Multiphysics CFD Modelling of Incompressible Flows at Low and Moderate Reynolds Numbers

László Könözsy

Submitted for the Degree of Ph.D.

Department of Engineering Physics,
School of Engineering, Cranfield University,
Cranfield, Bedfordshire, MK43 0AL, United Kingdom

2012

Except where acknowledged in the customary manner, the material presented in this thesis is, to the best of my knowledge, original and has not been submitted in whole or part for a degree in any university.

_____

László Könözsy

The author also confirms that the material presented in this thesis has been written by using original materials of the 9^{th} and 21^{st} month Ph.D. progress review reports [1, 2], which were submitted by the author for assessment at Cranfield University as a part of his Ph.D. study.

_____

László Könözsy

CRANFIELD UNIVERSITY

School of Engineering

Ph.D. Thesis

Academic Year: 2011-2012

László Könözsy

Multiphysics CFD Modelling of Incompressible Flows at Low and Moderate Reynolds Numbers

Supervisor:

Professor Dimitris Drikakis

Abstract

In this Ph.D. thesis, a novel high-resolution Godunov-type numerical procedure has been developed for solving the unsteady, incompressible Navier-Stokes equations for constant and variable density flows. The proposed FSAC-PP approach encompasses both artificial compressibility (AC) and fractional step (FS) pressure-projection (PP) methods of Chorin [3, 4] in a unified solution concept. To take advantage of different computational strategies, the FS and AC methods have been coupled (FSAC formulation), and further a PP step has been employed at each pseudo-time step. To provide time-accurate solutions, the dual-time stepping procedure is utilized. Taking the advantage of the hyperbolic nature of the inviscid part of the AC formulation, high-resolution characteristics-based (CB) Godunov-type scheme is employed to discretize the non-linear advective fluxes. High-order of accuracy is achieved by using from first- up to ninth-order interpolation schemes. Time integration is obtained from a fourth-order Runge-Kutta scheme. A non-linear full-multigrid, full-approximation storage (FMG-FAS) acceleration technique has been further extended to the FSAC-PP solution method to increase the efficiency and decrease the computational cost of the developed method and simulations.

The AC method has major value for solving stationary flow problems, but for unsteady and/or low Reynolds number flows, the stability condition of the dual-time stepping procedure and the choice of the AC parameter may become too restrictive, which could lead to slow convergence rates [5]. To overcome this problem of stiffness, the key motivation for developing the FSAC-PP method is to improve the stability, efficiency and decrease the computational cost of the classical AC method at both (very) low and moderate Reynolds numbers. Most of the mircofluidic industrial applications under the continuum hypothesis are complex multiphysics problems occurring at low Reynolds numbers. In these cases, the typical Reynolds number is from 10^{-1} up to 10^{2} [6], where the classical AC method could fail. Therefore, the main goal of this thesis is to develop, analyse and validate a new efficient high-resolution method based software package for modelling multiphysics problems. The proposed FSAC-PP solver based software tool, called HIRECOM-MULTIPHYSICS Unified Code v1.0, might be a bridge between the market leader packages and the daily engineering demand in the design of microfluidic devices.

Numerical validation test cases and examples have been presented in this thesis. In

Chapter 5, the FSAC-PP method has been validated by comparison to the AC, PP methods and an analytical solution for steady-state, incompressible, constant density, pressure-driven laminar flow in a straight microfluidic channel. Four-hundred and eighty simulations have been performed using three different methods with five different intercell flux interpolation formulas on four different girds at eight different Reynolds numbers from 10 to 10^{-4}. The AC method fails to give physically correct results at extremely low Reynolds number flows ($10^{-4} < Re < 0.1$), whereas both PP and FSAC-PP methods exhibit a good agreement with the analytical solution for the two-dimensional straight microfluidic benchmark channel. In Chapter 6, the FSAC-PP method in conjunction with the FMG-FAS multigrid technique [7] has been validated for steady-state, incompressible, constant density laminar flow in a lid driven square cavity at $Re = 100$, 400, and 1000. To provide numerical data for validation purposes, different intercell flux interpolation formulas have been employed from first- up to ninth-order. The numerical results have been summarized and compared to the computational data of Ghia et al. [8] in comparative tables in Appendix B. The FSAC-PP method has also been tested for unsteady turbulent flows in a lid driven cubical cavity at $Re = 3200$ and 10 000. The turbulent flow simulations have been performed by using the Implicit Large Eddy Simulation (ILES) method relying on the proposed FSAC-PP solution method. In Chapter 7, the variable density version of the FSAC-PP method has been tested for steady-state, incompressible, multi-species variable density flow, taking two different miscible liquids with different densities, in a three-dimensional Y-junction microfluidic channel at $Re = 50$ and $Pe = 1000$. In Chapter 8, the capability of the FSAC-PP method has been demonstrated for steady-state, incompressible, non-isothermal, Newtonian and non-Newtonian biofluid flow in the presence of a uniform magnetic field in a two-dimensional straight microfluidic channel at $Re = 300$. The model equations of Tzirtzilakis and Loukopoulos [9] have been further extended to use any types of constitutive equation for blood. In Chapter 9, the FSAC-PP method has been tested for acoustic wave (AW) modelling and for solving unsteady, incompressible, laminar flow problem in a three-dimensional microfluidic T-channel at $Re = 10$. A simplified AW model has been adopted and further developed to investigate the effects of AW on the Newtonian fluid flow pattern. In this benchmark test case, the AW interacted with ssDNA strands that have been released in the microfluidic T-channel, and have been modelled through a coupled Eulerian-Lagrangian dynamics [10, 11]. The reason for choosing these numerical examples is to demonstrate the capability of the proposed FSAC-PP method. The contribution to the knowledge is summarized in Chapter 10.

Acknowledgements

I am thankful indeed to Professor Dimitris Drikakis for encouraging me to write a second Ph.D. thesis in the field of computational multiphysics using high-resolution Godunov-type methods. I must say that the Godunov-type methods changed my point of view about computational fluid dynamics compared to the topic and content of my first Ph.D. thesis. The reason for this change is the fact that the aforementioned methods can handle complex fluid flow physics reliably at different length scales of nature. It is important to mention that the topic of my first Ph.D. thesis changed my point of view about the phenomenon of turbulence and its modelling rather than the methodology of computational science. Since, Godunov-type methods try to ensure physically reasonable mathematical solution of the governing equations compared to many existing versions of finite difference, finite volume and finite element methods; therefore, these methods returned me the hope that it is possible to compute complex fluid flow physics accurately and efficiently. Furthermore, I am also thankful to Professor Dimitris Drikakis for his effective and creative supervision to choose the right direction of the research work at Cranfield University.

My father as a mechanical engineer and applied mathematician encouraged me to study computer and natural sciences when I was teenager despite of the fact that I wanted to study art and philosophy. After thinking a lot, I decided to improve further my knowledge in the field of computer and engineering sciences, where I found the mathematics and fluid mechanics equally fascinating subject to the art and philosophy. In this path, I met with excellent teachers at the University of Miskolc, in Hungary, where I graduated as a mechanical engineer. Therefore, I am thankful indeed to Dr. Csaba Takács, Dr. Árpád Fáy, Dr. Béla Tolvaj, Dr. Ferenc Karaffa, Professor Tibor Czibere, Professor András Nyíri, Professor Szilárd Szabó, Professor László Baranyi, Professor György Szeidl, Professor Imre Kozák and Professor István Páczelt from whom I learnt a lot of knowledge gaining strong mathematical background. I would specially like to thank Professor Tibor Czibere from whom I learnt the analytical way of thinking and problem solution methodology, and who was the supervisor of my first Ph.D. thesis at the University of Miskolc.

It is always precise and detailed work to do a literature survey and process the collected resources. I would like to thank Dr. Marco Kalweit, Dr. Nikolaos Asproulis and Dr.

Mátyás Benke for providing me useful resources based on their research experiences in the fields of micro- and nanofluidics.

The research work is about commitment to further develop ideas, knowledge and methods, or to invent something unique, which can be applied to the theoretical and/or practical life. To achieve at least one of these goals, it is essential to exchange thoughts with other people and have discussions about questions from different point of views. I would like to thank Dr. Evgeniy Shapiro, Dr. Vladimir Titarev, Dr. Ben Thornber, Dr. Sanjay Patel, Dr. Philip Barton and Kay Rawley for giving me inspirations.

I would like to acknowledge Dr. Tommaso Oggian's co-operation in conjunction with the implementation of the pressure-Poisson solver. Furthermore, I would like to acknowledge Dr. Mátyás Benke's and Dr. Evgeniy Shapiro's co-operation in conjunction with the development and implementation of the ssDNA flow meta-model.

I would specially like to thank my wife Mrs. Martina Könözsy-Kovács and my whole family for their loving encouragement.

Finally, I dedicate this Ph.D. thesis in memoriam Mr. Roland Málik poet, who was one of my best Hungarian friend, and who passed away in an accident in Ecuador last year.

I also dedicate this thesis to my son, Alexander Teodor Könözsy, who was born in Bedford, in the United Kingdom, on 25^{th} of June, 2012.

László Könözsy

Contents

Abstract **vi**

Acknowledgements **viii**

List of Figures **xxv**

List of Tables **xxxv**

List of Algorithms **xxxvi**

Nomenclature **xl**

1 Introduction and Objectives **1**

1.1 Background and Motivation of the Research Work 5

1.2 Problem Statement 6

1.3 Thesis Structure 8

1.4 Publications 9

2 Literature Review **10**

2.1 Microfluidics and Its Applications 10

2.2 Numerical Methods for the Navier-Stokes Equations 19

2.3 Perspectives of the Present Research Work 20

3 Governing Equations and Computational Methodology **21**

3.1 Governing Equations 21

3.1.1 Validity of Continuum Hypothesis 21

3.1.2 System of Governing Equations 22

3.1.3 The Navier-Stokes Equations . . . 25
3.2 Numerical Solution of the Navier-Stokes Equations . . . 27
3.2.1 Artificial Compressibility (AC) Method . . . 27
3.2.2 Fractional-Step (FS) Pressure-Projection (PP) Method . . . 28
3.2.3 Arrangements of Primitive Variables . . . 38
3.3 Computations in Curvilinear Coordinate System . . . 41
3.3.1 The General Momentum Equation (Cauchy Equation) . . . 41
3.3.2 Pressure-Projection with Curvilinear Coordinates . . . 46
3.3.2.1 Constant Density Flows . . . 51
3.3.2.2 Variable Density Flows . . . 56
3.3.3 Solution of the Curvilinear Pressure-Poisson Equation . . . 58
3.3.3.1 Constant Density Flows . . . 58
3.3.3.2 Variable Density Flows . . . 61
3.4 Constitutive Equations . . . 65
3.4.1 Newtonian Fluid Model . . . 65
3.4.2 Non-Newtonian Fluid Models for Blood Flow . . . 67
3.4.2.1 Power-Law Fluid Model . . . 67
3.4.2.2 Casson-Model . . . 68
3.4.2.3 Quemada-Model . . . 68
3.4.3 Numerical Treatment of the Laplacian Term . . . 70

4 Numerical Method Development for Solving the Navier-Stokes Equations 73
4.1 Introduction . . . 73
4.1.1 Riemann Method and Characteristics-Based (CB) Schemes . . . 74
4.1.1.1 Constant Density Flows . . . 74
4.1.1.2 Multi-Species Variable Density Flows . . . 80
4.2 A FSAC-PP Method for Constant Density Flows . . . 84
4.2.1 FSAC-PP Solution Method in conjunction with the CB Scheme . 84
4.2.2 Boundary Condition for the Pressure . . . 88

4.2.3 FMG-FAS Multigrid Technique for the FSAC-PP Method 88
4.3 A FSAC-PP Method for Variable Density Flows 91
4.4 Pseudo-Time Stepping Strategy 95
4.4.1 Constant Density Flows 95
4.4.2 Multi-Species Variable Density Flows 95
4.5 Summary 96

5 Laminar Flow in a Straight Microchannel at Low Reynolds Numbers 97
5.1 Introduction 97
5.2 The Straight Microfluidic Channel Test Case 99
5.3 Validation of the FSAC-PP Method at Various Low Reynolds Numbers . 101
5.4 Summary and Conclusions 141

6 Lid Driven Cavity Flow at Moderate Reynolds Numbers 142
6.1 Introduction 142
6.2 Two-Dimensional Flow in a Lid Driven Cavity 143
6.2.1 Validation of the FSAC-PP Method at Re = 100, 400, and 1000 . 144
6.3 Three-Dimensional Flow in a Lid Driven Cavity 183
6.3.1 The Benchmark Cubical Cavity and Problem Setup 183
6.3.2 Unsteady Turbulent Flow at Re = 3200, and 10 000 185
6.4 Summary and Conclusions 195

7 Multi-Species Variable Density Flow in a Y-Junction Microfluidic Channel 196
7.1 Introduction 196
7.2 Governing Equations and Methodology 197
7.3 Three-Dimensional Y-Junction Microfluidic Test Case 199
7.4 Results and Discussion 201
7.5 Summary and Conclusions 206

8 Non-Newtonian Biofluid Flow in the Presence of Uniform Magnetic Field 207

8.1 Introduction 207

8.2 Governing Equations and Methodology 209

8.3 Microfluidic Benchmark Test Case 216

8.4 Results and Discussion 219

8.5 Summary and Conclusions 225

9 Acoustic Wave and ssDNA Flow Modelling in a Microfluidic T-Channel 226

9.1 Introduction 226

9.2 Acoustic Wave and ssDNA Flow Modelling 228

9.3 Three-Dimensional Microfluidic T-Channel Test Case 231

9.3.1 Grid Convergence Study 232

9.4 Results and Discussion 234

9.5 Summary and Conclusions 246

10 Summary and Conclusions 247

10.1 Summary and Conclusions of the Research Work 247

10.2 Contribution to the Knowledge 253

10.3 Future Work 255

Appendix 256

A Computation of the Derivatives of the Curvilinear Coordinates 256

A.1 First Derivatives in the Cell-Centres and Faces 256

A.2 Second Derivatives in the Cell-Centres and Faces 261

B Comparative Tables 267

B.1 Laminar Flow in a Lid Driven Cavity at Re = 100, 400, and 1000 267

Bibliography 299

List of Figures

1.1 Levels of Modelling Approaches at Spatial and Temporal Scales [12, p. 2] 2
1.2 Microfluidics related to different fields of science and technology [13, p. 1.]. 3
1.3 Portable microfluidic biomedical device for daily blood glucose monitoring: a) OneTouch Ultra Blood Glucose Biosensor [14, Newman and Turner, p. 2444]; b) Pelikan Sun Integrated Blood Glucose Device [14, Newman and Turner, p. 2451]. 4

3.1 Continuum control volume (V) and viscous stresses. 23
3.2 Band structure of the system of linear equations for five point schemes [15]. 35
3.3 Collocated arrangement of primitive variables for FDM-based discretization. 38
3.4 Collocated arrangement of primitive variables for FVM-based discretization. 39
3.5 Staggered arrangement of primitive variables. 40

4.1 Sketch of characteristics-based temporal and spatial discretization [16]. . 75
4.2 Multigrid V-cycle in the pseudo-time stepping process on three grid levels [6]. 89

5.1 Computational grid for the microchannel using dimensionless coordinates. 99
5.2 Contour lines of the velocity component U in the fully developed pressure-driven laminar flow in a straight microfluidic channel. 102
5.3 Comparison of analytically and numerically computed outlet velocity profiles relying on the solution of the AC, PP, and FSAC-PP methods in a pressure-driven laminar flow in a straight microfluidic channel using 1^{st}-order intercell flux interpolation on four different grids at $Re = 10$. 109

5.4 Comparison of analytically and numerically computed outlet velocity profiles relying on the solution of the AC, PP, and FSAC-PP methods in a pressure-driven laminar flow in a straight microfluidic channel using 2^{nd}-order intercell flux interpolation on four different grids at $Re = 10$. 109
5.5 Comparison of analytically and numerically computed outlet velocity profiles relying on the solution of the AC, PP, and FSAC-PP methods in a pressure-driven laminar flow in a straight microfluidic channel using 3^{rd}-order intercell flux interpolation on four different grids at $Re = 10$. 110
5.6 Comparison of analytically and numerically computed outlet velocity profiles relying on the solution of the AC, PP, and FSAC-PP methods in a pressure-driven laminar flow in a straight microfluidic channel using 5^{th}-order WENO reconstruction on four different grids at $Re = 10$. 110
5.7 Comparison of analytically and numerically computed outlet velocity profiles relying on the solution of the AC, PP, and FSAC-PP methods in a pressure-driven laminar flow in a straight microfluidic channel 9^{th}-order WENO intercell flux interpolation on four different grids at $Re = 10$. . . . 111
5.8 Comparison of analytically and numerically computed outlet velocity profiles relying on the solution of the AC, PP, and FSAC-PP methods in a pressure-driven laminar flow in a straight microfluidic channel using 1^{st}-order intercell flux interpolation on four different grids at $Re = 5$. 111
5.9 Comparison of analytically and numerically computed outlet velocity profiles relying on the solution of the AC, PP, and FSAC-PP methods in a pressure-driven laminar flow in a straight microfluidic channel using 2^{nd}-order intercell flux interpolation on four different grids at $Re = 5$. 112
5.10 Comparison of analytically and numerically computed outlet velocity profiles relying on the solution of the AC, PP, and FSAC-PP methods in a pressure-driven laminar flow in a straight microfluidic channel using 3^{rd}-order intercell flux interpolation on four different grids at $Re = 5$. 112
5.11 Comparison of analytically and numerically computed outlet velocity profiles relying on the solution of the AC, PP, and FSAC-PP methods in a pressure-driven laminar flow in a straight microfluidic channel using 5^{th}-order WENO reconstruction on four different grids at $Re = 5$. 113
5.12 Comparison of analytically and numerically computed outlet velocity profiles relying on the solution of the AC, PP, and FSAC-PP methods in a pressure-driven laminar flow in a straight microfluidic channel 9^{th}-order WENO intercell flux interpolation on four different grids at $Re = 5$. . . . 113

5.13 Comparison of analytically and numerically computed outlet velocity profiles relying on the solution of the AC, PP, and FSAC-PP methods in a pressure-driven laminar flow in a straight microfluidic channel using 1^{st}-order intercell flux interpolation on four different grids at $Re = 1$. 114
5.14 Comparison of analytically and numerically computed outlet velocity profiles relying on the solution of the AC, PP, and FSAC-PP methods in a pressure-driven laminar flow in a straight microfluidic channel using 2^{nd}-order intercell flux interpolation on four different grids at $Re = 1$. 114
5.15 Comparison of analytically and numerically computed outlet velocity profiles relying on the solution of the AC, PP, and FSAC-PP methods in a pressure-driven laminar flow in a straight microfluidic channel using 3^{rd}-order intercell flux interpolation on four different grids at $Re = 1$. 115
5.16 Comparison of analytically and numerically computed outlet velocity profiles relying on the solution of the AC, PP, and FSAC-PP methods in a pressure-driven laminar flow in a straight microfluidic channel using 5^{th}-order WENO reconstruction on four different grids at $Re = 1$. 115
5.17 Comparison of analytically and numerically computed outlet velocity profiles relying on the solution of the AC, PP, and FSAC-PP methods in a pressure-driven laminar flow in a straight microfluidic channel 9^{th}-order WENO intercell flux interpolation on four different grids at $Re = 1$. . . . 116
5.18 Comparison of analytically and numerically computed outlet velocity profiles relying on the solution of the AC, PP, and FSAC-PP methods in a pressure-driven laminar flow in a straight microfluidic channel using 1^{st}-order intercell flux interpolation on four different grids at $Re = 0.5$. 116
5.19 Comparison of analytically and numerically computed outlet velocity profiles relying on the solution of the AC, PP, and FSAC-PP methods in a pressure-driven laminar flow in a straight microfluidic channel using 2^{nd}-order intercell flux interpolation on four different grids at $Re = 0.5$. 117
5.20 Comparison of analytically and numerically computed outlet velocity profiles relying on the solution of the AC, PP, and FSAC-PP methods in a pressure-driven laminar flow in a straight microfluidic channel using 3^{rd}-order intercell flux interpolation on four different grids at $Re = 0.5$. 117
5.21 Comparison of analytically and numerically computed outlet velocity profiles relying on the solution of the AC, PP, and FSAC-PP methods in a pressure-driven laminar flow in a straight microfluidic channel using 5^{th}-order WENO reconstruction on four different grids at $Re = 0.5$. 118

5.22 Comparison of analytically and numerically computed outlet velocity profiles relying on the solution of the AC, PP, and FSAC-PP methods in a pressure-driven laminar flow in a straight microfluidic channel 9^{th}-order WENO intercell flux interpolation on four different grids at $Re = 0.5$. . . 118
5.23 Comparison of analytically and numerically computed outlet velocity profiles relying on the solution of the AC, PP, and FSAC-PP methods in a pressure-driven laminar flow in a straight microfluidic channel using 1^{st}-order intercell flux interpolation on four different grids at $Re = 0.1$. 119
5.24 Comparison of analytically and numerically computed outlet velocity profiles relying on the solution of the AC, PP, and FSAC-PP methods in a pressure-driven laminar flow in a straight microfluidic channel using 2^{nd}-order intercell flux interpolation on four different grids at $Re = 0.1$. 119
5.25 Comparison of analytically and numerically computed outlet velocity profiles relying on the solution of the AC, PP, and FSAC-PP methods in a pressure-driven laminar flow in a straight microfluidic channel using 3^{rd}-order intercell flux interpolation on four different grids at $Re = 0.1$. 120
5.26 Comparison of analytically and numerically computed outlet velocity profiles relying on the solution of the AC, PP, and FSAC-PP methods in a pressure-driven laminar flow in a straight microfluidic channel using 5^{th}-order WENO intercell flux interpolation on four different grids at $Re = 0.1$. 120
5.27 Comparison of analytically and numerically computed outlet velocity profiles relying on the solution of the AC, PP, and FSAC-PP methods in a pressure-driven laminar flow in a straight microfluidic channel using 9^{th}-order WENO intercell flux interpolation on four different grids at $Re = 0.1$. 121
5.28 Comparison of analytically and numerically computed outlet velocity profiles relying on the solution of the AC, PP, and FSAC-PP methods in a pressure-driven laminar flow in a straight microfluidic channel using 1^{st}-order intercell flux interpolation on four different grids at $Re = 0.01$. . . . 121
5.29 Comparison of analytically and numerically computed outlet velocity profiles relying on the solution of the AC, PP, and FSAC-PP methods in a pressure-driven laminar flow in a straight microfluidic channel using 2^{nd}-order intercell flux interpolation on four different grids at $Re = 0.01$. . . . 122
5.30 Comparison of analytically and numerically computed outlet velocity profiles relying on the solution of the AC, PP, and FSAC-PP methods in a pressure-driven laminar flow in a straight microfluidic channel using 3^{rd}-order intercell flux interpolation on four different grids at $Re = 0.01$. . . . 122

5.31 Comparison of analytically and numerically computed outlet velocity profiles relying on the solution of the AC, PP, and FSAC-PP methods in a pressure-driven laminar flow in a straight microfluidic channel using 5^{th}-order WENO reconstruction on four different grids at $Re = 0.01$. 123
5.32 Comparison of analytically and numerically computed outlet velocity profiles relying on the solution of the AC, PP, and FSAC-PP methods in a pressure-driven laminar flow in a straight microfluidic channel 9^{th}-order WENO intercell flux interpolation on four different grids at $Re = 0.01$. . . 123
5.33 Comparison of analytically and numerically computed outlet velocity profiles relying on the solution of the AC, PP, and FSAC-PP methods in a pressure-driven laminar flow in a straight microfluidic channel using 1^{st}-order intercell flux interpolation on four different grids at $Re = 0.001$. . . 124
5.34 Comparison of analytically and numerically computed outlet velocity profiles relying on the solution of the AC, PP, and FSAC-PP methods in a pressure-driven laminar flow in a straight microfluidic channel using 2^{nd}-order intercell flux interpolation on four different grids at $Re = 0.001$. . . 124
5.35 Comparison of analytically and numerically computed outlet velocity profiles relying on the solution of the AC, PP, and FSAC-PP methods in a pressure-driven laminar flow in a straight microfluidic channel using 3^{rd}-order intercell flux interpolation on four different grids at $Re = 0.001$. . . 125
5.36 Comparison of analytically and numerically computed outlet velocity profiles relying on the solution of the AC, PP, and FSAC-PP methods in a pressure-driven laminar flow in a straight microfluidic channel using 5^{th}-order WENO reconstruction on four different grids at $Re = 0.001$. 125
5.37 Comparison of analytically and numerically computed outlet velocity profiles relying on the solution of the AC, PP, and FSAC-PP methods in a pressure-driven laminar flow in a straight microfluidic channel 9^{th}-order WENO intercell flux interpolation on four different grids at $Re = 0.001$. . 126
5.38 Comparison of analytically and numerically computed outlet velocity profiles relying on the solution of the AC, PP, and FSAC-PP methods in a pressure-driven laminar flow in a straight microfluidic channel using 1^{st}-order intercell flux interpolation on four different grids at $Re = 0.0001$. . . 126
5.39 Comparison of analytically and numerically computed outlet velocity profiles relying on the solution of the AC, PP, and FSAC-PP methods in a pressure-driven laminar flow in a straight microfluidic channel using 2^{nd}-order intercell flux interpolation on four different grids at $Re = 0.0001$. . . 127

5.40 Comparison of analytically and numerically computed outlet velocity profiles relying on the solution of the AC, PP, and FSAC-PP methods in a pressure-driven laminar flow in a straight microfluidic channel using 3^{rd}-order intercell flux interpolation on four different grids at $Re = 0.0001$. . . 127
5.41 Comparison of analytically and numerically computed outlet velocity profiles relying on the solution of the AC, PP, and FSAC-PP methods in a pressure-driven laminar flow in a straight microfluidic channel using 5^{th}-order WENO intercell flux interpolation on four different grids at $Re = 0.0001$. 128
5.42 Comparison of analytically and numerically computed outlet velocity profiles relying on the solution of the AC, PP, and FSAC-PP methods in a pressure-driven laminar flow in a straight microfluidic channel using 9^{th}-order WENO intercell flux interpolation on four different grids at $Re = 0.0001$. 128
5.43 Comparison of the numerical convergence of the AC, PP, and FSAC-PP methods; maximum values of Runge-Kutta residuals RK_{maxres} versus total number of multigrid iterations N_{mg} on the fine grid at $Re = 10$. 133
5.44 Comparison of the numerical convergence of the AC, PP, and FSAC-PP methods; maximum values of Runge-Kutta residuals RK_{maxres} versus total number of multigrid iterations N_{mg} on the fine grid at $Re = 5$. 134
5.45 Comparison of the numerical convergence of the AC, PP, and FSAC-PP methods; maximum values of Runge-Kutta residuals RK_{maxres} versus total number of multigrid iterations N_{mg} on the fine grid at $Re = 1$. 135
5.46 Comparison of the numerical convergence of the AC, PP, and FSAC-PP methods; maximum values of Runge-Kutta residuals RK_{maxres} versus total number of multigrid iterations N_{mg} on the fine grid at $Re = 0.5$. 136
5.47 Comparison of the numerical convergence of the AC, PP, and FSAC-PP methods; maximum values of Runge-Kutta residuals RK_{maxres} versus total number of multigrid iterations N_{mg} on the fine grid at $Re = 0.1$. 137
5.48 Comparison of the numerical convergence of the AC, PP, and FSAC-PP methods; maximum values of Runge-Kutta residuals RK_{maxres} versus total number of multigrid iterations N_{mg} on the fine grid at $Re = 0.01$. 138
5.49 Comparison of the numerical convergence of the AC, PP, and FSAC-PP methods; maximum values of Runge-Kutta residuals RK_{maxres} versus total number of multigrid iterations N_{mg} on the fine grid at $Re = 0.001$. 139
5.50 Comparison of the numerical convergence of the AC, PP, and FSAC-PP methods; maximum values of Runge-Kutta residuals versus total number of multigrid iterations on the fine grid at $Re = 0.0001$. 140

6.1 Equidistant grid for the square cavity using dimensionless coordinates. . . 143
6.2 Streamline pattern for two-dimensional laminar flow in the lid driven square cavity obtained by Ghia et al. [8] at $Re = 100$. 144
6.3 Streamline pattern in the lid driven square cavity at $Re = 100$. 145
6.4 Streamline pattern for two-dimensional laminar flow in the lid driven square cavity obtained by Ghia et al. [8] at $Re = 400$. 147
6.5 Streamline pattern in the lid driven square cavity at $Re = 400$. 147
6.6 Streamline pattern for two-dimensional laminar flow in the lid driven square cavity obtained by Ghia et al. [8] at $Re = 1000$. 148
6.7 Streamline pattern in the lid driven square cavity at $Re = 1000$. 149
6.8 Results of the AC, PP, and FSAC-PP methods for dimensionless velocity components V and U along a) horizontal and b) vertical centre-lines of the square cavity using 1^{st}-order interpolation compared to the results of Ghia et al. [8] at $Re = 100$. 151
6.9 Results of the AC, PP, and FSAC-PP methods for dimensionless velocity components V and U along a) horizontal and b) vertical centre-lines of the square cavity using 2^{nd}-order interpolation compared to the results of Ghia et al. [8] at $Re = 100$. 152
6.10 Results of the AC, PP, and FSAC-PP methods for the dimensionless velocity components V and U along a) horizontal and b) vertical centre-lines of the square cavity using 3^{rd}-order interpolation compared to the results of Ghia et al. [8] at $Re = 100$. 153
6.11 Results of the AC, PP, and FSAC-PP methods for the dimensionless velocity components V and U along a) horizontal and b) vertical centre-lines of the square cavity using 5^{th}-order WENO interpolation compared to the results of Ghia et al. [8] at $Re = 100$. 154
6.12 Results of the AC, PP, and FSAC-PP methods for the dimensionless velocity components V and U along a) horizontal and b) vertical centre-lines of the square cavity using 9^{th}-order WENO interpolation compared to the results of Ghia et al. [8] at $Re = 100$. 155
6.13 Comparison of the numerical convergence of the AC, PP, and FSAC-PP methods; maximum values of Runge-Kutta residuals versus total number of multigrid iterations on the fine grid using 1^{st}-order interpolation at $Re = 100$. 156
6.14 Comparison of the numerical convergence of the AC, PP, and FSAC-PP methods; maximum values of Runge-Kutta residuals versus total number of multigrid iterations on the fine grid using 2^{nd}-order interpolation at $Re = 100$. 157

6.15 Comparison of the numerical convergence of the AC, PP, and FSAC-PP methods; maximum values of Runge-Kutta residuals versus total number of multigrid iterations on the fine grid using 3^{rd}-order interpolation at $Re = 100$. 158
6.16 Comparison of the numerical convergence of the AC, PP, and FSAC-PP methods; maximum values of Runge-Kutta residuals versus total number of multigrid iterations on the fine grid using 5^{th}-order WENO interpolation at $Re = 100$. 159
6.17 Comparison of the numerical convergence of the AC, PP, and FSAC-PP methods; maximum values of Runge-Kutta residuals versus total number of multigrid iterations on the fine grid using 9^{th}-order WENO interpolation at $Re = 100$. 160
6.18 Results of the AC, PP, and FSAC-PP methods for the dimensionless velocity components V and U along a) horizontal and b) vertical centre-lines of the square cavity using 1^{st}-order interpolation compared to the results of Ghia et al. [8] at $Re = 400$. 161
6.19 Results of the AC, PP, and FSAC-PP methods for the dimensionless velocity components V and U along a) horizontal and b) vertical centre-lines of the square cavity using 2^{nd}-order interpolation compared to the results of Ghia et al. [8] at $Re = 400$. 162
6.20 Results of the AC, PP, and FSAC-PP methods for the dimensionless velocity components V and U along a) horizontal and b) vertical centre-lines of the square cavity using 3^{rd}-order interpolation compared to the results of Ghia et al. [8] at $Re = 400$. 163
6.21 Results of the AC, PP, and FSAC-PP methods for the dimensionless velocity components V and U along a) horizontal and b) vertical centre-lines of the square cavity using 5^{th}-order WENO interpolation compared to the results of Ghia et al. [8] at $Re = 400$. 164
6.22 Results of the AC, PP, and FSAC-PP methods for the dimensionless velocity components V and U along a) horizontal and b) vertical centre-lines of the square cavity using 9^{th}-order WENO interpolation compared to the results of Ghia et al. [8] at $Re = 400$. 165
6.23 Comparison of the numerical convergence of the AC, PP, and FSAC-PP methods; maximum values of Runge-Kutta residuals versus total number of multigrid iterations on the fine grid using 1^{st}-order interpolation at $Re = 400$. 166

6.24 Comparison of the numerical convergence of the AC, PP, and FSAC-PP methods; maximum values of Runge-Kutta residuals versus total number of multigrid iterations on the fine grid using 2^{nd}-order interpolation at $Re = 400$. 167
6.25 Comparison of the numerical convergence of the AC, PP, and FSAC-PP methods; maximum values of Runge-Kutta residuals versus total number of multigrid iterations on the fine grid using 3^{rd}-order interpolation at $Re = 400$. 168
6.26 Comparison of the numerical convergence of the AC, PP, and FSAC-PP methods; maximum values of Runge-Kutta residuals versus total number of multigrid iterations on the fine grid using 5^{th}-order WENO interpolation at $Re = 400$. 169
6.27 Comparison of the numerical convergence of the AC, PP, and FSAC-PP methods; maximum values of Runge-Kutta residuals versus total number of multigrid iterations on the fine grid using 9^{th}-order WENO interpolation at $Re = 400$. 170
6.28 Results of the AC, PP, and FSAC-PP methods for the dimensionless velocity components V and U along a) horizontal and b) vertical centre-lines of the square cavity using 1^{st}-order interpolation compared to the results of Ghia et al. [8] at $Re = 1000$. 171
6.29 Results of the AC, PP, and FSAC-PP methods for the dimensionless velocity components V and U along a) horizontal and b) vertical centre-lines of the square cavity using 2^{nd}-order interpolation compared to the results of Ghia et al. [8] at $Re = 1000$. 172
6.30 Results of the AC, PP, and FSAC-PP methods for the dimensionless velocity components V and U along a) horizontal and b) vertical centre-lines of the square cavity using 3^{rd}-order interpolation compared to the results of Ghia et al. [8] at $Re = 1000$. 173
6.31 Results of the AC, PP, and FSAC-PP methods for the dimensionless velocity components V and U along a) horizontal and b) vertical centre-lines of the square cavity using 5^{th}-order WENO scheme compared to the results of Ghia et al. [8] at $Re = 1000$. 174
6.32 Results of the AC, PP, and FSAC-PP methods for the dimensionless velocity components V and U along a) horizontal and b) vertical centre-lines of the square cavity using 9^{th}-order WENO scheme compared to the results of Ghia et al. [8] at $Re = 1000$. 175

6.33 Comparison of the numerical convergence of the AC, PP, and FSAC-PP methods; maximum values of Runge-Kutta residuals versus total number of multigrid iterations on the fine grid using 1^{st}-order interpolation at $Re = 1000$. 176
6.34 Comparison of the numerical convergence of the AC, PP, and FSAC-PP methods; maximum values of Runge-Kutta residuals versus total number of multigrid iterations on the fine grid using 2^{nd}-order interpolation at $Re = 1000$. 177
6.35 Comparison of the numerical convergence of the AC, PP, and FSAC-PP methods; maximum values of Runge-Kutta residuals versus total number of multigrid iterations on the fine grid using 3^{rd}-order interpolation at $Re = 1000$. 178
6.36 Comparison of the numerical convergence of the AC, PP, and FSAC-PP methods; maximum values of Runge-Kutta residuals versus total number of multigrid iterations on the fine grid using 5^{th}-order WENO scheme at $Re = 1000$. 179
6.37 Comparison of the numerical convergence of the AC, PP, and FSAC-PP methods; maximum values of Runge-Kutta residuals versus total number of multigrid iterations on the fine grid using 9^{th}-order WENO scheme at $Re = 1000$. 180
6.38 Geometrical dimensions of the cubical cavity configuration measured by Prasad and Koseff (1989) [17, p. 209] at $L = B = D = 150\,mm$ with SAR of 1:1. 183
6.39 Equidistant computational grid of the cubical cavity using dimensionless coordinates, where $L = B = D = 150\,mm$ with SAR of 1:1. 184
6.40 Experimental data taken from Prasad and Koseff (1989) with SAR of 1:1 at $Re = 3200$ [17, p. 211]. 187
6.41 ILES results using the AC, PP, and FSAC-PP methods and experimental data of [17, p. 211] in the mid-plane $z/L = 0$ with SAR of 1:1 at $Re = 3200$; dimensionless mean velocity profiles along a) horizontal and b) vertical centre-lines. 188
6.42 ILES results using the AC, PP, and FSAC-PP methods and experimental data of [17, p. 211] in the mid-plane $z/L = 0$ with SAR of 1:1 at $Re = 3200$; dimensionless normal (main) stress profiles $10\sqrt{\overline{V'^2}}/U_b$ and $10\sqrt{\overline{U'^2}}/U_b$ along c) horizontal and d) vertical centre-lines. 189

6.43 ILES results using the AC, PP, and FSAC-PP methods and experimental data of [17, p. 211] in the mid-plane $z/L = 0$ with SAR of 1:1 at $Re = 3200$; shear stress profiles $500\sqrt{\overline{U'V'}}/U_b^2$ along e) horizontal and f) vertical centre-lines. 190
6.44 Experimental data taken from Prasad and Koseff (1989) with SAR of 1:1 at $Re = 10\,000$ [17, p. 212]. 191
6.45 ILES results using the AC, PP, and FSAC-PP methods and experimental data of [17, p. 211] in the mid-plane $z/L = 0$ with SAR of 1:1 at $Re = 10\,000$; dimensionless mean velocity profiles along a) horizontal and b) vertical centre-lines. 192
6.46 ILES results using the AC, PP, and FSAC-PP methods and experimental data of [17, p. 211] in the mid-plane $z/L = 0$ with SAR of 1:1 at $Re = 10\,000$; dimensionless normal (main) stress profiles $10\sqrt{\overline{V'^2}}/U_b$ and $10\sqrt{\overline{U'^2}}/U_b$ along c) horizontal and d) vertical centre-lines. 193
6.47 ILES results using the AC, PP, and FSAC-PP methods and experimental data of [17, p. 211] in the mid-plane $z/L = 0$ with SAR of 1:1 at $Re = 10\,000$; shear stress profiles $500\sqrt{\overline{U'V'}}/U_b^2$ along e) horizontal and f) vertical centre-lines. 194

7.1 Computational domain of the three-dimensional Y-junction microfluidic channel using dimensionless coordinates. 199
7.2 Distribution of the velocity component U using AC, PP, and FSAC-PP methods with 3^{rd}-order interpolation in the Y-junction channel at $Re = 50$ and $Pe = 1000$. 202
7.3 Distribution of species density using AC method with 3^{rd}-order interpolation in the Y-junction channel at $Re = 50$ and $Pe = 1000$. 202
7.4 Distribution of the velocity component U using AC method with 3^{rd}-order interpolation compared to the analytical solution of Marco and Han [18, 19, p. 5.67] at the outlet of the Y-junction channel at $Re = 50$ and $Pe = 1000$. 203
7.5 Distribution of the velocity component U using the PP method with 3^{rd}-order interpolation compared to the analytical solution of Marco and Han [18, 19, p. 5.67] at the outlet of the Y-junction channel at $Re = 50$ and $Pe = 1000$. 203
7.6 Distribution of the velocity component U using FSAC-PP method with 3^{rd}-order interpolation compared to the analytical solution of Marco and Han [18, 19, p. 5.67] at the outlet of the Y-junction channel at $Re = 50$ and $Pe = 1000$. 204

7.7 Comparison of the numerical convergence of the AC, PP, and FSAC-PP methods for incompressible, multi-species, variable density flow in a Y-junction microfluidic channel; maximum values of Runge-Kutta residuals versus total number of multigrid iterations on the fine grid using 3^{rd}-order interpolation at $Re = 50$ and $Pe = 1000$. 205

8.1 Fully developed velocity profiles using different constitutive equations of blood computed by Neofytou and Drikakis [20, p. 134] at $Re = 200$. . . 214
8.2 Location of the uniform magnetic field in the two-dimensional straight microfluidic channel. 216
8.3 Distribution of the velocity component U using the Newtonian fluid model at different X positions in the microfluidic channel compared to the computational data of Tzirtzilakis and Loukopoulos at $Re = 300$, $Mn_M = 40$, and $Mn_F = 0$. 221
8.4 Comparison of the numerical convergence of the AC and FSAC-PP methods using Newtonian fluid model in the presence of uniform localized magnetic field in the microfluidic straight channel; maximum values of Runge-Kutta residuals versus total number of multigrid iterations on the fine grid using 3^{rd}-order interpolation at $Re = 300$, $Mn_M = 40$, $Mn_F = 0$. 222
8.5 Distribution of the velocity component U using the non-Newtonian power law fluid model at different X positions in the microfluidic channel compared to the computational data of Tzirtzilakis and Loukopoulos at $Re = 300$, $Mn_M = 40$, and $Mn_F = 0$. 223
8.6 Comparison of the numerical convergence of the AC and FSAC-PP methods using non-Newtonian power law fluid model in the presence of uniform localized magnetic field in the microfluidic straight channel; maximum values of Runge-Kutta residuals versus total number of multigrid iterations on the fine grid using 3^{rd}-order interpolation at $Re = 300$, $Mn_M = 40$, $Mn_F = 0$. 224
8.7 Streamline pattern for two-dimensional, steady-state, incompressible, non-Newtonian power law fluid flow in the presence of uniform magnetic field obtained by the author of this thesis at $Re = 300$, $Mn_M = 0$, $Mn_F = 11.39$. 225

9.1 Sketch of the three-dimensional microfluidic T-channel geometry. 231
9.2 Velocity component U without the presence of AW at $Re = 10$. 236
9.3 Velocity component U with the presence of AW at $Re = 10$. 236
9.4 Velocity component V without the presence of AW at $Re = 10$. 237
9.5 Velocity component V with the presence of AW at $Re = 10$. 237
9.6 Velocity component W without the presence of AW at $Re = 10$. 238

9.7 Velocity component W with the presence of AW at $Re = 10$. 238
9.8 Velocity magnitude without the presence of AW at $Re = 10$. 239
9.9 Velocity magnitude with the presence of AW at $Re = 10$. 239
9.10 Comparison of the numerical convergence of the AC and FSAC-PP methods without modelling AW in the microfluidic T-channel; maximum values of Runge-Kutta residuals versus total number of multigrid iterations on the fine grid using 3^{rd}-order interpolation at $Re = 10$. 240
9.11 Distribution of the velocity component U and ssDNA pathlines without the presence of AW at $Re = 10$. 241
9.12 Distribution of the velocity component U and ssDNA pathlines with the presence of AW at $Re = 10$. 241
9.13 Distribution of the velocity component V and ssDNA pathlines without the presence of AW at $Re = 10$. 242
9.14 Distribution of the velocity component V and ssDNA pathlines with the presence of AW at $Re = 10$. 242
9.15 Distribution of the velocity component W and ssDNA pathlines without the presence of AW at $Re = 10$. 243
9.16 Distribution of the velocity component W and ssDNA pathlines with the presence of AW at $Re = 10$. 243
9.17 Distribution of velocity magnitude and ssDNA pathlines without the presence of AW at $Re = 10$. 244
9.18 Distribution of velocity magnitude and ssDNA pathlines with the presence of AW at $Re = 10$. 244
9.19 Comparison of the numerical convergence of the AC and FSAC-PP methods with modelling AW in the microfluidic T-channel; maximum values of Runge-Kutta residuals versus total number of multigrid iterations on the fine grid using 3^{rd}-order interpolation at $Re = 10$. 245

10.1 Problem classes of the developed multiphysics software. 248

List of Tables

2.1 A possible classification of biomedical sensors [21, Neuman, Section V, p. 2]. 11

3.1 Types of forces acting on fluid particles [22, p. 15]. 26

5.1 Geometrical sizes of the two-dimensional straight microfluidic channel. . 99
5.2 Simulation parameters of eight numerical test cases for the AC parameter β, for the CFL_{inv} and CFL_{vis} Courant-Friedrichs-Lewy numbers associated with the inviscid and viscous fluxes at various Reynolds numbers Re. 101
5.3 Number of node points and controll cells on different grid levels. 103
5.4 Grid refinement ratios r and the order of interpolation method relating to the truncation error p on different grid levels. 103
5.5 Grid Convergence Indices (GCI) at $Re = 10$. 105
5.6 Grid Convergence Indices (GCI) at $Re = 5$. 105
5.7 Grid Convergence Indices (GCI) at $Re = 1$. 106
5.8 Grid Convergence Indices (GCI) at $Re = 0.5$. 106
5.9 Grid Convergence Indices (GCI) at $Re = 0.1$. 107
5.10 Grid Convergence Indices (GCI) at $Re = 0.01$. 107
5.11 Grid Convergence Indices (GCI) at $Re = 0.001$. 108
5.12 Grid Convergence Indices (GCI) at $Re = 0.0001$. 108
5.13 Relative errors of the maximum norm at the outlet section at $Re = 10$. . . 129
5.14 Relative errors of the maximum norm at the outlet section at $Re = 5$. . . . 129
5.15 Relative errors of the maximum norm at the outlet section at $Re = 1$. . . . 130
5.16 Relative errors of the maximum norm at the outlet section at $Re = 0.5$. . . 130
5.17 Relative errors of the maximum norm at the outlet section at $Re = 0.1$. . . 131
5.18 Relative errors of the maximum norm at the outlet section at $Re = 0.01$. . 131
5.19 Relative errors of the maximum norm at the outlet section at $Re = 0.001$. . 132
5.20 Relative errors of the maximum norm at the outlet section at $Re = 0.0001$. 132

5.21 Total number of multigrid iterations on the fine grid and maximum values of Runge-Kutta residuals using different intercell flux interpolations at $Re = 10$. 133
5.22 Total number of multigrid iterations on the fine grid and maximum values of Runge-Kutta residuals using different intercell flux interpolations at $Re = 5$. 134
5.23 Total number of multigrid iterations on the fine grid and maximum values of Runge-Kutta residuals using different intercell flux interpolations at $Re = 1$. 135
5.24 Total number of multigrid iterations on the fine grid and maximum values of Runge-Kutta residuals using different intercell flux interpolations at $Re = 0.5$. 136
5.25 Total number of multigrid iterations on the fine grid and maximum values of Runge-Kutta residuals using different intercell flux interpolations at $Re = 0.1$. 137
5.26 Total number of multigrid iterations on the fine grid and maximum values of Runge-Kutta residuals using different intercell flux interpolations at $Re = 0.01$. 138
5.27 Total number of multigrid iterations on the fine grid and maximum values of Runge-Kutta residuals using different intercell flux interpolations at $Re = 0.001$. 139
5.28 Total number of multigrid iterations on the fine grid and maximum values of Runge-Kutta residuals using different intercell flux interpolations at $Re = 0.0001$. 140

6.1 Total number of multigrid iterations on the fine grid using 1^{st}-order intercell flux interpolation at $Re = 100$. 156
6.2 Total number of multigrid iterations on the fine grid using 2^{nd}-order intercell flux interpolation at $Re = 100$. 157
6.3 Total number of multigrid iterations on the fine grid using 3^{rd}-order intercell flux interpolation at $Re = 100$. 158
6.4 Total number of multigrid iterations on the fine grid using 5^{th}-order WENO intercell flux interpolation at $Re = 100$. 159
6.5 Total number of multigrid iterations on the fine grid using 9^{th}-order WENO intercell flux interpolation at $Re = 100$. 160
6.6 Total number of multigrid iterations on the fine grid using 1^{st}-order intercell flux interpolation at $Re = 400$. 166
6.7 Total number of multigrid iterations on the fine grid using 2^{nd}-order intercell flux interpolation at $Re = 400$. 167

6.8 Total number of multigrid iterations on the fine grid using 3^{rd}-order intercell flux interpolation at $Re = 400$. 168
6.9 Total number of multigrid iterations on the fine grid using 5^{th}-order WENO intercell flux interpolation at $Re = 400$. 169
6.10 Total number of multigrid iterations on the fine grid using 9^{th}-order WENO intercell flux interpolation at $Re = 400$. 170
6.11 Total number of multigrid iterations on the fine grid using 1^{st}-order intercell flux interpolation at $Re = 1000$. 176
6.12 Total number of multigrid iterations on the fine grid using 2^{nd}-order intercell flux interpolation at $Re = 1000$. 177
6.13 Total number of multigrid iterations on the fine grid using 3^{rd}-order intercell flux interpolation at $Re = 1000$. 178
6.14 Total number of multigrid iterations on the fine grid using 5^{th}-order WENO intercell flux interpolation at $Re = 1000$. 179
6.15 Total number of multigrid iterations on the fine grid using 9^{th}-order WENO intercell flux interpolation at $Re = 1000$. 180
6.16 Total number of multigrid iterations on the fine grid using different intercell flux interpolations at Re = 100, 400, and 1000. 181
6.17 Maximum relative errors of the AC, PP, and FSAC-PP methods for the dimensionless velocity component V along horizontal centre-line of the square cavity compared to the results of Ghia et al. [8] at Re = 100, 400, and 1000. 181
6.18 Maximum relative errors of the AC, PP, and FSAC-PP methods for dimensionless velocity component U along vertical centre-line of the square cavity compared to the results of Ghia et al. [8] at Re = 100, 400, and 1000. 182

7.1 Geometrical sizes of the mixing zone of the Y-junction microfluidic channel. 199
7.2 Absolute and relative errors of the AC, PP, and FSAC-PP methods for the dimensionless velocity distribution of velocity component U at the outlet of the Y-junction channel, using 3^{rd}-order interpolation, compared to the analytical solution of Marco and Han [18, 19, p. 5.67] at $Re = 50$ and $Pe = 1000$. 204
7.3 Comparison of the numerical convergence of the AC, PP, and FSAC-PP methods; total number of multigrid iterations on the fine grid and maximum values of Runge-Kutta residuals using 3^{rd}-order interpolations at $Re = 50$ and $Pe = 1000$. 205

List of Tables

8.1 Geometrical sizes of the two-dimensional straight microfluidic channel under the presence of uniform electromagnetic field. 216
8.2 Simulation parameters, dimensional and dimensionless physical quantities relying on the paper of Tzirtzilakis and Loukopoulos [9]. 218
8.3 Comparison of the numerical convergence of the AC and FSAC-PP methods using Newtonian fluid model in the presence of uniform localized magnetic field in the microfluidic straight channel; total number of multigrid iterations on the fine grid using 3^{rd}-order interpolation at $Re = 300$, $Mn_M = 40$, $Mn_F = 0$. 222
8.4 Comparison of the numerical convergence of the AC and FSAC-PP methods using non-Newtonian power law fluid model in the presence of uniform localized magnetic field in the microfluidic straight channel; total number of multigrid iterations on the fine grid using 3^{rd}-order interpolation at $Re = 300$, $Mn_M = 40$, $Mn_F = 0$. 224

9.1 Geometrical sizes of the three-dimensional T-channel. 232
9.2 Results of grid convergence study. 233
9.3 Comparison of the numerical convergence of the AC and FSAC-PP methods without modelling AW in the microfluidic T-channel; total number of multigrid iterations on the fine grid using 3^{rd}-order interpolation at $Re = 10.240$
9.4 Comparison of the numerical convergence of the AC and FSAC-PP methods with modelling AW in the microfluidic T-channel; total number of multigrid iterations on the fine grid using 3^{rd}-order interpolation at $Re = 10.245$

B.1 Results of the AC, PP, and FSAC-PP methods for the dimensionless velocity component V along horizontal centre-line of the square cavity using 1^{st}-order interpolation compared to the results of [8] at $Re = 100$. 269
B.2 Absolute and relative errors of the AC, PP, and FSAC-PP methods for the dimensionless velocity component V along horizontal centre-line of the square cavity using 1^{st}-order interpolation compared to the results of [8] at $Re = 100$. 269
B.3 Results of the AC, PP, and FSAC-PP methods for the dimensionless velocity component U along vertical centre-line of the square cavity using 1^{st}-order interpolation compared to the results of [8] at $Re = 100$. 270
B.4 Absolute and relative errors of the AC, PP, and FSAC-PP methods for the dimensionless velocity component U along vertical centre-line of the square cavity using 1^{st}-order interpolation compared to the results of [8] at $Re = 100$. 270

B.5 Results of the AC, PP, and FSAC-PP methods for the dimensionless velocity component V along horizontal centre-line of the square cavity using 2^{nd}-order interpolation compared to the results of [8] at $Re = 100$. 271
B.6 Absolute and relative errors of the AC, PP, and FSAC-PP methods for the dimensionless velocity component V along horizontal centre-line of the square cavity using 2^{nd}-order interpolation compared to the results of [8] at $Re = 100$. 271
B.7 Results of the AC, PP, and FSAC-PP methods for the dimensionless velocity component U along vertical centre-line of the square cavity using 2^{nd}-order interpolation compared to the results of [8] at $Re = 100$. 272
B.8 Absolute and relative errors of the AC, PP, and FSAC-PP methods for the dimensionless velocity component U along vertical centre-line of the square cavity using 2^{nd}-order interpolation compared to the results of [8] at $Re = 100$. 272
B.9 Results of the AC, PP, and FSAC-PP methods for the dimensionless velocity component V along horizontal centre-line of the square cavity using 3^{rd}-order interpolation compared to the results of [8] at $Re = 100$. 273
B.10 Absolute and relative errors of the AC, PP, and FSAC-PP methods for the dimensionless velocity component V along horizontal centre-line of the square cavity using 3^{rd}-order interpolation compared to the results of [8] at $Re = 100$. 273
B.11 Results of the AC, PP, and FSAC-PP methods for the dimensionless velocity component U along vertical centre-line of the square cavity using 3^{rd}-order interpolation compared to the results of [8] at $Re = 100$. 274
B.12 Absolute and relative errors of the AC, PP, and FSAC-PP methods for the dimensionless velocity component U along vertical centre-line of the square cavity using 3^{rd}-order interpolation compared to the results of [8] at $Re = 100$. 274
B.13 Results of the AC, PP, and FSAC-PP methods for the dimensionless velocity component V along horizontal centre-line of the square cavity using 5^{th}-order WENO interpolation compared to the results of [8] at $Re = 100$. 275
B.14 Absolute and relative errors of the AC, PP, and FSAC-PP methods for the dimensionless velocity component V along horizontal centre-line of the square cavity using 5^{th}-order WENO interpolation compared to the results of [8] at $Re = 100$. 275
B.15 Results of the AC, PP, and FSAC-PP methods for the dimensionless velocity component U along vertical centre-line of the square cavity using 5^{th}-order WENO interpolation compared to the results of [8] at $Re = 100$. 276

B.16 Absolute and relative errors of the AC, PP, and FSAC-PP methods for the dimensionless velocity component U along vertical centre-line of the square cavity using 5^{th}-order WENO interpolation compared to the results of [8] at $Re = 100$. 276
B.17 Results of the AC, PP, and FSAC-PP methods for the dimensionless velocity component V along horizontal centre-line of the square cavity using 9^{th}-order WENO interpolation compared to the results of [8] at $Re = 100$. 277
B.18 Absolute and relative errors of the AC, PP, and FSAC-PP methods for the dimensionless velocity component V along horizontal centre-line of the square cavity using 9^{th}-order WENO interpolation compared to the results of [8] at $Re = 100$. 277
B.19 Results of the AC, PP, and FSAC-PP methods for the dimensionless velocity component U along vertical centre-line of the square cavity using 9^{th}-order WENO interpolation compared to the results of [8] at $Re = 100$. 278
B.20 Absolute and relative errors of the AC, PP, and FSAC-PP methods for the dimensionless velocity component U along vertical centre-line of the square cavity using 9^{th}-order WENO interpolation compared to the results of [8] at $Re = 100$. 278
B.21 Results of the AC, PP, and FSAC-PP methods for the dimensionless velocity component V along horizontal centre-line of the square cavity using 1^{st}-order interpolation compared to the results of [8] at $Re = 400$. 279
B.22 Absolute and relative errors of the AC, PP, and FSAC-PP methods for the dimensionless velocity component V along horizontal centre-line of the square cavity using 1^{st}-order interpolation compared to the results of [8] at $Re = 400$. 279
B.23 Results of the AC, PP, and FSAC-PP methods for the dimensionless velocity component U along vertical centre-line of the square cavity using 1^{st}-order interpolation compared to the results of [8] at $Re = 400$. 280
B.24 Absolute and relative errors of the AC, PP, and FSAC-PP methods for the dimensionless velocity component U along vertical centre-line of the square cavity using 1^{st}-order interpolation compared to the results of [8] at $Re = 400$. 280
B.25 Results of the AC, PP, and FSAC-PP methods for the dimensionless velocity component V along horizontal centre-line of the square cavity using 2^{nd}-order interpolation compared to the results of [8] at $Re = 400$. 281

B.26 Absolute and relative errors of the AC, PP, and FSAC-PP methods for the dimensionless velocity component V along horizontal centre-line of the square cavity using 2^{nd}-order interpolation compared to the results of [8] at $Re = 400$. 281
B.27 Results of the AC, PP, and FSAC-PP methods for the dimensionless velocity component U along vertical centre-line of the square cavity using 2^{nd}-order interpolation compared to the results of [8] at $Re = 400$. 282
B.28 Absolute and relative errors of the AC, PP, and FSAC-PP methods for the dimensionless velocity component U along vertical centre-line of the square cavity using 2^{nd}-order interpolation compared to the results of [8] at $Re = 400$. 282
B.29 Results of the AC, PP, and FSAC-PP methods for the dimensionless velocity component V along horizontal centre-line of the square cavity using 3^{rd}-order interpolation compared to the results of [8] at $Re = 400$. 283
B.30 Absolute and relative errors of the AC, PP, and FSAC-PP methods for the dimensionless velocity component V along horizontal centre-line of the square cavity using 3^{rd}-order interpolation compared to the results of [8] at $Re = 400$. 283
B.31 Results of the AC, PP, and FSAC-PP methods for the dimensionless velocity component U along vertical centre-line of the square cavity using 3^{rd}-order interpolation compared to the results of [8] at $Re = 400$. 284
B.32 Absolute and relative errors of the AC, PP, and FSAC-PP methods for the dimensionless velocity component U along vertical centre-line of the square cavity using 3^{rd}-order interpolation compared to the results of [8] at $Re = 400$. 284
B.33 Results of the AC, PP, and FSAC-PP methods for the dimensionless velocity component V along horizontal centre-line of the square cavity using 5^{th}-order WENO interpolation compared to the results of [8] at $Re = 400$. 285
B.34 Absolute and relative errors of the AC, PP, and FSAC-PP methods for the dimensionless velocity component V along horizontal centre-line of the square cavity using 5^{th}-order WENO interpolation compared to the results of [8] at $Re = 400$. 285
B.35 Results of the AC, PP, and FSAC-PP methods for the dimensionless velocity component U along vertical centre-line of the square cavity using 5^{th}-order WENO interpolation compared to the results of [8] at $Re = 400$. 286

B.36 Absolute and relative errors of the AC, PP, and FSAC-PP methods for the dimensionless velocity component U along vertical centre-line of the square cavity using 5^{th}-order WENO interpolation compared to the results of [8] at $Re = 400$. 286
B.37 Results of the AC, PP, and FSAC-PP methods for the dimensionless velocity component V along horizontal centre-line of the square cavity using 9^{th}-order WENO interpolation compared to the results of [8] at $Re = 400$. 287
B.38 Absolute and relative errors of the AC, PP, and FSAC-PP methods for the dimensionless velocity component V along horizontal centre-line of the square cavity using 9^{th}-order WENO interpolation compared to the results of [8] at $Re = 400$. 287
B.39 Results of the AC, PP, and FSAC-PP methods for the dimensionless velocity component U along vertical centre-line of the square cavity using 9^{th}-order WENO interpolation compared to the results of [8] at $Re = 400$. 288
B.40 Absolute and relative errors of the AC, PP, and FSAC-PP methods for the dimensionless velocity component U along vertical centre-line of the square cavity using 9^{th}-order WENO interpolation compared to the results of [8] at $Re = 400$. 288
B.41 Results of the AC, PP, and FSAC-PP methods for the dimensionless velocity component V along horizontal centre-line of the square cavity using 1^{st}-order interpolation compared to the results of [8] at $Re = 1000$. 289
B.42 Absolute and relative errors of the AC, PP, and FSAC-PP methods for the dimensionless velocity component V along horizontal centre-line of the square cavity using 1^{st}-order interpolation compared to the results of [8] at $Re = 1000$. 289
B.43 Results of the AC, PP, and FSAC-PP methods for the dimensionless velocity component U along vertical centre-line of the square cavity using 1^{st}-order interpolation compared to the results of [8] at $Re = 1000$. 290
B.44 Absolute and relative errors of the AC, PP, and FSAC-PP methods for the dimensionless velocity component U along vertical centre-line of the square cavity using 1^{st}-order interpolation compared to the results of [8] at $Re = 1000$. 290
B.45 Results of the AC, PP, and FSAC-PP methods for the dimensionless velocity component V along horizontal centre-line of the square cavity using 2^{nd}-order interpolation compared to the results of [8] at $Re = 1000$. 291

B.46 Absolute and relative errors of the AC, PP, and FSAC-PP methods for the dimensionless velocity component V along horizontal centre-line of the square cavity using 2^{nd}-order interpolation compared to the results of [8] at $Re = 1000$. 291
B.47 Results of the AC, PP, and FSAC-PP methods for the dimensionless velocity component U along vertical centre-line of the square cavity using 2^{nd}-order interpolation compared to the results of [8] at $Re = 1000$. 292
B.48 Absolute and relative errors of the AC, PP, and FSAC-PP methods for the dimensionless velocity component U along vertical centre-line of the square cavity using 2^{nd}-order interpolation compared to the results of [8] at $Re = 1000$. 292
B.49 Results of the AC, PP, and FSAC-PP methods for the dimensionless velocity component V along horizontal centre-line of the square cavity using 3^{rd}-order interpolation compared to the results of [8] at $Re = 1000$. 293
B.50 Absolute and relative errors of the AC, PP, and FSAC-PP methods for the dimensionless velocity component V along horizontal centre-line of the square cavity using 3^{rd}-order interpolation compared to the results of [8] at $Re = 1000$. 293
B.51 Results of the AC, PP, and FSAC-PP methods for the dimensionless velocity component U along vertical centre-line of the square cavity using 3^{rd}-order interpolation compared to the results of [8] at $Re = 1000$. 294
B.52 Absolute and relative errors of the AC, PP, and FSAC-PP methods for the dimensionless velocity component U along vertical centre-line of the square cavity using 3^{rd}-order interpolation compared to the results of [8] at $Re = 1000$. 294
B.53 Results of the AC, PP, and FSAC-PP methods for the dimensionless velocity component V along horizontal centre-line of the square cavity using 5^{th}-order WENO interpolation compared to the results of [8] at $Re = 1000$. 295
B.54 Absolute and relative errors of the AC, PP, and FSAC-PP methods for the dimensionless velocity component V along horizontal centre-line of the square cavity using 5^{th}-order WENO interpolation compared to the results of [8] at $Re = 1000$. 295
B.55 Results of the AC, PP, and FSAC-PP methods for the dimensionless velocity component U along vertical centre-line of the square cavity using 5^{th}-order WENO interpolation compared to the results of [8] at $Re = 1000$. 296

B.56 Absolute and relative errors of the AC, PP, and FSAC-PP methods for the dimensionless velocity component U along vertical centre-line of the square cavity using 5^{th}-order WENO interpolation compared to the results of [8] at $Re = 1000$. 296
B.57 Results of the AC, PP, and FSAC-PP methods for the dimensionless velocity component V along horizontal centre-line of the square cavity using 9^{th}-order WENO interpolation compared to the results of [8] at $Re = 1000$. 297
B.58 Absolute and relative errors of the AC, PP, and FSAC-PP methods for the dimensionless velocity component V along horizontal centre-line of the square cavity using 9^{th}-order WENO interpolation compared to the results of [8] at $Re = 1000$. 297
B.59 Results of the AC, PP, and FSAC-PP methods for the dimensionless velocity component U along vertical centre-line of the square cavity using 9^{th}-order WENO interpolation compared to the results of [8] at $Re = 1000$. 298
B.60 Absolute and relative errors of the AC, PP, and FSAC-PP methods for the dimensionless velocity component U along vertical centre-line of the square cavity using 9^{th}-order WENO interpolation compared to the results of [8] at $Re = 1000$. 298

List of Algorithms

4.1 Extended non-linear FMG-FAS algorithm to the developed FSAC-PP solution method for solving unsteady, incompressible Navier-Stokes equations. 90
4.2 Extended non-linear FMG-FAS algorithm to the developed FSAC-PP solution method for solving unsteady, incompressible variable density flow problems. 94

Nomenclature

Symbol	Unit	Description
a, b, c, d, e, f_i	–	Coefficients or geometrical constants
$\mathbf{B}$	Tesla=$V{\cdot}s/m^2$	Magnetic field
c_p	$J/(kg{\cdot}K)$	Specific heat at constant pressure
c_s	m/s	Speed of sound in the medium
$\mathbf{D}$	C/m^2	Electric flux density (electric displacement field)
e	C=$A{\cdot}s$	Isolated electric charge
$\mathbf{E}$	V/m	Electric field
$\mathbf{f}$	N	External (additional) forces
$\mathbf{F}$	–	Dimensionless external (additional) forces
$\mathbf{g}$	m/s^2	Gravitational acceleration vector
$\mathbf{H}$	A/m	Magnetic field intensity
$\mathbf{i}_s$	W/m^2	Acoustic intensity vector
$\mathbf{I}_s$	–	Dimensionless acoustic intensity vector
$\underline{\underline{\mathrm{I}}}$	–	Idem tensor
J	–	Jacobian determinant
$\mathbf{J}_e$	m^2/s	Particle current density vector
$\mathbf{u}$	m/s	Velocity vector
u, v, w	m/s	Scalar velocity components
$\mathbf{u}_\infty$	m/s	Reference velocity vector
$u_\infty, v_\infty, w_\infty$	m/s	Reference scalar velocity components
$\mathbf{U}$	–	Dimensionless velocity vector
U, V, W	–	Dimensionless scalar velocity components
$\mathbf{U_p}$	–	Vector of dimensionless pseudo-time stepping unknowns
$\mathbf{U_r}$	–	Vector of dimensionless real-time stepping quantities
L	m	Length/Reference length
Ma	–	Mach number
M_A	kg/mol	Molar mass

N_A	$1/mol$	Avogadro's number
p	Pa	Pressure field
P	–	Dimensionless pressure field
Pe	–	Péclet number
r	–	Grid refinement ratio
Re	–	Reynolds number
s	m/s	Artificial speed of sound
$\underline{\underline{S}}$	$1/s$	Rate of strain (deformation) tensor
t	s	Time
t^*	–	Dimensionless time
Δt^*	s	Time-step
T	–	Dimensionless temperature field
x, y, z	m	Cartesian coordinates
X, Y, Z	–	Dimensionless Cartesian coordinates
β	–	Artificial compressibility parameter
γ_{t^*}	–	Safety-factor
ε	–	Dielectric constant
ϑ	K	Temperature field
λ_A	m	Average interatomic space
μ	$Pa{\cdot}s$	Dynamic viscosity
υ	m^2/s	Kinematic viscosity
$\underline{\underline{\sigma}}$	Pa	Total stress tensor
τ	s	Pseudo-time
$\underline{\underline{\tau}}$	Pa	Viscous stress tensor
ξ, η, ζ	m	Curvilinear coordinates
ρ	kg/m^3	Fluid density
ρ_e	C/m^3	Electric charge density
ρ_∞	kg/m^3	Reference (constant) density
ω_P	–	Relaxation factor for the pressure
Φ	m^2/s	Potential function of the irrotational velocity field
ψ	J/C	Potential function of the electric field

Abbreviations

AC	Artificial Compressibility
AW	Acoustic Wave(s)
Bio-MEMS	Biological-Micro-Electro-Mechanical Systems
CB	Characteristics-Based

CBD	Computational Biofluid Dynamics
CBM	Computational Biofluid Mechanics
CFD	Computational Fluid Dynamics
CFL	Courant-Friedrichs-Lewy
DNA	Deoxyribonucleic Acid
DNS	Direct Numerical Simulation
DPD	Dissipative Particle Dynamics
dsDNA	Double-Stranded Deoxyribonucleic Acid
DSMC	Direct Simulation Monte Carlo
EDL	Electric Double Layer
ENO	Essentially Non-Oscillatory
EOF	Electroosmotic Flow
EWOD	Electrowetting on Dielectric
FALCO	FAst Linear COrrector
FCM	Force Coupling Method
FDM	Finite Difference Method
FEM	Finite Element Method
FHD	Ferro-HydroDynamics
FMG-FAS	Full-Multigrid, Full-Approximation-Storage
FVM	Finite Volume Method
FS	Fractional Step
FSAC	Fractional Step Artificial Compressibility
FSAC-PP	Fractional Step Artificial Compressibility with Pressure-Projection
FS-PP	Fractional Step Pressure-Projection
FSTE	Flow-Structure-Thermal-Electrical
FSI	Fluid-Structure Interactions
FVGM	Finite Volume Godunov-type Method
GCI	Grid Convergence Index
HIV	Human Immunodeficiency Virus
HR-CBS	High-Resolution Characteristics-Based Scheme
ILES	Implicit Large Eddy Simulation
LBM	Lattice-Boltzmann Method
LES	Large Eddy Simulation
MAC	Marker-and-Cell
MCB	Multidimensional Characteristics-Based
MD	Molecular Dynamics
MHD	Magnetohydrodynamic
MM	Meshless Methods

MEMS	Micro-Electro-Mechanical Systems
MpCCI	Multiphysics Code Coupling Interface
MST	MicroSystem Technology
μTAS	Micro Total Analysis Systems
NPIV	Nano-Particle Image Velocimetry
PISO	Pressure Implicit with Splitting of Operators
PP	Pressure-Projection
PVC	Pressure-Velocity Coupling
QUICK	Quadratic Upwind Interpolation for Convective Kinematics
SAR	Spanwise Aspect Ratio
SIMPLE	Semi-Implicit Method for Pressure-Linked Equations
SIMPLEC	Semi-Implicit Method for Pressure-Linked Equations Consistent
SIMPLER	Semi-Implicit Method for Pressure-Linked Equations Revised
SEM	Spectral Element Method
S.O.R.	Successive Over-Relaxation
S.P.O.R.	Successive Point Over-Relaxation
ssDNA	Single-Stranded Deoxyribonucleic Acid
VOF	Volume of Fluid
VPH	Virtual Physiological Human
WENO	Weighted Essentially Non-Oscillatory

Subscripts

S	South corresponds to grid indices $(i, j-1, k)$
E	East corresponds to grid indices $(i-1, j, k)$
P	Point corresponds to grid indices (i, j, k)
W	West corresponds to grid indices $(i+1, j, k)$
N	North corresponds to grid indices $(i, j+1, k)$
T	Top corresponds to grid indices $(i, j, k+1)$
B	Bottom corresponds to grid indices $(i, j, k-1)$

Operators

∇	Hamilton (nabla) vector-type differential operator
∇^2	Laplacian second-order scalar-type differential operator
$\cdot\cdot$	Double dot product of two second-rank tensors

Chapter 1

Introduction and Objectives

Multiphysics modelling refers to multiple physical models combining different mathematical descriptions and solutions. For modelling complex phenomena and/or designing high level technological devices, it is indispensable to develop and integrate different mathematical models for a broad range of physics disciplines. Equations of the corresponding models are mostly coupled systems of partial differential equations, and it may be advantageous and required to couple various computational methods. The mathematical solution may happen considering model simplifications and assumptions.

Multiphysics software packages are available on the market, such as ANSYS Multiphysics, CFD-ACE+, CoventorWare^{TM} and COMSOL Multiphysics packages, requiring interdisciplinary knowledge from their users. These software packages are capable of modelling coupled physical phenomena, such as fluid flow, heat and chemical species transport, fluid-structure interactions (FSI), thermal stresses, chemical reaction kinetics, electromechanical interactions, electromagnetic-fluid interactions, and magnetohydrodynamics. Most of them are relying on the Finite Volume Method (FVM) and/or Finite Element Method (FEM) as discretization methods for solving the corresponding systems of transport equations. The different mathematical behaviour of partial differential equations are taken into account by single or multiple discretization techniques using optimization methods. The MpCCI (Multiphysics Code Coupling Interface) commercially available software package is capable of coupling simulation among different multiphysics packages simultaneously to model complex physical processes all together.

The above mentioned commercial multiphysics software packages cover a broad range of scientific and practical engineering applications, such as aerospace and defence, aircraft engineering, combustion, simulation of biomedical and life science processes, and designing biomedical devices using bioengineering technologies. These software packages provide a multiscale modelling environment to manage physical phenomena in macro-, micro-, and nanoscales. For example, it is possible to model microscale processes, such

as pressure and/or electrokinetically-driven flows, non-Newtonian fluid flows, mixing of chemical species, and take into account e.g. Joule heating. Modelling of these physical processes may be useful in designing Micro-Electro-Mechanical Systems (MEMS), Lab-on-a-Chip devices, micropumps, micromixers, biosensors, and other microfluidic devices.

There are different levels of physical modelling in terms of spatial and temporal scales (see Figure 1.1 [12, p. 2]). One of them is the continuum model under the continuum hypothesis, and the other main one is the Molecular Dynamics (MD) based model relating to the momentum equation for individual particles. These modelling approaches are often used for micro- and nanofluidic engineering applications. Micro- and nanofluidics deal with physical and chemical processes in micro- and nano spatial scale devices, which is related to different fields of science and technology (see Figure 1.2 [13, p. 1.]).

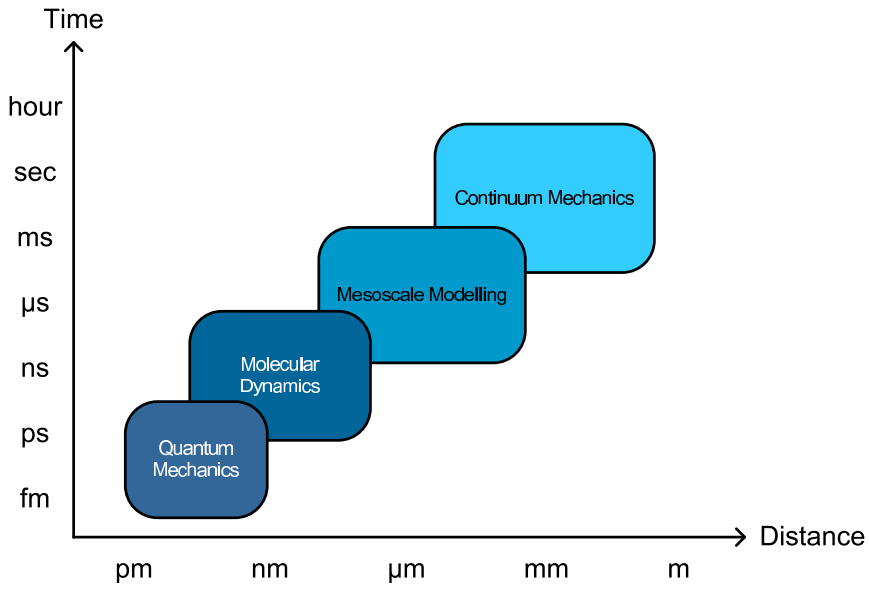

Figure 1.1: Levels of Modelling Approaches at Spatial and Temporal Scales [12, p. 2]

Karniadakis, Beskok and Aluru discussed the fundamentals of micro- and nanofluidics relying on continuum and MD simulation techniques for multiphysics and multiscale modelling of liquid and gas flows [23]. The main differences of fluid mechanics between the micro- and macroscale flow simulation approach were considered as the classification of non-continuum, surface-dominated, low Reynolds number, multiphysics, and multiscale effects. Multiscale modelling of gas microflows was described at the mesoscopic and atomistic levels based on the stochastical stationary and unsteady Direct Simulation Monte Carlo (DSMC) method. The Schwarz iterative method was presented for coupling the continuum and atomistic scales. The Lattice-Boltzmann Method (LBM) was discussed for incompressible, and compressible flows. Multiscale modelling of liquid microflows involves the MD method, the LBM, and the Dissipative Particle Dynamics

(DPD) method. For continuum simulation, the incompressible and compressible Navier-Stokes equations based on high-order Spectral Element Method (SEM), the Meshless Methods (MM), and the Force Coupling Method (FCM) were described in detail. Shear-driven flows, pressure-driven flows, surface-tension driven flows, electrokinetic flows, such as electroosmotic flow (EOF), electrophoresis and dielectrophoresis, and thermal effects were also discussed. Demonstrative examples can be found for micro- and nanofluidic systems, such as Lab-on-a-Chip systems, microfilters, micronozzle, micromixers, carbon nanotubes, micro/nanochannels, and full systems in heterogeneous domains.

Microfluidics also refers to science and microsystem technology that is related multidisciplinary to mathematics, physics, chemistry (including surface chemistry), biology, material science, microoptics, computational fluid dynamics (CFD), biofluid mechanics, computational biofluid dynamics (CBD), biomedical and life sciences, microfabrication, system and production engineering, bioengineering, and biotechnologies [24, 25].

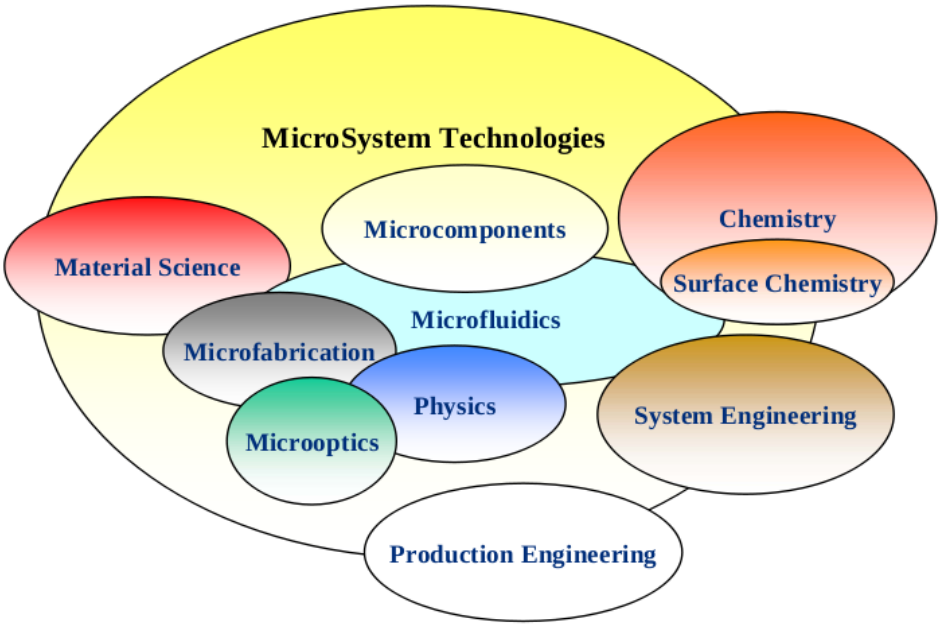

Figure 1.2: Microfluidics related to different fields of science and technology [13, p. 1.].

The modern age of computers started in the 20th century, because the break-through in the microelectronics and information technology with producing integrated circuits made miniaturization the centre of interest [23, 25, 26]. The scientific interest had a significant growth from the beginning of the 21th century, because it has become possible to produce cheap portable biomedical devices (see, e.g., Figure 1.3) [14]. The fabrication and development of microfluidic devices happens on micro- or smaller-scales, i.e. nano-, pico- and femtolitre volumes. This field enables a whole range of possibilities to study

fundamental physical, chemical, biological, biophysical, and biochemical processes. The flow is laminar, and the fluid may be Newtonian or non-Newtonian depending on the microfluidic device. In these devices, the surface forces, surface tension and viscosity dominate instead of the inertial forces at low Reynolds numbers. It may also be important to consider the magnetic field effect, e.g. during the modelling and design of biofluid magnetic particle separators. These physical phenomena are relevant to be taken into account in the design processes of microfluidic devices.

Figure 1.3: Portable microfluidic biomedical device for daily blood glucose monitoring: a) OneTouch Ultra Blood Glucose Biosensor [14, Newman and Turner, p. 2444]; b) Pelikan Sun Integrated Blood Glucose Device [14, Newman and Turner, p. 2451].

Microfluidic systems are used for diverse industrial fields, such as micro- and consumer electronics, biotechnology, diagnostics, pharmaceutics, chemistry, medical and process industry, environmental technology, automobile, and food industry. These relevant industrial applications may include Micro-Electro-Mechanical Systems (MEMS), Biological-Micro-Electro-Mechanical Systems (Bio-MEMS), Micro Total Analysis Systems (μTAS), Lab-on-a-Chip devices, commercial blood glucose biosensors (see Figure 1.3), cancer biomarker biosensors, cell based devices, DNA and protein chips, drug delivery, micropumps, microvalves, micromixers, and other microfluidic devices.

However, different multiphysics software packages are available on the market, but there are shortages of quick and reliable high-resolution Godunov-type method based software tools to design microfluidic biomedical devices, and/or biosensors. The reason is that the high-resolution methods are computationally expensive, therefore, the scope of this thesis is to develop and validate a new efficient high-resolution Godunov-type numerical procedure for solving the unsteady, incompressible Navier-Stokes equations; and implement a multiphysics software package for low and moderate Reynolds number flow problems. This software tool may be used in the design of microfluidic devices.

1.1 Background and Motivation of the Research Work

For microfluidic applications, the research work has been going on for almost ten years at the Department of Engineering Physics at Cranfield University. The Fluid Mechanics and Computational Science (FMCS) research group develops and uses in-house Computational Fluid Dynamics (CFD) FORTRAN 90/95 codes, called HIRECOM and CNS3D, for solving incompressible and compressible fluid flow, heat transfer and chemical multi-species problems for both scientific and industrial applications. These in-house codes are high-performance parallelized software packages relying on a high-resolution Finite Volume Godunov-type Method (FVGM), which have been developed by over 40 members of the FMCS research group led by Professor Dimitris Drikakis. These codes are also capable of handling scientifically and industrially relevant fluid dynamics problems, such as Implicit Large Eddy Simulation (ILES) for turbulent flows, instabilities, and mixing; aerodynamics in particular to unsteady flows; multiphase and multi-species problems; shock-material interactions; micro- and nanoflows, e.g. fluid-material interfaces, nanotubes, DNA flow modelling; and multiscale methods for flows and materials modelling. Therefore, the motivation of the present research work is to further develop high-resolution methods and implement a multiphysics modelling software tool, called HIRECOM-MULTIPHYSICS Unified Code v1.0, for microfluidic industrial applications.

The author of this Ph.D. thesis attaches importance to his personal interest and background in the development of numerical methods. He received his Ph.D. degree[1] in 2004 at the University of Miskolc, in Hungary. Prior to his position at Cranfield University, he was a guest research fellow at the University of Siegen in 2003, and at the Otto-von-Guericke-University Magdeburg in 2005, in Germany. He was working on mathematical modelling of isothermal and non-isothermal turbulent flows using a stochastical Reynolds Averaged Navier-Stokes (RANS) turbulence model. After being an assistant professor at the University of Miskolc, in Hungary, he became a postdoctoral research fellow in 2006 at the University of Leoben, in Austria. He took part in an industrially sponsored research project from 2006 to 2008 working on modelling of multiphase and multicomponent solidification and melting processes of ingot casting. After finishing the industrial research project in Austria, his interest turned to the field of microfluidics. He decided to further educate himself writing a second Ph.D. thesis under Professor Dimitris Drikakis supervision. His motivation is to integrate his previously gained knowledge in mathematical modelling and computer science in the field of computational multiphysics.

[1] L. Könözsy. Computation of Two-Dimensional Shear Flows with the Solution of the Turbulent Vorticity Transport Equation (in Hungarian), *University of Miskolc*, *Department of Fluid and Heat Engineering,* PhD thesis, Miskolc, Hungary, 2004. The research project was sponsored by the DAAD-MÖB German-Hungarian fund in co-operation with the University of Siegen and the Otto-von-Guericke-University Magdeburg, Institutes of Fluid- and Thermodynamics, in Germany.

1.2 Problem Statement

The main outcomes of this Ph.D. project are a novel numerical treatment of the unsteady, incompressible Navier-Stokes equations; and a high-resolution Godunov-type method based FORTRAN 90/95 multiphysics software tool for solving constant and variable density flows, taking into account interface tracking, electric- and electromagnetic forces. Multiphysics modelling refers to multiple physical models combining different mathematical approaches and solutions. For microfluidic industrial applications, the flow is laminar, and the fluid is Newtonian (e.g. water) or non-Newtonian (e.g. a biofluid such as blood) depending on the microfluidic device. In these cases, the surface forces, surface tension and viscosity dominate instead of the inertial forces at low Reynolds numbers. The classical artificial compressibility method has major value for solving stationary flow problems, but for unsteady and/or low Reynolds number flows, the stability condition of the dual-time stepping procedure and the choice of the artificial compressibility parameter may become too restrictive, which could lead to slow convergence rates [5, 27].

In this thesis, to overcome the stiffness of the classical artificial compressibility method, a novel high-resolution Godunov-type numerical procedure has been developed for solving the unsteady, incompressible Navier-Stokes equations. For constant and variable density flows, the proposed numerical method encompasses both artificial compressibility (AC) and fractional step (FS) pressure-projection (PP) methods of Chorin [3, 4] in a unified solution concept, which is labelled as FSAC-PP method in this thesis. To take advantage of the best numerical features of different computational strategies, the FS and AC methods have been coupled (FSAC formulation), and further a PP step has been employed at each pseudo-time step. To provide time-accurate solutions, the dual-time stepping procedure is utilized. Taking the advantage of the hyperbolic nature of the inviscid part of the AC formulation, high-resolution characteristics-based (CB) Godunov-type scheme is employed to discretize the non-linear advective fluxes. Five different interpolation schemes have been used for the advective term discretization from first- up to ninth-order of accuracy. An adaptive time stepping method with an appropriately chosen safety factor has been used to compute the time step in each control cell locally. Time integration is obtained from a fourth-order Runge-Kutta scheme. In the presented thesis, the proposed FSAC-PP method has been coupled with a non-linear full-multigrid, full-approximation storage (FMG-FAS) acceleration technique to further increase the efficiency and decrease the computational cost of the developed unsteady, incompressible Navier-Stokes solver.

Most of the mircofluidic industrial applications under the continuum hypothesis are complex multiphysics problems occurring at low Reynolds numbers. In these practical cases, the typical Reynolds number changes from 10^{-1} up to 10^{2} [6], where the classical AC method could fail for $Re < 1$. Therefore, the key motivation for developing the FSAC-

PP method is to improve the stability, efficiency and decrease the computational cost of the classical AC method at both (very) low and moderate Reynolds numbers. Since, microfluidics refers to science and microsystem technology multidisciplinary related to mathematics, physics, chemistry, biology, material science, computational fluid dynamics (CFD), biofluid mechanics, computational biofluid dynamics (CBD), biomedical and life sciences [24, 25]; therefore, another reasonable objective is to implement a new efficient high-resolution Godunov-type method based multiphysics software package relying on the proposed FSAC-PP unsteady, incompressible Navier-Stokes solver.

One of the main reasons for using multiphysics software packages is to gain scientific understanding about the physical behaviour of complex processes, and their mathematical descriptions in many practical cases. On the other hand, the computational cost might be too expensive in the daily engineering design process of microfluidic devices. However, different software packages are available on the market, such as ANSYS Multiphysics, CFD-ACE+, CoventorWare^{TM} and COMSOL Multiphysics packages, but there are shortages of quick and reliable high-resolution Godunov-type method based software tools to design microfluidic biomedical devices, and/or biosensors.

The aims of this project can be summarized as follows:

1. To develop and analyse a new efficient high-resolution Godunov-type numerical procedure for solving the unsteady, incompressible Navier-Stokes equations at (very) low and moderate Reynolds numbers. For constant and variable density flows, the proposed FSAC-PP numerical approach encompasses both artificial compressibility (AC) and fractional step (FS) pressure-projection (PP) methods of Chorin [3, 4] in a unified solution concept.

2. To implement a high-resolution Godunov-type method based FORTRAN 90/95 multiphysics software package relying on the proposed FSAC-PP unsteady, incompressible Navier-Stokes solver. This multiphysics software tool, called HIRECOM-MULTIPHYSICS Unified Code v1.0, might be a bridge between the market leader packages and the daily engineering demand in the design of microfluidic devices.

3. To perform, validate and investigate numerical simulations in conjunction with physical processes for constant and variable density flows, taking into account interface tracking, and the presence of magnetic field, and ssDNA flow.

1.3 Thesis Structure

The thesis is divided into ten chapters.

Chapter 1 describes the background and problem statement of the research work.

Chapter 2 provides an overview of the literature of models and numerical methods for microfluidics and its applications due to the author's background. The corresponding literature of the development for solving the unsteady, incompressible Navier-Stokes equations numerically has been reviewed only briefly.

Chapter 3 introduces the governing equations and computational methodology.

Chapter 4 describes a high-resolution Godunov-type numerical method development for solving the unsteady, incompressible Navier-Stokes equations. For constant and variable density flows, this chapter proposes a novel FSAC-PP solution method in conjunction with a characteristics-based (CB) scheme.

Chapter 5 presents numerical results of a pressure-driven laminar flow in a two-dimensional straight microfluidic channel at (very) low Reynolds numbers.

Chapter 6 presents numerical results of steady-state laminar and unsteady turbulent flows in a lid-driven square and cubical cavity at higher Reynolds numbers, respectively.

Chapter 7 presents numerical results of steady-state, incompressible, multi-species variable density flow in a three-dimensional Y-junction microfluidic channel.

Chapter 8 presents numerical results of steady-state, incompressible, non-isothermal, Newtonian and non-Newtonian biofluid flow in the presence of a uniform magnetic field in a two-dimensional microfluidic channel.

Chapter 9 presents numerical results of acoustic wave modelling and for solving unsteady, incompressible, laminar flow problem in a three-dimensional microfluidic T-channel.

Chapter 10 summarizes the conclusions of the present research work and the results of the contribution to the knowledge including the future work.

1.4 Publications

In the framework of the Ph.D. research project, one book chapter, two conference papers, furthermore six technical and two review reports have been written. The technical reports have been delivered to the scientific and industrial community of the 6^{th} European Commission Framework Program in the project DINAMICS, NMP4-CT-2007-026804. Review reports [1, 2] have been written and submitted at Cranfield University, and presentations have been held as a part of the Ph.D. program.

- **Book chapter:**

1. D. Mantzalis, K. Karantonis, N. Asproulis, **L. Könözsy**, and D. Drikakis, "Computational Modelling of Aqueous Environments in Micro and Nanochannels", pp. 135-161. Edited by G. Zuccheri and N. Asproulis, "Detection of Pathogens in Water Using Micro and Nano-Technology", *IWA Publishing*, London, New York, 2012.

- **Conference papers:**

1. **L. Könözsy**, D. Drikakis: "A Coupled High-Resolution Fractional-Step Artificial Compressibility and Pressure-Projection Formulation for Solving Incompressible Multi-Species Variable Density Flow Problem at Low Reynolds Numbers", *CD-ROM Proceedings of the 6th European Congress on Computational Methods in Applied Sciences and Engineering (ECCOMAS 2012)*, September 10-14, 2012, Vienna, Austria, Eds.: Eberhardsteiner, J.; Böhm, H.J.; Rammerstorfer, F.G., Publisher: Vienna University of Technology, Austria, ISBN: 978-3-9502481-9-7.

2. **L. Könözsy**, N. Asproulis, D. Drikakis, "High-Resolution Characteristics-based Godunov-type Method for Modelling Acoustic Waves in conjunction with Incompressible Microscale Laminar Flow", *The 15th International Conference on Fluid Flow Technologies, Conference on Modelling Fluid Flow (CMFF'2012)*, Budapest, Hungary, September 4-7, Vol. II, 2012, pp. 899-906, ISBN: 978-963-08-4588-5.

Chapter 2

Literature Review

2.1 Microfluidics and Its Applications

Microfluidics related to biological sciences is one of the most rapidly developing research fields and industries in the second part of the 20^{th} century, but mainly in the last two decades. Therefore, the key motivation of the present research work is to further develop high-resolution methods and implement a FORTRAN 90/95 multiphysics modelling software tools for microfluidic industrial applications. A number of books, monographs, articles, reports, and theses related to microfluidics and its applications have appeared since Richard P. Feynman held his famous speech "*There's Plenty of Room at the Bottom*" in 1959 [28, 29]. In this chapter, some of these writings have been collected, reviewed, and analyzed in relation to the topic of this thesis.

Biomedical engineering is an assembly between the medical and the engineering sciences. All aspects of knowledge in this field are involved to solve health care related problems including the development and design of biomedical devices. The biomechanics, physiological modelling, biomaterials, biomedical instrumentation and devices (e.g. biosensors), biotechnology, and bionanotechnology are related to biomedical engineering. Biofluid mechanics within biomechanics is a discipline to study the mechanical behaviour of various biological fluids. Biological fluids are called biofluids such as sweat, blood, urine, bile, blister and cyst fluids, or e.g. the breast milk. Most of the biomedical devices work with various biofluids, thus the material properties, and fluid dynamics behaviour of biofluids have been significant to describe them physically.

Mazumdar dealt with the fundamentals of biofluid mechanics studying a certain class of biological problems from the fluid mechanics point of view [30]. Governing equations of fluid- and circulatory biofluid mechanics, blood rheology and non-Newtonian fluid behaviour, models of biofluid flow and its applications (e.g. flows in capillary blood

vessels and in kidneys), as well as peristaltic flows, fluid mechanics of heart valves, and numerical methods for computational biofluid mechanics (CBM) were discussed. This book is an important resource to develop models for classical biological problems.

Twenty fields of biomedical engineering are encompassed in the first volume of "*The Biomedical Engineering Handbook*" edited by Bronzino [21]. Bioengineering is represented as a modern multidisciplinary science covering mathematical, physical, chemical, biological, engineering, and manufacturing details. Biomaterials and working principles of biomedical sensors were also described in [21] providing a comprehensive summary how to utilize material properties and how to use ideas to develop the basis of computational models.

In general, sensors convert information by a transducer for further use. Biomedical sensors are devices used for measuring physical and/or chemical quantities for biomedical applications. Three types of these sensors exist such as physical, chemical and bioanalytical sensors, where the third one is used for measuring quantities in biological systems. A possible classification of different types of biomedical sensors relying on their measured quantities can be shown in Table 2.1 [21, Neuman, Section V, p. 2].

Physical Sensors	Chemical Sensors
Mechanical	Electrochemical
Thermal	Gas
Optical	Photometric
Electric	Bioanalytic Sensors
Hydraulic	
Geometric	

Table 2.1: A possible classification of biomedical sensors [21, Neuman, Section V, p. 2].

Biomedical sensors may be defined as interfaces between a biological and an electrical system identifying physical and/or chemical information for biomedical applications. Pure physical sensors measure only physical quantities, and these can be mechanical for arterial blood flow, thermal for body temperature, electric for electric signals produced by the heart, hydraulic for blood pressure, and geometric for muscle displacement. Chemical sensors measure chemical quantities and these devices can be electrochemical sensors for sensing chemical concentration of blood glucose, gas sensors e.g. measuring oxygen concentration in the pulmonary system, and photometric sensors to detect chemical concentrations based on changes in light transmission, reflection or colour. Bioanalytic sensors also fall into the group of chemical sensors, but it can be classified as a separate category related only to biological systems. Biomedical sensors can be used for diagnostic or therapeutic purposes in clinical medicine, and for data collection in biomedical research (see more details in [21, Neuman, Section V, p. 2]).

2. Literature Review

Biotechnology involves diverse technologies and methods, such as techniques how to manipulate genetic materials, DNA technology, applications of nucleic acid chemistry, cancer detection and treatment, genome analysis, viral vaccines development, gene therapy, and several clinical measurements. Since, biotechnology covers different fields of biomedical engineering, therefore, Nill summarized definitions, phrases and terms to various specialists working in the field of biotechnology [31]. More details can be found about modern biotechnology by Yarmush, Toner, Plonsey and Bronzino [32], and about its applications by Moore and Zouridakis [33].

Computational power is permanently increasing, therefore, simulation of different physical phenomena from the quantum scale to the macroscale, called multiscale simulation, is in the centre of scientific and engineering interest for gaining deeper understanding of natural processes than ever before. Even nowadays, the computational cost is still time consuming, because multiscale problems consist of many unknowns. Engquist, Lötstedt and Runborg collected studies about multiscale simulation methods in science and engineering practice [34]. Homogenization techniques, stochastic differential equations, subdomain-subgrid models, multiscale discontinuous finite element Galerkin methods, multigrid techniques, micro- and macroscale coupling methods were described. Using multiscale methods is advantageous, because it provides possibilities to understand behaviour of different materials in smaller scales, which can help to develop constitutive relationships for macroscale modelling.

Drikakis and Kalweit discussed the flow and mass transport modelling techniques for a continuum simulation approach including non-Newtonian constitutive equations for shear stress transport, and quantum mechanics considering the Schrödinger equation [35]. The DSMC method and MD dynamics approaches for equilibrium and non-equilibrium were considered, and an MD case study of a protein molecule was presented in the field of computational nanotechnology [35]. Kumar, Hormes, and Leuschner encompassed the nanofabrication technologies and methods for biomedical applications [36]. Müller and Nicolau dealt with the microarray technology and its applications [37]. Enderle, Blanchard, and Bronzino's edited handbook is a comprehensive introduction to biomedical engineering [38]. Malsch summarized methods for biomedical nanotechnology [39].

The age of Micro-Electro-Mechanical Systems (MEMS) started in the late 1970s when silicon technology was extended to machining mechanical microdevices [25, p. 1], [40]. MEMS have characteristic length between 1 μm and 1 mm, and consist of electrical and mechanical elements. A few typical examples of MEMS are microsensors, micromotors, microvalves, micropumps, and microducts. Nguyen and Wereley provided an extensive summary of fundamentals and applications of microfluidics, including MEMS, in particular to fabrication and design of microfluidic devices, such as microvalves, micropumps, microflow sensors, microneedles, micromixers, microdispensers, microfilters, mi-

croseparators, and microreactors [25]. According to them, the MEMS is an inappropriate term, because the "*MicroSystem Technology*" (MST) with fluidic and optical components in microdevices would be a more accurate description [25, p. 1]. Biological applications of MEMS are called Biological-Micro-Electro-Mechanical Systems (Bio-MEMS). Since the MEMS term became the most widely used expression, it has been employed in this thesis following the general convention.

"*The MEMS Handbook*", edited by Gad-el-Hak [26], discussed several aspects of microfluidics and its applications, e.g. scaling of micromechanics devices, mechanical properties of MEMS materials, flow physics, coupling Flow-Structure-Thermal-Electrical (FSTE) domains, slip flow simulations based on LBM, liquid and gas flows modelling, bubble/drop transport in microchannels, and molecular-based simulations. The flow characteristics in microdevices are different from macrodevices due to the small characteristic sizes. The flow tends to be laminar, and it can occur with Newtonian or non-Newtonian medium. Surface forces, surface tension, and viscosity dominate instead of the inertial forces at low Reynolds numbers. Brownian-motion and Joule heating need to be taken into account depending on the microfluidic device. Electrophoresis can also occur which is an electrokinetic phenomenon where the motion of dispersed particles relative to a fluid is under the influence of a uniform electric field. When this motion occurs in a non-uniform electric field is called dielectrophoresis. The particles can be solid, liquid or gas bubbles with sizes in micro- and nanoscales. It may also be important to consider the magnetic field effect, for example, during modelling, designing, and fabricating of biofluid magnetic particle separators [26].

Microfluidics related to biomedical engineering enables a whole range of scientific and technological possibilities in the development of biomedical devices. Akay edited an encyclopedia on biomedical engineering [41] as a glossary of articles involving basic mathematical descriptions related to diverse biomedical disciplines. Webster edited a six-volume encyclopedia for medical devices and instrumentation [42] covering engineering, physics, and computer sciences related to the general areas of medicine. Since, it looks that mathematics has the possibility to describe natural processes numerically, modelling has gained importance in all sciences nowadays. The theory of probability is a tool to predict natural processes numerically and analyse random aspects of complex biological problems in a deductive way. For biomedical engineers, Enderle, Farden, and Krause introduced the probability theory in a series of books on [43, 44, 45] to present a unified treatment of the subject [43, p. ix]. Important examples can be found in this field, such as diffusion of ions across a cell membrane, biochemical reactions, mathematical modelling of DNA mutation processes, genetics, and biostatistics [43, p. 2].

The development of Bio-MEMS plays an important role in the design of microfluidic biomedical devices as well as the development of MEMS in the design of integrated

circuit. Ozkan and Heller discussed micro- and nanotechnologies for genomics and proteomics Bio-MEMS [46], in particular to recently developed, commercialized and miniaturized DNA microarray, DNA chip, Lab-on-a-Chip, and biosensor devices. The handbook, edited by Bashir and Wereley, dealt with biomolecular sensing, processing and analyzing methods [47] with special consideration to micro/nanoscale sensing and materials, such as biosensors and biochips [47, Vo-Dinh, pp. 3-20], cantilever arrays [47, Yue, Majumdar and Thundat, pp. 21-34], cell-based sensing technologies [47, Ozkan et al., pp. 55-92], and fabricating of Bio-MEMS [47, Nguyen, pp. 93-116]. This handbook also dealt with processing and integrated systems, such as Micro Total Analysis Systems (μTAS) [47, Lee, Collins, and Lemoff, pp. 135-158], Bio-MEMS for cellular manipulation [47, Li, Gómez-Sjöberg, and Bashir, pp. 187-204], and microfluidic tectonics [47, Gimm and Beebe, pp. 223-242]. Characterization of microfluidics is an important issue, such as particle dynamics in a dielectrophoretic device [47, Wereley and Whitacre, pp. 259-276], microflow simulation for electrokinetic and Lab-on-a-Chip applications [47, Erickson and Li, pp. 277-300], electroosmotic flow (EOF) in nanochannels [47, Conlisk and Singer, pp. 301-330], Nano-Particle Image Velocimetry (NPIV) measuring technique [47, Yoda, pp. 331-348], optical MEMS-based sensor development [47, Fourguette, Arik, and Wilson, pp. 349-370], and vascular cell responses to fluid shear stress [47, McCann, Webster, and Haberstroh, pp. 371-394]. More details can be found about Bio-MEMS technology and its applications by Wang and Soper [48]. These handbooks focused on the perspectives for the future as well in the fields of microfluidics, biomedical engineering, and medical science, therefore, it was necessary to reference them.

Waite and Fine considered the modern problems of applied biofluid mechanics starting from a brief historical introduction of the discipline [49]. The authors provided a substantial description of the topic with useful mathematical examples. Cardiovascular structure and function with clinical features, pulmonary anatomy and physiology, respiration, minute description of hematology and blood rheology, physiological behaviour of blood vessels, mechanics of heart valves, pulsatile flow in large arteries, flow and pressure measurements, and mathematical modelling issues were covered. The fluid dynamics researchers can also get a deep insight into the behaviour of blood elements when various infections, such as e.g. tuberculosis, mononucleosis, rubella, mumps, hepatitis, syphilis, and Human Immunodeficiency Virus (HIV) are present in the blood. As a matter of fact, it is difficult to develop continuum and/or molecular type constitutive blood models for understanding specific blood flow behaviour, therefore, the book's provided knowledge is indispensable in the development of biosensors to detect bacterial and/or viral infections.

The scientific interest has a significant growth from the beginning of the 21^{th} century, because it has become possible to produce cheap portable biomedical devices. Bruus investigated the theoretical aspects of microfluidics, in particular to complex flow pat-

terns, acoustofluidics, optofluidics, and nanofluidics [24]. Berthier dealt with digital microfluidic systems, electrowetting on dielectric (EWOD) microsystems in biological and chemical utilizations, physics of droplets, and multiphase microflows [50]. Tian and Finehout discussed the microfluidic techniques for biological applications [51]. Peterson and Bronzino assorted the biomechanical principles and its applications [52].

Non-Newtonian fluids show non-linear relationship between the shear stress and the shear strain rate [20]. Blood is a well-known non-Newtonian fluid. In order to model the rheological behaviour of blood flow in microfluidic biomedical devices, the literature for the blood biorheology has to be considered. Neofytou and Drikakis [20] made a first attempt to investigate the bifurcation of a two-dimensional blood flow, which occurs through a plane symmetric sudden expansion, employing Casson [53], a version of the Power-Law as proposed by Walburn and Schneck [54], and Quemada [55] non-Newtonian fluid models. The Casson constitutive equation exhibits discontinuous behaviour, therefore, its numerical discretization has to be made with particular consideration [20]. Walburn and Schneck's suggested Power-Law model employs a coefficient, a power exponent and a characteristic parameter which have to be adjusted for simulations. Quemada predicts the viscosity of a concentrated disperse system taking into account the shear rate and haematocrit level of the blood.

Himeno [56] investigated the blood flow in the human vascular system and pointed out that blood has a weak non-Newtonian effect in arteries, but strong one in capillaries. Grinberg and Karniadakis [57], furthermore, Grinberg et al. [58] considered the blood as a Newtonian medium in the arterial flow and in the virtual physiological human (VPH) arterial tree simulations. Sherwin et al. [59], Neofytou and Tsangaris [60], Ikbal et al. [61], and Kim et al. [62] considered non-Newtonian blood flow effects in their haemodynamics simulations. Ikbal et al. [61] investigated the unsteady response of blood flow through a stenosed artery in a magnetic field. Kim et al. [62] dealt with the multiphase non-Newtonian effects of pulsatile haemodynamics in a coronary artery using the Carreau-Yasuda [63], Quemada [64], Cross [65], and a modified version of Casson [66] biorheological fluid models. These constitutive equations are used mostly for a continuum approach of non-Newtonian blood flow in the field of biomedical engineering, computational haemodynamics, and arterial flow modelling. More details can be found about haemodynamic modelling and blood flow simulations by Franke et al. [67] and Sherwin et al. [68]. Bitsch [69] discussed blood flow in microchannels.

Tang et al. [70] investigated a non-Newtonian power-law electroosmotic flow (EOF) using a LBM in microchannels. The computational results were compared to analytical solutions in the pressure-driven non-Newtonian flow, therefore, this study provides possibility to analyse the effects of the power-law exponent for the rheological behaviour of non-Newtonian fluids in electroosmotic microflows [70].

Das and Chakraborty [71] derived an analytical solution for velocity, temperature, and concentration distribution of a non-Newtonian biofluid in electroosmotic microchannel flows. They emphasized that the biorheological behaviour of human blood can be described accurately with higher-order constitutive equations, because it shows non-linear, time-dependent, viscoelastic and neglectable Bingham plastic characteristics. Bingham plastic behaviour was described in detail by Fortin, Côté, and Tanguy [72]. Kornev and Neimark studied numerically the spontaneous penetration of viscoelastic fluids and biofluids into capillaries [73]. Xiao, Yang, and Pitchumani [74] proposed a generalized analysis of capillary flows in channels.

Chakraborty and Paul [75] developed a mathematical model to study the combined influences of electromagnetohydrodynamic forces in rectangular microchannels. The classical Poisson-Boltzmann equation was used to model the Electric Double Layer (EDL) effects. A parametric study emphasized that with the aid of a relatively low-magnitude magnetic field, a substantial augmentation in volumetric flow rates can be achieved. Non-dimensional parameters were investigated in the flow mechanism as well [75].

Das, Das, and Chakraborty [76] derived analytical solutions for the rate of DNA hybridization in electroosmotic and pressure-driven flows in a microchannel. Second-order hybridization kinetics was used for modelling the diffusion-reaction mechanism. Time-dependent reactive boundary conditions were considered at the channel walls for the species conservation taking into account advection and diffusion fluxes. According to this model, a saturation state of the hybridization reaction was obtained faster in a pure EOF compared to a pressure-driven flow [76]. These results can be used in the design of DNA microchips and microarrays in the field of bioanalytical chemistry for gene identification, DNA sequencing, and clinical diagnostics [76].

Das, Das, and Chakraborty [77] investigated the momentum, heat and solute transport during DNA hybridization considering electroosmotic effects and axial pressure gradients in a microchannel. An integrated thermofluidic analysis was presented for DNA hybridization combining electrokinetically and/or pressure-driven microflows. The bulk and surface transport of momentum, heat, and solute with the pertinent hybridization kinetics was encompassed in the model. According to the results, electrokinetic accumulation of DNA occurs in a shorter time (within a few seconds or minutes) than passive hybridization that could take sometimes several hours [77]. It was also observed that significantly higher DNA can be achieved at the capture probes by increasing the accumulation time. These results can be used to investigate the rate of DNA hybridization [77].

Shapiro et al. [78] studied an interface capturing dual-fluid xylene/water flow in a microchannel at low Reynolds number using the High-Resolution Characteristics-Based Scheme (HR-CBS); the SIMPLE (Semi-Implicit Method for Pressure-Linked Equations) pressure-velocity coupling (PVC) technique, and the Volume of Fluid (VOF) interface

tracking methods. This study focused on the interface positioning in xylene/water flows used in polymer membrane fabrication in microfluidics. The computational results were compared with the analytical solution. It was concluded that the HR-CBS model yields better resolution of the contact discontinuity than the PVC-VOF solutions. These methods can be used for *in-situ* polymer, and biological membrane fabrication [78].

Gargiuli et al. [79] dealt with microfluidic systems for *in-situ* formation of nylon 6,6 membranes. This study focused on glass fabricated structures used with adipoyl chloride and hexamethylenediamine in the organic and aqueous phases, in order to achieve nylon 6,6 interfacial polymerization [79]. Different geometries and flow rates were investigated at various Reynolds numbers to characterize flow stability and wall shear stress patterns. It was concluded that the best membranes were observed for Y-shaped structures with a 45° degree entry angle, curved input walls, and a single exit [79].

Chakraborty [80] described foremost the electroosmotically-driven capillary transport of non-Newtonian biofluids in rectangular microchannels. A semi-analytical mathematical model was developed to study the capillary filling employing a power law constitutive relationship for the blood biorheology. The main electroosmotic forces were derived by taking into account both liquid and vapour phases in the capillary. A case study was presented to illustrate the blood sample behaviour for different haematocrit levels. It was concluded that a) the meniscus dynamics has strongly dependence on the blood haematocrit level; b) higher capillary speed obtained at lower haematocrit levels; and c) higher haematocrit levels can be characterized with a capillary retracting phenomenon [80, p. 183]. Microfluidic applications of capillary-driven filling are e.g. Lab-on-a-Chip devices and Micro Total Analysis Systems (μTAS). These results can also be used for designing blood transporting microsystems, e.g. continuous blood glucose monitoring [80].

Chakraborty and Srivastava [81] developed a generalized model for a time periodic EOF with overlapping EDL. In this article, an analytical model was developed for analyzing time periodic EOF in nanochannels within the continuum regime, but the validity of the Boltzmann distribution of ionic charges was neglected. The charge density distributions were obtained from the individual ionic species conservation and from other thermochemical constraints. The potential distribution within the EDL were derived based on the charge density distribution. The derived model equations were coupled with the time-dependent Navier-Stokes equation under the overlapped EDL conditions. The results were validated in asymptotic limits of a thin EDL, and an analysis was carried out to investigate the influences of the electrical field frequency on the EOF [81].

Paul and Chakraborty [82] established a theoretical model to describe the wall effects in microchannel-based macromolecular separation under electromagnetohydrodynamic influences. The near-wall interaction potentials and the consequent migratory fluxes on the size-based separation of macromolecules were investigated. The results showed that

one can obtain a significantly faster separation under the application of a strong external magnetic field, however, it can also cause reduced resolution of the species. According to this theoretical analysis, one can select optimal combinations of the electrical and magnetic fields for microchannel-based macromolecular separation systems [82].

Benke, Shapiro, and Drikakis [10] proposed an efficient multiscale macromolecule modelling approach for single-stranded DNA (ssDNA) motion in fluid flow introducing a new FAst Linear COrrector (FALCO) algorithm. A multiscale modelling strategy was provided by using a meta-modelling approach based on the coupled solution of governing equations. A simplified mechanical macromolecule model was considered in the momentum equations, which enables individual macromolecule simulations at macroscopic time scales. The introduced new algorithm significantly improves computational efficiency and numerical stability compared to the widely used SHAKE algorithm. The ssDNA motion was tested in a lid-driven microcavity. This method can be used for simulating flow of macromolecules in biomedical devices, such as separators, detection and analysis systems [10]. More details can be found about biosensors, biomaterials and its biomedical applications in the thesis of Schneider [83], and in the books of Eggins [84], Wong and Bronzino [85], Mozafari [86], Takeuchi et al. [87], and Zourob et al. [88].

Novel microfluidic designs in conjunction with multiphysics modelling were reported by the Microfluidics Theory and Simulation Group (MIFTS) at the Technical University of Denmark, which can be found in the M.Sc. and Ph.D. theses of Jensen [89], Hansen [90], Brask [91], Bitsch [69], Goranovic [92], Olesen [93], Belmon [94], Heller [95], Jensen [96], Xueyu [97], Brask [98], Gregersen [99], Mikkelsen [100], Bitsch [101], Olesen [102], Hansen [103], Heller [104], Andersen [105], and Gregersen [106].

After reviewing briefly the literature of microfluidics and its applications, one may conclude that the design and mathematical modelling of physical processes are not common tasks in small-scale devices at low Reynolds numbers [107]. The research and development on numerical methods for solving the unsteady, incompressible Navier-Stokes equations at low Reynolds numbers are indispensable; for example, biomedical sciences need novel design and development of biomedical devices to treat special medical cases. Moreover, microfluidic devices can also be used for biomolecule recognition, detection of bacteria and viruses, drug development, and in-house medical diagnosis for cholesterol and blood glucose level [88]. Furthermore, other application fields may include environmental field monitoring, water protection, and food analysis for quality control. To get insight into the method development for solving the unsteady, incompressible Navier-Stokes equations, the literature has been reviewed briefly in the following section.

2.2 Numerical Methods for the Navier-Stokes Equations

The numerical solution of unsteady, incompressible Navier-Stokes equations is in the centre of interest using different approaches, because one of the major problems lies in that no independent partial differential equation exists for the pressure. Therefore, Chorin [3] introduced a perturbed continuity equation in order to decouple the continuity and momentum equations, which is a method known as "artificial compressibility method" (AC method). Another method was introduced by Chorin [4] and Temam [108], the fractional step (FS) pressure-projection (PP) method, which is based on the orthogonality theorem of Ladyzhenskaya [109]. According to this theorem, a vector field can be decomposed into a solenoidal (divergence-free) part and an irrotational part. The first FS estimates an intermediate velocity field neglecting the pressure term from the momentum equation. The second FS projects the predicted intermediate velocity field into a divergence-free (exact projection), or numerically nearly divergence-free (approximate projection) vector field updating the velocity values based on the solution of a pressure-Poisson equation. Kim and Moin [110] proposed an application of the FS method for solving three-dimensional, time-dependent, incompressible Navier-Stokes equations.

Eberle [111] developed a characteristics-based (CB) method for three-dimensional, compressible Euler equations using characteristic flux extrapolation, which was further extended by Drikakis, Govatsos, and Papatonis [112] to unsteady, incompressible Navier-Stokes equations using the high-resolution Godunov-type method. To overcome the stiffness of the solution of the AC method, Turkel [113] solved incompressible and low-speed compressible flow problems using preconditioning techniques, and the stiffness was eliminated from the system of eigenvalues. Bell, Colella, and Trangenstein [114] dealt with hyperbolic conservation laws using high-resolution method. Bell, Colella, and Glaz [115] developed a second-order exact projection method in conjunction with high-resolution Godunov-type methods for incompressible Navier-Stokes equations using an approximate Riemann solver. Colella [116] established a multidimensional upwind method for hyperbolic equations. Karniadakis, Israeli, and Orszag [117] introduced a spectral element discretization-based high-order time splitting method with consistent Neumann-type boundary conditions for the pressure field. Bell and Marcus [118] established a second-order projection method for variable-density, incompressible flows. Perot [119] accomplished a detailed analysis on the FS method to overcome the first-order temporal accuracy using generalized block LU decomposition of the governing equations for the primitive variables. For three-dimensional, incompressible flow, Drikakis [120] developed a parallel multiblock method using an AC formulation of Navier-Stokes equations. For unsteady, incompressible flow, Drikakis, Iliev, and Vassileva [7] proposed a non-linear full-multigrid (FMG) and full-approximation storage (FAS) algorithm coupled with the

AC method in conjunction with a high-resolution third-order upwind CB scheme. Almgren et al. [121] introduced a conservative and adaptive projection method for variable-density, incompressible Navier-Stokes equations.

Turkel [122] presented a comprehensive review in conjunction with preconditioning techniques. For avoiding numerical instabilities and stiffness of the AC method, Patel and Drikakis [123] investigated the effects of a preconditioning approach on accuracy and efficiency relating to high-resolution CB scheme for non-linear bifurcation phenomena. They concluded that the preconditioning technique reduced the number of multigrid cycles at high Reynolds numbers, but their approach did not have significant influence on the convergence rate of the process [123]. Shapiro and Drikakis [16, 6] derived CB schemes for variable density, incompressible and multi-species flows. Furthermore, Shapiro and Drikakis [78] investigated non-conservative and conservative formulations of CB numerical reconstructions, and presented an eigenvalue analysis for the aforementioned schemes. They emphasized that CB schemes provide high accuracy results in the wide range of applications for both Newtonian and non-Newtonian flows. In order to improve the efficiency of the AC method, Tang and Sotiropoulos [124] proposed a time-accurate approach for solving unsteady, incompressible flow problems on non-staggered grids using a second-order accurate hybrid FSAC method. Their approach is not fallen into the class of non-linear and non-oscillatory high-resolution methods, and the projection of the velocity field was carried out via a dual-time stepping AC formulation instead of solving a pressure-Poisson equation. Zamzamian and Razavi [125] introduced and investigated the numerical behaviour of the multidimensional CB scheme (MCB). They concluded that the MCB scheme shows faster convergence properties than the conventional CB scheme, and their results were validated against experimental data.

2.3 Perspectives of the Present Research Work

The present research work focuses on a new efficient numerical method development for solving the unsteady, incompressible Navier-Stokes equations, in particular to low Reynolds numbers. A reliable high-resolution Godunov-type method based multiphysics software tool has been implemented for providing input parameters to designers. The present research work can have a positive outcome for both academic and industrial sides, because a multiphysics software tool can open perspectives of novel microfluidic designs and inventions. The numerical procedure developed in this thesis can be further extended to other cases that may also be used in different microfluidic industrial applications.

Chapter 3

Governing Equations and Computational Methodology

3.1 Governing Equations

3.1.1 Validity of Continuum Hypothesis

Continuum modelling of fluid flow is a mathematical flow field description approach, where the unknown physical quantities are assumed to be continuously differentiable functions in the governing equations. For focusing on numerical method development and microfluidic applications, it is important to determine the validity of the continuum hypothesis. The continuum modelling approach is limited, because it breaks down below a certain length scale of the physical problem, which is relevant from the multiphysics CFD modelling point of view. To determine this limitation, the atomistic length scale of the fluid and the typical length scale of the investigated microfluidic system have to be compared [95, p. 8]. The average interatomic space is defined [95, p. 8] as

$$\lambda_A = \left(\frac{M_A}{\rho N_A} \right)^{\frac{1}{3}}, \tag{3.1}$$

where ρ is the fluid density, $N_A = 6.022 \cdot 10^{23}\ 1/mol$ is the Avogadro's number, and M_A is the molar mass. According to Heller [95, p. 8], for investigating microfluidic systems under the contiuum hypothesis, the characteristic length scale of the fabricated system has to be a bigger value than the average interatomic space λ_A [95, p. 8]. After satisfying this criterion, the mass, momentum, energy and species transport equations of continuum physics are considered to be valid for multiphysics problems in microfluidic systems.

3.1.2 System of Governing Equations

We focus on mathematical investigations under the continuum hypothesis, therefore, the mass, momentum, energy and species transport equations consist of the governing equations [27, pp. 7-49]. For fluid flow continuum modelling, the continuity equation is derived from the principle of conservation of mass [22], which can be written as

$$\frac{\partial \rho}{\partial t} + \nabla \cdot (\rho \mathbf{u}) = 0, \tag{3.2}$$

where ρ is the fluid density, and $\mathbf{u}$ is the velocity vector. The conservation of momentum in its general form, which is also known as Cauchy equation, is derived from Newton's second law for fluid motion as

$$\rho \frac{D\mathbf{u}}{Dt} = \rho \mathbf{g} + \nabla \cdot \underline{\underline{\sigma}} + \rho \mathbf{f}, \tag{3.3}$$

where D/Dt denotes the total or substantial derivative, $\mathbf{g}$ is the gravity field, $\underline{\underline{\sigma}}$ is the total stress tensor [27, pp. 7-49], and $\mathbf{f}$ represents external (additional) forces. The total stress tensor $\underline{\underline{\sigma}}$ consists of two main parts as

$$\underline{\underline{\sigma}} = -p\underline{\underline{\mathrm{I}}} + \underline{\underline{\tau}} = \begin{bmatrix} \sigma_x & \tau_{xy} & \tau_{xz} \\ \tau_{yx} & \sigma_y & \tau_{yz} \\ \tau_{zx} & \tau_{zy} & \sigma_z \end{bmatrix} = \begin{bmatrix} -p+\tau_{xx} & \tau_{xy} & \tau_{xz} \\ \tau_{yx} & -p+\tau_{yy} & \tau_{yz} \\ \tau_{zx} & \tau_{zy} & -p+\tau_{zz} \end{bmatrix}, \tag{3.4}$$

where the first part represents the surface forces with the hydrodynamic pressure p, $\underline{\underline{\mathrm{I}}}$ is the unit tensor, and the second part is the viscous stress tensor $\underline{\underline{\tau}}$. The viscous part $\underline{\underline{\tau}}$ plays an important role to derive various momentum equations for different fluid flow problems; therefore, it has to be chosen according to the constitutive equation that is going to be solved. For an ideal fluid, the viscous stress tensor

$$\underline{\underline{\tau}} = 0 \tag{3.5}$$

is equal to zero; and by substitution of Eq. (3.5) into Eq. (3.4), the Eq. (3.3) yields the Euler momentum equation for inviscid and incompressible fluid in a vector form as

$$\rho \frac{D\mathbf{u}}{Dt} = \rho \mathbf{g} - \nabla p + \rho \mathbf{f}. \tag{3.6}$$

For a Newtonian viscous incompressible fluid, the Navier-Stokes momentum equation is valid, which is described in details in the following subsection. The relationship between the continuum control volume *(V)* and the viscous stresses can be seen in Figure 3.1.

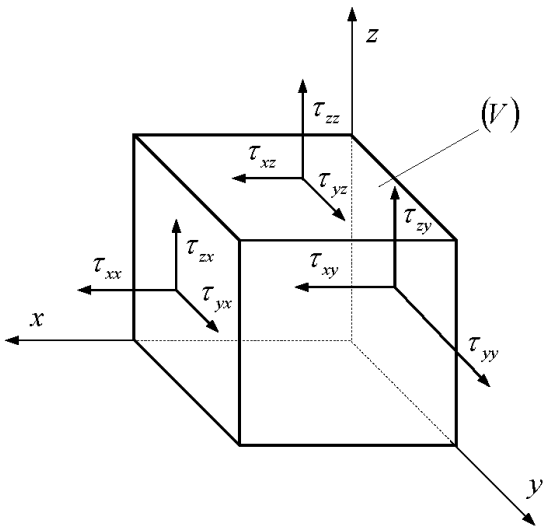

Figure 3.1: Continuum control volume (V) and viscous stresses.

The principle of conservation of energy is written as

$$\rho\frac{DE}{Dt} = -\nabla\cdot(p\mathbf{u}) + \nabla\cdot\left(\underline{\underline{\tau}}\cdot\mathbf{u}\right) + \nabla\cdot(\lambda\nabla\vartheta) + \varphi_E + \varphi_D \tag{3.7}$$

where the specific energy E is the sum of the internal energy i, kinetic energy $k = \frac{1}{2}\rho\mathbf{u}^2$ and potential energy U; and ϑ is the temperature, φ_E is the source of internal heat, and

$$\varphi_D = \underline{\underline{\tau}}\cdot\cdot(\nabla\otimes\mathbf{u}) \tag{3.8}$$

is the dissipation function. In order to obtain conservation equations for the internal energy and the temperature field, the mechanical kinetic energy equation has to be used [22]; which is derived from the general momentum equation (3.3) multiplying it by the velocity vector $\mathbf{u}$, and we obtain the following

$$\rho\frac{Dk}{Dt} = \rho\mathbf{u}\cdot\mathbf{g} - \mathbf{u}\cdot\nabla p + \mathbf{u}\cdot\left(\nabla\cdot\underline{\underline{\tau}}\right) + \rho\mathbf{u}\cdot\mathbf{f} \tag{3.9}$$

transport equation for the mechanical kinetic energy. By subtracting Eq. (3.9) from the conservation of energy equation (3.7), the changes of internal energy is obtained as

$$\rho\frac{Di}{Dt} = -p\,(\nabla\cdot\mathbf{u}) + \nabla\cdot(\lambda\nabla\vartheta) + \varphi_E + \underline{\underline{\tau}}\cdot\cdot(\nabla\otimes\mathbf{u}) - \rho\mathbf{u}\cdot\mathbf{f}. \tag{3.10}$$

For an incompressible fluid, the internal energy is expressed as $i = c_p\vartheta$ and taking into account the divergence-free constraint ($\nabla\cdot\mathbf{u} = 0$), the conservation of energy for the tem-

perature field can be written as

$$\rho c_p \frac{D\vartheta}{Dt} = \nabla \cdot (\lambda \nabla \vartheta) + \varphi_E + \underline{\underline{\tau}} \cdot\cdot (\nabla \otimes \mathbf{u}) - \rho \mathbf{u} \cdot \mathbf{f} \tag{3.11}$$

where c_p is the specific heat at constant pressure. The conservation of species for a multicomponent fluid is

$$\frac{\partial c_i}{\partial t} + \nabla \cdot \mathbf{J}_i = 0 \tag{3.12}$$

where c_i is the concentration of i^{th} species, and $\mathbf{J}_i$ is the i^{th} species flux.

Magnetohydrodynamic effects can occur in microfluidic systems [100], therefore, the Maxwell's equations have to be taken into account [126, p. 928]. The first law is Faraday's law of induction [126, p. 928], which is

$$\nabla \times \mathbf{E} + \frac{\partial \mathbf{B}}{\partial t} = \mathbf{0}, \tag{3.13}$$

where $\mathbf{E}$ is the electric- and $\mathbf{B}$ is the magnetic field. The second law is Ampere's circuital law [126, p. 928], which is

$$\nabla \times \mathbf{H} + \frac{\partial \mathbf{D}}{\partial t} = \mathbf{J}_e, \tag{3.14}$$

where $\mathbf{H}$ is the magnetic field intensity, $\mathbf{D}$ is the electric flux density (which is also called electric displacement field), and $\mathbf{J}_e$ is the (particle) current density vector. The magnetic field is divergence-free [126, p. 928] as

$$\nabla \cdot \mathbf{B} = 0, \tag{3.15}$$

and the divergence of the electric flux density [126, p. 928]

$$\nabla \cdot \mathbf{D} = \rho_e \tag{3.16}$$

is equal to the electric charge density ρ_e. For magnetohydrodynamic flows, the electromagnetic force appears in the momentum equation (3.3) as an external (additional) force [126, p. 931] as

$$\mathbf{f} = \mathbf{J}_e \times \mathbf{B} + e\mathbf{E} = (\nabla \times \mathbf{B}) \times \mathbf{B} + e\mathbf{E} \tag{3.17}$$

where e is the isolated electric charge. For electrokinetically-driven flow, an additional

Poisson-type equation has to be solved for the electric potential [90, p. 7] as

$$\nabla^2 \psi = -\frac{1}{\varepsilon}\rho_e, \tag{3.18}$$

where ψ is the electric field potential, ε is the dielectric constant, and ρ_e is the electric charge density. An additional elecrokinetic force appears in Eq. (3.3), which was given by Stratton [127] as

$$\mathbf{f}_{EK} = \rho_e \mathbf{E} - \frac{1}{2}\mathbf{E}\cdot\mathbf{E}\cdot\varepsilon_0\nabla\varepsilon + \frac{\varepsilon_0}{2}\nabla\left(\rho\frac{\partial\varepsilon}{\partial\rho}\mathbf{E}\cdot\mathbf{E}\right), \tag{3.19}$$

where $\mathbf{f}_{EK}$ is the electrokinetic body force [23, p. 263]. For electrokinetically-driven flow, the charged species fluxes for a multicomponent fluid [23, p. 263] is

$$\mathbf{J}_i = -D_i\nabla c_i + c_i\left(\mathbf{u} + \mu_{EK,i}\mathbf{E}\right) = -D_i\nabla c_i + c_i\mathbf{u} + c_i\mu_{EK,i}\mathbf{E}, \tag{3.20}$$

therefore, Eq. (3.12) yields [23, p. 263]

$$\frac{\partial c_i}{\partial t} + \nabla\cdot(c_i\mathbf{u}) = D_i\nabla^2 c_i - \nabla\cdot(c_i\mu_{EK,i}\mathbf{E}). \tag{3.21}$$

More details about the governing equation of multiphysics can be found in the books of Chung [126], Drikakis and Rider [27], and Karniadakis, Beskok, and Aluru [23].

3.1.3 The Navier-Stokes Equations

The Navier-Stokes momentum equation in a vector form can be derived from the general momentum equation (3.3) by substitution of the following

$$\underline{\underline{\tau}} = 2\mu\underline{\underline{\mathrm{S}}} - \frac{2}{3}\mu\left(\nabla\cdot\mathbf{u}\right)\cdot\underline{\underline{\mathrm{I}}} = \mu\left(\mathbf{u}\otimes\nabla + \nabla\otimes\mathbf{u}\right) - \frac{2}{3}\mu\left(\nabla\cdot\mathbf{u}\right)\cdot\underline{\underline{\mathrm{I}}} \tag{3.22}$$

viscous stress tensor into the equation of the total stress tensor (3.4), which yields

$$\underline{\underline{\sigma}} = -p\underline{\underline{\mathrm{I}}} + 2\mu\underline{\underline{\mathrm{S}}} - \frac{2}{3}\mu\left(\nabla\cdot\mathbf{u}\right)\cdot\underline{\underline{\mathrm{I}}} = -p\underline{\underline{\mathrm{I}}} + \mu\left(\mathbf{u}\otimes\nabla + \nabla\otimes\mathbf{u}\right) - \frac{2}{3}\mu\left(\nabla\cdot\mathbf{u}\right)\cdot\underline{\underline{\mathrm{I}}} \tag{3.23}$$

as a relationship between the total and viscous stress tensors, where μ is the dynamic viscosity of the fluid, and $\underline{\underline{\mathrm{S}}}$ is the rate of strain (deformation) tensor. The viscous stress tensor (3.22) is an extension of the Hooke's law to Newtonian viscous compressible fluid

by Navier and Stokes. The divergence of the total stress tensor (3.23) yields

$$\nabla \cdot \underline{\underline{\sigma}} = -\nabla p + \mu \nabla^2 \mathbf{u} - \frac{\mu}{3} \nabla (\nabla \cdot \mathbf{u}), \tag{3.24}$$

consequently, the Navier-Stokes momentum equation based on the general momentum equation (3.3) can be written in a vector form as

$$\rho \frac{D\mathbf{u}}{Dt} = \rho \mathbf{g} - \nabla p + \mu \nabla^2 \mathbf{u} - \frac{\mu}{3} \nabla (\nabla \cdot \mathbf{u}) + \rho \mathbf{f}. \tag{3.25}$$

Assuming that the fluid is incompressible, and we consider constant density, thus

$$\nabla \cdot \mathbf{u} = 0 \tag{3.26}$$

the divergence-free velocity field and the Navier-Stokes momentum equation for incompressible fluid in a conservative and vector form are obtained as

$$\rho \frac{\partial \mathbf{u}}{\partial t} + \nabla \cdot (\rho \mathbf{u} \otimes \mathbf{u}) = \rho \mathbf{g} - \nabla p + \mu \nabla^2 \mathbf{u} + \rho \mathbf{f}. \tag{3.27}$$

The surface and body forces acting on fluid particles are summarized in Table 3.1.

Surface forces	Body forces
Pressure forces	Gravity force
Viscous forces	Centrifugal force
	Coriolis force
	Electromagnetic force

Table 3.1: Types of forces acting on fluid particles [22, p. 15].

3.2 Numerical Solution of the Navier-Stokes Equations

3.2.1 Artificial Compressibility (AC) Method

For solving three-dimensional, Newtonian, unsteady, incompressible laminar flow problems, the governing equations of conservation of mass and momentum, using conservative flux form and vector notation, are written as follows

$$\nabla \cdot \mathbf{u} = 0, \tag{3.28}$$

$$\frac{\partial \mathbf{u}}{\partial t} + \nabla \cdot (\mathbf{u} \otimes \mathbf{u}) = \mathbf{g} - \frac{1}{\rho}\nabla p + \upsilon \nabla^2 \mathbf{u} + \mathbf{f}, \tag{3.29}$$

on a domain $\partial\Gamma$, where t is the physical time, $\mathbf{u}$ is the velocity field, $\mathbf{g}$ is the gravity force, p is the hydrodynamic pressure, ρ is the fluid density, υ is the kinematic viscosity of the fluid, and $\mathbf{f}$ represents external forces. For non-dimensionalising, the following

$$t^* = \frac{t u_\infty}{L},\ X = \frac{x}{L},\ Y = \frac{y}{L},\ Z = \frac{z}{L},$$

$$U = \frac{u}{u_\infty},\ V = \frac{v}{u_\infty},\ W = \frac{w}{u_\infty},$$

$$\mathbf{G} = \frac{L}{u_\infty^2}\mathbf{g},\ P = \frac{p}{\rho_\infty u_\infty^2},\ Re = \frac{L u_\infty}{\upsilon},\ \mathbf{F} = \frac{L}{u_\infty^2}\mathbf{f},$$

dimensionless quantities are introduced for time, spatial coordinates, velocity components, gravity force, pressure field, and external forces, where L, u_∞, ρ_∞ are constant reference quantities for the characteristic length, velocity and fluid density; and Re is the Reynolds number, which is a ratio between momentum transported by convection and by viscous diffusion. Using these quantities and neglecting the gravity force field $\mathbf{G}$, the dimensionless governing equations of Newtonian incompressible fluid flow are written as

$$\nabla \cdot \mathbf{U} = 0, \tag{3.30}$$

$$\frac{\partial \mathbf{U}}{\partial t^*} + \nabla \cdot (\mathbf{U} \otimes \mathbf{U}) = -\nabla P + \frac{1}{Re}\nabla^2 \mathbf{U} + \mathbf{F}. \tag{3.31}$$

Since an independent equation for the pressure field does not exist, Chorin [3] introduced a perturbed continuity equation in order to decouple the continuity and momentum equations. The perturbed continuity equation contains a pseudo-time derivative for the

pressure that has no physical meaning until the steady-state solution is achieved. For unsteady, incompressible fluid flows, pseudo-time derivatives are also introduced for the velocity components in the scalar momentum equations, therefore, the following

$$\frac{1}{\beta}\frac{\partial P}{\partial \tau} = -\nabla \cdot \mathbf{U}, \tag{3.32}$$

$$\frac{\partial \mathbf{U}}{\partial \tau} = -\frac{\partial \mathbf{U}}{\partial t^*} - \nabla \cdot (\mathbf{U} \otimes \mathbf{U}) - \nabla P + \frac{1}{Re}\nabla^2 \mathbf{U} + \mathbf{F}, \tag{3.33}$$

hyperbolic system of partial differential equations has to be solved, where

$$\beta \gg \left(1 + \frac{4L}{Re}\right)^2 - 1 \tag{3.34}$$

is the artificial compressibility parameter (AC parameter) for low-speed laminar flows related to the numerical convergence, and τ is the pseudo-time step [27].

The system of governing equations (3.32)-(3.33) are solved iteratively in pseudo-time until the divergence-free continuity equation (3.30) is satisfied [16, 6]. This method has major value for solving steady-state (stationary) flow problems, but for unsteady and/or low Reynolds number flows, the stability conditions of the dual-time stepping procedure, and the choice of AC parameter may become too restrictive, which could lead to a slow convergence rate [5]. For avoiding numerical instabilities and stiffness of the AC method, Patel and Drikakis [123] investigated the effects of a preconditioning approach on accuracy and efficiency relating to high-resolution characteristics-based (CB) scheme for non-linear bifurcation phenomena. They concluded that their preconditioning technique reduced the number of multigrid cycles at high Reynolds numbers, but their approach did not have a significant influence on the convergence rate of the AC process.

3.2.2 Fractional-Step (FS) Pressure-Projection (PP) Method

For solving unsteady, incompressible Navier-Stokes equations, Chorin [4] and Temam [108] introduced a fractional step (FS) pressure-projection (PP) method, which is based on the orthogonality theorem of Ladyzhenskaya [109]; which is also called Helmholtz-Hodge decomposition or Hodge decomposition in the literature [3, 4, 115, 118, 121, 128]. According to this theorem, a vector field can be decomposed into a solenoidal (divergence-free) part and an irrotational part as

$$\mathbf{U} = \mathbf{U}_{solenoidal} + \mathbf{U}_{irrotational}, \tag{3.35}$$

where the irrotational vector field can be written as

$$\mathbf{U}_{irrotational} = \nabla\Phi, \tag{3.36}$$

where Φ is a scalar (potential) function, and the scalar components of gradient Φ provide the scalar components of the irrotational vector field. According to the potential theory, a scalar function Φ exists in any case of an irrotational vector field [109], because the following vector identity is valid as

$$\nabla \times \mathbf{U}_{irrotational} = \nabla \times (\nabla\Phi) = 0. \tag{3.37}$$

Using Eq. (3.36) and re-arranging Eq. (3.35), we obtain that

$$\mathbf{U}_{solenoidal} = \mathbf{U} - \nabla\Phi, \tag{3.38}$$

and since, the solenoidal vector field is divergence-free, therefore, taking the divergence of Eq. (3.38), the following

$$\nabla^2\Phi = \nabla \cdot \mathbf{U} \tag{3.39}$$

equality is gained for the potential function Φ, which is a second-order elliptical partial differential equation, which is also called Poisson-equation. Relying on the above described Helmholtz-Hodge decomposition, Chorin [4] constructed a pressure-Poisson equation considering the pressure as a potential function of the irrotational velocity field. Since, the correct pressure field is unknown in the momentum equation at time level n, therefore, the continuity equation is not satisfied as follows

$$\nabla \cdot \mathbf{U}^{(n)} \neq 0, \tag{3.40}$$

but considering the solenoidal velocity field as $\mathbf{U}^{(n+1)} = \mathbf{U}_{solenoidal}$ at time level $n+1$, the continuity equation will be satisfied as

$$\nabla \cdot \mathbf{U}^{(n+1)} = 0. \tag{3.41}$$

In consequence of Eq. (3.38), the first fractional step estimates an intermediate velocity field $\hat{\mathbf{U}}$ neglecting the pressure term from the momentum equation. To determine this intermediate vector field, Chorin [4] employed a first-order backward Euler temporal discretization, and all quantities were considered in the right hand side of the momentum equation at time level n. After re-arrangement, Eq. (3.31) can also be written in a semi-

discrete form as

$$\frac{\hat{\mathbf{U}}-\mathbf{U}^{(n)}}{\Delta t^*} = -\nabla\cdot(\mathbf{U}\otimes\mathbf{U})^{(n)} + \frac{1}{Re}\nabla^2\mathbf{U}^{(n)} + \mathbf{F}^{(n)}, \tag{3.42}$$

and intermediate velocity field can be expressed as

$$\hat{\mathbf{U}} = \mathbf{U}^{(n)} + \Delta t^* \left[-\nabla\cdot(\mathbf{U}\otimes\mathbf{U}) + \frac{1}{Re}\nabla^2\mathbf{U} + \mathbf{F}\right]^{(n)}. \tag{3.43}$$

In consequence of Eq. (3.39) in the second fractional step, the pressure field is computed to update the velocity field taking into account the divergence-free constraint based on Eq. (3.41). Furthermore, taking the divergence of

$$\frac{\mathbf{U}^{(n+1)}-\hat{\mathbf{U}}}{\Delta t^*} = -\nabla P^{(n+1)} \tag{3.44}$$

the semi-discrete equation, a second-order elliptical partial differential equation (Poisson-equation) is obtained for the pressure [4, 119] at time level $n+1$ as

$$\nabla^2 P^{(n+1)} = \frac{1}{\Delta t^*}\nabla\cdot\hat{\mathbf{U}}. \tag{3.45}$$

Similarly to Eq. (3.38), the second fractional step projects the predicted intermediate velocity field (3.43) into a divergence-free (exact projection), or numerically nearly divergence-free (approximate projection) vector field, updating the velocity values relying on the solution of the pressure-Poisson equation (3.45) as

$$\mathbf{U}^{(n+1)} = \hat{\mathbf{U}} - \Delta t^*\nabla P^{(n+1)}. \tag{3.46}$$

For solving unsteady, incompressible Navier-Stokes equations, the pressure-Poisson equation (3.45) has to be solved to estimate the pressure field values at each time level, then the velocity field has to be updated by using Eq. (3.46) in order to satisfy the divergence-free constraint (3.30). For the numerical treatment of two-dimensional Navier-Stokes equations, Chorin [4] employed a version of Peaceman-Rachford scheme proposed by Wilkes [129] using the Finite Difference Method (FDM) based spatial discretization. For solving the pressure-Poisson equation, Chorin [4] used the Successive Point Over-Relaxation (S.P.O.R.) method in conjunction with Dufort-Frankel scheme. In order to describe Chorin's and Temam's FS-PP method in practice, a two-dimensional numerical solution example has been presented in this subsection.

The spatial non-linear convective/advective term in the right hand side of Eq. (3.42) has been discretized by using Torrance's [130] non-oscillatory spatial approach on a col-

located grid (see Figure 3.3). The second-order diffusive term in Eq. (3.42) has been discretized by employing second-order accurate central difference approximations. Both of the non-linear convective/advective and the linear second-order diffusive terms have been treated explicitly, and the pressure-Poisson equation has been solved implicitly by applying the Gauss-Seidel-type Successive Over-Relaxation (S.O.R.) method. More details can be found about the practical applications of spatial discretization strategy in the works of Torrance and Rockett [131], Kopecky and Torrance [132], Raithby and Torrance [133], and Chuen-Yen Chow [134, pp. 336-359].

For two-dimensional incompressible fluid flow problem, the scalar continuity equation in dimensionless form is

$$\frac{\partial U}{\partial X}+\frac{\partial V}{\partial Y}=0, \tag{3.47}$$

and the two scalar dimensionless Navier-Stokes momentum equations are

$$\frac{\partial U}{\partial t^*}+\frac{\partial\left(U^2\right)}{\partial X}+\frac{\partial\left(VU\right)}{\partial Y}=-\frac{\partial P}{\partial X}+\frac{1}{Re}\left(\frac{\partial^2 U}{\partial X^2}+\frac{\partial^2 U}{\partial Y^2}\right), \tag{3.48}$$

$$\frac{\partial V}{\partial t^*}+\frac{\partial\left(UV\right)}{\partial X}+\frac{\partial\left(V^2\right)}{\partial Y}=-\frac{\partial P}{\partial Y}+\frac{1}{Re}\left(\frac{\partial^2 V}{\partial X^2}+\frac{\partial^2 V}{\partial Y^2}\right). \tag{3.49}$$

According to the example presented hereby, the discretized continuity equation has been satisfied using first-order backward spatial discretization scheme as follows

$$\frac{U_{i,j}^{(n+1)}-U_{i-1,j}^{(n+1)}}{\Delta X}+\frac{V_{i,j}^{(n+1)}-V_{i,j-1}^{(n+1)}}{\Delta Y}=0 \tag{3.50}$$

at time level $n+1$, because it is assumed that the continuity equation is not satisfied at time level n relying on Chorin's method [4]. In the first fractional step, two semi-discrete scalar momentum equation using backward Euler time-discretization based on Eq. (3.42) and after the re-arrangement of Eqs. (3.48)-(3.49) can be written as

$$\frac{\hat{U}_{i,j}-U_{i,j}^{(n)}}{\Delta t^*}=-\left[\frac{\partial\left(U^2\right)}{\partial X}\right]_{i,j}^{(n)}-\left[\frac{\partial\left(VU\right)}{\partial Y}\right]_{i,j}^{(n)}+\frac{1}{Re}\left(\frac{\partial^2 U}{\partial X^2}+\frac{\partial^2 U}{\partial Y^2}\right)_{i,j}^{(n)}, \tag{3.51}$$

$$\frac{\hat{V}_{i,j}-V_{i,j}^{(n)}}{\Delta t^*}=-\left[\frac{\partial\left(UV\right)}{\partial X}\right]_{i,j}^{(n)}-\left[\frac{\partial\left(V^2\right)}{\partial Y}\right]_{i,j}^{(n)}+\frac{1}{Re}\left(\frac{\partial^2 V}{\partial X^2}+\frac{\partial^2 V}{\partial Y^2}\right)_{i,j}^{(n)}, \tag{3.52}$$

where the non-linear advective terms have been discretized by using forward and back-

ward average velocities [130, 131, 132, 133, 134, pp. 336-359] in the following ways

$$\left[\frac{\partial\left(U^2\right)}{\partial X}\right]_{i,j}^{(n)} \approx -\frac{\bar{U}_{b,X}^{(n)}+\left|\bar{U}_{b,X}^{(n)}\right|}{2\Delta X}U_{i-1,j}^{(n)}+$$

$$+\frac{\bar{U}_{f,X}^{(n)}+\left|\bar{U}_{f,X}^{(n)}\right|-\bar{U}_{b,X}^{(n)}+\left|\bar{U}_{b,X}^{(n)}\right|}{2\Delta X}U_{i,j}^{(n)}+\frac{\bar{U}_{f,X}^{(n)}+\left|\bar{U}_{f,X}^{(n)}\right|}{2\Delta X}U_{i+1,j}^{(n)}, \tag{3.53}$$

$$\left[\frac{\partial\left(VU\right)}{\partial Y}\right]_{i,j}^{(n)} \approx -\frac{\bar{V}_{b,Y}^{(n)}+\left|\bar{V}_{b,Y}^{(n)}\right|}{2\Delta Y}U_{i,j-1}^{(n)}+$$

$$+\frac{\bar{V}_{f,Y}^{(n)}+\left|\bar{V}_{f,Y}^{(n)}\right|-\bar{V}_{b,Y}^{(n)}+\left|\bar{V}_{b,Y}^{(n)}\right|}{2\Delta Y}U_{i,j}^{(n)}+\frac{\bar{V}_{f,Y}^{(n)}+\left|\bar{V}_{f,Y}^{(n)}\right|}{2\Delta Y}U_{i,j+1}^{(n)}, \tag{3.54}$$

$$\left[\frac{\partial\left(UV\right)}{\partial X}\right]_{i,j}^{(n)} \approx -\frac{\bar{U}_{b,X}^{(n)}+\left|\bar{U}_{b,X}^{(n)}\right|}{2\Delta X}V_{i-1,j}^{(n)}+$$

$$+\frac{\bar{U}_{f,X}^{(n)}+\left|\bar{U}_{f,X}^{(n)}\right|-\bar{U}_{b,X}^{(n)}+\left|\bar{U}_{b,X}^{(n)}\right|}{2\Delta X}V_{i,j}^{n}+\frac{\bar{U}_{f,X}^{(n)}+\left|\bar{U}_{f,X}^{(n)}\right|}{2\Delta X}V_{i+1,j}^{(n)}, \tag{3.55}$$

$$\left[\frac{\partial\left(V^2\right)}{\partial Y}\right]_{i,j}^{(n)} \approx -\frac{\bar{V}_{b,Y}^{(n)}+\left|\bar{V}_{b,Y}^{(n)}\right|}{2\Delta Y}V_{i,j-1}^{(n)}+$$

$$+\frac{\bar{V}_{f,Y}^{(n)}+\left|\bar{V}_{f,Y}^{(n)}\right|-\bar{V}_{b,Y}^{(n)}+\left|\bar{V}_{b,Y}^{(n)}\right|}{2\Delta Y}V_{i,j}^{(n)}+\frac{\bar{V}_{f,Y}^{(n)}+\left|\bar{V}_{f,Y}^{(n)}\right|}{2\Delta Y}V_{i,j+1}^{(n)}, \tag{3.56}$$

where the forward and backward average velocities for velocity component U are

$$\bar{U}_{f,X}^{(n)}=\frac{U_{i,j}^{(n)}+U_{i+1,j}^{(n)}}{2}, \tag{3.57}$$

$$\bar{U}_{b,X}^{(n)}=\frac{U_{i,j}^{(n)}+U_{i-1,j}^{(n)}}{2}, \tag{3.58}$$

and for velocity component V are

$$\bar{V}_{f,Y}^{(n)}=\frac{V_{i,j}^{(n)}+V_{i,j+1}^{(n)}}{2}, \tag{3.59}$$

$$\bar{V}_{b,Y}^{(n)}=\frac{V_{i,j}^{(n)}+V_{i,j-1}^{(n)}}{2}. \tag{3.60}$$

The second-order viscous terms have been approximated by using second-order accurate central difference schemes as

$$\left(\frac{\partial^2 U}{\partial X^2}+\frac{\partial^2 U}{\partial Y^2}\right)_{i,j}^{(n)} \approx \frac{U_{i+1,j}^{(n)}-2U_{i,j}^{(n)}+U_{i-1,j}^{(n)}}{(\Delta X)^2}+\frac{U_{i,j+1}^{(n)}-2U_{i,j}^{(n)}+U_{i,j-1}^{(n)}}{(\Delta Y)^2}, \tag{3.61}$$

$$\left(\frac{\partial^2 V}{\partial X^2}+\frac{\partial^2 V}{\partial Y^2}\right)_{i,j}^{(n)} \approx \frac{V_{i+1,j}^{(n)}-2V_{i,j}^{(n)}+V_{i-1,j}^{(n)}}{(\Delta X)^2}+\frac{V_{i,j+1}^{(n)}-2V_{i,j}^{(n)}+V_{i,j-1}^{(n)}}{(\Delta Y)^2}. \tag{3.62}$$

Analogue to Eq. (3.43), using approximations (3.53)-(3.62), the two-dimensional intermediate scalar velocity components $\hat{U}$ and $\hat{V}$ have been computed as

$$\hat{U}_{i,j}=U_{i,j}^{(n)}+\Delta t^*\left[\frac{1}{Re}\left(\frac{\partial^2 U}{\partial X^2}+\frac{\partial^2 U}{\partial Y^2}\right)-\frac{\partial\left(U^2\right)}{\partial X}-\frac{\partial\left(VU\right)}{\partial Y}\right]_{i,j}^{(n)},$$

$$\hat{V}_{i,j}=V_{i,j}^{(n)}+\Delta t^*\left[\frac{1}{Re}\left(\frac{\partial^2 V}{\partial X^2}+\frac{\partial^2 V}{\partial Y^2}\right)-\frac{\partial\left(UV\right)}{\partial X}-\frac{\partial\left(V^2\right)}{\partial Y}\right]_{i,j}^{(n)}.$$

In order to satisfy the continuity equation (3.41) at time level $n+1$, the divergence of Eq. (3.44) has to be taken in the second fractional step, which yields two scalar equations for velocity components $U^{(n+1)}$ and $V^{(n+1)}$ as

$$\frac{\partial U^{(n+1)}}{\partial X}=\frac{\partial \hat{U}}{\partial X}-\Delta t^*\frac{\partial^2 P^{(n+1)}}{\partial X^2}, \tag{3.63}$$

$$\frac{\partial V^{(n+1)}}{\partial Y}=\frac{\partial \hat{V}}{\partial Y}-\Delta t^*\frac{\partial^2 P^{(n+1)}}{\partial Y^2}, \tag{3.64}$$

and the sum of these Eqs. (3.63)-(3.64) has to satisfy the continuity equation

$$\frac{\partial U^{(n+1)}}{\partial X}+\frac{\partial V^{(n+1)}}{\partial Y}=0 \tag{3.65}$$

at time level $n+1$ leading to a pressure-Poisson equation as

$$\frac{\partial^2 P^{(n+1)}}{\partial X^2}+\frac{\partial^2 P^{(n+1)}}{\partial Y^2}=\frac{1}{\Delta t^*}\left(\frac{\partial \hat{U}}{\partial X}+\frac{\partial \hat{V}}{\partial Y}\right)^{(n)}, \tag{3.66}$$

which is a second-order elliptical partial differential equation for the pressure field. The pressure-Poisson equation has been solved implicitly by applying the Gauss-Seidel-type S.O.R. method. The standard approach for appropriate boundary conditions for the pres-

sure leads the Neumann-type conditions (see [4, 119]). For fully Neumann-type boundary conditions, the coefficient matrix of system of linear equations becomes singular [135, p. 38], therefore, the pressure value has to be prescribed at least in one point on the domain. The boundary conditions for the pressure is an important issue in the field of computational fluid dynamics and it will be discussed in details in the next chapter.

After discretizing the pressure-Poisson equation (3.66) using second-order central difference schemes, it can be written as

$$\frac{P_{i-1,j}^{(m+1)} - 2P_{i,j}^{(m+1)} + P_{i+1,j}^{(m+1)}}{(\Delta X)^2} + \frac{P_{i,j-1}^{(m+1)} - 2P_{i,j}^{(m+1)} + P_{i,j+1}^{(m+1)}}{(\Delta Y)^2} = RHS_{i,j}^{(m)}, \tag{3.67}$$

where the right hand side of the equation is equal to

$$RHS_{i,j}^{(m)} = \frac{1}{\Delta t^*}\left[\frac{F_{i,j}^{(m)} - F_{i-1,j}^{(m)}}{\Delta X} + \frac{G_{i,j}^{(m)} - G_{i,j-1}^{(m)}}{\Delta Y}\right], \tag{3.68}$$

where the first-order derivatives have been discretized by using first-order backward difference schemes. In order to solve the system of linear equations for the discretized pressure-Poisson equation (3.67), the coefficients of this system have to be determined, therefore, we are looking for the coefficients of the following

$$\begin{aligned} &a_S^{(m+1)} P_S^{(m+1)} + a_W^{(m+1)} P_W^{(m+1)} + \\ &+ a_P^{(m+1)} P_P^{(m+1)} + \\ &+ a_E^{(m+1)} P_E^{(m+1)} + a_N^{(m+1)} P_N^{(m+1)} = b_P^{(m)} \end{aligned} \tag{3.69}$$

linear algebraic equation in the interior points of the domain, which are

$$a_S^{(m+1)} = \frac{1}{(\Delta Y)^2}, \tag{3.70}$$

$$a_W^{(m+1)} = \frac{1}{(\Delta X)^2}, \tag{3.71}$$

$$a_P^{(m+1)} = -2\left[\frac{1}{(\Delta X)^2} + \frac{1}{(\Delta Y)^2}\right], \tag{3.72}$$

$$a_E^{(m+1)} = \frac{1}{(\Delta X)^2}, \tag{3.73}$$

$$a_N^{(m+1)} = \frac{1}{(\Delta Y)^2}, \tag{3.74}$$

and the right hand side of the linear algebraic equation (3.69) is

$$b_P^{(m)} = RHS_{i,j}^{(m)}, \tag{3.75}$$

which will satisfy the discretized continuity equation (3.50) at time level $n+1$ using first-order backward spatial difference approximations. The coefficients (3.70)-(3.74) of the system of linear equations and the right hand side of system (3.75) have to be arranged and modified according to the corresponding boundary conditions. The band structure of the system of linear equations has been shown in Figure 3.2 [15, p. 57].

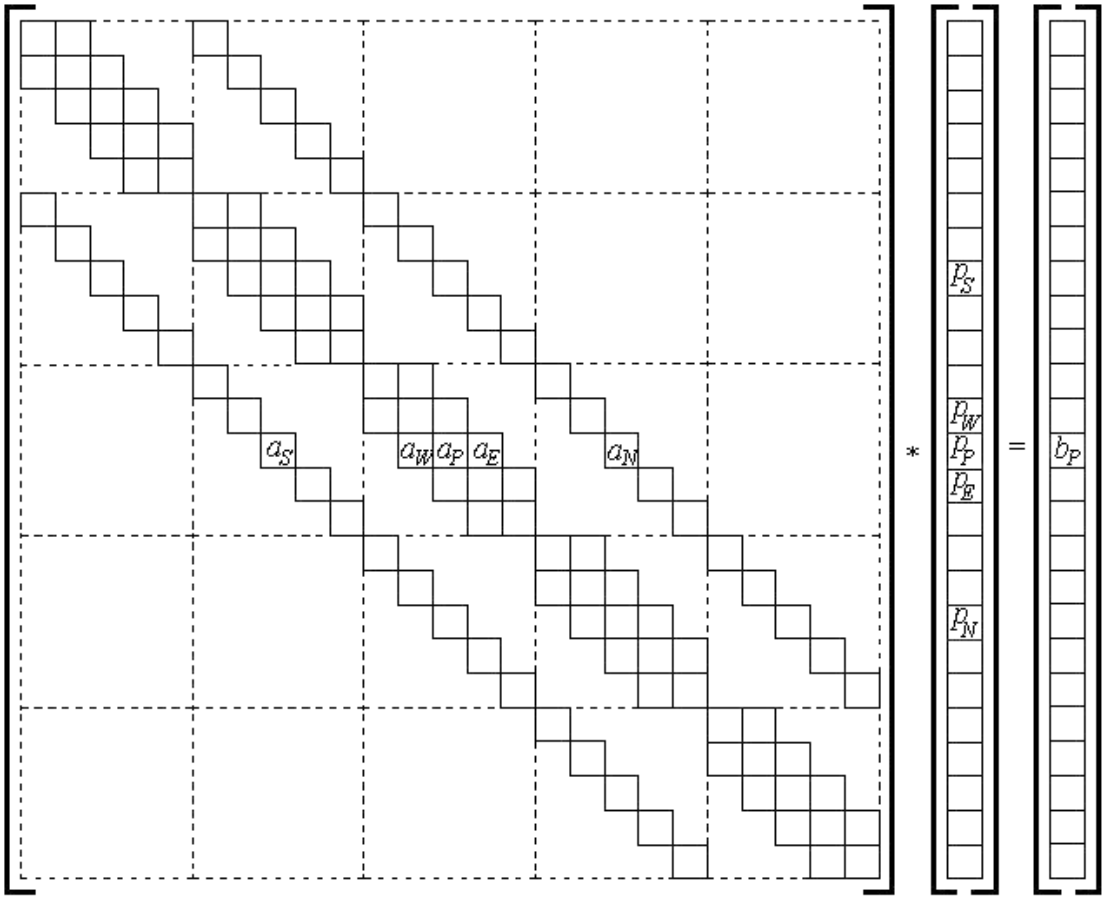

Figure 3.2: Band structure of the system of linear equations for five point schemes [15].

For solving the system of linear equations for the pressure field, Eq. (3.67) according

to the Gauss-Seidel iterative method yields

$$P_{i,j}^{(m+1)} = \left\{ P_{i-1,j}^{(m+1)} + P_{i+1,j}^{(m)} + \alpha_P \left[P_{i,j-1}^{(m+1)} + P_{i,j+1}^{(m)} \right] - RHS_{i,j}^{(m)} (\Delta X)^2 \right\} \cdot \beta_P^{-1}, \quad (3.76)$$

where upper index m denotes the sub-iteration steps, and where

$$\alpha_P = \frac{(\Delta X)^2}{(\Delta Y)^2}, \quad (3.77)$$

$$\beta_P = 2(1 + \alpha_P). \quad (3.78)$$

For solving the system of linear equations with the S.O.R. method, which is an improved version of the original Gauss-Seidel method, a relaxation parameter ω_P is introduced to accelerate the rate of convergence. This parameter has to be chosen between 1 and 2, appropriately [136, p. 11]. Using the S.O.R. iterative method, Eq. (3.76) is modified resulting the following equation for the discrete pressure values as

$$P_{i,j}^{(m+1)} = (1 - \omega_P) P_{i,j}^{(m)} +$$

$$+ \gamma_P \cdot \left\{ P_{i-1,j}^{(m+1)} + P_{i+1,j}^{(m)} + \alpha_P \left[P_{i,j-1}^{(m+1)} + P_{i,j+1}^{(m)} \right] - RHS_{i,j}^{(m)} (\Delta X)^2 \right\} \cdot \beta_P^{-1}. \quad (3.79)$$

After solving the system of linear equations for the pressure field, the velocity field has to be updated based on the updated pressure field, and Eq. (3.46) yields

$$U_{i,j}^{(n+1)} = \hat{U}_{i,j} - \Delta t^* \frac{P_{i+1,j}^{(n+1)} - P_{i,j}^{(n+1)}}{\Delta X}, \quad (3.80)$$

$$V_{i,j}^{(n+1)} = \hat{V}_{i,j} - \Delta t^* \frac{P_{i,j+1}^{(n+1)} - P_{i,j}^{(n+1)}}{\Delta Y}, \quad (3.81)$$

two algebraic equations, where the first-order spatial pressure derivatives have been discretized by applying first-order forward difference approximations. Note that any other numerical solution method of system of linear equations can be used to solve the discretized pressure-Poisson equation (3.67) implicitly.

Since the non-linear convective/advective and the linear second-order diffusive terms are treated explicitly, there is a limitation for choosing the time-step size. In order to ensure numerical convergence and stability, and avoid oscillatory behaviour of the numerical solution of the Navier-Stokes equations, it is necessary to satisfy additional conditions for the time-step size [137, 135, p. 39]. The *Courant-Friedrichs-Lewy* (CFL) conditions are used in the field of computational sciences [135, p. 39], which are

$$|U_{\max}| \Delta t^* < \Delta X,$$

$$|V_{\max}|\,\Delta t^* < \Delta Y,$$

and for adaptive time stepping, the appropriately chosen dimensionless time-step size is

$$\Delta t^* \cong \gamma_{t^*} \min\left(\frac{\Delta X}{|U_{\max}|}; \frac{\Delta Y}{|V_{\max}|}\right), \tag{3.82}$$

where $\gamma_{t^*} \in]\,0,1]$ is a safety factor [137, 135, p. 39]. More details can be found about stability analysis in the books of Roache [138] and Peyret and Taylor [5].

It is important to mention that one can find two types of approach to obtain divergence-free numerical solution for incompressible fluid flow problems in the literature. One group is the above discussed FS-PP method proposed by Chorin [4] and Temam [108]. Another type is the pressure-correction methods, such as SIMPLE-method (Semi-Implicit Method for Pressure-Linked Equations) developed by Patankar and Spalding [139], which is relying on a semi-implicit time discretization and uses mostly the higher-order QUICK (Quadratic Upwind Interpolation for Convective Kinematics) spatial discretization scheme for the non-linear convective/advective fluxes [135, p. 9] proposed by Leonard [140]. A revised version of the SIMPLE-method is called SIMPLER, which was also developed by Patankar [141, p. 131-134]. Van Doormal and Raithby [142] further improved Patankar's methods, which is called the SIMPLEC-method (Semi-Implicit Method for Pressure-Linked Equations Consistent). Issa [143] established an implicit type pressure-correction method called as PISO (Pressure Implicit with Splitting of Operators). One can find more details about pressure-correction methods in the book of Patankar [141].

3.2.3 Arrangements of Primitive Variables

From the point of view of the numerical solution, another important issue is the arrangement of primitive variables on the computational grid. Two arrangements are commonly used for treating the Navier-Stokes equations, such as collocated and staggered arrangement. Collocated solution considers the velocity and pressure quantities at the same grid location (see Figure 3.3 and Figure 3.4).

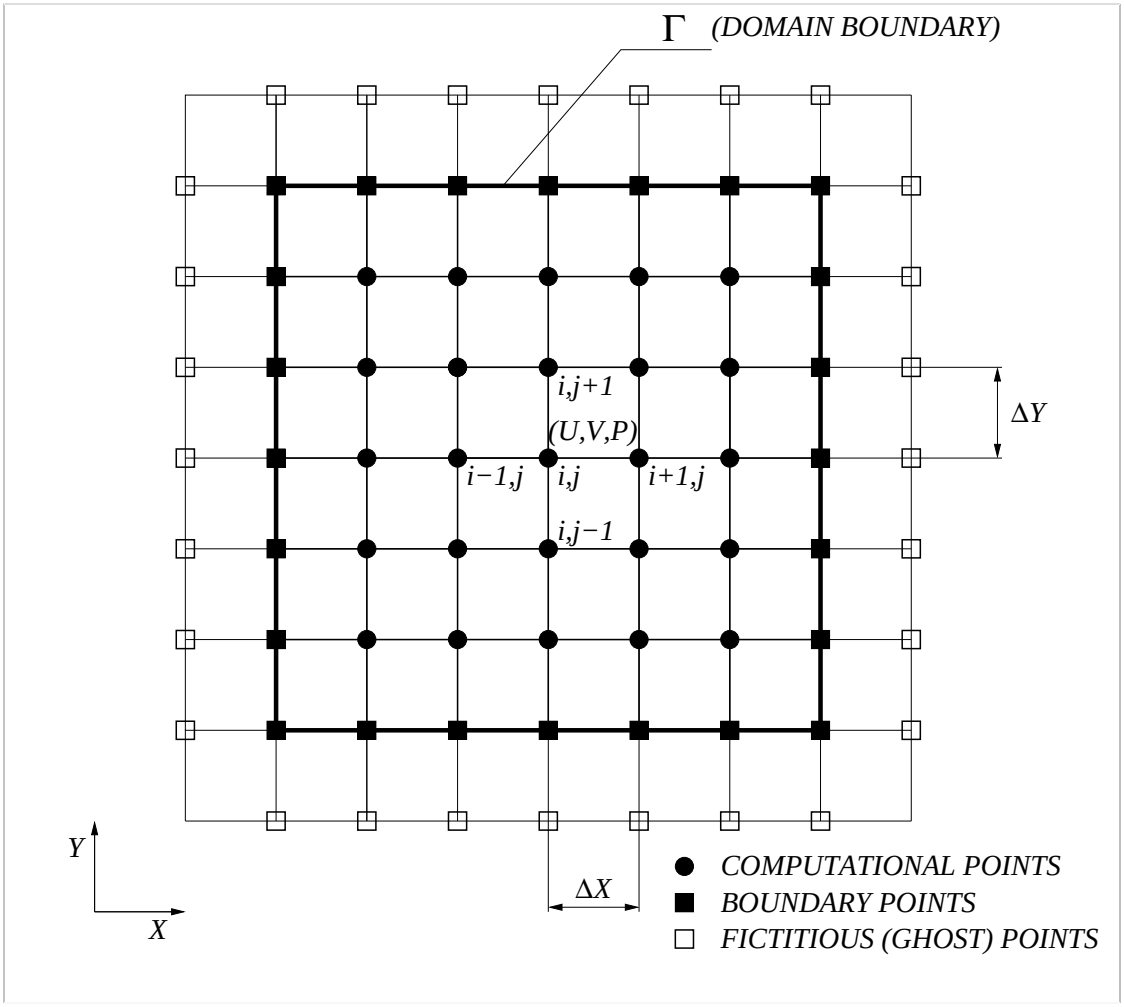

Figure 3.3: Collocated arrangement of primitive variables for FDM-based discretization.

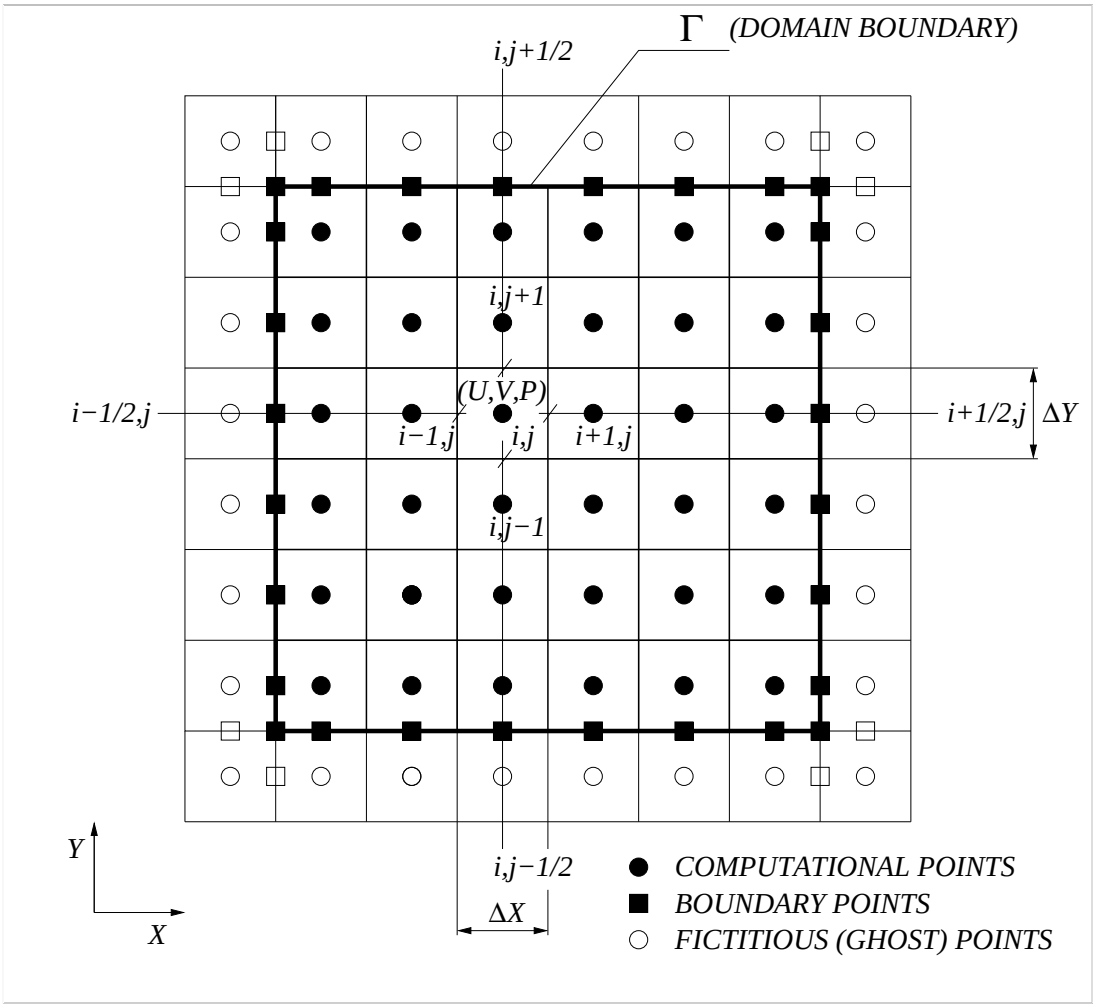

Figure 3.4: Collocated arrangement of primitive variables for FVM-based discretization.

Staggered arrangement considers the velocity components that are located in the mid-points of the cell edges while the pressure values are located in the cell centres (see Figure 3.5), which is the solution strategy called Marker-and-Cell (MAC) method developed by Harlow and Welch [144]. Note that the staggered arrangement has advantageous numerical behaviour, because it prevents oscillations of the pressure field, which could occur in the case of a collocated arrangement [145, 135]. For using the MAC method, different types of application can be found in the literature. Daly and Pracht [146] used the MAC method for multiphase flows in a numerical study of density current surges, while Amsden and Harlow [147] developed a simplified MAC method. Nichols and Hirt [148] further improved the MAC method for solving free-surface flows. Viecelli [149] established a method to treat moving boundaries. Hirt and Cook [150] extended the MAC technique to three-dimensions. Miyata, Nishimura, and Masuko [151] proposed a modification of

this method for simulating waves generated by ships. Miyata [152] used this method to compute breaking waves. Peric, Kessler, and Scheuerer [145] compared the FVM-based solutions for two-dimensional incompressible fluid with staggered and collocated grid arrangements [145]. Tome and McKee [137] developed a variant of the MAC method for the simulation of injection molding plastics [135, p. 9]. More details can be found about the MAC method applications in Hirt and Nichols [153], Lafaurie et al. [154], and in the book of Griebel, Dornseifer, and Neunhoeffer [135]. The following section deals with velocity and pressure coupling using a collocated arrangement of the primitive variables in a three-dimensional curvilinear coordinate system.

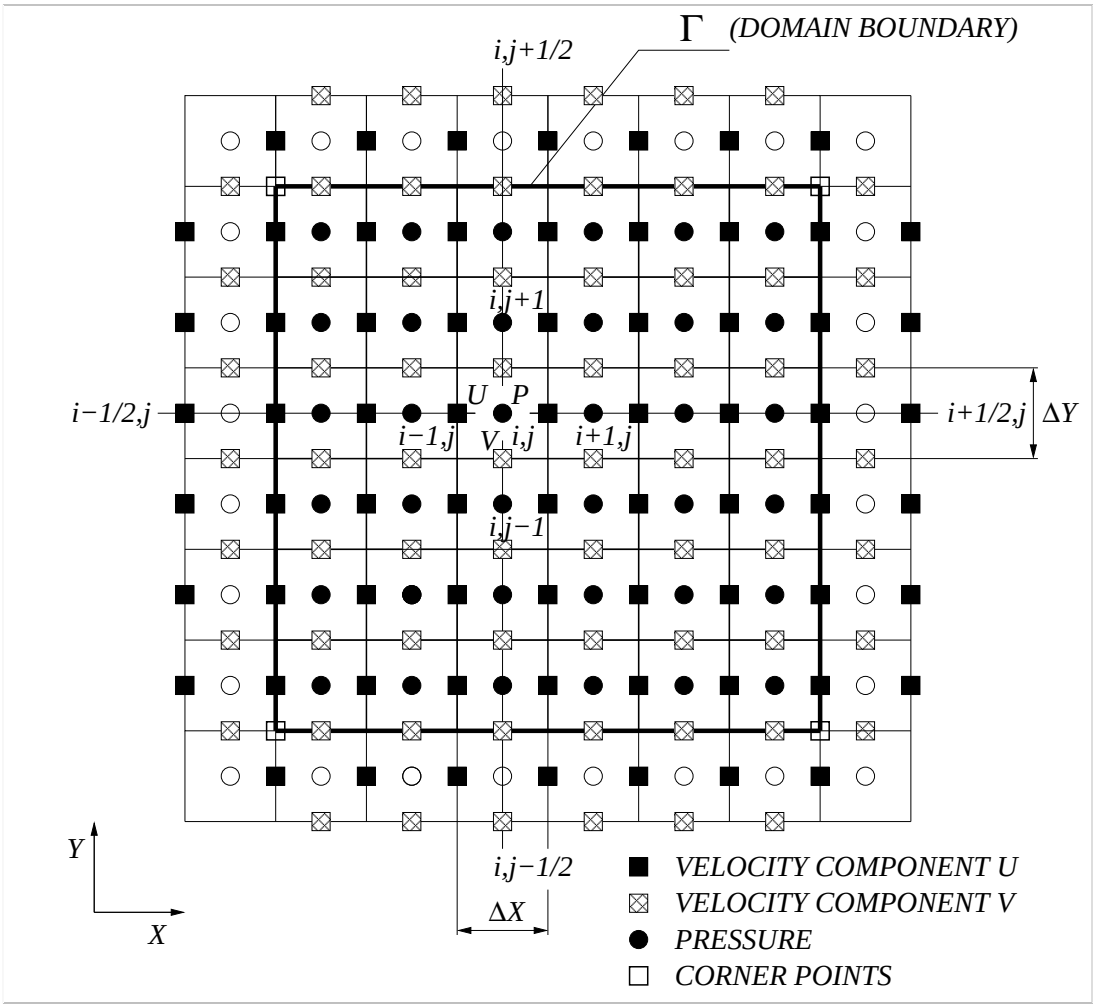

Figure 3.5: Staggered arrangement of primitive variables.

3.3 Computations in Curvilinear Coordinate System

3.3.1 The General Momentum Equation (Cauchy Equation)

In favour of compactness, curvilinear coordinate system has been used in order to be capable of handling complex geometries. In this case, the governing equations are transformed from the Cartesian coordinate system (x,y,z) into curvilinear coordinate system (ξ,η,ζ). Since the fluid can also be Newtonian or non-Newtonian depending on the elements of viscous stress tensor $\underline{\underline{\tau}}$, therefore, the general momentum equation (3.3) (Cauchy equation) has been taken into account in the derivation of dimensionless scalar momentum equations in a curvilinear coordinate system. For multiphysics CFD modelling, we devote attention to the coordinate transformation in order to set up the full three-dimensional general scalar system of governing equations for the pressure-projection method. More details can be found about generalised curvilinear coordinates and about coordinate transformation in the book of Drikakis and Rider [27, pp. 57-63] in a different context.

For incompressible fluid, the scalar form of continuity equation is

$$\frac{\partial u}{\partial x}+\frac{\partial v}{\partial y}+\frac{\partial w}{\partial z}=0, \tag{3.83}$$

and the three scalar momentum equations for velocity components u, v, and w are

$$\rho\left[\frac{\partial u}{\partial t}+\frac{\partial\left(u^2\right)}{\partial x}+\frac{\partial\left(vu\right)}{\partial y}+\frac{\partial\left(wu\right)}{\partial z}\right]=\rho g_x-\frac{\partial p}{\partial x}+\frac{\partial\tau_{xx}}{\partial x}+\frac{\partial\tau_{yx}}{\partial y}+\frac{\partial\tau_{zx}}{\partial z}+\rho f_x, \tag{3.84}$$

$$\rho\left[\frac{\partial v}{\partial t}+\frac{\partial\left(uv\right)}{\partial x}+\frac{\partial\left(v^2\right)}{\partial y}+\frac{\partial\left(wv\right)}{\partial z}\right]=\rho g_y-\frac{\partial p}{\partial y}+\frac{\partial\tau_{xy}}{\partial x}+\frac{\partial\tau_{yy}}{\partial y}+\frac{\partial\tau_{zy}}{\partial z}+\rho f_y, \tag{3.85}$$

$$\rho\left[\frac{\partial w}{\partial t}+\frac{\partial\left(uw\right)}{\partial x}+\frac{\partial\left(vw\right)}{\partial y}+\frac{\partial\left(w^2\right)}{\partial z}\right]=\rho g_z-\frac{\partial p}{\partial z}+\frac{\partial\tau_{xz}}{\partial x}+\frac{\partial\tau_{yz}}{\partial y}+\frac{\partial\tau_{zz}}{\partial z}+\rho f_z, \tag{3.86}$$

where g_x, g_y, g_z are the scalar components of the gravity vector, $\tau_{xx}, \tau_{yx}, \tau_{zx}, \tau_{xy}, \tau_{yy}, \tau_{zy}, \tau_{xz}$, τ_{yz}, τ_{zz} are the elements of viscous stress tensor $\underline{\underline{\tau}}$, and f_x, f_y, f_z are the scalar components of external (additional) forces. For incompressible fluid, the dimensionless scalar form of continuity equation (3.83) is

$$\frac{\partial U}{\partial X}+\frac{\partial V}{\partial Y}+\frac{\partial W}{\partial Z}=0, \tag{3.87}$$

and the three scalar momentum equations for velocity components U, V, and W are

$$\frac{\partial U}{\partial t^*}+\frac{\partial\left(U^2\right)}{\partial X}+\frac{\partial\left(VU\right)}{\partial Y}+\frac{\partial\left(WU\right)}{\partial Z}=-\frac{\partial P}{\partial X}+\frac{\partial\tau_{XX}}{\partial X}+\frac{\partial\tau_{YX}}{\partial Y}+\frac{\partial\tau_{ZX}}{\partial Z}+F_X, \quad (3.88)$$

$$\frac{\partial V}{\partial t^*}+\frac{\partial\left(UV\right)}{\partial X}+\frac{\partial\left(V^2\right)}{\partial Y}+\frac{\partial\left(WV\right)}{\partial Z}=-\frac{\partial P}{\partial Y}+\frac{\partial\tau_{XY}}{\partial X}+\frac{\partial\tau_{YY}}{\partial Y}+\frac{\partial\tau_{ZY}}{\partial Z}+F_Y, \quad (3.89)$$

$$\frac{\partial W}{\partial t^*}+\frac{\partial\left(UW\right)}{\partial X}+\frac{\partial\left(VW\right)}{\partial Y}+\frac{\partial\left(W^2\right)}{\partial Z}=-\frac{\partial P}{\partial Z}+\frac{\partial\tau_{XZ}}{\partial X}+\frac{\partial\tau_{YZ}}{\partial Y}+\frac{\partial\tau_{ZZ}}{\partial Z}+F_Z, \quad (3.90)$$

which scalar system of general momentum equations can also be written as

$$\frac{\partial\mathbf{U}}{\partial t^*}+\frac{\partial\mathbf{E_I}}{\partial X}+\frac{\partial\mathbf{F_I}}{\partial Y}+\frac{\partial\mathbf{G_I}}{\partial Z}=\frac{\partial\mathbf{E_V}}{\partial X}+\frac{\partial\mathbf{F_V}}{\partial Y}+\frac{\partial\mathbf{G_V}}{\partial Z}+\mathbf{F}, \quad (3.91)$$

where the following vector notations are introduced as

$$\mathbf{U}=\begin{bmatrix}0\\U\\V\\W\end{bmatrix},\ \mathbf{E_I}=\begin{bmatrix}U\\U^2+P\\UV\\UW\end{bmatrix},\ \mathbf{F_I}=\begin{bmatrix}V\\VU\\V^2+P\\VW\end{bmatrix},\ \mathbf{G_I}=\begin{bmatrix}W\\WU\\WV\\W^2+P\end{bmatrix},$$

$$\mathbf{E_V}=\begin{bmatrix}0\\\tau_{XX}\\\tau_{XY}\\\tau_{XZ}\end{bmatrix},\ \mathbf{F_V}=\begin{bmatrix}0\\\tau_{YX}\\\tau_{YY}\\\tau_{YZ}\end{bmatrix},\ \mathbf{G_V}=\begin{bmatrix}0\\\tau_{ZX}\\\tau_{ZY}\\\tau_{ZZ}\end{bmatrix},\ \mathbf{F}=\begin{bmatrix}0\\F_X\\F_Y\\F_Z\end{bmatrix}.$$

The first-order derivatives in the three-dimensional scalar continuity (3.87) and general momentum equations (3.88)-(3.90) can be expressed by using the chain-rule as

$$\frac{\partial}{\partial X}=\left(\frac{\partial\xi}{\partial X}\right)\frac{\partial}{\partial\xi}+\left(\frac{\partial\eta}{\partial X}\right)\frac{\partial}{\partial\eta}+\left(\frac{\partial\zeta}{\partial X}\right)\frac{\partial}{\partial\zeta}=\xi_X\frac{\partial}{\partial\xi}+\eta_X\frac{\partial}{\partial\eta}+\zeta_X\frac{\partial}{\partial\zeta}, \quad (3.92)$$

$$\frac{\partial}{\partial Y}=\left(\frac{\partial\xi}{\partial Y}\right)\frac{\partial}{\partial\xi}+\left(\frac{\partial\eta}{\partial Y}\right)\frac{\partial}{\partial\eta}+\left(\frac{\partial\zeta}{\partial Y}\right)\frac{\partial}{\partial\zeta}=\xi_Y\frac{\partial}{\partial\xi}+\eta_Y\frac{\partial}{\partial\eta}+\zeta_Y\frac{\partial}{\partial\zeta}, \quad (3.93)$$

$$\frac{\partial}{\partial Z}=\left(\frac{\partial\xi}{\partial Z}\right)\frac{\partial}{\partial\xi}+\left(\frac{\partial\eta}{\partial Z}\right)\frac{\partial}{\partial\eta}+\left(\frac{\partial\zeta}{\partial Z}\right)\frac{\partial}{\partial\zeta}=\xi_Z\frac{\partial}{\partial\xi}+\eta_Z\frac{\partial}{\partial\eta}+\zeta_Z\frac{\partial}{\partial\zeta}, \quad (3.94)$$

where the derivatives of curvilinear coordinates (ξ,η,ζ), according to Cartesian coordinates (X,Y,Z), are computed [27, p. 60] as

$$\xi_X=\frac{Y_\eta Z_\zeta-Y_\zeta Z_\eta}{J},\ \ \xi_Y=\frac{X_\zeta Z_\eta-X_\eta Z_\zeta}{J},\ \ \xi_Z=\frac{X_\eta Y_\zeta-X_\zeta Y_\eta}{J}, \quad (3.95)$$

$$\eta_X = \frac{Y_\zeta Z_\xi - Y_\xi Z_\zeta}{J}, \quad \eta_Y = \frac{X_\xi Z_\zeta - X_\zeta Z_\xi}{J}, \quad \eta_Z = \frac{X_\zeta Y_\xi - X_\xi Y_\zeta}{J}, \tag{3.96}$$

$$\zeta_X = \frac{Y_\xi Z_\eta - Y_\eta Z_\xi}{J}, \quad \zeta_Y = \frac{X_\eta Z_\xi - X_\xi Z_\eta}{J}, \quad \zeta_Z = \frac{X_\xi Y_\eta - X_\eta Y_\xi}{J}, \tag{3.97}$$

where

$$J = X_\xi \left(Y_\eta Z_\zeta - Y_\zeta Z_\eta\right) + X_\eta \left(Y_\zeta Z_\xi - Y_\xi Z_\zeta\right) + X_\zeta \left(Y_\xi Z_\eta - Y_\eta Z_\xi\right) \tag{3.98}$$

is the Jacobian determinant. The derivatives of the curvilinear coordinates (ξ, η, ζ), according to Cartesian coordinates (X, Y, Z), can be approximated numerically in the cell-centres and cell faces (see more details in Appendix A). After applying the chain-rule and multiplying the system of equations with the Jacobian determinant (3.98), the three-dimensional scalar curvilinear system of governing equations are written [27] as

$$\begin{aligned}
&J\frac{\partial \mathbf{U}}{\partial t^*} + J\xi_X \frac{\partial \mathbf{E_I}}{\partial \xi} + J\eta_X \frac{\partial \mathbf{E_I}}{\partial \eta} + J\zeta_X \frac{\partial \mathbf{E_I}}{\partial \zeta} + \\
&+J\xi_Y \frac{\partial \mathbf{F_I}}{\partial \xi} + J\eta_Y \frac{\partial \mathbf{F_I}}{\partial \eta} + J\zeta_Y \frac{\partial \mathbf{F_I}}{\partial \zeta} + \\
&+J\xi_Z \frac{\partial \mathbf{G_I}}{\partial \xi} + J\eta_Z \frac{\partial \mathbf{G_I}}{\partial \eta} + J\zeta_Z \frac{\partial \mathbf{G_I}}{\partial \zeta} = \\
&= J\xi_X \frac{\partial \mathbf{E_V}}{\partial \xi} + J\eta_X \frac{\partial \mathbf{E_V}}{\partial \eta} + J\zeta_X \frac{\partial \mathbf{E_V}}{\partial \zeta} + \\
&+J\xi_Y \frac{\partial \mathbf{F_V}}{\partial \xi} + J\eta_Y \frac{\partial \mathbf{F_V}}{\partial \eta} + J\zeta_Y \frac{\partial \mathbf{F_V}}{\partial \zeta} + \\
&+J\xi_Z \frac{\partial \mathbf{G_V}}{\partial \xi} + J\eta_Z \frac{\partial \mathbf{G_V}}{\partial \eta} + J\zeta_Z \frac{\partial \mathbf{G_V}}{\partial \zeta} + J\mathbf{F},
\end{aligned} \tag{3.99}$$

where the following term can be expressed as

$$J\xi_X \frac{\partial \mathbf{E_I}}{\partial \xi} = \frac{\partial \left(J\xi_X \mathbf{E_I}\right)}{\partial \xi} - \mathbf{E_I} \frac{\partial \left(J\xi_X\right)}{\partial \xi}, \tag{3.100}$$

which can also be written as

$$\begin{aligned}
&\frac{\partial \left(J\xi_X \mathbf{E_I}\right)}{\partial \xi} - \mathbf{E_I} \frac{\partial \left(J\xi_X\right)}{\partial \xi} = \xi_X \mathbf{E_I} \frac{\partial J}{\partial \xi} + J\mathbf{E_I} \frac{\partial \xi_X}{\partial \xi} + J\xi_X \frac{\partial \mathbf{E_I}}{\partial \xi} - \mathbf{E_I}\xi_X \frac{\partial J}{\partial \xi} - \mathbf{E_I} J \frac{\partial \xi_X}{\partial \xi} = \\
&= \xi_X \mathbf{E_I} \frac{\partial J}{\partial \xi} + J\mathbf{E_I} \frac{\partial \xi_X}{\partial \xi} + J\xi_X \frac{\partial \mathbf{E_I}}{\partial \xi} - \xi_X \mathbf{E_I} \frac{\partial J}{\partial \xi} - J\mathbf{E_I} \frac{\partial \xi_X}{\partial \xi} =
\end{aligned}$$

$$= \xi_X \mathbf{E_I} \frac{\partial J}{\partial \xi} - \xi_X \mathbf{E_I} \frac{\partial J}{\partial \xi} + J\mathbf{E_I} \frac{\partial \xi_X}{\partial \xi} - J\mathbf{E_I} \frac{\partial \xi_X}{\partial \xi} + J\xi_X \frac{\partial \mathbf{E_I}}{\partial \xi} = J\xi_X \frac{\partial \mathbf{E_I}}{\partial \xi}, \tag{3.101}$$

therefore, the other derivative terms in Eq. (3.99) can be taken into account similarly to Eq. (3.101). By substitution of these terms into Eq. (3.99) and re-arranging the resulted vector equation to be equal to zero, we obtain the following vector equation as

$$\begin{aligned}
&J\frac{\partial \mathbf{U}}{\partial t^*} + \frac{\partial}{\partial \xi}\left(J\xi_X \mathbf{E_I} + J\xi_Y \mathbf{F_I} + J\xi_Z \mathbf{G_I} - J\xi_X \mathbf{E_V} - J\xi_Y \mathbf{F_V} - J\xi_Z \mathbf{G_V}\right) + \\
&+\frac{\partial}{\partial \eta}\left(J\eta_X \mathbf{E_I} + J\eta_Y \mathbf{F_I} + J\eta_Z \mathbf{G_I} - J\eta_X \mathbf{E_V} - J\eta_Y \mathbf{F_V} - J\eta_Z \mathbf{G_V}\right) + \\
&+\frac{\partial}{\partial \zeta}\left(J\zeta_X \mathbf{E_I} + J\zeta_Y \mathbf{F_I} + J\zeta_Z \mathbf{G_I} - J\zeta_X \mathbf{E_V} - J\zeta_Y \mathbf{F_V} - J\zeta_Z \mathbf{G_V}\right) - \\
&-\mathbf{E_I}\left[\frac{\partial (J\xi_X)}{\partial \xi} + \frac{\partial (J\eta_X)}{\partial \eta} + \frac{\partial (J\zeta_X)}{\partial \zeta}\right] - \\
&-\mathbf{F_I}\left[\frac{\partial (J\xi_Y)}{\partial \xi} + \frac{\partial (J\eta_Y)}{\partial \eta} + \frac{\partial (J\zeta_Y)}{\partial \zeta}\right] - \\
&-\mathbf{G_I}\left[\frac{\partial (J\xi_Z)}{\partial \xi} + \frac{\partial (J\eta_Z)}{\partial \eta} + \frac{\partial (J\zeta_Z)}{\partial \zeta}\right] + \\
&+\mathbf{E_V}\left[\frac{\partial (J\xi_X)}{\partial \xi} + \frac{\partial (J\eta_X)}{\partial \eta} + \frac{\partial (J\zeta_X)}{\partial \zeta}\right] + \\
&+\mathbf{F_V}\left[\frac{\partial (J\xi_Y)}{\partial \xi} + \frac{\partial (J\eta_Y)}{\partial \eta} + \frac{\partial (J\zeta_Y)}{\partial \zeta}\right] + \\
&+\mathbf{G_V}\left[\frac{\partial (J\xi_Z)}{\partial \xi} + \frac{\partial (J\eta_Z)}{\partial \eta} + \frac{\partial (J\zeta_Z)}{\partial \zeta}\right] - J\mathbf{F} = 0,
\end{aligned} \tag{3.102}$$

where taking into account that the following terms

$$\frac{\partial (J\xi_X)}{\partial \xi} + \frac{\partial (J\eta_X)}{\partial \eta} + \frac{\partial (J\zeta_X)}{\partial \zeta} = 0, \tag{3.103}$$

$$\frac{\partial (J\xi_Y)}{\partial \xi} + \frac{\partial (J\eta_Y)}{\partial \eta} + \frac{\partial (J\zeta_Y)}{\partial \zeta} = 0, \tag{3.104}$$

$$\frac{\partial (J\xi_Z)}{\partial \xi} + \frac{\partial (J\eta_Z)}{\partial \eta} + \frac{\partial (J\zeta_Z)}{\partial \zeta} = 0, \tag{3.105}$$

are vanishing, Eq. (3.99) can also be written as

$$J\frac{\partial \mathbf{U}}{\partial t^*} + \frac{\partial \left(J\xi_X \mathbf{E_I} + J\xi_Y \mathbf{F_I} + J\xi_Z \mathbf{G_I}\right)}{\partial \xi} +$$

$$
\begin{aligned}
&+\frac{\partial\left(J\eta_X\mathbf{E_I}+J\eta_Y\mathbf{F_I}+J\eta_Z\mathbf{G_I}\right)}{\partial\eta}+\\
&+\frac{\partial\left(J\zeta_X\mathbf{E_I}+J\zeta_Y\mathbf{F_I}+J\zeta_Z\mathbf{G_I}\right)}{\partial\zeta}=\\
&=\frac{\partial\left(J\xi_X\mathbf{E_V}+J\xi_Y\mathbf{F_V}+J\xi_Z\mathbf{G_V}\right)}{\partial\xi}+\\
&+\frac{\partial\left(J\eta_X\mathbf{E_V}+J\eta_Y\mathbf{F_V}+J\eta_Z\mathbf{G_V}\right)}{\partial\eta}+\\
&+\frac{\partial\left(J\zeta_X\mathbf{E_V}+J\zeta_Y\mathbf{F_V}+J\zeta_Z\mathbf{G_V}\right)}{\partial\zeta}+J\mathbf{F}.
\end{aligned}
\tag{3.106}
$$

Similarly to the notations of Vinokur [155] and Viviand [156], the inviscid flux terms are introduced [27] as

$$
\begin{cases}
\mathbf{E_I^\xi}=J\left(\xi_X\mathbf{E_I}+\xi_Y\mathbf{F_I}+\xi_Z\mathbf{G_I}\right),\\
\mathbf{F_I^\eta}=J\left(\eta_X\mathbf{E_I}+\eta_Y\mathbf{F_I}+\eta_Z\mathbf{G_I}\right),\\
\mathbf{G_I^\zeta}=J\left(\zeta_X\mathbf{E_I}+\zeta_Y\mathbf{F_I}+\zeta_Z\mathbf{G_I}\right),
\end{cases}
\tag{3.107}
$$

and the viscous flux terms are

$$
\begin{cases}
\mathbf{E_V^\xi}=J\left(\xi_X\mathbf{E_V}+\xi_Y\mathbf{F_V}+\xi_Z\mathbf{G_V}\right),\\
\mathbf{F_V^\eta}=J\left(\eta_X\mathbf{E_V}+\eta_Y\mathbf{F_V}+\eta_Z\mathbf{G_V}\right),\\
\mathbf{G_V^\zeta}=J\left(\zeta_X\mathbf{E_V}+\zeta_Y\mathbf{F_V}+\zeta_Z\mathbf{G_V}\right),
\end{cases}
\tag{3.108}
$$

therefore, Eq. (3.91) can be written in a curvilinear coordinate system as

$$
J\frac{\partial\mathbf{U}}{\partial t^*}+\frac{\partial\mathbf{E_I^\xi}}{\partial\xi}+\frac{\partial\mathbf{F_I^\eta}}{\partial\eta}+\frac{\partial\mathbf{G_I^\zeta}}{\partial\zeta}=\frac{\partial\mathbf{E_V^\xi}}{\partial\xi}+\frac{\partial\mathbf{F_V^\eta}}{\partial\eta}+\frac{\partial\mathbf{G_V^\zeta}}{\partial\zeta}+J\mathbf{F},
\tag{3.109}
$$

where the dimensionless vectors of inviscid fluxes can also be expressed as

$$
\mathbf{E_I^\xi}=J\begin{bmatrix}
\xi_XU+\xi_YV+\xi_ZW\\
\xi_XU^2+\xi_YVU+\xi_ZWU+\xi_XP\\
\xi_XUV+\xi_YV^2+\xi_ZWV+\xi_YP\\
\xi_XUW+\xi_YVW+\xi_ZW^2+\xi_ZP
\end{bmatrix},
\tag{3.110}
$$

$$\mathbf{F}_{\mathbf{I}}^{\eta} = J \begin{bmatrix} \eta_X U + \eta_Y V + \eta_Z W \\ \eta_X U^2 + \eta_Y VU + \eta_Z WU + \eta_X P \\ \eta_X UV + \eta_Y V^2 + \eta_Z WV + \eta_Y P \\ \eta_X UW + \eta_Y VW + \eta_Z W^2 + \eta_Z P \end{bmatrix}, \tag{3.111}$$

$$\mathbf{G}_{\mathbf{I}}^{\zeta} = J \begin{bmatrix} \zeta_X U + \zeta_Y V + \zeta_Z W \\ \zeta_X U^2 + \zeta_Y VU + \zeta_Z WU + \zeta_X P \\ \zeta_X UV + \zeta_Y V^2 + \zeta_Z WV + \zeta_Y P \\ \zeta_X UW + \zeta_Y VW + \zeta_Z W^2 + \zeta_Z P \end{bmatrix}, \tag{3.112}$$

and the dimensionless vectors of viscous fluxes $\mathbf{E}_{\mathbf{V}}^{\xi}$, $\mathbf{F}_{\mathbf{V}}^{\eta}$, $\mathbf{G}_{\mathbf{V}}^{\zeta}$ have to be expressed based on the corresponding constitutive equation of the fluid. The derivatives of inviscid fluxes with curvilinear coordinates in Eq. (3.109) are approximated by using intercell flux values relying on FVM discretization strategy as

$$\begin{cases} \frac{\partial \mathbf{E}_{\mathbf{I}}^{\xi}}{\partial \xi} \cong \frac{\left(\mathbf{E}_{\mathbf{I}}^{\xi}\right)_{i+1/2,j,k} - \left(\mathbf{E}_{\mathbf{I}}^{\xi}\right)_{i-1/2,j,k}}{\Delta \xi}, \\ \\ \frac{\partial \mathbf{F}_{\mathbf{I}}^{\eta}}{\partial \eta} \cong \frac{\left(\mathbf{F}_{\mathbf{I}}^{\eta}\right)_{i,j+1/2,k} - \left(\mathbf{F}_{\mathbf{I}}^{\eta}\right)_{i,j-1/2,k}}{\Delta \eta}, \\ \\ \frac{\partial \mathbf{G}_{\mathbf{I}}^{\zeta}}{\partial \zeta} \cong \frac{\left(\mathbf{G}_{\mathbf{I}}^{\zeta}\right)_{i,j,k+1/2} - \left(\mathbf{G}_{\mathbf{I}}^{\zeta}\right)_{i,j,k-1/2}}{\Delta \zeta}, \end{cases} \tag{3.113}$$

where the i, j, k subscripts correspond to the cell-centre coordinates in the domain.

3.3.2 Pressure-Projection with Curvilinear Coordinates

The pressure-projection method of Chorin [4] and Temam [108] has been coupled with fractional pseudo time-step artificial compressibility formulation in a unified solution concept in the next chapter of this thesis. In order to perform this coupling, the pressure-projection step has been inserted into the dual pseudo-time stepping procedure of the artificial compressibility method. The artificial compressibility formulation does not contain any pressure-projection steps [119], because the pressure field is determined by the perturbed continuity equation. To incorporate the pressure-projection method with the high-resolution characteristics-based Godunov-type scheme for non-linear convective/advective fluxes, it is necessary to keep the hyperbolic nature of the classical artificial compressibility formulation; leading to a fractional step artificial compressibility (FSAC) formulation. The reason for this is to gain advantageous convergence proper-

ties of the characteristics-based scheme. Since the various corresponding characteristics-based schemes derived by Shapiro and Drikakis [16] are relying on the Riemann method in curvilinear coordinate system, the inclusion of the pressure-projection step has to be implemented with curvilinear coordinates. Consequently, the curvilinear pressure-projection method and its formulation in conjunction with the general momentum equation have been presented in this subsection. The presented formulation has been used as the immanent part of the proposed FSAC-PP solution method in this thesis.

For modelling fluid flow with curvilinear coordinates, the system of governing equations (3.109) yield four scalar equations corresponding to the continuity and three scalar momentum equations for velocity components U, V, and W. The dimensionless continuity equation in curvilinear coordinate system relying on Eq. (3.109) can be written as

$$\begin{aligned}
&\xi_X \frac{\partial U}{\partial \xi} + \eta_X \frac{\partial U}{\partial \eta} + \zeta_X \frac{\partial U}{\partial \zeta} + \\
&+\xi_Y \frac{\partial V}{\partial \xi} + \eta_Y \frac{\partial V}{\partial \eta} + \zeta_Y \frac{\partial V}{\partial \zeta} + \\
&+\xi_Z \frac{\partial W}{\partial \xi} + \eta_Z \frac{\partial W}{\partial \eta} + \zeta_Z \frac{\partial W}{\partial \zeta} = 0,
\end{aligned} \tag{3.114}$$

and the scalar momentum equation for velocity component U is

$$\begin{aligned}
&\frac{\partial U}{\partial t^*} + \xi_X \frac{\partial \left(U^2\right)}{\partial \xi} + \eta_X \frac{\partial \left(U^2\right)}{\partial \eta} + \zeta_X \frac{\partial \left(U^2\right)}{\partial \zeta} + \\
&+\xi_Y \frac{\partial (VU)}{\partial \xi} + \eta_Y \frac{\partial (VU)}{\partial \eta} + \zeta_Y \frac{\partial (VU)}{\partial \zeta} + \\
&+\xi_Z \frac{\partial (WU)}{\partial \xi} + \eta_Z \frac{\partial (WU)}{\partial \eta} + \zeta_Z \frac{\partial (WU)}{\partial \zeta} = \\
&= \xi_X \frac{\partial \tau_{XX}}{\partial \xi} + \eta_X \frac{\partial \tau_{XX}}{\partial \eta} + \zeta_X \frac{\partial \tau_{XX}}{\partial \zeta} + \\
&+\xi_Y \frac{\partial \tau_{YX}}{\partial \xi} + \eta_Y \frac{\partial \tau_{YX}}{\partial \eta} + \zeta_Y \frac{\partial \tau_{YX}}{\partial \zeta} + \\
&+\xi_Z \frac{\partial \tau_{ZX}}{\partial \xi} + \eta_Z \frac{\partial \tau_{ZX}}{\partial \eta} + \zeta_Z \frac{\partial \tau_{ZX}}{\partial \zeta} - \\
&-\xi_X \frac{\partial P}{\partial \xi} - \eta_X \frac{\partial P}{\partial \eta} - \zeta_X \frac{\partial P}{\partial \zeta} + F_\xi,
\end{aligned} \tag{3.115}$$

and the scalar momentum equation for velocity component V is

$$\begin{aligned}
&\frac{\partial V}{\partial t^*}+\xi_X\frac{\partial\left(UV\right)}{\partial\xi}+\eta_X\frac{\partial\left(UV\right)}{\partial\eta}+\zeta_X\frac{\partial\left(UV\right)}{\partial\zeta}+\\
&+\xi_Y\frac{\partial\left(V^2\right)}{\partial\xi}+\eta_Y\frac{\partial\left(V^2\right)}{\partial\eta}+\zeta_Y\frac{\partial\left(V^2\right)}{\partial\zeta}+\\
&+\xi_Z\frac{\partial\left(WV\right)}{\partial\xi}+\eta_Z\frac{\partial\left(WV\right)}{\partial\eta}+\zeta_Z\frac{\partial\left(WV\right)}{\partial\zeta}=\\
&=\xi_X\frac{\partial\tau_{XY}}{\partial\xi}+\eta_X\frac{\partial\tau_{XY}}{\partial\eta}+\zeta_X\frac{\partial\tau_{XY}}{\partial\zeta}+\\
&+\xi_Y\frac{\partial\tau_{YY}}{\partial\xi}+\eta_Y\frac{\partial\tau_{YY}}{\partial\eta}+\zeta_Y\frac{\partial\tau_{YY}}{\partial\zeta}+\\
&+\xi_Z\frac{\partial\tau_{ZY}}{\partial\xi}+\eta_Z\frac{\partial\tau_{ZY}}{\partial\eta}+\zeta_Z\frac{\partial\tau_{ZY}}{\partial\zeta}-\\
&-\xi_Y\frac{\partial P}{\partial\xi}-\eta_Y\frac{\partial P}{\partial\eta}-\zeta_Y\frac{\partial P}{\partial\zeta}+F_\eta,
\end{aligned}\tag{3.116}$$

and the scalar momentum equation for velocity component W is

$$\begin{aligned}
&\frac{\partial W}{\partial t^*}+\xi_X\frac{\partial\left(UW\right)}{\partial\xi}+\eta_X\frac{\partial\left(UW\right)}{\partial\eta}+\zeta_X\frac{\partial\left(UW\right)}{\partial\zeta}+\\
&+\xi_Y\frac{\partial\left(VW\right)}{\partial\xi}+\eta_Y\frac{\partial\left(VW\right)}{\partial\eta}+\zeta_Y\frac{\partial\left(VW\right)}{\partial\zeta}+\\
&+\xi_Z\frac{\partial\left(W^2\right)}{\partial\xi}+\eta_Z\frac{\partial\left(W^2\right)}{\partial\eta}+\zeta_Z\frac{\partial\left(W^2\right)}{\partial\zeta}=\\
&=\xi_X\frac{\partial\tau_{XZ}}{\partial\xi}+\eta_X\frac{\partial\tau_{XZ}}{\partial\eta}+\zeta_X\frac{\partial\tau_{XZ}}{\partial\zeta}+\\
&+\xi_Y\frac{\partial\tau_{YZ}}{\partial\xi}+\eta_Y\frac{\partial\tau_{YZ}}{\partial\eta}+\zeta_Y\frac{\partial\tau_{YZ}}{\partial\zeta}+\\
&+\xi_Z\frac{\partial\tau_{ZZ}}{\partial\xi}+\eta_Z\frac{\partial\tau_{ZZ}}{\partial\eta}+\zeta_Z\frac{\partial\tau_{ZZ}}{\partial\zeta}-\\
&-\xi_Z\frac{\partial P}{\partial\xi}-\eta_Z\frac{\partial P}{\partial\eta}-\zeta_Z\frac{\partial P}{\partial\zeta}+F_\zeta.
\end{aligned}\tag{3.117}$$

According to the fractional step pressure-projection method of Chorin [4] and Temam [108], an intermediate velocity field is determined in the first fractional step relying on Eq. (3.43) and neglecting the pressure gradient terms in the scalar momentum equations.

Using the divergence form of the viscous stress tensor $\underline{\underline{\tau}}$ in the right hand side of the momentum equations, similarly to Eq. (3.43), the intermediate velocity component $\hat{U}$ is

$$\begin{aligned}\hat{U} = U^{(n)} + \Delta t^* \Bigg[& -\xi_X \frac{\partial \left(U^2\right)}{\partial \xi} - \eta_X \frac{\partial \left(U^2\right)}{\partial \eta} - \zeta_X \frac{\partial \left(U^2\right)}{\partial \zeta} - \\ & -\xi_Y \frac{\partial (VU)}{\partial \xi} - \eta_Y \frac{\partial (VU)}{\partial \eta} - \zeta_Y \frac{\partial (VU)}{\partial \zeta} - \\ & -\xi_Z \frac{\partial (WU)}{\partial \xi} - \eta_Z \frac{\partial (WU)}{\partial \eta} - \zeta_Z \frac{\partial (WU)}{\partial \zeta} + \\ & +\xi_X \frac{\partial \tau_{XX}}{\partial \xi} + \eta_X \frac{\partial \tau_{XX}}{\partial \eta} + \zeta_X \frac{\partial \tau_{XX}}{\partial \zeta} + \\ & +\xi_Y \frac{\partial \tau_{YX}}{\partial \xi} + \eta_Y \frac{\partial \tau_{YX}}{\partial \eta} + \zeta_Y \frac{\partial \tau_{YX}}{\partial \zeta} + \\ & +\xi_Z \frac{\partial \tau_{ZX}}{\partial \xi} + \eta_Z \frac{\partial \tau_{ZX}}{\partial \eta} + \zeta_Z \frac{\partial \tau_{ZX}}{\partial \zeta} + F_\xi \Bigg]^{(n)}, \end{aligned} \tag{3.118}$$

and the intermediate velocity component $\hat{V}$ is

$$\begin{aligned}\hat{V} = V^{(n)} + \Delta t^* \Bigg[& -\xi_X \frac{\partial (UV)}{\partial \xi} - \eta_X \frac{\partial (UV)}{\partial \eta} - \zeta_X \frac{\partial (UV)}{\partial \zeta} - \\ & -\xi_Y \frac{\partial \left(V^2\right)}{\partial \xi} - \eta_Y \frac{\partial \left(V^2\right)}{\partial \eta} - \zeta_Y \frac{\partial \left(V^2\right)}{\partial \zeta} - \\ & -\xi_Z \frac{\partial (WV)}{\partial \xi} - \eta_Z \frac{\partial (WV)}{\partial \eta} - \zeta_Z \frac{\partial (WV)}{\partial \zeta} + \\ & +\xi_X \frac{\partial \tau_{XY}}{\partial \xi} + \eta_X \frac{\partial \tau_{XY}}{\partial \eta} + \zeta_X \frac{\partial \tau_{XY}}{\partial \zeta} + \\ & +\xi_Y \frac{\partial \tau_{YY}}{\partial \xi} + \eta_Y \frac{\partial \tau_{YY}}{\partial \eta} + \zeta_Y \frac{\partial \tau_{YY}}{\partial \zeta} + \\ & +\xi_Z \frac{\partial \tau_{ZY}}{\partial \xi} + \eta_Z \frac{\partial \tau_{ZY}}{\partial \eta} + \zeta_Z \frac{\partial \tau_{ZY}}{\partial \zeta} + F_\eta \Bigg]^{(n)}, \end{aligned} \tag{3.119}$$

and the intermediate velocity component $\hat{W}$ is

$$\hat{W} = W^{(n)} + \Delta t^* \Bigg[-\xi_X \frac{\partial (UW)}{\partial \xi} - \eta_X \frac{\partial (UW)}{\partial \eta} - \zeta_X \frac{\partial (UW)}{\partial \zeta} -$$

$$
\begin{aligned}
&-\xi_Y \frac{\partial (VW)}{\partial \xi} - \eta_Y \frac{\partial (VW)}{\partial \eta} - \zeta_Y \frac{\partial (VW)}{\partial \zeta} - \\
&-\xi_Z \frac{\partial \left(W^2\right)}{\partial \xi} - \eta_Z \frac{\partial \left(W^2\right)}{\partial \eta} - \zeta_Z \frac{\partial \left(W^2\right)}{\partial \zeta} + \\
&+\xi_X \frac{\partial \tau_{XZ}}{\partial \xi} + \eta_X \frac{\partial \tau_{XZ}}{\partial \eta} + \zeta_X \frac{\partial \tau_{XZ}}{\partial \zeta} + \\
&+\xi_Y \frac{\partial \tau_{YZ}}{\partial \xi} + \eta_Y \frac{\partial \tau_{YZ}}{\partial \eta} + \zeta_Y \frac{\partial \tau_{YZ}}{\partial \zeta} + \\
&+\xi_Z \frac{\partial \tau_{ZZ}}{\partial \xi} + \eta_Z \frac{\partial \tau_{ZZ}}{\partial \eta} + \zeta_Z \frac{\partial \tau_{ZZ}}{\partial \zeta} + F_\zeta \Bigg]^{(n)} .
\end{aligned} \tag{3.120}
$$

By taking the divergence of Eq. (3.44) in the curvilinear coordinate system to satisfy the continuity equation (3.41) in the second fractional step for constant density flow, three scalar system of equations are obtained for velocity components U, V, and W at time level $n+1$. The scalar equation for velocity component U is

$$
\begin{aligned}
&\xi_X \frac{\partial U^{(n+1)}}{\partial \xi} + \eta_X \frac{\partial U^{(n+1)}}{\partial \eta} + \zeta_X \frac{\partial U^{(n+1)}}{\partial \zeta} = \\
&= \xi_X \frac{\partial \hat{U}}{\partial \xi} + \eta_X \frac{\partial \hat{U}}{\partial \eta} + \zeta_X \frac{\partial \hat{U}}{\partial \zeta} - \\
&-\Delta t^* \Bigg[\xi_X^2 \frac{\partial^2 P^{(n+1)}}{\partial \xi^2} + \eta_X^2 \frac{\partial^2 P^{(n+1)}}{\partial \eta^2} + \zeta_X^2 \frac{\partial^2 P^{(n+1)}}{\partial \zeta^2} + \\
&+2\xi_X \eta_X \frac{\partial^2 P^{(n+1)}}{\partial \xi \partial \eta} + 2\xi_X \zeta_X \frac{\partial^2 P^{(n+1)}}{\partial \xi \partial \zeta} + 2\eta_X \zeta_X \frac{\partial^2 P^{(n+1)}}{\partial \eta \partial \zeta} + \\
&+\xi_{XX} \frac{\partial P^{(n+1)}}{\partial \xi} + \eta_{XX} \frac{\partial P^{(n+1)}}{\partial \eta} + \zeta_{XX} \frac{\partial P^{(n+1)}}{\partial \zeta} \Bigg],
\end{aligned} \tag{3.121}
$$

and the scalar equation for velocity component V is

$$
\begin{aligned}
&\xi_Y \frac{\partial V^{(n+1)}}{\partial \xi} + \eta_Y \frac{\partial V^{(n+1)}}{\partial \eta} + \zeta_Y \frac{\partial V^{(n+1)}}{\partial \zeta} = \\
&= \xi_Y \frac{\partial \hat{V}}{\partial \xi} + \eta_Y \frac{\partial \hat{V}}{\partial \eta} + \zeta_Y \frac{\partial \hat{V}}{\partial \zeta} - \\
&-\Delta t^* \Bigg[\xi_Y^2 \frac{\partial^2 P^{(n+1)}}{\partial \xi^2} + \eta_Y^2 \frac{\partial^2 P^{(n+1)}}{\partial \eta^2} + \zeta_Y^2 \frac{\partial^2 P^{(n+1)}}{\partial \zeta^2} +
\end{aligned}
$$

$$+2\xi_Y\eta_Y\frac{\partial^2 P^{(n+1)}}{\partial\xi\,\partial\eta}+2\xi_Y\zeta_Y\frac{\partial^2 P^{(n+1)}}{\partial\xi\,\partial\zeta}+2\eta_Y\zeta_Y\frac{\partial^2 P^{(n+1)}}{\partial\eta\,\partial\zeta}+$$
$$+\xi_{YY}\frac{\partial P^{(n+1)}}{\partial\xi}+\eta_{YY}\frac{\partial P^{(n+1)}}{\partial\eta}+\zeta_{YY}\frac{\partial P^{(n+1)}}{\partial\zeta}\Bigg], \tag{3.122}$$

and the scalar equation for velocity component W is

$$\xi_Z\frac{\partial W^{(n+1)}}{\partial\xi}+\eta_Z\frac{\partial W^{(n+1)}}{\partial\eta}+\zeta_Z\frac{\partial W^{(n+1)}}{\partial\zeta}=$$
$$=\xi_Z\frac{\partial\hat{W}}{\partial\xi}+\eta_Z\frac{\partial\hat{W}}{\partial\eta}+\zeta_Z\frac{\partial\hat{W}}{\partial\zeta}-$$
$$-\Delta t^*\Bigg[\xi_Z^2\frac{\partial^2 P^{(n+1)}}{\partial\xi^2}+\eta_Z^2\frac{\partial^2 P^{(n+1)}}{\partial\eta^2}+\zeta_Z^2\frac{\partial^2 P^{(n+1)}}{\partial\zeta^2}+$$
$$+2\xi_Z\eta_Z\frac{\partial^2 P^{(n+1)}}{\partial\xi\,\partial\eta}+2\xi_Z\zeta_Z\frac{\partial^2 P^{(n+1)}}{\partial\xi\,\partial\zeta}+2\eta_Z\zeta_Z\frac{\partial^2 P^{(n+1)}}{\partial\eta\,\partial\zeta}+$$
$$+\xi_{ZZ}\frac{\partial P^{(n+1)}}{\partial\xi}+\eta_{ZZ}\frac{\partial P^{(n+1)}}{\partial\eta}+\zeta_{ZZ}\frac{\partial P^{(n+1)}}{\partial\zeta}\Bigg]. \tag{3.123}$$

Relying on the fractional step pressure-projection method of Chorin [4] and Temam [108], the elliptical pressure-Poisson equation has to be solved in the second fractional step; then the velocity field has to be updated based on the updated pressure field values in order to satisfy the divergence-free constraint (3.41) at time level $n+1$. Since the system of equations (3.121)-(3.123) for velocity components U, V, and W is different in the cases of constant and variable density flows, the pressure-Poisson equation will also be different in these cases. Consequently, the different forms of pressure-Poisson equation and the corresponding velocity field update are discussed in the next two sub-subsection.

3.3.2.1 Constant Density Flows

For constant density flows, after adding of Eqs. (3.121), (3.122) and (3.123), a partial differential equation is obtained in the curvilinear coordinate system. The left hand side of this equation is equal to the scalar continuity equation (3.114), which has to be equal to zero according to the incompressibility constraint at time level $n+1$ as

$$\xi_X\frac{\partial U^{(n+1)}}{\partial\xi}+\eta_X\frac{\partial U^{(n+1)}}{\partial\eta}+\zeta_X\frac{\partial U^{(n+1)}}{\partial\zeta}+$$

$$+\xi_Y \frac{\partial V^{(n+1)}}{\partial \xi} + \eta_Y \frac{\partial V^{(n+1)}}{\partial \eta} + \zeta_Y \frac{\partial V^{(n+1)}}{\partial \zeta} +$$
$$+\xi_Z \frac{\partial W^{(n+1)}}{\partial \xi} + \eta_Z \frac{\partial W^{(n+1)}}{\partial \eta} + \zeta_Z \frac{\partial W^{(n+1)}}{\partial \zeta} = 0. \tag{3.124}$$

By taking into account the divergence-free constraint relying on Eq. (3.124), the system of equations (3.121)-(3.123) yields an elliptical three-dimensional pressure-Poisson equation in a curvilinear coordinate system as

$$\left(\xi_X^2 + \xi_Y^2 + \xi_Z^2\right) \frac{\partial^2 P^{(n+1)}}{\partial \xi^2} +$$
$$+ \left(\eta_X^2 + \eta_Y^2 + \eta_Z^2\right) \frac{\partial^2 P^{(n+1)}}{\partial \eta^2} +$$
$$+ \left(\zeta_X^2 + \zeta_Y^2 + \zeta_Z^2\right) \frac{\partial^2 P^{(n+1)}}{\partial \zeta^2} +$$
$$+2\left(\xi_X \eta_X + \xi_Y \eta_Y + \xi_Z \eta_Z\right) \frac{\partial^2 P^{(n+1)}}{\partial \xi \partial \eta} +$$
$$+2\left(\xi_X \zeta_X + \xi_Y \zeta_Y + \xi_Z \zeta_Z\right) \frac{\partial^2 P^{(n+1)}}{\partial \xi \partial \zeta} +$$
$$+2\left(\eta_X \zeta_X + \eta_Y \zeta_Y + \eta_Z \zeta_Z\right) \frac{\partial^2 P^{(n+1)}}{\partial \eta \partial \zeta} +$$
$$+\left(\xi_{XX} + \xi_{YY} + \xi_{ZZ}\right) \frac{\partial P^{(n+1)}}{\partial \xi} +$$
$$+\left(\eta_{XX} + \eta_{YY} + \eta_{ZZ}\right) \frac{\partial P^{(n+1)}}{\partial \eta} +$$
$$+\left(\zeta_{XX} + \zeta_{YY} + \zeta_{ZZ}\right) \frac{\partial P^{(n+1)}}{\partial \zeta} =$$
$$= \frac{1}{\Delta t^*} \left(\xi_X \frac{\partial \hat{U}}{\partial \xi} + \eta_X \frac{\partial \hat{U}}{\partial \eta} + \zeta_X \frac{\partial \hat{U}}{\partial \zeta} + \right.$$
$$+\xi_Y \frac{\partial \hat{V}}{\partial \xi} + \eta_Y \frac{\partial \hat{V}}{\partial \eta} + \zeta_Y \frac{\partial \hat{V}}{\partial \zeta} +$$
$$\left. +\xi_Z \frac{\partial \hat{W}}{\partial \xi} + \eta_Z \frac{\partial \hat{W}}{\partial \eta} + \zeta_Z \frac{\partial \hat{W}}{\partial \zeta} \right)^{(n)}, \tag{3.125}$$

where the notations of second derivatives of the curvilinear coordinates (ξ, η, ζ), accord-

ing to Cartesian coordinates (X,Y,Z), are introduced as

$$\xi_{XX} = \frac{\partial^2 \xi}{\partial X^2}, \quad \eta_{XX} = \frac{\partial^2 \eta}{\partial X^2}, \quad \zeta_{XX} = \frac{\partial^2 \zeta}{\partial X^2},$$

$$\xi_{YY} = \frac{\partial^2 \xi}{\partial Y^2}, \quad \eta_{YY} = \frac{\partial^2 \eta}{\partial Y^2}, \quad \zeta_{YY} = \frac{\partial^2 \zeta}{\partial Y^2},$$

$$\xi_{ZZ} = \frac{\partial^2 \xi}{\partial Z^2}, \quad \eta_{ZZ} = \frac{\partial^2 \eta}{\partial Z^2}, \quad \zeta_{ZZ} = \frac{\partial^2 \zeta}{\partial Z^2}.$$

After solving the elliptical pressure-Poisson equation (3.125) numerically, the velocity field has to be updated based on the intermediate velocity components $\hat{U}$, $\hat{V}$, and $\hat{W}$ by using the solution of Eqs. (3.118)-(3.120); and based on the updated solution of the pressure-Poisson equation. Note that the numerical solution of the elliptical curvilinear Poisson equation (3.125) for the pressure field has been discussed for constant density flows in the following subsection. For constant density flows, the updated velocity components in curvilinear coordinate system at time level $n+1$, relying on the Helmholtz-Hodge decomposition (3.38), are written as

$$U^{(n+1)} = \hat{U} - \Delta t^* \left[\xi_X \frac{\partial P^{(n+1)}}{\partial \xi} + \eta_X \frac{\partial P^{(n+1)}}{\partial \eta} + \zeta_X \frac{\partial P^{(n+1)}}{\partial \zeta} \right], \tag{3.126}$$

$$V^{(n+1)} = \hat{V} - \Delta t^* \left[\xi_Y \frac{\partial P^{(n+1)}}{\partial \xi} + \eta_Y \frac{\partial P^{(n+1)}}{\partial \eta} + \zeta_Y \frac{\partial P^{(n+1)}}{\partial \zeta} \right], \tag{3.127}$$

$$W^{(n+1)} = \hat{W} - \Delta t^* \left[\xi_Z \frac{\partial P^{(n+1)}}{\partial \xi} + \eta_Z \frac{\partial P^{(n+1)}}{\partial \eta} + \zeta_Z \frac{\partial P^{(n+1)}}{\partial \zeta} \right]. \tag{3.128}$$

In order to satisfy the incompressibility (divergence-free) constraint for constant density flows (3.124), an iterative algorithm has to be performed relying on the discretized Eqs. (3.118) -(3.128). This algorithm has to be repeated iteratively until an appropriately chosen convergence criterion will be satisfied within small values of ε_i $(i = 1,\ldots,m)$, where m is the number of unknown functions. Since this thesis focuses on the explicit Godunov procedure, after applying a high-order interpolation formula for computing the intercell flux values, the characteristic fluxes are evaluated based on the solution of the local Riemann problem at the cell faces (see in Chapter 4). To obtain the divergence-free velocity field based on Eqs. (3.126)-(3.128) at time level $n+1$, the following intercell flux based discretization has been used for the cell-centred intermediate velocity component $\hat{U}_{i,j,k}$ as

$$\hat{U}_{i,j,k} = U^{(n)}_{i,jk} - \Delta t^* \xi_X \frac{\left(U^2\right)^{(n)}_{i+1/2,j,k} - \left(U^2\right)^{(n)}_{i-1/2,j,k}}{\Delta \xi} -$$

$$-\Delta t^* \eta_X \frac{\left(U^2\right)^{(n)}_{i,j+1/2,k} - \left(U^2\right)^{(n)}_{i,j-1/2,k}}{\Delta\eta} - \Delta t^* \zeta_X \frac{\left(U^2\right)^{(n)}_{i,j,k+1/2} - \left(U^2\right)^{(n)}_{i,j,k-1/2}}{\Delta\zeta} -$$

$$-\Delta t^* \xi_Y \frac{(VU)^{(n)}_{i+1/2,j,k} - (VU)^{(n)}_{i-1/2,j,k}}{\Delta\xi} -$$

$$-\Delta t^* \eta_Y \frac{(VU)^{(n)}_{i,j+1/2,k} - (VU)^{(n)}_{i,j-1/2,k}}{\Delta\eta} - \Delta t^* \zeta_Y \frac{(VU)^{(n)}_{i,j,k+1/2} - (VU)^{(n)}_{i,j,k-1/2}}{\Delta\zeta} -$$

$$-\Delta t^* \xi_Z \frac{(WU)^{(n)}_{i+1/2,j,k} - (WU)^{(n)}_{i-1/2,j,k}}{\Delta\xi} -$$

$$-\Delta t^* \eta_Z \frac{(WU)^{(n)}_{i,j+1/2,k} - (WU)^{(n)}_{i,j-1/2,k}}{\Delta\eta} - \Delta t^* \zeta_Z \frac{(WU)^{(n)}_{i,j,k+1/2} - (WU)^{(n)}_{i,j,k-1/2}}{\Delta\zeta} +$$

$$+\Delta t^* \left(\nabla \cdot \underline{\underline{\tau_\xi}}\right)^{(n)}_{i,j,k}, \tag{3.129}$$

and the cell-centred intermediate velocity component $\hat{V}_{i,j,k}$ is

$$\hat{V}_{i,j,k} = V^{(n)}_{i,j,k} - \Delta t^* \xi_X \frac{(UV)^{(n)}_{i+1/2,j,k} - (UV)^{(n)}_{i-1/2,j,k}}{\Delta\xi} -$$

$$-\Delta t^* \eta_X \frac{(UV)^{(n)}_{i,j+1/2,k} - (UV)^{(n)}_{i,j-1/2,k}}{\Delta\eta} - \Delta t^* \zeta_X \frac{(UV)^{(n)}_{i,j,k+1/2} - (UV)^{(n)}_{i,j,k-1/2}}{\Delta\zeta} -$$

$$-\Delta t^* \xi_Y \frac{\left(V^2\right)^{(n)}_{i+1/2,j,k} - \left(V^2\right)^{(n)}_{i-1/2,j,k}}{\Delta\xi} -$$

$$-\Delta t^* \eta_Y \frac{\left(V^2\right)^{(n)}_{i,j+1/2,k} - \left(V^2\right)^{(n)}_{i,j-1/2,k}}{\Delta\eta} - \Delta t^* \zeta_Y \frac{\left(V^2\right)^{(n)}_{i,j,k+1/2} - \left(V^2\right)^{(n)}_{i,j,k-1/2}}{\Delta\zeta} -$$

$$-\Delta t^* \xi_Z \frac{(WV)^{(n)}_{i+1/2,j,k} - (WV)^{(n)}_{i-1/2,j,k}}{\Delta\xi} -$$

$$-\Delta t^* \eta_Z \frac{(WV)^{(n)}_{i,j+1/2,k} - (WV)^{(n)}_{i,j-1/2,k}}{\Delta\eta} - \Delta t^* \zeta_Z \frac{(WV)^{(n)}_{i,j,k+1/2} - (WV)^{(n)}_{i,j,k-1/2}}{\Delta\zeta} +$$

$$+\Delta t^* \left(\nabla \cdot \underline{\underline{\tau_\eta}}\right)^{(n)}_{i,j,k}, \tag{3.130}$$

and the cell-centred intermediate velocity component $\hat{W}_{i,j,k}$ is

$$\hat{W}_{i,j,k} = W^{(n)}_{i,j,k} - \Delta t^* \xi_X \frac{(UW)^{(n)}_{i+1/2,j,k} - (UW)^{(n)}_{i-1/2,j,k}}{\Delta\xi} -$$

$$-\Delta t^* \eta_X \frac{(UW)^{(n)}_{i,j+1/2,k} - (UW)^{(n)}_{i,j-1/2,k}}{\Delta\eta} - \Delta t^* \zeta_X \frac{(UW)^{(n)}_{i,j,k+1/2} - (UW)^{(n)}_{i,j,k-1/2}}{\Delta\zeta} -$$

$$-\Delta t^* \xi_Y \frac{(VW)^{(n)}_{i+1/2,j,k} - (VW)^{(n)}_{i-1/2,j,k}}{\Delta\xi} -$$

$$-\Delta t^* \eta_Y \frac{(VW)^{(n)}_{i,j+1/2,k} - (VW)^{(n)}_{i,j-1/2,k}}{\Delta\eta} - \Delta t^* \zeta_Y \frac{(VW)^{(n)}_{i,j,k+1/2} - (VW)^{(n)}_{i,j,k-1/2}}{\Delta\zeta} -$$

$$-\Delta t^* \xi_Z \frac{\left(W^2\right)^{(n)}_{i+1/2,j,k} - \left(W^2\right)^{(n)}_{i-1/2,j,k}}{\Delta\xi} -$$

$$-\Delta t^* \eta_Z \frac{\left(W^2\right)^{(n)}_{i,j+1/2,k} - \left(W^2\right)^{(n)}_{i,j-1/2,k}}{\Delta\eta} - \Delta t^* \zeta_Z \frac{\left(W^2\right)^{(n)}_{i,j,k+1/2} - \left(W^2\right)^{(n)}_{i,j,k-1/2}}{\Delta\zeta} +$$

$$+\Delta t^* \left(\nabla \cdot \underline{\underline{\tau_\zeta}}\right)^{(n)}_{i,j,k}, \tag{3.131}$$

where $\nabla \cdot \underline{\underline{\tau_i}}$ $(i = \xi, \eta, \zeta)$ represents the tensor divergence of the viscous stress tensor $\underline{\underline{\tau}}$ for each direction of the curvilinear coordinates (ξ, η, ζ). After updating the cell-centred pressure field values based on the numerical solution of the elliptic pressure-Poisson equation (3.125), the projected cell-centred velocity field can be updated as

$$U^{(n+1)}_{i,j,k} = \hat{U}_{i,j,k} -$$

$$-\Delta t^* \left[\xi_X \frac{P^{(n+1)}_{i+1,j,k} - P^{(n+1)}_{i-1,j,k}}{2\Delta\xi} + \eta_X \frac{P^{(n+1)}_{i,j+1,k} - P^{(n+1)}_{i,j-1,k}}{2\Delta\eta} + \zeta_X \frac{P^{(n+1)}_{i,j,k+1} - P^{(n+1)}_{i,j,k-1}}{2\Delta\zeta}\right], \tag{3.132}$$

$$V^{(n+1)}_{i,j,k} = \hat{V}_{i,j,k} -$$

$$-\Delta t^* \left[\xi_Y \frac{P^{(n+1)}_{i+1,j,k} - P^{(n+1)}_{i-1,j,k}}{2\Delta\xi} + \eta_Y \frac{P^{(n+1)}_{i,j+1,k} - P^{(n+1)}_{i,j-1,k}}{2\Delta\eta} + \zeta_Y \frac{P^{(n+1)}_{i,j,k+1} - P^{(n+1)}_{i,j,k-1}}{2\Delta\zeta}\right], \tag{3.133}$$

$$W^{(n+1)}_{i,j,k} = \hat{W}_{i,j,k} -$$

$$-\Delta t^{*}\left[\xi_{Z}\frac{P_{i+1,j,k}^{(n+1)}-P_{i-1,j,k}^{(n+1)}}{2\Delta\xi}+\eta_{Z}\frac{P_{i,j+1,k}^{(n+1)}-P_{i,j-1,k}^{(n+1)}}{2\Delta\eta}+\zeta_{Z}\frac{P_{i,j,k+1}^{(n+1)}-P_{i,j,k-1}^{(n+1)}}{2\Delta\zeta}\right]. \quad (3.134)$$

Since, the discretized system of equations (3.129)-(3.134) has been solved iteratively, the convergence criterion might be chosen as the maximum norm of the numerical solution between two different time levels with a value smaller than a prescribed small ε threshold. Note that any other convergence criterion can be used and being valid, ensuring that the numerical solution of the system is converged to the boundary conditions.

3.3.2.2 Variable Density Flows

For variable density flows, the pressure-Poisson equation is different from the constant density case (3.125), because the fluid density ρ or its reciprocal $\sigma = {}^{1}/_{\rho}$ appears in the governing equations. Multiplying the system of equations (3.121)-(3.123) by the density of the fluid ρ, and adding them together, the following

$$\begin{aligned}
&\xi_{X}\frac{\partial\left[\rho U^{(n+1)}\right]}{\partial\xi}+\eta_{X}\frac{\partial\left[\rho U^{(n+1)}\right]}{\partial\eta}+\zeta_{X}\frac{\partial\left[\rho U^{(n+1)}\right]}{\partial\zeta}+\\
&+\xi_{Y}\frac{\partial\left[\rho V^{(n+1)}\right]}{\partial\xi}+\eta_{Y}\frac{\partial\left[\rho V^{(n+1)}\right]}{\partial\eta}+\zeta_{Y}\frac{\partial\left[\rho V^{(n+1)}\right]}{\partial\zeta}+\\
&+\xi_{Z}\frac{\partial\left[\rho W^{(n+1)}\right]}{\partial\xi}+\eta_{Z}\frac{\partial\left[\rho W^{(n+1)}\right]}{\partial\eta}+\zeta_{Z}\frac{\partial\left[\rho W^{(n+1)}\right]}{\partial\zeta}=0
\end{aligned} \quad (3.135)$$

continuity equation is valid for incompressible variable density flows at time level $n+1$. By taking into account the incompressibility (divergence-free) constraint relying on Eq. (3.135), the system of equations (3.121)-(3.123) multiplied by the fluid density ρ yields an elliptical three-dimensional pressure-Poisson equation for incompressible variable density flows in a curvilinear coordinate system as

$$\begin{aligned}
&\left(\xi_{X}^{2}+\xi_{Y}^{2}+\xi_{Z}^{2}\right)\frac{\partial}{\partial\xi}\left[\sigma\frac{\partial P^{(n+1)}}{\partial\xi}\right]+\\
&+\left(\eta_{X}^{2}+\eta_{Y}^{2}+\eta_{Z}^{2}\right)\frac{\partial}{\partial\eta}\left[\sigma\frac{\partial P^{(n+1)}}{\partial\eta}\right]+\\
&+\left(\zeta_{X}^{2}+\zeta_{Y}^{2}+\zeta_{Z}^{2}\right)\frac{\partial}{\partial\zeta}\left[\sigma\frac{\partial P^{(n+1)}}{\partial\zeta}\right]+
\end{aligned}$$

$$
\begin{aligned}
&+2\left(\xi_X\eta_X+\xi_Y\eta_Y+\xi_Z\eta_Z\right)\frac{\partial}{\partial\xi}\left[\sigma\frac{\partial P^{(n+1)}}{\partial\eta}\right]+\\
&+2\left(\xi_X\zeta_X+\xi_Y\zeta_Y+\xi_Z\zeta_Z\right)\frac{\partial}{\partial\xi}\left[\sigma\frac{\partial P^{(n+1)}}{\partial\zeta}\right]+\\
&+2\left(\eta_X\zeta_X+\eta_Y\zeta_Y+\eta_Z\zeta_Z\right)\frac{\partial}{\partial\eta}\left[\sigma\frac{\partial P^{(n+1)}}{\partial\zeta}\right]+\\
&+\left(\xi_{XX}+\xi_{YY}+\xi_{ZZ}\right)\left[\sigma\frac{\partial P^{(n+1)}}{\partial\xi}\right]+\\
&+\left(\eta_{XX}+\eta_{YY}+\eta_{ZZ}\right)\left[\sigma\frac{\partial P^{(n+1)}}{\partial\eta}\right]+\\
&+\left(\zeta_{XX}+\zeta_{YY}+\zeta_{ZZ}\right)\left[\sigma\frac{\partial P^{(n+1)}}{\partial\zeta}\right]=\\
&=\frac{1}{\Delta t^*}\left(\xi_X\frac{\partial\hat{U}}{\partial\xi}+\eta_X\frac{\partial\hat{U}}{\partial\eta}+\zeta_X\frac{\partial\hat{U}}{\partial\zeta}+\right.\\
&+\xi_Y\frac{\partial\hat{V}}{\partial\xi}+\eta_Y\frac{\partial\hat{V}}{\partial\eta}+\zeta_Y\frac{\partial\hat{V}}{\partial\zeta}+\\
&\left.+\xi_Z\frac{\partial\hat{W}}{\partial\xi}+\eta_Z\frac{\partial\hat{W}}{\partial\eta}+\zeta_Z\frac{\partial\hat{W}}{\partial\zeta}\right)^{(n)}. \qquad (3.136)
\end{aligned}
$$

After solving the elliptical pressure-Poisson equation (3.136) numerically, the velocity field has to be updated based on the intermediate velocity components $\rho\hat{U}$, $\rho\hat{V}$, and $\rho\hat{W}$ by using the solution of Eqs. (3.118)-(3.120) multiplied by the fluid density ρ; and based on the updated solution of the pressure-Poisson equation. Note that the numerical solution of the elliptical curvilinear Poisson equation (3.136) for the pressure field has been discussed for variable density flows in the following subsection. For incompressible variable density flows, the updated velocity components in a curvilinear coordinate system at time level $n+1$, relying on the Helmholtz-Hodge decomposition (3.38), are written as

$$
\rho U^{(n+1)}=\rho\hat{U}-\Delta t^*\left[\xi_X\frac{\partial P^{(n+1)}}{\partial\xi}+\eta_X\frac{\partial P^{(n+1)}}{\partial\eta}+\zeta_X\frac{\partial P^{(n+1)}}{\partial\zeta}\right], \qquad (3.137)
$$

$$
\rho V^{(n+1)}=\rho\hat{V}-\Delta t^*\left[\xi_Y\frac{\partial P^{(n+1)}}{\partial\xi}+\eta_Y\frac{\partial P^{(n+1)}}{\partial\eta}+\zeta_Y\frac{\partial P^{(n+1)}}{\partial\zeta}\right], \qquad (3.138)
$$

$$\rho W^{(n+1)} = \rho \hat{W} - \Delta t^* \left[\xi_Z \frac{\partial P^{(n+1)}}{\partial \xi} + \eta_Z \frac{\partial P^{(n+1)}}{\partial \eta} + \zeta_Z \frac{\partial P^{(n+1)}}{\partial \zeta} \right]. \tag{3.139}$$

The cell-centred intermediate velocity components $\rho \hat{U}_{i,j,k}$, $\rho \hat{V}_{i,j,k}$, $\rho \hat{W}_{i,j,k}$, and the updated velocity components $\rho U_{i,j,k}^{(n+1)}$, $\rho V_{i,j,k}^{(n+1)}$, $\rho W_{i,j,k}^{(n+1)}$ at time level $n+1$ have to be computed similarly to Eqs. (3.129)-(3.134) multiplying them by the density of fluid ρ (see more details about incompressible variable density flows in conjunction with the pressure-projection method in the papers of Bell et al. [118] and Almgren et al. [121]).

3.3.3 Solution of the Curvilinear Pressure-Poisson Equation

3.3.3.1 Constant Density Flows

For constant density flows, the discretized system of linear equations of the second-order elliptical pressure-Poisson equation (3.125) has been solved by the Gauss-Seidel-type Successive Over-Relaxation (S.O.R.) iterative method in a curvilinear coordinate system. Central difference approximations have been employed for second-order, mixed and first-order derivatives of the pressure. In the present case, the formulation of the finite volume discretization is equivalent to the finite difference approach, because $\Delta\xi = \Delta\eta = \Delta\zeta = 1$ in the curvilinear coordinate system. The derivatives of the curvilinear coordinates (ξ, η, ζ), according to Cartesian coordinates (X, Y, Z), has been computed by using finite difference approximations, which can be found in detail in Appendix A.

The discretized form of the pressure-Poisson equation (3.125) using the S.O.R. iterative method formulation in the curvilinear coordinate system can be written as

$$\left(\xi_X^2 + \xi_Y^2 + \xi_Z^2\right) \frac{\omega_P P_{i-1,j,k}^{(m+1)} - 2P_{i,j,k}^{(m+1)} + 2\left(1-\omega_P\right) P_{i,j,k}^{(m)} + \omega_P P_{i+1,j,k}^{(m)}}{\left(\Delta\xi\right)^2} +$$

$$+ \left(\eta_X^2 + \eta_Y^2 + \eta_Z^2\right) \frac{\omega_P P_{i,j-1,k}^{(m+1)} - 2P_{i,j,k}^{(m+1)} + 2\left(1-\omega_P\right) P_{i,j,k}^{(m)} + \omega_P P_{i,j+1,k}^{(m)}}{\left(\Delta\eta\right)^2} +$$

$$+ \left(\zeta_X^2 + \zeta_Y^2 + \zeta_Z^2\right) \frac{\omega_P P_{i,j,k-1}^{(m+1)} - 2P_{i,j,k}^{(m+1)} + 2\left(1-\omega_P\right) P_{i,j,k}^{(m)} + \omega_P P_{i,j,k+1}^{(m)}}{\left(\Delta\zeta\right)^2} +$$

$$+ \omega_P \left(\xi_X \eta_X + \xi_Y \eta_Y + \xi_Z \eta_Z\right) \frac{P_{i+1,j+1,k}^{(m)} - P_{i+1,j-1,k}^{(m+1)} - P_{i-1,j+1,k}^{(m)} + P_{i-1,j-1,k}^{(m+1)}}{2\Delta\xi\Delta\eta} +$$

$$+ \omega_P \left(\xi_X \zeta_X + \xi_Y \zeta_Y + \xi_Z \zeta_Z\right) \frac{P_{i+1,j,k+1}^{(m)} - P_{i+1,j,k-1}^{(m+1)} - P_{i-1,j,k+1}^{(m)} + P_{i-1,j,k-1}^{(m+1)}}{2\Delta\xi\Delta\zeta} +$$

$$+\omega_P\left(\eta_X\zeta_X+\eta_Y\zeta_Y+\eta_Z\zeta_Z\right)\frac{P^{(m)}_{i,j+1,k+1}-P^{(m+1)}_{i,j+1,k-1}-P^{(m)}_{i,j-1,k+1}+P^{(m+1)}_{i,j-1,k-1}}{2\Delta\eta\Delta\zeta}+$$

$$+\omega_P\left(\xi_{XX}+\xi_{YY}+\xi_{ZZ}\right)\frac{P^{(m)}_{i+1,j,k}-P^{(m+1)}_{i-1,j,k}}{2\Delta\xi}+$$

$$+\omega_P\left(\eta_{XX}+\eta_{YY}+\eta_{ZZ}\right)\frac{P^{(m)}_{i,j+1,k}-P^{(m+1)}_{i,j-1,k}}{2\Delta\eta}+$$

$$+\omega_P\left(\zeta_{XX}+\zeta_{YY}+\zeta_{ZZ}\right)\frac{P^{(m)}_{i,j,k+1}-P^{(m+1)}_{i,j,k-1}}{2\Delta\zeta}=\omega_P\varphi^{(m)}_{i,j,k}, \tag{3.140}$$

where ω_P is the relaxation factor (parameter) introduced to accelerate the rate of convergence of the Gauss-Seidel method [136, p. 11], the m superscript denotes the m^{th} sub-iteration step, and the discrete function in the right hand side of (3.140) is

$$\varphi^{(m)}_{i,j,k}=\frac{1}{\Delta t^*}\left(\xi_X\frac{\hat{U}_{i+1,j,k}-\hat{U}_{i-1,j,k}}{2\Delta\xi}+\eta_X\frac{\hat{U}_{i,j+1,k}-\hat{U}_{i,j-1,k}}{2\Delta\eta}+\zeta_X\frac{\hat{U}_{i,j,k+1}-\hat{U}_{i,j,k-1}}{2\Delta\zeta}+\right.$$

$$+\xi_Y\frac{\hat{V}_{i+1,j,k}-\hat{V}_{i-1,j,k}}{2\Delta\xi}+\eta_Y\frac{\hat{V}_{i,j+1,k}-\hat{V}_{i,j-1,k}}{2\Delta\eta}+\zeta_Y\frac{\hat{V}_{i,j,k+1}-\hat{V}_{i,j,k-1}}{2\Delta\zeta}+$$

$$\left.+\xi_Z\frac{\hat{W}_{i+1,j,k}-\hat{W}_{i-1,j,k}}{2\Delta\xi}+\eta_Z\frac{\hat{W}_{i,j+1,k}-\hat{W}_{i,j-1,k}}{2\Delta\eta}+\zeta_Z\frac{\hat{W}_{i,j,k+1}-\hat{W}_{i,j,k-1}}{2\Delta\zeta}\right)^{(n)}, \tag{3.141}$$

where $\hat{U}$, $\hat{V}$, and $\hat{W}$ are the intermediate velocity components of the FS-PP method of Chorin [4] and Temam [108]. After re-arranging the discretized form of the second-order elliptical pressure-Poisson equation (3.140), the following

$$P^{(m+1)}_{i,j,k}=\left(1-\omega_P\right)P^{(m)}_{i,j,k}-$$

$$-\frac{\omega_P}{a_P}\left(a_WP^{(m+1)}_{i-1,j,k}+a_EP^{(m)}_{i+1,j,k}+a_SP^{(m+1)}_{i,j-1,k}+a_NP^{(m)}_{i,j+1,k}+a_BP^{(m+1)}_{i,j,k-1}+a_TP^{(m)}_{i,j,k+1}+\right.$$

$$+a_{NE}P^{(m)}_{i+1,j+1,k}+a_{SE}P^{(m+1)}_{i+1,j-1,k}+a_{NW}P^{(m)}_{i-1,j+1,k}+a_{SW}P^{(m+1)}_{i-1,j-1,k}+$$

$$+a_{TE}P^{(m)}_{i+1,j,k+1}+a_{BE}P^{(m+1)}_{i+1,j,k-1}+a_{TW}P^{(m)}_{i-1,j,k+1}+a_{BW}P^{(m+1)}_{i-1,j,k-1}+$$

$$\left.+a_{TN}P^{(m)}_{i,j+1,k+1}+a_{BN}P^{(m+1)}_{i,j+1,k-1}+a_{TS}P^{(m)}_{i,j-1,k+1}+a_{BS}P^{(m+1)}_{i,j-1,k-1}-\varphi^{(m)}_{i,j,k}\right) \tag{3.142}$$

algebraic equation is obtained in the internal curvilinear domain, where the coefficients

of the sparse band system of linear equations corresponding to the cell indices are

$$a_{BS} = \frac{\eta_X \zeta_X + \eta_Y \zeta_Y + \eta_Z \zeta_Z}{2\Delta\eta\Delta\zeta}, \tag{3.143}$$

$$a_{BW} = \frac{\xi_X \zeta_X + \xi_Y \zeta_Y + \xi_Z \zeta_Z}{2\Delta\xi\Delta\zeta}, \tag{3.144}$$

$$a_B = \frac{\zeta_X^2 + \zeta_Y^2 + \zeta_Z^2}{(\Delta\zeta)^2} - \frac{\zeta_{XX} + \zeta_{YY} + \zeta_{ZZ}}{2\Delta\zeta}, \tag{3.145}$$

$$a_{BE} = -\frac{\xi_X \zeta_X + \xi_Y \zeta_Y + \xi_Z \zeta_Z}{2\Delta\xi\Delta\zeta}, \tag{3.146}$$

$$a_{BN} = -\frac{\eta_X \zeta_X + \eta_Y \zeta_Y + \eta_Z \zeta_Z}{2\Delta\eta\Delta\zeta}, \tag{3.147}$$

$$a_{SW} = \frac{\xi_X \eta_X + \xi_Y \eta_Y + \xi_Z \eta_Z}{2\Delta\xi\Delta\eta}, \tag{3.148}$$

$$a_S = \frac{\eta_X^2 + \eta_Y^2 + \eta_Z^2}{(\Delta\eta)^2} - \frac{\eta_{XX} + \eta_{YY} + \eta_{ZZ}}{2\Delta\eta}, \tag{3.149}$$

$$a_{SE} = -\frac{\xi_X \eta_X + \xi_Y \eta_Y + \xi_Z \eta_Z}{2\Delta\xi\Delta\eta}, \tag{3.150}$$

$$a_W = \frac{\xi_X^2 + \xi_Y^2 + \xi_Z^2}{(\Delta\xi)^2} - \frac{\xi_{XX} + \xi_{YY} + \xi_{ZZ}}{2\Delta\xi}, \tag{3.151}$$

$$a_P = -2\left[\frac{\xi_X^2 + \xi_Y^2 + \xi_Z^2}{(\Delta\xi)^2} + \frac{\eta_X^2 + \eta_Y^2 + \eta_Z^2}{(\Delta\eta)^2} + \frac{\zeta_X^2 + \zeta_Y^2 + \zeta_Z^2}{(\Delta\zeta)^2}\right], \tag{3.152}$$

$$a_E = \frac{\xi_X^2 + \xi_Y^2 + \xi_Z^2}{(\Delta\xi)^2} + \frac{\xi_{XX} + \xi_{YY} + \xi_{ZZ}}{2\Delta\xi}, \tag{3.153}$$

$$a_{NW} = -\frac{\xi_X \eta_X + \xi_Y \eta_Y + \xi_Z \eta_Z}{2\Delta\xi\Delta\eta}, \tag{3.154}$$

$$a_N = \frac{\eta_X^2 + \eta_Y^2 + \eta_Z^2}{(\Delta\eta)^2} + \frac{\eta_{XX} + \eta_{YY} + \eta_{ZZ}}{2\Delta\eta}, \tag{3.155}$$

$$a_{NE} = \frac{\xi_X \eta_X + \xi_Y \eta_Y + \xi_Z \eta_Z}{2\Delta\xi\Delta\eta}, \tag{3.156}$$

$$a_{TS} = -\frac{\eta_X \zeta_X + \eta_Y \zeta_Y + \eta_Z \zeta_Z}{2\Delta\eta\Delta\zeta}, \tag{3.157}$$

$$a_{TW} = -\frac{\xi_X \zeta_X + \xi_Y \zeta_Y + \xi_Z \zeta_Z}{2\Delta\xi\Delta\zeta}, \tag{3.158}$$

$$a_T = \frac{\zeta_X^2 + \zeta_Y^2 + \zeta_Z^2}{(\Delta\zeta)^2} + \frac{\zeta_{XX} + \zeta_{YY} + \zeta_{ZZ}}{2\Delta\zeta}, \tag{3.159}$$

$$a_{TE} = \frac{\xi_X \zeta_X + \xi_Y \zeta_Y + \xi_Z \zeta_Z}{2\Delta\xi\Delta\zeta}, \tag{3.160}$$

$$a_{TN} = \frac{\eta_X \zeta_X + \eta_Y \zeta_Y + \eta_Z \zeta_Z}{2\Delta\eta\Delta\zeta}, \tag{3.161}$$

and the right hand side of the algebraic system of equations is equal to

$$b_P = \omega_P \varphi_{i,j,k}^{(m)}. \tag{3.162}$$

For incompressible constant density flows, the sparse band system of linear equations of the discretized second-order elliptical pressure-Poisson equation (3.140) consists of 19 bands in a curvilinear coordinate system. The S.O.R. method for solving the sparse band system of linear equations for constant density flows has been implemented in the HIRECOM-MULTIPHYSICS v1.0 in-house FORTRAN 90/95 software package, which has been developed as a part of the Ph.D. project.

3.3.3.2 Variable Density Flows

For variable density flows, the second-order elliptical pressure-Poisson equation (3.136) is different from the equation of the constant density case (3.125), because the fluid density ρ or its reciprocal $\sigma = 1/\rho$ appears in the Laplacian term. The sparse band system of linear equations of the Poisson equation for incompressible variable density flow (3.136) has again been solved by the Gauss-Seidel-type Successive Over-Relaxation (S.O.R.) iterative method in curvilinear coordinate system. As before, central difference approximations have been employed for second-order, mixed and first-order derivatives of the pressure. In the present case, the formulation of the finite volume discretization is equivalent to the finite difference approach, because $\Delta\xi = \Delta\eta = \Delta\zeta = 1$ in the curvilinear coordinate system. The derivatives of the curvilinear coordinates (ξ, η, ζ), according to Cartesian coordinates (X, Y, Z), has been computed by using finite difference approximations, which can be found in detail in Appendix A (see details in [27] as well).

The discretized form of the pressure-Poisson equation (3.136) using S.O.R. iterative method formulation in curvilinear coordinate system can be written as

$$\left(\xi_X^2 + \xi_Y^2 + \xi_Z^2\right) \frac{\sigma_{i-1,j,k}\left[\omega_P P_{i-1,j,k}^{(m+1)} - P_{i,j,k}^{(m+1)} + (1-\omega_P) P_{i,j,k}^{(m)}\right]}{(\Delta\xi)^2} +$$

$$
\begin{aligned}
&+\left(\xi_X^2+\xi_Y^2+\xi_Z^2\right)\frac{\sigma_{i+1,j,k}\left[\omega_P P_{i+1,j,k}^{(m)}-P_{i,j,k}^{(m+1)}+(1-\omega_P)P_{i,j,k}^{(m)}\right]}{(\Delta\xi)^2}+\\
&+\left(\eta_X^2+\eta_Y^2+\eta_Z^2\right)\frac{\sigma_{i,j-1,k}\left[\omega_P P_{i,j-1,k}^{(m+1)}-P_{i,j,k}^{(m+1)}+(1-\omega_P)P_{i,j,k}^{(m)}\right]}{(\Delta\eta)^2}+\\
&+\left(\eta_X^2+\eta_Y^2+\eta_Z^2\right)\frac{\sigma_{i,j+1,k}\left[\omega_P P_{i,j+1,k}^{(m)}-P_{i,j,k}^{(m+1)}+(1-\omega_P)P_{i,j,k}^{(m)}\right]}{(\Delta\eta)^2}+\\
&+\left(\zeta_X^2+\zeta_Y^2+\zeta_Z^2\right)\frac{\sigma_{i,j,k-1}\left[\omega_P P_{i,j,k-1}^{(m+1)}-P_{i,j,k}^{(m+1)}+(1-\omega_P)P_{i,j,k}^{(m)}\right]}{(\Delta\zeta)^2}+\\
&+\left(\zeta_X^2+\zeta_Y^2+\zeta_Z^2\right)\frac{\sigma_{i,j,k+1}\left[\omega_P P_{i,j,k+1}^{(m)}-P_{i,j,k}^{(m+1)}+(1-\omega_P)P_{i,j,k}^{(m)}\right]}{(\Delta\zeta)^2}+\\
&+\omega_P\left(\xi_X\eta_X+\xi_Y\eta_Y+\xi_Z\eta_Z\right)\frac{\sigma_{i+1,j+1,k}P_{i+1,j+1,k}^{(m)}-\sigma_{i+1,j-1,k}P_{i+1,j-1,k}^{(m+1)}}{2\Delta\xi\Delta\eta}-\\
&-\omega_P\left(\xi_X\eta_X+\xi_Y\eta_Y+\xi_Z\eta_Z\right)\frac{\sigma_{i-1,j+1,k}P_{i-1,j+1,k}^{(m)}-\sigma_{i-1,j-1,k}P_{i-1,j-1,k}^{(m+1)}}{2\Delta\xi\Delta\eta}+\\
&+\omega_P\left(\xi_X\zeta_X+\xi_Y\zeta_Y+\xi_Z\zeta_Z\right)\frac{\sigma_{i+1,j,k+1}P_{i+1,j,k+1}^{(m)}-\sigma_{i+1,j,k-1}P_{i+1,j,k-1}^{(m+1)}}{2\Delta\xi\Delta\zeta}-\\
&-\omega_P\left(\xi_X\zeta_X+\xi_Y\zeta_Y+\xi_Z\zeta_Z\right)\frac{\sigma_{i-1,j,k+1}P_{i-1,j,k+1}^{(m)}-\sigma_{i-1,j,k-1}P_{i-1,j,k-1}^{(m+1)}}{2\Delta\xi\Delta\zeta}+\\
&+\omega_P\left(\eta_X\zeta_X+\eta_Y\zeta_Y+\eta_Z\zeta_Z\right)\frac{\sigma_{i,j+1,k+1}P_{i,j+1,k+1}^{(m)}-\sigma_{i,j+1,k-1}P_{i,j+1,k-1}^{(m+1)}}{2\Delta\eta\Delta\zeta}-\\
&-\omega_P\left(\eta_X\zeta_X+\eta_Y\zeta_Y+\eta_Z\zeta_Z\right)\frac{\sigma_{i,j-1,k+1}P_{i,j-1,k+1}^{(m)}-\sigma_{i,j-1,k-1}P_{i,j-1,k-1}^{(m+1)}}{2\Delta\eta\Delta\zeta}+\\
&+\omega_P\left(\xi_{XX}+\xi_{YY}+\xi_{ZZ}\right)\frac{\sigma_{i+1,j,k}P_{i+1,j,k}^{(m)}-\sigma_{i-1,j,k}P_{i-1,j,k}^{(m+1)}}{2\Delta\xi}+\\
&+\omega_P\left(\eta_{XX}+\eta_{YY}+\eta_{ZZ}\right)\frac{\sigma_{i,j+1,k}P_{i,j+1,k}^{(m)}-\sigma_{i,j-1,k}P_{i,j-1,k}^{(m+1)}}{2\Delta\eta}+\\
&+\omega_P\left(\zeta_{XX}+\zeta_{YY}+\zeta_{ZZ}\right)\frac{\sigma_{i,j,k+1}P_{i,j,k+1}^{(m)}-\sigma_{i,j,k-1}P_{i,j,k-1}^{(m+1)}}{2\Delta\zeta}=\omega_P\varphi_{i,j,k}^{(m)},
\end{aligned}
\tag{3.163}
$$

where similarly to the discretized pressure-Poisson equation (3.140) for constant density flows, ω_P is the relaxation factor (parameter) introduced to accelerate the rate of convergence of the Gauss-Seidel method, the m superscript denotes the m^{th} sub-iteration step, and the discrete disturbing function in the right hand side is equal to Eq. (3.141). After re-arranging the discretized form of the second-order elliptical pressure-Poisson equation (3.163), the same algebraic equation is obtained as Eq. (3.142) in the internal curvilinear domain, where the coefficients of the sparse band system of linear equations, corresponding to the cell indices, are different compared to the constant density case as

$$a_{BS} = \frac{\eta_X \zeta_X + \eta_Y \zeta_Y + \eta_Z \zeta_Z}{2\Delta\eta\Delta\zeta} \sigma_{i,j-1,k-1}, \tag{3.164}$$

$$a_{BW} = \frac{\xi_X \zeta_X + \xi_Y \zeta_Y + \xi_Z \zeta_Z}{2\Delta\xi\Delta\zeta} \sigma_{i-1,j,k-1}, \tag{3.165}$$

$$a_B = \frac{\zeta_X^2 + \zeta_Y^2 + \zeta_Z^2}{(\Delta\zeta)^2} \sigma_{i,j,k-1} - \frac{\zeta_{XX} + \zeta_{YY} + \zeta_{ZZ}}{2\Delta\zeta} \sigma_{i,j,k-1}, \tag{3.166}$$

$$a_{BE} = -\frac{\xi_X \zeta_X + \xi_Y \zeta_Y + \xi_Z \zeta_Z}{2\Delta\xi\Delta\zeta} \sigma_{i+1,j,k-1}, \tag{3.167}$$

$$a_{BN} = -\frac{\eta_X \zeta_X + \eta_Y \zeta_Y + \eta_Z \zeta_Z}{2\Delta\eta\Delta\zeta} \sigma_{i,j+1,k-1}, \tag{3.168}$$

$$a_{SW} = \frac{\xi_X \eta_X + \xi_Y \eta_Y + \xi_Z \eta_Z}{2\Delta\xi\Delta\eta} \sigma_{i-1,j-1,k}, \tag{3.169}$$

$$a_S = \frac{\eta_X^2 + \eta_Y^2 + \eta_Z^2}{(\Delta\eta)^2} \sigma_{i,j-1,k} - \frac{\eta_{XX} + \eta_{YY} + \eta_{ZZ}}{2\Delta\eta} \sigma_{i,j-1,k}, \tag{3.170}$$

$$a_{SE} = -\frac{\xi_X \eta_X + \xi_Y \eta_Y + \xi_Z \eta_Z}{2\Delta\xi\Delta\eta} \sigma_{i+1,j-1,k}, \tag{3.171}$$

$$a_W = \frac{\xi_X^2 + \xi_Y^2 + \xi_Z^2}{(\Delta\xi)^2} \sigma_{i-1,j,k} - \frac{\xi_{XX} + \xi_{YY} + \xi_{ZZ}}{2\Delta\xi} \sigma_{i-1,j,k}, \tag{3.172}$$

$$a_P = -\frac{\xi_X^2 + \xi_Y^2 + \xi_Z^2}{(\Delta\xi)^2} \left(\sigma_{i-1,j,k} + \sigma_{i+1,j,k}\right) - \tag{3.173}$$

$$-\frac{\eta_X^2 + \eta_Y^2 + \eta_Z^2}{(\Delta\eta)^2} \left(\sigma_{i,j-1,k} + \sigma_{i,j+1,k}\right) - \tag{3.174}$$

$$-\frac{\zeta_X^2 + \zeta_Y^2 + \zeta_Z^2}{(\Delta\zeta)^2} \left(\sigma_{i,j,k-1} + \sigma_{i,j,k+1}\right), \tag{3.175}$$

$$a_E = \frac{\xi_X^2 + \xi_Y^2 + \xi_Z^2}{(\Delta\xi)^2}\sigma_{i+1,j,k} + \frac{\xi_{XX} + \xi_{YY} + \xi_{ZZ}}{2\Delta\xi}\sigma_{i+1,j,k}, \tag{3.176}$$

$$a_{NW} = -\frac{\xi_X\eta_X + \xi_Y\eta_Y + \xi_Z\eta_Z}{2\Delta\xi\Delta\eta}\sigma_{i-1,j+1,k}, \tag{3.177}$$

$$a_N = \frac{\eta_X^2 + \eta_Y^2 + \eta_Z^2}{(\Delta\eta)^2}\sigma_{i,j+1,k} + \frac{\eta_{XX} + \eta_{YY} + \eta_{ZZ}}{2\Delta\eta}\sigma_{i,j+1,k}, \tag{3.178}$$

$$a_{NE} = \frac{\xi_X\eta_X + \xi_Y\eta_Y + \xi_Z\eta_Z}{2\Delta\xi\Delta\eta}\sigma_{i+1,j+1,k}, \tag{3.179}$$

$$a_{TS} = -\frac{\eta_X\zeta_X + \eta_Y\zeta_Y + \eta_Z\zeta_Z}{2\Delta\eta\Delta\zeta}\sigma_{i,j-1,k+1}, \tag{3.180}$$

$$a_{TW} = -\frac{\xi_X\zeta_X + \xi_Y\zeta_Y + \xi_Z\zeta_Z}{2\Delta\xi\Delta\zeta}\sigma_{i-1,j,k+1}, \tag{3.181}$$

$$a_T = \frac{\zeta_X^2 + \zeta_Y^2 + \zeta_Z^2}{(\Delta\zeta)^2}\sigma_{i,j,k+1} + \frac{\zeta_{XX} + \zeta_{YY} + \zeta_{ZZ}}{2\Delta\zeta}\sigma_{i,j,k+1}, \tag{3.182}$$

$$a_{TE} = \frac{\xi_X\zeta_X + \xi_Y\zeta_Y + \xi_Z\zeta_Z}{2\Delta\xi\Delta\zeta}\sigma_{i+1,j,k+1}, \tag{3.183}$$

$$a_{TN} = \frac{\eta_X\zeta_X + \eta_Y\zeta_Y + \eta_Z\zeta_Z}{2\Delta\eta\Delta\zeta}\sigma_{i,j+1,k+1}, \tag{3.184}$$

and similarly to the constant density case, the right hand side of the algebraic system of equations is equal to

$$b_P = \omega_P\varphi_{i,j,k}^{(m)}. \tag{3.185}$$

For incompressible variable density flows, the sparse system of linear equations of the discretized second-order elliptical pressure-Poisson equation (3.163), similarly to the discretized pressure-Poisson equation for constant density flows (3.140), consists of 19 bands in curvilinear coordinate system. For variable density flows, again the S.O.R. method for solving the sparse system of linear equations has been implemented in the HIRECOM-MULTIPHYSICS Unified Code v1.0 in-house FORTRAN 90/95 software package.

3.4 Constitutive Equations

3.4.1 Newtonian Fluid Model

For microfluidic applications, the viscous terms become dominant as the flow is characterized by a low Reynolds number. For an incompressible Newtonian fluid using Stokes' hypothesis [27, p. 31], the elements of the viscous stress tensor $\underline{\underline{\tau}}$ in Cartesian coordinate system (x, y, z) in dimensional form are written as

$$\begin{cases} \tau_{XX} = 2\mu \frac{\partial u}{\partial x}, \\ \tau_{YY} = 2\mu \frac{\partial v}{\partial y}, \\ \tau_{ZZ} = 2\mu \frac{\partial w}{\partial z}, \\ \tau_{XY} = \tau_{YX} = \mu \left(\frac{\partial v}{\partial x} + \frac{\partial u}{\partial y} \right), \\ \tau_{XZ} = \tau_{ZX} = \mu \left(\frac{\partial w}{\partial x} + \frac{\partial u}{\partial z} \right), \\ \tau_{YZ} = \tau_{ZY} = \mu \left(\frac{\partial w}{\partial y} + \frac{\partial v}{\partial z} \right), \end{cases} \tag{3.186}$$

and the dimensionless vectors of the viscous fluxes in Eq. (3.109) in the curvilinear coordinate system can be written as

$$\mathbf{E}_{\mathbf{V}}^{\xi} = J \begin{bmatrix} 0 \\ a_{\xi}^{\mathbf{E}_V^{\xi}} U_{\xi} + b_{\eta}^{\mathbf{E}_V^{\xi}} U_{\eta} + c_{\zeta}^{\mathbf{E}_V^{\xi}} U_{\zeta} \\ a_{\xi}^{\mathbf{E}_V^{\xi}} V_{\xi} + b_{\eta}^{\mathbf{E}_V^{\xi}} V_{\eta} + c_{\zeta}^{\mathbf{E}_V^{\xi}} V_{\zeta} \\ a_{\xi}^{\mathbf{E}_V^{\xi}} W_{\xi} + b_{\eta}^{\mathbf{E}_V^{\xi}} W_{\eta} + c_{\zeta}^{\mathbf{E}_V^{\xi}} W_{\zeta} \end{bmatrix}, \tag{3.187}$$

$$\mathbf{F}_{\mathbf{V}}^{\eta} = J \begin{bmatrix} 0 \\ a_{\xi}^{\mathbf{F}_{\mathbf{V}}^{\eta}} U_{\xi} + b_{\eta}^{\mathbf{F}_{\mathbf{V}}^{\eta}} U_{\eta} + c_{\zeta}^{\mathbf{F}_{\mathbf{V}}^{\eta}} U_{\zeta} \\ a_{\xi}^{\mathbf{F}_{\mathbf{V}}^{\eta}} V_{\xi} + b_{\eta}^{\mathbf{F}_{\mathbf{V}}^{\eta}} V_{\eta} + c_{\zeta}^{\mathbf{F}_{\mathbf{V}}^{\eta}} V_{\zeta} \\ a_{\xi}^{\mathbf{F}_{\mathbf{V}}^{\eta}} W_{\xi} + b_{\eta}^{\mathbf{F}_{\mathbf{V}}^{\eta}} W_{\eta} + c_{\zeta}^{\mathbf{F}_{\mathbf{V}}^{\eta}} W_{\zeta} \end{bmatrix}, \tag{3.188}$$

$$\mathbf{G}_{\mathbf{V}}^{\zeta} = J \begin{bmatrix} 0 \\ a_{\xi}^{\mathbf{G}_{\mathbf{V}}^{\zeta}} U_{\xi} + b_{\eta}^{\mathbf{G}_{\mathbf{V}}^{\zeta}} U_{\eta} + c_{\zeta}^{\mathbf{G}_{\mathbf{V}}^{\zeta}} U_{\zeta} \\ a_{\xi}^{\mathbf{G}_{\mathbf{V}}^{\zeta}} V_{\xi} + b_{\eta}^{\mathbf{G}_{\mathbf{V}}^{\zeta}} V_{\eta} + c_{\zeta}^{\mathbf{G}_{\mathbf{V}}^{\zeta}} V_{\zeta} \\ a_{\xi}^{\mathbf{G}_{\mathbf{V}}^{\zeta}} W_{\xi} + b_{\eta}^{\mathbf{G}_{\mathbf{V}}^{\zeta}} W_{\eta} + c_{\zeta}^{\mathbf{G}_{\mathbf{V}}^{\zeta}} W_{\zeta} \end{bmatrix}, \tag{3.189}$$

where $a_{\xi}^{\mathbf{E}_V^{\xi}}, b_{\eta}^{\mathbf{F}_{\mathbf{V}}^{\eta}}, c_{\zeta}^{\mathbf{G}_{\mathbf{V}}^{\zeta}}, a_{\xi}^{\mathbf{F}_{\mathbf{V}}^{\eta}} = b_{\eta}^{\mathbf{E}_V^{\xi}}, a_{\xi}^{\mathbf{G}_{\mathbf{V}}^{\zeta}} = c_{\zeta}^{\mathbf{E}_V^{\xi}}, b_{\eta}^{\mathbf{G}_{\mathbf{V}}^{\zeta}} = c_{\zeta}^{\mathbf{F}_{\mathbf{V}}^{\eta}}$ are coefficients corresponding to the derivatives of the curvilinear coordinates (ξ, η, ζ) with respect to Cartesian coordinates (X, Y, Z) on the transformed computational map as

$$\begin{cases} a_{\xi}^{\mathbf{E}_V^{\xi}} = \xi_X^2 + \xi_Y^2 + \xi_Z^2, \\ b_{\eta}^{\mathbf{F}_{\mathbf{V}}^{\eta}} = \eta_X^2 + \eta_Y^2 + \eta_Z^2, \\ c_{\zeta}^{\mathbf{G}_{\mathbf{V}}^{\zeta}} = \zeta_X^2 + \zeta_Y^2 + \zeta_Z^2, \\ a_{\xi}^{\mathbf{F}_{\mathbf{V}}^{\eta}} = b_{\eta}^{\mathbf{E}_V^{\xi}} = \xi_X \eta_X + \xi_Y \eta_Y + \xi_Z \eta_Z, \\ a_{\xi}^{\mathbf{G}_{\mathbf{V}}^{\zeta}} = c_{\zeta}^{\mathbf{E}_V^{\xi}} = \xi_X \zeta_X + \xi_Y \zeta_Y + \xi_Z \zeta_Z, \\ b_{\eta}^{\mathbf{G}_{\mathbf{V}}^{\zeta}} = c_{\zeta}^{\mathbf{F}_{\mathbf{V}}^{\eta}} = \eta_X \zeta_X + \eta_Y \zeta_Y + \eta_Z \zeta_Z. \end{cases} \tag{3.190}$$

The derivatives of viscous fluxes in Eq. (3.109) have been approximated using intercell flux values relying on FVM discretization strategy as

$$\begin{cases} \frac{\partial \mathbf{E}_{\mathbf{V}}^{\xi}}{\partial \xi} \cong \frac{\left(\mathbf{E}_{\mathbf{V}}^{\xi}\right)_{i+1/2,j,k} - \left(\mathbf{E}_{\mathbf{V}}^{\xi}\right)_{i-1/2,j,k}}{\Delta \xi}, \\ \frac{\partial \mathbf{F}_{\mathbf{V}}^{\eta}}{\partial \eta} \cong \frac{\left(\mathbf{F}_{\mathbf{V}}^{\eta}\right)_{i,j+1/2,k} - \left(\mathbf{F}_{\mathbf{V}}^{\eta}\right)_{i,j-1/2,k}}{\Delta \eta}, \\ \frac{\partial \mathbf{G}_{\mathbf{V}}^{\zeta}}{\partial \zeta} \cong \frac{\left(\mathbf{G}_{\mathbf{V}}^{\zeta}\right)_{i,j,k+1/2} - \left(\mathbf{G}_{\mathbf{V}}^{\zeta}\right)_{i,j,k-1/2}}{\Delta \zeta}. \end{cases} \tag{3.191}$$

where the i, j, k subscripts correspond to the cell-centre coordinates in the domain.

3.4.2 Non-Newtonian Fluid Models for Blood Flow

Non-Newtonian fluids show non-linear relationship between the shear stress and the shear strain rate. Blood is a non-Newtonian fluid, and in order to model its rheological behaviour in microfluidic biomedical devices, the literature of blood biorheology has to be considered. Neofytou and Drikakis [20] made a first attempt to investigate the bifurcation of a two-dimensional blood flow, which occurs through a plane symmetric sudden expansion. They employed a version of Power-Law proposed by Walburn and Schneck [54], Casson [53] and Quemada [55] blood fluid models. Other constitutive equations are also used to describe the rheological behaviour of blood as per the generalized Maxwell model [69, p. 50] and the viscoelastic Oldroyd-B constitutive model [157].

For Newtonian fluids, the dynamic viscosity coefficient μ is a constant value, but for non-Newtonian fluids, it is a function of shear rate $\dot{\gamma}$. The shear rate tensor can be expressed [20] as

$$\underline{\underline{\dot{\gamma}}} = 2\underline{\underline{\mathrm{S}}} = \mathbf{u} \otimes \nabla + \nabla \otimes \mathbf{u}, \tag{3.192}$$

where the rate of strain (deformation) tensor is

$$\underline{\underline{\mathrm{S}}} = \frac{1}{2}\left(\mathbf{u} \otimes \nabla + \nabla \otimes \mathbf{u}\right) = \begin{bmatrix} \frac{\partial u}{\partial x} & \frac{1}{2}\left(\frac{\partial u}{\partial y} + \frac{\partial v}{\partial x}\right) & \frac{1}{2}\left(\frac{\partial u}{\partial z} + \frac{\partial w}{\partial x}\right) \\ \frac{1}{2}\left(\frac{\partial v}{\partial x} + \frac{\partial u}{\partial y}\right) & \frac{\partial v}{\partial y} & \frac{1}{2}\left(\frac{\partial v}{\partial z} + \frac{\partial w}{\partial y}\right) \\ \frac{1}{2}\left(\frac{\partial w}{\partial x} + \frac{\partial u}{\partial z}\right) & \frac{1}{2}\left(\frac{\partial w}{\partial y} + \frac{\partial v}{\partial z}\right) & \frac{\partial w}{\partial z} \end{bmatrix}, \tag{3.193}$$

and is relying on the generalized Newtonian behaviour of the fluid, assuming that elasticity and stress relaxation are not taken into account [20], the relationship between the viscous stress and the shear rate tensor can be described as

$$\underline{\underline{\tau}} = \mu\left(\left|\underline{\underline{\dot{\gamma}}}\right|\right)\left|\underline{\underline{\dot{\gamma}}}\right|, \tag{3.194}$$

where $\left|\underline{\underline{\dot{\gamma}}}\right|$ is the magnitude of shear rate tensor defined by the second invariant of rate of strain (deformation) tensor as

$$\left|\underline{\underline{\dot{\gamma}}}\right| = \sqrt{2\mathrm{tr}\left(\underline{\underline{\mathrm{S}}}^2\right)}. \tag{3.195}$$

3.4.2.1 Power-Law Fluid Model

For using the Power-Law Fluid Model, a coefficient, a power exponent and a characteristic parameter have to be adjusted for numerical simulations [20]. A version of this model was

proposed by Walburn and Schneck [54]. In this model, the shear stress is given by

$$\tau = k_0 \cdot \dot{\gamma}^n, \tag{3.196}$$

and Walburn and Schneck [54] suggested parameters are $k_0 = 14.67 \cdot 10^{-3}\ Pas^n$ and $n = 0.7755$ for blood flow. The Reynolds number for Power-Law Fluid can be defined [20] as

$$Re_{Power-Law} = \frac{\rho l^n}{k_0 u_\infty^{n-2}}, \tag{3.197}$$

which is the dimensionless characteristic parameter of the model [20].

3.4.2.2 Casson-Model

The Casson [53] rheological model is a widely used description of blood flow. Referring to Papanastasiou [158], this model can cause difficulties in numerical modelling, because it has a discontinuous character, therefore, the Casson equation can be re-written as

$$\tau = \left[\sqrt{\mu_\infty} + \sqrt{\frac{\tau_y}{|\dot{\gamma}|}}\left(1 - e^{-\sqrt{m|\dot{\gamma}|}}\right)\right]^2 \cdot \dot{\gamma}, \tag{3.198}$$

where τ_y is the yield stress and μ_∞ is the asymptotic viscosity [20]. Charm et al. [159], and Charm and Kurland [160] suggested parameters are $\tau_y = 10.82\ mPa$ and $\mu_\infty = 3.1 \cdot 10^{-3}$ *Pas* for $m > 100$ [20]. The Bingham number is defined [20] as

$$Bi_{Casson} = \frac{\tau_y l}{\mu_\infty u_\infty}, \tag{3.199}$$

and the Reynolds number of the Casson model is

$$Re_{Casson} = \frac{\rho u_\infty l}{\mu_\infty}, \tag{3.200}$$

which are the dimensionless characteristic parameters of the Casson model [20].

3.4.2.3 Quemada-Model

Quemada [55] developed a model to estimate the viscosity of concentrated disperse systems based on the shear rate and haematocrit level of blood [20]. According to this model,

the shear rate is given by

$$\tau = \mu_F \left[1 - \frac{k_0 + k_\infty \sqrt{\frac{\dot{\gamma}}{\dot{\gamma}_c}}}{2\left(1 + \sqrt{\frac{\dot{\gamma}}{\dot{\gamma}_c}}\right)} \varphi \right]^{-2} \cdot \dot{\gamma}, \tag{3.201}$$

where μ_F is viscosity of blood plasma, which is suggested to be $\mu_F = 1.2 \cdot 10^{-3}$ *Pas* [20]. The other parameters for haematocrit level are $\varphi = 0.45$, $\gamma_c = 1.88$ *s*, $k_\infty = 2.07$, $k_0 = 4.33$ [20], and $\dot{\gamma}_c^*$ is

$$\dot{\gamma}_c^* = \frac{\dot{\gamma}_c l}{U_\infty}, \tag{3.202}$$

and the Reynolds number of the Quemada model is

$$Re_{Quemada} = \frac{\rho U_\infty l}{\mu_F}, \tag{3.203}$$

which are the dimensionless characteristic parameters of the Quemada model [20].

3.4.3 Numerical Treatment of the Laplacian Term

For microfluidic applications, the numerical treatment of the Laplacian term of viscous fluxes for both Newtonian and non-Newtonian fluid models is a relevant issue, because the viscous effect becomes dominant. These terms contain second-order derivatives, which can be approximated by employing second-order central differences, and can be constructed in curvilinear coordinate system by using Eqs. (3.92)-(3.94) as

$$\frac{\partial^2}{\partial X^2} = \left(\frac{\partial \xi}{\partial X}\right)^2 \frac{\partial^2}{\partial \xi^2} + \left(\frac{\partial \eta}{\partial X}\right)^2 \frac{\partial^2}{\partial \eta^2} + \left(\frac{\partial \zeta}{\partial X}\right)^2 \frac{\partial^2}{\partial \zeta^2} +$$
$$+2\left(\frac{\partial \xi}{\partial X}\frac{\partial \eta}{\partial X}\right)\frac{\partial^2}{\partial \xi \partial \eta} + 2\left(\frac{\partial \xi}{\partial X}\frac{\partial \zeta}{\partial X}\right)\frac{\partial^2}{\partial \xi \partial \zeta} + 2\left(\frac{\partial \eta}{\partial X}\frac{\partial \zeta}{\partial X}\right)\frac{\partial^2}{\partial \eta \partial \zeta} +$$
$$+\left(\frac{\partial^2 \xi}{\partial X^2}\right)\frac{\partial}{\partial \xi} + \left(\frac{\partial^2 \eta}{\partial X^2}\right)\frac{\partial}{\partial \eta} + \left(\frac{\partial^2 \zeta}{\partial X^2}\right)\frac{\partial}{\partial \zeta}, \tag{3.204}$$

$$\frac{\partial^2}{\partial Y^2} = \left(\frac{\partial \xi}{\partial Y}\right)^2 \frac{\partial^2}{\partial \xi^2} + \left(\frac{\partial \eta}{\partial Y}\right)^2 \frac{\partial^2}{\partial \eta^2} + \left(\frac{\partial \zeta}{\partial Y}\right)^2 \frac{\partial^2}{\partial \zeta^2} +$$
$$+2\left(\frac{\partial \xi}{\partial Y}\frac{\partial \eta}{\partial Y}\right)\frac{\partial^2}{\partial \xi \partial \eta} + 2\left(\frac{\partial \xi}{\partial Y}\frac{\partial \zeta}{\partial Y}\right)\frac{\partial^2}{\partial \xi \partial \zeta} + 2\left(\frac{\partial \eta}{\partial Y}\frac{\partial \zeta}{\partial Y}\right)\frac{\partial^2}{\partial \eta \partial \zeta} +$$
$$+\left(\frac{\partial^2 \xi}{\partial Y^2}\right)\frac{\partial}{\partial \xi} + \left(\frac{\partial^2 \eta}{\partial Y^2}\right)\frac{\partial}{\partial \eta} + \left(\frac{\partial^2 \zeta}{\partial Y^2}\right)\frac{\partial}{\partial \zeta}, \tag{3.205}$$

$$\frac{\partial^2}{\partial Z^2} = \left(\frac{\partial \xi}{\partial Z}\right)^2 \frac{\partial^2}{\partial \xi^2} + \left(\frac{\partial \eta}{\partial Z}\right)^2 \frac{\partial^2}{\partial \eta^2} + \left(\frac{\partial \zeta}{\partial Z}\right)^2 \frac{\partial^2}{\partial \zeta^2} +$$
$$+2\left(\frac{\partial \xi}{\partial Z}\frac{\partial \eta}{\partial Z}\right)\frac{\partial^2}{\partial \xi \partial \eta} + 2\left(\frac{\partial \xi}{\partial Z}\frac{\partial \zeta}{\partial Z}\right)\frac{\partial^2}{\partial \xi \partial \zeta} + 2\left(\frac{\partial \eta}{\partial Z}\frac{\partial \zeta}{\partial Z}\right)\frac{\partial^2}{\partial \eta \partial \zeta} +$$
$$+\left(\frac{\partial^2 \xi}{\partial Z^2}\right)\frac{\partial}{\partial \xi} + \left(\frac{\partial^2 \eta}{\partial Z^2}\right)\frac{\partial}{\partial \eta} + \left(\frac{\partial^2 \zeta}{\partial Z^2}\right)\frac{\partial}{\partial \zeta}, \tag{3.206}$$

therefore, the Laplacian term of the momentum equation U can be written as

$$\nabla^2 U = \left(\xi_X^2 + \xi_Y^2 + \xi_Z^2\right)\frac{\partial^2 U}{\partial \xi^2} +$$
$$+\left(\eta_X^2 + \eta_Y^2 + \eta_Z^2\right)\frac{\partial^2 U}{\partial \eta^2} +$$
$$+\left(\zeta_X^2 + \zeta_Y^2 + \zeta_Z^2\right)\frac{\partial^2 U}{\partial \zeta^2} +$$

$$
\begin{aligned}
&+2\left(\xi_X\eta_X+\xi_Y\eta_Y+\xi_Z\eta_Z\right)\frac{\partial^2 U}{\partial\xi\,\partial\eta}+\\
&+2\left(\xi_X\zeta_X+\xi_Y\zeta_Y+\xi_Z\zeta_Z\right)\frac{\partial^2 U}{\partial\xi\,\partial\zeta}+\\
&+2\left(\eta_X\zeta_X+\eta_Y\zeta_Y+\eta_Z\zeta_Z\right)\frac{\partial^2 U}{\partial\eta\,\partial\zeta}+\\
&+\left(\xi_{XX}+\xi_{YY}+\xi_{ZZ}\right)\frac{\partial U}{\partial\xi}+\\
&+\left(\eta_{XX}+\eta_{YY}+\eta_{ZZ}\right)\frac{\partial U}{\partial\eta}+\\
&+\left(\zeta_{XX}+\zeta_{YY}+\zeta_{ZZ}\right)\frac{\partial U}{\partial\zeta},
\end{aligned}
\tag{3.207}
$$

where the second-, mixed- and first derivatives, respectively, are

$$\frac{\partial^2 U^n}{\partial\xi^2}\approx\frac{U^n_{i-1,j,k}-2U^n_{i,j,k}+U^n_{i+1,j,k}}{(\Delta\xi)^2},\tag{3.208}$$

$$\frac{\partial^2 U^n}{\partial\eta^2}\approx\frac{U^n_{i,j-1,k}-2U^n_{i,j,k}+U^n_{i,j+1,k}}{(\Delta\eta)^2},\tag{3.209}$$

$$\frac{\partial^2 U^n}{\partial\zeta^2}\approx\frac{U^n_{i,j,k-1}-2U^n_{i,j,k}+U^n_{i,j,k+1}}{(\Delta\zeta)^2},\tag{3.210}$$

$$\frac{\partial^2 U^n}{\partial\xi\,\partial\eta}\approx\frac{U^n_{i+1,j+1,k}-U^n_{i+1,j-1,k}-U^n_{i-1,j+1,k}+U^n_{i-1,j-1,k}}{4\Delta\xi\Delta\eta},\tag{3.211}$$

$$\frac{\partial^2 U^n}{\partial\xi\,\partial\zeta}\approx\frac{U^n_{i+1,j,k+1}-U^n_{i+1,j,k-1}-U^n_{i-1,j,k+1}+U^n_{i-1,j,k-1}}{4\Delta\xi\Delta\zeta},\tag{3.212}$$

$$\frac{\partial^2 U^n}{\partial\eta\,\partial\zeta}\approx\frac{U^n_{i,j+1,k+1}-U^n_{i,j+1,k-1}-U^n_{i,j-1,k+1}+U^n_{i,j-1,k-1}}{4\Delta\eta\Delta\zeta}.\tag{3.213}$$

$$\frac{\partial U^n}{\partial\xi}\approx\frac{U^n_{i+1,j,k}-U^n_{i-1,j,k}}{\Delta\xi},\tag{3.214}$$

$$\frac{\partial U^n}{\partial\eta}\approx\frac{U^n_{i,j+1,k}-U^n_{i,j-1,k}}{\Delta\eta},\tag{3.215}$$

$$\frac{\partial U^n}{\partial\zeta}\approx\frac{U^n_{i,j,k+1}-U^n_{i,j,k-1}}{\Delta\zeta}.\tag{3.216}$$

The Laplacian terms of momentum equations V and W can also be constructed in a similar manner; thus, the discretized Laplacian term of the momentum equation U in the curvilinear coordinate system can be written as

$$
\begin{aligned}
\left(\nabla^2 U\right)^n_{i,j,k} \approx & \left(\xi_X^2+\xi_Y^2+\xi_Z^2\right)\frac{U^n_{i-1,j,k}-2U^n_{i,j,k}+U^n_{i+1,j,k}}{(\Delta\xi)^2}+\\
&+\left(\eta_X^2+\eta_Y^2+\eta_Z^2\right)\frac{U^n_{i,j-1,k}-2U^n_{i,j,k}+U^n_{i,j+1,k}}{(\Delta\eta)^2}+\\
&+\left(\zeta_X^2+\zeta_Y^2+\zeta_Z^2\right)\frac{U^n_{i,j,k-1}-2U^n_{i,j,k}+U^n_{i,j,k+1}}{(\Delta\zeta)^2}+\\
&+\left(\xi_X\eta_X+\xi_Y\eta_Y+\xi_Z\eta_Z\right)\frac{U^n_{i+1,j+1,k}-U^n_{i+1,j-1,k}-U^n_{i-1,j+1,k}+U^n_{i-1,j-1,k}}{2\Delta\xi\Delta\eta}+\\
&+\left(\xi_X\zeta_X+\xi_Y\zeta_Y+\xi_Z\zeta_Z\right)\frac{U^n_{i+1,j,k+1}-U^n_{i+1,j,k-1}-U^n_{i-1,j,k+1}+U^n_{i-1,j,k-1}}{2\Delta\xi\Delta\zeta}+\\
&+\left(\eta_X\zeta_X+\eta_Y\zeta_Y+\eta_Z\zeta_Z\right)\frac{U^n_{i,j+1,k+1}-U^n_{i,j+1,k-1}-U^n_{i,j-1,k+1}+U^n_{i,j-1,k-1}}{2\Delta\eta\Delta\zeta}+\\
&+\left(\xi_{XX}+\xi_{YY}+\xi_{ZZ}\right)\frac{U^n_{i+1,j,k}-U^n_{i-1,j,k}}{\Delta\xi}+\\
&+\left(\eta_{XX}+\eta_{YY}+\eta_{ZZ}\right)\frac{U^n_{i,j+1,k}-U^n_{i,j-1,k}}{\Delta\eta}+\\
&+\left(\zeta_{XX}+\zeta_{YY}+\zeta_{ZZ}\right)\frac{U^n_{i,j,k+1}-U^n_{i,j,k-1}}{\Delta\zeta},
\end{aligned}
\tag{3.217}
$$

where the derivatives of the curvilinear coordinates (ξ,η,ζ), according to Cartesian coordinates (X,Y,Z), can be approximated numerically in the cell-centres. More details about these derivatives can be found in Appendix A.

Chapter 4

Numerical Method Development for Solving the Navier-Stokes Equations

4.1 Introduction

In this chapter, a high-resolution Godunov-type numerical procedure has been developed for solving the unsteady, incompressible Navier-Stokes equations for constant and variable density flows. The proposed FSAC-PP approach unifies the artificial compressibility (AC) and fractional step (FS) pressure-projection (PP) methods of Chorin [3, 4]. The objectives of the numerical method development are a) to improve further the accuracy and efficiency of the classical AC method, and b) to combine the accuracy properties of the CB Godunov-type discretization with PP methods by solving the Riemann problem with the Riemann method. The proposed FSAC-PP method is fallen into the group of pseudo-time splitting FSAC approaches including a PP step at each pseudo-time step of the dual-time stepping procedure to accelerate the satisfaction of the divergence-free (incompressibility) constraint; thus, a pressure-Poisson equation has been solved for the pressure field to update the velocity field at each pseudo-time level. The CB scheme has been obtained from the hyperbolic system of the classical AC formulation, under consideration to be singe-directional in space. The arrangement of primitive variables has been taken to be collocated on the computational domain. Recently, Tang and Sotiropoulos [124] proposed a time-accurate approach on non-staggered grids using a second-order accurate hybrid FSAC method to advance the efficiency of the AC method, but their solution does not fall into the class of non-linear high-resolution methods. In their case, the projection of the velocity field was carried out via a dual-time stepping of the AC formulation instead of solving a pressure-Poisson equation. Nithiarasu [161] developed a fully explicit CB split scheme that takes advantage of both, the velocity correction and the

classical AC schemes using finite element method (FEM). Massarotti et al. [162] compared the classical semi-implicit CB split scheme to a fully explicit AC formulation type scheme using FEM as well. This chapter deals with a FSAC formulation coupled with the PP method in conjunction with a CB Godunov-type discretization for the non-linear advective fluxes relying on the Riemann method for solving the Riemann problem.

4.1.1 Riemann Method and Characteristics-Based (CB) Schemes

4.1.1.1 Constant Density Flows

In favour of completeness, for unsteady, incompressible flows, the dimensionless artificial compressibility (AC) formulation relying on Eqs. (3.32)-(3.33) has been transformed from the Cartesian coordinate system (X,Y,Z) into a curvilinear coordinate system (ξ,η,ζ). Thus the system of governing equations can be written in vector form as

$$\frac{\partial J\mathbf{U_p}}{\partial \tau} = -\frac{\partial J\mathbf{U_r}}{\partial t^*} - \left(\frac{\partial \mathbf{E_I^\xi}}{\partial \xi} + \frac{\partial \mathbf{F_I^\eta}}{\partial \eta} + \frac{\partial \mathbf{G_I^\zeta}}{\partial \zeta}\right)$$

$$+\frac{1}{Re}\left(\frac{\partial \mathbf{E_V^\xi}}{\partial \xi} + \frac{\partial \mathbf{F_V^\eta}}{\partial \eta} + \frac{\partial \mathbf{G_V^\zeta}}{\partial \zeta}\right) + J\mathbf{F}, \tag{4.1}$$

where the $\mathbf{U_p} = \begin{bmatrix} P/\beta & U & V & W \end{bmatrix}^T$ vector stands for pseudo-time stepping unknowns, and $\mathbf{U_r} = \begin{bmatrix} 0 & U & V & W \end{bmatrix}^T$ represents the vector of real-time stepping quantities.

To obtain CB intercell advective fluxes, the system of governing equations (4.1) has to be used to derive the reconstructed formulas for primitive variables (see Figure 4.1). Riemann's method has been employed for deriving the singe-directional transport CB scheme [16, 6] with respect to direction ξ. The solution of the Riemann initial value problem is an immanent part of the Godunov procedure to obtain physically reasonable inviscid intercell fluxes from the dependent variables using a high-order interpolation ("reconstruction") formula [27]. In order to couple the PP method with CB scheme by using the Riemann method and the Godunov-type discretization, it is necessary to keep the hyperbolic system of the AC formulation. The derivation of CB inviscid fluxes based on the Riemann method has been discussed in this subsection, because it is an indispensable part of the proposed FSAC-PP method for solving the Navier-Stokes equations.

Introducing the notation $L_\xi = \sqrt{\xi_X^2 + \xi_Y^2 + \xi_Z^2}$ metrics and notations

$$\tilde{X} = \frac{\xi_X}{L_\xi}, \quad \tilde{Y} = \frac{\xi_Y}{L_\xi}, \quad \tilde{Z} = \frac{\xi_Z}{L_\xi},$$

for direction ξ, because we seek the reconstructed CB dependent variables for computing inviscid intercell flux values along these characteristics (see Figure 4.1).

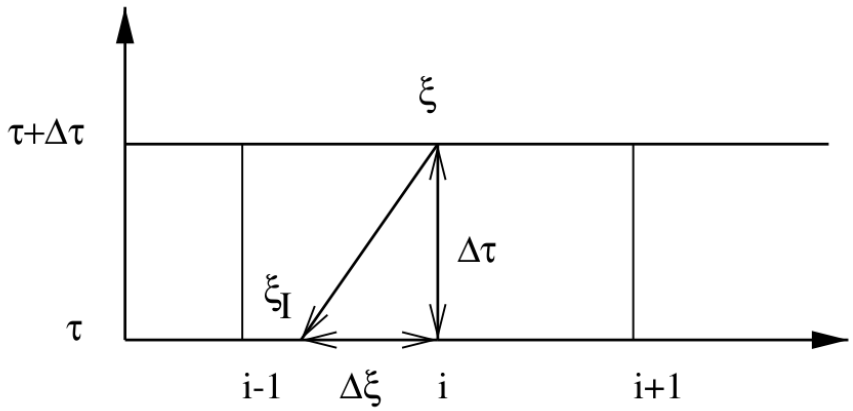

Figure 4.1: Sketch of characteristics-based temporal and spatial discretization [16].

Hereby, the viscous flux terms are considered to be equal to zero, and the vectorial system of equations (4.1) yields

$$\begin{cases} \frac{1}{\beta L_\xi}\frac{\partial P}{\partial \tau}+\tilde{X}\frac{\partial U}{\partial \xi}+\tilde{Y}\frac{\partial V}{\partial \xi}+\tilde{Z}\frac{\partial W}{\partial \xi}=0, \\ \frac{1}{L_\xi}\frac{\partial U}{\partial \tau}+\tilde{X}\frac{\partial \left(U^2\right)}{\partial \xi}+\tilde{Y}\frac{\partial (UV)}{\partial \xi}+\tilde{Z}\frac{\partial (UW)}{\partial \xi}+\tilde{X}\frac{\partial P}{\partial \xi}=0, \\ \frac{1}{L_\xi}\frac{\partial V}{\partial \tau}+\tilde{X}\frac{\partial (UV)}{\partial \xi}+\tilde{Y}\frac{\partial \left(V^2\right)}{\partial \xi}+\tilde{Z}\frac{\partial (VW)}{\partial \xi}+\tilde{Y}\frac{\partial P}{\partial \xi}=0, \\ \frac{1}{L_\xi}\frac{\partial W}{\partial \tau}+\tilde{X}\frac{\partial (UW)}{\partial \xi}+\tilde{Y}\frac{\partial (VW)}{\partial \xi}+\tilde{Z}\frac{\partial \left(W^2\right)}{\partial \xi}+\tilde{Z}\frac{\partial P}{\partial \xi}=0, \end{cases} \tag{4.2}$$

a system of non-linear scalar partial differential equations. After expressing the derivatives of system (4.2), and taking into account the

$$\tilde{X}\frac{\partial U}{\partial \xi}+\tilde{Y}\frac{\partial V}{\partial \xi}+\tilde{Z}\frac{\partial W}{\partial \xi}=0 \tag{4.3}$$

divergence-free constraint, the following system can be written as

$$\begin{cases} \frac{1}{\beta L_\xi}\frac{\partial P}{\partial \tau}+\tilde{X}\frac{\partial U}{\partial \xi}+\tilde{Y}\frac{\partial V}{\partial \xi}+\tilde{Z}\frac{\partial W}{\partial \xi}=0, \\ \frac{1}{L_\xi}\frac{\partial U}{\partial \tau}+\lambda_0\frac{\partial U}{\partial \xi}+\tilde{X}\frac{\partial P}{\partial \xi}=0, \\ \frac{1}{L_\xi}\frac{\partial V}{\partial \tau}+\lambda_0\frac{\partial V}{\partial \xi}+\tilde{Y}\frac{\partial P}{\partial \xi}=0, \\ \frac{1}{L_\xi}\frac{\partial W}{\partial \tau}+\lambda_0\frac{\partial W}{\partial \xi}+\tilde{Z}\frac{\partial P}{\partial \xi}=0, \end{cases} \tag{4.4}$$

where $\lambda_0 = U\tilde{X}+V\tilde{Y}+W\tilde{Z}$ is one of the eigenvalue of system (4.4). This system can also be expressed in a compacted vector form as

$$\frac{1}{L_\xi}\frac{\partial \mathbf{U_p}}{\partial \tau}+\mathbf{A}\frac{\partial \mathbf{U_p}}{\partial \xi}=0, \tag{4.5}$$

where the 4×4 coefficient matrix for constant density flow is

$$\mathbf{A}=\begin{bmatrix} 0 & \tilde{X} & \tilde{Y} & \tilde{Z} \\ \beta\tilde{X} & \lambda_0 & 0 & 0 \\ \beta\tilde{Y} & 0 & \lambda_0 & 0 \\ \beta\tilde{Z} & 0 & 0 & \lambda_0 \end{bmatrix}, \tag{4.6}$$

which have distinct eigenvalues λ_0, $\lambda_1=\lambda_0+s$ and $\lambda_2=\lambda_0-s$, where $s=\left(\lambda_0^2+\beta\right)^{1/2}$ is the artificial speed of sound [16, 6]. The pseudo-time derivatives in the system (4.5) are approximated based on the characteristic directions (ξ,η,ζ) as

$$\begin{cases} \frac{\partial \mathbf{U_p}(\xi,\tau)}{\partial \tau}\cong\frac{\tilde{\mathbf{U}}_\mathbf{p}(\xi,\tau+\Delta\tau)-\mathbf{U_p}(\xi_l,\tau)}{\Delta\tau}-\frac{\partial \mathbf{U_p}(\xi_l,\tau)}{\partial \xi}\lambda_l L_\xi, \\ \frac{\partial \mathbf{U_p}(\eta,\tau)}{\partial \tau}\cong\frac{\tilde{\mathbf{U}}_\mathbf{p}(\eta,\tau+\Delta\tau)-\mathbf{U_p}(\eta_l,\tau)}{\Delta\tau}-\frac{\partial \mathbf{U_p}(\eta_l,\tau)}{\partial \eta}\lambda_l L_\eta, \\ \frac{\partial \mathbf{U_p}(\zeta,\tau)}{\partial \tau}\cong\frac{\tilde{\mathbf{U}}_\mathbf{p}(\zeta,\tau+\Delta\tau)-\mathbf{U_p}(\zeta_l,\tau)}{\Delta\tau}-\frac{\partial \mathbf{U_p}(\zeta_l,\tau)}{\partial \zeta}\lambda_l L_\zeta, \end{cases} \tag{4.7}$$

where $l=0,1,2$ stands for sub-indices of distinct eigenvalues λ_l, and $L_\eta=\sqrt{\eta_X^2+\eta_Y^2+\eta_Z^2}$ and $L_\zeta=\sqrt{\zeta_X^2+\zeta_Y^2+\zeta_Z^2}$ denote metrics in directions (η,ζ). By using the previously introduced approximation of pseudo-time derivatives, the system of scalar governing equations (4.4) in direction ξ can also be written as

$$\begin{cases} \frac{1}{\beta L_\xi}\frac{\tilde{P}-P_l}{\Delta\tau} - \frac{\lambda_l}{\beta}\frac{\partial P}{\partial \xi} + \tilde{X}\frac{\partial U}{\partial \xi} + \tilde{Y}\frac{\partial V}{\partial \xi} + \tilde{Z}\frac{\partial W}{\partial \xi} = 0, \\ \frac{1}{L_\xi}\frac{\tilde{U}-U_l}{\Delta\tau} + (\lambda_0-\lambda_l)\frac{\partial U}{\partial \xi} + \tilde{X}\frac{\partial P}{\partial \xi} = 0, \\ \frac{1}{L_\xi}\frac{\tilde{V}-V_l}{\Delta\tau} + (\lambda_0-\lambda_l)\frac{\partial V}{\partial \xi} + \tilde{Y}\frac{\partial P}{\partial \xi} = 0, \\ \frac{1}{L_\xi}\frac{\tilde{W}-W_l}{\Delta\tau} + (\lambda_0-\lambda_l)\frac{\partial W}{\partial \xi} + \tilde{Z}\frac{\partial P}{\partial \xi} = 0. \end{cases} \tag{4.8}$$

Hereby, the Riemann method [163, 112, 120, 16] has been employed to eliminate the spatial derivatives from the system (4.8) in direction ξ, therefore, the arbitrarily chosen coefficients a,b,c,d have been introduced for the derivatives of the dimensionless pressure P and velocity components U,V,W, respectively. After re-arranging the temporal and spatial derivatives, and adding all terms together, it yields the following

$$\begin{aligned} & a\frac{1}{\beta L_\xi}\frac{\tilde{P}-P_l}{\Delta\tau} + b\frac{1}{L_\xi}\frac{\tilde{U}-U_l}{\Delta\tau} + c\frac{1}{L_\xi}\frac{\tilde{V}-V_l}{\Delta\tau} + d\frac{1}{L_\xi}\frac{\tilde{W}-W_l}{\Delta\tau} - \\ & -a\frac{\lambda_l}{\beta} + b\tilde{X} + c\tilde{Y} + d\tilde{Z} + \\ & + a\tilde{X} + b(\lambda_0-\lambda_l) + \\ & + a\tilde{Y} + c(\lambda_0-\lambda_l) + \\ & + a\tilde{Z} + d(\lambda_0-\lambda_l) = 0, \end{aligned} \tag{4.9}$$

algebraic equation. By taking $\lambda_l = \lambda_0$, Eq. (4.9) yields a system of equations as

$$\begin{cases} \frac{a}{\beta}(\tilde{P}-P_0) + b(\tilde{U}-U_0) + c(\tilde{V}-V_0) + d(\tilde{W}-W_0) = 0, \\ a = \frac{\beta}{\lambda_0}(b\tilde{X} + c\tilde{Y} + d\tilde{Z}), \\ a\tilde{X} = \frac{\beta}{\lambda_0}(b\tilde{X} + c\tilde{Y} + d\tilde{Z})\tilde{X} = 0, \\ a\tilde{Y} = \frac{\beta}{\lambda_0}(b\tilde{X} + c\tilde{Y} + d\tilde{Z})\tilde{Y} = 0, \\ a\tilde{Z} = \frac{\beta}{\lambda_0}(b\tilde{X} + c\tilde{Y} + d\tilde{Z})\tilde{Z} = 0. \end{cases} \tag{4.10}$$

It can be seen from the system (4.10) that

$$b\tilde{X} + c\tilde{Y} + d\tilde{Z} = 0, \tag{4.11}$$

therefore $a = 0$, thus the first algebraic equation of the system (4.10) leads to be

$$b(\tilde{U} - U_0) + c(\tilde{V} - V_0) + d(\tilde{W} - W_0) = 0, \tag{4.12}$$

where

$$b = -c(\tilde{Y}/\tilde{X}) - d(\tilde{Z}/\tilde{X}) \tag{4.13}$$

is expressed from Eq. (4.11), and substituting Eq. (4.13) into Eq. (4.12), the following

$$c\left[(\tilde{V} - V_0)\tilde{X} - (\tilde{U} - U_0)\tilde{Y}\right] + d\left[(\tilde{W} - W_0)\tilde{X} - (\tilde{U} - U_0)\tilde{Z}\right] = 0, \tag{4.14}$$

algebraic equation is obtained, which yields a system of algebraic equations as

$$\begin{cases} (\tilde{V} - V_0)\tilde{X} - (\tilde{U} - U_0)\tilde{Y} = 0, \\ \\ (\tilde{W} - W_0)\tilde{X} - (\tilde{U} - U_0)\tilde{Z} = 0. \end{cases} \tag{4.15}$$

After re-arranging the system (4.15), we obtain that

$$\begin{cases} \tilde{U} = U_0 + (\tilde{V} - V_0)\frac{\tilde{X}}{\tilde{Y}}, \\ \\ \tilde{V} = V_0 + (\tilde{U} - U_0)\frac{\tilde{Y}}{\tilde{X}}, \\ \\ \tilde{W} = W_0 + (\tilde{U} - U_0)\frac{\tilde{Z}}{\tilde{X}}, \\ \\ \frac{\tilde{V} - V_0}{\tilde{Y}} = \frac{\tilde{U} - U_0}{\tilde{X}}, \\ \\ \frac{\tilde{W} - W_0}{\tilde{Z}} = \frac{\tilde{U} - U_0}{\tilde{X}}. \end{cases} \tag{4.16}$$

These relationships play an important role for expressing the final form of the reconstructed characteristic velocity components $\tilde{U}, \tilde{V}, \tilde{W}$ subsequently. To derive the reconstructed pressure $\tilde{P}$ for using the classical AC method, we take $\lambda_l = \lambda_1 = \lambda_0 + s$, which also leads to a set of algebraic system of equations as

$$\begin{cases} \tilde{P} - P_1 + \beta \left[\frac{b}{a}(\tilde{U} - U_1) + \frac{c}{a}(\tilde{V} - V_1) + \frac{d}{a}(\tilde{W} - W_1) \right] = 0, \\ -\frac{\lambda_1}{\beta} + \frac{b}{a}\tilde{X} + \frac{c}{a}\tilde{Y} + \frac{d}{a}\tilde{Z} = 0, \\ a\tilde{X} + b\,(\lambda_0 - \lambda_1) = a\tilde{X} - bs = 0, \\ a\tilde{Y} + c\,(\lambda_0 - \lambda_1) = a\tilde{Y} - cs = 0, \\ a\tilde{Z} + d\,(\lambda_0 - \lambda_1) = a\tilde{Z} - ds = 0, \end{cases} \tag{4.17}$$

where $\frac{b}{a} = \frac{\tilde{X}}{s}$, $\frac{c}{a} = \frac{\tilde{Y}}{s}$, and $\frac{d}{a} = \frac{\tilde{Z}}{s}$ can be expressed from the last three equations of system (4.17). By taking into account that $\tilde{X}^2 + \tilde{Y}^2 + \tilde{Z}^2 = 1$ and $\lambda_1 = \frac{\beta}{s}$, the characteristic pressure $\tilde{P}$ using λ_1 eigenvalue is given by

$$\tilde{P} = P_1 - \lambda_1 \left[\tilde{X}(\tilde{U} - U_1) + \tilde{Y}(\tilde{V} - V_1) + \tilde{Z}(\tilde{W} - W_1) \right], \tag{4.18}$$

and similarly, for $\lambda_l = \lambda_2 = \lambda_0 - s$, we obtain

$$\tilde{P} = P_2 - \lambda_2 \left[\tilde{X}(\tilde{U} - U_2) + \tilde{Y}(\tilde{V} - V_2) + \tilde{Z}(\tilde{W} - W_2) \right]. \tag{4.19}$$

By subtracting Eq. (4.18) from Eq. (4.19) after dividing them by the eigenvalues λ_1 and λ_2 eigenvalues, and after re-arranging the obtained equation taking into account that $\lambda_1 \lambda_2 = -\frac{\beta}{\rho}$, the characteristic pressure for constant density flow will be given by

$$\begin{aligned} \tilde{P} = \tfrac{1}{2s} \{ & \lambda_1 P_2 - \lambda_2 P_1 - \beta \left[\tilde{X}(\tilde{U} - U_1) + \tilde{Y}(\tilde{V} - V_1) + \tilde{Z}(\tilde{W} - W_1) \right] + \\ & + \beta \left[\tilde{X}(\tilde{U} - U_2) + \tilde{Y}(\tilde{V} - V_2) + \tilde{Z}(\tilde{W} - W_2) \right] \}, \end{aligned} \tag{4.20}$$

where sub-index "1" is relating to the "Left", and sub-index "2" is relating to the "Right" hand side reconstructed intercell pressure values using high-order interpolation. For using the classical AC method, Eq. (4.20) can be employed to compute the pressure gradient terms in the right hand side of the scalar momentum equations in each direction. Unlike when the subsequently proposed FSAC-PP method is used at each pseudo-time step, the cell-centered pressure values are obtained by solving a pressure-Poisson equation.

To derive the characteristic velocity components $\tilde{U}, \tilde{V}, \tilde{W}$, Eq. (4.18) has to be subtracted from Eq. (4.19), and after that using the relationships of system (4.16), the fol-

lowing algebraic equations are obtained for the characteristic velocity components as

$$\begin{cases} \tilde{U} = U_0 + \frac{\tilde{X}}{2s}R, \\ \\ \tilde{V} = V_0 + \frac{\tilde{Y}}{2s}R, \\ \\ \tilde{W} = W_0 + \frac{\tilde{Z}}{2s}R, \end{cases} \tag{4.21}$$

where

$$\begin{aligned} R = P_1 - P_2 + \lambda_2 \left[\tilde{X}\left(U_0 - U_1\right) + \tilde{Y}\left(V_0 - V_1\right) + \tilde{Z}\left(W_0 - W_1\right)\right] - \\ -\lambda_1 \left[\tilde{X}\left(U_0 - U_2\right) + \tilde{Y}\left(V_0 - V_2\right) + \tilde{Z}\left(W_0 - W_2\right)\right] \end{aligned} \tag{4.22}$$

is an auxiliary function to write the system of characteristic velocity components (4.21) in a compact form. Having obtained these velocity components, the algebraic system of unsteady, incompressible Navier-Stokes equations along the characteristics can be constructed in a curvilinear coordinate system.

4.1.1.2 Multi-Species Variable Density Flows

For unsteady, incompressible multi-species variable density flows using the classical AC formulation, the dimensionless governing equations for the continuity, momentum, total- and partial densities in vector form are written [16] as

$$\begin{cases} \frac{1}{\beta}\frac{\partial P}{\partial \tau} = -\nabla \cdot \mathbf{U}, \\ \\ \frac{\partial \mathbf{U}}{\partial \tau} = -\frac{\partial \mathbf{U}}{\partial t^*} - \nabla \cdot (\mathbf{U} \otimes \mathbf{U}) + \frac{1}{Re}\nabla^2 \mathbf{U} - \frac{1}{\rho}\nabla P + \mathbf{F}, \\ \\ \frac{\partial \rho}{\partial \tau} = -\frac{\partial \rho}{\partial t^*} - (\mathbf{U} \cdot \nabla)\rho, \\ \\ \frac{\partial \rho_i}{\partial \tau} = -\frac{\partial \rho_i}{\partial t^*} - (\mathbf{U} \cdot \nabla)\rho_i + \frac{1}{Pe}\nabla \cdot \left(\sum_{j=1}^{N-1} D_{ji}\rho \nabla \frac{\rho_j}{\rho}\right), \\ \\ i = 1, N-1, \end{cases} \tag{4.23}$$

where $\rho = \sum \rho_i \ (i = 1, \ldots, N)$ is the total density, ρ_i is the partial density of i^{th} species, D_{ji} are the elements of multicomponent $(N-1) \times (N-1)$ diffusion matrix, Pe is the Péclet number. The multicomponent diffusion matrix contains $(N-1) \times (N-1)$ elements, because a conservation equation is solved for the total density to avoid the system of govern-

ing equations (4.23) to be over-defined [16]. For incompressible multi-species variable density flows, the system of governing equations (4.23) can be transformed into a curvilinear coordinate-system similarly to the system of governing equations (4.1) for constant density flows. The pseudo-time stepping vector $\mathbf{U_p} = \begin{bmatrix} P/\beta & U & V & W & \rho & \rho_i \end{bmatrix}^T$ and the real-time stepping vector $\mathbf{U_r} = \begin{bmatrix} 0 & U & V & W & \rho & \rho_i \end{bmatrix}^T$ are different from the constant density flow case. By taking into account the divergence-free constraint (4.3) for the scalar momentum equation in direction ξ, similarly to the system of equation (4.4), a scalar partial differential system of equations can be obtained for the continuity, the three scalar momentum equations, and the total- and partial densities as

$$\begin{cases} \frac{1}{\beta L_\xi}\frac{\partial P}{\partial \tau} + \tilde{X}\frac{\partial U}{\partial \xi} + \tilde{Y}\frac{\partial V}{\partial \xi} + \tilde{Z}\frac{\partial W}{\partial \xi} = 0, \\ \frac{1}{L_\xi}\frac{\partial U}{\partial \tau} + \lambda_0\frac{\partial U}{\partial \xi} + \tilde{X}\frac{1}{\rho}\frac{\partial P}{\partial \xi} = 0, \\ \frac{1}{L_\xi}\frac{\partial V}{\partial \tau} + \lambda_0\frac{\partial V}{\partial \xi} + \tilde{Y}\frac{1}{\rho}\frac{\partial P}{\partial \xi} = 0, \\ \frac{1}{L_\xi}\frac{\partial W}{\partial \tau} + \lambda_0\frac{\partial W}{\partial \xi} + \tilde{Z}\frac{1}{\rho}\frac{\partial P}{\partial \xi} = 0, \\ \frac{1}{L_\xi}\frac{\partial \rho}{\partial \tau} + \lambda_0\frac{\partial \rho}{\partial \xi} + \left(\tilde{X}\frac{\partial U}{\partial \xi} + \tilde{Y}\frac{\partial V}{\partial \xi} + \tilde{Z}\frac{\partial W}{\partial \xi}\right)\rho = 0, \\ \frac{1}{L_\xi}\frac{\partial \rho_i}{\partial \tau} + \lambda_0\frac{\partial \rho_i}{\partial \xi} + \left(\tilde{X}\frac{\partial U}{\partial \xi} + \tilde{Y}\frac{\partial V}{\partial \xi} + \tilde{Z}\frac{\partial W}{\partial \xi}\right)\rho_i = 0. \end{cases} \tag{4.24}$$

The coefficient matrix of the eigenvalue system based on the system of scalar differential equations (4.24), similarly to the coefficient matrix (4.6), can be written as

$$\mathbf{A} = \begin{bmatrix} 0 & \tilde{X} & \tilde{Y} & \tilde{Z} & 0 & 0 & \dots & 0 \\ \frac{\beta}{\rho}\tilde{X} & \lambda_0 & 0 & 0 & 0 & 0 & \dots & 0 \\ \frac{\beta}{\rho}\tilde{Y} & 0 & \lambda_0 & 0 & 0 & 0 & \dots & 0 \\ \frac{\beta}{\rho}\tilde{Z} & 0 & 0 & \lambda_0 & 0 & 0 & \dots & 0 \\ 0 & \tilde{X}\rho & \tilde{Y}\rho & \tilde{Z}\rho & \lambda_0 & 0 & \dots & 0 \\ 0 & \tilde{X}\rho_1 & \tilde{Y}\rho_1 & \tilde{Z}\rho_1 & 0 & \lambda_0 & \dots & 0 \\ . & . & . & . & . & . & \dots & . \\ 0 & \tilde{X}\rho_{N-1} & \tilde{Y}\rho_{N-1} & \tilde{Z}\rho_{N-1} & 0 & 0 & 0 & \lambda_0 \end{bmatrix}, \tag{4.25}$$

which have distinct eigenvalues λ_0, $\lambda_1 = \lambda_0 + s$ and $\lambda_2 = \lambda_0 - s$, where $s = \left(\lambda_0^2 + \frac{\beta}{\rho}\right)^{1/2}$ denotes the artificial speed of sound [16, 6]. The Riemann method [163, 112, 120, 16] has been employed to eliminate the spatial derivatives from the system of equations (4.24) in

direction ξ, therefore, arbitrarily chosen coefficients a,b,c,d,e,f_i have been introduced for the derivatives of the dimensionless pressure P, velocity components U,V,W, the total density ρ and the partial densities ρ_i, respectively.

After re-arranging the temporal and spatial derivatives, adding all terms together, and setting all of them to be equal to zero, it yields the following

$$\begin{cases} \frac{a}{\beta}(\tilde{P}-P_l)+b(\tilde{U}-U_l)+c(\tilde{V}-V_l)+ \\ +d(\tilde{W}-W_l)+e(\tilde{\rho}-\rho_0)+\sum\limits_{i=1}^{N-1} f_i(\tilde{\rho}_i-\rho_{il})=0, \\ \\ -a\frac{\lambda_l}{\beta}+b\tilde{X}+c\tilde{Y}+d\tilde{Z}=0, \\ \\ a\tilde{X}+b(\lambda_0-\lambda_l)+e\rho\tilde{X}+\sum\limits_{i=1}^{N-1} f_i\rho_i\tilde{X}=0, \\ \\ a\tilde{Y}+c(\lambda_0-\lambda_l)+e\rho\tilde{Y}+\sum\limits_{i=1}^{N-1} f_i\rho_i\tilde{Y}=0, \\ \\ a\tilde{Z}+d(\lambda_0-\lambda_l)+e\rho\tilde{Z}+\sum\limits_{i=1}^{N-1} f_i\rho_i\tilde{Z}=0, \\ \\ e(\lambda_0-\lambda_l)=0, \\ \\ f_i(\lambda_0-\lambda_l)=0, \\ \\ i=1,N-1, \end{cases} \tag{4.26}$$

algebraic system of equations, which has to be solved by substituting the eigenvalues λ_0, λ_1 and λ_2 into each equation. The non-trivial solution of the system (4.26) leads to

$$\begin{cases} \tilde{U}=U_0+\frac{\tilde{X}}{\rho s}R_*, \\ \tilde{V}=V_0+\frac{\tilde{Y}}{\rho s}R_*, \\ \tilde{W}=W_0+\frac{\tilde{Z}}{\rho s}R_*, \\ \tilde{\rho}=\rho_0+\frac{\rho}{\beta}\left(P-P_0+\frac{\lambda_0}{s}R_*\right), \\ \tilde{\rho}_i=\rho_{i0}+\frac{\rho_i}{\beta}\left(P-P_0+\frac{\lambda_0}{s}R_*\right), \\ i=1,\ N-1, \end{cases} \tag{4.27}$$

where tilde denotes the characteristic variables [16], and

$$\begin{aligned} R_* = P_1 - P_2 + \lambda_2\rho\left[\tilde{X}(U_0-U_1)+\tilde{Y}(V_0-V_1)+\tilde{Z}(W_0-W_1)\right] - \\ -\lambda_1\rho\left[\tilde{X}(U_0-U_2)+\tilde{Y}(V_0-V_2)+\tilde{Z}(W_0-W_2)\right] \end{aligned} \tag{4.28}$$

is an auxiliary function to write the characteristic quantities in a compact form. For incompressible multi-species variable density flows, the following

$$\begin{aligned} \tilde{P} = \tfrac{1}{s}\left\{\lambda_1 P_2 - \lambda_2 P_1 - \beta\left[\tilde{X}(\tilde{U}-U_1)+\tilde{Y}(\tilde{V}-V_1)+\tilde{Z}(\tilde{W}-W_1)\right] + \right. \\ \left. +\beta\left[\tilde{X}(\tilde{U}-U_2)+\tilde{Y}(\tilde{V}-V_2)+\tilde{Z}(\tilde{W}-W_2)\right]\right. \end{aligned} \tag{4.29}$$

characteristic pressure equation is obtained [16], which has to be taken into account in the right hand side of the scalar momentum equations. The first step of the Godunov procedure is to use a high-order interpolation ("reconstruction") formula to approximate the left and right side values of the characteristic variables. Before evaluating the cell-centred velocity components, the second step is to compute the inviscid intercell velocity components a) for constant density flows based on the system (4.21), and b) for multi-species variable density flows based on the system (4.27) [16]. In the third step, the non-linear cell-centered advective fluxes can be computed in a conservative $\nabla\cdot(\mathbf{U}\otimes\mathbf{U})$ form by using the FV discretization technique relying on approximation formulas according to (3.113). In the present thesis, for evaluating the pressure field, a fractional pseudo-time stepping method has been employed to couple the PP method with a high-resolution CB Godunov-type discretization by solving a pressure-Poisson equation. This method refers to the FSAC-PP method as proposed in the next two sections.

4.2 A FSAC-PP Method for Constant Density Flows

4.2.1 FSAC-PP Solution Method in conjunction with the CB Scheme

To provide time-accurate solution, the dual-time stepping procedure has been utilised. The advantage of the hyperbolic nature of the inviscid part of the AC formulation has been taken and high-resolution CB Godunov-type discretization has been employed for the non-linear advective fluxes.

In the first fractional step of the dual-time stepping procedure, the pressure term is neglected in the momentum equation as in the classical FS-PP method [4, 119], and the corresponding perturbed dimensionless system of governing equations in a semi-discrete vector form can be written as

$$\frac{P^{(n)} - P^{(n-1)}}{\Delta\tau} = -\beta \left(\nabla \cdot \mathbf{U}\right)^{(n)}, \tag{4.30}$$

$$\frac{\hat{\mathbf{U}} - \mathbf{U}^{(n)}}{\Delta\tau} = -\frac{\partial \mathbf{U}^{(n)}}{\partial t^*} - \nabla \cdot (\tilde{\mathbf{U}} \otimes \tilde{\mathbf{U}})^{(n)} + \frac{1}{Re}\nabla^2 \mathbf{U}^{(n)} + \mathbf{F}^{(n)}, \tag{4.31}$$

where $\hat{\mathbf{U}} = \begin{bmatrix} \hat{U} & \hat{V} & \hat{W} \end{bmatrix}^T$ represents the intermediate velocity field vector. In the first iteration step, the pressure and velocity fields are equal to the initial values of the problem. The intercell velocity components of the non-linear advective flux term in each direction are computed at time level n using the CB scheme [16, 6] based on the Riemann method [163], which has been discussed in the previous section. According to the transport CB scheme, the intercell velocity components are given [16] by

$$\tilde{\mathbf{U}}^{(n)} = \begin{bmatrix} \tilde{U} \\ \tilde{V} \\ \tilde{W} \end{bmatrix}^{(n)} = \begin{bmatrix} U_0 + \frac{\tilde{X}}{2s}R \\ V_0 + \frac{\tilde{Y}}{2s}R \\ W_0 + \frac{\tilde{Z}}{2s}R \end{bmatrix}^{(n)}, \tag{4.32}$$

where

$$\tilde{X} = \frac{k_X}{L_k}, \quad \tilde{Y} = \frac{k_Y}{L_k}, \quad \tilde{Z} = \frac{k_Z}{L_k},$$

are the coefficients of the scalar curvilinear governing equations, with k_X, k_Y, k_Z being the derivatives of the curvilinear coordinates $(k = \xi, \eta, \zeta)$ according to Cartesian (X, Y, Z)

dimensionless coordinates, and the notation $L_k = \left(k_X^2 + k_Y^2 + k_Z^2\right)^{1/2}$ is applied to the metrics. The distinct eigenvalues of the characteristic equations are $\lambda_0 = U\tilde{X} + V\tilde{Y} + W\tilde{Z}$, $\lambda_1 = \lambda_0 + s$ and $\lambda_2 = \lambda_0 - s$, where $s = \left(\lambda_0^2 + \beta\right)^{1/2}$ denotes the artificial speed of sound [16]. To compute the intercell CB velocity components $\tilde{U}, \tilde{V}, \tilde{W}$ of the advective term $\nabla \cdot (\tilde{\mathbf{U}} \otimes \tilde{\mathbf{U}})^{(n)}$ in conservative form at time level n, the following

$$\begin{aligned} R^{(n)} = {} & P_L - P_R + \lambda_2 \left[\tilde{X}\left(U_0 - U_R\right) + \tilde{Y}\left(V_0 - V_R\right) + \tilde{Z}\left(W_0 - W_R\right)\right] - \\ & - \lambda_1 \left[\tilde{X}\left(U_0 - U_L\right) + \tilde{Y}\left(V_0 - V_L\right) + \tilde{Z}\left(W_0 - W_L\right)\right] \end{aligned} \tag{4.33}$$

auxiliary function is introduced to write the intercell CB velocity components in (4.32) in a short form, where the "L" and "R" sub-indices denote the "Left" and "Right" sides of the scalar intercell flux quantities in the subdomain cells. These intercell flux quantities have been determined by applying first-, second- and third-order interpolations and fifth- and ninth-order WENO interpolations [164, 165, 166] with the values taken from the pseudo-time level n. These interpolations of the advective intercell fluxes are also employed in the pressure-projection step to obtain the high-accurate updated velocity field. Note that any appropriately chosen order of interpolation can be used. The cell-centred pressure values are obtained by solving the pressure-Poisson equation (3.125) at each pseudo-time step using the FSAC formulation. It is important to mention that the CB scheme is derived from the hyperbolic system of AC formulation, including the pressure gradient term [16, 6], therefore, the intercell pressure values P_L and P_R appear in the advective flux term based on Eq. (4.33). Although the pressure term is neglected in the first fractional step in the momentum equation (4.31), the intercell pressure values, as an initial guess of the pressure-projection step, can be determined from the perturbed continuity equation (4.30) in order to provide the consistency of the solution.

For computing the non-linear advective terms according to (4.32) in the momentum equation (4.31), the Godunov-type discretization has been employed to compute the velocity components U_0, V_0, W_0 corresponding to the λ_0 eigenvalue as

$$\mathbf{U}_0^{(n)} = \begin{bmatrix} U_0 \\ V_0 \\ W_0 \end{bmatrix}^{(n)} = \frac{1}{2} \begin{bmatrix} U_L + U_R + sign(\lambda_0)(U_L - U_R) \\ V_L + V_R + sign(\lambda_0)(V_L - V_R) \\ W_L + W_R + sign(\lambda_0)(W_L - W_R) \end{bmatrix}^{(n)}, \tag{4.34}$$

where

$$sign(\lambda_0) = \begin{cases} -1 & \lambda_0 > 0 \\ 1 & \lambda_0 < 0 \end{cases}. \tag{4.35}$$

After determining the right hand side of (4.31), an intermediate velocity field $\hat{\mathbf{U}}$ is estimated at each pseudo-time step. The Laplacian viscous flux terms are discretized by second-order accurate central approximations in the cell-centre.

The first-order temporal accuracy of pseudo-time stepping is advanced by applying an explicit fourth-order Runge-Kutta integration scheme [16, 167], thus improving the solution of the intermediate velocity field as

$$\begin{cases} \hat{\mathbf{U}}_{RK,1} = \hat{\mathbf{U}}_{RK}^{(n)}, \\ \hat{\mathbf{U}}_{RK,2} = \hat{\mathbf{U}}_{RK}^{(n)} + \frac{\Delta\tau}{2}\mathrm{RHS}(\hat{\mathbf{U}}_{RK,1}), \\ \hat{\mathbf{U}}_{RK,3} = \hat{\mathbf{U}}_{RK}^{(n)} + \frac{\Delta\tau}{2}\mathrm{RHS}(\hat{\mathbf{U}}_{RK,2}), \\ \hat{\mathbf{U}}_{RK,4} = \hat{\mathbf{U}}_{RK}^{(n)} + \Delta\tau\mathrm{RHS}(\hat{\mathbf{U}}_{RK,3}), \\ \hat{\mathbf{U}}_{RK} = \hat{\mathbf{U}}_{RK}^{(n)} + \frac{\Delta\tau}{6}\left[\sum_{i=1,4}\mathrm{RHS}(\hat{\mathbf{U}}_{RK,i}) + 2\sum_{i=2,3}\mathrm{RHS}(\hat{\mathbf{U}}_{RK,i})\right]. \end{cases} \tag{4.36}$$

where the $\hat{\mathbf{U}}_{RK} = \begin{bmatrix} P/\beta & \hat{U} & \hat{V} & \hat{W} \end{bmatrix}^T$ vector stands for the stages of the pseudo-time advancement, and $\mathrm{RHS}(\hat{\mathbf{U}}_{RK})$ represents the right hand side of the system of governing equations (4.30)-(4.31) in each integration step. After performing the pseudo-time advancement, the pressure field is computed to update the velocity field at each pseudo-time step by taking into account the divergence-free constraint, $\nabla\cdot\mathbf{U}^{(n+1)} = 0$. In the second fractional step of the dual-time stepping procedure. By taking the divergence of

$$\frac{\mathbf{U}^{(n+1)} - \hat{\mathbf{U}}}{\Delta\tau} = -\nabla P^{(n+1)}, \tag{4.37}$$

a second-order elliptical pressure-Poisson equation can be obtained [4, 119] as

$$\nabla^2 P^{(n+1)} = \frac{1}{\Delta\tau}\nabla\cdot\hat{\mathbf{U}}, \tag{4.38}$$

thus the pressure field is approximated by solving a pressure-Poisson equation (4.38). This second-order elliptical equation (4.38) is discretized in a curvilinear coordinate system using the Gauss-Seidel-type Successive Over Relaxation (S.O.R) iteration method [168, 135] (see in subsection 3.3.3). The numerical solution provides an approximately divergence-free velocity field at each pseudo-time step, which means that the pseudo-pressure term gradually tends to be zero in the perturbed continuity equation (3.32). The

velocity field is updated via the solution of the pressure-Poisson equation (4.38) as

$$\mathbf{U}^{(n+1)} = \hat{\mathbf{U}} - \Delta\tau \nabla P^{(n+1)}. \tag{4.39}$$

In order to satisfy the divergence-free constraint (3.30), the FSAC-PP procedure at each pseudo-time step has to be repeated until the continuity equation (3.30) and the pseudo-time derivatives in each scalar momentum equation approach very small values (near the machine-zero in computing terms). When the continuity equation (3.30) is satisfied, the pseudo-pressure term in the perturbed continuity equation (3.32) becomes equal to the threshold defined by the user as the machine-zero value. The convergence criterion for steady-state solution in pseudo-time is defined for constant density flows by

$$\max\left(\beta\left|\nabla\cdot\mathbf{U}^{(n+1)} - \nabla\cdot\mathbf{U}^{(n)}\right|, \left|\frac{\mathbf{U}^{(n+1)} - \mathbf{U}^{(n)}}{\Delta\tau}\right|\right) \leq \varepsilon. \tag{4.40}$$

When this criterion is satisfied, the continuity equation (3.30) will also be satisfied. Note that the perturbed continuity equation (3.32) is appropriate for controlling the pseudo-time stepping process, because when the right hand side of (4.30) becomes equal to zero, the steady-state solution of the system is achieved. Due to the velocity field update at each pseudo-time step, the difference between the divergence of the velocity fields in pseudo-time levels $n+1$ and n will decrease. Therefore, the following

$$\max\left(\beta\left|\nabla\cdot\mathbf{U}^{(n+1)} - \nabla\cdot\mathbf{U}^{(n)}\right|\right) \leq \varepsilon \tag{4.41}$$

strict criterion provides the compatibility with the classical AC method, hence satisfying the perturbed continuity equation (3.32). Since the divergence-free constraint is satisfied iteratively due to the pressure-projection and velocity field update at each pseudo-time step, the pseudo-pressure term in the perturbed continuity equation (3.32) will tend to be zero step by step. Note that it is necessary to perform sufficiently enough sub-iterations for solving the pressure-Poisson equation (3.140) to avoid possible oscillations in the pressure field solution. The convergence criterion of the pseudo-time stepping process (4.40) is a very strict imposition in order to satisfy the divergence-free continuity equation (3.30). For unsteady, time-accurate flow problems, when the steady-state solution is achieved in pseudo-time, the process has also to be advanced in real-time [16, 6].

4.2.2 Boundary Condition for the Pressure

In the classical FS-PP method, a Neumann-type boundary condition was used by Chorin [4] and Perot [119], which is written as

$$\frac{\partial P^{(n+1)}}{\partial n} = 0, \tag{4.42}$$

This is also called *"inviscid-type boundary condition"* for the pressure [23, 169]. Karniadakis et al. [117] introduced a consistent Neumann-type boundary condition for the pressure field using a spectral element discretization employing a high-order time splitting method for solving unsteady, incompressible Navier-Stokes equations. They also pointed out that the inviscid-type boundary condition (4.42) for the pressure is valid at high Reynolds number flows, but not for low Reynolds number microflows, because this condition leads to a divergence error at the boundary [23]. For microflows, using the dimensionless form of the governing equations, the following consistent boundary condition is suggested by Karniadakis et al. [23, pp. 514-517] as

$$\frac{\partial P^{(n+1)}}{\partial n} = \frac{1}{Re}\mathbf{n}\nabla^2\mathbf{U}^{(n+1)} - \mathbf{n}\hat{\mathbf{U}}, \tag{4.43}$$

where $\mathbf{n}$ is the normal vector, which is perpendicular to the surface with outward direction. The Neumann-type boundary condition for the pressure prescribed at all boundaries introduces a difficulty; specifically, the coefficient matrix of the system of linear equations of the discretized pressure-Poisson equation (3.140) becomes singular. To overcome this problem, the pressure value has to be prescribed at least in one point of the domain as an additive constant [135]. Moreover, the inviscid Neumann-type boundary condition is not a physical condition for the pressure as emphasized by Guermond et al. [170] among others. Bell et al. [115] and Guermond et al. [170] also pointed out, in consequence of Ladyzhenskaya's [109] orthogonality theorem, that there is no need for a boundary condition for the pressure, because the system will be over-determined [115]. Guermond et al. [170] considers the Neumann-type boundary condition mathematically correct for the pressure-Poisson equation in the incremental projection method. More details can be found about the orthogonality theorem of Ladyzhenskaya and the orthogonality of the pressure gradient with a solenoidal vector field in the book of Ladyzhenskaya [109].

4.2.3 FMG-FAS Multigrid Technique for the FSAC-PP Method

A non-linear full-multigrid and full-approximation storage (FMG-FAS) acceleration technique was developed by Drikakis et al. [7] in conjunction with the classical AC formu-

lation. In this thesis, we further extend the aforementioned technique to solve unsteady, incompressible Navier-Stokes equations using the proposed FSAC-PP method. The main difference between the original [7] and the present algorithm is the inclusion of the FSAC-PP step with the velocity field update into the pre- and post-relaxation steps of the FMG-FAS solution based on multigrid V-cycles. Note that the choice of the number of pre- and post-relaxation steps is depending on the fluid flow problem [6, p. 616].

The schematic representation of the multigrid V-cycle in the pseudo-time stepping process on three grid levels is shown in Figure 4.2 (see more details in [6]). The notations m_1 and m_1^* correspond to the pre-relaxation steps, and similarly, m_2 and m_2^* correspond to the post-relaxation steps on the fine and intermediate grid levels, respectively. The restriction and prolongation operators are denoted by R and P, where the employed restriction functions are according to [171]. The FSAC-PP solution of the Navier-Stokes equations in pseudo-time are denoted with N_{fg}, N_{ig}, N_{cg} corresponding to the fine, intermediate, and coarse grids; and, similarly, $PP_{fg}, PP_{ig}, PP_{cg}$ and $VU_{fg}, VU_{ig}, VU_{cg}$ notations stand for the pressure-projection step and the velocity field update, respectively. The initial conditions for the primitive variables on the fine grid are denoted by 0_{fg}.

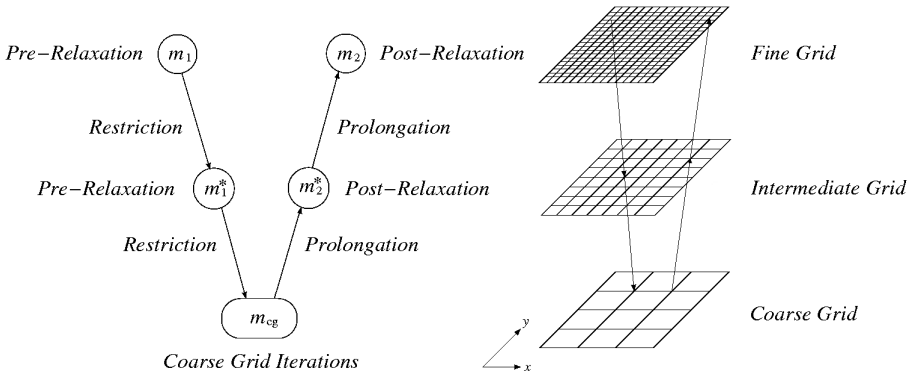

Figure 4.2: Multigrid V-cycle in the pseudo-time stepping process on three grid levels [6].

The further extended non-linear FMG-FAS algorithm to the developed FSAC-PP solution method consists of 17 steps in Algorithm 4.1. The pseudo-time marching is advanced by applying an explicit fourth-order Runge-Kutta integration scheme using adaptive time stepping with an appropriately chosen safety factor. The developed FSAC-PP method combines the features of classical FS and AC method using a PP step to gain high accuracy and excellent convergence properties via the CB scheme. The aim of coupling the non-linear FMG-FAS acceleration technique with the FSAC-PP method is to improve further the efficiency of the solution via a roboust numerical procedure. This method can be applicable to different practical problems in diverse fields of science and engineering, therefore, numerical examples have been presented in this thesis from Chapter 5 to 9.

Algorithm 4.1 Extended non-linear FMG-FAS algorithm to the developed FSAC-PP solution method for solving unsteady, incompressible Navier-Stokes equations.

1. Perform m_1 pre-relaxation iterations on the fine grid including the PP step and velocity field update: $V_{fg} := S_{fg}\left(V_{fg}, 0_{fg}, PP_{fg}, VU_{fg}, m_1\right)$.
2. Compute the fine grid defect: $d_{fg} := N_{fg}U_{fg}$.
3. Restriction from the finest grid to the intermediate grid: $d_{ig} := Rd_{fg}$.
4. Computation of the right hand side of (4.31) with the pressure gradient term on the intermediate grid: $f_{ig} := -d_{ig} + N_{ig}RV_{fg}$.
5. Perform m_1^* pre-relaxation iterations on the intermediate grid including the PP step and velocity field update: $V_{ig} := S_{ig}\left(V_{ig}, f_{ig}, PP_{ig}, VU_{ig}, m_1^*\right)$.
6. Computation of the intermediate grid defect: $d_{ig} := -f_{ig} + N_{ig}V_{ig}$.
7. Restriction from the intermediate grid to the coarse grid: $d_{cg} := Rd_{ig}$.
8. Computation of the right hand side of (4.31) with the pressure gradient term on the coarse grid: $f_{cg} := -d_{cg} + N_{cg}RV_{ig}$.
9. Approximate solution on the coarse grid: $V_{cg} := N_{cg}^{-1} f_{cg}$.
10. Perform correction on the coarse grid: $c_{cg} := V_{cg} - RV_{ig}$.
11. Prolongation from the coarse grid to the intermediate grid: $c_{ig} := Pc_{cg}$.
12. Compute the correct solution on the intermediate grid: $V_{ig} := V_{ig} + c_{ig}$.
13. Perform m_2^* post-relaxation iterations on the intermediate grid including the PP step and velocity field update: $V_{ig} := S_{ig}\left(V_{ig}, f_{ig}, PP_{ig}, VU_{ig}, m_2^*\right)$.
14. Perform correction on the intermediate grid: $c_{cg} := V_{ig} - RV_{fg}$.
15. Prolongation from the intermediate grid to the fine grid: $c_{fg} := Pc_{ig}$.
16. Compute the correct solution on the fine grid: $V_{fg} := V_{fg} + c_{fg}$.
17. Perform m_2 post-relaxation iterations on the fine grid including the PP step and velocity field update: $V_{fg} := S_{fg}\left(V_{fg}, 0_{fg}, PP_{fg}, VU_{fg}, m_2\right)$.

4.3 A FSAC-PP Method for Variable Density Flows

The proposed FSAC-PP solution method for constant density flows can be further extended to the solution of the momentum equation of the system (4.23) for multi-species variable density flows. In the first fractional step of the dual-time stepping procedure, similarly to the constant density flow case, the pressure term is neglected in the momentum equation as in the classical FS-PP method [4, 119]; therefore, the corresponding dimensionless momentum equation in semi-discrete vector form can be written as

$$\frac{\rho\hat{\mathbf{U}}-(\rho\mathbf{U})^{(n)}}{\Delta\tau}=-\frac{\partial\,(\rho\mathbf{U})^{(n)}}{\partial t^{*}}-\nabla\cdot(\rho\tilde{\mathbf{U}}\otimes\tilde{\mathbf{U}})^{(n)}+\frac{1}{Re}\nabla^{2}\mathbf{U}^{(n)}+\mathbf{F}^{(n)}, \tag{4.44}$$

where $\hat{\mathbf{U}}=\left[\begin{array}{ccc}\hat{U} & \hat{V} & \hat{W}\end{array}\right]^{T}$ represents the intermediate velocity field vector. In the first iteration step, the pressure and velocity fields are equal to the initial values of the problem. The intercell velocity components of the non-linear advective flux term in each direction are computed at time level n using the CB scheme [16, 6] based on the Riemann method [163]. According to the transport CB scheme for incompressible multi-species variable density flows, the intercell velocity components are given [16] by

$$\tilde{\mathbf{U}}^{(n)}=\left[\begin{array}{c}\tilde{U}\\ \tilde{V}\\ \tilde{W}\end{array}\right]^{(n)}=\left[\begin{array}{c}U_0+\frac{\tilde{X}}{2\rho s}R_{*}\\ V_0+\frac{\tilde{Y}}{2\rho s}R_{*}\\ W_0+\frac{\tilde{Z}}{2\rho s}R_{*}\end{array}\right]^{(n)}, \tag{4.45}$$

where

$$\begin{aligned}R_{*}^{(n)}=P_L-P_R+\lambda_2\rho\left[\tilde{X}(U_0-U_L)+\tilde{Y}(V_0-V_L)+\tilde{Z}(W_0-W_L)\right]-\\ -\lambda_1\rho\left[\tilde{X}(U_0-U_R)+\tilde{Y}(V_0-V_R)+\tilde{Z}(W_0-W_R)\right]\end{aligned} \tag{4.46}$$

is an auxiliary function introduced to write the intercell CB velocity components in (4.32) in a short form, where again the "L" and "R" sub-indices denote the "Left" and "Right" sides of the scalar intercell flux quantities in the subdomain cells. These intercell flux quantities have been determined by applying first-, second- and third-order interpolations and fifth- and ninth-order WENO interpolations [164, 165, 166] with the values taken from the pseudo-time level n (as in the case of the FSAC-PP method for constant density flow). These interpolations of the advective intercell fluxes are also employed in the pressure-projection step to obtain the high-accurate updated velocity field. Note that any appropriately chosen order of interpolation can be used. The cell-centred pressure values are obtained by solving the pressure-Poisson equation (3.136) for variable density flow at each pseudo-time step using the FSAC formulation. It is important to mention that

the CB scheme is derived from the hyperbolic system of AC formulation, including the pressure gradient term [16, 6], therefore, the intercell pressure values P_L and P_R appear in the advective flux term based on (4.33). Although the pressure term is neglected in the first fractional step in the momentum equation (4.44), the intercell pressure values, as an initial guess of the pressure-projection step, can be determined from the perturbed continuity equation (4.30) in order to provide the consistency of the solution.

For computing the non-linear advective terms according to (4.45) in the momentum equation (4.44), the Godunov-type discretization has been employed again to compute the velocity components U_0, V_0, W_0 corresponding to the eigenvalue λ_0 as

$$\mathbf{U}_0^{(n)} = \begin{bmatrix} U_0 \\ V_0 \\ W_0 \end{bmatrix}^{(n)} = \frac{1}{2} \begin{bmatrix} U_L + U_R + sign(\lambda_0)(U_L - U_R) \\ V_L + V_R + sign(\lambda_0)(V_L - V_R) \\ W_L + W_R + sign(\lambda_0)(W_L - W_R) \end{bmatrix}^{(n)}, \tag{4.47}$$

where $sign(\lambda_0)$ is computed based on Eq. (4.35). After determining the right hand side of (4.44), an intermediate velocity field multiplied by the total density $\rho\hat{\mathbf{U}}$ is estimated at each pseudo-time step. The Laplacian viscous flux terms are discretized by second-order accurate central approximations in the cell-centre. The first-order temporal accuracy of pseudo-time stepping is advanced by applying an explicit fourth-order Runge-Kutta integration scheme [16, 167]; thus improving the solution of the intermediate velocity field. Note that the Runge-Kutta pseudo-time integration scheme has also been employed for the total and the partial density equations depending on the number of species. After performing the pseudo-time advancement, the pressure field is computed to update the velocity field at each pseudo-time step. By taking the divergence of

$$\frac{\mathbf{U}^{(n+1)} - \hat{\mathbf{U}}}{\Delta\tau} = -\frac{1}{\rho}\nabla P^{(n+1)}, \tag{4.48}$$

a second-order elliptical pressure-Poisson equation can be obtained [118] including the total density as

$$\nabla \cdot \left(\frac{1}{\rho}\nabla P\right)^{(n+1)} = \frac{1}{\Delta\tau}\nabla \cdot \hat{\mathbf{U}}, \tag{4.49}$$

thus the pressure field is approximated by solving a pressure-Poisson equation (4.49). This second-order elliptical equation (4.49) is discretized in curvilinear coordinate system using the Gauss-Seidel-type Successive Over Relaxation (S.O.R) iteration method [168, 135] (see in subsection 3.3.3). The numerical solution provides an approximately divergence-free velocity field at each pseudo-time step, which means that the pseudo-pressure term approximates zero in the perturbed continuity equation (3.32). The velocity

field is updated via the solution of the pressure-Poisson equation (4.49) as

$$\rho \mathbf{U}^{(n+1)} = \rho \hat{\mathbf{U}} - \Delta\tau \nabla P^{(n+1)}. \tag{4.50}$$

In order to satisfy the divergence-free constraint (3.30) for incompressible variable density flows, the FSAC-PP procedure at each pseudo-time step has to be repeated until the continuity equation (3.30) and the pseudo-time derivatives in each scalar momentum equation, total and partial density equations approach very small values (near the machine-zero in computing terms). When the continuity equation (3.30) is satisfied, the pseudo-pressure term in the perturbed continuity equation (3.32) becomes equal to the threshold defined by the user as the machine-zero value. The convergence criterion for steady-state solution in pseudo-time is defined for variable density flows by

$$\max\left(\left|\nabla\cdot(\rho\mathbf{U})^{(n+1)} - \nabla\cdot(\rho\mathbf{U})^{(n)}\right|, \left|\frac{\rho\mathbf{U}^{(n+1)} - \rho\mathbf{U}^{(n)}}{\Delta\tau}\right|\right) \leq \varepsilon. \tag{4.51}$$

When this criterion is satisfied, the continuity equation (3.30) will also be satisfied. Note that the perturbed continuity equation (3.32) is appropriate for controlling the pseudo-time stepping process, because when the right hand side of (4.30) becomes equal to zero, the steady-state solution of the system is achieved. Due to the velocity field update at each pseudo-time step, the difference between the divergence of the velocity fields in pseudo-time levels $n+1$ and n will decrease. Therefore, the following

$$\max\left[\beta\left|\nabla\cdot(\rho\mathbf{U})^{(n+1)} - \nabla\cdot(\rho\mathbf{U})^{(n)}\right|\right] \leq \varepsilon \tag{4.52}$$

strict criterion provides the compatibility with the classical AC method, hence satisfying the perturbed continuity equation (3.32). Note that it is necessary to perform sufficiently enough sub-iterations for solving the pressure-Poisson equation (3.163) to avoid oscillations in the pressure field solution. The convergence criterion of the pseudo-time stepping process (4.51) is also a very strict imposition to satisfy the divergence-free continuity equation (3.30). To further increase the efficiency of the proposed FSAC-PP method for incompressible variable density flows, the FMG-FAS multigrid acceleration technique, discussed in subsection 4.2.3, has been further extended to solve incompressible variable density flow problems by using Algorithm 4.2.

Algorithm 4.2 Extended non-linear FMG-FAS algorithm to the developed FSAC-PP solution method for solving unsteady, incompressible variable density flow problems.

1. Perform m_1 pre-relaxation iterations on the fine grid including the variable density PP step and velocity field update: $V_{fg} := S_{fg}\left(V_{fg}, 0_{fg}, PP_{fg}^{vd}, VU_{fg}, m_1\right)$.
2. Compute the fine grid defect: $d_{fg} := N_{fg}U_{fg}$.
3. Restriction from the finest grid to the intermediate grid: $d_{ig} := Rd_{fg}$.
4. Computation of the right hand side of (4.44) with the pressure gradient term on the intermediate grid: $f_{ig} := -d_{ig} + N_{ig}RV_{fg}$.
5. Perform m_1^* pre-relaxation iterations on the intermediate grid including the variable density PP step and velocity field update: $V_{ig} := S_{ig}\left(V_{ig}, f_{ig}, PP_{ig}^{vd}, VU_{ig}, m_1^*\right)$.
6. Computation of the intermediate grid defect: $d_{ig} := -f_{ig} + N_{ig}V_{ig}$.
7. Restriction from the intermediate grid to the coarse grid: $d_{cg} := Rd_{ig}$.
8. Computation of the right hand side of (4.44) with the pressure gradient term on the coarse grid: $f_{cg} := -d_{cg} + N_{cg}RV_{ig}$.
9. Approximate solution on the coarse grid: $V_{cg} := N_{cg}^{-1} f_{cg}$.
10. Perform correction on the coarse grid: $c_{cg} := V_{cg} - RV_{ig}$.
11. Prolongation from the coarse grid to the intermediate grid: $c_{ig} := Pc_{cg}$.
12. Compute the correct solution on the intermediate grid: $V_{ig} := V_{ig} + c_{ig}$.
13. Perform m_2^* post-relaxation iterations on the intermediate grid including the variable density PP step and velocity field update: $V_{ig} := S_{ig}\left(V_{ig}, f_{ig}, PP_{ig}^{vd}, VU_{ig}, m_2^*\right)$.
14. Perform correction on the intermediate grid: $c_{cg} := V_{ig} - RV_{fg}$.
15. Prolongation from the intermediate grid to the fine grid: $c_{fg} := Pc_{ig}$.
16. Compute the correct solution on the fine grid: $V_{fg} := V_{fg} + c_{fg}$.
17. Perform m_2 post-relaxation iterations on the fine grid including the variable density PP step and velocity field update: $V_{fg} := S_{fg}\left(V_{fg}, 0_{fg}, PP_{fg}^{vd}, VU_{fg}, m_2\right)$.

4.4 Pseudo-Time Stepping Strategy

4.4.1 Constant Density Flows

The discretized system of governing equations is solved via a dual-time stepping Godunov-type explicit method, therefore, a pseudo-time stepping strategy is required for stability reasons. The accuracy and convergence properties of CB schemes were discussed by Shapiro and Drikakis [16] based on an eigenvalue analysis to estimate the locally computed pseudo-time step. The pseudo-time step is determined in each computational cell in the domain. The relationship between the pseudo-time step and characteristic condition numbers provides the stability of the numerical procedure, which are given [16] by

$$\begin{cases} \Delta\tau_{i,j,k}^{\text{Inviscid}} = \dfrac{\text{CFL}_{\text{Inviscid}}}{[\max_{\text{m=1-6}}(|\lambda_1|,|\lambda_2|)_m]_{i,j,k}}, \\ \\ \Delta\tau_{i,j,k}^{\text{Viscous}} = \dfrac{\text{CFL}_{\text{Viscous}}Re}{4[\max_{\text{n=1,2,3}}(dl_n)]_{i,j,k}}, \end{cases} \tag{4.53}$$

where $\text{CFL}_{\text{Inviscid}}$ and $\text{CFL}_{\text{Viscous}}$ are the *Courant-Friedrichs-Lewy* (CFL) numbers of the inviscid and viscous fluxes, respectively, and dl_n represents the cell dimension according to the coordinate directions (ξ,η,ζ). The CFL numbers are characteristic condition numbers relating to the stiffness of the solution. The locally computed pseudo-time step is computed based on the minimum value of the locally determined pseudo-time steps for the inviscid and viscous fluxes as

$$\Delta\tau_{i,j,k} = \gamma \cdot \min\left(\Delta\tau_{i,j,k}^{\text{Inviscid}}, \Delta\tau_{i,j,k}^{\text{Viscous}}\right), \tag{4.54}$$

where $\gamma \in]\,0,1]$ is an appropriately chosen safety factor to ensure numerical stability [137]. The pseudo-time step depends on the CFL numbers and the eigenvalues, which in turn depend on the AC parameter, therefore, these appropriately chosen parameters ensure the stability and convergence of the iterative numerical procedure [138, 5].

4.4.2 Multi-Species Variable Density Flows

The accuracy and convergence properties of CB schemes were discussed by Shapiro and Drikakis [16] for solving multi-species variable density flow problems as well. The relationships between the locally computed pseudo-time step and characteristic condition

numbers are defined [16] by

$$\begin{cases} \Delta\tau_{i,j,k}^{\text{Inviscid}} = \dfrac{\text{CFL}_{\text{Inviscid}}}{[\max_{\text{m=1-6}}(|\lambda_1|,|\lambda_2|)_m]_{i,j,k}}, \\ \Delta\tau_{i,j,k}^{\text{Viscous}} = \dfrac{\text{CFL}_{\text{Viscous}}Re}{4[\max_{\text{n=1,2,3}}(dl_n)]_{i,j,k}}, \\ \Delta\tau_{i,j,k}^{\text{Diffusive}} = \dfrac{\text{CFL}_{\text{Viscous}}Pe}{4[\max_{\text{n=1,2,3}}(dl_n)]_{i,j,k}}, \end{cases} \tag{4.55}$$

where $\text{CFL}_{\text{Inviscid}}$, and $\text{CFL}_{\text{Viscous}}$ are again the *Courant-Friedrichs-Lewy* (CFL) numbers of the inviscid and viscous flux terms, respectively, and dl_n represents again the cell dimension according to the coordinate directions (ξ,η,ζ). For stability reasons, we assume that the locally computed pseudo-time step size is determined by the minimum value of the locally computed pseudo-time step of the inviscid, viscous and diffusive fluxes as

$$\Delta\tau_{i,j,k} = \gamma \cdot \min\left(\Delta\tau_{i,j,k}^{\text{Inviscid}}, \Delta\tau_{i,j,k}^{\text{Viscous}}, \Delta\tau_{i,j,k}^{\text{Diffusive}}\right), \tag{4.56}$$

where $\gamma \in]\,0,1]$ is a safety factor of stability [137]. Similarly to constant density flows, the time step size depends on the CFL numbers and on the eigenvalue structure of system of equations. The eigenvalues also depend on the AC parameter, therefore, these parameters have to be chosen appropriately to ensure the stability and convergence of the iterative process for multi-species variable density flow problems as well. More details can be found about stability analysis in the books of Roache [138], and Peyret and Taylor [5].

4.5 Summary

To circumvent convergence and associated accuracy problems of the original AC formulation when used for low Reynolds and/or unsteady problems, a new FSAC-PP approach has been proposed in this chapter that couples the fractional step (FS), artificial compressibility (AC), and pressure-projection (PP) methods. The FSAC-PP method incorporates the CB scheme with PP methods via the FSAC formulation. This method retains the hyperbolic, inviscid counterpart of the AC formulation to enable the use of Riemann method for solving the Riemann problem. In this thesis, the pressure field has been updated by solving a pressure-Poisson equation. Relying on the idea of the proposed FSAC-PP method, it is possible to further improve the efficiency of the classical AC method, because excellent convergence properties of the high-resolution CB Godunov-type schemes can be gained to avoid spurious oscillations in the non-linear convective/advective terms.

Chapter 5

Laminar Flow in a Straight Microchannel at Low Reynolds Numbers

5.1 Introduction

An in-house FORTRAN 90/95 HIRECOM-MULTIPHYSICS Unified Code v1.0 software package has been developed for solving the unsteady, incompressible Navier-Stokes equations relying on the proposed FSAC-PP solution method discussed in Chapter 4. The validation of the proposed FSAC-PP method is indispensable compared to other methods in terms of accuracy and efficiency. In this chapter, the FSAC-PP method has been validated for steady-state, incompressible, constant density flow by comparing it to the AC, PP methods and an analytical solution. For microfluidic applications, the two-dimensional straight microfluidic channel is a widely used benchmark test case for pressure-driven laminar flow. An analytical solution exists for the fully developed laminar velocity profile, which has to be obtained at the outlet section of the microfluidic channel. Therefore, the computational results can be compared to analytical solutions at different Reynolds numbers taking into account also extremely low Reynolds number cases. Furthermore, the physical boundary and initial conditions can be prescribed accurately, thus the mathematical task may be considered as well-posed. More details can be found about pressure-driven laminar flows in two-dimensional channels in the works of Kotake, Hijikata and Fusegi [172, pp. 99-122], Chen et al. [173], and of Chakraborty [174, 80].

For steady-state, incompressible, constant density flow in a straight microfluidic channel, according to the analytical solution for the one dimensional case, the axial velocity component depends on the coordinate of the radial direction $u = u(y)$ while the other

velocity components vanish ($v = w = 0$). It is well-known that the AC method is efficient at Reynolds numbers from 1 up to 10^3 [5, 27]. The reasons are the restriction for the locally computed pseudo-time step in Eq. (4.55) and the choice of AC parameter in Eq. (3.34) that may lead to a slow convergence rate at $Re \ll 1$. For microfluidic applications under the continuum hypothesis, the typical Reynolds numbers range from 10^{-1} up to 10^2 (see, e.g., [6]). Therefore, it is pertinent to validate the FSAC-PP method at different low Reynolds numbers (including extremely low regimes), which is defined by

$$Re = \frac{2h\tilde{u}}{\upsilon}, \tag{5.1}$$

where h is the height of the microfluidic channel, $\tilde{u}$ is the average velocity, and υ is the kinematic viscosity of the fluid. From wall to wall, the divergence-free steady-state velocity distribution [93, p. 10] can be derived as

$$u(y) = \rho \frac{\Delta\Pi}{2\mu l} y(h-y), \tag{5.2}$$

where ρ is the density of the fluid, μ is the dynamic viscosity of the fluid, l is the length of the straight microfluidic channel, and Π is the total potential, which is proportional to the pressure difference between the inlet and the outlet sections as

$$\Delta\Pi = \frac{\Delta p}{\rho}. \tag{5.3}$$

The characteristic quantities can also be computed such as the volume flow rate which is

$$Q = w_c \int_0^h u(y)\, dy = w_c \frac{\Delta\Pi}{2\upsilon l} \int_0^h y(h-y)\, dy = w_c \frac{\Delta\Pi}{12\upsilon l} h^3, \tag{5.4}$$

and the average velocity can be expressed as

$$\tilde{u} = \frac{Q}{A} = \frac{\Delta p}{12\mu l} h^2, \tag{5.5}$$

and the pressure difference between the inlet and outlet sections is written as

$$\Delta p = \frac{12\mu l}{h^2} \tilde{u}. \tag{5.6}$$

By using Eqs. (5.1)-(5.6), all physical quantities of the pressure-driven laminar flow can be computed; thus a numerical benchmark test case can be set up for validating the FSAC-PP method, which has been described in the following section.

5.2 The Straight Microfluidic Channel Test Case

The computational grid is shown in Figure 5.1, which consists of 181×41 node points $(180 \times 40 \text{ control cells})$ on the fine grid.

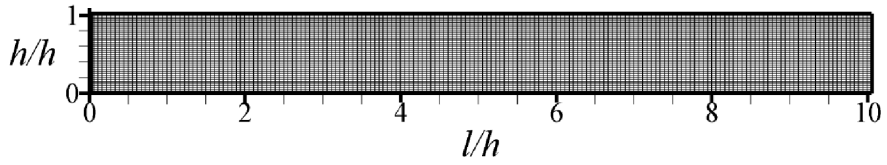

Figure 5.1: Computational grid for the microchannel using dimensionless coordinates.

The height h of the benchmark straight microfluidic channel is $10\mu m$, and the length l is equal to $100\mu m$. The dimensional and dimensionless geometrical sizes of the two-dimensional microfluidic channel have been summarized in Table 5.1.

	Microfluidic channel	
Sizes	μm	dimensionless
l	100	10
h	10	1

Table 5.1: Geometrical sizes of the two-dimensional straight microfluidic channel.

A mathematical task can be formulated in terms of boundary conditions for the pressure-driven laminar flow in the straight microfluidic channel. Dimensionless quantities have been used in the simulations, therefore, the spatial coordinates have been normalized by the height h of the channel. From wall to wall, the inlet velocity profile normalized by the average flow velocity $\tilde{u}$ and can be derived based on Eqs. (5.2)-(5.6) as

$$U_{inlet}(0,Y) = \frac{u}{u_*}\frac{u_*}{\tilde{u}} = 6Y(1-Y), \tag{5.7}$$

where u_* is the wall-friction velocity [172]. The dimensionless pressure has been prescribed equally to be zero at the inlet section, which can be written as $P_{inlet}(0,Y) = 0$. Thus, the boundary conditions are Dirichlet-type in the inlet section. The outlet boundary conditions for the dimensionless velocity components can be prescribed as

$$\frac{\partial U(L,Y)}{\partial X} = 0 \text{ and } \frac{\partial V(L,Y)}{\partial X} = 0, \tag{5.8}$$

which are Neumann-type boundary conditions, where L is the dimensionless spatial coordinate of the outlet section. The dimensionless pressure has been prescribed equally to be one at the outlet section, which is a Dirichlet-type boundary condition, and can be written as $P_{outlet}(L,Y) = 1$. The wall is non-moving, therefore, the dimensionless velocity components U and V are equal to zero on the bottom and upper walls as

$$U_{upperwall}(X,1) = U_{bottomwall}(X,0) = V_{upperwall}(X,1) = V_{bottomwall}(X,0) = 0. \quad (5.9)$$

Neumann-type and consistent boundary conditions are prescribed for the dimensionless pressure on the bottom and upper walls suggested by Karniadakis et al. [23, pp. 514-517] based on Eq. (4.43). More details can be found in subsection 4.2.2.

The continuum model is limited at small physical length scales, therefore, a criterion exists to determine the validity of continuum hypothesis (see in Chapter 3). According to Heller [95, p. 8], for investigating microfluidic systems under the contiuum hypothesis, the characteristic length scale of the fabricated system has to be a bigger value than the average interatomic space λ_A [95, p. 8]. The average interatomic space [95, p. 8] has been determined relying on Eq. (3.1). In the present test case, the working fluid is water, and the interatomic space of water λ_{water} is calculated as

$$\lambda_{water} = \left(\frac{M_{water}}{\rho_{water} N_A} \right)^{\frac{1}{3}} = 0.3 \cdot 10^{-9}\, m, \quad (5.10)$$

where $\rho_{water} = 1000\ kg/m^3$ is the density of water, $M_{water} = 18.0153 \cdot 10^{-3}\ kg/mol$ is the molar mass of water, and $N_A = 6.022 \cdot 10^{23}\ 1/mol$ is the Avogadro's number. The biggest characteristic length of the two-dimensional straight microfluidic channel (see Table 5.1) is $100 \cdot 10^{-6}\ m$ (100 *micron*), which is a greater value than $0.3 \cdot 10^{-9}\ m$ (0.3 *nm*); consequently, the continuum model can be considered to be valid for the present physical and numerical test case. Furthermore, this example demonstrates the overall limitation of the continuum hypothesis for water, because when the geometrical size of the investigated microfluidic system is smaller than 0.3 *nm*, the continuum model can not be used for modelling physical phenomena at those small physical length scales.

5.3 Validation of the FSAC-PP Method at Various Low Reynolds Numbers

For the validation of the FSAC-PP method compared to the AC, PP methods and an analytical solution for steady-state, incompressible, constant density flow from $Re = 10$ to 10^{-4}, 480 simulations have been performed using 3 different methods with 5 different intercell flux interpolations on 4 different girds at 8 different Reynolds numbers as

$$480\,\text{Simulations} = 3\,\text{Method} \times 5\,\text{Interpolation Formulas} \times 4\,\text{Grids} \times 8\,Re\,\text{Numbers}.$$

The non-linear full-multigrid, full-approximation-storage (FMG-FAS) technique, discussed in subsection 4.2.3, has been used in order to accelerate the numerical process using 100 pre- and post-smoothing iterations on the fine grid, 10 pre- and post-smoothing iterations on the medium grid, and 10 iterations on the coarse grid, respectively. Note that the choice of the number of pre- and post-relaxation steps is depending on the fluid flow case [6, p. 616]. The CFL numbers for computing the inviscid and viscous fluxes, and the simulation parameters have been summarized in Table 5.2.

	Reynolds Numbers (Re)							
	10	5	1	0.5	0.1	0.01	0.001	0.0001
	Simulation Parameters							
β	10	10^2	10^2	10^3	10^3	10^4	10^5	10^6
CFL_{inv}	0.2	0.2	0.05	0.015	0.015	0.015	0.015	0.015
CFL_{vis}	0.15	0.15	0.05	0.015	0.015	0.015	0.015	0.015

Table 5.2: Simulation parameters of eight numerical test cases for the AC parameter β, for the CFL_{inv} and CFL_{vis} Courant-Friedrichs-Lewy numbers associated with the inviscid and viscous fluxes at various Reynolds numbers Re.

The numerical convergence has been measured using the maximum value of the Runge-Kutta residuals, which is defined by

$$\max\left(\left|\frac{\mathbf{U}_{RK}^{(n+1)} - \mathbf{U}_{RK}^{(n)}}{\Delta\tau}\right|\right) \leq \varepsilon, \tag{5.11}$$

where $\mathbf{U}_{RK} = \begin{bmatrix} P/\beta & U & V & W \end{bmatrix}^T$ represents the numerical solution of the governing equations between two pseudo-time level. The pseudo-time stepping iterations of the AC, PP and FSAC-PP methods have been carried out until the steady-state solution is achieved; which means that the Runge-Kutta residuals do not change significantly below

a very small ε threshold value. The contour lines of the dimensionless velocity component U in the fully developed laminar flow is shown in Figure 5.2.

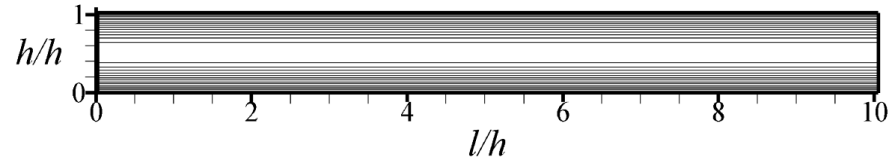

Figure 5.2: Contour lines of the velocity component U in the fully developed pressure-driven laminar flow in a straight microfluidic channel.

The grid convergence study is part of the validation process, therefore, Roache [175] introduced the Grid Convergence Index (GCI) to measure the rate of grid convergence avoiding inconsistency in the way of reporting grid convergence studies in the field of engineering sciences [138, pp. 107-119]. Relying on the generalization of the Richardson extrapolation, Roach [138, p. 115] defined the GCI as

$$\mathrm{GCI} = F_s \frac{|\varepsilon_r|}{r^p - 1}, \tag{5.12}$$

where F_s is the safety factor, ε_r is the relative error between the solutions for the investigated quantity (e.g. velocity and/or pressure field values) using two different grids, r is the grid refinement ratio; and p is the order of the method, which is related to the order of the truncation error. In the present thesis in conjunction with the grid convergence studies, the safety factor has been chosen to be equal to one $(F_s = 1)$, and the relative error of the solution on two different grids (e.g. between the coarse and fine grid) as

$$\varepsilon_r = \frac{\left\|U_{coarse\,grid}\right\|_{(\infty)} - \left\|U_{fine\,grid}\right\|_{(\infty)}}{\left\|U_{fine\,grid}\right\|_{(\infty)}}, \tag{5.13}$$

where the maximum norm of the velocity component U on the chosen grid is defined as

$$\|U\|_{(\infty)} = \max_i \left(\sum_{j=1}^{N} \left| U_{i,j} \right| \right),$$

where N is the number of the control cells in the computational domain. In the present thesis, four different grid levels G1, G2, G3, G4 have been used for validating the proposed FSAC-PP method compared to the AC, PP methods and an analytical solution, respectively (see Table 5.3). For investigating the grid convergence on different grid levels systematically, the grid refinement ratio r and the order of the intercell flux interpolation method relating to the truncation error p have been summarized in Table 5.4.

Grid Levels	Number of Node Points	Number of Controll Cells
G1	$21 \times 11 = 231$	$20 \times 10 = 200$
G2	$41 \times 21 = 861$	$40 \times 20 = 800$
G3	$81 \times 41 = 3321$	$80 \times 40 = 3200$
G4	$181 \times 41 = 7421$	$180 \times 40 = 7200$

Table 5.3: Number of node points and controll cells on different grid levels.

Grid	Grid Refinement Ratio r	Order of Truncation Error p
G1÷G2	4	1,2,3,5,9
G2÷G3	4	1,2,3,5,9
G3÷G4	2.25	1,2,3,5,9

Table 5.4: Grid refinement ratios r and the order of interpolation method relating to the truncation error p on different grid levels.

A systematic grid convergence study has been performed by using 3 different methods and by employing 5 different intercell flux interpolations on 4 different grid levels. The GCI indices of the grid convergence studies for the AC, PP and FSAC-PP methods using different intercell flux interpolations have been summarized from Tables 5.5 to 5.12. The results show that grid convergence has been observed in the most cases of AC, PP and FSAC-PP methods from $Re = 10$ to 0.1 based on the simulation parameters (see Table 5.2) at different grid levels (see Table 5.3). Grid convergence has only been observed in the most cases of PP and FSAC-PP methods from $Re = 0.01$ to 0.0001; see Tables from 5.10 to 5.12. The GCI mostly exhibits minor changes between the grid levels (G1÷G2) and (G2÷G3), and mostly exhibits more significant decrement between the meshes (G2÷G3) and (G3÷G4). Thus, the results do not show significant changes by using more than 180×40 control cells on the domain for this microfluidic benchmark test case.

The characteristic condition numbers as CFL_{inv} and CFL_{vis} for inviscid and viscous fluxes, respectively, have to be decreased, and the AC parameter β has to be increased when the Reynolds number has been decreased from 10 to 0.0001. Small CFL numbers lead to very small values of the locally computed pseudo-time step and the large values of parameter β ensure the numerical convergence (see Table 5.2). The computational cost of the AC, PP and FSAC-PP methods has been measured based on the required number of multigrid cycles N_{mg} on the fine grid until the lowest maximum Runge-Kutta residuals RK_{maxres} are achieved, which have been summarized in Tables 5.21 to 5.28 and in Figures 5.43 to 5.50. The results show that the FSAC-PP method requires the lowest number of multigrid iterations N_{mg} on the fine grid compared to the AC and PP methods in each test case. For example, the total CPU time, on a Dual-Core E5300 2.60 Ghz computer with 8GB RAM, was 41 minutes for the AC method, 15 minutes for the PP method, and

14 minutes for the FSAC-PP method by using a 3^{rd}-order intercell flux interpolation at $Re = 10$. The FSAC-PP method consumes 5 and 52 times less N_{mg} at $Re = 10$ (see Table 5.21 and Figure 5.43); 2.5 and 27 times less N_{mg} at $Re = 5$ (see Table 5.22 and Figure 5.44); 40 and 29 times less N_{mg} at $Re = 1$ (see Table 5.23 and Figure 5.45); 29 and 9 times less N_{mg} at $Re = 0.5$ (see Table 5.24 and Figure 5.46); 110 and 14 times less N_{mg} at $Re = 0.1$ (see Table 5.25 and Figure 5.47); 14.5 and 14 times less N_{mg} at $Re = 0.01$ (see Table 5.26 and Figure 5.48); 12 and 10 times less N_{mg} at $Re = 0.001$ (see Table 5.27 and Figure 5.49); furthermore, 9 and 8 times less N_{mg} at $Re = 0.0001$ (see Table 5.28 and Figure 5.50) than the AC and PP methods in average, respectively.

The relative errors of the maximum norm of the outlet velocity component U compared to the maximum norm of the analytical solution have been computed at the outlet section of the channel from $Re = 10$ up to 10^{-4} (see Tables from 5.13 to 5.20). On the coarsest grid level G1, the results show that the FSAC-PP method exhibits agreement in $\sim 0.63624\%$ maximum relative error with the analytically computed outlet velocity profiles up to $Re = 1$ while the AC and PP methods exhibit $\sim 0.35687\%$ and $\sim 11.39831\%$ maximum relative errors, respectively. On the finest grid level G4, the FSAC-PP method exhibits agreement in $\sim 0.17535\%$ maximum relative error up to $Re = 1$ while the AC and PP methods exhibit $\sim 0.50831\%$ and $\sim 1.25491\%$ maximum relative errors, respectively (see Tables from 5.13 to 5.15). Decreasing the Reynolds number, the maximum relative error of the AC, PP and FSAC-PP methods compared to the analytical solution is $\sim 4.19308\%$, $\sim 0.00563\%$ and $\sim 0.14231\%$ on the finest grid at $Re = 0.1$, respectively. The AC method shows agreement with the analytically computed outlet velocity profiles up to $Re = 0.1$ on each grid level; unlike the PP and the FSAC-PP methods exhibit agreement with the analytical solution up to $Re = 0.0001$, respectively. Since, the lowest maximum Runge-Kutta residual of the AC method is in between 0.19437 and $0.24087 \cdot 10^3$ when the Reynolds number is smaller than 0.1 (see from Tables 5.26 to 5.28), the numerical solution is not able to resolve the fully developed laminar velocity profile at the outlet section. These results can be seen in Figures 5.28 to 5.42 at $Re = 0.01$, 0.001, and 0.0001. The velocity values computed by the AC method are almost equal to zero, which means they are nearly equal to the initial condition of the velocity field. Despite of this fact, the PP and FSAC-PP methods show agreement with the analytical solution at $Re = 0.01$, 0.001, and 0.0001 as well. For $Re < 0.1$, the AC method fails to give physically reasonable results (see Figures from 5.28 to 5.42). When the Reynolds number is decreased by using the PP and FSAC-PP methods, the lowest maximum Runge-Kutta residual is achieved by employing third- and fifth-order interpolation schemes, therefore, at least third-order interpolation is recommended for the intercell fluxes at low Reynolds numbers (see Table 5.28). All in all, both PP and FSAC-PP methods are capable of handling extremely low Reynolds numbers compared to the AC method for this test case.

Reynolds Number ($Re = 10$)		Grid Convergence Index [%]		
Intercell Flux Interpolation	Solution Method	Grid Levels		
		G1÷G2	G2÷G3	G3÷G4
1^{st}-Order	AC	$4.15217 \cdot 10^{-1}$	$2.27508 \cdot 10^{-1}$	$6.48428 \cdot 10^{-4}$
	PP	2.88112	1.86577	$7.35134 \cdot 10^{-1}$
	FSAC-PP	$4.68341 \cdot 10^{-1}$	$2.57152 \cdot 10^{-1}$	$2.18638 \cdot 10^{-3}$
2^{nd}-Order	AC	$8.36038 \cdot 10^{-2}$	$4.57280 \cdot 10^{-2}$	$1.63216 \cdot 10^{-4}$
	PP	$1.47308 \cdot 10^{-2}$	$5.17153 \cdot 10^{-2}$	$8.85167 \cdot 10^{-3}$
	FSAC-PP	$9.33061 \cdot 10^{-2}$	$5.10805 \cdot 10^{-2}$	$1.26119 \cdot 10^{-3}$
3^{rd}-Order	AC	$2.00130 \cdot 10^{-2}$	$1.09143 \cdot 10^{-2}$	$8.37118 \cdot 10^{-5}$
	PP	$3.54762 \cdot 10^{-3}$	$1.76900 \cdot 10^{-2}$	$7.26692 \cdot 10^{-7}$
	FSAC-PP	$2.23611 \cdot 10^{-2}$	$1.22472 \cdot 10^{-2}$	$2.86851 \cdot 10^{-4}$
5^{th}-WENO	AC	$1.25795 \cdot 10^{-3}$	$6.75378 \cdot 10^{-4}$	$1.99655 \cdot 10^{-5}$
	PP	$7.23818 \cdot 10^{-4}$	$9.87718 \cdot 10^{-4}$	$1.90396 \cdot 10^{-5}$
	FSAC-PP	$1.37091 \cdot 10^{-3}$	$7.56585 \cdot 10^{-4}$	$3.38822 \cdot 10^{-5}$
9^{th}-WENO	AC	$4.92886 \cdot 10^{-6}$	$2.64698 \cdot 10^{-6}$	$8.78931 \cdot 10^{-7}$
	PP	$1.10911 \cdot 10^{-5}$	$5.05514 \cdot 10^{-6}$	$7.68508 \cdot 10^{-7}$
	FSAC-PP	$5.37030 \cdot 10^{-6}$	$2.95649 \cdot 10^{-6}$	$1.06505 \cdot 10^{-6}$

Table 5.5: Grid Convergence Indices (GCI) at $Re = 10$.

Reynolds Number ($Re = 5$)		Grid Convergence Index [%]		
Intercell Flux Interpolation	Solution Method	Grid Levels		
		G1÷G2	G2÷G3	G3÷G4
1^{st}-Order	AC	$4.15522 \cdot 10^{-1}$	$2.27343 \cdot 10^{-1}$	$1.64429 \cdot 10^{-3}$
	PP	2.79045	$8.52475 \cdot 10^{-1}$	$5.10451 \cdot 10^{-2}$
	FSAC-PP	$5.15235 \cdot 10^{-1}$	$2.85967 \cdot 10^{-1}$	$1.05935 \cdot 10^{-1}$
2^{nd}-Order	AC	$8.36267 \cdot 10^{-2}$	$4.57003 \cdot 10^{-2}$	$1.43499 \cdot 10^{-5}$
	PP	$8.42093 \cdot 10^{-3}$	$7.18193 \cdot 10^{-2}$	$1.12122 \cdot 10^{-2}$
	FSAC-PP	$1.02229 \cdot 10^{-1}$	$5.65146 \cdot 10^{-2}$	$3.06634 \cdot 10^{-2}$
3^{rd}-Order	AC	$2.00401 \cdot 10^{-2}$	$1.09230 \cdot 10^{-2}$	$2.63472 \cdot 10^{-5}$
	PP	$1.16161 \cdot 10^{-2}$	$1.97647 \cdot 10^{-2}$	$1.63898 \cdot 10^{-3}$
	FSAC-PP	$2.46276 \cdot 10^{-2}$	$1.36392 \cdot 10^{-2}$	$1.29173 \cdot 10^{-2}$
5^{th}-WENO	AC	$1.27747 \cdot 10^{-3}$	$6.78820 \cdot 10^{-4}$	$5.19421 \cdot 10^{-6}$
	PP	$7.99412 \cdot 10^{-4}$	$1.13693 \cdot 10^{-3}$	$1.11238 \cdot 10^{-3}$
	FSAC-PP	$1.52101 \cdot 10^{-3}$	$8.42226 \cdot 10^{-4}$	$2.37335 \cdot 10^{-3}$
9^{th}-WENO	AC	$4.88962 \cdot 10^{-6}$	$2.64909 \cdot 10^{-6}$	$2.35682 \cdot 10^{-7}$
	PP	$2.25684 \cdot 10^{-6}$	$4.65415 \cdot 10^{-6}$	$1.66382 \cdot 10^{-5}$
	FSAC-PP	$5.95205 \cdot 10^{-6}$	$3.29554 \cdot 10^{-6}$	$9.25433 \cdot 10^{-5}$

Table 5.6: Grid Convergence Indices (GCI) at $Re = 5$.

Reynolds Number ($Re = 1$)		Grid Convergence Index [%]		
Intercell Flux Interpolation	Solution Method	Grid Levels		
		G1÷G2	G2÷G3	G3÷G4
1^{st}-Order	AC	$4.16643 \cdot 10^{-1}$	$2.27508 \cdot 10^{-1}$	$9.53024 \cdot 10^{-3}$
	PP	2.88136	1.86744	$7.31858 \cdot 10^{-1}$
	FSAC-PP	$4.59582 \cdot 10^{-1}$	$2.53041 \cdot 10^{-1}$	$1.78027 \cdot 10^{-4}$
2^{nd}-Order	AC	$8.35818 \cdot 10^{-2}$	$4.57002 \cdot 10^{-2}$	$3.21369 \cdot 10^{-5}$
	PP	$1.52065 \cdot 10^{-2}$	$5.18616 \cdot 10^{-2}$	$6.70398 \cdot 10^{-4}$
	FSAC-PP	$9.20011 \cdot 10^{-2}$	$5.04852 \cdot 10^{-2}$	$1.22959 \cdot 10^{-4}$
3^{rd}-Order	AC	$1.99955 \cdot 10^{-2}$	$1.09106 \cdot 10^{-2}$	$3.40900 \cdot 10^{-5}$
	PP	$6.09283 \cdot 10^{-3}$	$1.17284 \cdot 10^{-2}$	$3.19098 \cdot 10^{-3}$
	FSAC-PP	$2.18994 \cdot 10^{-2}$	$1.20565 \cdot 10^{-2}$	$2.67494 \cdot 10^{-5}$
5^{th}-WENO	AC	$1.27277 \cdot 10^{-3}$	$6.81216 \cdot 10^{-4}$	$1.65752 \cdot 10^{-5}$
	PP	$9.99759 \cdot 10^{-4}$	$1.01349 \cdot 10^{-3}$	$8.59210 \cdot 10^{-5}$
	FSAC-PP	$1.34837 \cdot 10^{-3}$	$7.42747 \cdot 10^{-4}$	$7.12396 \cdot 10^{-6}$
9^{th}-WENO	AC	$4.99724 \cdot 10^{-6}$	$2.54742 \cdot 10^{-6}$	$2.58761 \cdot 10^{-4}$
	PP	$1.96233 \cdot 10^{-6}$	$4.72875 \cdot 10^{-6}$	$1.71518 \cdot 10^{-5}$
	FSAC-PP	$5.26120 \cdot 10^{-6}$	$2.89906 \cdot 10^{-6}$	$2.82494 \cdot 10^{-7}$

Table 5.7: Grid Convergence Indices (GCI) at $Re = 1$.

Reynolds Number ($Re = 0.5$)		Grid Convergence Index [%]		
Intercell Flux Interpolation	Solution Method	Grid Levels		
		G1÷G2	G2÷G3	G3÷G4
1^{st}-Order	AC	$4.17704 \cdot 10^{-1}$	$2.61049 \cdot 10^{-1}$	$8.34931 \cdot 10^{-2}$
	PP	2.79071	1.02369	$4.42098 \cdot 10^{-1}$
	FSAC-PP	$4.25794 \cdot 10^{-1}$	$2.33243 \cdot 10^{-1}$	$1.52982 \cdot 10^{-4}$
2^{nd}-Order	AC	$8.36102 \cdot 10^{-2}$	$6.08240 \cdot 10^{-2}$	$5.52737 \cdot 10^{-2}$
	PP	$9.08911 \cdot 10^{-3}$	$8.29998 \cdot 10^{-2}$	$1.42106 \cdot 10^{-2}$
	FSAC-PP	$8.90082 \cdot 10^{-2}$	$4.85910 \cdot 10^{-2}$	$8.11372 \cdot 10^{-3}$
3^{rd}-Order	AC	$2.00053 \cdot 10^{-2}$	$1.45382 \cdot 10^{-2}$	$8.10165 \cdot 10^{-3}$
	PP	$2.01686 \cdot 10^{-2}$	$1.11265 \cdot 10^{-2}$	$9.72977 \cdot 10^{-4}$
	FSAC-PP	$2.11069 \cdot 10^{-2}$	$1.15925 \cdot 10^{-2}$	$3.26134 \cdot 10^{-3}$
5^{th}-WENO	AC	$1.26661 \cdot 10^{-3}$	$2.30576 \cdot 10^{-3}$	$2.61435 \cdot 10^{-2}$
	PP	$7.85120 \cdot 10^{-4}$	$1.11724 \cdot 10^{-3}$	$1.68843 \cdot 10^{-4}$
	FSAC-PP	$1.29936 \cdot 10^{-3}$	$7.13955 \cdot 10^{-4}$	$6.00235 \cdot 10^{-4}$
9^{th}-WENO	AC	$5.10320 \cdot 10^{-6}$	$1.00586 \cdot 10^{-5}$	$1.10504 \cdot 10^{-3}$
	PP	$2.22193 \cdot 10^{-6}$	$4.64488 \cdot 10^{-6}$	$1.52025 \cdot 10^{-6}$
	FSAC-PP	$5.06986 \cdot 10^{-6}$	$2.78640 \cdot 10^{-6}$	$2.30804 \cdot 10^{-5}$

Table 5.8: Grid Convergence Indices (GCI) at $Re = 0.5$.

Reynolds Number ($Re = 0.1$)		Grid Convergence Index [%]		
Intercell Flux Interpolation	Solution Method	Grid Levels		
		G1÷G2	G2÷G3	G3÷G4
1^{st}-Order	AC	$3.25837 \cdot 10^{-1}$	$7.77264 \cdot 10^{-1}$	$7.66117 \cdot 10^{-1}$
	PP	2.88139	1.86883	$9.24901 \cdot 10^{-3}$
	FSAC-PP	$4.57557 \cdot 10^{-1}$	$2.52135 \cdot 10^{-1}$	$4.44994 \cdot 10^{-4}$
2^{nd}-Order	AC	$8.18355 \cdot 10^{-2}$	$2.42630 \cdot 10^{-1}$	$4.46816 \cdot 10^{-1}$
	PP	$1.51842 \cdot 10^{-2}$	$5.17927 \cdot 10^{-2}$	$3.84025 \cdot 10^{-3}$
	FSAC-PP	$9.15312 \cdot 10^{-2}$	$5.04197 \cdot 10^{-2}$	$1.15053 \cdot 10^{-4}$
3^{rd}-Order	AC	$2.07035 \cdot 10^{-2}$	$5.79134 \cdot 10^{-2}$	$2.20398 \cdot 10^{-1}$
	PP	$7.44690 \cdot 10^{-3}$	$1.03598 \cdot 10^{-2}$	$3.21562 \cdot 10^{-3}$
	FSAC-PP	$2.17896 \cdot 10^{-2}$	$1.20094 \cdot 10^{-2}$	$5.71814 \cdot 10^{-5}$
5^{th}-WENO	AC	$1.27316 \cdot 10^{-3}$	$4.24940 \cdot 10^{-3}$	$9.87817 \cdot 10^{-3}$
	PP	$1.38070 \cdot 10^{-3}$	$6.33737 \cdot 10^{-4}$	$2.50955 \cdot 10^{-5}$
	FSAC-PP	$1.34183 \cdot 10^{-3}$	$7.39621 \cdot 10^{-4}$	$1.07216 \cdot 10^{-5}$
9^{th}-WENO	AC	$4.85195 \cdot 10^{-6}$	$2.66548 \cdot 10^{-6}$	$3.58004 \cdot 10^{-4}$
	PP	$4.34032 \cdot 10^{-6}$	$2.38586 \cdot 10^{-6}$	$1.16451 \cdot 10^{-5}$
	FSAC-PP	$5.23636 \cdot 10^{-6}$	$2.88640 \cdot 10^{-6}$	$4.13814 \cdot 10^{-7}$

Table 5.9: Grid Convergence Indices (GCI) at $Re = 0.1$.

Reynolds Number ($Re = 0.01$)		Grid Convergence Index [%]		
Intercell Flux Interpolation	Solution Method	Grid Levels		
		G1÷G2	G2÷G3	G3÷G4
1^{st}-Order	AC	-	-	-
	PP	$9.18199 \cdot 10^{-1}$	$2.05915 \cdot 10^{-1}$	$9.19230 \cdot 10^{-3}$
	FSAC-PP	$4.80705 \cdot 10^{-1}$	$2.65889 \cdot 10^{-1}$	$3.07851 \cdot 10^{-4}$
2^{nd}-Order	AC	-	-	-
	PP	$2.35784 \cdot 10^{-1}$	$1.11514 \cdot 10^{-1}$	$3.89595 \cdot 10^{-3}$
	FSAC-PP	$9.61565 \cdot 10^{-2}$	$5.31842 \cdot 10^{-2}$	$9.55466 \cdot 10^{-5}$
3^{rd}-Order	AC	-	-	-
	PP	$2.28540 \cdot 10^{-2}$	$7.35615 \cdot 10^{-3}$	$3.21809 \cdot 10^{-3}$
	FSAC-PP	$2.28947 \cdot 10^{-2}$	$1.26650 \cdot 10^{-2}$	$4.19674 \cdot 10^{-5}$
5^{th}-WENO	AC	-	-	-
	PP	$5.65356 \cdot 10^{-4}$	$1.21599 \cdot 10^{-3}$	$8.42584 \cdot 10^{-4}$
	FSAC-PP	$1.40994 \cdot 10^{-3}$	$7.79972 \cdot 10^{-4}$	$7.76634 \cdot 10^{-6}$
9^{th}-WENO	AC	-	-	-
	PP	$1.93962 \cdot 10^{-6}$	$4.85897 \cdot 10^{-6}$	$1.43405 \cdot 10^{-5}$
	FSAC-PP	$5.50222 \cdot 10^{-6}$	$3.04384 \cdot 10^{-6}$	$3.00103 \cdot 10^{-7}$

Table 5.10: Grid Convergence Indices (GCI) at $Re = 0.01$.

Reynolds Number ($Re = 0.001$)		Grid Convergence Index [%]		
Intercell Flux Interpolation	Solution Method	Grid Levels		
		G1÷G2	G2÷G3	G3÷G4
1^{st}-Order	AC	-	-	-
	PP	$9.18245 \cdot 10^{-1}$	$2.05879 \cdot 10^{-1}$	$9.18663 \cdot 10^{-3}$
	FSAC-PP	$4.80720 \cdot 10^{-1}$	$2.65917 \cdot 10^{-1}$	$3.21445 \cdot 10^{-4}$
2^{nd}-Order	AC	-	-	-
	PP	$2.35665 \cdot 10^{-1}$	$1.11400 \cdot 10^{-1}$	$3.90151 \cdot 10^{-3}$
	FSAC-PP	$9.61581 \cdot 10^{-2}$	$5.31936 \cdot 10^{-2}$	$1.08162 \cdot 10^{-4}$
3^{rd}-Order	AC	-	-	-
	PP	$2.28533 \cdot 10^{-2}$	$7.35676 \cdot 10^{-3}$	$3.21834 \cdot 10^{-3}$
	FSAC-PP	$2.28948 \cdot 10^{-2}$	$1.26657 \cdot 10^{-2}$	$4.36071 \cdot 10^{-5}$
5^{th}-WENO	AC	-	-	-
	PP	$5.65084 \cdot 10^{-4}$	$1.21627 \cdot 10^{-3}$	$8.42737 \cdot 10^{-4}$
	FSAC-PP	$1.40995 \cdot 10^{-3}$	$7.80006 \cdot 10^{-4}$	$8.01154 \cdot 10^{-6}$
9^{th}-WENO	AC	-	-	-
	PP	$1.84297 \cdot 10^{-6}$	$4.85766 \cdot 10^{-6}$	$1.43765 \cdot 10^{-5}$
	FSAC-PP	$5.50225 \cdot 10^{-6}$	$3.04395 \cdot 10^{-6}$	$3.08153 \cdot 10^{-7}$

Table 5.11: Grid Convergence Indices (GCI) at $Re = 0.001$.

Reynolds Number ($Re = 0.0001$)		Grid Convergence Index [%]		
Intercell Flux Interpolation	Solution Method	Grid Levels		
		G1÷G2	G2÷G3	G3÷G4
1^{st}-Order	AC	-	-	-
	PP	$9.18250 \cdot 10^{-1}$	$2.05875 \cdot 10^{-1}$	$9.18606 \cdot 10^{-3}$
	FSAC-PP	$4.80724 \cdot 10^{-1}$	$2.65925 \cdot 10^{-1}$	$3.25196 \cdot 10^{-4}$
2^{nd}-Order	AC	-	-	-
	PP	$2.35653 \cdot 10^{-1}$	$1.11389 \cdot 10^{-1}$	$3.90207 \cdot 10^{-3}$
	FSAC-PP	$9.61584 \cdot 10^{-2}$	$5.31962 \cdot 10^{-2}$	$1.11672 \cdot 10^{-4}$
3^{rd}-Order	AC	-	-	-
	PP	$2.28533 \cdot 10^{-2}$	$7.35682 \cdot 10^{-3}$	$3.21836 \cdot 10^{-3}$
	FSAC-PP	$2.28949 \cdot 10^{-2}$	$1.26660 \cdot 10^{-2}$	$4.40641 \cdot 10^{-5}$
5^{th}-WENO	AC	-	-	-
	PP	$5.65056 \cdot 10^{-4}$	$1.21629 \cdot 10^{-3}$	$8.42753 \cdot 10^{-4}$
	FSAC-PP	$1.40995 \cdot 10^{-3}$	$7.80016 \cdot 10^{-4}$	$8.08416 \cdot 10^{-6}$
9^{th}-WENO	AC	-	-	-
	PP	$1.91958 \cdot 10^{-6}$	$4.85753 \cdot 10^{-6}$	$1.43817 \cdot 10^{-5}$
	FSAC-PP	$5.50225 \cdot 10^{-6}$	$3.04398 \cdot 10^{-6}$	$3.10423 \cdot 10^{-7}$

Table 5.12: Grid Convergence Indices (GCI) at $Re = 0.0001$.

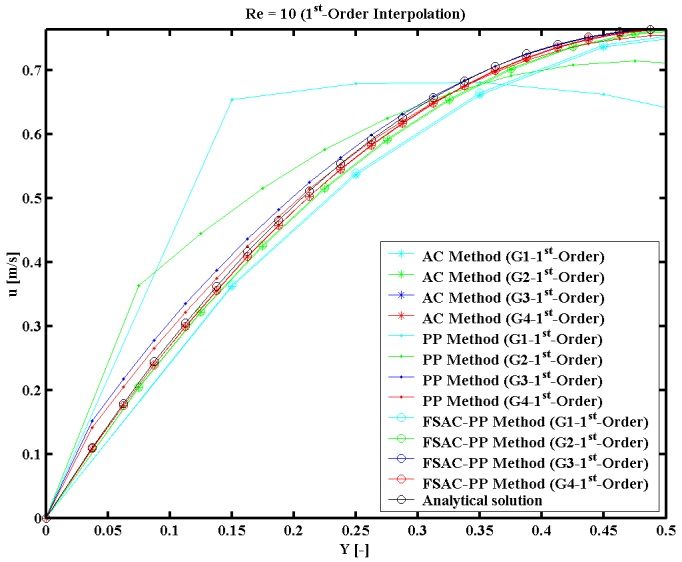

Figure 5.3: Comparison of analytically and numerically computed outlet velocity profiles relying on the solution of the AC, PP, and FSAC-PP methods in a pressure-driven laminar flow in a straight microfluidic channel using 1^{st}-order intercell flux interpolation on four different grids at $Re = 10$.

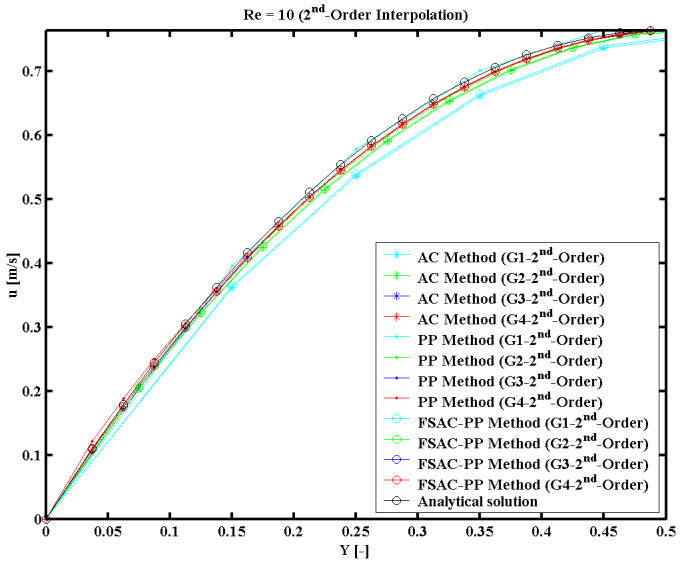

Figure 5.4: Comparison of analytically and numerically computed outlet velocity profiles relying on the solution of the AC, PP, and FSAC-PP methods in a pressure-driven laminar flow in a straight microfluidic channel using 2^{nd}-order intercell flux interpolation on four different grids at $Re = 10$.

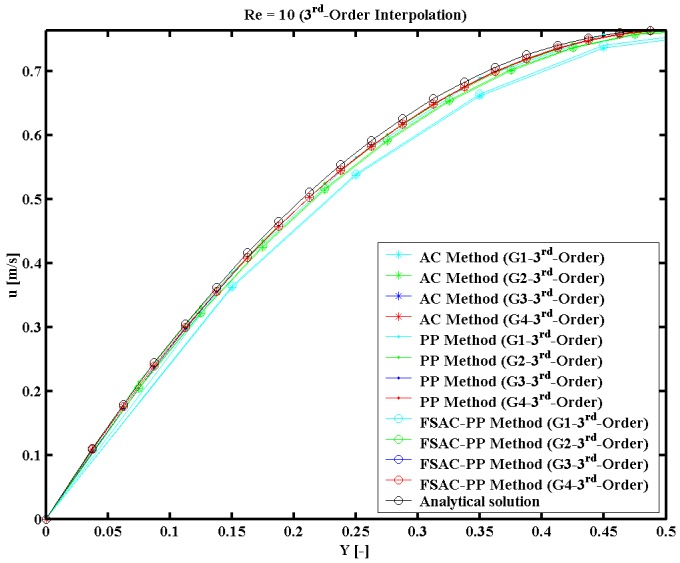

Figure 5.5: Comparison of analytically and numerically computed outlet velocity profiles relying on the solution of the AC, PP, and FSAC-PP methods in a pressure-driven laminar flow in a straight microfluidic channel using 3^{rd}-order intercell flux interpolation on four different grids at $Re = 10$.

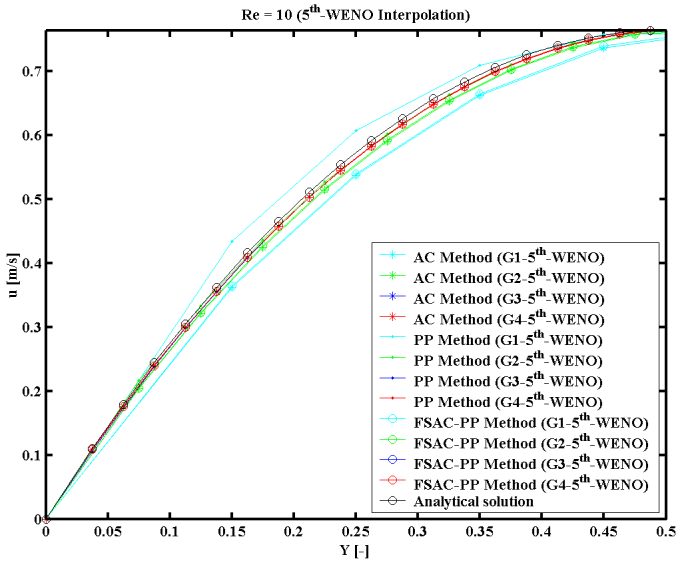

Figure 5.6: Comparison of analytically and numerically computed outlet velocity profiles relying on the solution of the AC, PP, and FSAC-PP methods in a pressure-driven laminar flow in a straight microfluidic channel using 5^{th}-order WENO reconstruction on four different grids at $Re = 10$.

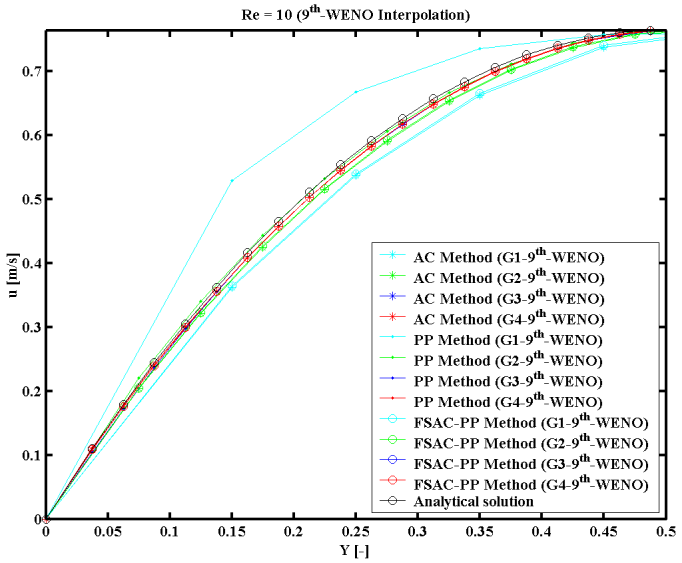

Figure 5.7: Comparison of analytically and numerically computed outlet velocity profiles relying on the solution of the AC, PP, and FSAC-PP methods in a pressure-driven laminar flow in a straight microfluidic channel 9^{th}-order WENO intercell flux interpolation on four different grids at $Re = 10$.

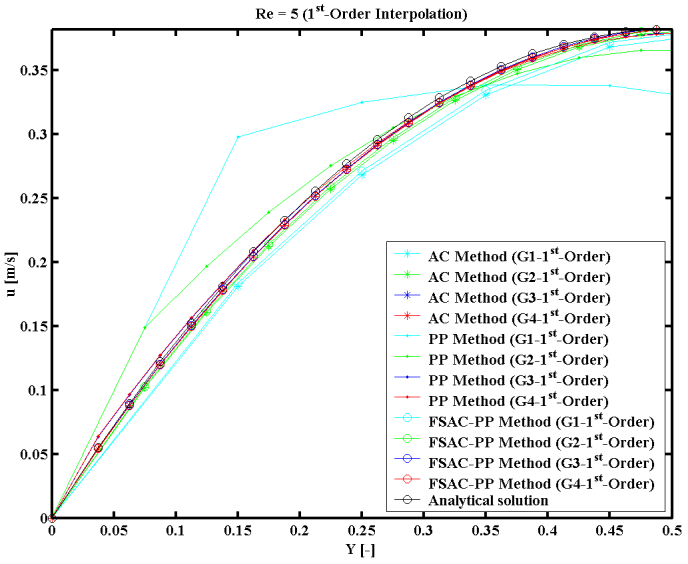

Figure 5.8: Comparison of analytically and numerically computed outlet velocity profiles relying on the solution of the AC, PP, and FSAC-PP methods in a pressure-driven laminar flow in a straight microfluidic channel using 1^{st}-order intercell flux interpolation on four different grids at $Re = 5$.

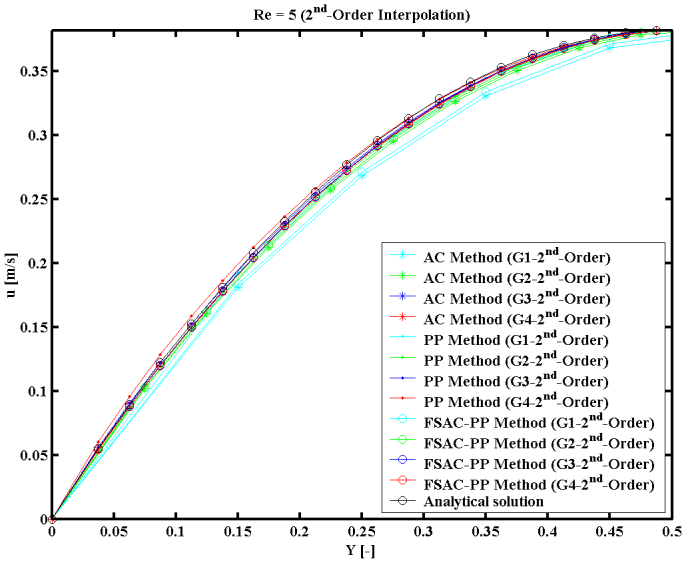

Figure 5.9: Comparison of analytically and numerically computed outlet velocity profiles relying on the solution of the AC, PP, and FSAC-PP methods in a pressure-driven laminar flow in a straight microfluidic channel using 2^{nd}-order intercell flux interpolation on four different grids at $Re = 5$.

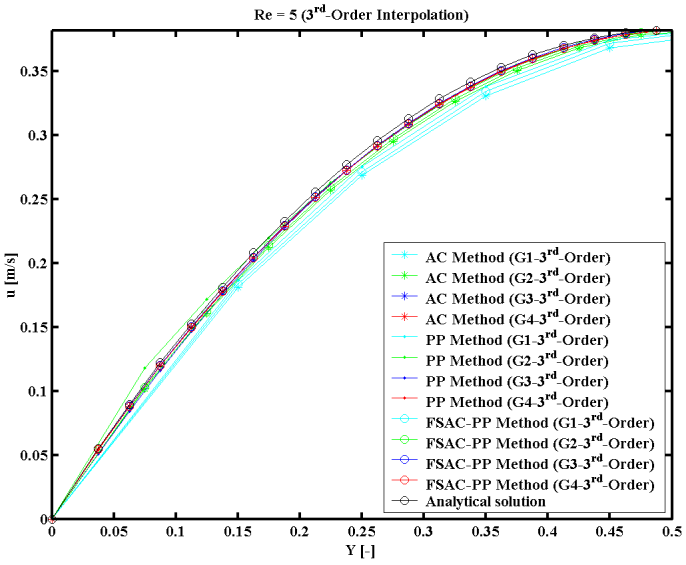

Figure 5.10: Comparison of analytically and numerically computed outlet velocity profiles relying on the solution of the AC, PP, and FSAC-PP methods in a pressure-driven laminar flow in a straight microfluidic channel using 3^{rd}-order intercell flux interpolation on four different grids at $Re = 5$.

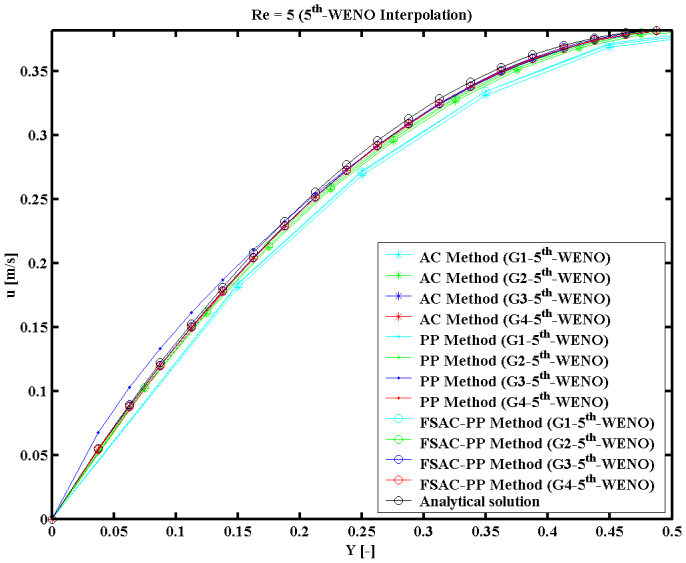

Figure 5.11: Comparison of analytically and numerically computed outlet velocity profiles relying on the solution of the AC, PP, and FSAC-PP methods in a pressure-driven laminar flow in a straight microfluidic channel using 5^{th}-order WENO reconstruction on four different grids at $Re = 5$.

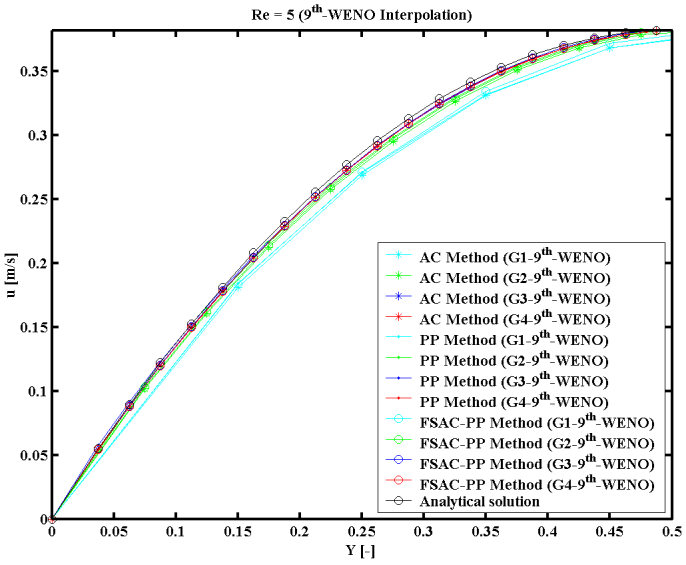

Figure 5.12: Comparison of analytically and numerically computed outlet velocity profiles relying on the solution of the AC, PP, and FSAC-PP methods in a pressure-driven laminar flow in a straight microfluidic channel 9^{th}-order WENO intercell flux interpolation on four different grids at $Re = 5$.

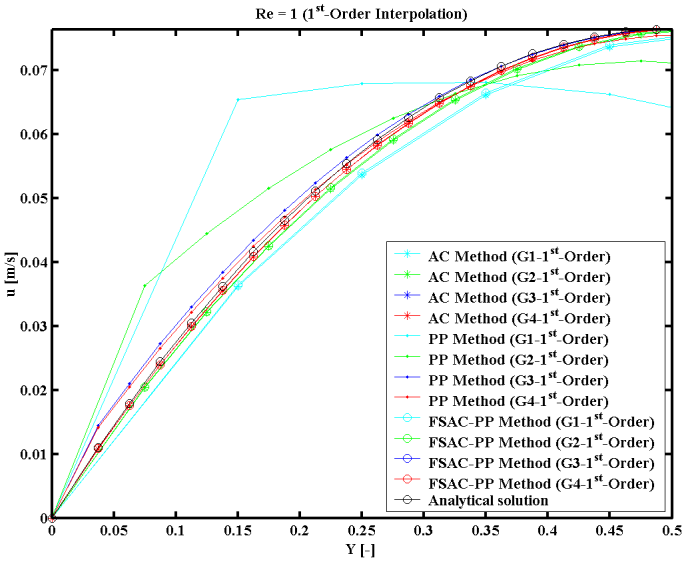

Figure 5.13: Comparison of analytically and numerically computed outlet velocity profiles relying on the solution of the AC, PP, and FSAC-PP methods in a pressure-driven laminar flow in a straight microfluidic channel using 1^{st}-order intercell flux interpolation on four different grids at $Re = 1$.

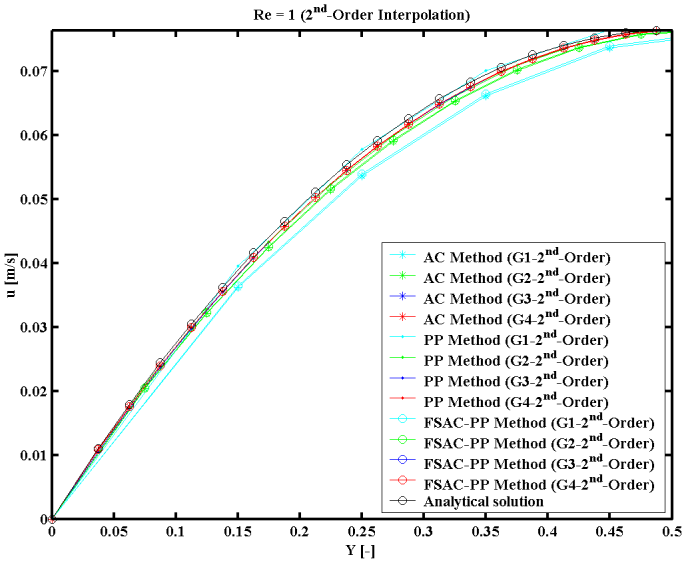

Figure 5.14: Comparison of analytically and numerically computed outlet velocity profiles relying on the solution of the AC, PP, and FSAC-PP methods in a pressure-driven laminar flow in a straight microfluidic channel using 2^{nd}-order intercell flux interpolation on four different grids at $Re = 1$.

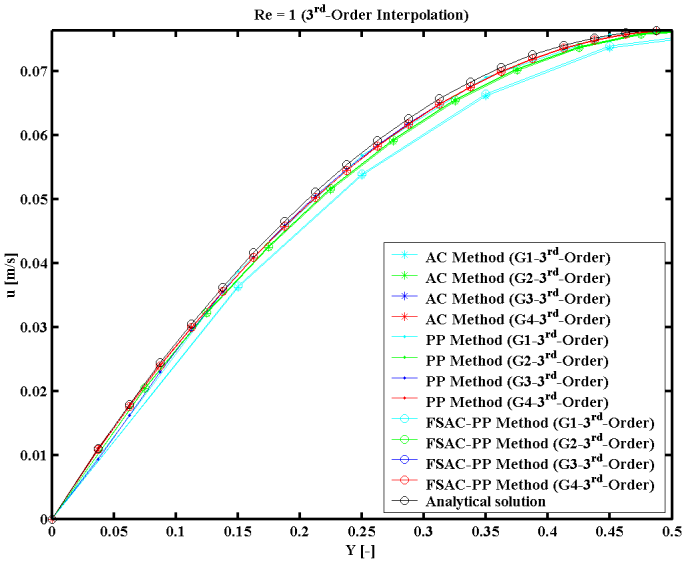

Figure 5.15: Comparison of analytically and numerically computed outlet velocity profiles relying on the solution of the AC, PP, and FSAC-PP methods in a pressure-driven laminar flow in a straight microfluidic channel using 3^{rd}-order intercell flux interpolation on four different grids at $Re = 1$.

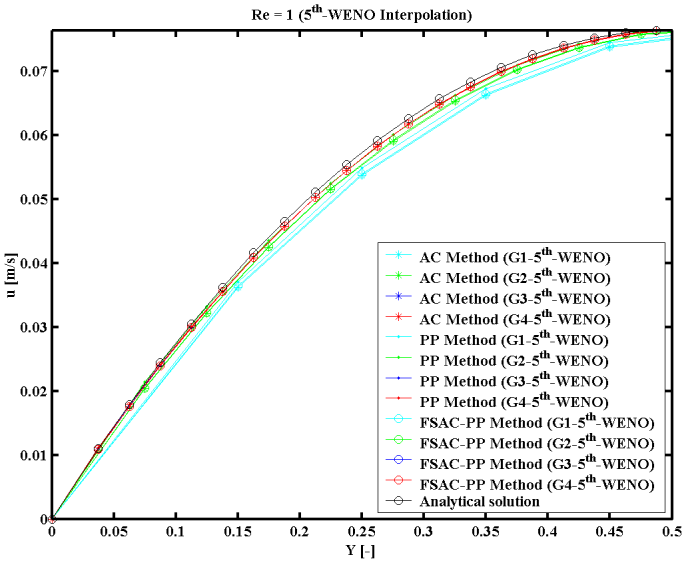

Figure 5.16: Comparison of analytically and numerically computed outlet velocity profiles relying on the solution of the AC, PP, and FSAC-PP methods in a pressure-driven laminar flow in a straight microfluidic channel using 5^{th}-order WENO reconstruction on four different grids at $Re = 1$.

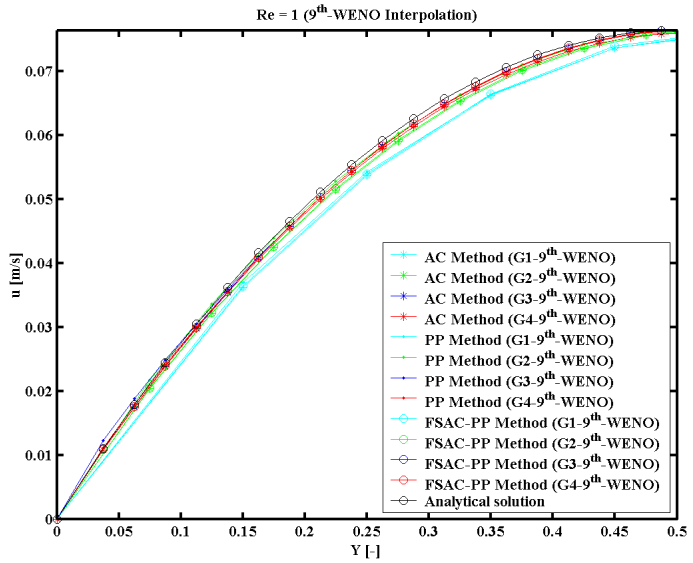

Figure 5.17: Comparison of analytically and numerically computed outlet velocity profiles relying on the solution of the AC, PP, and FSAC-PP methods in a pressure-driven laminar flow in a straight microfluidic channel 9^{th}-order WENO intercell flux interpolation on four different grids at $Re = 1$.

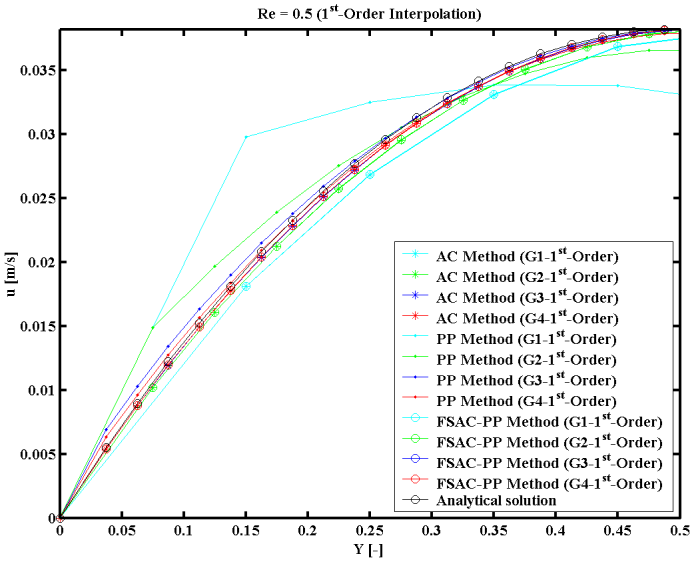

Figure 5.18: Comparison of analytically and numerically computed outlet velocity profiles relying on the solution of the AC, PP, and FSAC-PP methods in a pressure-driven laminar flow in a straight microfluidic channel using 1^{st}-order intercell flux interpolation on four different grids at $Re = 0.5$.

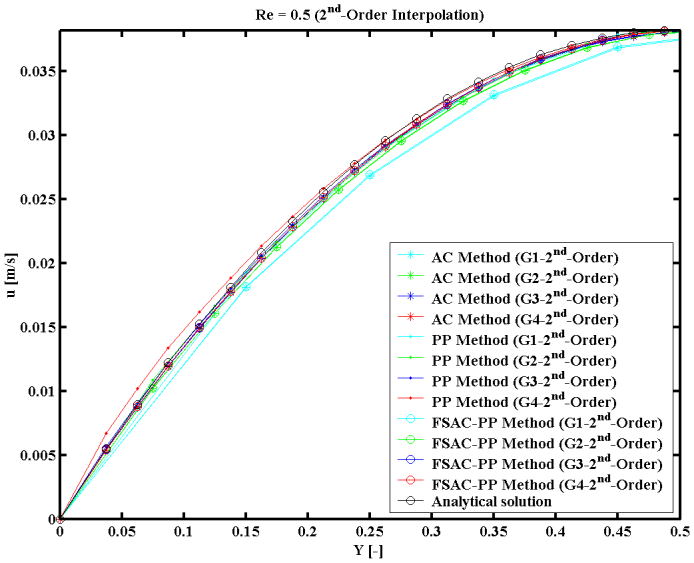

Figure 5.19: Comparison of analytically and numerically computed outlet velocity profiles relying on the solution of the AC, PP, and FSAC-PP methods in a pressure-driven laminar flow in a straight microfluidic channel using 2^{nd}-order intercell flux interpolation on four different grids at $Re = 0.5$.

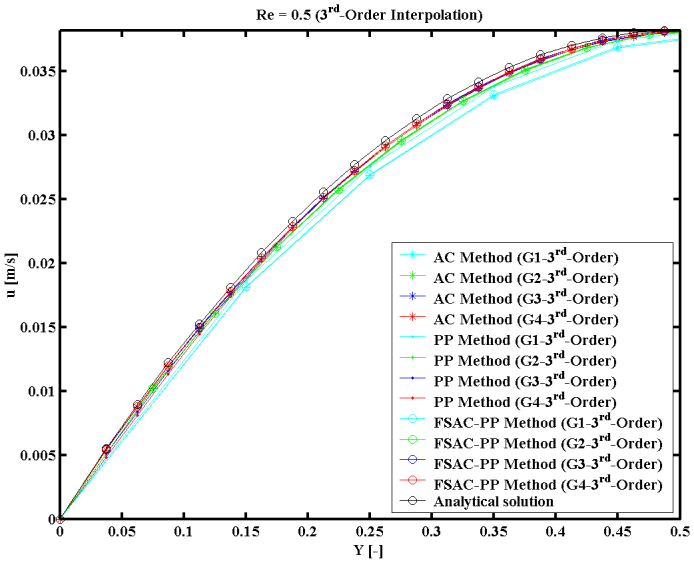

Figure 5.20: Comparison of analytically and numerically computed outlet velocity profiles relying on the solution of the AC, PP, and FSAC-PP methods in a pressure-driven laminar flow in a straight microfluidic channel using 3^{rd}-order intercell flux interpolation on four different grids at $Re = 0.5$.

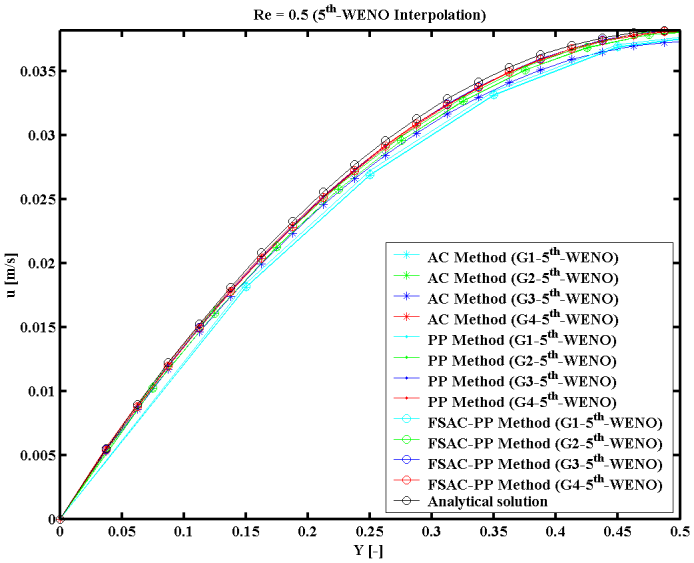

Figure 5.21: Comparison of analytically and numerically computed outlet velocity profiles relying on the solution of the AC, PP, and FSAC-PP methods in a pressure-driven laminar flow in a straight microfluidic channel using 5^{th}-order WENO reconstruction on four different grids at $Re = 0.5$.

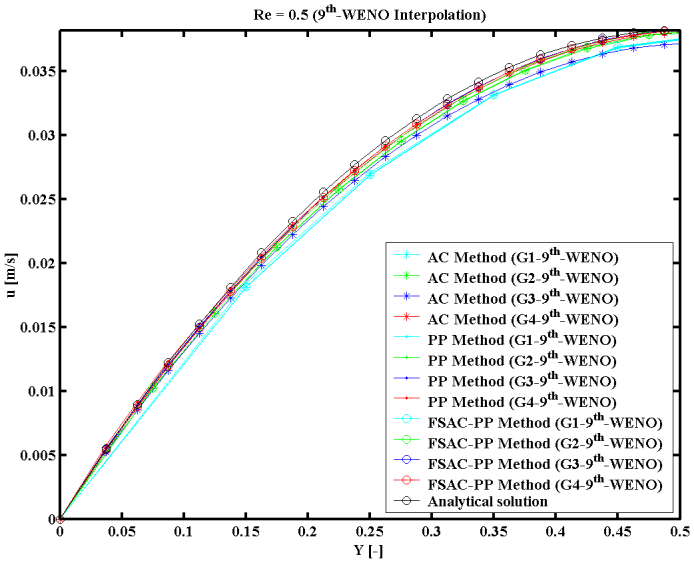

Figure 5.22: Comparison of analytically and numerically computed outlet velocity profiles relying on the solution of the AC, PP, and FSAC-PP methods in a pressure-driven laminar flow in a straight microfluidic channel 9^{th}-order WENO intercell flux interpolation on four different grids at $Re = 0.5$.

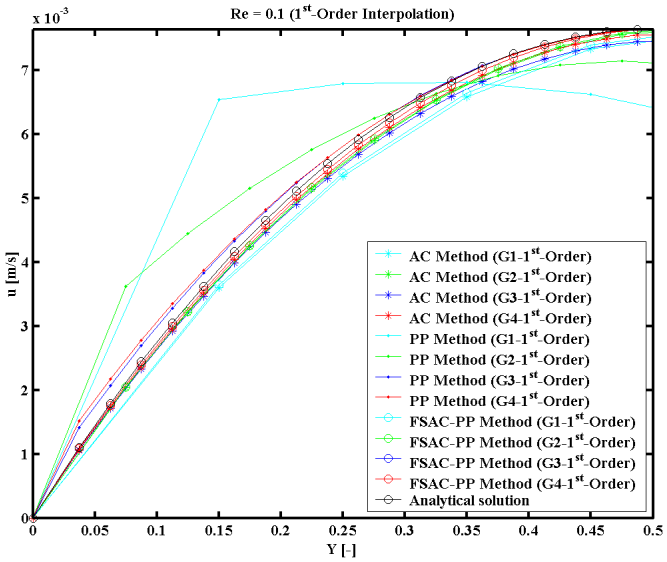

Figure 5.23: Comparison of analytically and numerically computed outlet velocity profiles relying on the solution of the AC, PP, and FSAC-PP methods in a pressure-driven laminar flow in a straight microfluidic channel using 1^{st}-order intercell flux interpolation on four different grids at $Re = 0.1$.

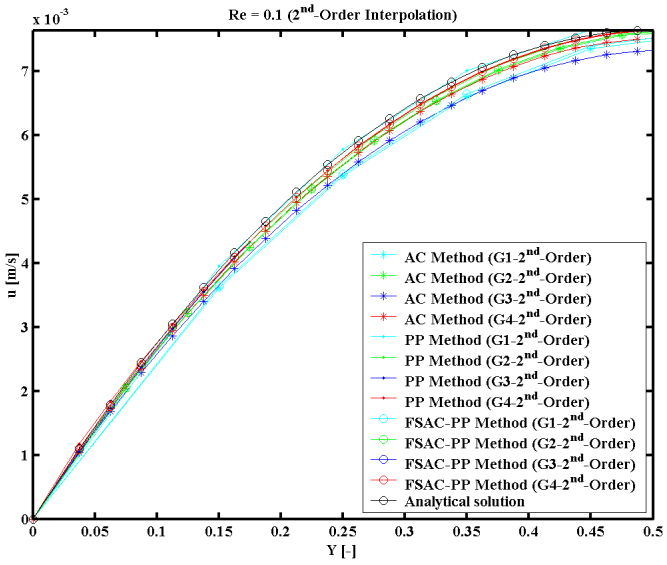

Figure 5.24: Comparison of analytically and numerically computed outlet velocity profiles relying on the solution of the AC, PP, and FSAC-PP methods in a pressure-driven laminar flow in a straight microfluidic channel using 2^{nd}-order intercell flux interpolation on four different grids at $Re = 0.1$.

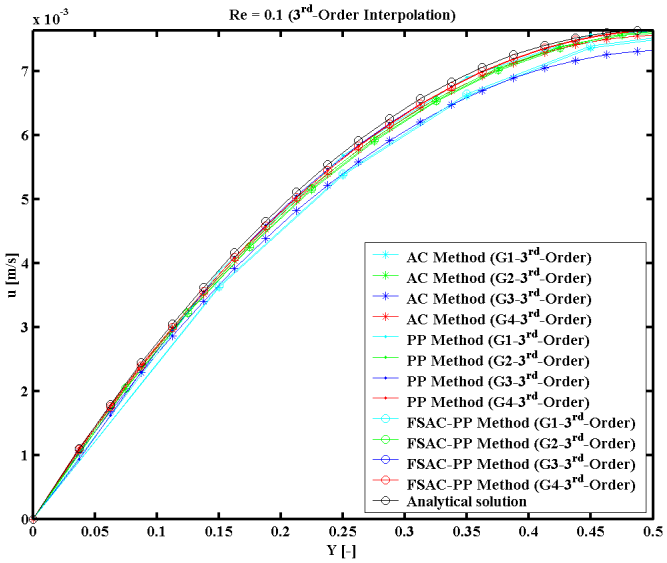

Figure 5.25: Comparison of analytically and numerically computed outlet velocity profiles relying on the solution of the AC, PP, and FSAC-PP methods in a pressure-driven laminar flow in a straight microfluidic channel using 3^{rd}-order intercell flux interpolation on four different grids at $Re = 0.1$.

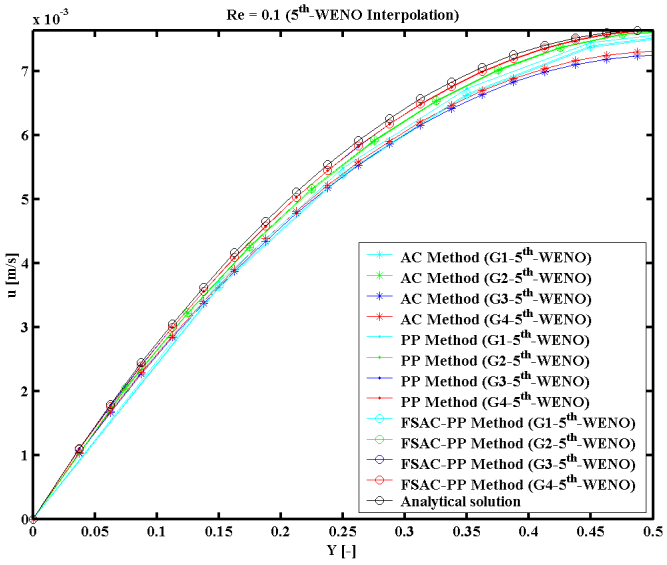

Figure 5.26: Comparison of analytically and numerically computed outlet velocity profiles relying on the solution of the AC, PP, and FSAC-PP methods in a pressure-driven laminar flow in a straight microfluidic channel using 5^{th}-order WENO intercell flux interpolation on four different grids at $Re = 0.1$.

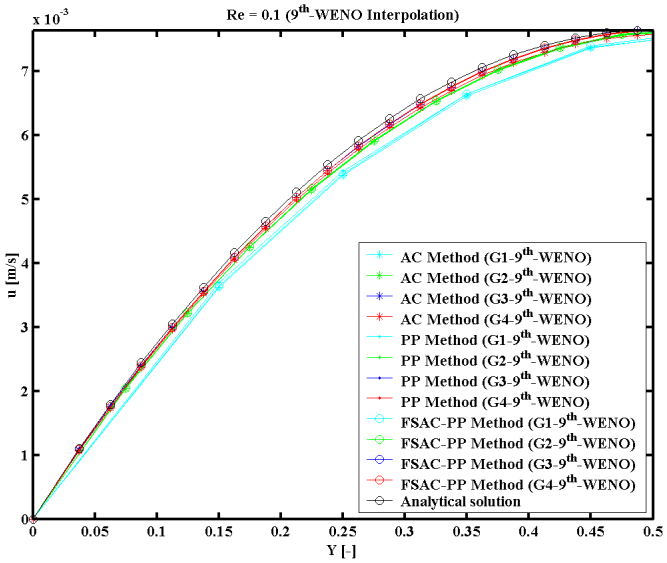

Figure 5.27: Comparison of analytically and numerically computed outlet velocity profiles relying on the solution of the AC, PP, and FSAC-PP methods in a pressure-driven laminar flow in a straight microfluidic channel using 9^{th}-order WENO intercell flux interpolation on four different grids at $Re = 0.1$.

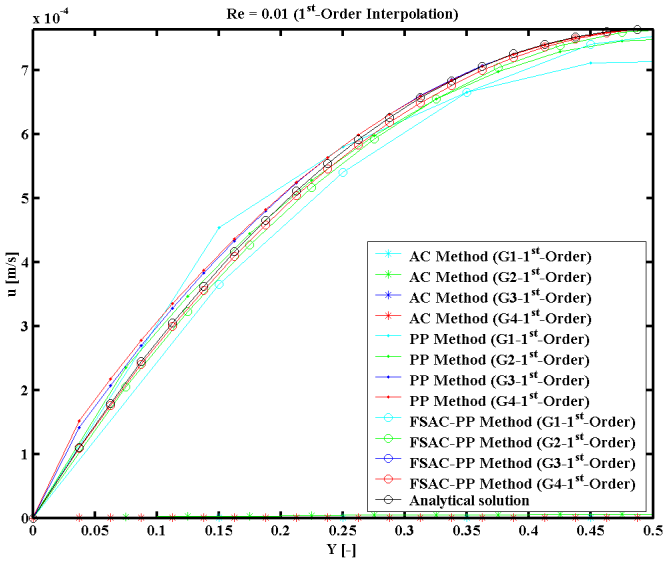

Figure 5.28: Comparison of analytically and numerically computed outlet velocity profiles relying on the solution of the AC, PP, and FSAC-PP methods in a pressure-driven laminar flow in a straight microfluidic channel using 1^{st}-order intercell flux interpolation on four different grids at $Re = 0.01$.

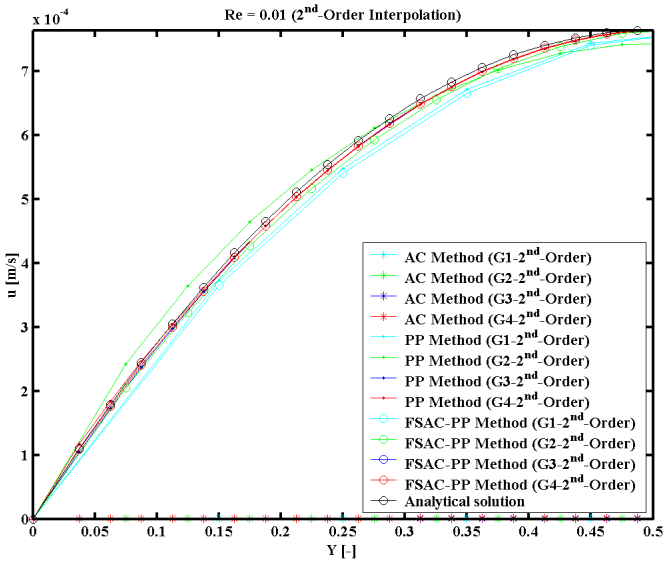

Figure 5.29: Comparison of analytically and numerically computed outlet velocity profiles relying on the solution of the AC, PP, and FSAC-PP methods in a pressure-driven laminar flow in a straight microfluidic channel using 2^{nd}-order intercell flux interpolation on four different grids at $Re = 0.01$.

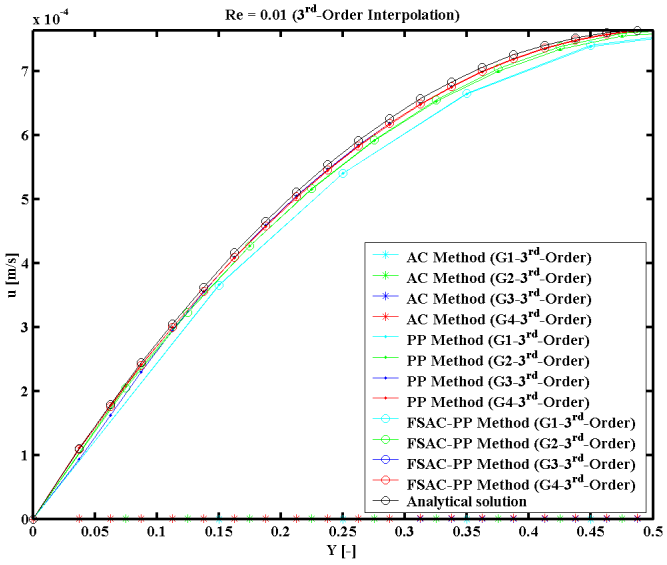

Figure 5.30: Comparison of analytically and numerically computed outlet velocity profiles relying on the solution of the AC, PP, and FSAC-PP methods in a pressure-driven laminar flow in a straight microfluidic channel using 3^{rd}-order intercell flux interpolation on four different grids at $Re = 0.01$.

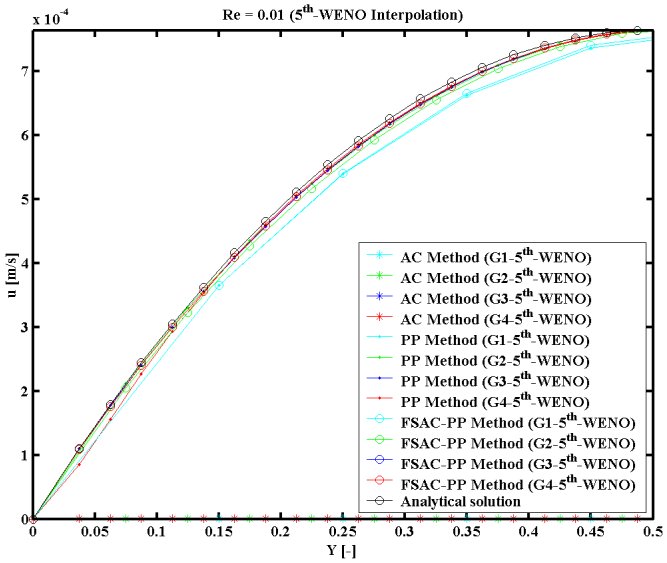

Figure 5.31: Comparison of analytically and numerically computed outlet velocity profiles relying on the solution of the AC, PP, and FSAC-PP methods in a pressure-driven laminar flow in a straight microfluidic channel using 5^{th}-order WENO reconstruction on four different grids at $Re = 0.01$.

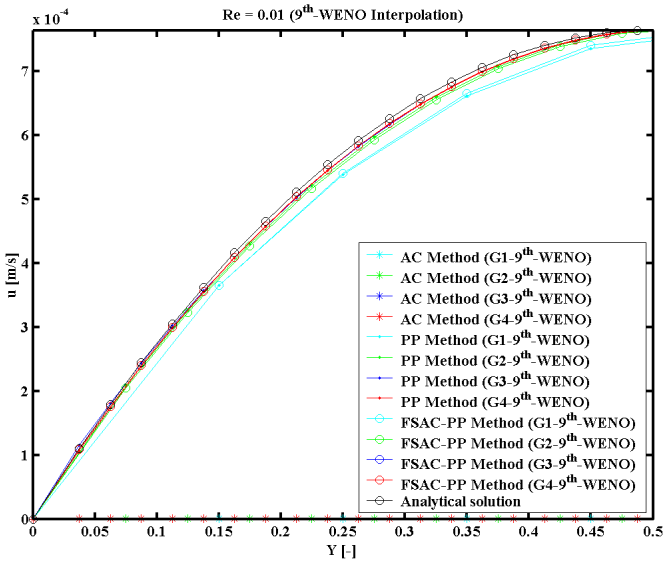

Figure 5.32: Comparison of analytically and numerically computed outlet velocity profiles relying on the solution of the AC, PP, and FSAC-PP methods in a pressure-driven laminar flow in a straight microfluidic channel 9^{th}-order WENO intercell flux interpolation on four different grids at $Re = 0.01$.

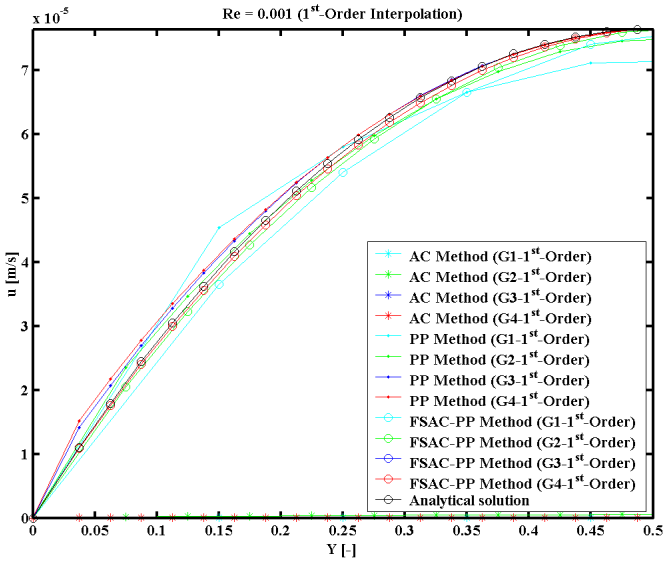

Figure 5.33: Comparison of analytically and numerically computed outlet velocity profiles relying on the solution of the AC, PP, and FSAC-PP methods in a pressure-driven laminar flow in a straight microfluidic channel using 1^{st}-order intercell flux interpolation on four different grids at $Re = 0.001$.

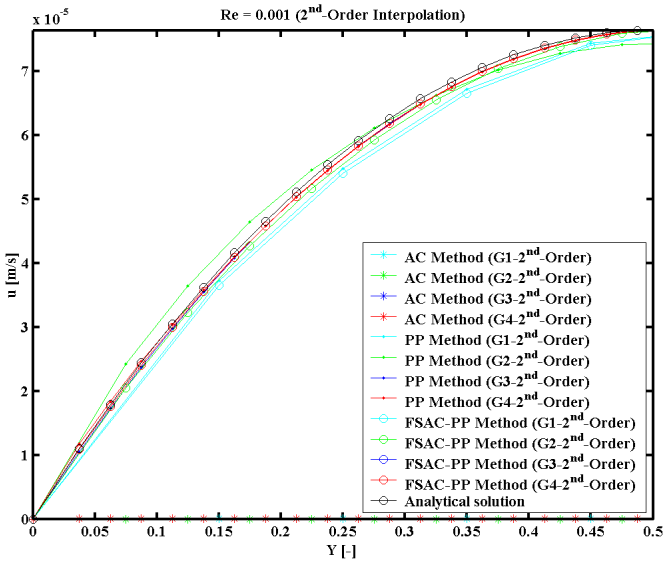

Figure 5.34: Comparison of analytically and numerically computed outlet velocity profiles relying on the solution of the AC, PP, and FSAC-PP methods in a pressure-driven laminar flow in a straight microfluidic channel using 2^{nd}-order intercell flux interpolation on four different grids at $Re = 0.001$.

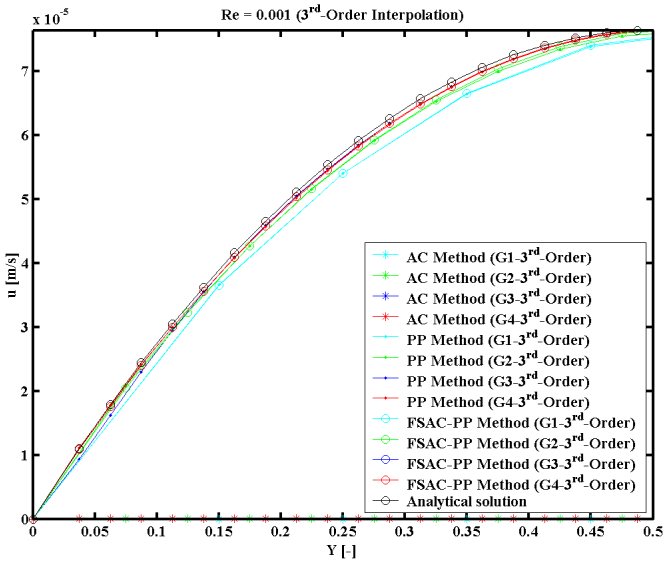

Figure 5.35: Comparison of analytically and numerically computed outlet velocity profiles relying on the solution of the AC, PP, and FSAC-PP methods in a pressure-driven laminar flow in a straight microfluidic channel using 3^{rd}-order intercell flux interpolation on four different grids at $Re = 0.001$.

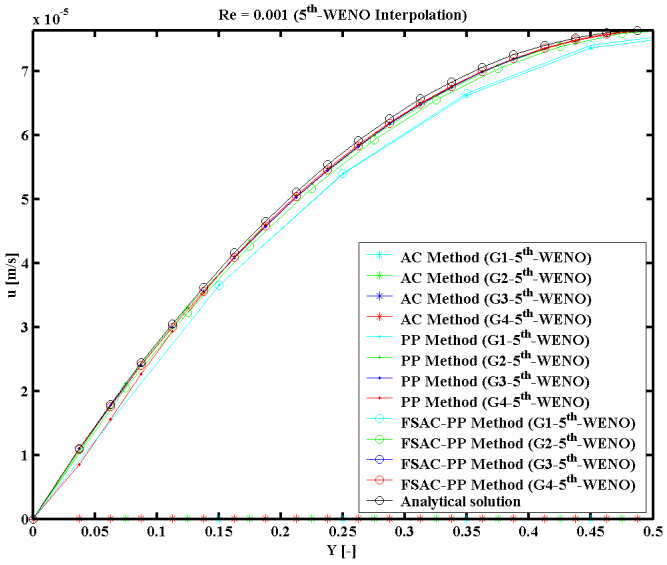

Figure 5.36: Comparison of analytically and numerically computed outlet velocity profiles relying on the solution of the AC, PP, and FSAC-PP methods in a pressure-driven laminar flow in a straight microfluidic channel using 5^{th}-order WENO reconstruction on four different grids at $Re = 0.001$.

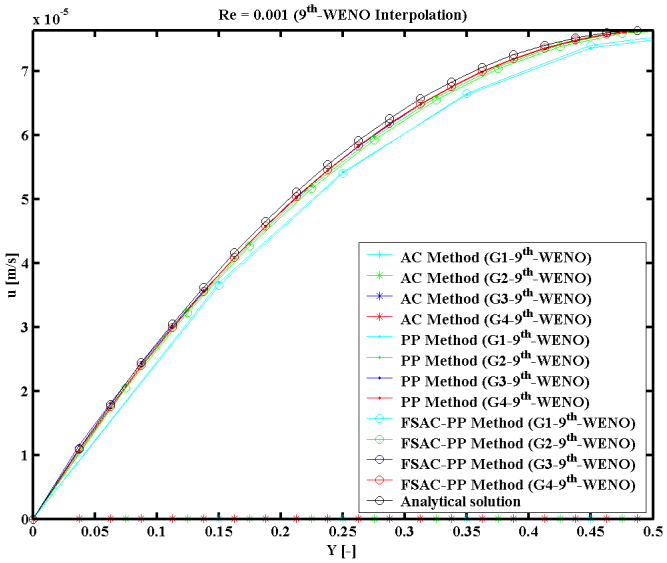

Figure 5.37: Comparison of analytically and numerically computed outlet velocity profiles relying on the solution of the AC, PP, and FSAC-PP methods in a pressure-driven laminar flow in a straight microfluidic channel 9^{th}-order WENO intercell flux interpolation on four different grids at $Re = 0.001$.

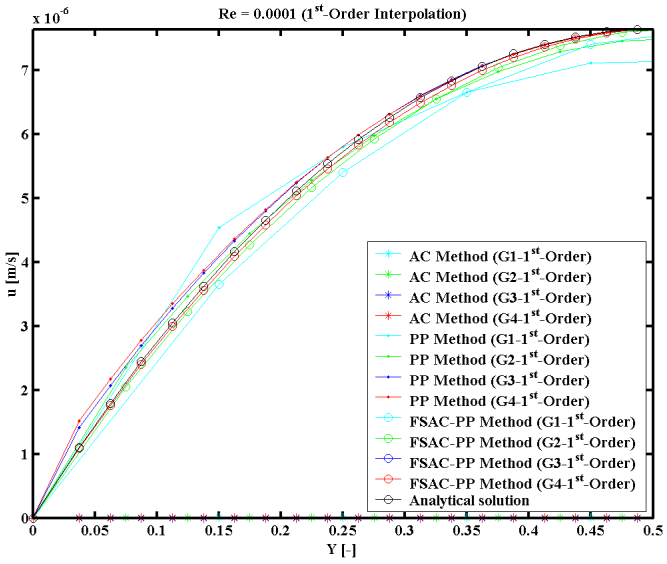

Figure 5.38: Comparison of analytically and numerically computed outlet velocity profiles relying on the solution of the AC, PP, and FSAC-PP methods in a pressure-driven laminar flow in a straight microfluidic channel using 1^{st}-order intercell flux interpolation on four different grids at $Re = 0.0001$.

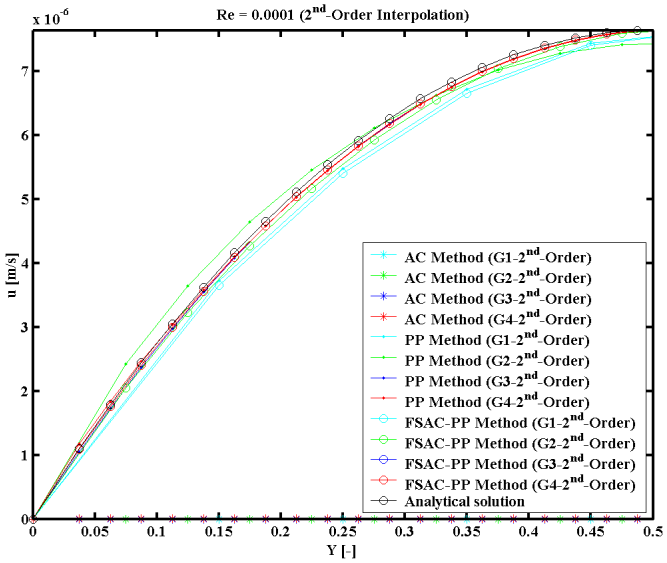

Figure 5.39: Comparison of analytically and numerically computed outlet velocity profiles relying on the solution of the AC, PP, and FSAC-PP methods in a pressure-driven laminar flow in a straight microfluidic channel using 2^{nd}-order intercell flux interpolation on four different grids at $Re = 0.0001$.

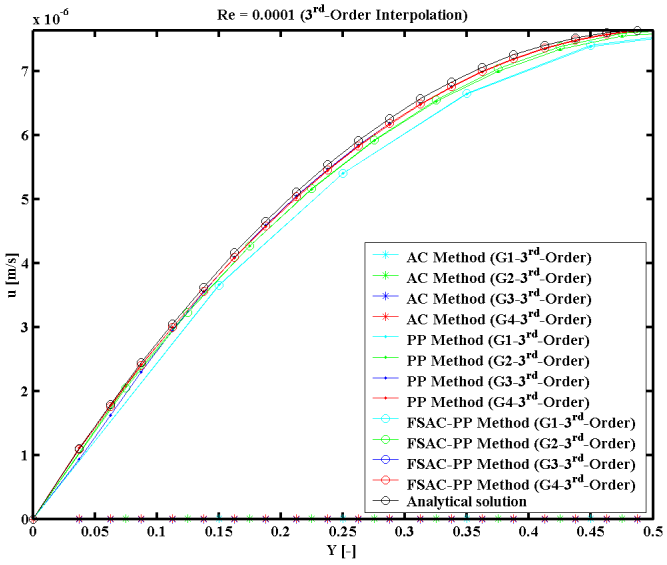

Figure 5.40: Comparison of analytically and numerically computed outlet velocity profiles relying on the solution of the AC, PP, and FSAC-PP methods in a pressure-driven laminar flow in a straight microfluidic channel using 3^{rd}-order intercell flux interpolation on four different grids at $Re = 0.0001$.

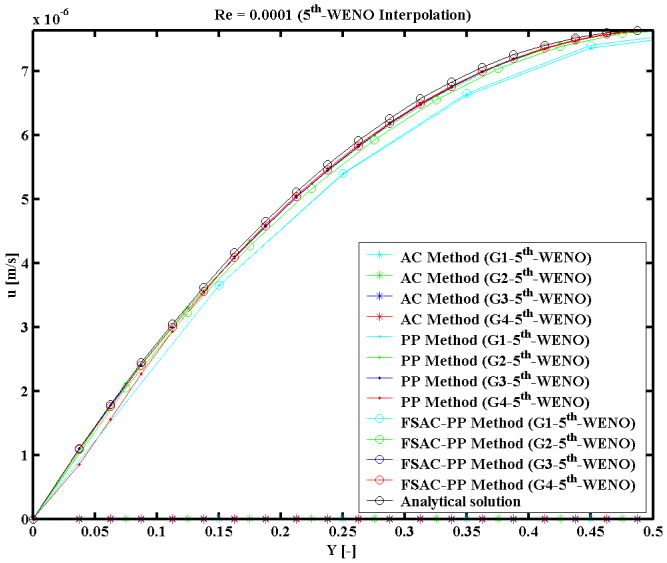

Figure 5.41: Comparison of analytically and numerically computed outlet velocity profiles relying on the solution of the AC, PP, and FSAC-PP methods in a pressure-driven laminar flow in a straight microfluidic channel using 5^{th}-order WENO intercell flux interpolation on four different grids at $Re = 0.0001$.

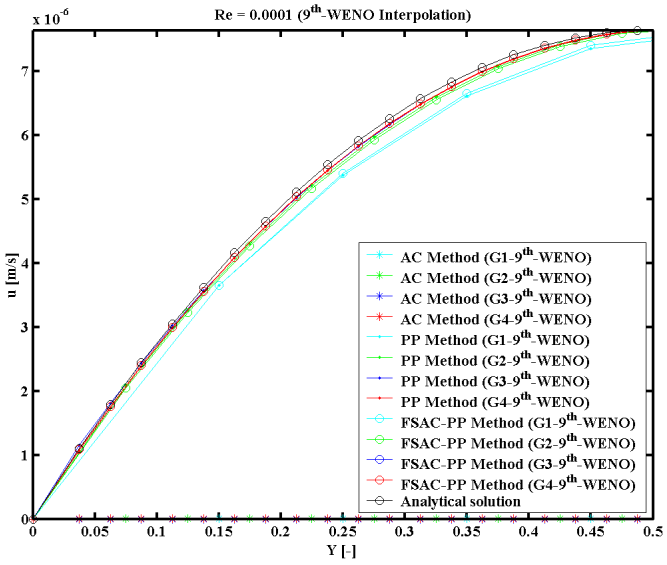

Figure 5.42: Comparison of analytically and numerically computed outlet velocity profiles relying on the solution of the AC, PP, and FSAC-PP methods in a pressure-driven laminar flow in a straight microfluidic channel using 9^{th}-order WENO intercell flux interpolation on four different grids at $Re = 0.0001$.

Reynolds Number ($Re = 10$)		Relative Errors of the Maximum Norm [%]			
Intercell Flux Interpolation	Solution Method	Grid Levels			
		G1	G2	G3	G4
1^{st}-Order	AC	0.35622	0.05689	0.02961	0.02846
	PP	10.83861	6.54441	0.00242	1.25491
	FSAC-PP	0.13552	0.20810	0.16926	0.17315
2^{nd}-Order	AC	0.33673	0.04946	0.03220	0.03126
	PP	1.10628	0.52134	0.00325	0.00454
	FSAC-PP	0.11128	0.19230	0.16107	0.16837
3^{rd}-Order	AC	0.32415	0.04655	0.03272	0.03148
	PP	0.74304	0.61379	0.00342	0.00014
	FSAC-PP	0.14252	0.20903	0.16997	0.17423
5^{th}-WENO	AC	0.28178	0.04143	0.03313	0.03152
	PP	0.67525	0.56522	0.00491	0.00034
	FSAC-PP	0.13824	0.21372	0.17122	0.17396
9^{th}-WENO	AC	0.26969	0.03678	0.03354	0.03169
	PP	0.66130	0.61215	0.00260	0.00212
	FSAC-PP	0.14931	0.21708	0.17310	0.17535

Table 5.13: Relative errors of the maximum norm at the outlet section at $Re = 10$.

Reynolds Number ($Re = 5$)		Relative Errors of the Maximum Norm [%]			
Intercell Flux Interpolation	Solution Method	Grid Levels			
		G1	G2	G3	G4
1^{st}-Order	AC	0.35687	0.05883	0.02839	0.03132
	PP	11.39831	4.28545	0.74571	0.82193
	FSAC-PP	0.59933	0.47027	0.30918	0.12373
2^{nd}-Order	AC	0.33606	0.04929	0.03296	0.03305
	PP	0.69447	0.62730	0.00362	0.00148
	FSAC-PP	0.55281	0.44250	0.29616	0.12178
3^{rd}-Order	AC	0.32079	0.04565	0.03284	0.03324
	PP	0.64077	0.64235	0.00141	0.00056
	FSAC-PP	0.61299	0.47487	0.31177	0.12380
5^{th}-WENO	AC	0.24779	0.03599	0.03356	0.03314
	PP	0.01694	0.68191	0.00500	0.00620
	FSAC-PP	0.62325	0.47869	0.31226	0.12392
9^{th}-WENO	AC	0.28310	0.03552	0.03401	0.03352
	PP	0.41296	0.70001	0.00174	0.00577
	FSAC-PP	0.63624	0.48544	0.31564	0.12423

Table 5.14: Relative errors of the maximum norm at the outlet section at $Re = 5$.

Reynolds Number ($Re = 1$)		Relative Errors of the Maximum Norm [%]			
Intercell Flux Interpolation	Solution Method	Grid Levels			
		G1	G2	G3	G4
1^{st}-Order	AC	0.35086	0.05763	0.02888	0.01191
	PP	10.83821	6.54310	0.00361	1.24045
	FSAC-PP	0.05988	0.16919	0.14760	0.14727
2^{nd}-Order	AC	0.33707	0.04934	0.03291	0.03273
	PP	1.10713	0.51880	0.00037	0.00386
	FSAC-PP	0.05667	0.16435	0.14549	0.14620
3^{rd}-Order	AC	0.32517	0.04601	0.03358	0.03308
	PP	0.58529	0.17654	0.00296	0.00616
	FSAC-PP	0.06249	0.17039	0.14817	0.14777
5^{th}-WENO	AC	0.25007	0.03145	0.03461	0.03327
	PP	0.32209	0.60142	0.00421	0.00438
	FSAC-PP	0.06289	0.17117	0.14856	0.14798
9^{th}-WENO	AC	0.28080	0.07313	0.03431	0.50831
	PP	0.43465	0.64140	0.00630	0.00613
	FSAC-PP	0.06300	0.17156	0.14875	0.14815

Table 5.15: Relative errors of the maximum norm at the outlet section at $Re = 1$.

Reynolds Number ($Re = 0.5$)		Relative Errors of the Maximum Norm [%]			
Intercell Flux Interpolation	Solution Method	Grid Levels			
		G1	G2	G3	G4
1^{st}-Order	AC	0.35267	0.06393	0.11966	0.02907
	PP	11.39793	4.28381	0.00565	0.76861
	FSAC-PP	0.26095	0.00703	0.05516	0.05489
2^{nd}-Order	AC	0.33615	0.04903	0.28715	0.03286
	PP	0.69201	0.63010	0.24687	0.00469
	FSAC-PP	0.09129	0.07958	0.10099	0.05479
3^{rd}-Order	AC	0.32349	0.04522	0.28836	0.16865
	PP	0.64121	0.04080	0.00622	0.00184
	FSAC-PP	0.09581	0.08342	0.10246	0.05493
5^{th}-WENO	AC	0.25542	0.02785	2.27571	0.16758
	PP	0.01758	0.68802	0.00399	0.00090
	FSAC-PP	0.09624	0.08370	0.10265	0.05495
9^{th}-WENO	AC	0.27637	0.10799	2.73369	0.41539
	PP	0.40626	0.69033	0.00292	0.00254
	FSAC-PP	0.09635	0.08390	0.10277	0.05496

Table 5.16: Relative errors of the maximum norm at the outlet section at $Re = 0.5$.

Reynolds Number ($Re = 0.1$)		Relative Errors of the Maximum Norm [%]			
Intercell Flux Interpolation	Solution Method	Grid Levels			
		G1	G2	G3	G4
1^{st}-Order	AC	0.81873	0.13628	2.34479	0.98989
	PP	10.83817	6.54297	0.00297	0.00201
	FSAC-PP	0.04302	0.16089	0.14311	0.14231
2^{nd}-Order	AC	0.46225	0.13638	4.11292	1.55503
	PP	1.10721	0.51945	0.00167	0.00084
	FSAC-PP	0.04295	0.16041	0.14278	0.14211
3^{rd}-Order	AC	0.32646	0.11035	4.09989	0.85682
	PP	0.58513	0.01970	0.00217	0.00563
	FSAC-PP	0.04364	0.16140	0.14335	0.14250
5^{th}-WENO	AC	0.26687	0.04865	4.96713	4.19308
	PP	0.32227	0.07147	0.00471	0.00024
	FSAC-PP	0.04370	0.16154	0.14343	0.14256
9^{th}-WENO	AC	0.30192	0.04021	0.02326	0.72620
	PP	0.43383	0.12627	0.00579	0.00303
	FSAC-PP	0.04376	0.16161	0.14348	0.14260

Table 5.17: Relative errors of the maximum norm at the outlet section at $Re = 0.1$.

Reynolds Number ($Re = 0.01$)		Relative Errors of the Maximum Norm [%]			
Intercell Flux Interpolation	Solution Method	Grid Levels			
		G1	G2	G3	G4
1^{st}-Order	AC	-	-	-	-
	PP	6.40150	1.77022	0.00242	0.00136
	FSAC-PP	0.26466	0.28313	0.20706	0.20651
2^{nd}-Order	AC	-	-	-	-
	PP	0.05727	2.62672	0.00187	0.00027
	FSAC-PP	0.26510	0.28324	0.20703	0.20648
3^{rd}-Order	AC	-	-	-	-
	PP	0.19093	0.33923	0.00209	0.00557
	FSAC-PP	0.26555	0.28366	0.20726	0.20664
5^{th}-WENO	AC	-	-	-	-
	PP	0.44139	0.65025	0.00476	0.00493
	FSAC-PP	0.26561	0.28371	0.20729	0.20666
9^{th}-WENO	AC	-	-	-	-
	PP	0.53620	0.71227	0.00501	0.00308
	FSAC-PP	0.26565	0.28375	0.20731	0.20668

Table 5.18: Relative errors of the maximum norm at the outlet section at $Re = 0.01$.

Reynolds Number ($Re = 0.001$)		Relative Errors of the Maximum Norm [%]			
Intercell Flux Interpolation	Solution Method	Grid Levels			
		G1	G2	G3	G4
1^{st}-Order	AC	-	-	-	-
	PP	6.40149	1.77007	0.00237	0.00129
	FSAC-PP	0.26499	0.28339	0.20719	0.20662
2^{nd}-Order	AC	-	-	-	-
	PP	0.05730	2.62487	0.00189	0.00021
	FSAC-PP	0.26559	0.28368	0.20727	0.20664
3^{rd}-Order	AC	-	-	-	-
	PP	0.19092	0.33918	0.00209	0.00557
	FSAC-PP	0.26572	0.28381	0.20734	0.20669
5^{th}-WENO	AC	-	-	-	-
	PP	0.44138	0.65061	0.00476	0.00491
	FSAC-PP	0.26573	0.28382	0.20735	0.20670
9^{th}-WENO	AC	-	-	-	-
	PP	0.44996	0.71220	0.00502	0.00308
	FSAC-PP	0.26575	0.28383	0.20736	0.20671

Table 5.19: Relative errors of the maximum norm at the outlet section at $Re = 0.001$.

Reynolds Number ($Re = 0.0001$)		Relative Errors of the Maximum Norm [%]			
Intercell Flux Interpolation	Solution Method	Grid Levels			
		G1	G2	G3	G4
1^{st}-Order	AC	-	-	-	-
	PP	6.40149	1.77006	0.00236	0.00128
	FSAC-PP	0.26508	0.28346	0.20724	0.20666
2^{nd}-Order	AC	-	-	-	-
	PP	0.05731	2.62469	0.00189	0.00020
	FSAC-PP	0.26572	0.28381	0.20734	0.20669
3^{rd}-Order	AC	-	-	-	-
	PP	0.19092	0.33917	0.00209	0.00557
	FSAC-PP	0.26576	0.28385	0.20736	0.20671
5^{th}-WENO	AC	-	-	-	-
	PP	0.44138	0.65064	0.00477	0.00491
	FSAC-PP	0.26577	0.28385	0.20737	0.20671
9^{th}-WENO	AC	-	-	-	-
	PP	0.56149	0.71219	0.00502	0.00308
	FSAC-PP	0.26577	0.28386	0.20737	0.20671

Table 5.20: Relative errors of the maximum norm at the outlet section at $Re = 0.0001$.

Reynolds Number ($Re = 10$)			
Intercell Flux Interpolation	Solution Method	N_{mg}	RK_{maxres}
1^{st}-Order	AC	166	$0.19995 \cdot 10^{-8}$
	PP	2699	$0.17488 \cdot 10^{-8}$
	FSAC-PP	32	$0.79310 \cdot 10^{-7}$
2^{nd}-Order	AC	166	$0.19994 \cdot 10^{-8}$
	PP	751	$0.14190 \cdot 10^{-3}$
	FSAC-PP	32	$0.40928 \cdot 10^{-7}$
3^{rd}-Order	AC	166	$0.19995 \cdot 10^{-8}$
	PP	1878	$0.18354 \cdot 10^{-5}$
	FSAC-PP	31	$0.13352 \cdot 10^{-6}$
5^{th}-WENO	AC	166	$0.19994 \cdot 10^{-8}$
	PP	1897	$0.10196 \cdot 10^{-5}$
	FSAC-PP	32	$0.65440 \cdot 10^{-7}$
9^{th}-WENO	AC	166	$0.22137 \cdot 10^{-8}$
	PP	1162	$0.30575 \cdot 10^{-4}$
	FSAC-PP	33	$0.12724 \cdot 10^{-8}$

Table 5.21: Total number of multigrid iterations on the fine grid and maximum values of Runge-Kutta residuals using different intercell flux interpolations at $Re = 10$.

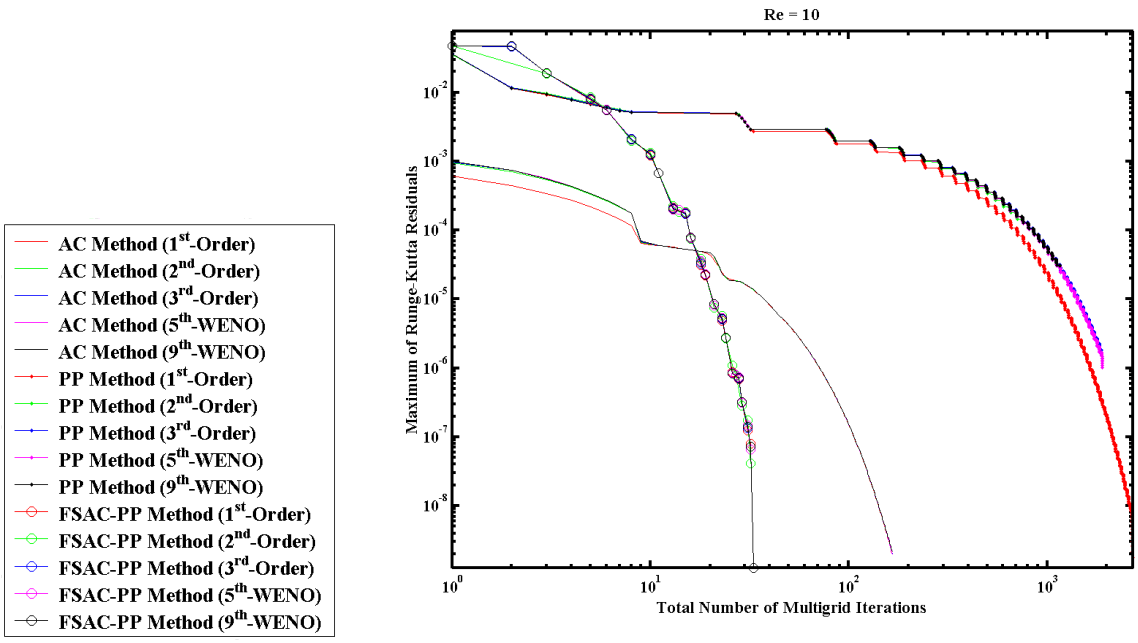

Figure 5.43: Comparison of the numerical convergence of the AC, PP, and FSAC-PP methods; maximum values of Runge-Kutta residuals RK_{maxres} versus total number of multigrid iterations N_{mg} on the fine grid at $Re = 10$.

Reynolds Number ($Re = 5$)			
Intercell Flux Interpolation	Solution Method	N_{mg}	RK_{maxres}
1^{st}-Order	AC	121	$0.19973 \cdot 10^{-8}$
	PP	2215	$0.19304 \cdot 10^{-8}$
	FSAC-PP	46	$0.14204 \cdot 10^{-8}$
2^{nd}-Order	AC	121	$0.19981 \cdot 10^{-8}$
	PP	710	$0.30551 \cdot 10^{-4}$
	FSAC-PP	46	$0.29082 \cdot 10^{-6}$
3^{rd}-Order	AC	121	$0.19990 \cdot 10^{-8}$
	PP	1529	$0.14656 \cdot 10^{-5}$
	FSAC-PP	46	$0.10803 \cdot 10^{-8}$
5^{th}-WENO	AC	121	$0.19972 \cdot 10^{-8}$
	PP	707	$0.95896 \cdot 10^{-4}$
	FSAC-PP	46	$0.26707 \cdot 10^{-6}$
9^{th}-WENO	AC	121	$0.24606 \cdot 10^{-8}$
	PP	1121	$0.13174 \cdot 10^{-4}$
	FSAC-PP	45	$0.18573 \cdot 10^{-8}$

Table 5.22: Total number of multigrid iterations on the fine grid and maximum values of Runge-Kutta residuals using different intercell flux interpolations at $Re = 5$.

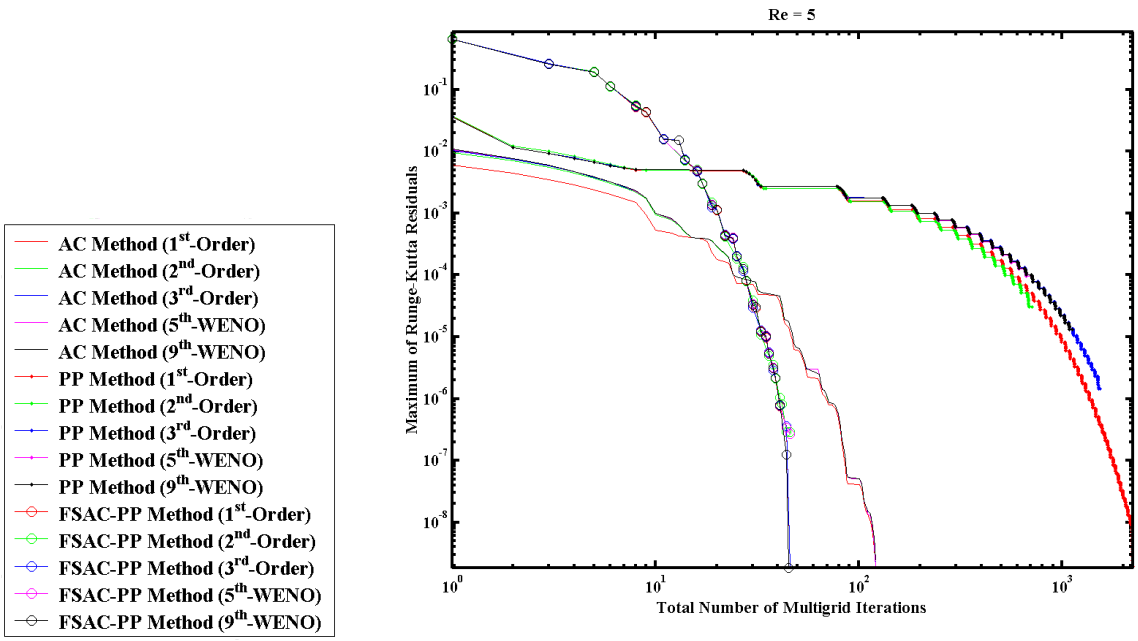

Figure 5.44: Comparison of the numerical convergence of the AC, PP, and FSAC-PP methods; maximum values of Runge-Kutta residuals RK_{maxres} versus total number of multigrid iterations N_{mg} on the fine grid at $Re = 5$.

Reynolds Number ($Re = 1$)			
Intercell Flux Interpolation	Solution Method	N_{mg}	RK_{maxres}
1^{st}-Order	AC	1686	$0.17147 \cdot 10^{-6}$
	PP	2610	$0.98816 \cdot 10^{-7}$
	FSAC-PP	50	$0.12885 \cdot 10^{-8}$
2^{nd}-Order	AC	2548	$0.19999 \cdot 10^{-8}$
	PP	1216	$0.23133 \cdot 10^{-3}$
	FSAC-PP	50	$0.24190 \cdot 10^{-6}$
3^{rd}-Order	AC	2548	$0.20027 \cdot 10^{-8}$
	PP	1161	$0.33209 \cdot 10^{-3}$
	FSAC-PP	51	$0.15745 \cdot 10^{-8}$
5^{th}-WENO	AC	2548	$0.19999 \cdot 10^{-8}$
	PP	1162	$0.31189 \cdot 10^{-3}$
	FSAC-PP	52	$0.60556 \cdot 10^{-9}$
9^{th}-WENO	AC	1032	$0.58068 \cdot 10^{-5}$
	PP	1162	$0.32380 \cdot 10^{-3}$
	FSAC-PP	54	$0.82197 \cdot 10^{-7}$

Table 5.23: Total number of multigrid iterations on the fine grid and maximum values of Runge-Kutta residuals using different intercell flux interpolations at $Re = 1$.

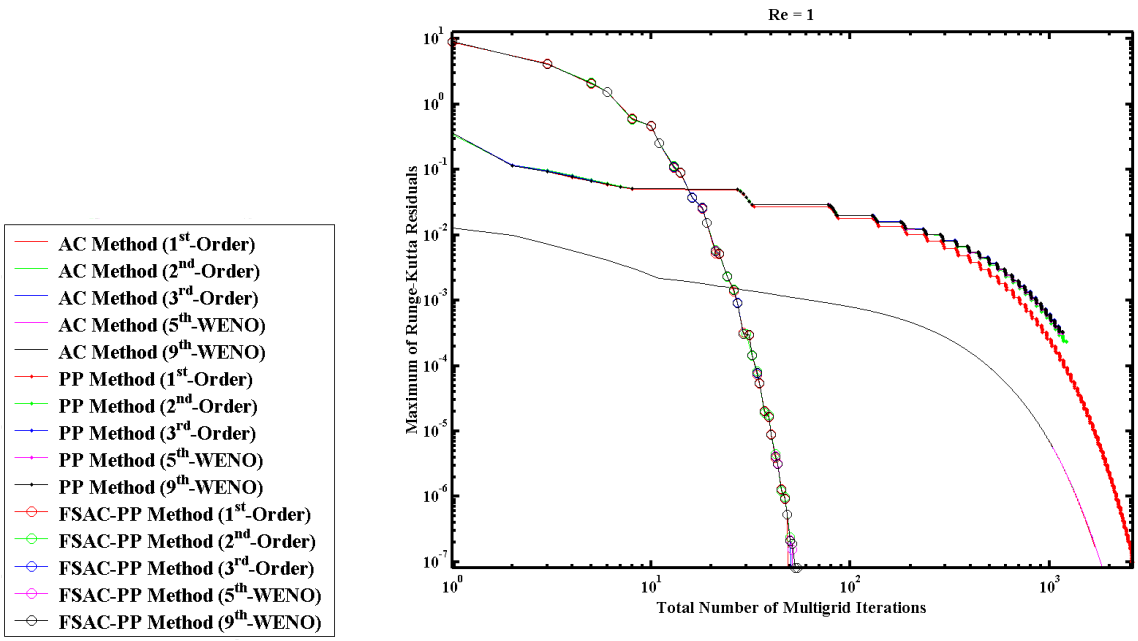

Figure 5.45: Comparison of the numerical convergence of the AC, PP, and FSAC-PP methods; maximum values of Runge-Kutta residuals RK_{maxres} versus total number of multigrid iterations N_{mg} on the fine grid at $Re = 1$.

Reynolds Number ($Re = 0.5$)			
Intercell Flux Interpolation	Solution Method	N_{mg}	RK_{maxres}
1^{st}-Order	AC	5916	$0.20004 \cdot 10^{-8}$
	PP	2580	$0.58763 \cdot 10^{-8}$
	FSAC-PP	112	$0.51164 \cdot 10^{-6}$
2^{nd}-Order	AC	6013	$0.20014 \cdot 10^{-8}$
	PP	458	$0.22789 \cdot 10^{-2}$
	FSAC-PP	116	$0.63931 \cdot 10^{-6}$
3^{rd}-Order	AC	2473	$0.21411 \cdot 10^{-4}$
	PP	603	$0.17201 \cdot 10^{-2}$
	FSAC-PP	116	$0.61200 \cdot 10^{-6}$
5^{th}-WENO	AC	611	$0.28258 \cdot 10^{-2}$
	PP	974	$0.25913 \cdot 10^{-3}$
	FSAC-PP	115	$0.21583 \cdot 10^{-6}$
9^{th}-WENO	AC	2168	$0.47640 \cdot 10^{-4}$
	PP	761	$0.78613 \cdot 10^{-3}$
	FSAC-PP	142	$0.20473 \cdot 10^{-7}$

Table 5.24: Total number of multigrid iterations on the fine grid and maximum values of Runge-Kutta residuals using different intercell flux interpolations at $Re = 0.5$.

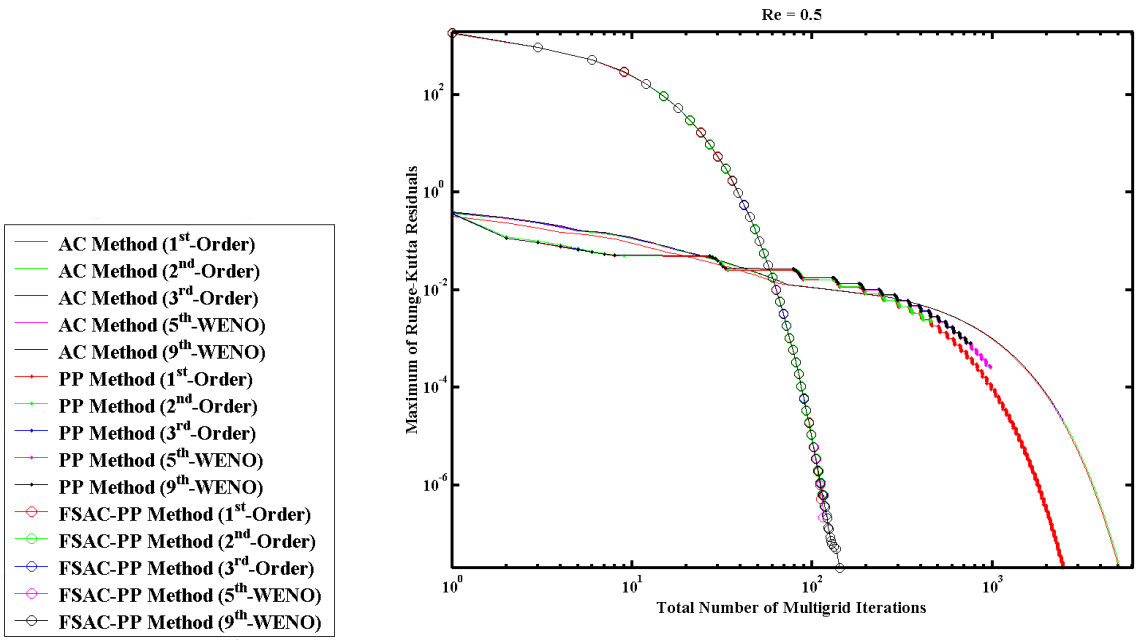

Figure 5.46: Comparison of the numerical convergence of the AC, PP, and FSAC-PP methods; maximum values of Runge-Kutta residuals RK_{maxres} versus total number of multigrid iterations N_{mg} on the fine grid at $Re = 0.5$.

Reynolds Number ($Re = 0.1$)			
Intercell Flux Interpolation	Solution Method	N_{mg}	RK_{maxres}
1^{st}-Order	AC	8816	$0.11695 \cdot 10^{-3}$
	PP	764	$0.67944 \cdot 10^{-2}$
	FSAC-PP	65	$0.39556 \cdot 10^{-6}$
2^{nd}-Order	AC	8755	$0.16735 \cdot 10^{-3}$
	PP	854	$0.99766 \cdot 10^{-2}$
	FSAC-PP	66	$0.20061 \cdot 10^{-6}$
3^{rd}-Order	AC	9913	$0.93892 \cdot 10^{-4}$
	PP	1161	$0.33399 \cdot 10^{-2}$
	FSAC-PP	65	$0.39317 \cdot 10^{-6}$
5^{th}-WENO	AC	6797	$0.44584 \cdot 10^{-3}$
	PP	1725	$0.34530 \cdot 10^{-3}$
	FSAC-PP	66	$0.97704 \cdot 10^{-9}$
9^{th}-WENO	AC	10229	$0.80224 \cdot 10^{-4}$
	PP	1213	$0.26800 \cdot 10^{-2}$
	FSAC-PP	364	$0.82944 \cdot 10^{-7}$

Table 5.25: Total number of multigrid iterations on the fine grid and maximum values of Runge-Kutta residuals using different intercell flux interpolations at $Re = 0.1$.

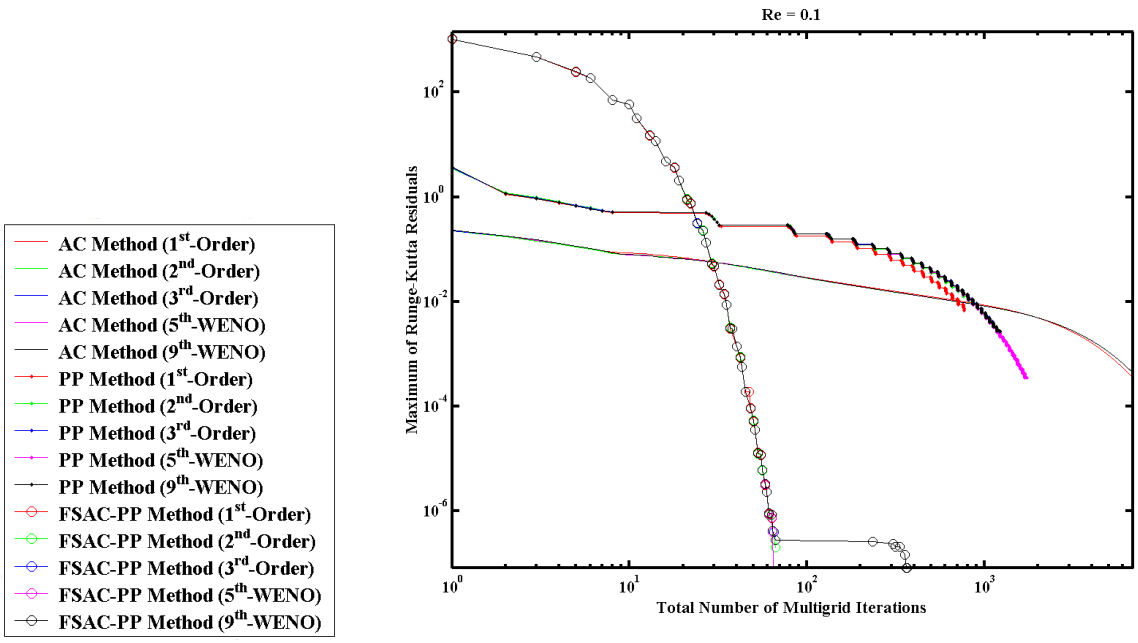

Figure 5.47: Comparison of the numerical convergence of the AC, PP, and FSAC-PP methods; maximum values of Runge-Kutta residuals RK_{maxres} versus total number of multigrid iterations N_{mg} on the fine grid at $Re = 0.1$.

Reynolds Number ($Re = 0.01$)			
Intercell Flux Interpolation	Solution Method	N_{mg}	RK_{maxres}
1^{st}-Order	AC	912	0.25786
	PP	764	$0.67973 \cdot 10^{-1}$
	FSAC-PP	63	$0.18301 \cdot 10^{-8}$
2^{nd}-Order	AC	1241	0.19437
	PP	854	$0.99824 \cdot 10^{-1}$
	FSAC-PP	63	$0.19609 \cdot 10^{-8}$
3^{rd}-Order	AC	1230	0.19621
	PP	1161	$0.33418 \cdot 10^{-1}$
	FSAC-PP	62	$0.19609 \cdot 10^{-8}$
5^{th}-WENO	AC	815	0.24683
	PP	594	0.29520
	FSAC-PP	64	$0.12575 \cdot 10^{-6}$
9^{th}-WENO	AC	349	0.42662
	PP	1213	$0.26827 \cdot 10^{-1}$
	FSAC-PP	76	$0.20311 \cdot 10^{-5}$

Table 5.26: Total number of multigrid iterations on the fine grid and maximum values of Runge-Kutta residuals using different intercell flux interpolations at $Re = 0.01$.

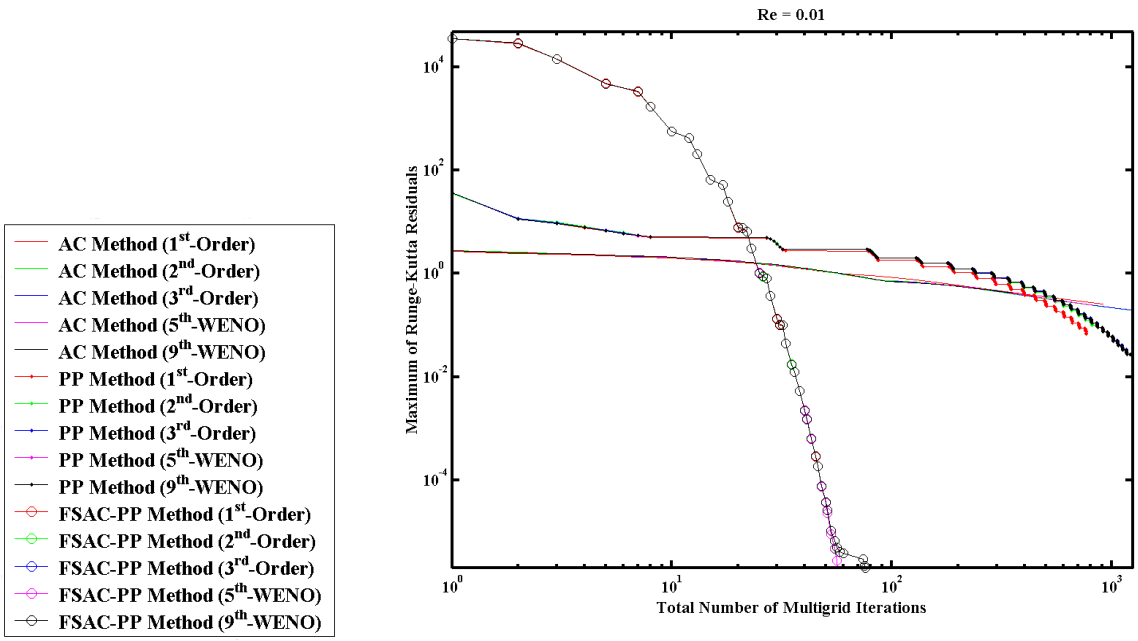

Figure 5.48: Comparison of the numerical convergence of the AC, PP, and FSAC-PP methods; maximum values of Runge-Kutta residuals RK_{maxres} versus total number of multigrid iterations N_{mg} on the fine grid at $Re = 0.01$.

Reynolds Number ($Re = 0.001$)			
Intercell Flux Interpolation	Solution Method	N_{mg}	RK_{maxres}
1^{st}-Order	AC	1487	7.69911
	PP	764	0.67976
	FSAC-PP	147	$0.13595 \cdot 10^{-6}$
2^{nd}-Order	AC	1481	6.52887
	PP	854	0.99830
	FSAC-PP	84	$0.17256 \cdot 10^{-6}$
3^{rd}-Order	AC	1470	6.54560
	PP	1161	0.33420
	FSAC-PP	77	$0.16733 \cdot 10^{-6}$
5^{th}-WENO	AC	930	7.30634
	PP	594	0.29521
	FSAC-PP	104	$0.15164 \cdot 10^{-6}$
9^{th}-WENO	AC	387	1.33459
	PP	1213	0.26830
	FSAC-PP	100	$0.10183 \cdot 10^{-3}$

Table 5.27: Total number of multigrid iterations on the fine grid and maximum values of Runge-Kutta residuals using different intercell flux interpolations at $Re = 0.001$.

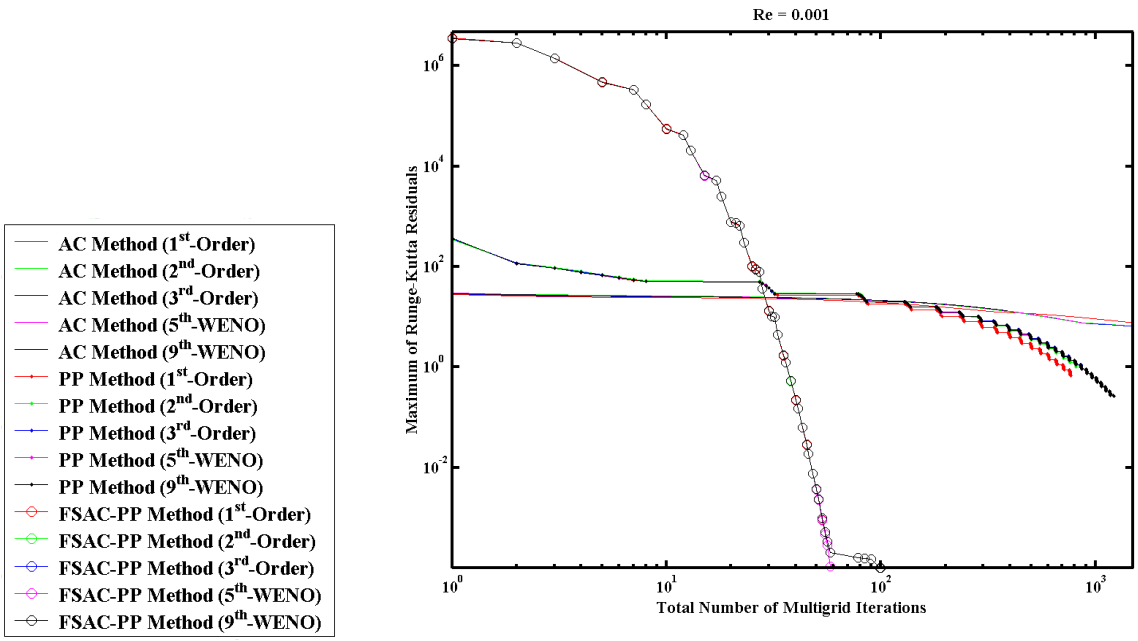

Figure 5.49: Comparison of the numerical convergence of the AC, PP, and FSAC-PP methods; maximum values of Runge-Kutta residuals RK_{maxres} versus total number of multigrid iterations N_{mg} on the fine grid at $Re = 0.001$.

Reynolds Number ($Re = 0.0001$)			
Intercell Flux Interpolation	Solution Method	N_{mg}	RK_{maxres}
1^{st}-Order	AC	1172	$0.16354 \cdot 10^{3}$
	PP	764	6.79768
	FSAC-PP	81	$0.11713 \cdot 10^{-4}$
2^{nd}-Order	AC	1169	$0.20113 \cdot 10^{3}$
	PP	854	9.98313
	FSAC-PP	76	$0.13386 \cdot 10^{-4}$
3^{rd}-Order	AC	1165	$0.20293 \cdot 10^{3}$
	PP	1161	3.34202
	FSAC-PP	123	$0.15059 \cdot 10^{-4}$
5^{th}-WENO	AC	741	$0.22363 \cdot 10^{3}$
	PP	594	$0.29521 \cdot 10^{2}$
	FSAC-PP	122	$0.11713 \cdot 10^{-4}$
9^{th}-WENO	AC	387	$0.24087 \cdot 10^{3}$
	PP	1213	2.68312
	FSAC-PP	303	$0.21485 \cdot 10^{-2}$

Table 5.28: Total number of multigrid iterations on the fine grid and maximum values of Runge-Kutta residuals using different intercell flux interpolations at $Re = 0.0001$.

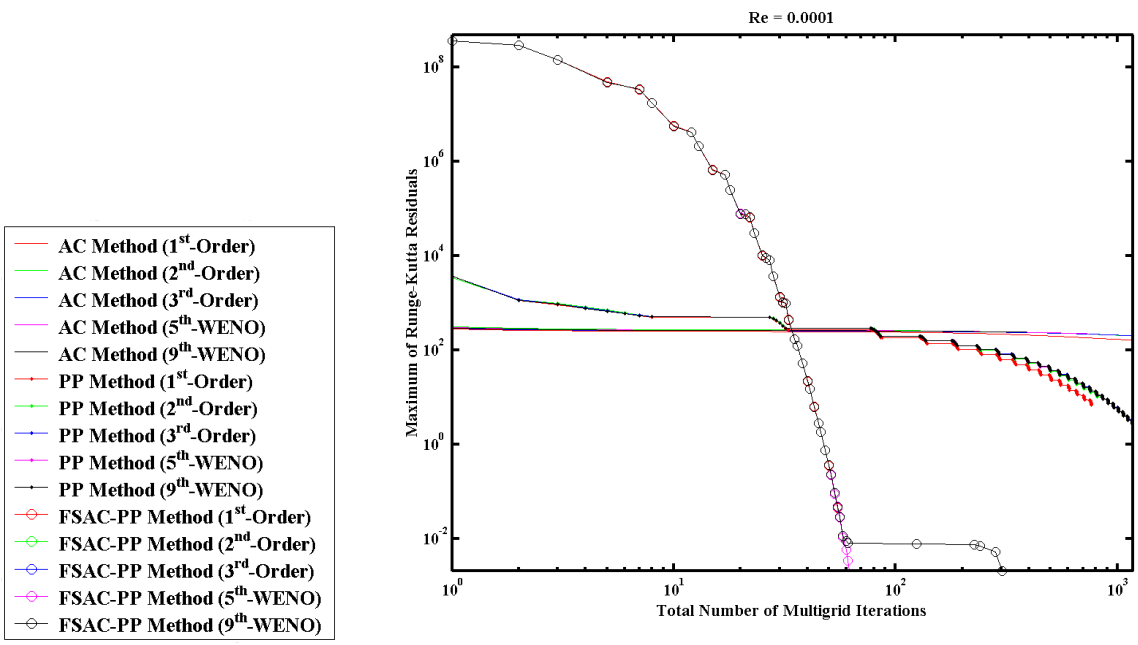

Figure 5.50: Comparison of the numerical convergence of the AC, PP, and FSAC-PP methods; maximum values of Runge-Kutta residuals versus total number of multigrid iterations on the fine grid at $Re = 0.0001$.

5.4 Summary and Conclusions

In this chapter, the proposed FSAC-PP method has been validated compared to the AC, PP methods and an analytical solution for steady-state, incompressible, constant density, pressure-driven laminar flow in a straight microfluidic channel. Four-hundred and eighty simulations have been performed using three different methods with five different inter-cell flux interpolation formulas on four different girds at eight different Reynolds numbers. The values of the characteristic condition numbers such as CFL_{inv} and CFL_{vis} have to be decreased, and the AC parameter β has to be increased as the Reynolds number reduces from 10 to 10^{-4} (see Table 5.2). The convergence histories overall show that the FSAC-PP method requires significantly smaller number of multigrid iterations than the classical AC and PP methods to achieve convergence at each Reynolds number (see Tables from 5.21 to 5.28). For $Re < 0.1$, the convergence of the AC method exhibits relatively high values related to the lowest maximum Runge-Kutta residuals, therefore, the numerical solution is not able to resolve the fully developed laminar velocity profile at the outlet boundary section. Thus, the AC method fails to give physically correct results at extremely low Reynolds number flows ($10^{-4} < Re < 0.1$), whereas both PP and FSAC-PP methods exhibited a good agreement with the analytical solution. Numerical solutions to the AC formulation of the Navier-Stokes equations exhibit slow convergence rates irrespective of the values of the AC parameter. In the case of the PP method, the rate of convergence is also slow and the number of multigrid cycles is the highest, because a) small time-step size has to be chosen as $\triangle t = 0.001s$ to achieve numerically stable solution; and b) relatively high number of sub-iterations is required for solving the pressure-Poisson equation to obtain accurate results. Due to these reasons, the proposed FSAC-PP solution method has been developed and investigated as an alternative method. The presented results showed that the FSAC-PP method is more efficient than the classical AC and PP methods for the investigated two-dimensional microfluidic benchmark channel. From the present benchmark test case, it can also be concluded that both PP and FSAC-PP methods are capable of handling extremely low Reynolds numbers more accurately than the classical AC method. The computational experience gained in this study has shown that the FSAC-PP method performs at a very slow convergence rate when the Reynolds number is smaller than 10^{-4}. In the present study, the numerical experiments also show that the FSAC-PP method is valid for Reynolds numbers up to 10^{-4}. Therefore, further investigation is required to understand the convergence properties of the FSAC-PP method for $Re < 10^{-4}$; furthermore, the FSAC-PP method has to be tested for complex microfluidic problems when small Reynolds number flow occurs.

Chapter 6

Lid Driven Cavity Flow at Moderate Reynolds Numbers

6.1 Introduction

For the validation of the proposed FSAC-PP method for incompressible, constant density laminar and turbulent flows at moderate and higher Reynolds numbers, the benchmark test case is the flow in a lid driven square and cubical cavity, respectively. This test case is a classical benchmark in the field of computational fluid dynamics, because for both two- and three-dimensional cases, computational data relying on Direct Numerical Simulation (DNS) and/or experimental data are available in the literature [8, 110, 176, 177, 178, 17]. Therefore, the FSAC-PP method has been validated compared to AC and PP methods, and DNS based computational data of Ghia et al. [8] for two-dimensional laminar flow in a lid driven square cavity at $Re = 100$, 400, and 1000 in this chapter. For the two-dimensional case, the convergence properties and the numerical errors of each employed method have been presented in conjunction with the non-linear FMG-FAS three-level multigrid algorithm discussed in Chapter 4. However, the main objective of this thesis is to develop an accurate and efficient method for solving low Reynolds number laminar flow problems in microfluidic systems, but in order to examine the capability of the FSAC-PP method at higher Reynolds numbers, the unsteady turbulent flow in a lid driven cubical cavity has been tested at $Re = 3200$ and 10 000. For this three-dimensional problem, experimental results are available in the article of Prasad and Koseff [17]. Furthermore, several authors have used the same benchmark to verify their computer codes and validate their numerical methods [110, 176, 177, 178]. The turbulent flow simulations have been performed by using the Implicit Large Eddy Simulation (ILES) method.

6.2 Two-Dimensional Flow in a Lid Driven Cavity

For the validation of the proposed FSAC-PP method compared to AC and PP methods and the DNS based computational data of Ghia et al. [8] for two-dimensional laminar flow in a lid driven square cavity, 45 simulations have been performed using 3 different methods with 5 different intercell flux interpolation formulas at 3 different Reynolds numbers as

$$45\,\text{Simulations} = 3\,\text{Method} \times 5\,\text{Interpolation Formulas} \times 3\,Re\,\text{Numbers}.$$

The computational grid is shown in Figure 6.1, which consists of 129×129 node points $(128 \times 128$ control cells$)$ on the fine grid, which is the same grid used by Ghia et al. [8] at $Re = 100$, 400, and 1000. Since the computational results have been computed and compared on the same grid as taken from the literature [8], a grid convergence study has not been performed for this benchmark test case.

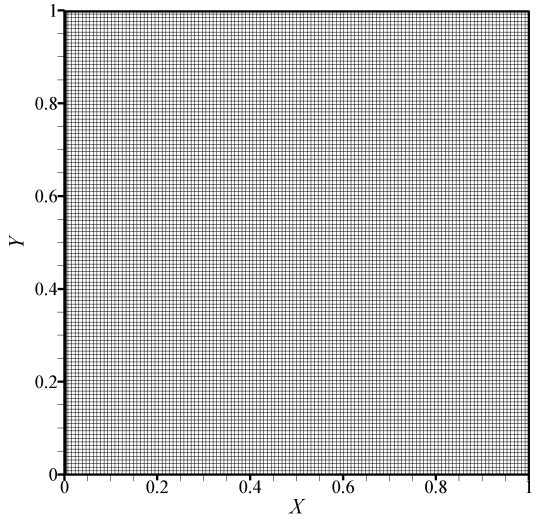

Figure 6.1: Equidistant grid for the square cavity using dimensionless coordinates.

A mathematical task can be formulated in terms of boundary and initial conditions for the two-dimensional laminar flow in the lid driven square cavity. Dimensionless quantities have been used in the simulations, therefore, the spatial coordinates have been normalized by the characteristic length l of the square cavity. The dimensional velocity components u and v are normalized by the average velocity $\tilde{u}$ of the moving lid on the top. No-slip boundary conditions have been prescribed for the dimensionless velocity components U and V on the non-moving side and bottom walls as $U_{wall} = V_{wall} = 0$. Dirichlet-type boundary conditions have also been imposed for the dimensionless velocity components

U and V on the moving top wall as $U_{lid} = 1$ and $V_{lid} = 0$. To obtain a unique solution of the incompressible Navier-Stokes equation for this benchmark test case, the reference static pressure has been taken to be equal to zero in the lower left corner of the square cavity. Consequently, Neumann-type boundary conditions have been prescribed for the pressure on both non-moving and moving walls; which means that the normal derivative of the pressure vanishes as $\partial P/\partial n = 0$. Note that the Neumann-type boundary conditions have been considered mathematically correct for the pressure, see more details in [170].

The incompressible Navier-Stokes equations have numerically been solved by using pseudo-time stepping procedure until the steady-state solution is achieved. The numerical results of the AC, PP and FSAC-PP methods for the dimensionless velocity components V and U along the horizontal and vertical centre-lines, using 5 different intercell flux interpolations (from first- up to ninth-order), have been compared to the DNS computational data of Ghia et al. [8] at $Re = 100$, 400, and 1000, respectively. Comparative tables of the dimensionless velocity profiles and of the minimum/maximum absolute and relative errors have been documented and summarized in Appendix B.

6.2.1 Validation of the FSAC-PP Method at *Re* = 100, 400, and 1000

All of the simulation results have been discussed and compared to the DNS data of Ghia et al. [8] in conjunction with the order of intercell flux interpolation formula in this subsection. The intercell fluxes have been interpolated by employing first-, second-, third-order interpolations, and fifth- and ninth-order WENO schemes, respectively. The streamline pattern for two-dimensional, incompressible, constant density laminar flow in the lid driven square cavity as obtained by Ghia et al. [8] at Re = 100, can be seen in Figure 6.2.

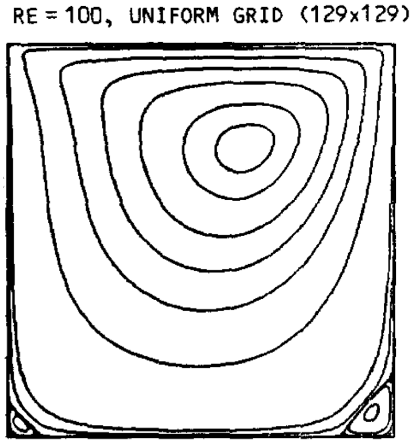

Figure 6.2: Streamline pattern for two-dimensional laminar flow in the lid driven square cavity obtained by Ghia et al. [8] at $Re = 100$.

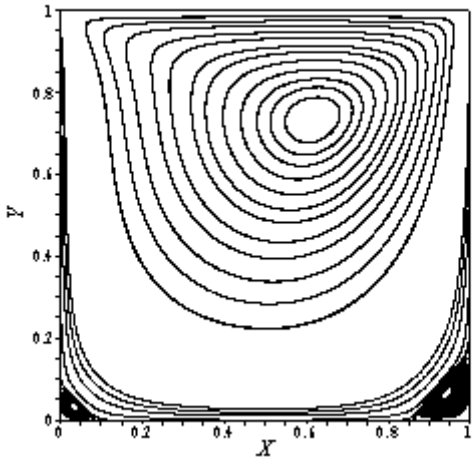

Figure 6.3: Streamline pattern in the lid driven square cavity at $Re = 100$.

The same streamline pattern has been obtained here with respect to the streamline structure of the primary large eddy and the corner vortices, which is shown in Figure 6.3. For the dimensionless velocity components V and U along horizontal and vertical centre-lines using first-order intercell flux interpolation, the results of the AC, PP and FSAC-PP methods, compared to the DNS data of Ghia et al. [8], can be seen in Figure 6.8. For the velocity component V along the horizontal centre-line, the maximum relative errors of the AC, PP and FSAC-PP methods are ~ 0.19925, ~ 0.42650 and ~ 0.07362, respectively (see Table B.2 in Appendix B). For the velocity component U along the vertical centre-line, the maximum relative errors of the AC, PP and FSAC-PP methods are ~ 15.67207, ~ 13.76639 and ~ 0.70087, respectively (see Table B.4 in Appendix B). The convergence history of the pseudo-time stepping procedure has been plotted in Figure 6.13, which can be characterized by the maximum value of the Runge-Kutta residuals versus the total number of multigrid iterations on the fine grid until the steady-state solution is achieved. The total number of multigrid iteration of the AC, PP and FSAC-PP methods are 107, 7280 and 97, respectively (see Figure 6.13 and Table 6.1). In terms of accuracy, these numerical results show that the FSAC-PP method gives the most accurate agreement with the DNS data of Ghia et al. [8] for both velocity components V and U. In terms of efficiency, the FSAC-PP method consumes the lowest number of multigrid cycles of 97 compared to the AC and PP methods; and the highest number of multigrid cycles of 7280 has been obtained by using the PP method (see Figure 6.13 and Table 6.1). The FSAC-PP method consumes approximately 1.1 and 75.05 times less multigrid iterations than the AC and PP methods, respectively. These results suggest that the FSAC-PP method is the most accurate and efficient method compared to the AC and PP methods when a

first-order interpolation is used for the present two-dimensional benchmark at $Re = 100$.

For velocity components V and U using second- and third-order interpolations, and fifth- and ninth-order WENO schemes, the results of the AC, PP and FSAC-PP methods can be seen from Figures 6.9 to 6.12. When second-order interpolation is used for the velocity component V, the maximum relative errors of the AC, PP and FSAC-PP methods are ~ 0.05110, ~ 0.27482 and ~ 0.05531, respectively (see Table B.6 in Appendix B). For the velocity component U, the maximum relative errors of the AC, PP and FSAC-PP methods are ~ 0.27663, ~ 0.63502 and ~ 0.08482, respectively (see Table B.8 in Appendix B). For velocity components V and U, these numerical results show that the AC and FSAC-PP methods are more accurate than the PP method. Unlike the first-order interpolation, the FSAC-PP method is overall more accurate than the AC and PP methods (see Figure 6.8). When third-order interpolation is used for the velocity component V, the maximum relative errors of the AC, PP and FSAC-PP methods are ~ 0.05420, ~ 0.07968 and ~ 0.05270, respectively (see Table B.10 in Appendix B). For the velocity component U, the maximum relative errors of the AC, PP and FSAC-PP methods are ~ 0.23427, ~ 0.22983 and ~ 0.11597, respectively (see Table B.12 in Appendix B). One can see from these numerical results that the accuracy of the AC and PP methods are similar to each other for the velocity component V, and the proposed FSAC-PP method is the most accurate for the velocity component U. The relative errors of the fifth- and ninth-order WENO interpolation schemes are summarized in Tables B.14 and B.16, and in Tables B.18 and B.20 in Appendix B, respectively. The numerical results for these high-order schemes suggest, similarly to the third-order interpolation, that the accuracy of the AC and FSAC-PP methods are similar to each other for the velocity component V, and the proposed FSAC-PP method is the most accurate for the horizontal velocity component U. This also means that the numerically computed velocity profiles in the centre-lines do not change significantly by employing higher than third-order interpolation for this benchmark at $Re = 100$. The reason for this is the computational grid resolution of 129×129 node points, which is a fine mesh for this two-dimensional test case, therefore, the high-order schemes do not improve further the accuracy of the solution. In terms of efficiency, these results show that the FSAC-PP method requires the lowest number of multigrid iterations N_{mg} on the fine grid compared to the AC and PP methods at $Re = 100$ (see Figures from 6.13 to 6.17 and Tables from 6.1 to 6.5).

The streamline pattern for two-dimensional incompressible, constant density laminar flow in the lid driven square cavity, obtained by Ghia et al. [8], can be seen in Figure 6.4 at $Re = 400$. A similar streamline pattern has been obtained here, which is shown in Figure 6.5. For the dimensionless velocity components V and U, the results of the AC, PP and FSAC-PP methods can be seen in Figures from 6.18 to 6.22.

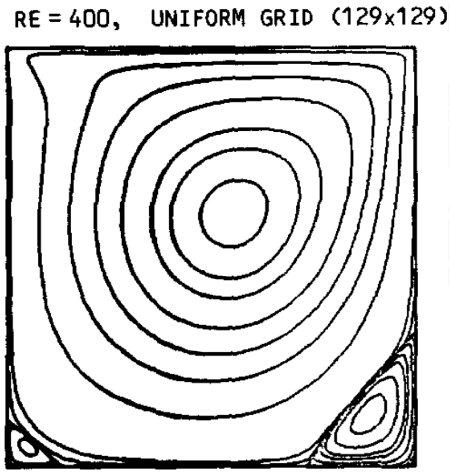

Figure 6.4: Streamline pattern for two-dimensional laminar flow in the lid driven square cavity obtained by Ghia et al. [8] at $Re = 400$.

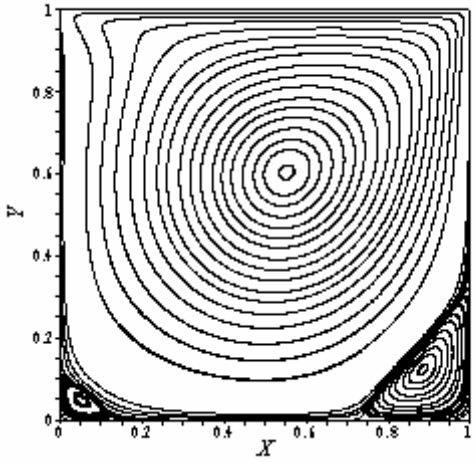

Figure 6.5: Streamline pattern in the lid driven square cavity at $Re = 400$.

When first-order interpolation is used again for the velocity component V, the maximum relative errors of the AC, PP and FSAC-PP methods are ~ 0.61997, ~ 0.53882 and ~ 0.56081, respectively (see Table B.22 in Appendix B). For the velocity component U, the maximum relative errors of the AC, PP and FSAC-PP methods are ~ 3.11797, ~ 8.12039 and ~ 0.19398, respectively (see Table B.24 in Appendix B). These results show that the accuracy of the PP and FSAC-PP methods are similar to each other for the velocity component V, and the FSAC-PP method is the most accurate for the velocity component U for this benchmark test case at $Re = 400$. In terms of efficiency, the FSAC-

PP method consumes again the lowest number of multigrid cycles of 113; and the highest number of multigrid cycles of 12360 has again been obtained by using the PP method (see Figure 6.23 and Table 6.6). In the case of the second-order interpolation for the velocity components V and U (see Tables B.26 and B.28 in Appendix B), the PP method is more accurate than the AC and FSAC-PP methods for the velocity component V, and the FSAC-PP method is again the most accurate for the velocity component U. These results are also valid for the velocity component V by employing a third-order interpolation (see Table B.30 in Appendix B). Unlike the second-order interpolation, the AC method exhibits the lowest maximum relative error for the velocity component U (see Table B.32 in Appendix B). In the cases of fifth- and ninth-order WENO schemes (see Tables B.34 and B.36, and Tables B.38 and B.39 in Appendix B), the PP method is more accurate than the AC and FSAC-PP methods for the velocity component V, and the AC and FSAC-PP methods are more accurate than the PP method for the velocity component U. The results of these schemes exhibit the same order of magnitude, which means again that the numerically computed velocity profiles do not change significantly by employing higher than third-order interpolation for this benchmark at $Re = 400$. In terms of efficiency, the FSAC-PP method required again the lowest number of multigrid iterations N_{mg} (see Figures from 6.23 to 6.27 and Tables from 6.6 to 6.10).

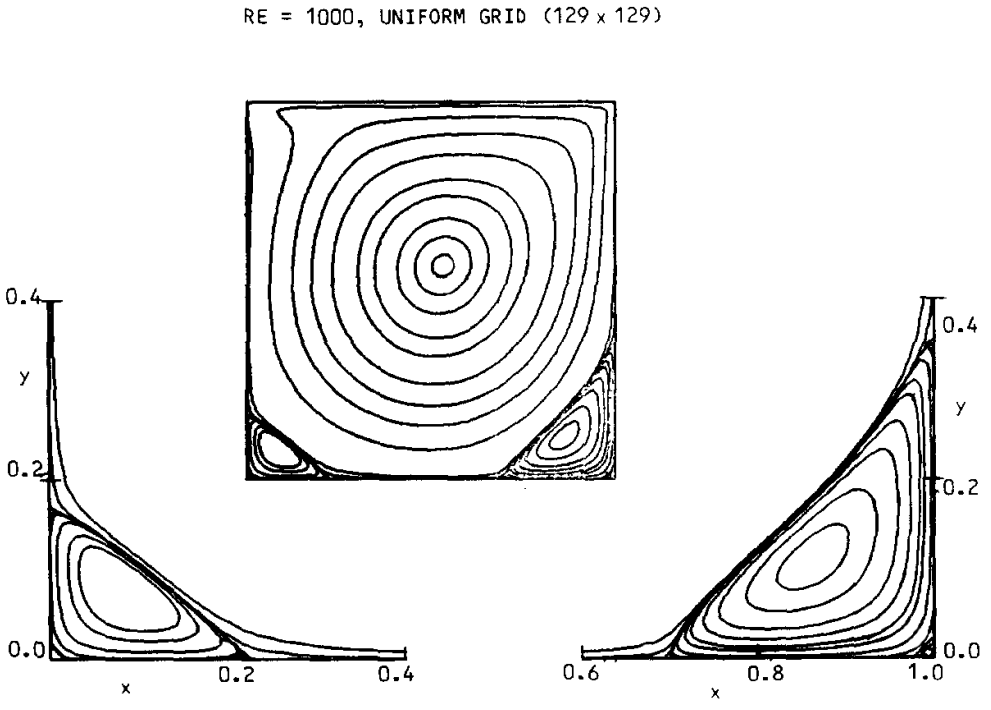

Figure 6.6: Streamline pattern for two-dimensional laminar flow in the lid driven square cavity obtained by Ghia et al. [8] at $Re = 1000$.

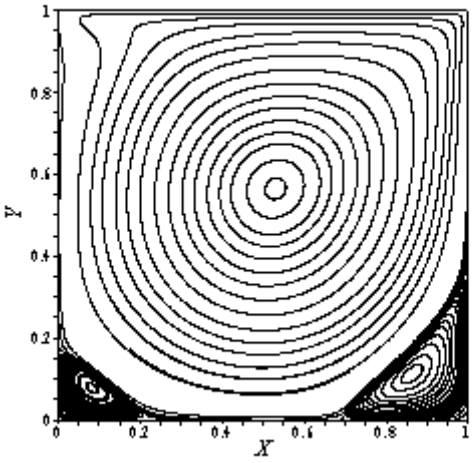

Figure 6.7: Streamline pattern in the lid driven square cavity at $Re = 1000$.

The streamline pattern for incompressible, constant density laminar flow in the lid driven square cavity, obtained by Ghia et al. [8], can be seen in Figure 6.6 at $Re = 1000$. A similar streamline pattern has been obtained in respect to the streamline structure of the primary large eddy and the corner vortices, which is shown in Figure 6.7. For the dimensionless velocity components V and U, the results of the AC, PP and FSAC-PP methods can be seen in Figures from 6.28 to 6.32. In the case of the first-order interpolation for the velocity component V, the maximum relative errors of the AC, PP and FSAC-PP methods are ~ 1.15918, ~ 0.82317 and ~ 0.28518, respectively (see Table B.42 in Appendix B). For the velocity components U, the maximum relative errors of the AC, PP and FSAC-PP methods are ~ 1.16409, ~ 3.42777 and ~ 0.13116, respectively (see Table B.44 in Appendix B). These results show again that the FSAC-PP method gives the most accurate agreement with the DNS data of [8] for both velocity components V and U along the horizontal and vertical centre-lines by employing a first-order interpolation for this benchmark test case at $Re = 1000$. In terms of efficiency, the FSAC-PP method consumes the lowest number of multigrid cycles of 162; and the highest number of multigrid cycles of 14490 has again been obtained by using the PP method (see Figure 6.33 and Table 6.11). When second-order interpolation is used for the velocity components V and U (see Tables B.45 and B.47 in Appendix B), the AC method is more accurate than the PP and FSAC-PP methods for both velocity components V and U. In the case of the third-order interpolation (see Tables B.50 and B.52 in Appendix B), the FSAC-PP method is more accurate than the AC and PP methods for the velocity component V, and the AC method shows the most accurate agreement with the velocity component U. The relative errors exhibit similar order of magnitude compared to the results of the third-order interpolation

when the high-order fifth- and ninth-order WENO schemes are used for velocity components V and U (see Tables B.53 and B.55, and Tables B.57 and B.60 in Appendix B). For both velocity components V and U when using these high-order schemes, the AC method is more accurate than the PP and FSAC-PP methods for this test case at $Re = 1000$. This means again that the FSAC-PP method shows good agreement with the DNS data of Ghia et al. [8] by employing low-order intercell flux interpolations as well. In terms of efficiency, the FSAC-PP method required again the lowest number of multigrid iterations N_{mg} (see Figures from 6.33 to 6.37 and Tables from 6.11 to 6.15).

The overall results suggest that the accuracy of the AC and FSAC-PP methods are similar to each other. The FSAC-PP method is the most efficient method, compared to the classical AC and PP methods, for the present two-dimensional benchmark for all interpolation orders at Re = 100, 400, and 1000. Furthermore, the FSAC-PP method is capable of providing accurate and efficient solution by employing low-order interpolation schemes for the present benchmark for all considered Reynolds numbers.

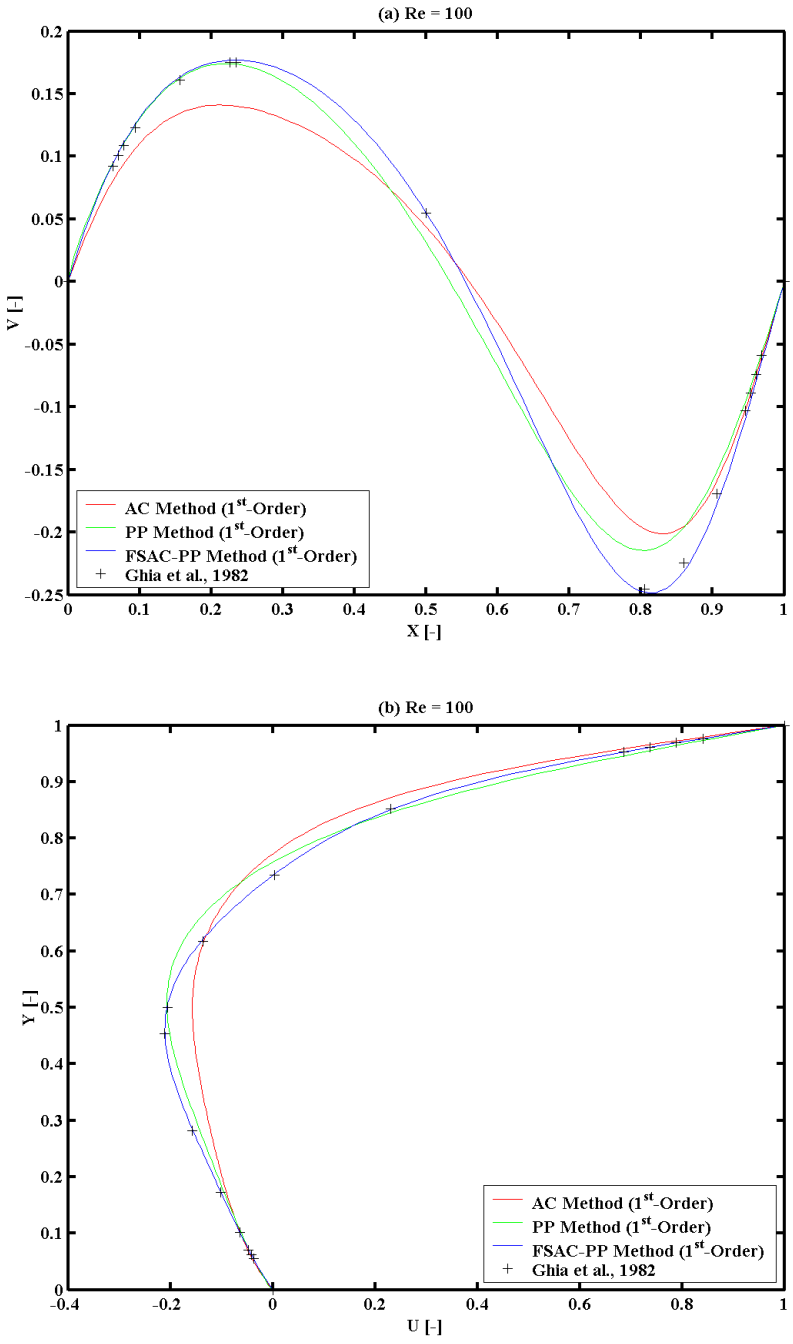

Figure 6.8: Results of the AC, PP, and FSAC-PP methods for dimensionless velocity components V and U along a) horizontal and b) vertical centre-lines of the square cavity using 1^{st}-order interpolation compared to the results of Ghia et al. [8] at $Re = 100$.

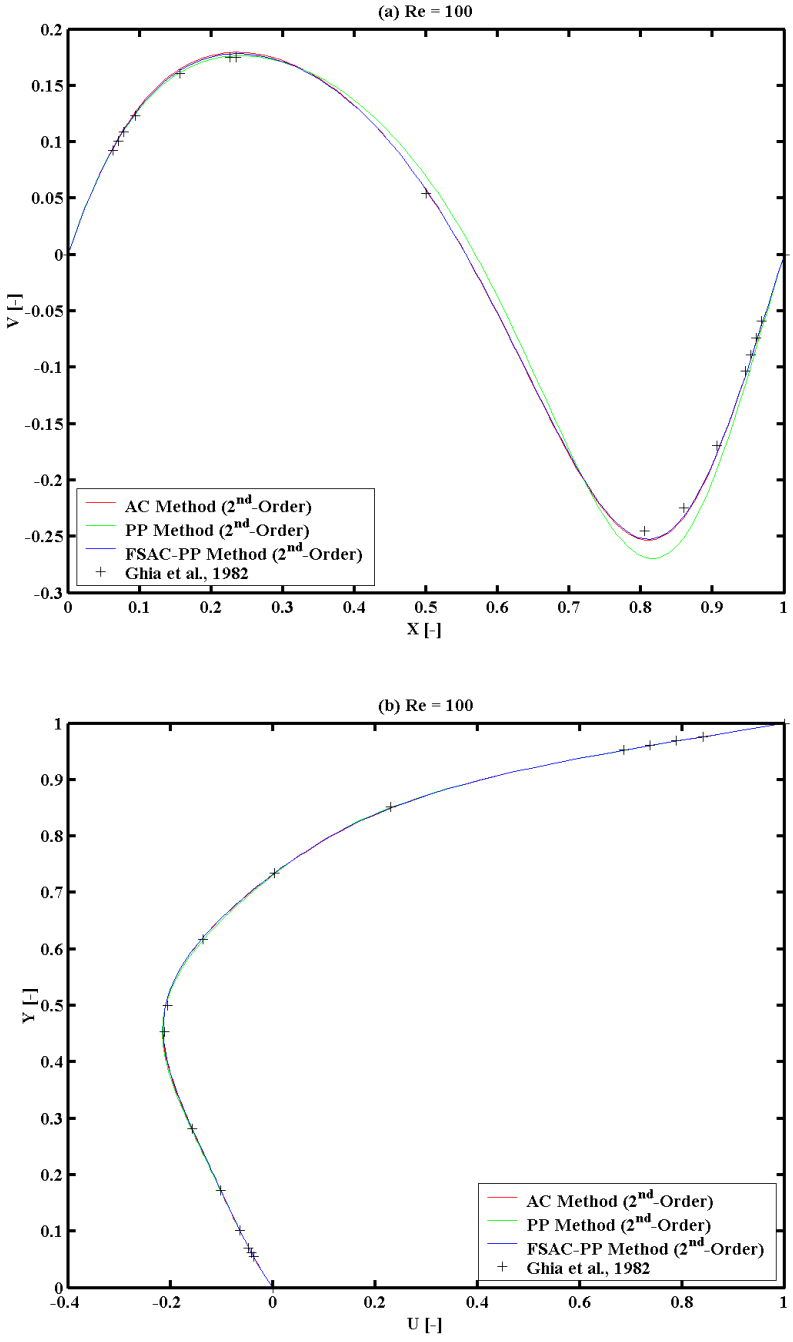

Figure 6.9: Results of the AC, PP, and FSAC-PP methods for dimensionless velocity components V and U along a) horizontal and b) vertical centre-lines of the square cavity using 2^{nd}-order interpolation compared to the results of Ghia et al. [8] at $Re = 100$.

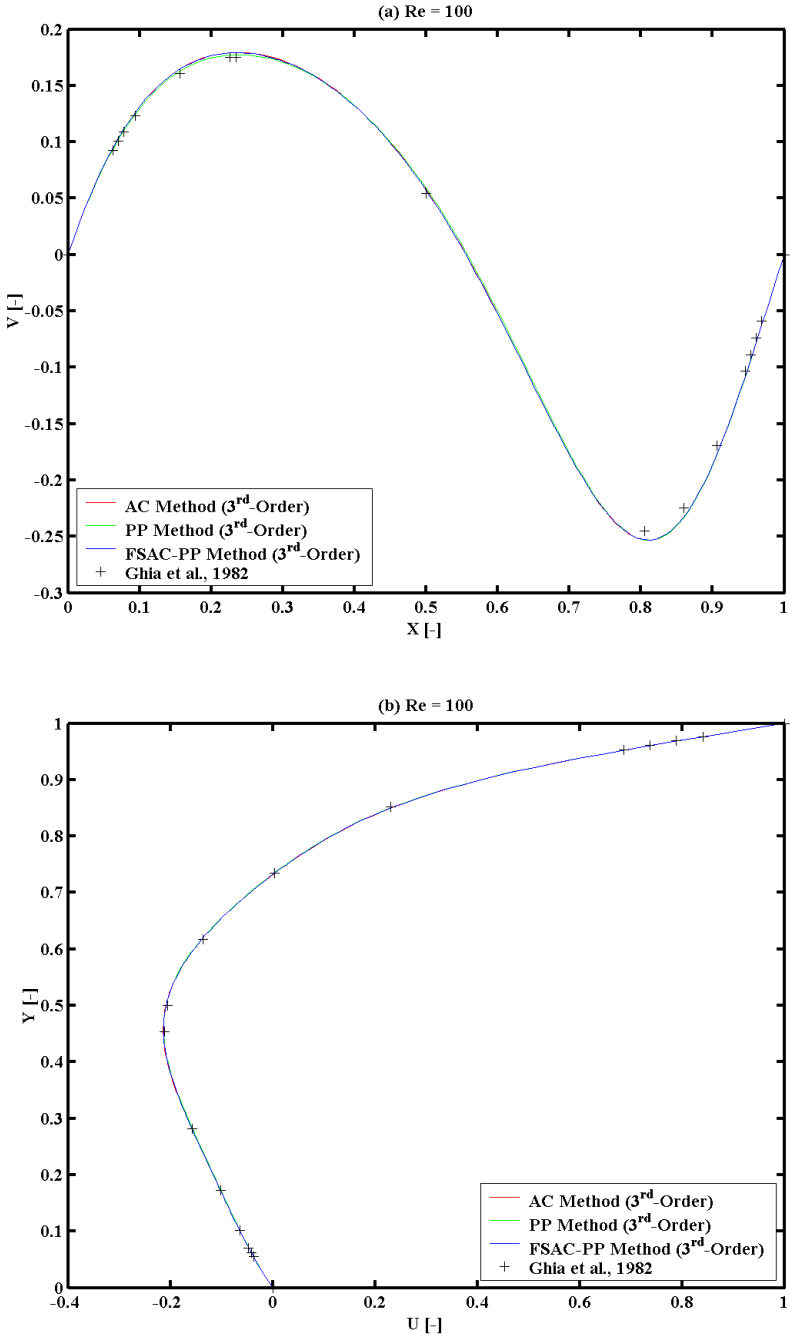

Figure 6.10: Results of the AC, PP, and FSAC-PP methods for the dimensionless velocity components V and U along a) horizontal and b) vertical centre-lines of the square cavity using 3^{rd}-order interpolation compared to the results of Ghia et al. [8] at $Re = 100$.

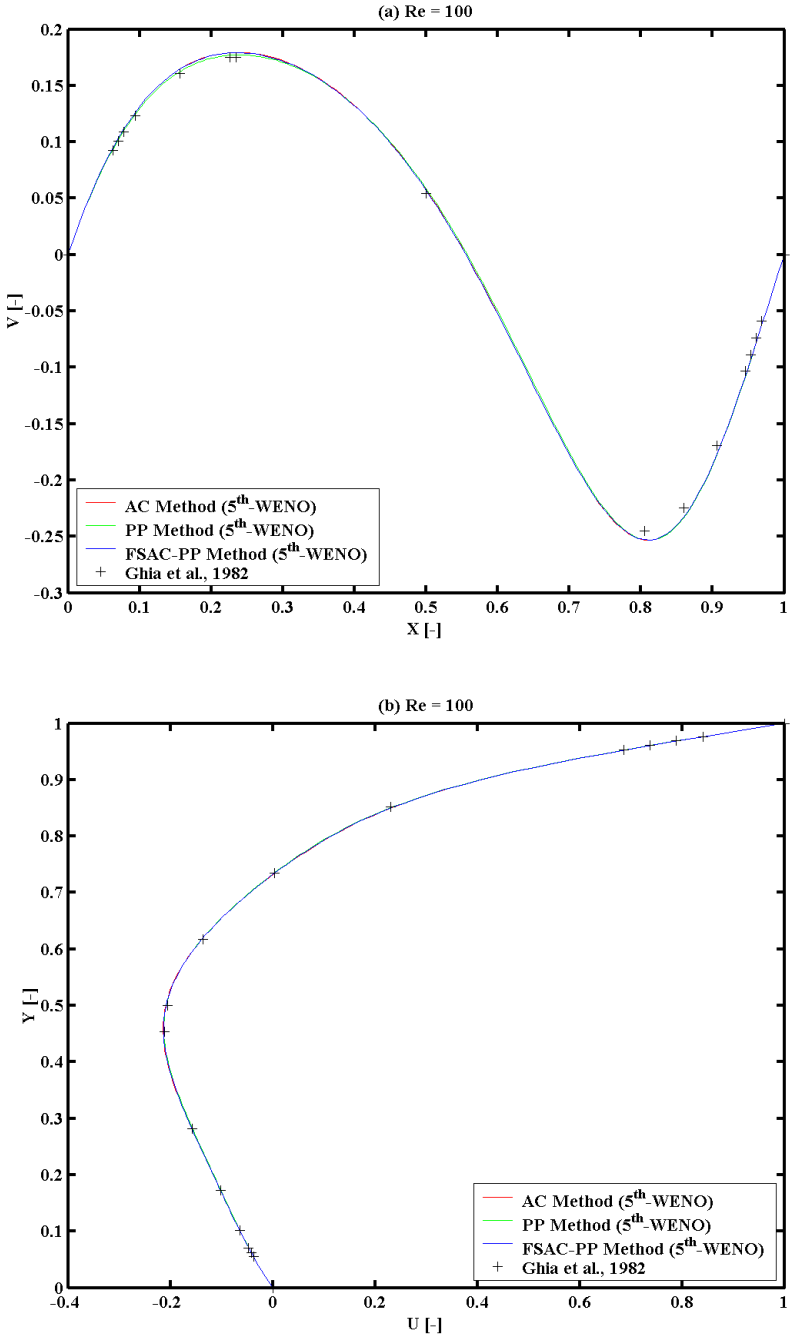

Figure 6.11: Results of the AC, PP, and FSAC-PP methods for the dimensionless velocity components V and U along a) horizontal and b) vertical centre-lines of the square cavity using 5^{th}-order WENO interpolation compared to the results of Ghia et al. [8] at $Re = 100$.

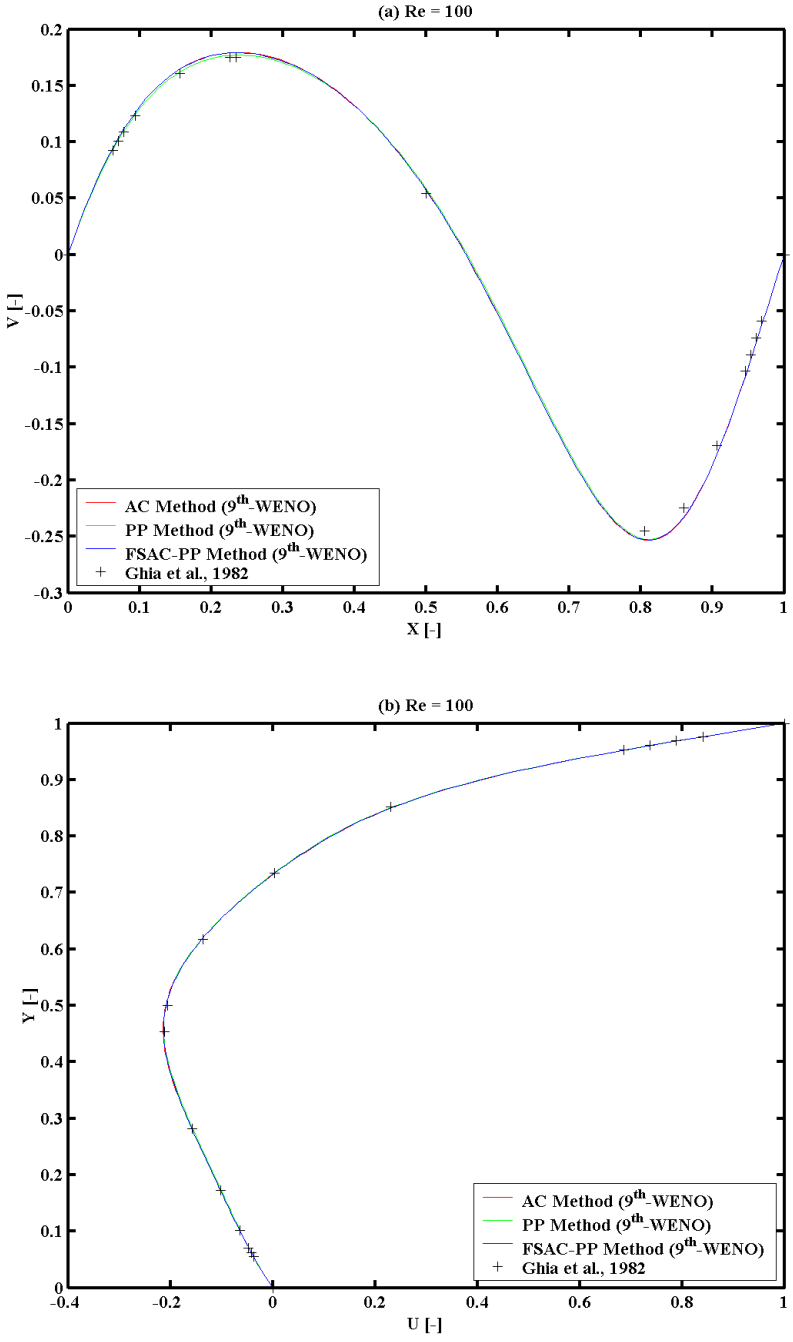

Figure 6.12: Results of the AC, PP, and FSAC-PP methods for the dimensionless velocity components V and U along a) horizontal and b) vertical centre-lines of the square cavity using 9^{th}-order WENO interpolation compared to the results of Ghia et al. [8] at $Re = 100$.

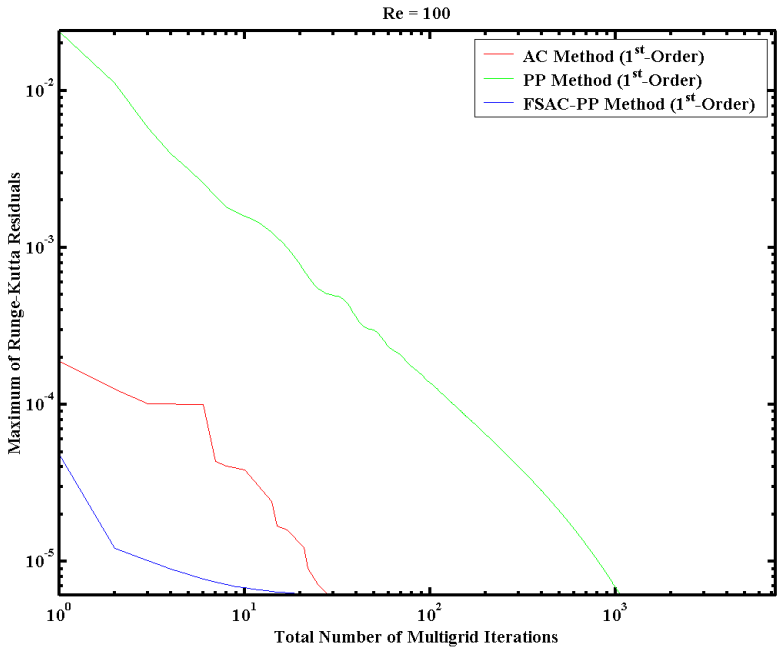

Figure 6.13: Comparison of the numerical convergence of the AC, PP, and FSAC-PP methods; maximum values of Runge-Kutta residuals versus total number of multigrid iterations on the fine grid using 1^{st}-order interpolation at $Re = 100$.

	$Re = 100$
	Order of Intercell Flux Interpolation: 1^{st}-Order
	Total Number of Multigrid Iterations N_{mg} on the Fine Grid
AC Method	107
PP Method	7280
FSAC-PP Method	97

Table 6.1: Total number of multigrid iterations on the fine grid using 1^{st}-order intercell flux interpolation at $Re = 100$.

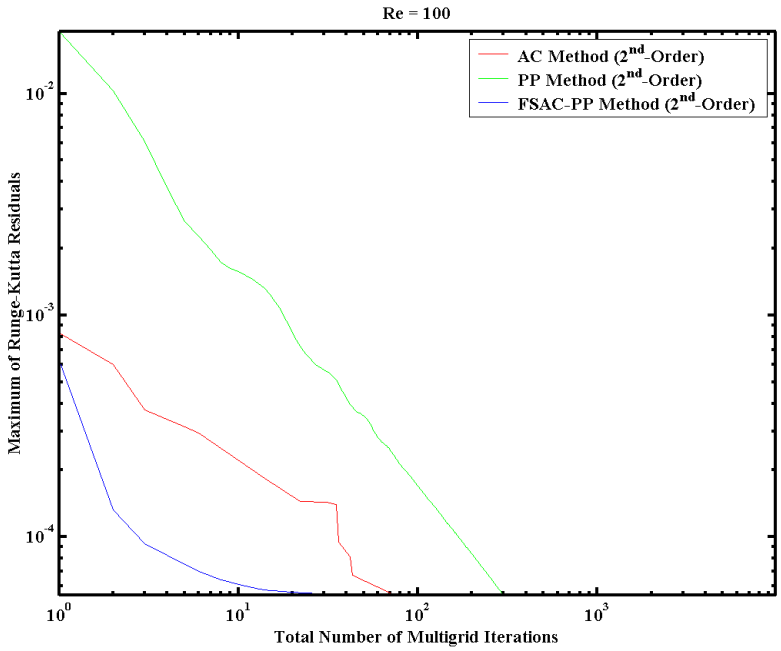

Figure 6.14: Comparison of the numerical convergence of the AC, PP, and FSAC-PP methods; maximum values of Runge-Kutta residuals versus total number of multigrid iterations on the fine grid using 2^{nd}-order interpolation at $Re = 100$.

	$Re = 100$
	Order of Intercell Flux Interpolation: 2^{nd}-Order
	Total Number of Multigrid Iterations N_{mg} on the Fine Grid
AC Method	788
PP Method	9780
FSAC-PP Method	202

Table 6.2: Total number of multigrid iterations on the fine grid using 2^{nd}-order intercell flux interpolation at $Re = 100$.

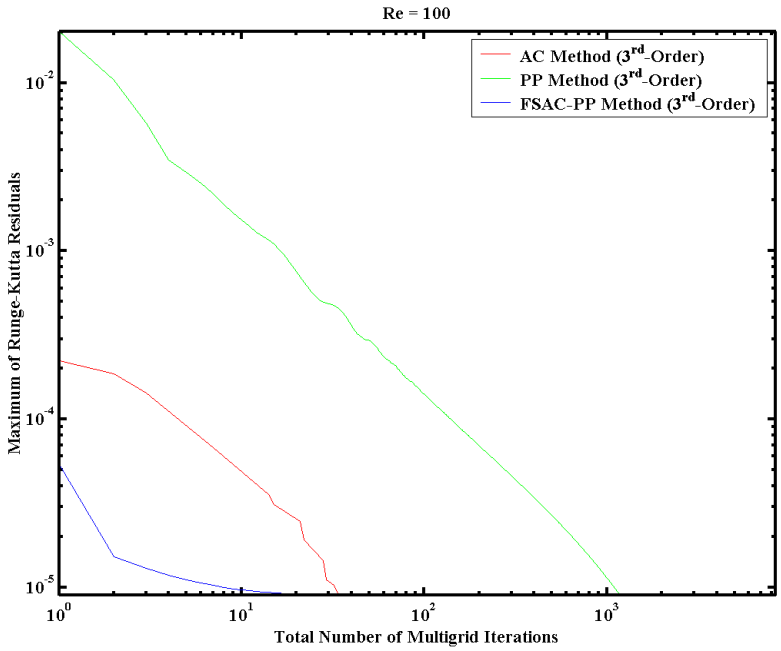

Figure 6.15: Comparison of the numerical convergence of the AC, PP, and FSAC-PP methods; maximum values of Runge-Kutta residuals versus total number of multigrid iterations on the fine grid using 3^{rd}-order interpolation at $Re = 100$.

	$Re = 100$
	Order of Intercell Flux Interpolation: 3^{rd}-Order
	Total Number of Multigrid Iterations N_{mg} on the Fine Grid
AC Method	157
PP Method	8350
FSAC-PP Method	107

Table 6.3: Total number of multigrid iterations on the fine grid using 3^{rd}-order intercell flux interpolation at $Re = 100$.

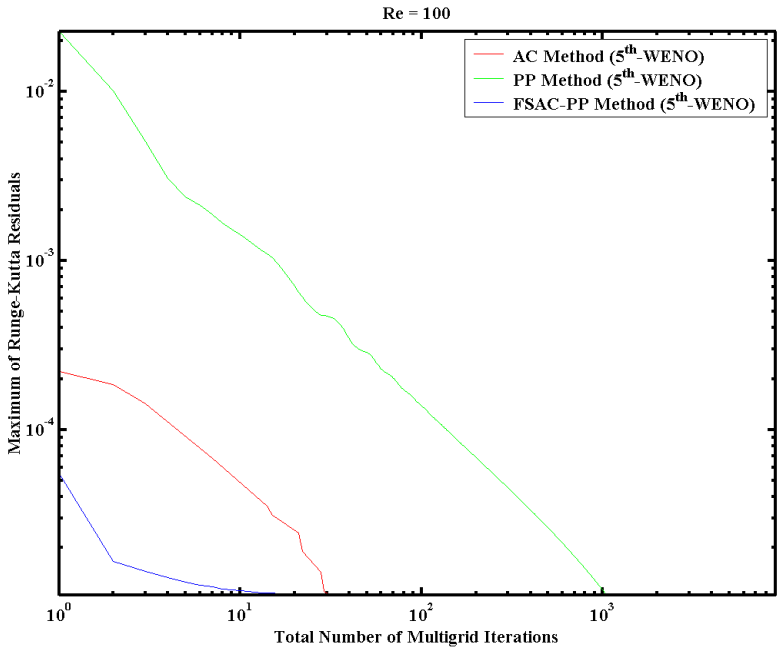

Figure 6.16: Comparison of the numerical convergence of the AC, PP, and FSAC-PP methods; maximum values of Runge-Kutta residuals versus total number of multigrid iterations on the fine grid using 5^{th}-order WENO interpolation at $Re = 100$.

	$Re = 100$
	Order of Intercell Flux Interpolation: 5^{th}-WENO
	Total Number of Multigrid Iterations N_{mg} on the Fine Grid
AC Method	157
PP Method	8940
FSAC-PP Method	102

Table 6.4: Total number of multigrid iterations on the fine grid using 5^{th}-order WENO intercell flux interpolation at $Re = 100$.

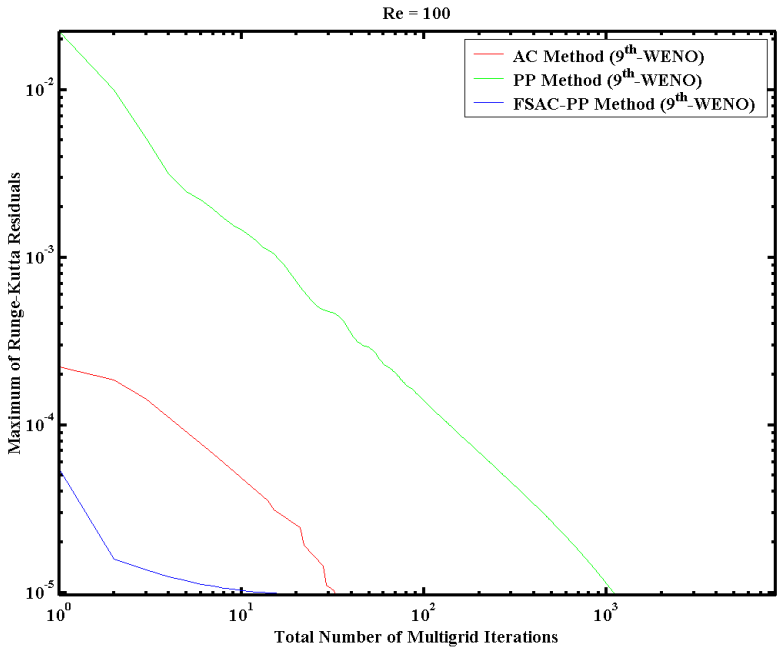

Figure 6.17: Comparison of the numerical convergence of the AC, PP, and FSAC-PP methods; maximum values of Runge-Kutta residuals versus total number of multigrid iterations on the fine grid using 9^{th}-order WENO interpolation at $Re = 100$.

	$Re = 100$
	Order of Intercell Flux Interpolation: 9^{th}-WENO
	Total Number of Multigrid Iterations N_{mg} on the Fine Grid
AC Method	157
PP Method	8370
FSAC-PP Method	105

Table 6.5: Total number of multigrid iterations on the fine grid using 9^{th}-order WENO intercell flux interpolation at $Re = 100$.

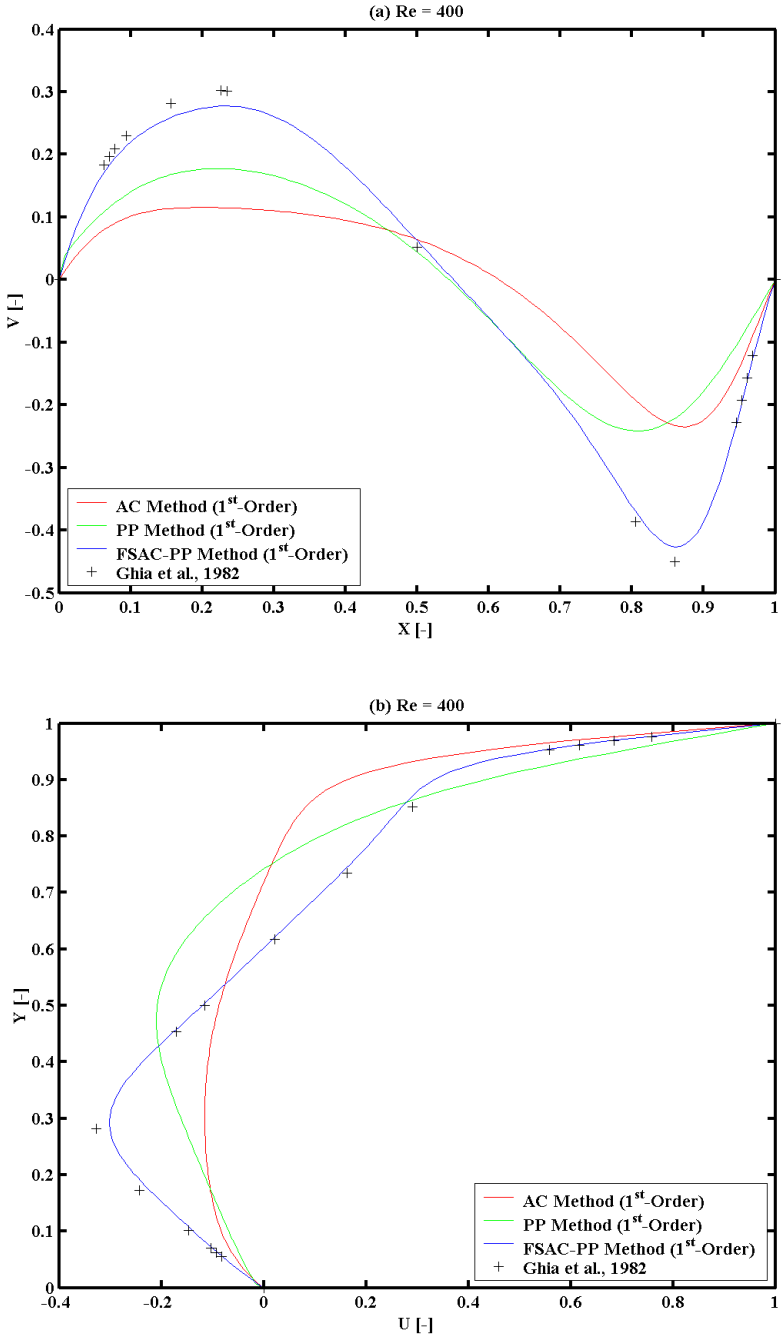

Figure 6.18: Results of the AC, PP, and FSAC-PP methods for the dimensionless velocity components V and U along a) horizontal and b) vertical centre-lines of the square cavity using 1^{st}-order interpolation compared to the results of Ghia et al. [8] at $Re = 400$.

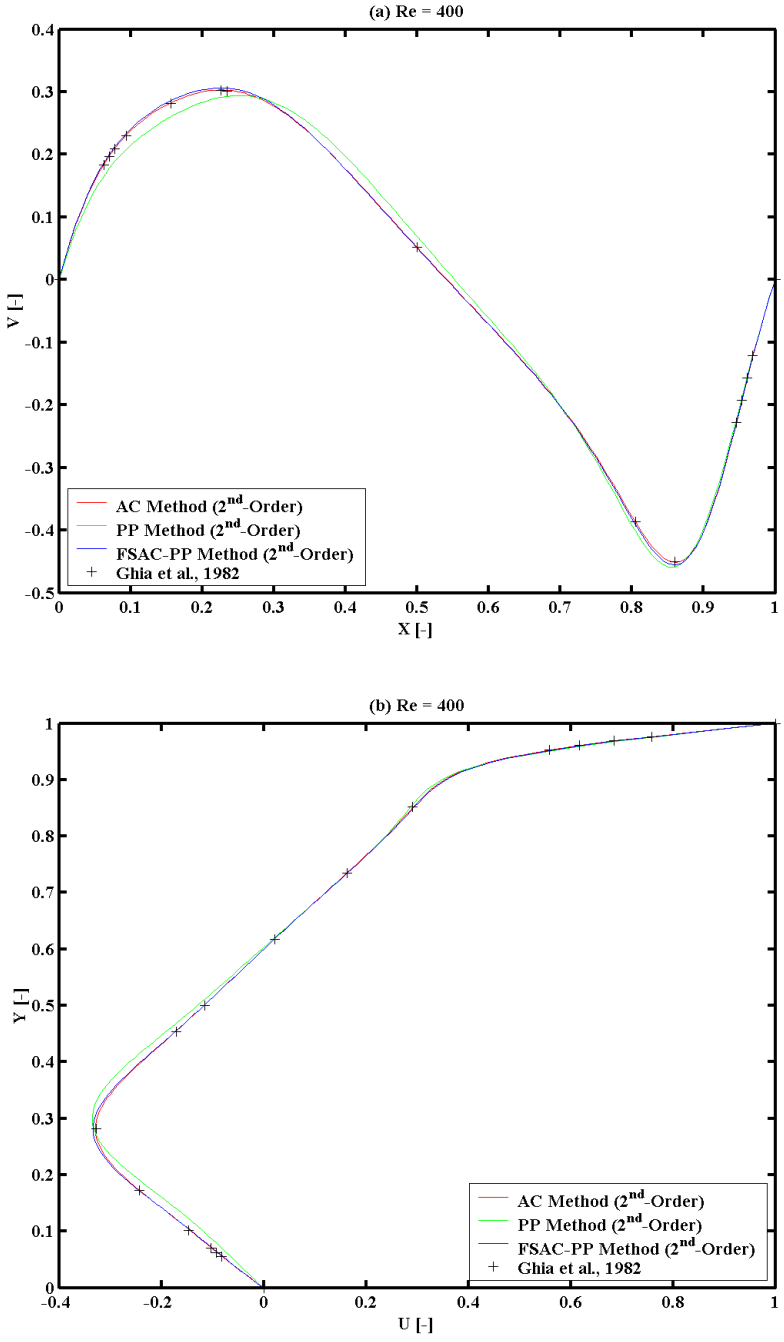

Figure 6.19: Results of the AC, PP, and FSAC-PP methods for the dimensionless velocity components V and U along a) horizontal and b) vertical centre-lines of the square cavity using 2^{nd}-order interpolation compared to the results of Ghia et al. [8] at $Re = 400$.

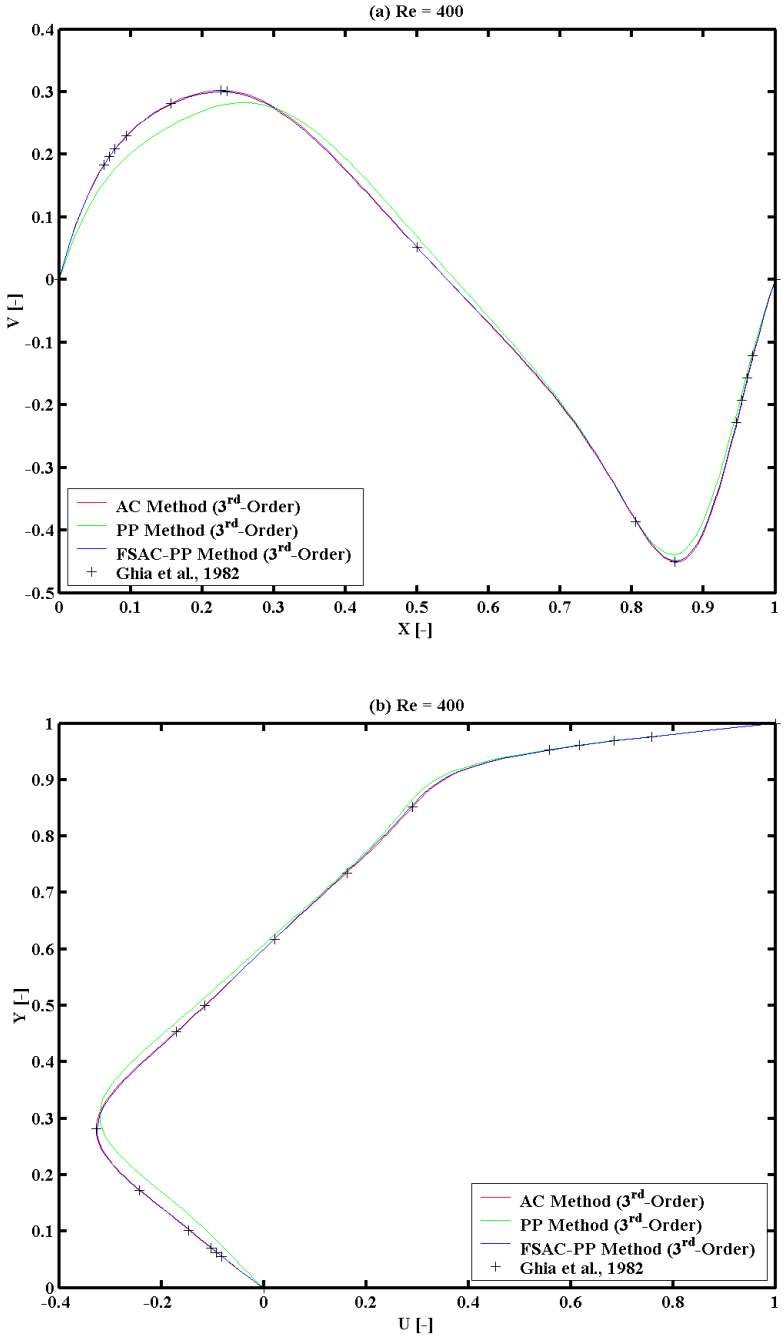

Figure 6.20: Results of the AC, PP, and FSAC-PP methods for the dimensionless velocity components V and U along a) horizontal and b) vertical centre-lines of the square cavity using 3^{rd}-order interpolation compared to the results of Ghia et al. [8] at $Re = 400$.

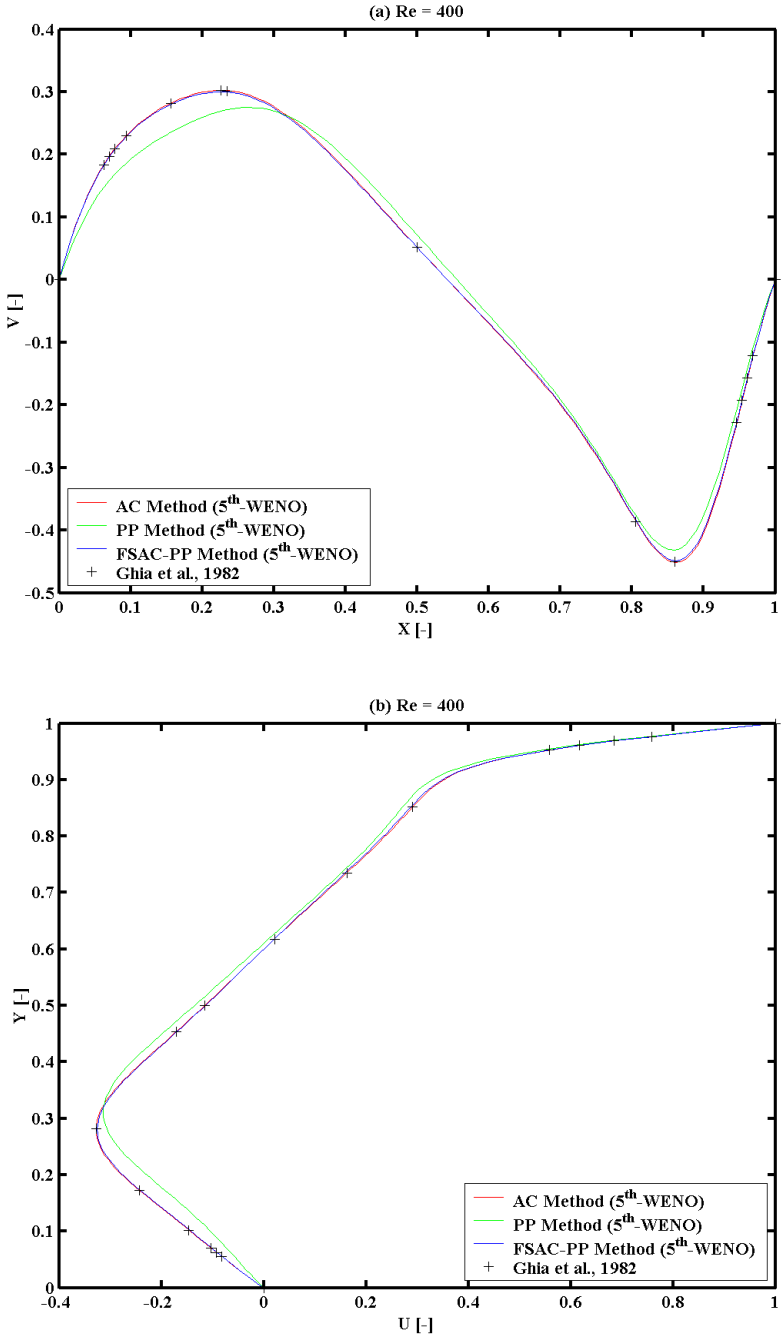

Figure 6.21: Results of the AC, PP, and FSAC-PP methods for the dimensionless velocity components V and U along a) horizontal and b) vertical centre-lines of the square cavity using 5^{th}-order WENO interpolation compared to the results of Ghia et al. [8] at $Re = 400$.

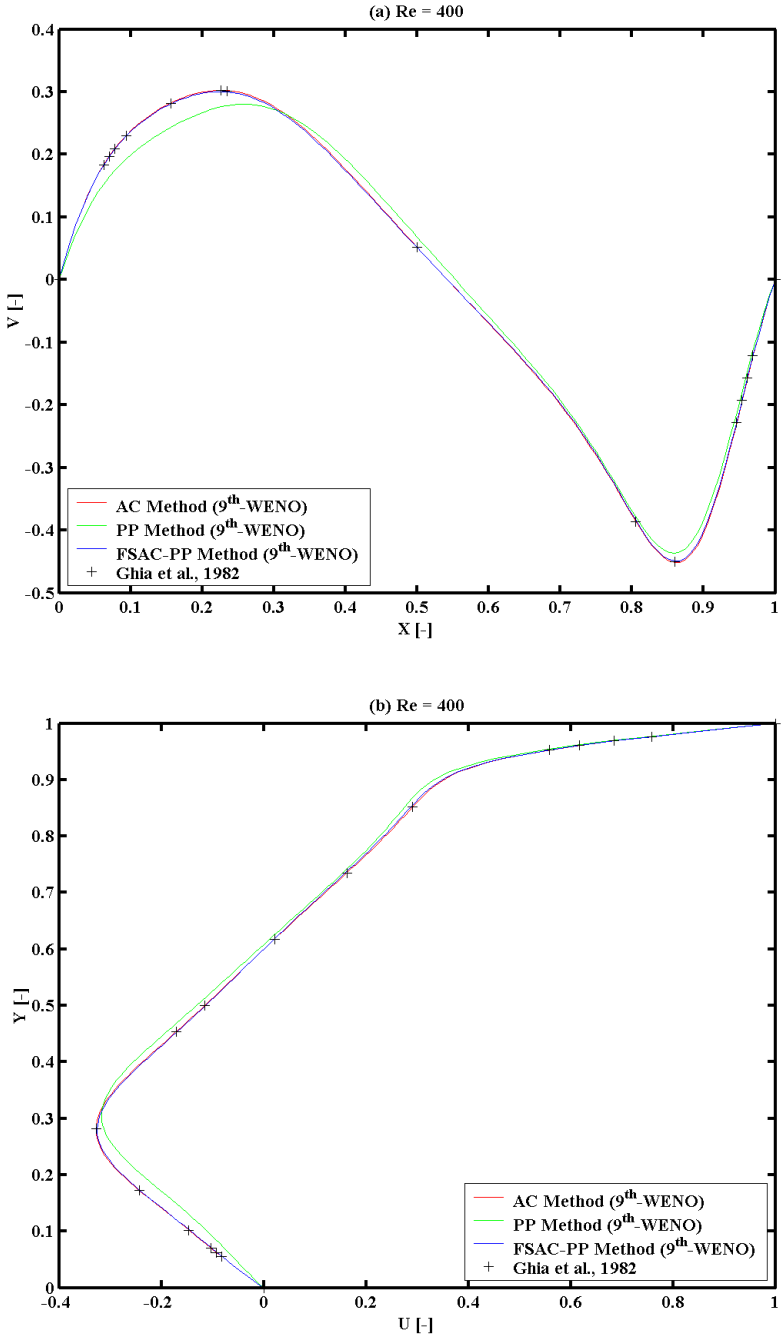

Figure 6.22: Results of the AC, PP, and FSAC-PP methods for the dimensionless velocity components V and U along a) horizontal and b) vertical centre-lines of the square cavity using 9^{th}-order WENO interpolation compared to the results of Ghia et al. [8] at $Re = 400$.

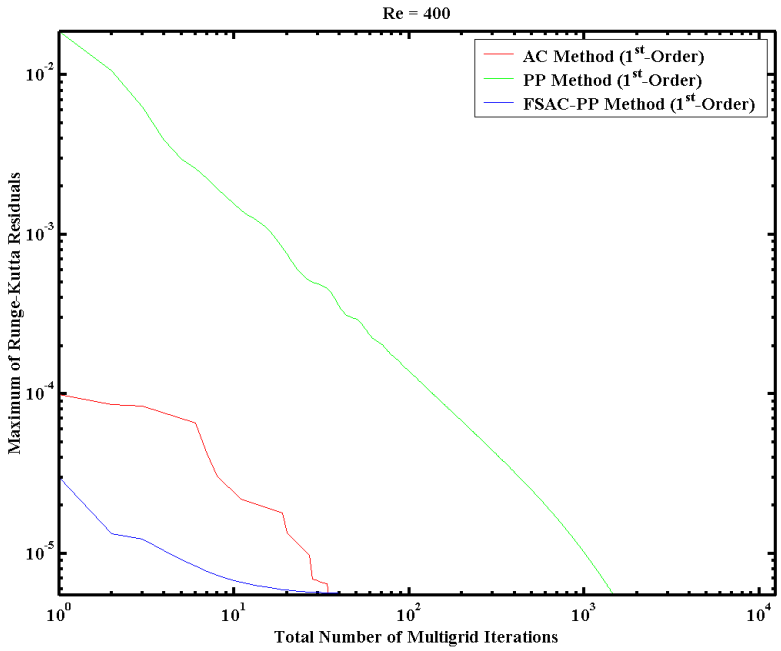

Figure 6.23: Comparison of the numerical convergence of the AC, PP, and FSAC-PP methods; maximum values of Runge-Kutta residuals versus total number of multigrid iterations on the fine grid using 1^{st}-order interpolation at $Re = 400$.

	$Re = 400$
	Order of Intercell Flux Interpolation: 1^{st}-Order
	Total Number of Multigrid Iterations N_{mg} on the Fine Grid
AC Method	159
PP Method	12360
FSAC-PP Method	113

Table 6.6: Total number of multigrid iterations on the fine grid using 1^{st}-order intercell flux interpolation at $Re = 400$.

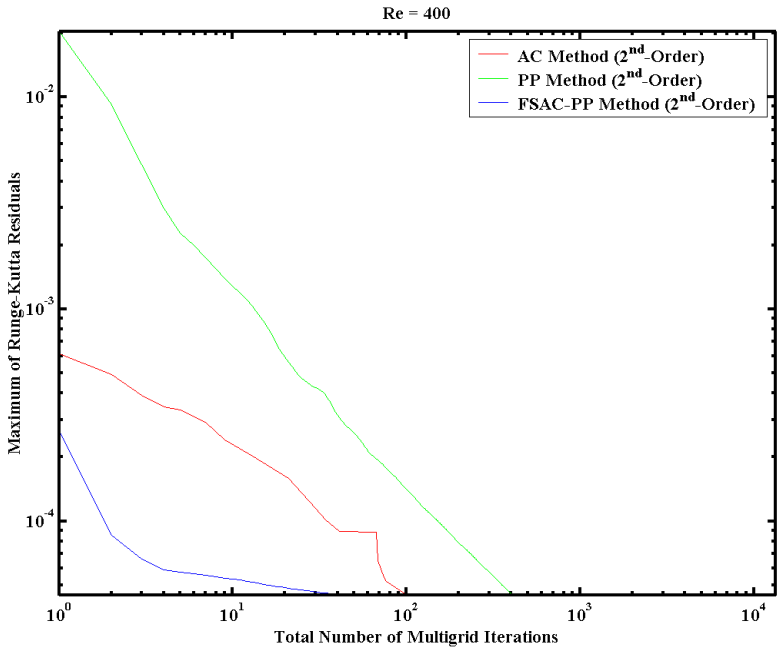

Figure 6.24: Comparison of the numerical convergence of the AC, PP, and FSAC-PP methods; maximum values of Runge-Kutta residuals versus total number of multigrid iterations on the fine grid using 2^{nd}-order interpolation at $Re = 400$.

	$Re = 400$
	Order of Intercell Flux Interpolation: 2^{nd}-Order
	Total Number of Multigrid Iterations N_{mg} on the Fine Grid
AC Method	1716
PP Method	13180
FSAC-PP Method	722

Table 6.7: Total number of multigrid iterations on the fine grid using 2^{nd}-order intercell flux interpolation at $Re = 400$.

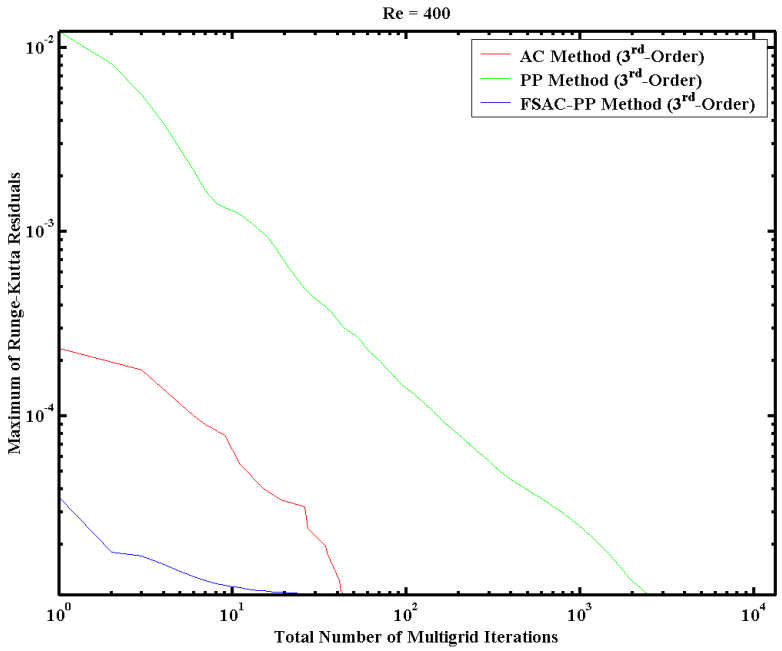

Figure 6.25: Comparison of the numerical convergence of the AC, PP, and FSAC-PP methods; maximum values of Runge-Kutta residuals versus total number of multigrid iterations on the fine grid using 3^{rd}-order interpolation at $Re = 400$.

	$Re = 400$
	Order of Intercell Flux Interpolation: 3^{rd}-Order
	Total Number of Multigrid Iterations N_{mg} on the Fine Grid
AC Method	175
PP Method	13180
FSAC-PP Method	115

Table 6.8: Total number of multigrid iterations on the fine grid using 3^{rd}-order intercell flux interpolation at $Re = 400$.

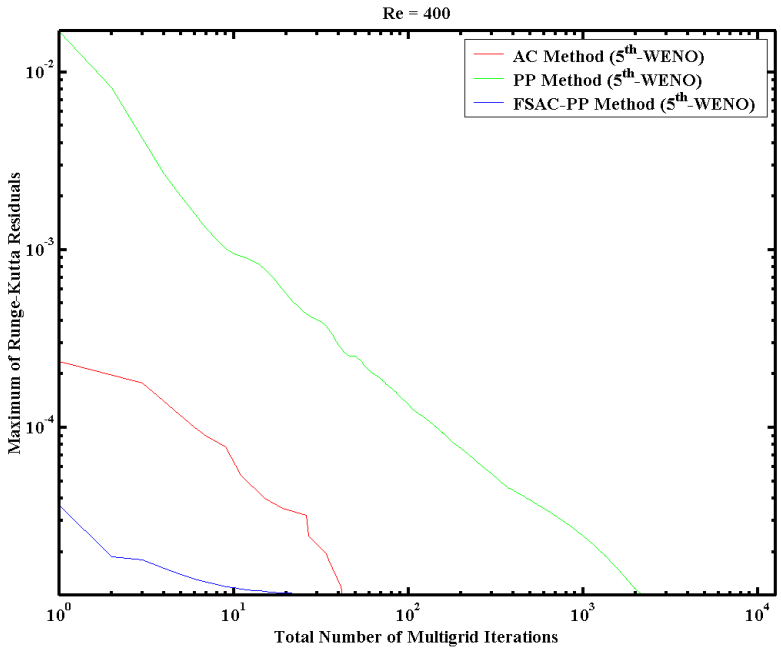

Figure 6.26: Comparison of the numerical convergence of the AC, PP, and FSAC-PP methods; maximum values of Runge-Kutta residuals versus total number of multigrid iterations on the fine grid using 5^{th}-order WENO interpolation at $Re = 400$.

	$Re = 400$
	Order of Intercell Flux Interpolation: 5^{th}-WENO
	Total Number of Multigrid Iterations N_{mg} on the Fine Grid
AC Method	346
PP Method	12600
FSAC-PP Method	114

Table 6.9: Total number of multigrid iterations on the fine grid using 5^{th}-order WENO intercell flux interpolation at $Re = 400$.

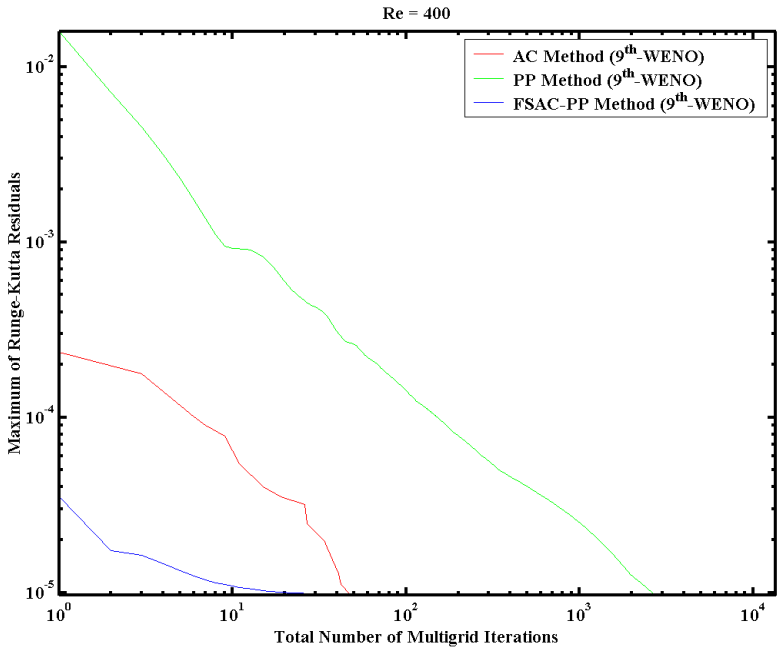

Figure 6.27: Comparison of the numerical convergence of the AC, PP, and FSAC-PP methods; maximum values of Runge-Kutta residuals versus total number of multigrid iterations on the fine grid using 9^{th}-order WENO interpolation at $Re = 400$.

	$Re = 400$
	Order of Intercell Flux Interpolation: 9^{th}-WENO
	Total Number of Multigrid Iterations N_{mg} on the Fine Grid
AC Method	283
PP Method	13400
FSAC-PP Method	125

Table 6.10: Total number of multigrid iterations on the fine grid using 9^{th}-order WENO intercell flux interpolation at $Re = 400$.

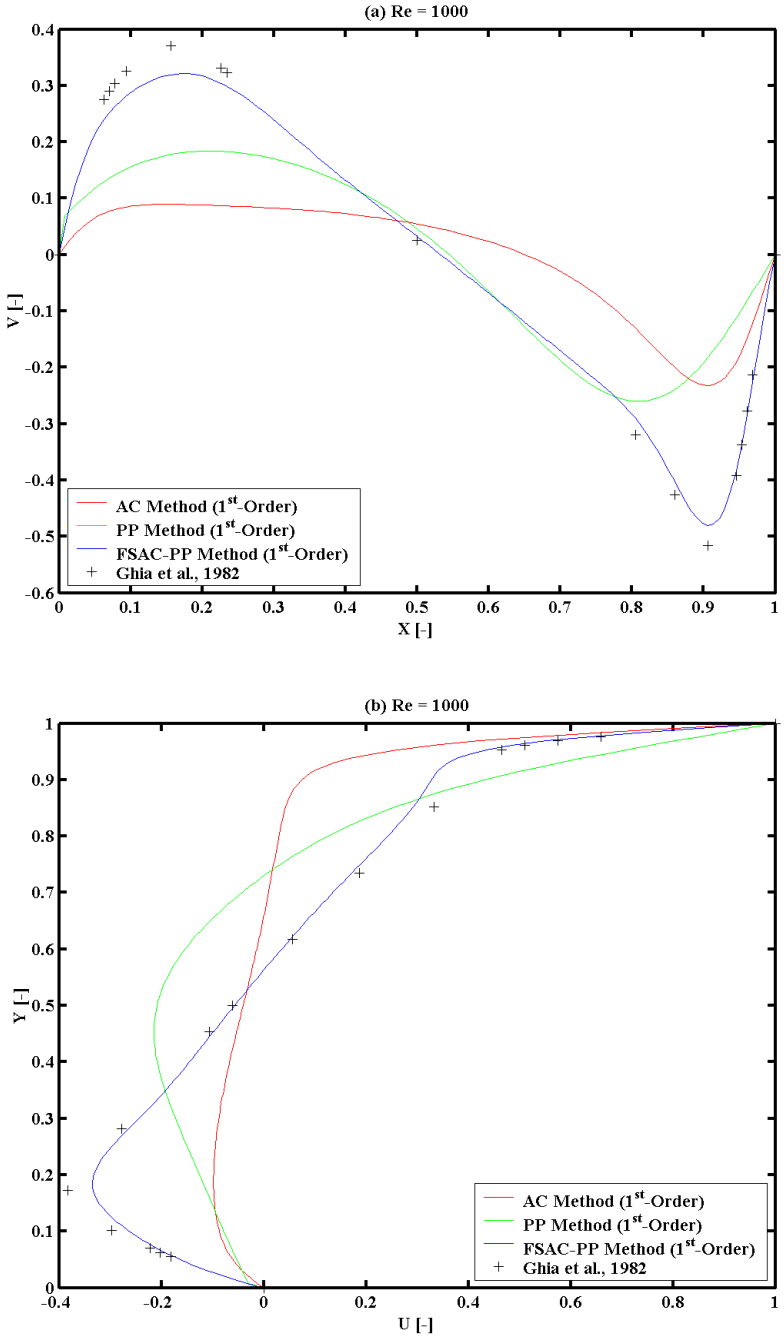

Figure 6.28: Results of the AC, PP, and FSAC-PP methods for the dimensionless velocity components V and U along a) horizontal and b) vertical centre-lines of the square cavity using 1^{st}-order interpolation compared to the results of Ghia et al. [8] at $Re = 1000$.

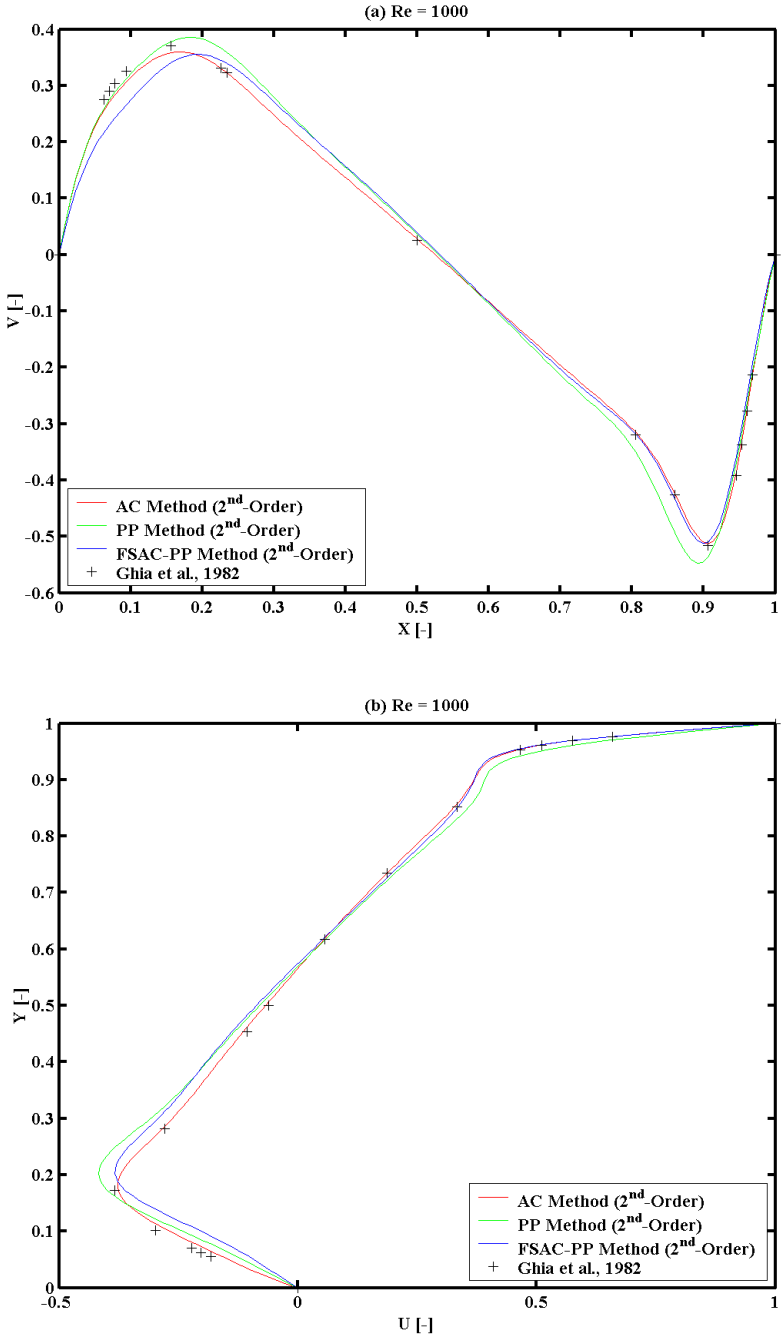

Figure 6.29: Results of the AC, PP, and FSAC-PP methods for the dimensionless velocity components V and U along a) horizontal and b) vertical centre-lines of the square cavity using 2^{nd}-order interpolation compared to the results of Ghia et al. [8] at $Re = 1000$.

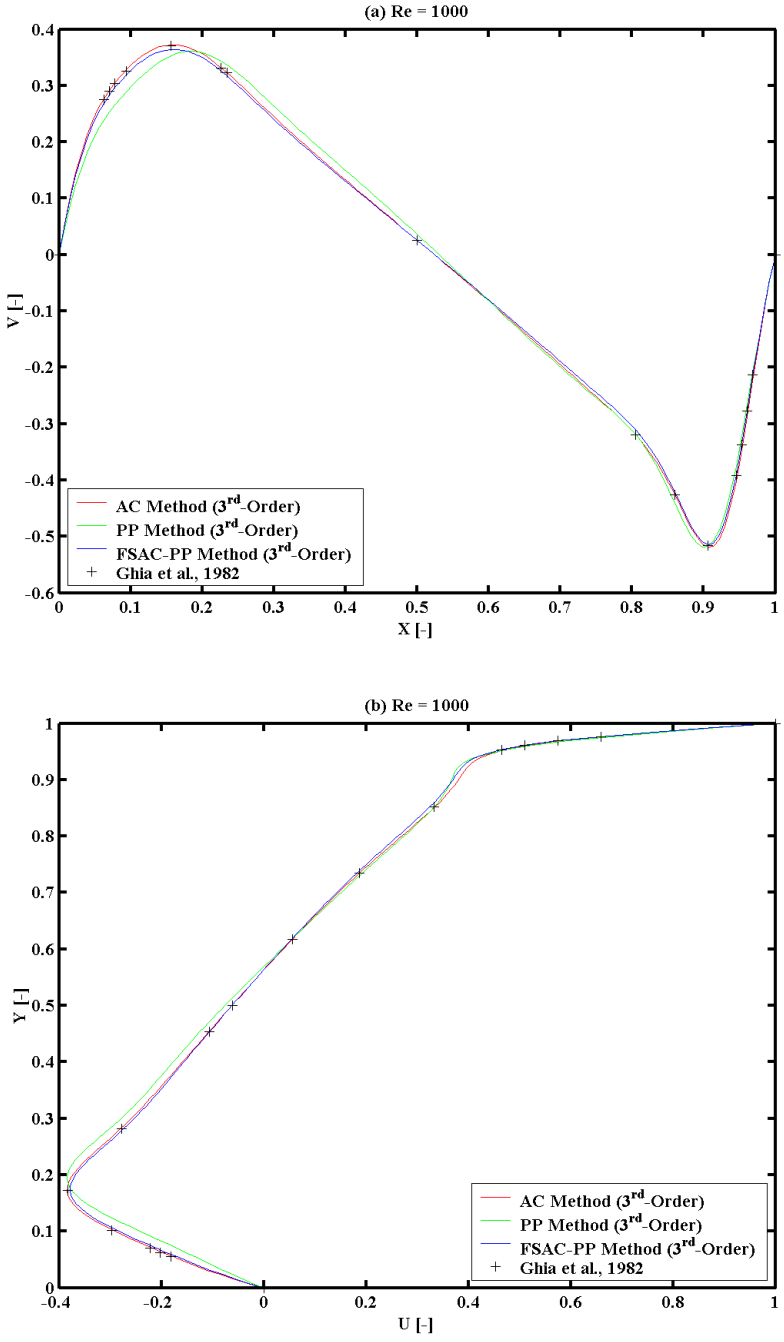

Figure 6.30: Results of the AC, PP, and FSAC-PP methods for the dimensionless velocity components V and U along a) horizontal and b) vertical centre-lines of the square cavity using 3^{rd}-order interpolation compared to the results of Ghia et al. [8] at $Re = 1000$.

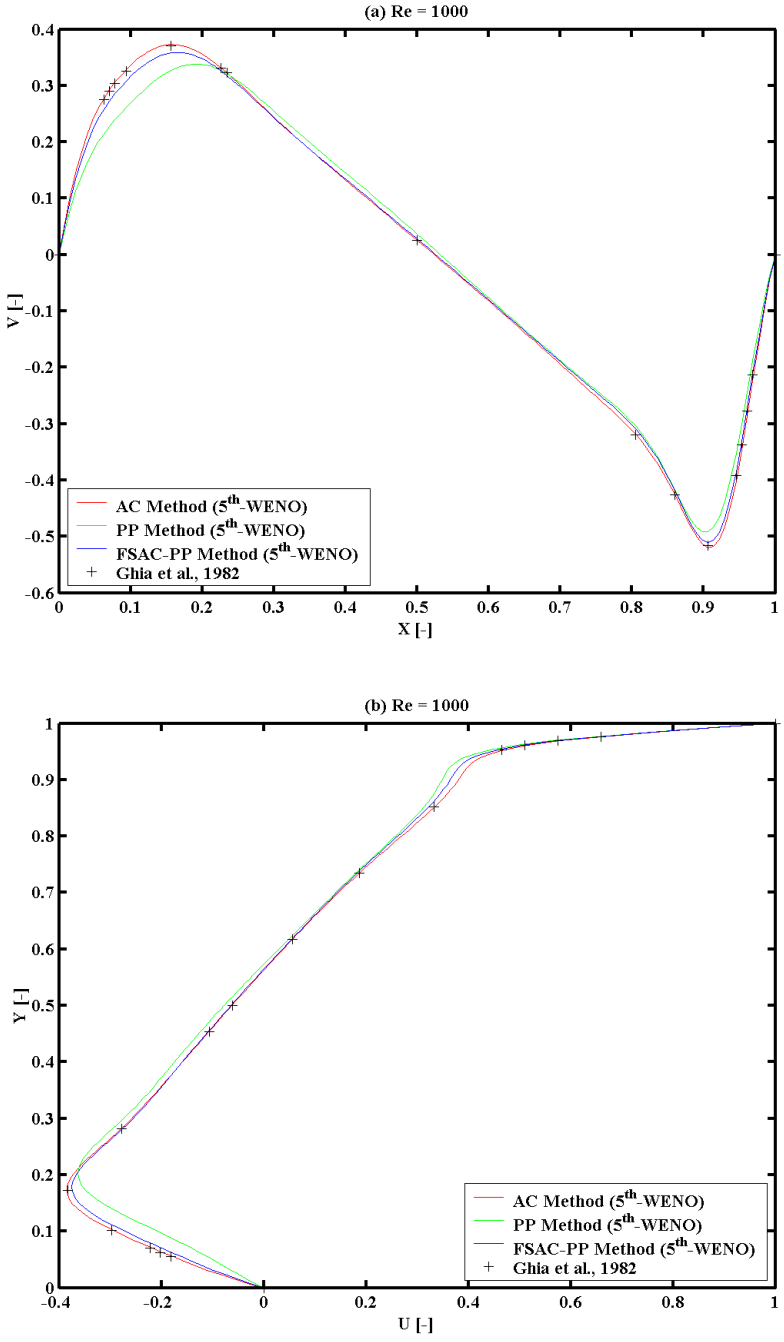

Figure 6.31: Results of the AC, PP, and FSAC-PP methods for the dimensionless velocity components V and U along a) horizontal and b) vertical centre-lines of the square cavity using 5^{th}-order WENO scheme compared to the results of Ghia et al. [8] at $Re = 1000$.

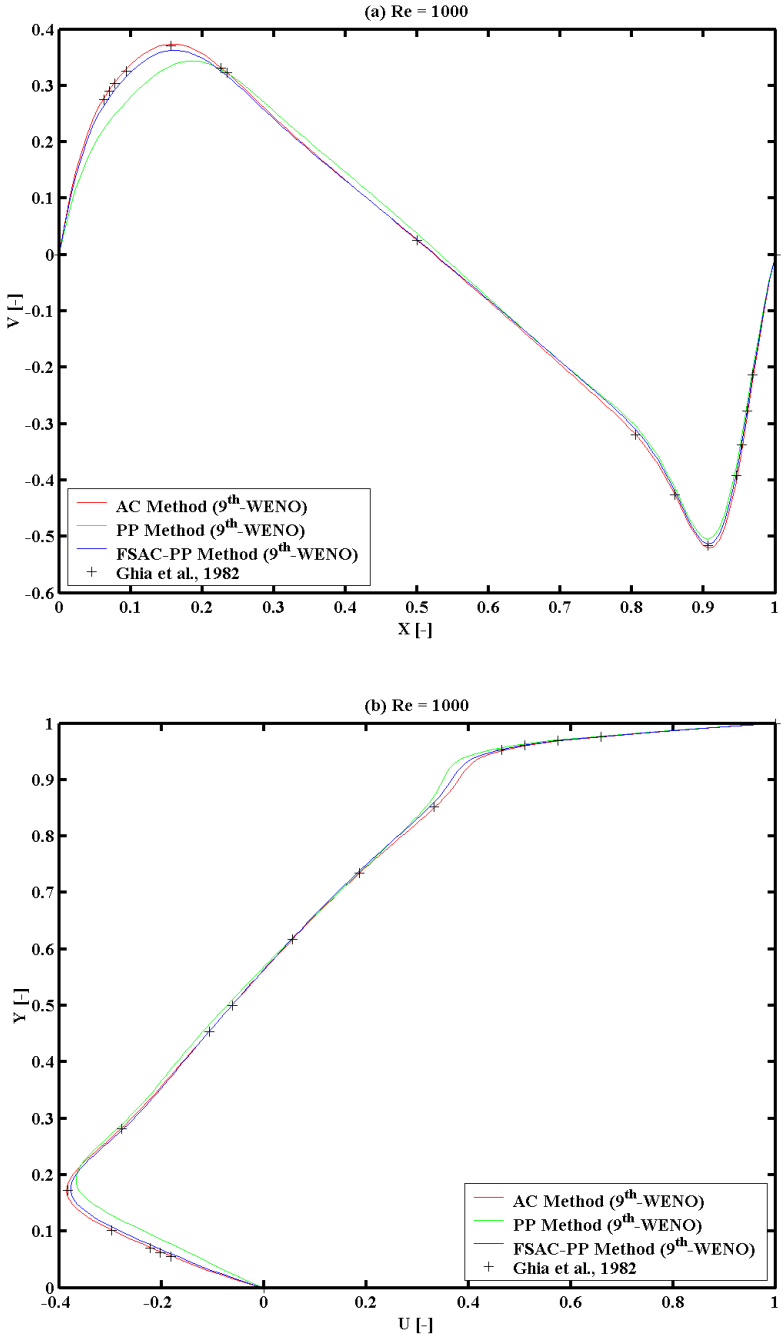

Figure 6.32: Results of the AC, PP, and FSAC-PP methods for the dimensionless velocity components V and U along a) horizontal and b) vertical centre-lines of the square cavity using 9^{th}-order WENO scheme compared to the results of Ghia et al. [8] at $Re = 1000$.

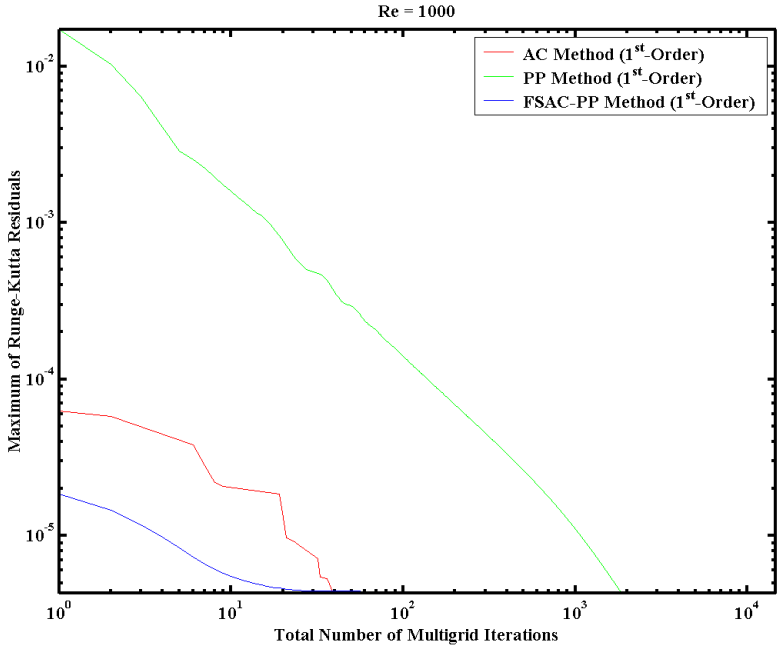

Figure 6.33: Comparison of the numerical convergence of the AC, PP, and FSAC-PP methods; maximum values of Runge-Kutta residuals versus total number of multigrid iterations on the fine grid using 1^{st}-order interpolation at $Re = 1000$.

	$Re = 1000$
	Order of Intercell Flux Interpolation: 1^{st}-Order
	Total Number of Multigrid Iterations N_{mg} on the Fine Grid
AC Method	189
PP Method	14490
FSAC-PP Method	162

Table 6.11: Total number of multigrid iterations on the fine grid using 1^{st}-order intercell flux interpolation at $Re = 1000$.

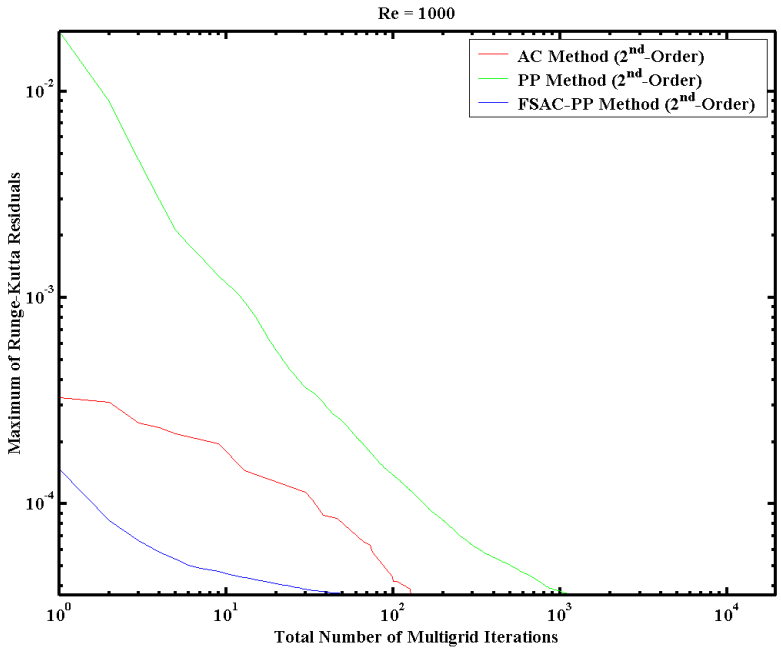

Figure 6.34: Comparison of the numerical convergence of the AC, PP, and FSAC-PP methods; maximum values of Runge-Kutta residuals versus total number of multigrid iterations on the fine grid using 2^{nd}-order interpolation at $Re = 1000$.

	$Re = 1000$
	Order of Intercell Flux Interpolation: 2^{nd}-Order
	Total Number of Multigrid Iterations N_{mg} on the Fine Grid
AC Method	526
PP Method	19380
FSAC-PP Method	403

Table 6.12: Total number of multigrid iterations on the fine grid using 2^{nd}-order intercell flux interpolation at $Re = 1000$.

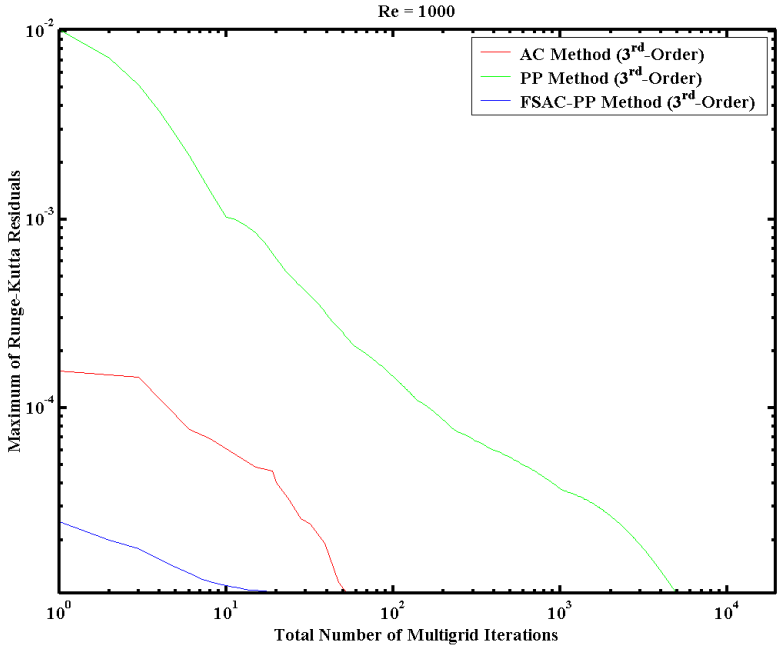

Figure 6.35: Comparison of the numerical convergence of the AC, PP, and FSAC-PP methods; maximum values of Runge-Kutta residuals versus total number of multigrid iterations on the fine grid using 3^{rd}-order interpolation at $Re = 1000$.

	$Re = 1000$
	Order of Intercell Flux Interpolation: 3^{rd}-Order
	Total Number of Multigrid Iterations N_{mg} on the Fine Grid
AC Method	521
PP Method	19310
FSAC-PP Method	118

Table 6.13: Total number of multigrid iterations on the fine grid using 3^{rd}-order intercell flux interpolation at $Re = 1000$.

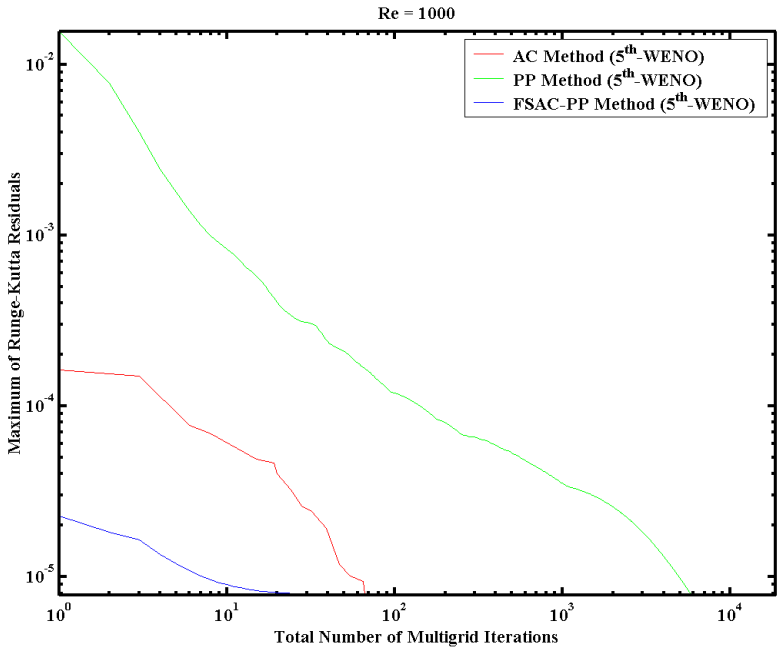

Figure 6.36: Comparison of the numerical convergence of the AC, PP, and FSAC-PP methods; maximum values of Runge-Kutta residuals versus total number of multigrid iterations on the fine grid using 5^{th}-order WENO scheme at $Re = 1000$.

	$Re = 1000$
	Order of Intercell Flux Interpolation: 5^{th}-WENO
	Total Number of Multigrid Iterations N_{mg} on the Fine Grid
AC Method	521
PP Method	18460
FSAC-PP Method	104

Table 6.14: Total number of multigrid iterations on the fine grid using 5^{th}-order WENO intercell flux interpolation at $Re = 1000$.

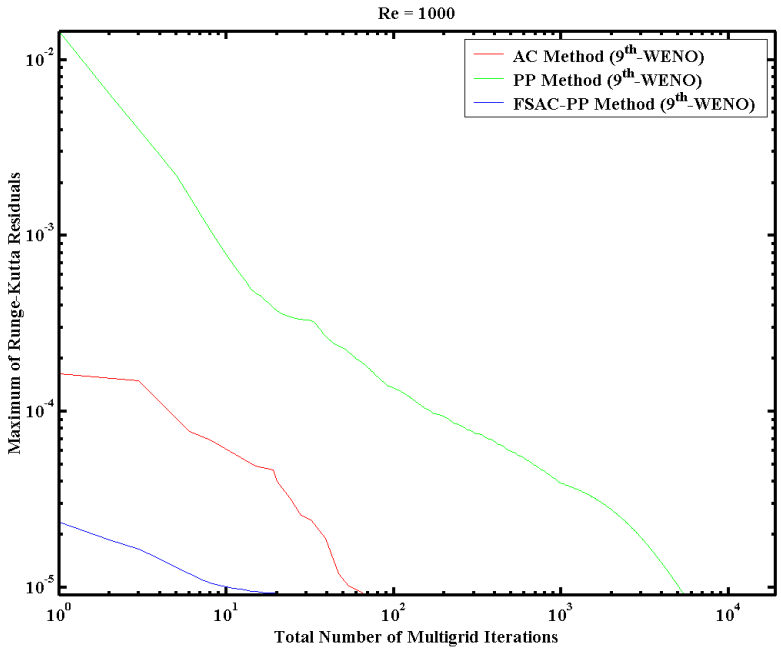

Figure 6.37: Comparison of the numerical convergence of the AC, PP, and FSAC-PP methods; maximum values of Runge-Kutta residuals versus total number of multigrid iterations on the fine grid using 9^{th}-order WENO scheme at $Re = 1000$.

	$Re = 1000$
	Order of Intercell Flux Interpolation: 9^{th}-WENO
	Total Number of Multigrid Iterations N_{mg} on the Fine Grid
AC Method	521
PP Method	18990
FSAC-PP Method	112

Table 6.15: Total number of multigrid iterations on the fine grid using 9^{th}-order WENO intercell flux interpolation at $Re = 1000$.

Total Number of Multigrid Iterations on the Fine Grid				
Intercell Flux Interpolation	Solution Method	$Re = 100$	$Re = 400$	$Re = 1000$
1^{st}-Order	AC	107	159	189
	PP	7280	12360	14490
	FSAC-PP	97	113	162
2^{nd}-Order	AC	788	1716	526
	PP	9780	13180	19380
	FSAC-PP	202	722	403
3^{rd}-Order	AC	157	175	521
	PP	8350	13180	19310
	FSAC-PP	107	115	118
5^{th}-WENO	AC	157	346	521
	PP	8940	12600	18460
	FSAC-PP	102	114	104
9^{th}-WENO	AC	157	283	521
	PP	8370	13400	18990
	FSAC-PP	105	125	112

Table 6.16: Total number of multigrid iterations on the fine grid using different intercell flux interpolations at $Re = 100$, 400, and 1000.

Maximum Relative Errors along Horizontal Centre-Line [-]				
Intercell Flux Interpolation	Solution Method	$Re = 100$	$Re = 400$	$Re = 1000$
1^{st}-Order	AC	0.19925	0.61997	1.15918
	PP	0.42650	0.53882	0.82317
	FSAC-PP	0.07362	0.56081	0.28518
2^{nd}-Order	AC	0.05110	0.61561	0.10497
	PP	0.27482	0.58735	0.45352
	FSAC-PP	0.05531	0.61311	0.57405
3^{rd}-Order	AC	0.05420	0.62387	0.04062
	PP	0.07968	0.53539	0.43522
	FSAC-PP	0.05270	0.61038	0.02942
5^{th}-WENO	AC	0.05415	0.62492	0.03863
	PP	0.07575	0.50669	0.45148
	FSAC-PP	0.05283	0.60976	0.10794
9^{th}-WENO	AC	0.05391	0.62612	0.04084
	PP	0.07455	0.53552	0.47184
	FSAC-PP	0.05277	0.61141	0.05262

Table 6.17: Maximum relative errors of the AC, PP, and FSAC-PP methods for the dimensionless velocity component V along horizontal centre-line of the square cavity compared to the results of Ghia et al. [8] at $Re = 100$, 400, and 1000.

Maximum Relative Errors along Vertical Centre-Line [-]				
Intercell Flux Interpolation	Solution Method	$Re = 100$	$Re = 400$	$Re = 1000$
1^{st}-Order	AC	15.67207	3.11797	1.16409
	PP	13.76639	8.12039	3.42777
	FSAC-PP	0.70087	0.19398	0.13116
2^{nd}-Order	AC	0.27663	0.05174	0.12761
	PP	0.63502	0.21816	0.31473
	FSAC-PP	0.08482	0.03716	0.44063
3^{rd}-Order	AC	0.23427	0.03705	0.02469
	PP	0.22983	0.46706	0.26077
	FSAC-PP	0.11597	0.05844	0.06324
5^{th}-WENO	AC	0.24897	0.03432	0.02355
	PP	0.29880	0.58807	0.39702
	FSAC-PP	0.12395	0.06039	0.11584
9^{th}-WENO	AC	0.24727	0.03205	0.02236
	PP	0.36641	0.46733	0.28609
	FSAC-PP	0.12054	0.05240	0.07939

Table 6.18: Maximum relative errors of the AC, PP, and FSAC-PP methods for dimensionless velocity component U along vertical centre-line of the square cavity compared to the results of Ghia et al. [8] at $Re = 100$, 400, and 1000.

6.3 Three-Dimensional Flow in a Lid Driven Cavity

In this section, the implemented FSAC-PP method has been tested for incompressible turbulent flows compared to AC and PP methods, and experimental data of Prasad and Koseff [17] in a lid driven cubical cavity at $Re = 3200$, and $10\,000$. However, the main scope of this thesis is to develop an accurate and efficient method for solving low Reynolds number laminar flow problems in microfluidic systems, but the proposed FSAC-PP method is a new approach, therefore, it is indispensable to test at least the capability of this method at higher Reynolds numbers as well. The FSAC-PP method is relying on the Godunov procedure in this thesis, therefore, the numerical treatment of non-linear advective fluxes makes unnecessary any restrictions for cell Reynolds numbers at high-speed flows [115, 27]. It means that the proposed FSAC-PP method provides the possibility to simulate flows relying on the Implicit Large Eddy Simulation (ILES) technique at high Reynolds numbers; in which case the subgrid scale modelling is not required. Consequently, the turbulent flow simulations have been performed by using the ILES method.

6.3.1 The Benchmark Cubical Cavity and Problem Setup

The unsteady, incompressible turbulent flow in the lid driven cubical cavity is of central interest in the field of CFD, because both simulation benchmark cases and measurement are available in the literature [177, 178, 17]. The geometry of the full measurement configuration of Prasad and Koseff can be seen in Figure 6.38 [17, p. 209].

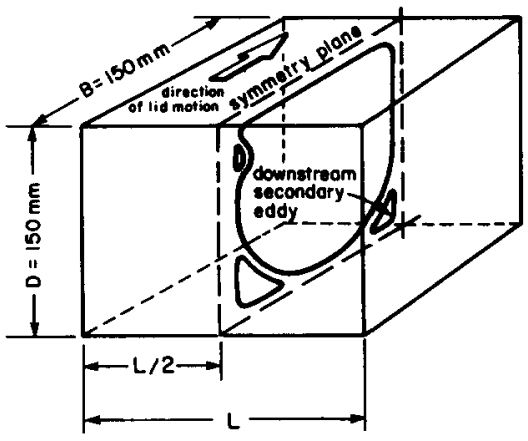

Figure 6.38: Geometrical dimensions of the cubical cavity configuration measured by Prasad and Koseff (1989) [17, p. 209] at $L = B = D = 150\,mm$ with SAR of 1:1.

The geometrical dimensions of the numerically investigated three-dimensional benchmark are equal to the cubical cavity of the experiment: $L = B = D = 150\,mm$ at a spanwise aspect ratio (SAR) of 1:1 [17] (see Figure 6.38). The computational grid has been shown in Figure 6.39, which consists of $64 \times 64 \times 64$ node points $(63 \times 63 \times 63$ control cells$)$ on the fine grid as the extension of the two-dimensional test case to three-dimensions.

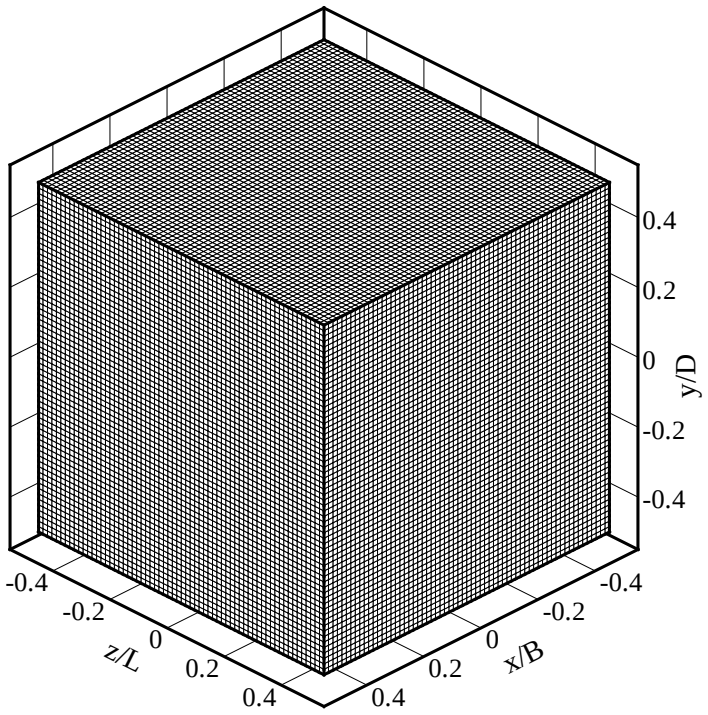

Figure 6.39: Equidistant computational grid of the cubical cavity using dimensionless coordinates, where $L = B = D = 150\,mm$ with SAR of 1:1.

Similarly to the two-dimensional case, a mathematical task can be formulated in terms of boundary and initial conditions for the three-dimensional turbulent flow in the lid driven cubical cavity. Dimensionless quantities have also been used in the simulations, therefore, the spatial coordinates have been normalized by the characteristic length L of the square cavity (see Figure 6.39). The dimensional velocity components *u, v* and *w* are normalized by the average velocity U_b of the moving lid on the top. No-slip Dirichlet-type boundary conditions have been prescribed for the dimensionless velocity components *U, V* and *W* on the non-moving wall as $U_{wall} = V_{wall} = W_{wall} = 0$. Dirichlet-type boundary conditions have also been imposed for the dimensionless velocity components U, V and W on the moving wall as $U_{lid} = 1$, $V_{lid} = 0$ and $W_{lid} = 0$. To obtain a unique solution of the incompressible Navier-Stokes equation using the ILES method for this benchmark case,

the reference static pressure was set to be zero in the lower left corner of the front side of the cubical cavity. Consequently, Neumann-type boundary conditions, in other words the inviscid-type boundary conditions (see in section 4.2.2), have been prescribed for the pressure on both non-moving and moving walls; which means that the normal derivative of the pressure vanishes as $\partial P/\partial n = 0$. Similarly to the two-dimensional case, it is important to mention that the Neumann-type boundary conditions have been considered to be mathematically correct for the pressure, see more details in [170].

The unsteady, incompressible Navier-Stokes equations have numerically been solved by using the ILES method via a dual-time stepping procedure. It means that the pseudo-time stepping procedure has to be performed until the steady-state solution is achieved, then the process has to be advanced at real time. The dimensionless velocity profiles for velocity components V and U have been compared to the aforementioned experimental data along the horizontal and vertical centre-lines of the mid-plane of the cubical cavity at $z/L = 0$ based on Figure 6.39. The intercell fluxes of the non-linear advective terms in the Navier-Stokes equations have been interpolated by employing the 9^{th}-order WENO scheme, because the computational grid is relatively coarse for this benchmark test case. Note that when the PP method has been used itself, the non-linear advective terms of the scalar momentum equations have been discretized by employing the well-known Lax-Friedrichs scheme with a small time-step size as $\triangle t = 0.001s$.

6.3.2 Unsteady Turbulent Flow at *Re* = 3200, and 10 000

For solving the three-dimensional high-speed turbulent flow problem in the lid driven cubical cavity, the third velocity component becomes significant due to the presence of strong velocity fluctuations, which have a high-frequency. At the early stage of the flow field formation, a clockwise-rotating primary large eddy appears in the upper right corner, which slowly flows downstream [135]. During this period of time, the counter-rotating downstream secondary eddy starts to develop from nearly the mid-point of the right side of the cubical cavity towards the lower right corner. In the finally developed steady-state, the primary large eddy is located in the middle of the symmetry plane; two counter-rotating secondary eddies appear in the lower corners; and a third vortex formation appears slightly lower than the left upper corner [135, 17].

The laminar-turbulent transition flow region at $Re = 3200$ and the strongly turbulent flow at $Re = 10000$ have also been simulated, and the horizontal and vertical velocity profiles have been compared against experimental data [17] in the mid-plane at $z/L = 0$. The experimental data of Prasad and Koseff [17] for the dimensionless mean velocity profiles, the dimensionless root-mean-square (RMS) profiles, and the dimensionless shear stress $\overline{U'V'}$ profiles can be seen at $Re = 3200$ and at $Re = 10000$ in Figures 6.40 and

6.44, respectively. The RMS profiles represent the normal stresses in the Reynolds stress tensor. By employing the ILES method, the elements of the Reynolds stress tensor are modelled implicitly, but these values can be recovered by using spatial averaging. The relationship between the Reynolds Averaged Navier-Stokes (RANS) and the ILES method based turbulence modelling can be expressed [27] as

$$\mathbf{U}_T = \overline{\mathbf{U}} + \mathbf{U}', \tag{6.1}$$

where $\mathbf{U}_T$ is the instantaneous (turbulent) velocity field, $\overline{\mathbf{U}}$ is the spatial averaged mean velocity field, and $\mathbf{U}'$ is the fluctuating velocity field. The instantaneous velocity field $\mathbf{U}_{ILES} = \mathbf{U}_T$ is obtained as the result of the ILES method, and the spatial averaged velocity field may be computed by

$$\overline{\mathbf{U}} = \frac{1}{N} \sum_{i,j,k}^{N} (\mathbf{U}_{ILES})_{i,j,k}\,, \tag{6.2}$$

where N is the number of computational cells of the domain. Relying on the Reynolds decomposition (6.1), the fluctuating velocity field can be approximated as

$$\mathbf{U}' = \mathbf{U}_{ILES} - \overline{\mathbf{U}}, \tag{6.3}$$

and averaging of the products of fluctuating velocity components U', V' and W', the elements of the Reynolds stress tensor can be recovered. The mean velocity-, normal and shear stress profiles have been computed by employing the AC, PP and FSAC-PP methods in the framework of the ILES method [179]. The computational results have been shown in Figures 6.41 to 6.43 and in Figures 6.45 to 6.47 at $Re = 3200$ and at $Re = 10000$, respectively. The lid driven cubical cavity flow at high Reynolds number was also investigated by Leriche [178] and Leriche et al. [177] using Direct Numerical Simulation (DNS). The present numerical results show that the AC, PP and FSAC-PP methods capture the mean velocity components better than the RMS main and shear stress profiles compared to the experimental data of [17]. The RMS main and shear stress profiles follow the tendency of the measured values with significant deviations between experiments and simulations, which are similar to the DNS results of Leriche et al. [177]. According to Leriche et al. [177], the differences in the fluctuating field between the simulation and the experiment are caused by the measurement errors approaching the moving wall. Therefore, the deviations observed in the present simulations may be due to the same reason. Overall, the FSAC-PP method leads to a fairly good and acceptable agreement with the experimental data for these high Reynolds number flows.

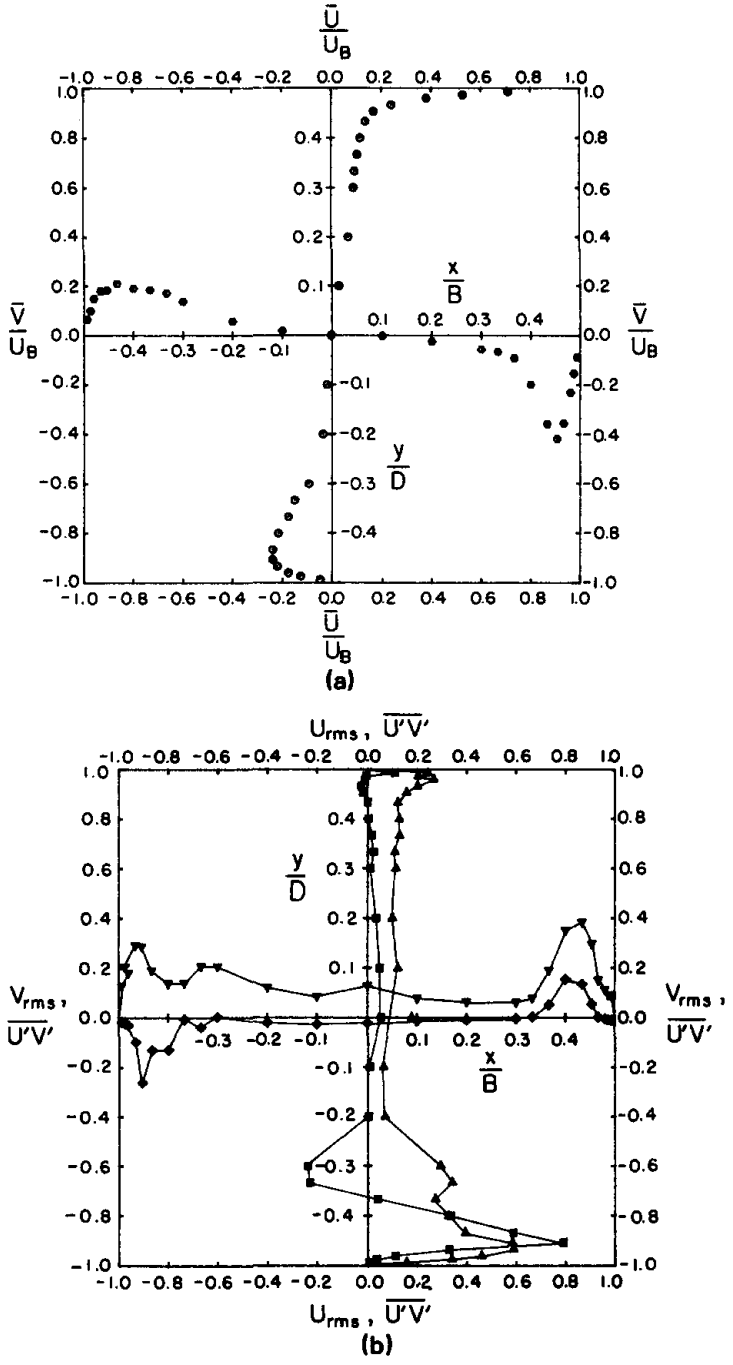

FIG. 5. Mean, rms, and $\overline{U'V'}$ profiles (Re = 3200, SAR = 1:1). (a) ⊙: $\overline{U}/U_B$, ○: $\overline{V}/U_B$; (b) △: $10\sqrt{\overline{U'^2}}/U_B$, ▽:$10\sqrt{\overline{V'^2}}/U_B$, □, ◇: $500\,\overline{U'V'}/U_B^2$.

Figure 6.40: Experimental data taken from Prasad and Koseff (1989) with SAR of 1:1 at $Re = 3200$ [17, p. 211].

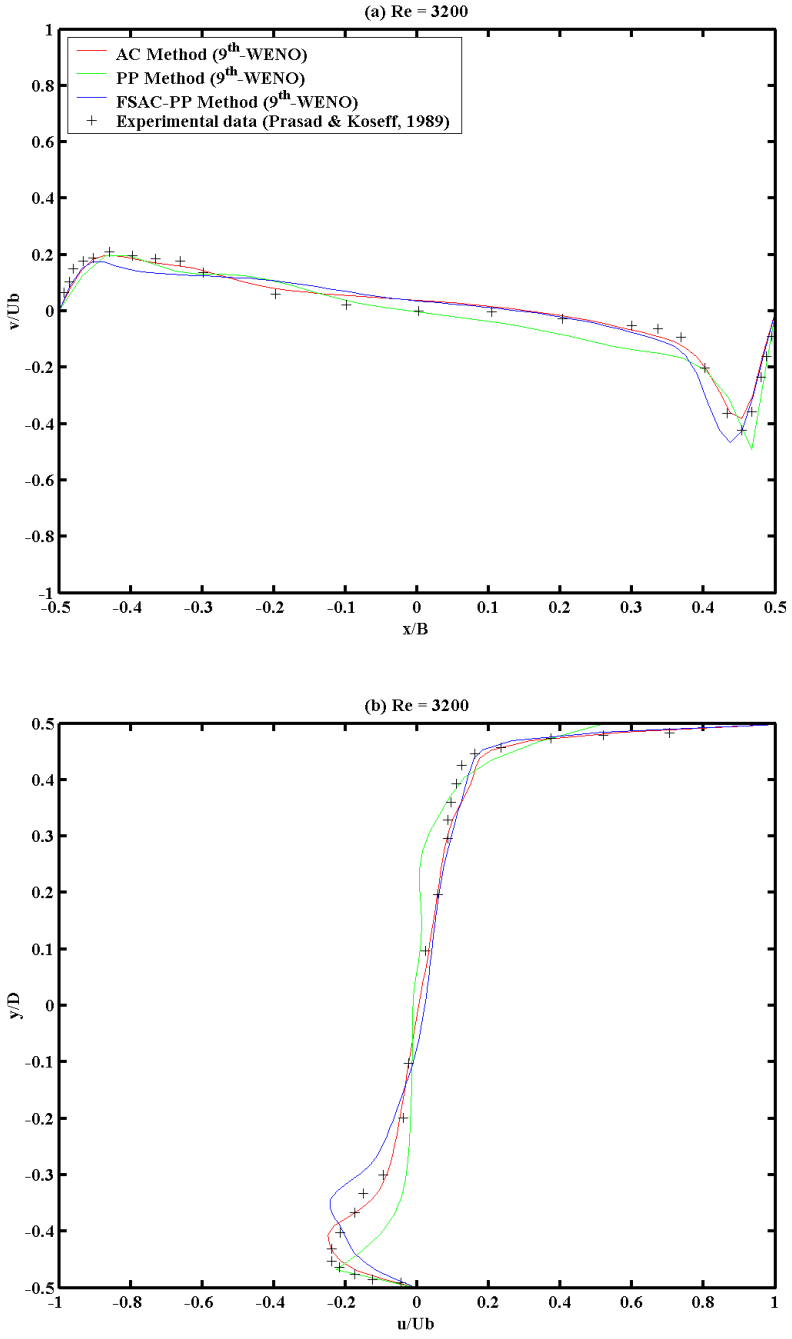

Figure 6.41: ILES results using the AC, PP, and FSAC-PP methods and experimental data of [17, p. 211] in the mid-plane $z/L = 0$ with SAR of 1:1 at $Re = 3200$; dimensionless mean velocity profiles along a) horizontal and b) vertical centre-lines.

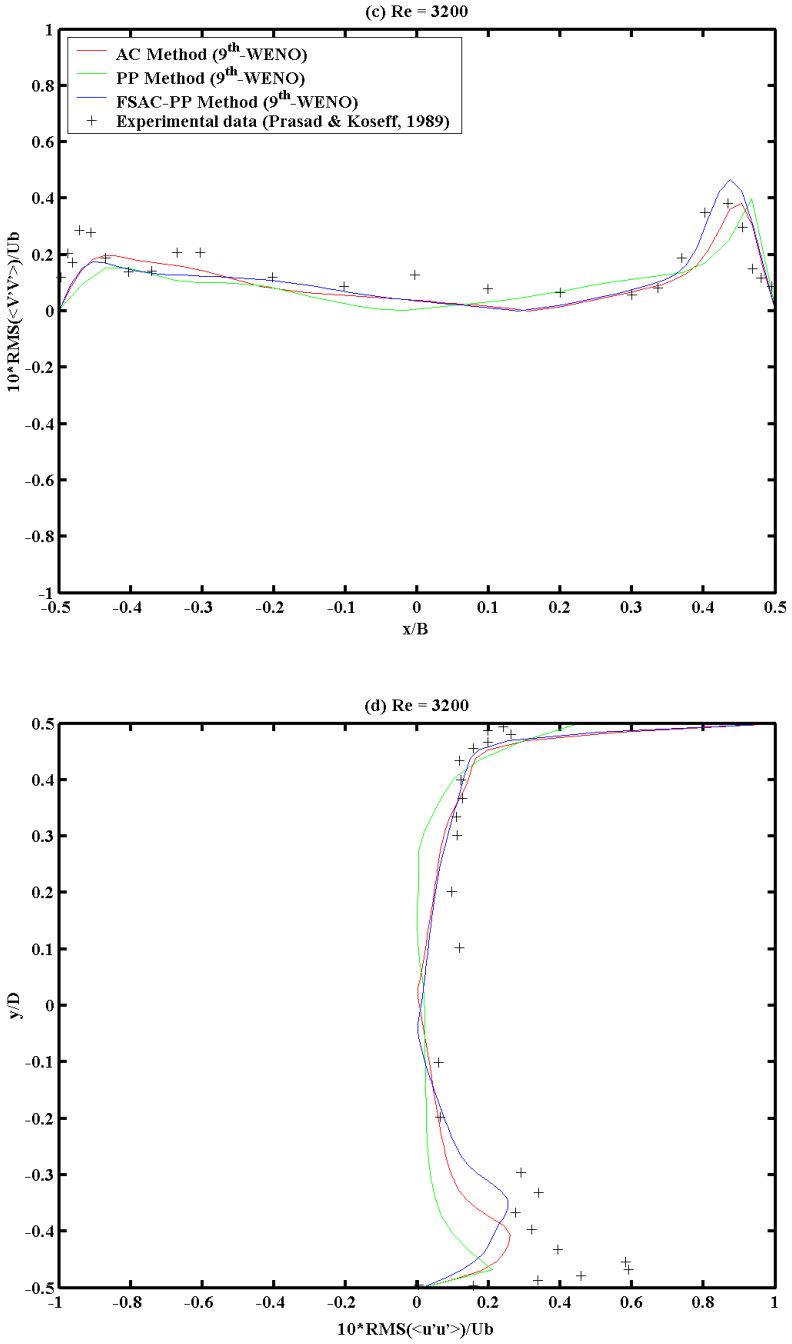

Figure 6.42: ILES results using the AC, PP, and FSAC-PP methods and experimental data of [17, p. 211] in the mid-plane $z/L = 0$ with SAR of 1:1 at $Re = 3200$; dimensionless normal (main) stress profiles $10\sqrt{\overline{V'^2}}/U_b$ and $10\sqrt{\overline{U'^2}}/U_b$ along c) horizontal and d) vertical centre-lines.

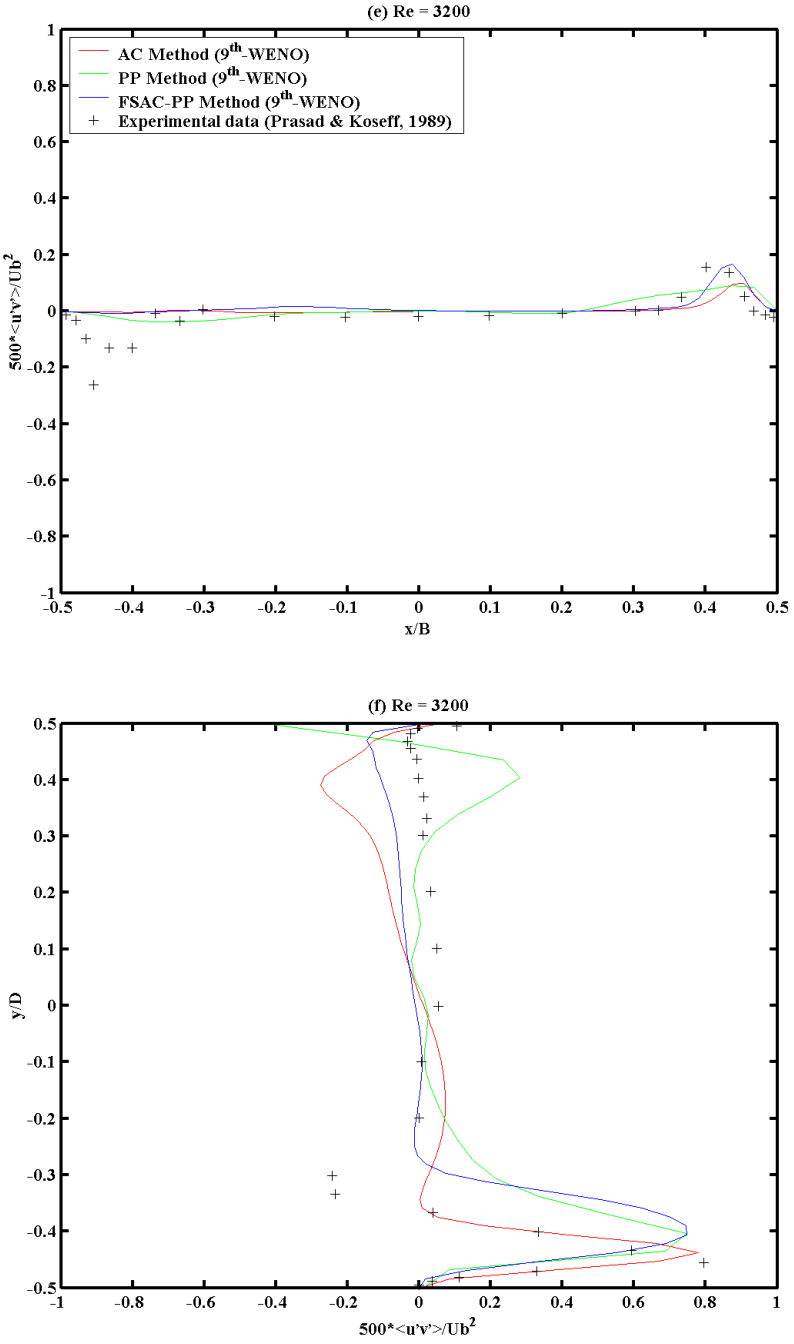

Figure 6.43: ILES results using the AC, PP, and FSAC-PP methods and experimental data of [17, p. 211] in the mid-plane $z/L = 0$ with SAR of 1:1 at $Re = 3200$; shear stress profiles $500\sqrt{\overline{U'V'}}/U_b^2$ along e) horizontal and f) vertical centre-lines.

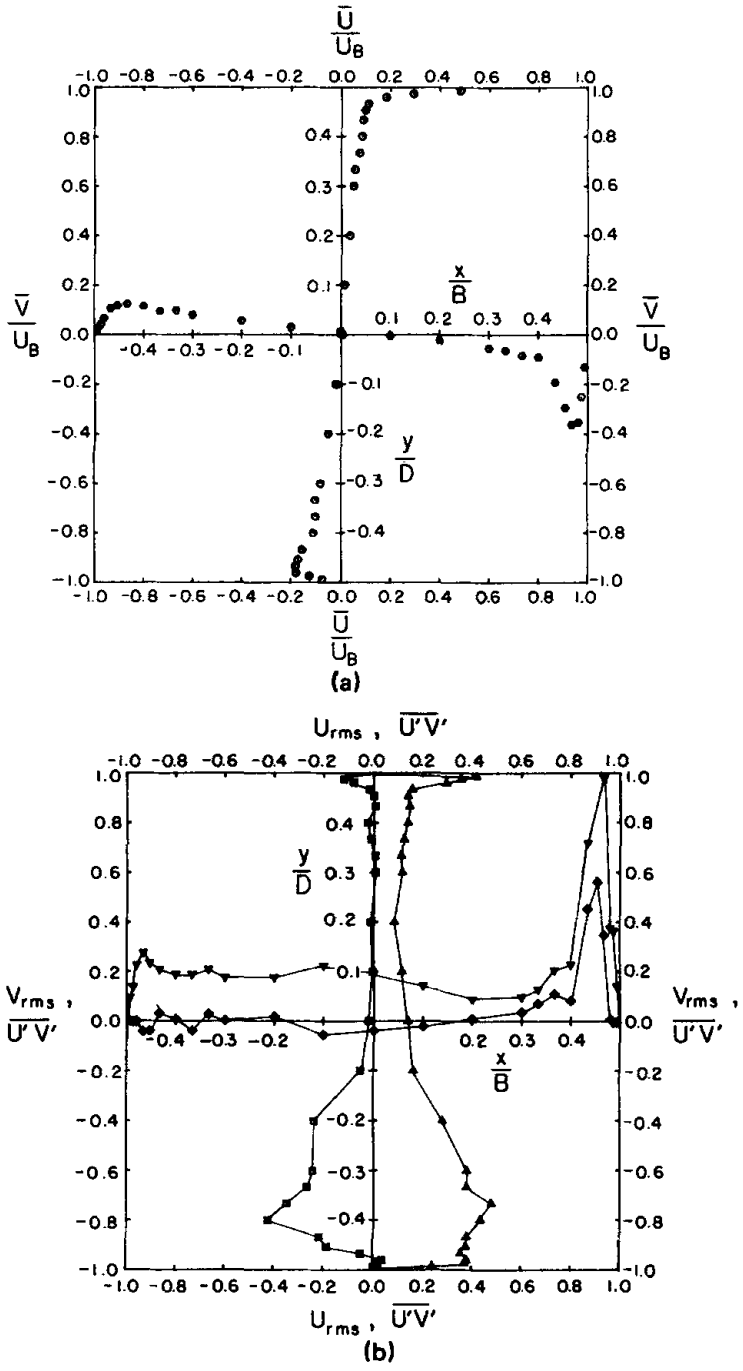

FIG. 7. Mean, rms, and $\overline{U'V'}$ profiles (Re = 10 000, SAR = 1:1). (a) ⊙: $\overline{U}/U_B$, ⊙: $\overline{V}/U_B$; (b) △: $10\sqrt{\overline{U'^2}}/U_B$, ▽: $10\sqrt{\overline{V'^2}}/U_B$, □, ◇: $500\ \overline{U'V'}/U_B^2$.

Figure 6.44: Experimental data taken from Prasad and Koseff (1989) with SAR of 1:1 at $Re = 10000$ [17, p. 212].

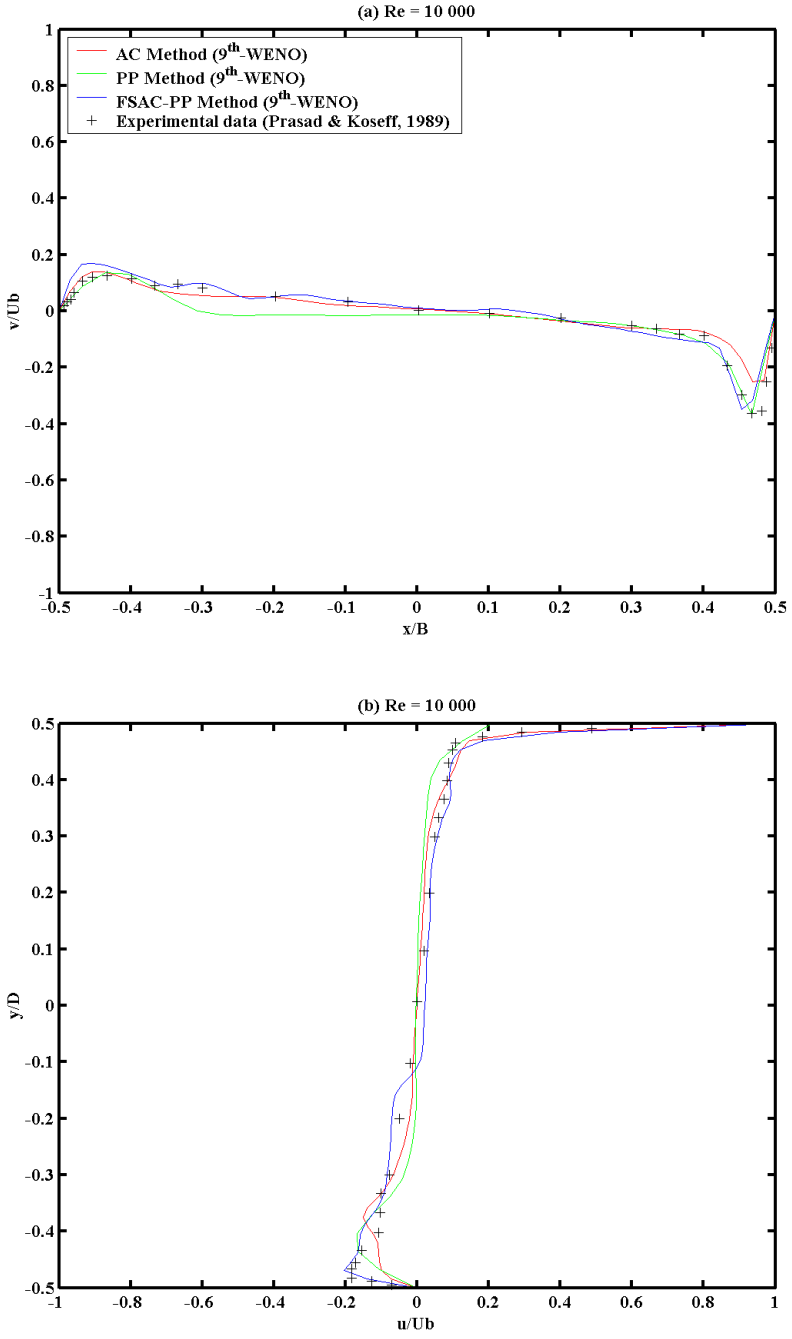

Figure 6.45: ILES results using the AC, PP, and FSAC-PP methods and experimental data of [17, p. 211] in the mid-plane $z/L = 0$ with SAR of 1:1 at $Re = 10\,000$; dimensionless mean velocity profiles along a) horizontal and b) vertical centre-lines.

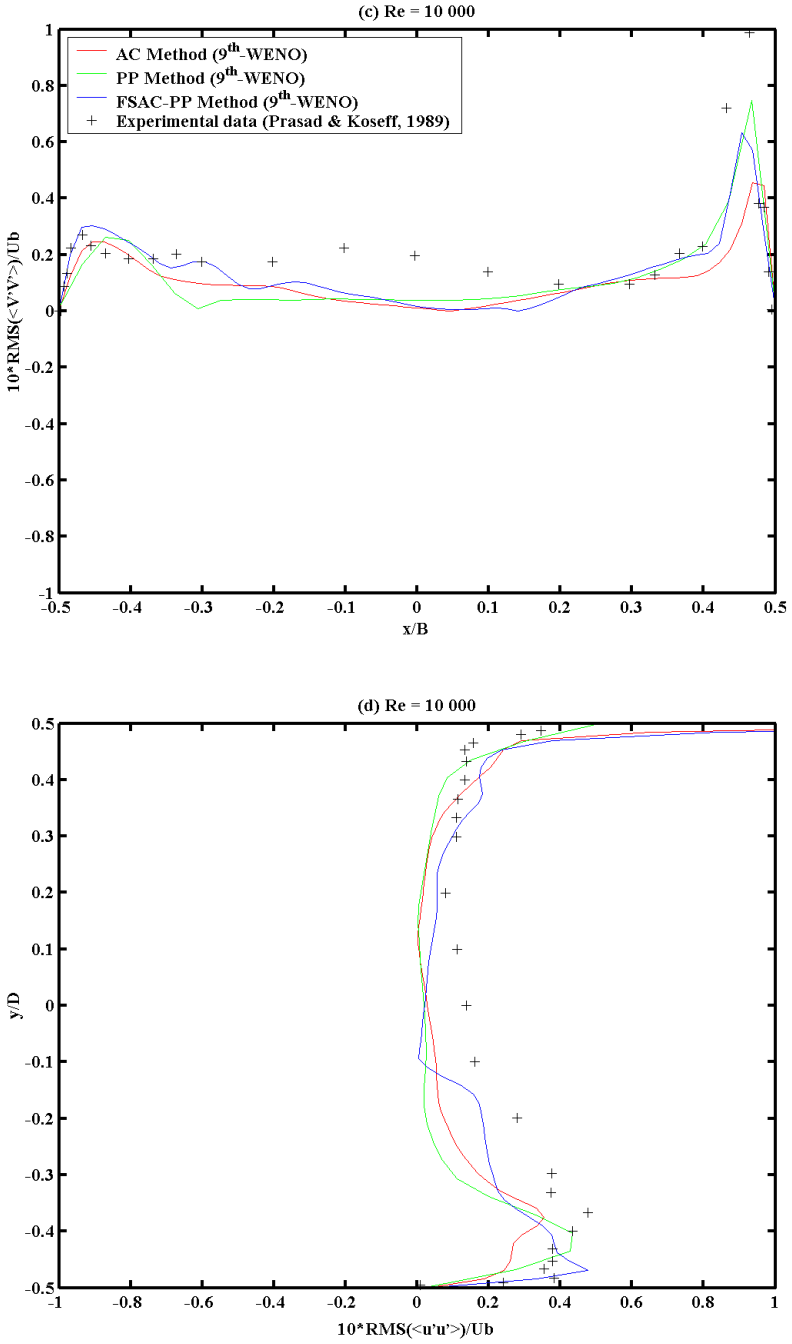

Figure 6.46: ILES results using the AC, PP, and FSAC-PP methods and experimental data of [17, p. 211] in the mid-plane $z/L = 0$ with SAR of 1:1 at $Re = 10\,000$; dimensionless normal (main) stress profiles $10\sqrt{\overline{V'^2}}/U_b$ and $10\sqrt{\overline{U'^2}}/U_b$ along c) horizontal and d) vertical centre-lines.

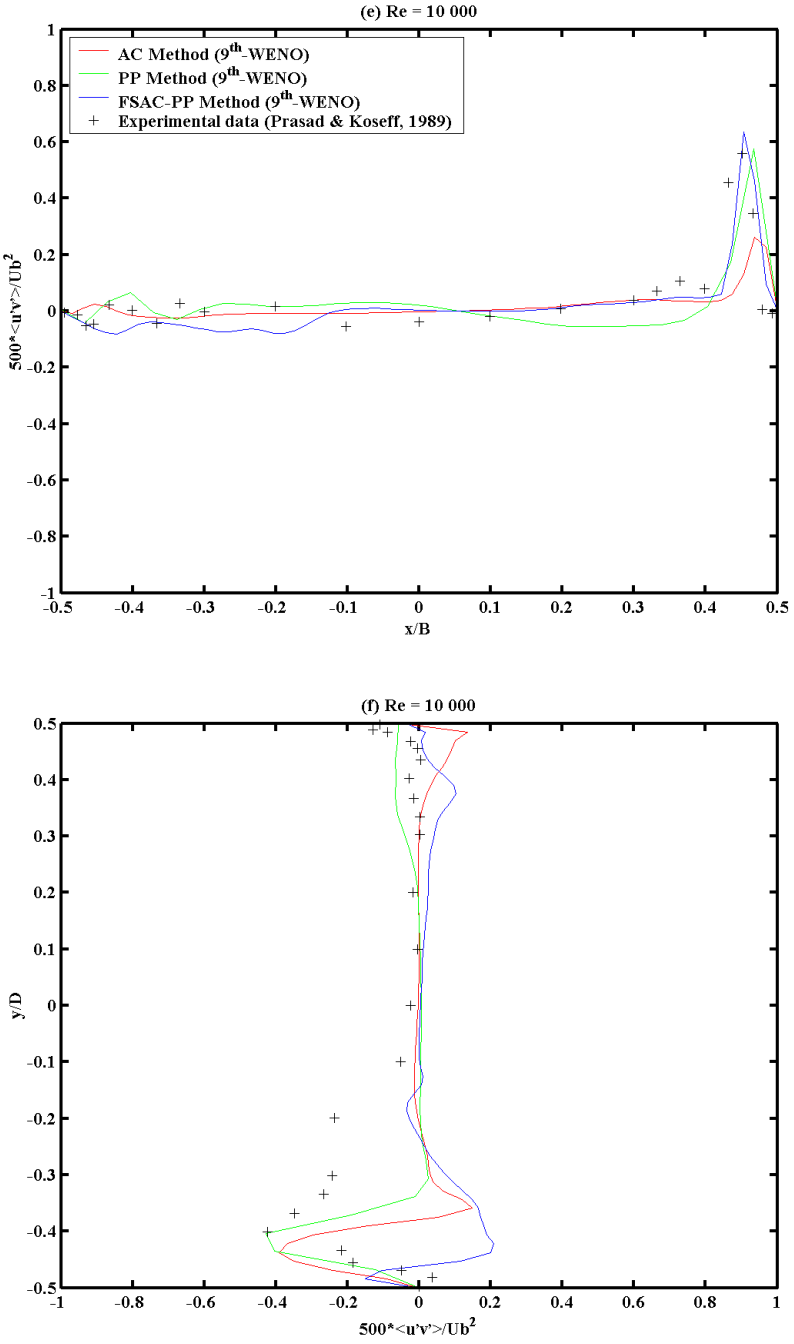

Figure 6.47: ILES results using the AC, PP, and FSAC-PP methods and experimental data of [17, p. 211] in the mid-plane $z/L = 0$ with SAR of 1:1 at $Re = 10\,000$; shear stress profiles $500\sqrt{\overline{U'V'}}/U_b^2$ along e) horizontal and f) vertical centre-lines.

6.4 Summary and Conclusions

In this chapter, the proposed FSAC-PP method in conjunction with the FMG-FAS multigrid technique [7] has been validated for steady-state, incompressible, constant density laminar flow in a lid driven square cavity at $Re = 100, 400,$ and 1000. The proposed FSAC-PP method has also been tested for unsteady turbulent flows in a lid driven cubical cavity at $Re = 3200,$ and $10\,000$. The numerical results of the FSAC-PP method has been compared to the classical AC and PP methods; and to Direct Numerical Simulation (DNS) based computational data of Ghia et al. [8] for two-dimensional laminar flows; and to experimental data of Prasad and Koseff [17] for three-dimensional turbulent flows. The aforementioned turbulent flow simulations have been performed by using the Implicit Large Eddy Simulation (ILES) method. For two-dimensional laminar flows, the overall results suggest that in terms of accuracy, the FSAC-PP method shows better results in most cases compared to the AC and PP methods; especially when low-order (first- and second-order) intercell flux interpolation schemes have been employed. In terms of efficiency, the FSAC-PP method is the most efficient method compared to the AC and PP methods for the presented two-dimensional benchmark at $Re = 100, 400,$ and 1000. It is important to emphasize that the FSAC-PP method required and consumed the lowest number of multigrid iterations in each two-dimensional test case. To provide numerical data for validaton purposes, different intercell flux interpolation formulas have been employed from first- up to ninth-order for the lid driven square cavity test case; and the numerical results have been summarized and compared to the computational data of Ghia et al. [8] in comparative tables in Appendix B at $Re = 100, 400,$ and 1000. For the three-dimensional, unsteady turbulent flows, the overall results show that the AC, PP and FSAC-PP methods capture the mean velocity components better than the RMS main and shear stress profiles compared to the experimental data of Prasad and Koseff [17] at $Re = 3200,$ and $10\,000$. The RMS main and shear stress profiles follow the tendency of the measured values with significant discrepancy between experiments and simulations, which are similar to the DNS results of Leriche et al. [177]. According to Leriche et al. [177], the differences between the simulation and the experiment are caused by the measurement errors approaching the moving wall. Overall, the FSAC-PP method has to be further investigated at high Reynolds numbers for unsteady flows, which is a scope of the future work.

Chapter 7

Multi-Species Variable Density Flow in a Y-Junction Microfluidic Channel

7.1 Introduction

In this chapter, the proposed FSAC-PP method in conjunction with the FMG-FAS multigrid technique [7] has numerically been tested for steady-state, incompressible, multi-species variable density flow in a three-dimensional Y-junction microfluidic channel. The aforementioned three-level multigrid technique [7] has been further extended to the incompressible, variable density version of the FSAC-PP method in this thesis (see in section 4.3). Shapiro and Drikakis [6] investigated this multigrid method [7] combined with the classical AC formulation for different variable density flows; and pointed out that this combination has not been found previously in the literature. Consequently, the FMG-FAS multigrid technique [7] in conjunction with the proposed FSAC-PP method has also not been discussed in any other work yet. Therefore, it is difficult to find a representative numerical example in the literature in order to compare the results of the FSAC-PP method to other numerical methods and/or experimental data. Shapiro and Drikakis [6] presented numerical examples for a two- and three-dimensional diffusion broadening problem of two miscible liquids in microfluidic channels. Ismagilov et al. [180] investigated experimentally and theoretically the diffusion broadening problem, including a Y-shaped channel, in pressure-driven laminar microflows at high Péclet numbers. Relying on these works, a numerical example has been discussed in this chapter. The dimensionless outlet velocity distribution of the AC, PP and FSAC-PP methods has numerically been compared to the analytical solution of Marco and Han [18, 19, p. 5.67], which was derived for constant density pressure-driven laminar flow in rectangular ducts.

7.2 Governing Equations and Methodology

For steady-state, incompressible, multi-species variable density flow, the dimensionless system of perturbed governing equations for the conservation of mass, momentum, total- and partial densities in vector form (see in Chapter 4) can be written [16] as

$$\begin{cases} \frac{1}{\beta}\frac{\partial P}{\partial \tau} = -\nabla \cdot \mathbf{U}, \\ \frac{\partial \mathbf{U}}{\partial \tau} = -\nabla \cdot (\mathbf{U} \otimes \mathbf{U}) + \frac{1}{Re}\nabla^2 \mathbf{U} - \frac{1}{\rho}\nabla P, \\ \frac{\partial \rho}{\partial \tau} = -(\mathbf{U} \cdot \nabla)\rho, \\ \frac{\partial \rho_i}{\partial \tau} = -(\mathbf{U} \cdot \nabla)\rho_i + \frac{1}{Pe}\nabla \cdot \left(\sum_{j=1}^{N-1} D_{ji} \rho \nabla \frac{\rho_j}{\rho} \right), \\ i = 1, N-1, \end{cases} \tag{7.1}$$

where $\rho = \sum \rho_i \ (i = 1, \ldots, N)$ is the total density, ρ_i is the partial density of i^{th} species, D_{ji} are the elements of multicomponent $(N-1) \times (N-1)$ diffusion matrix, Pe is the Péclet number. The multicomponent diffusion matrix contains $(N-1) \times (N-1)$ elements, because a conservation equation has been solved for the total density to avoid the system of perturbed governing equations (7.1) to be over-defined [16]. The system of governing equations (7.1) has numerically been solved by using the FSAC-PP method in conjunction with the FMG-FAS multigrid technique [7] proposed in Chapter 4.

Marco and Han [18, 19, p. 5.67] derived an analytical solution for steady-state, incompressible, constant density pressure-driven laminar flow in rectangular ducts as

$$u(y,z) = -\frac{16a^2}{\mu \pi^3} \left(\frac{dp}{dx} \right) \sum_{i=1,3,\ldots}^{\infty} \frac{(-1)^{\frac{(i-1)}{2}}}{i^3} \left(1 - \frac{\cosh(i\pi z/2a)}{\cosh(i\pi b/2a)} \right) \cos\left(\frac{i\pi y}{2a} \right), \tag{7.2}$$

where $-a \leq y \leq a$ and $-b \leq z \leq b$ are the dimensional width and height of the rectangular cross-section of the channel, respectively; and the pressure gradient $\left(\frac{dp}{dx}\right)$ is related to the mean velocity u_m of the laminar flow [19, p. 5.67] as

$$u_m = -\frac{a^2}{3\mu} \left(\frac{dp}{dx} \right) \left[1 - \frac{192}{\pi^5} \left(\frac{a}{b} \right) \sum_{i=1,3,\ldots}^{\infty} \frac{1}{i^5} \tanh\left(\frac{i\pi b}{2a} \right) \right]. \tag{7.3}$$

Rohsenow [19, p. 5.67] pointed out that it is possible to avoid computational difficulties

by using an approximation, suggested by Purday [181], to compute the fully developed dimensionless velocity surface from the symmetry line to the wall as

$$U(Y,Z) = \frac{u(y,z)}{u_{max}} = \left[1 - \left(\frac{y}{a}\right)^n\right] \cdot \left[1 - \left(\frac{z}{b}\right)^m\right], \tag{7.4}$$

where u_{max} is the maximum velocity of the flow; and the values of exponents n and m are provided by Natarajan and Lakshmanan [182]. The numerical results of the AC, PP and FSAC-PP methods have been computed from wall to wall, which means that the fully developed dimensionless velocity profile based on (7.4) has to be extended to the full cross-sectional area, which has been approximated by

$$U(Y,Z) \approx 8\frac{y}{a}\left[1 - \left(\frac{y}{a}\right)^n\right] \cdot \frac{z}{b}\left[1 - \left(\frac{z}{b}\right)^m\right], \tag{7.5}$$

where the exponents, in favour of simplicity, $n = 2$ and $m = 2$, respectively. For fluid flow in a rectangular duct, the dimensionless Reynolds number is defined [19, p. 5.3] by

$$Re = \frac{u_m D_h}{\upsilon}, \tag{7.6}$$

where D_h is the hydraulic diameter, which can be expressed [19, p. 5.3] as

$$D_h = \frac{4A_{cross-section}}{W_{perimeter}}, \tag{7.7}$$

where $A_{cross-section}$ is the cross-sectional area and $W_{perimeter}$ is the wetted perimeter of the rectangular duct, respectively. The dimensionless Péclet number number is defined by

$$Pe = \frac{u_m L}{D}, \tag{7.8}$$

where L is the characteristic length of the physical problem, and D is the mass diffusion coefficient [19], which represents the ratio of convection to diffusion in the physical process. The dimensionless simulation results have been compared to the analytical solution of Marco and Han [18, 19, p. 5.67] at the outlet rectangular cross-section of the Y-junction microfluidic channel at $Re = 50$ and $Pe = 1000$. The numerical results of the FSAC-PP method has been compared to the classical AC and PP methods in this chapter. The geometrical dimensions of the three-dimensional microfluidic benchmark and the boundary conditions are described in the following section.

7.3 Three-Dimensional Y-Junction Microfluidic Test Case

To test the proposed FSAC-PP method for incompressible, multi-species, variable density flow, compared to the classical AC and PP methods and to the analytical solution of Marco and Han [18, 19, p. 5.67] at the outlet rectangular cross-section of the Y-junction microfluidic channel, 3 simulations have been performed by employing 3^{rd}-order interpolation for the intercell fluxes at $Re = 50$ and $Pe = 1000$. The geometry and the computational domain of the three-dimensional Y-junction microfluidic channel with a $\alpha = 25^{o}$ degree entry angle has been shown in Figure 7.1.

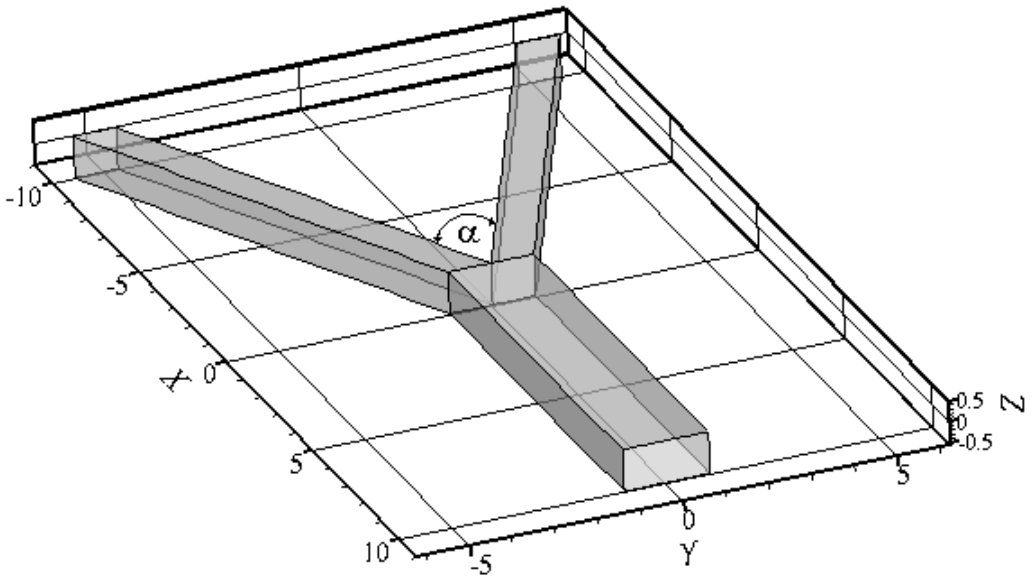

Figure 7.1: Computational domain of the three-dimensional Y-junction microfluidic channel using dimensionless coordinates.

The length l, width d and height h of the mixing zone of the Y-junction microfluidic channel are equal to $1000\mu m$, $200\mu m$, and $100\mu m$, respectively (see Figure 7.1). The dimensional and dimensionless geometrical sizes of the mixing zone of the three-dimensional Y-junction microfluidic channel have been summarized in Table 7.1.

	Mixing Zone of the Y-Junction Microfluidic Channel	
Sizes	μm	dimensionless
l	1000	10
d	200	2
h	100	1

Table 7.1: Geometrical sizes of the mixing zone of the Y-junction microfluidic channel.

The computational domain on the fine grid consists of $25 \times 17 \times 17$ node points $(24 \times 16 \times 16$ control cells) in the two inlet sections with a 25º degree entry angle, and $25 \times 33 \times 17$ node points $(24 \times 32 \times 16$ control volumes) in the main mixing zone for the three-dimensional simulations. Since the numerical results have been computed on a similar grid resolution as taken from the literature [6], a grid convergence study has not been performed for this benchmark.

A mathematical task can be formulated in terms of boundary and initial conditions for the steady-state, incompressible, multi-species, variable density pressure-driven laminar flow in the three-dimensional Y-junction microfluidic channel. Dimensionless quantities and curvilinear coordinates have been used in the simulations, therefore, the spatial coordinates have been normalized by the height h of the channel. From wall to wall at the two inlet sections, the velocity on the surface normalized by the maximum velocity of the flow u_{max} and have been approximated based on (7.5) as

$$U_{inlet\,sections}(0,\eta,\zeta) = \frac{u(0,\eta,\zeta)}{u_{max}} \approx 8\eta\,[1-\eta^n]\cdot\zeta\,[1-\zeta^m]. \tag{7.9}$$

where the exponents n and m have been taken to be equal to 2, respectively. Furthermore, the partial density of the fluids are two different constant values at the two inlet sections, which can be expressed as

$$\rho_{inlet\,sections}(0,\eta,\zeta) = \rho_1^* \;\text{ and }\; \rho_{i,inlet\,sections}(0,\eta,\zeta) = \rho_2^*, \tag{7.10}$$

which means that each inlet section is occupied by one fluid with constant density [6]. The dimensionless pressure has been prescibed as equal to zero at the two inlet sections, which can be written as $P_{inlet}(0,\eta,\zeta) = 0$. Thus, all boundary conditions are Dirichlet-type at the inlet sections. The outlet boundary conditions for the dimensionless velocity components, and for total- and partial densities can be prescribed as

$$\frac{\partial \mathbf{U}(L,\eta,\zeta)}{\partial\xi} = 0, \quad \frac{\partial \rho(L,\eta,\zeta)}{\partial\xi} = 0, \;\text{ and }\; \frac{\partial \rho_i(L,\eta,\zeta)}{\partial\xi} = 0, \tag{7.11}$$

where L is the dimensionless spatial coordinate of the outlet section, and $i = 1,\ldots,N$; which are Neumann-type outlet boundary conditions. The dimensionless pressure has been prescibed as equal to one at the outlet section, which is a Dirichlet-type boundary condition, and can be written as $P_{outlet}(L,\eta,\zeta) = 1$. For the velocity components, the no-slip boundary condition has been prescribed for each wall. The dimensionless initial conditions of the three-dimensional diffusion broadening problem are that parabolic surfaces have been prescribed for the velocity component U based on (7.5), and the pressure has been set equal to one in the whole Y-junction channel as $P_{inital}(\xi,\eta,\zeta) = 1$.

7.4 Results and Discussion

For steady-state, incompressible, multi-species variable density flow, two different miscible liquids are mixing with different densities $\rho_1^* = 0.1$ and $\rho_2^* = 0.9$ in the mixing zone (main channel) of the three-dimensional Y-junction microfluidic benchmark. For simulating the diffusion broadening problem with intense mixing, a low Reynolds number ($Re = 50$) and a high Péclet number ($Pe = 1000$) have been chosen [6, p. 619]. Ismagilov et al. [180, p. 2377] considered the elements of the multicomponent $(N-1)\times(N-1)$ diffusion matrix D_{ji} to be constant and equal to 10^{-9} m^2/s in the experiment. To provide a stable numerical solution for the proposed FSAC-PP and the classical AC methods, the CFL numbers for the inviscid and viscous flux terms have been taken as 0.3 and 0.1, respectively. The AC parameter β has been chosen to be equal to 25. One of the fluids is heavier than the other one in the upper left and right hand side of the Y-junction channel, respectively. Three simulations have been performed by using three different method as AC, PP and FSAC-PP methods with the same boundary and initial conditions. The distribution of the dimensionless velocity component U and distribution of species density have been shown in Figures 7.2 and 7.3 using the FSAC-PP method with the 3^{rd}-order intercell flux interpolation in the Y-junction channel at $Re = 50$ and $Pe = 1000$. The corresponding dimensionless velocity distributions at the outlet section can be seen in Figures 7.4 to 7.6 using AC, PP, and FSAC-PP methods, respectively. The numerical results of these methods have been compared to the analytical solution of Marco and Han [18, 19, p. 5.67]. The maximum absolute and relative errors of the AC, PP and FSAC-PP methods were compared to the analytical solution and have been summarized in Table 7.2. In terms of accuracy, the results show that the FSAC-PP method exhibits the smallest maximum absolute error compared to the analytical solution [18, 19, p. 5.67]. The reason for the difference between the numerically and analytically computed dimensionless velocity distributions at the outlet of the Y-junction channel is that both results are approximate solutions for the fully developed pressure-driven laminar flow in a rectangular duct. In terms of efficiency, the FSAC-PP method requires the lowest number of multigrid iterations on the fine grid compared to the AC and PP methods for steady-state, incompressible, multi-species variable density flow. It means that the FSAC-PP method consumes 8.14 and 37.89 times less multigrid iterations than the AC and PP methods in average at $Re = 50$ and $Pe = 1000$, respectively (see Figure 7.7 and Table 7.3). In terms of accuracy, the FSAC-PP method exhibits minor differences compared to the AC and PP methods; and in terms of efficiency, the FSAC-PP method is more efficient than the AC method, but significantly more efficient than the PP method for the presented test case. The obtained results show good agreement with the theoretical investigations of Ismagilov et al. [180] as well as the numerical investigations of Shapiro and Drikakis [6].

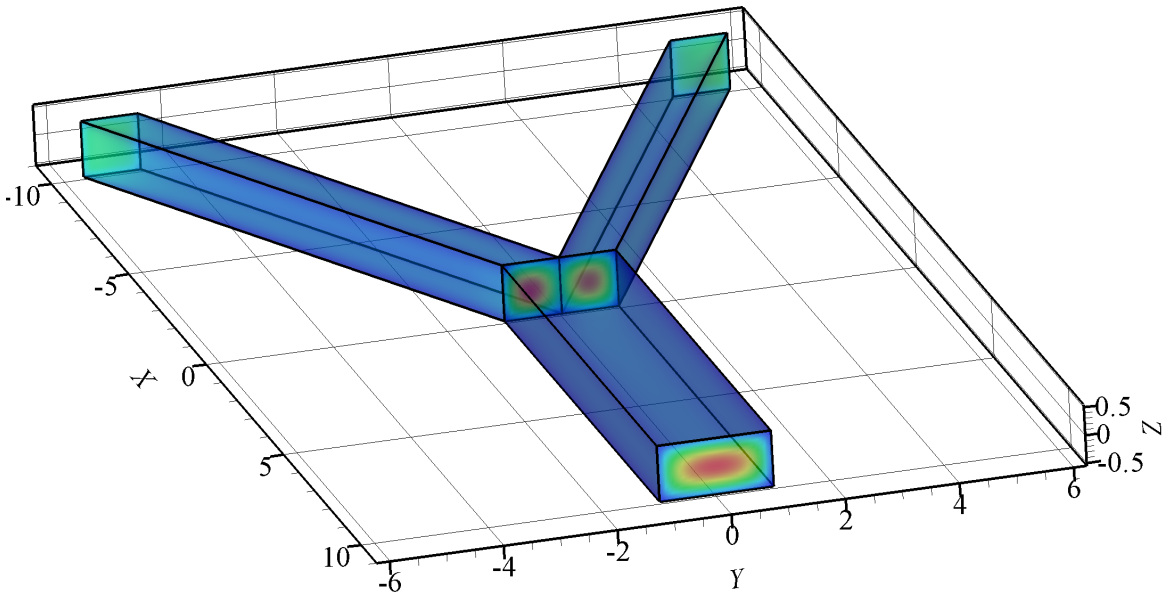

Figure 7.2: Distribution of the velocity component U using AC, PP, and FSAC-PP methods with 3^{rd}-order interpolation in the Y-junction channel at $Re = 50$ and $Pe = 1000$.

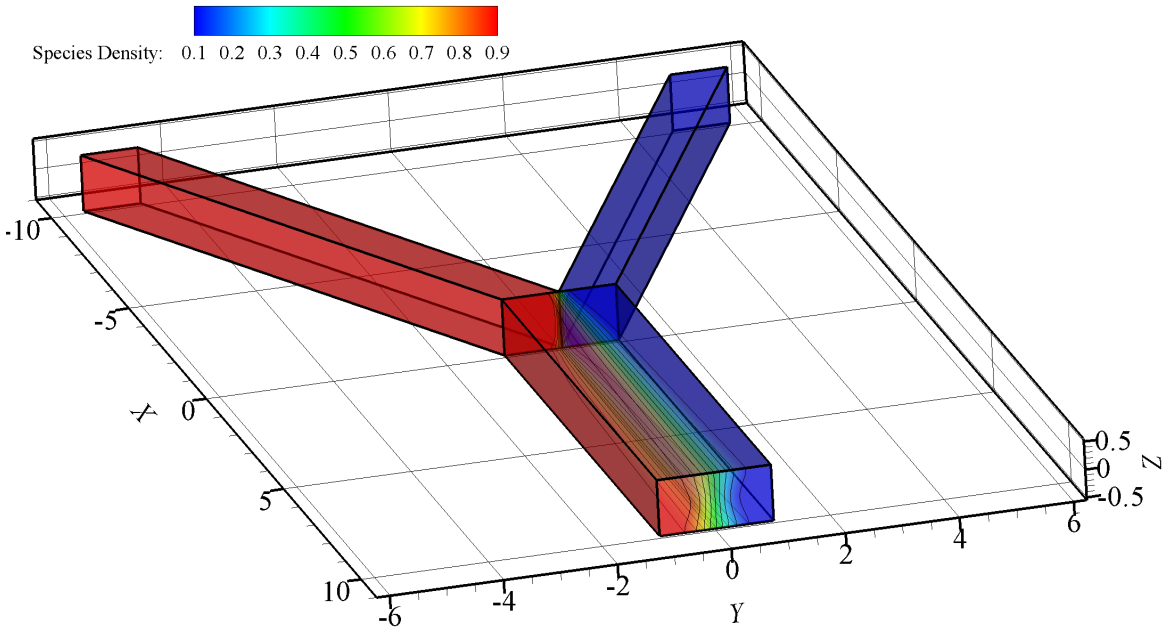

Figure 7.3: Distribution of species density using AC method with 3^{rd}-order interpolation in the Y-junction channel at $Re = 50$ and $Pe = 1000$.

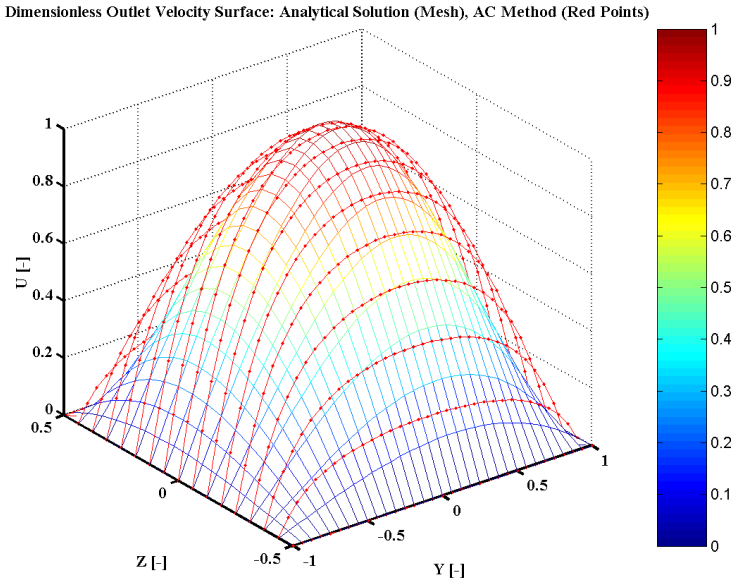

Figure 7.4: Distribution of the velocity component U using AC method with 3^{rd}-order interpolation compared to the analytical solution of Marco and Han [18, 19, p. 5.67] at the outlet of the Y-junction channel at $Re = 50$ and $Pe = 1000$.

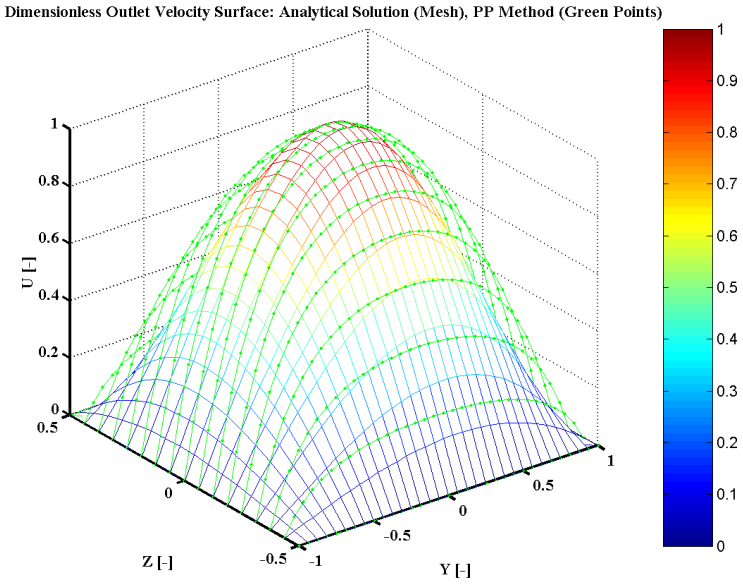

Figure 7.5: Distribution of the velocity component U using the PP method with 3^{rd}-order interpolation compared to the analytical solution of Marco and Han [18, 19, p. 5.67] at the outlet of the Y-junction channel at $Re = 50$ and $Pe = 1000$.

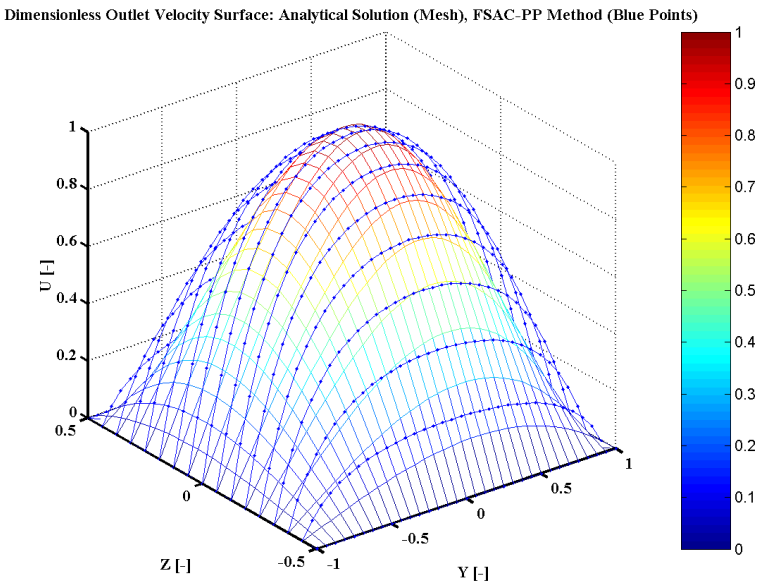

Figure 7.6: Distribution of the velocity component U using FSAC-PP method with 3^{rd}-order interpolation compared to the analytical solution of Marco and Han [18, 19, p. 5.67] at the outlet of the Y-junction channel at $Re = 50$ and $Pe = 1000$.

AC Method	
Maximum Absolute Error [-]	Maximum Relative Error [-]
0.30333	3.37317
PP Method	
Maximum Absolute Error [-]	Maximum Relative Error [-]
0.30710	3.46972
FSAC-PP Method	
Maximum Absolute Error [-]	Maximum Relative Error [-]
0.30203	3.38622

Table 7.2: Absolute and relative errors of the AC, PP, and FSAC-PP methods for the dimensionless velocity distribution of velocity component U at the outlet of the Y-junction channel, using 3^{rd}-order interpolation, compared to the analytical solution of Marco and Han [18, 19, p. 5.67] at $Re = 50$ and $Pe = 1000$.

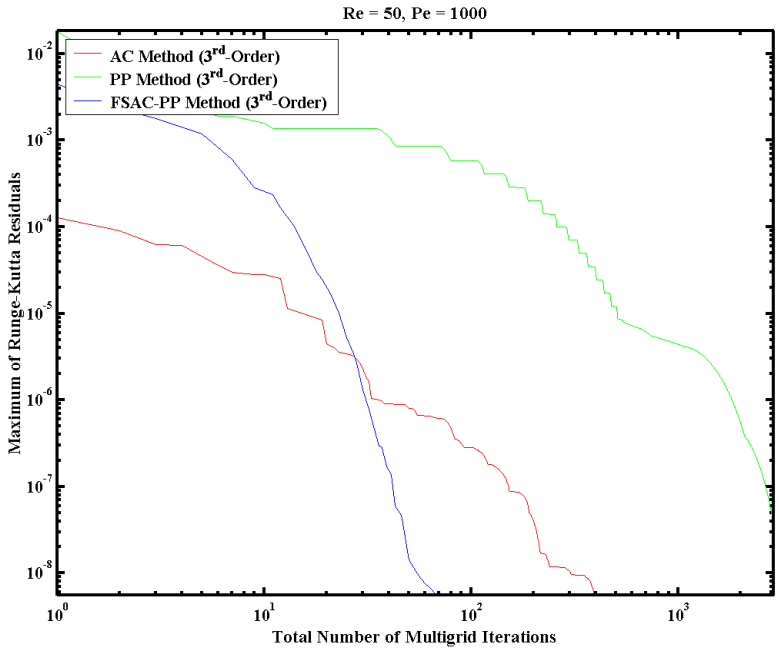

Figure 7.7: Comparison of the numerical convergence of the AC, PP, and FSAC-PP methods for incompressible, multi-species, variable density flow in a Y-junction microfluidic channel; maximum values of Runge-Kutta residuals versus total number of multigrid iterations on the fine grid using 3^{rd}-order interpolation at $Re = 50$ and $Pe = 1000$.

Reynolds Number ($Re = 50$), Péclet Number ($Pe = 1000$)			
Intercell Flux Interpolation	Solution Method	N_{mg}	RK_{maxres}
3^{rd}-Order	AC	619	$0.1 \cdot 10^{-8}$
	PP	2880	$0.3 \cdot 10^{-7}$
	FSAC-PP	76	$0.5 \cdot 10^{-8}$

Table 7.3: Comparison of the numerical convergence of the AC, PP, and FSAC-PP methods; total number of multigrid iterations on the fine grid and maximum values of Runge-Kutta residuals using 3^{rd}-order interpolations at $Re = 50$ and $Pe = 1000$.

7.5 Summary and Conclusions

In this chapter, the proposed FSAC-PP method in conjunction with the FMG-FAS multigrid technique [7] has been tested for steady-state, incompressible, multi-species variable density flow, taking two different miscible liquids with different densities, in a three-dimensional Y-junction microfluidic channel at $Re = 50$ and $Pe = 1000$. The dimensionless outlet velocity distribution has numerically been compared to the analytical solution of Marco and Han [18, 19, p. 5.67], which was derived for constant density pressure-driven laminar flow in rectangular ducts. Overall, the obtained results show that in terms of accuracy, the proposed FSAC-PP method exhibits only minor differences compared to the classical AC and PP methods; and in terms of efficiency, the FSAC-PP method is more efficient than the AC and PP methods for this benchmark test case. Furthermore, the presented results show good agreement with the experimental and theoretical investigations of Ismagilov et al. [180], and the numerical investigations of Shapiro and Drikakis [6].

Chapter 8

Non-Newtonian Biofluid Flow in the Presence of Uniform Magnetic Field

8.1 Introduction

In this chapter, the proposed FSAC-PP method, compared to the classical AC method, has been used for simulating non-Newtonian biofluid flow under the presence of a uniform magnetic field relying on the work of Tzirtzilakis and Loukopoulos [9]. The first main scope of this chapter is to demonstrate that the FSAC-PP method is capable of solving complex multiphysics flow problems. The aforementioned authors considered blood as a Newtonian biofluid, but since blood is a non-Newtonian fluid, the original model equations of Tzirtzilakis and Loukopoulos [9] have been further extended to use with any other constitutive equations. The second main scope of this chapter is to generalise the model of Tzirtzilakis and Loukopoulos [9] in the framework of the high-resolution Godunov-type method using the FSAC-PP solution method as a novel numerical treatment of the steady-state, incompressible Navier-Stokes equations. The computational results have been compared to the classical AC method and to the computational data of Tzirtzilakis and Loukopoulos [9]. However, the literature survey related to non-Newtonian blood flows has been reviewed comprehensively in Chapter 2, but the main works in conjunction with the present topic have also been revisited in this chapter.

Tzirtzilakis and Loukopoulos [9], among others, investigated the blood flow as a biomagnetic, steady-state, incompressible, non-isothermal, Newtonian fluid flow in the presence of a uniform magnetic field in a two-dimensional microfluidic channel. Their solution method is relying on the streamfunction-vorticity formulation and on a novel finite difference (FD) treatment of the governing equations. This research field generates great interest, because of the various biomedical applications; and this subject is related to the

mathematical modelling of Biomagnetic Fluid Dynamics (BDF) developed originally by Haik et al. [183, 184, 185]. In the last decade, researchers investigate biofluid (blood) flows in different physical circumstances, because the theoretical and engineering interests differ from each other. Neofytou and Drikakis [20] investigated the bifurcation of a two-dimensional blood flow, which occurs through a plane symmetric sudden expansion, employing the Casson [53], a version of Power-Law as proposed by Walburn and Schneck [54], and Quemada [55] non-Newtonian fluid models. The Casson constitutive equation exhibits discontinuous behaviour, therefore, its numerical discretization has to be made considerately [20]. Quemada predicts the viscosity of a concentrated disperse system taking into account both the shear rate and haematocrit level of the blood. Himeno [56] investigated the blood flow in the human vascular system and pointed out that the blood has a weak non-Newtonian effect in arteries, but a strong one in capillaries. Grinberg and Karniadakis [57], furthermore, Grinberg et al. [58] considered blood as a Newtonian medium in the arterial flow and in the virtual physiological human (VPH) arterial tree simulations. Sherwin et al. [59], Neofytou and Tsangaris [60], Ikbal et al. [61], and Kim et al. [62] considered non-Newtonian blood flow effect in haemodynamics simulations. Ikbal et al. [61] investigated the unsteady response of blood flow through a stenosed artery in a magnetic field. Kim et al. [62] dealt with the multiphase non-Newtonian effects on pulsatile haemodynamics in a coronary artery using Carreau-Yasuda [63], Quemada [64], Cross [65], and a modified version of Casson [66] biorheological fluid models. Das and Chakraborty [71] derived an analytical solution for velocity, temperature and concentration distribution in electroosmotic microchannel flows of a non-Newtonian biofluid. They emphasized that the biorheological behaviour of blood can be described accurately with higher-order constitutive equations, because it shows non-linear, time-dependent, viscoelastic and neglectable Bingham plastic characteristics. Bingham plasticity appears mostly at higher haematocrit percentages due to the presence of the protein fibrinogen [71]. Kornev and Neimark studied numerically the spontaneous penetration of viscoelastic fluids and biofluids into capillaries [73]. Recently, Chakraborty [80] described the electroosmotically-driven capillary transport of non-Newtonian biofluids in rectangular microfluidic channels. A semi-analytical mathematical model was developed to study the capillary filling employing a power law constitutive relationship for the blood biorheology. A case study was presented to illustrate the blood sample behaviour for different haematocrit levels. These results can also be used for designing blood transporting microsystems, e.g. blood glucose monitoring [80]. Since the proposed FSAC-PP method for solving the momentum equation is a new approach, it has been used for modelling biofluid flow in the presence of a uniform magnetic field in this thesis.

8.2 Governing Equations and Methodology

In this section, the model equations of Tzirtzilakis and Loukopoulos [9] for Newtonian biomagnetic fluid flow has been further extended to use constitutive equations for non-Newtonian blood flow under the presence of uniform magnetic field. For steady-state, incompressible, non-izothermal, Newtonain biomagnetic fluid flow in the presence of uniform magnetic field neglecting the gravity force **g**, the governing equations consist of the conservation of mass, momentum and energy; thus the model equations of Tzirtzilakis and Loukopoulos [9] may be written in general vector form as

$$\nabla \cdot \mathbf{u} = 0, \tag{8.1}$$

$$(\mathbf{u} \cdot \nabla)\,\mathbf{u} = -\frac{1}{\rho}\nabla p + \frac{\mu}{\rho}\nabla^2 \mathbf{u} + \frac{\mu_0}{\rho} M\,(\nabla H) - \frac{\sigma}{\rho}\mathbf{B}^2 \mathbf{u}, \tag{8.2}$$

$$(\mathbf{u} \cdot \nabla)\,\vartheta = \frac{k}{\rho c_p}\nabla^2 \vartheta - \frac{\mu_0}{\rho c_p}\vartheta \frac{\partial M}{\partial \vartheta}(\mathbf{u} \cdot \nabla) H + \frac{\sigma}{\rho c_p}\mathbf{B}^2 \mathbf{u} + \frac{1}{\rho c_p}\varphi_D, \tag{8.3}$$

where ρ is the density of the fluid, p is the hydrodynamic pressure, μ is the dynamic viscosity of the fluid, μ_0 is the magnetic permeability of vacuum, $\mathbf{u}$ is the velocity vector, M is the variation of magnetization, H is the magnetic field strength, σ is the electrical conductivity, $\mathbf{B}$ is the induction vector of the magnetic field, ϑ is the temperature field, k is the thermal conductivity, c_p is the specific heat at constant pressure, and φ_D is the function of dissipation. The second and third terms in the right hand side of the momentum equation (8.2) represent the magnetic and the Lorentz force per unit volume [9], respectively. The second and third terms in the right hand side of the temperature equation (8.3) represent the thermal power and Joule heating per unit volume of the magnetocaloric effect [9], respectively. In the above described system of equations (8.1)-(8.3), the constitutive equation (3.4) is relying on the Navier-Stokes hypothesis of the viscous stress tensor (3.22) taking into account the divergence-free (incompressibility) constraint (8.4). For modelling the blood flow as a biomagnetic non-Newtonian fluid flow, the system of governing equations (8.1)-(8.3) has to be generalized to use any other appropriately chosen constitutive equation. To achieve this goal, the general momentum equation (3.3), which is also known as Cauchy equation (see in Chapter 3), and the general function of dissipation (3.8) have to be used with the external force including the presence of a uniform magnetic field. Consequently, the generalized system of governing equations of Tzirtzilakis and Loukopoulos [9] may be written in vector form as

$$\nabla \cdot \mathbf{u} = 0, \tag{8.4}$$

$$(\mathbf{u}\cdot\nabla)\,\mathbf{u} = -\frac{1}{\rho}\nabla p + \frac{1}{\rho}\nabla\cdot\underline{\underline{\tau}} + \frac{\mu_0}{\rho}M\,(\nabla H) - \frac{\sigma}{\rho}\mathbf{B}^2\mathbf{u}, \tag{8.5}$$

$$(\mathbf{u}\cdot\nabla)\,\vartheta = \frac{k}{\rho c_p}\nabla^2\vartheta - \frac{\mu_0}{\rho c_p}\vartheta\frac{\partial M}{\partial\vartheta}\,(\mathbf{u}\cdot\nabla)\,H + \frac{\sigma}{\rho c_p}\mathbf{B}^2\mathbf{u} + \frac{1}{\rho c_p}\left[\underline{\underline{\tau}}\cdot\cdot\,(\nabla\otimes\mathbf{u})\right], \tag{8.6}$$

where the viscous stress tensor $\underline{\underline{\tau}}$ and the function of dissipation $\varphi_D = \underline{\underline{\tau}}\cdot\cdot\,(\nabla\otimes\mathbf{u})$ have to be expressed relying on the non-Newtonian constitutive equation, e.g. as a version of the power law (3.196), Casson (3.198) or Quemada (3.201) fluid models, which may be employed in the momentum (8.5) and temperature equations (8.6), respectively.

In the system of equations (8.4)-(8.6), there are two terms, where

$$M = KH\,(\vartheta_C - \vartheta) \tag{8.7}$$

appears, which is the variation of magnetization of the biomagnetic fluid, where K is an appropriately chosen constant, ϑ_C is the Curie temperature [9], and

$$H\,(x,y) = \frac{H_0}{2}\left\{\tanh\left[a_1\,(x-x_1)\right] - \tanh\left[a_2\,(x-x_2)\right]\right\} \tag{8.8}$$

is the strength of magnetic field [9], where H_0 is determined by the induction of the applied magnetic field $B = \mu_0 H_0$, which is the second scalar component of the magnetic induction vector $\mathbf{B} = (0,B,0)$. The strength of the magnetic field, taken from the literature [9], defined by function (8.8), which is acting with the magnetic induction in the vertical direction in the test case presented in this chapter (see Figure 8.2). To non-dimensionalise the system of governing equations (8.4)-(8.6), the following

$$X = \frac{x}{h},\;\; Y = \frac{y}{h},\;\; Z = \frac{z}{h},$$

$$U = \frac{u}{u_{max}},\;\; V = \frac{v}{u_{max}},\;\; W = \frac{w}{u_{max}},$$

$$P = \frac{p}{\rho_\infty u_{max}^2},\;\; H^* = \frac{H}{H_0},\;\; T = \frac{\vartheta - \vartheta_{lw}}{\vartheta_{uw} - \vartheta_{lw}},$$

dimensionless quantities are introduced for spatial coordinates, velocity components, pressure field, magnetic field strength, and temperature field, where L, u_{max}, ρ_∞ are constant reference quantities for characteristics length, velocity and fluid density; ϑ_{lw} and ϑ_{uw} are the temperature of the lower and upper wall of the microfluidic channel, respectively. After the non-dimensionalization by using these dimensionless quantities, the system of governing equations (8.4)-(8.6), can be written in vector form as

$$\nabla\cdot\mathbf{U} = 0, \tag{8.9}$$

$$(\mathbf{U}\cdot\nabla)\,\mathbf{U} = -\nabla P + \frac{1}{Re}\nabla\cdot\underline{\underline{\tau}} +$$
$$+\,(\mathrm{Mn}_{FC} - \mathrm{Mn}_F T)\,H^*\,(\nabla H^*) - \frac{\mathrm{Mn}_M}{Re}\,(H^*)^2\,\mathbf{U}, \tag{8.10}$$
$$(\mathbf{U}\cdot\nabla)\,T = \frac{1}{RePr}\nabla^2 T +$$
$$+\mathrm{Mn}_F \mathrm{Ec} H\,(T+\varepsilon)\,(\mathbf{U}\cdot\nabla)\,H^* + \frac{\mathrm{Mn}_M \mathrm{Ec}}{Re}\,(H^*)^2\,\mathbf{U}^2 + \frac{\mathrm{Ec}}{Re}\Phi_D, \tag{8.11}$$

where the following

$$Re = \frac{\rho u_{max} h}{\mu},\ \ \mathrm{Pr} = \frac{c_p \mu}{k},\ \ \mathrm{Ec} = \frac{u_{max}^2}{c_p\,(\vartheta_{uw} - \vartheta_{lw})},\ \ \varepsilon = \frac{\vartheta_{lw}}{\vartheta_{uw} - \vartheta_{lw}},$$
$$\mathrm{Mn}_F = \frac{\mu_0 H_0^2 K\,(\vartheta_{uw} - \vartheta_{lw})}{\rho u_{max}^2},\ \ \mathrm{Mn}_{FC} = \frac{\mu_0 H_0^2 K\,(\vartheta_C - \vartheta_{lw})}{\rho u_{max}^2},\ \ \mathrm{Mn}_M = \frac{\mu_0^2 H_0^2 h^2 \sigma}{\mu},$$

dimensionless quantities are the Reynolds number for Newtonian fluid, Prandtl number, Eckert number, temperature number, magnetic number defined by the temperature of upper wall from the field of ferro-hydrodynamics (FHD) [9], magnetic number defined by the Curie temperature, and magnetic number from the field of magnetohydrodynamics (MHD) [9], respectively. To use the classical AC and the proposed FSAC-PP solution methods, the pseudo-time derivatives have to be introduced in the continuity (8.9), momentum (8.10) and energy equation for the temperature (8.11); thus the perturbed hyperbolic system of governing equations can be written as

$$\frac{\partial P}{\partial \tau} = -\beta \nabla\cdot\mathbf{U}, \tag{8.12}$$
$$\frac{\partial \mathbf{U}}{\partial \tau} = -\,(\mathbf{U}\cdot\nabla)\,\mathbf{U} - \nabla P + \frac{1}{Re}\nabla\cdot\underline{\underline{\tau}} +$$
$$+\,(\mathrm{Mn}_{FC} - \mathrm{Mn}_F T)\,H^*\,(\nabla H^*) - \frac{\mathrm{Mn}_M}{Re}\,(H^*)^2\,\mathbf{U}, \tag{8.13}$$
$$\frac{\partial T}{\partial \tau} = -\,(\mathbf{U}\cdot\nabla)\,T + \frac{1}{RePr}\nabla^2 T +$$
$$+\mathrm{Mn}_F \mathrm{Ec} H^*\,(T+\varepsilon)\,(\mathbf{U}\cdot\nabla)\,H^* + \frac{\mathrm{Mn}_M \mathrm{Ec}}{Re}\,(H^*)^2\,\mathbf{U}^2 + \frac{\mathrm{Ec}}{Re}\Phi_D, \tag{8.14}$$

where the elements of the dimensionless viscous stress tensor $\underline{\underline{\tau}}$ for Newtonian fluid in

curvilinear coordinate system can be expressed as

$$\begin{cases} \tau_{XX} = 2\mu \left(\xi_X \frac{\partial U}{\partial \xi} + \eta_X \frac{\partial U}{\partial \eta} + \zeta_X \frac{\partial U}{\partial \zeta} \right), \\ \tau_{YY} = 2\mu \left(\xi_Y \frac{\partial V}{\partial \xi} + \eta_Y \frac{\partial V}{\partial \eta} + \zeta_Y \frac{\partial V}{\partial \zeta} \right), \\ \tau_{ZZ} = 2\mu \left(\xi_Z \frac{\partial W}{\partial \xi} + \eta_Z \frac{\partial W}{\partial \eta} + \zeta_Z \frac{\partial W}{\partial \zeta} \right), \\ \tau_{XY} = \tau_{YX} = \mu \left(\xi_X \frac{\partial V}{\partial \xi} + \eta_X \frac{\partial V}{\partial \eta} + \zeta_X \frac{\partial V}{\partial \zeta} + \xi_Y \frac{\partial U}{\partial \xi} + \eta_Y \frac{\partial U}{\partial \eta} + \zeta_Y \frac{\partial U}{\partial \zeta} \right), \\ \tau_{XZ} = \tau_{ZX} = \mu \left(\xi_X \frac{\partial W}{\partial \xi} + \eta_X \frac{\partial W}{\partial \eta} + \zeta_X \frac{\partial W}{\partial \zeta} + \xi_Z \frac{\partial U}{\partial \xi} + \eta_Z \frac{\partial U}{\partial \eta} + \zeta_Z \frac{\partial U}{\partial \zeta} \right), \\ \tau_{YZ} = \tau_{ZY} = \mu \left(\xi_Y \frac{\partial W}{\partial \xi} + \eta_Y \frac{\partial W}{\partial \eta} + \zeta_Y \frac{\partial W}{\partial \zeta} + \xi_Z \frac{\partial V}{\partial \xi} + \eta_Z \frac{\partial V}{\partial \eta} + \zeta_Z \frac{\partial V}{\partial \zeta} \right), \end{cases} \tag{8.15}$$

and for employing the non-Newtonian power law fluid, the elements of the dimensionless viscous stress tensor $\underline{\underline{\tau}}$ in curvilinear coordinate system can be expressed as

$$\begin{cases} \tau_{XX} = -2m \left| \underline{\underline{\dot{\gamma}}} \right|^{n-1} \left(\xi_X \frac{\partial U}{\partial \xi} + \eta_X \frac{\partial U}{\partial \eta} + \zeta_X \frac{\partial U}{\partial \zeta} \right), \\ \tau_{YY} = -2m \left| \underline{\underline{\dot{\gamma}}} \right|^{n-1} \left(\xi_Y \frac{\partial V}{\partial \xi} + \eta_Y \frac{\partial V}{\partial \eta} + \zeta_Y \frac{\partial V}{\partial \zeta} \right), \\ \tau_{ZZ} = -2m \left| \underline{\underline{\dot{\gamma}}} \right|^{n-1} \left(\xi_Z \frac{\partial W}{\partial \xi} + \eta_Z \frac{\partial W}{\partial \eta} + \zeta_Z \frac{\partial W}{\partial \zeta} \right), \\ \tau_{XY} = \tau_{YX} = -m \left| \underline{\underline{\dot{\gamma}}} \right|^{n-1} \left(\xi_X \frac{\partial V}{\partial \xi} + \eta_X \frac{\partial V}{\partial \eta} + \zeta_X \frac{\partial V}{\partial \zeta} + \xi_Y \frac{\partial U}{\partial \xi} + \eta_Y \frac{\partial U}{\partial \eta} + \zeta_Y \frac{\partial U}{\partial \zeta} \right), \\ \tau_{XZ} = \tau_{ZX} = -m \left| \underline{\underline{\dot{\gamma}}} \right|^{n-1} \left(\xi_X \frac{\partial W}{\partial \xi} + \eta_X \frac{\partial W}{\partial \eta} + \zeta_X \frac{\partial W}{\partial \zeta} + \xi_Z \frac{\partial U}{\partial \xi} + \eta_Z \frac{\partial U}{\partial \eta} + \zeta_Z \frac{\partial U}{\partial \zeta} \right), \\ \tau_{YZ} = \tau_{ZY} = -m \left| \underline{\underline{\dot{\gamma}}} \right|^{n-1} \left(\xi_Y \frac{\partial W}{\partial \xi} + \eta_Y \frac{\partial W}{\partial \eta} + \zeta_Y \frac{\partial W}{\partial \zeta} + \xi_Z \frac{\partial V}{\partial \xi} + \eta_Z \frac{\partial V}{\partial \eta} + \zeta_Z \frac{\partial V}{\partial \zeta} \right), \end{cases} \tag{8.16}$$

where m and n are the exponents of the non-Newtonian power law fluid; the Reynolds number is differ from the Newtonian fluid case and defined by Eq. (3.197); and where the magnitude of the dimensionless shear rate tensor $\left| \underline{\underline{\dot{\gamma}}} \right|$ is defined by Eq. (3.195) can be

written in curvilinear coordinate system as

$$
\begin{aligned}
&\left|\underline{\underline{\dot{\gamma}}}\right| = \sqrt{\frac{1}{2}\left(\underline{\underline{\dot{\gamma}}}\cdot\cdot\underline{\underline{\dot{\gamma}}}\right)} = \\
&= \left\{ 2\left[\left(\xi_X \frac{\partial U}{\partial \xi} + \eta_X \frac{\partial U}{\partial \eta} + \zeta_X \frac{\partial U}{\partial \zeta} \right)^2 + \right.\right. \\
&+ \left(\xi_Y \frac{\partial V}{\partial \xi} + \eta_Y \frac{\partial V}{\partial \eta} + \zeta_Y \frac{\partial V}{\partial \zeta} \right)^2 + \\
&\left.\left. + \left(\xi_Z \frac{\partial W}{\partial \xi} + \eta_Z \frac{\partial W}{\partial \eta} + \zeta_Z \frac{\partial W}{\partial \zeta} \right)^2 \right] + \right. \\
&+ \left(\xi_X \frac{\partial V}{\partial \xi} + \eta_X \frac{\partial V}{\partial \eta} + \zeta_X \frac{\partial V}{\partial \zeta} + \xi_Y \frac{\partial U}{\partial \xi} + \eta_Y \frac{\partial U}{\partial \eta} + \zeta_Y \frac{\partial U}{\partial \zeta} \right)^2 + \\
&+ \left(\xi_X \frac{\partial W}{\partial \xi} + \eta_X \frac{\partial W}{\partial \eta} + \zeta_X \frac{\partial W}{\partial \zeta} + \xi_Z \frac{\partial U}{\partial \xi} + \eta_Z \frac{\partial U}{\partial \eta} + \zeta_Z \frac{\partial U}{\partial \zeta} \right)^2 + \\
&\left. + \left(\xi_Y \frac{\partial W}{\partial \xi} + \eta_Y \frac{\partial W}{\partial \eta} + \zeta_Y \frac{\partial W}{\partial \zeta} + \xi_Z \frac{\partial V}{\partial \xi} + \eta_Z \frac{\partial V}{\partial \eta} + \zeta_Z \frac{\partial V}{\partial \zeta} \right)^2 \right\}^{1/2}. \qquad (8.17)
\end{aligned}
$$

The Prandtl number and the magnetic number are also differ from the Newtonian fluid case and defined by the apparent viscosity of the non-Newtonian fluid [19, 61]. Tzirtzilakis and Loukopoulos [9, p. 361] pointed out that their blood rheology approach is not realistic, because they considered the blood as a Newtonian fluid. However, the blood is a weak non-Newtonian fluid, therefore, the fully developed laminar velocity profile by employing different constitutive equations are slightly differ from each other, especially at $Re = 100 \div 300$ (see the computational results of Neofytou and Drikakis [20, p. 134] in Figure 8.1 at $Re = 200$). In this thesis, both Newtonian fluid and non-Newtonian power law fluid models have been used for simulating the blood flow in the presence of a uniform magnetic field. In terms of momentum equation (8.13) for a non-Newtonian blood rheology approach, the elements of the viscous stress tensor $\underline{\underline{\tau}}$ is differ from the implementation of Newtonian fluid model. A non-Newtonian power law fluid model has been used for the computational example of this chapter relying on the elements of the viscous stress tensor (8.16) and on the magnitude of the shear rate tensor (8.17) in curvilinear coordinate system. The derivatives appear in the viscous stress tensor $\underline{\underline{\tau}}$ and in the magnitude of the shear rate tensor $\left|\underline{\underline{\dot{\gamma}}}\right|$ have been approximated by second-order central differences; see more details about the discretization of viscous flux terms in Chapter 3.

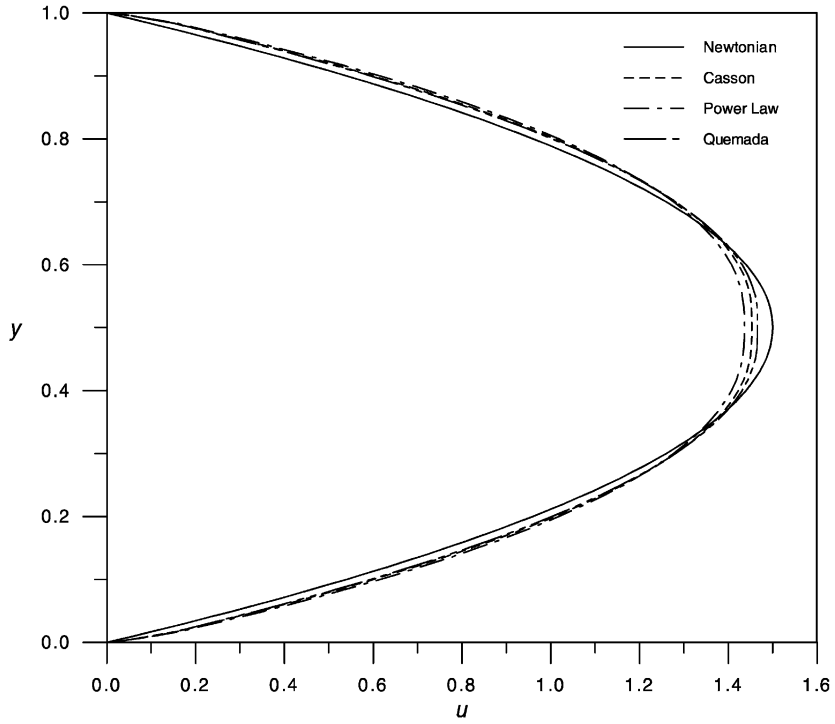

Figure 8.1: Fully developed velocity profiles using different constitutive equations of blood computed by Neofytou and Drikakis [20, p. 134] at $Re = 200$.

In terms of the energy equation for the temperature (8.14), the dimensionless viscous stress tensor $\underline{\underline{\tau}}$ appears in the dimensionless function of dissipation, which can be written in curvilinear coordinate system as

$$\Phi_D = \underline{\underline{\tau}} \cdot\cdot (\nabla \otimes \mathbf{U}) =$$

$$= \left(\xi_X \frac{\partial \mathbf{U}}{\partial \xi} + \eta_X \frac{\partial \mathbf{U}}{\partial \eta} + \zeta_X \frac{\partial \mathbf{U}}{\partial \zeta}\right) \cdot \left(\tau_{XX} \cdot \mathbf{e}_\xi + \tau_{YX} \cdot \mathbf{e}_\eta + \tau_{ZX} \cdot \mathbf{e}_\zeta\right) +$$

$$+ \left(\xi_Y \frac{\partial \mathbf{U}}{\partial \xi} + \eta_Y \frac{\partial \mathbf{U}}{\partial \eta} + \zeta_Y \frac{\partial \mathbf{U}}{\partial \zeta}\right) \cdot \left(\tau_{XY} \cdot \mathbf{e}_\xi + \tau_{YY} \cdot \mathbf{e}_\eta + \tau_{ZY} \cdot \mathbf{e}_\zeta\right) +$$

$$+ \left(\xi_Z \frac{\partial \mathbf{U}}{\partial \xi} + \eta_Z \frac{\partial \mathbf{U}}{\partial \eta} + \zeta_Z \frac{\partial \mathbf{U}}{\partial \zeta}\right) \cdot \left(\tau_{XZ} \cdot \mathbf{e}_\xi + \tau_{YZ} \cdot \mathbf{e}_\eta + \tau_{ZZ} \cdot \mathbf{e}_\zeta\right) =$$

$$= \tau_{XX} \left(\xi_X \frac{\partial U}{\partial \xi} + \eta_X \frac{\partial U}{\partial \eta} + \zeta_X \frac{\partial U}{\partial \zeta}\right) +$$

$$+ \tau_{XY} \left(\xi_Y \frac{\partial U}{\partial \xi} + \eta_Y \frac{\partial U}{\partial \eta} + \zeta_Y \frac{\partial U}{\partial \zeta}\right) +$$

$$
\begin{aligned}
&+\tau_{XZ}\left(\xi_Z\frac{\partial U}{\partial \xi}+\eta_Z\frac{\partial U}{\partial \eta}+\zeta_Z\frac{\partial U}{\partial \zeta}\right)+\\
&+\tau_{YX}\left(\xi_X\frac{\partial V}{\partial \xi}+\eta_X\frac{\partial V}{\partial \eta}+\zeta_X\frac{\partial V}{\partial \zeta}\right)+\\
&+\tau_{YY}\left(\xi_Y\frac{\partial V}{\partial \xi}+\eta_Y\frac{\partial V}{\partial \eta}+\zeta_Y\frac{\partial V}{\partial \zeta}\right)+\\
&+\tau_{YZ}\left(\xi_Z\frac{\partial V}{\partial \xi}+\eta_Z\frac{\partial V}{\partial \eta}+\zeta_Z\frac{\partial V}{\partial \zeta}\right)+\\
&+\tau_{ZX}\left(\xi_X\frac{\partial W}{\partial \xi}+\eta_X\frac{\partial W}{\partial \eta}+\zeta_X\frac{\partial W}{\partial \zeta}\right)+\\
&+\tau_{ZY}\left(\xi_Y\frac{\partial W}{\partial \xi}+\eta_Y\frac{\partial W}{\partial \eta}+\zeta_Y\frac{\partial W}{\partial \zeta}\right)+\\
&+\tau_{ZZ}\left(\xi_Z\frac{\partial W}{\partial \xi}+\eta_Z\frac{\partial W}{\partial \eta}+\zeta_Z\frac{\partial W}{\partial \zeta}\right),
\end{aligned}
\tag{8.18}
$$

where $\mathbf{e}_\xi, \mathbf{e}_\eta, \mathbf{e}_\zeta$ are the base unit vectors of the curvilinear coordinate system. The first derivatives appear in the dimensionless function of dissipation (8.18) have also been approximated by employing second-order central differences similarly to the discretization of viscous flux terms for both Newtonian fluid and non-Newtonian fluid models. The essential part of the generalization of the governing equations of Tzirtzilakis and Loukopoulos [9] for using any other constitutive equation is the inclusion of the elements of the viscous stress tensor of any kind of fluid in the momentum equation (8.13) and in the function of dissipation (8.18) in the temperature equation (8.14). For steady-state, incompressible, non-isothermal, Newtonian and non-Newtonian biomagnetic fluid flow in the presence of a uniform magnetic field, the perturbed system of equations (8.12)-(8.14) has been solved by using both, the classical AC and the proposed FSAC-PP solution methods (see more details about the FSAC-PP method in Chapter 4). The scope of this chapter is to present a numerical example to investigate the capability of the proposed FSAC-PP solution method for complex multiphysics flow problem. Although the geometry of the benchmark test case is relatively simple, the background of the investigated problem is very complex from both physical and mathematical modelling point of view. The present chapter also focuses on the numerical modelling and its consequences of the multiphysics problem compared to the classical AC method and the computational data of Tzirtzilakis and Loukopoulos [9]. More details can be found about the physical aspects of the examined problem in [9]. The two-dimensional microfluidic benchmark test case for the multiphysics problem has been presented in the next section.

8.3 Microfluidic Benchmark Test Case

To use the proposed FSAC-PP method for simulating non-Newtonian biofluid flow under the presence of uniform magnetic field, compared to the classical AC method and to the computational data of Tzirtzilakis and Loukopoulos [9], two simulations have been performed by employing 3^{rd}-order interpolation for the intercell fluxes at $Re = 300$, $Mn_M = 40$, and $Mn_F = 0$. The geometry of the two-dimensional straight microfluidic channel with the location of the uniform magnetic field has been shown in Figure 8.2.

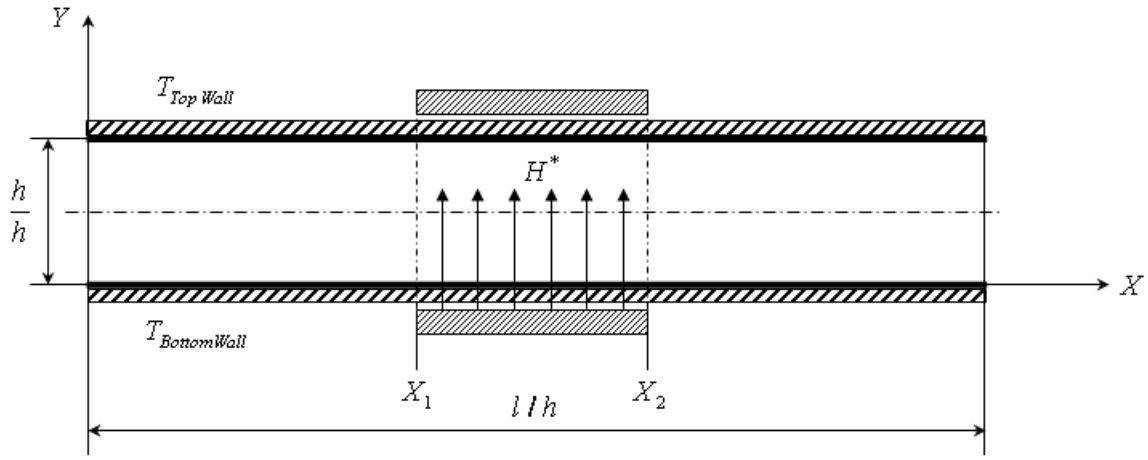

Figure 8.2: Location of the uniform magnetic field in the two-dimensional straight microfluidic channel.

The computational domain consists of 181×40 node points $(180 \times 39$ control cells$)$ on the fine grid. Since the computational results have been computed on a similar grid resolution as used for the microfluidic channel in Chapter 5, a grid convergence study has not been performed for this two-dimensional benchmark test case. The height h of the present straight microfluidic channel is $10\mu m$, and the length l is equal to $180\mu m$. The magnetic field is located between the dimensionless coordinates X_1 and X_2, respectively, which can appropriately be chosen. The dimensional and dimensionless geometrical sizes of the two-dimensional microfluidic channel have been summarized in Table 8.1.

	Two-dimensional straight microfluidic channel	
Sizes	μm	dimensionless
l	180	18
h	10	1

Table 8.1: Geometrical sizes of the two-dimensional straight microfluidic channel under the presence of uniform electromagnetic field.

A mathematical task can be formulated in terms of boundary and initial conditions for the non-isothermal pressure-driven laminar flow in the straight microfluidic channel. Dimensionless quantities have been used in the simulations, therefore, the spatial coordinates have been normalized by the height h of the channel. From wall to wall, the inlet velocity profile normalized by the maximum velocity of the flow u_{max} can be derived based on Eqs. (5.2)-(5.6) as

$$U_{inlet}(0,Y) = \frac{u}{u_{max}} = 4Y(1-Y), \tag{8.19}$$

and a Dirichlet-type inlet boundary condition has also been prescribed for the dimensionless temperature assuming that the inlet temperature profile is a linear function as

$$T_{inlet}(0,Y) = Y. \tag{8.20}$$

The dimensionless pressure has been prescibed as equal to zero at the inlet section, which can be written as $P_{inlet}(0,Y) = 0$. Thus, the boundary conditions are Dirichlet-type in the inlet section. The outlet boundary conditions for the dimensionless velocity components and temperature can be prescribed as

$$\frac{\partial U(L,Y)}{\partial X} = 0, \quad \frac{\partial V(L,Y)}{\partial X} = 0, \quad \text{and} \quad \frac{\partial T(L,Y)}{\partial X} = 0, \tag{8.21}$$

which are Neumann-type boundary conditions, where L is the dimensionless spatial coordinate of the outlet section. The dimensionless pressure has been set to one at the outlet section, which is a Dirichlet-type boundary condition, and can be written as $P_{outlet}(L,Y) = 1$. The wall is non-moving, therefore, the dimensionless velocity components U and V are equal to zero on the bottom and upper walls as

$$U_{upperwall}(X,1) = U_{bottomwall}(X,0) = V_{upperwall}(X,1) = V_{bottomwall}(X,0) = 0. \tag{8.22}$$

Dirichlet-type boundary conditions have also been prescribed for the dimensionless temperature on the bottom and upper walls as

$$T_{upperwall}(X,1) = 1, \quad \text{and} \quad T_{bottomwall}(X,0) = 0. \tag{8.23}$$

Neumann-type and consistent boundary conditions are prescribed for the dimensionless pressure on the bottom and upper walls as suggested by Karniadakis et al. [23, pp. 514-517] based on Eq. (4.43). More details can be found in subsection 4.2.2. The simulation parameters have been summarized in Table 8.2.

Simulation Parameters	
Physical Quantities with Units	Description of the Physical Quantity
$\rho = 1050\ kg/m^3$	Density of the biomagnetic fluid
$\mu = 3.2 \cdot 10^{-3}\ kg/ms$	Dynamic viscosity of blood
$k = 1.832 \cdot 10^{-3}\ J/msK$	Thermal conductivity
$c_p = 14.286\ J/kgK$	Specific heat at constant pressure
$\sigma = 0.7\ S/m$	Electrical conductivity of stationary blood
$\vartheta_{uw} = 42\ °C$	Upper wall temperature
$\vartheta_{lw} = 10.5\ °C$	Lower wall temperature
$B = 8\ Tesla$	Induction of magnetic field
$H = 40\ A/m$	Magnetic field strength
$a_1 = 5$	Coefficient to compute the magnetic field gradient
$a_2 = 5$	Coefficient to compute the magnetic field gradient
$u_{max} = 1.828 \cdot 10^{-2} m/s$	Maximum velocity
$Re = 300$	Reynolds number
$\mathrm{Pr} = 25$	Prandtl number
$\mathrm{Ec} = 7.43 \cdot 10^{-7}$	Eckert number
$\varepsilon = 9$	Temperature number
$Mn_F = 0$	Magnetic number based on upper wall temperature
$Mn_{FC} = 0$	Magnetic number based on the Curie temperature
$Mn_M = 40$	Magnetic number from the field of MHD

Table 8.2: Simulation parameters, dimensional and dimensionless physical quantities relying on the paper of Tzirtzilakis and Loukopoulos [9].

Note that according to the paper [9], the electrical conductivity of stationary blood, $\sigma = 0.7\ S/m$, is a measured value (see Table 8.2), and the temperature independent electrical conductivity of stationary blood, $\sigma = 0.8\ S/m$, is a computed value [9]. The numerical results of the performed simulations for Newtonian fluid and non-Newtonian power law fluid have been reported and discussed in the following section.

8.4 Results and Discussion

For steady-state, incompressible, non-isothermal, Newtonian biofluid flow under the presence of uniform magnetic field, the importance of the model of Tzirtzilakis and Loukopoulos [9] is that it takes into account the effects of ferro-hydrodynamics (FHD) and magnetohydrodynamics (MHD) jointly. Originally, Haik et al. [183, 184, 185] assumed that blood is an electrically non-conducting fluid, thus the model equations were constructed relying on the FHD approach [186, 187, 188, 189, 190]. Since blood, as observed by different authors is an electrically conducting fluid (e.g., see in [191, 192]), the Lorentz force needs also to be taken into account. The Lorentz force becomes dominant, where the uniform magnetic field is applied between the dimensionless coordinates X_1 and X_2 (see Figure 8.2); because the magnetic field strength H^* is high in this region [9]. Tzirtzilakis and Loukopoulos [9] pointed out that the electrical conductivity of blood changes at different flow rates. In this thesis, the measured electrical conductivity value of stationary blood flow has been taken into account in the simulations (see Table 8.2); which was measured by Gabriel et al. [192].

Both Newtonian and non-Newtonian blood flow (relying on a power law fluid model) have been simulated by employing the proposed FSAC-PP and the classical AC methods at $Re = 300$, $Mn_M = 40$, and $Mn_F = 0$; which means that the effects of MHD have been taken into account and the effects of FHD have been neglected. The reason for choosing this test case is that Tzirtzilakis and Loukopoulos [9] published computational data in order to show the effect of the uniform localized magnetic field on the dimensionless velocity component U at different cross-sections. In the first test case, a Newtonian fluid model has been employed for modelling the electrically conducting blood flow in the presence of a uniform magnetic field. Both, the AC and FSAC-PP methods show discrepancy closed to the wall compared to the computational data of Tzirtzilakis and Loukopoulos [9]; especially in the region where the magnetic field is applied; but the maximum values of velocity profiles have been found nearly the same compared to [9] at different volume flow rates. The reason for this difference might be that the FSAC-PP and AC methods employ pseudo-time stepping procedure, which is a pseudo-transient approach for solving steady-state problems, but the solution method of Tzirtzilakis and Loukopoulos [9] is relying on the purely stationary streamfunction-vorticity formulation. The results show that the maximum values of the flow velocity decreased when the biofluid entered into the zone of applied uniform magnetic field (see Figure 8.3). In terms of efficiency of the Newtonian fluid flow approach, the FSAC-PP method consumes 1.43 times less total number of multigrid iterations on the fine grid than the AC method; which means that the FSAC-PP method is slightly more efficient than the AC method for this test case (see Figure 8.4 and Table 8.3). The numerical results of both AC and FSAC-PP methods

show discrepancy closed to the wall compared to the computational data of Tzirtzilakis and Loukopoulos [9] when the non-Newtonian power law fluid approach as proposed by Walburn and Schneck [54], has been employed relying on Eqs. (3.196)-(3.197). Although, the difference might be minor between the Newtonian and non-Newtonian fluid models (see an example in Figure 8.1, and see Figure 8.5), the non-Newtonian effect of the fluid might become significant in the flow region where the uniform magnetic field is applied. The non-Newtonian fluid approach is much more realistic than the Newtonian blood rheological model despite of the fact that the blood is a weak non-Newtonian fluid [56]. In terms of accuracy, the non-Newtonian fluid flow approach relying on the FSAC-PP and AC methods exhibit slightly better agreement with the results of Tzirtzilakis and Loukopoulos [9] than the Newtonian fluid flow approach. In terms of efficiency of the non-Newtonian fluid flow approach, the FSAC-PP method consumes 1.08 times less total number of multigrid iterations than the AC method; which means that the FSAC-PP method is also slightly more efficient than the classical AC method in the present test case (see Figure 8.6 and Table 8.4). The current study also suggests that the importance of the non-Newtonian effect may be significant when the Lorentz force is present in the fluid flow. Overall, the accuracy and efficiency of FSAC-PP and AC methods exhibit minor differences for the present two-dimensional benchmark.

Although the model equations of Tzirtzilakis and Loukopoulos [9] have been further extended and generalized to steady-state, incompressible, non-Newtonian biofluid flows under the presence of a uniform magnetic field, the velocity field in the magnetic source term has not been taken into account in the eigenvalue system of the scalar governing equations (4.2). This assumption may lead to a numerical instability, because of the numerical solution of hyperbolic systems becomes sensitive when high values appear in the source terms [27]. In the present test case, when the magnetic field strength is increased by the FHD effect, which also means that the FHD magnetic number Mn_F is increased, the magnitude of source terms may become relatively high in the momentum and temperature equations (8.13)-(8.14); therefore, numerical instabilities may arise by employing both of the FSAC-PP and AC methods. Consequently, the inclusion of the velocity field of the magnetic source terms in the eigenvalue system of scalar equations (4.2) may further improve the numerical stability of the FSAC-PP and AC methods. Note that by taking into account only the FHD terms of the perturbed governing equations (8.12)-(8.14), the streamline pattern of the flow is also changed, which has been shown in Figure 8.7 at $Re = 300$, $Mn_M = 0$, and $Mn_F = 11.39$. More details can be found about the effect of dimensionless numbers on the fluid flow pattern in the work of Tzirtzilakis and Loukopoulos [9]. As a future work, other types of non-Newtonian blood fluid models may be further investigated on the present two-dimensional benchmark.

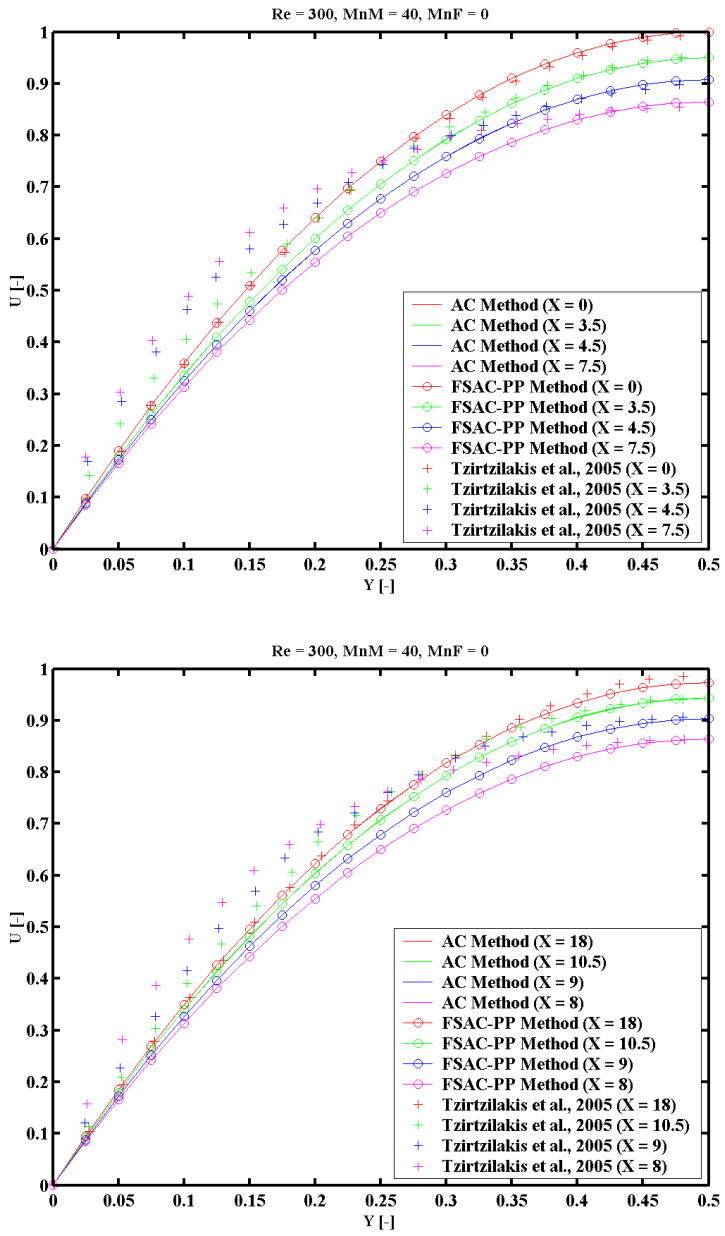

Figure 8.3: Distribution of the velocity component U using the Newtonian fluid model at different X positions in the microfluidic channel compared to the computational data of Tzirtzilakis and Loukopoulos at $Re = 300$, $Mn_M = 40$, and $Mn_F = 0$.

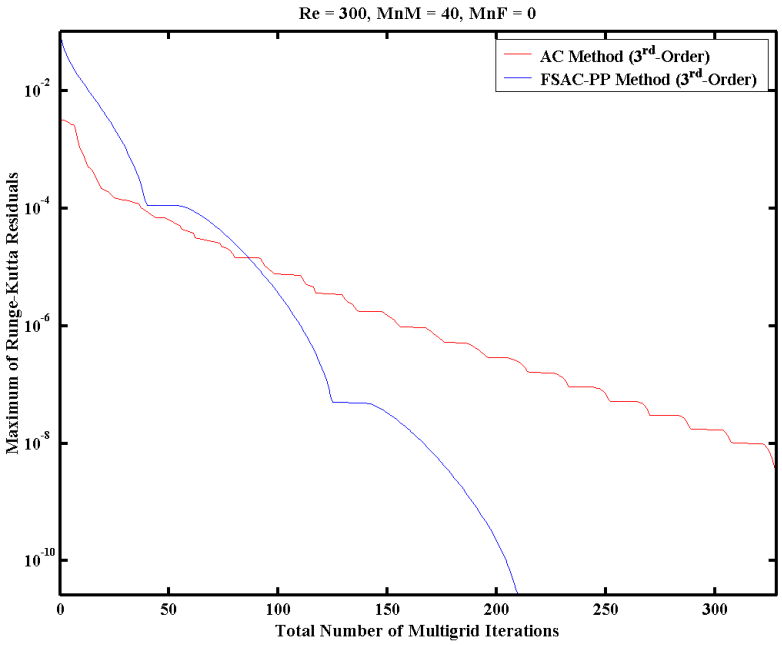

Figure 8.4: Comparison of the numerical convergence of the AC and FSAC-PP methods using Newtonian fluid model in the presence of uniform localized magnetic field in the microfluidic straight channel; maximum values of Runge-Kutta residuals versus total number of multigrid iterations on the fine grid using 3^{rd}-order interpolation at $Re = 300$, $Mn_M = 40$, $Mn_F = 0$.

	$Re = 300$, $Mn_M = 40$, $Mn_F = 0$
	Order of Intercell Flux Interpolation: 3^{rd}-Order
	Total Number of Multigrid Iterations on the Fine Grid
AC Method	328
FSAC-PP Method	228

Table 8.3: Comparison of the numerical convergence of the AC and FSAC-PP methods using Newtonian fluid model in the presence of uniform localized magnetic field in the microfluidic straight channel; total number of multigrid iterations on the fine grid using 3^{rd}-order interpolation at $Re = 300$, $Mn_M = 40$, $Mn_F = 0$.

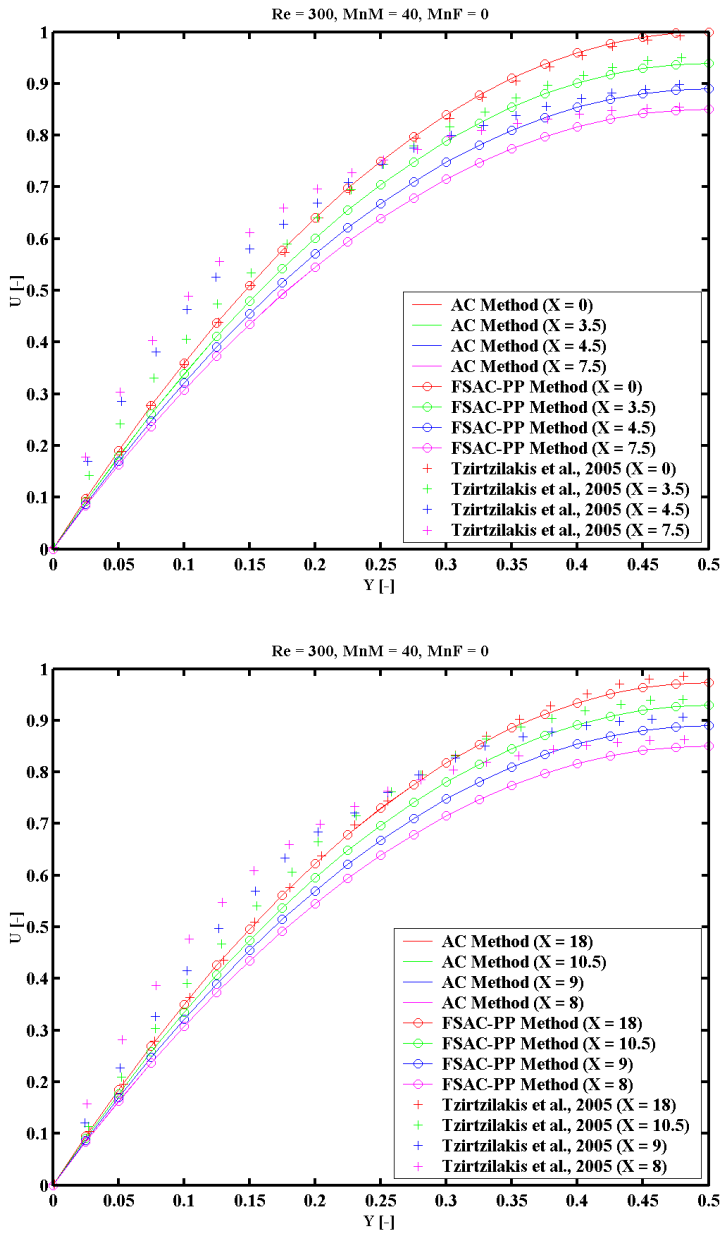

Figure 8.5: Distribution of the velocity component U using the non-Newtonian power law fluid model at different X positions in the microfluidic channel compared to the computational data of Tzirtzilakis and Loukopoulos at $Re = 300$, $Mn_M = 40$, and $Mn_F = 0$.

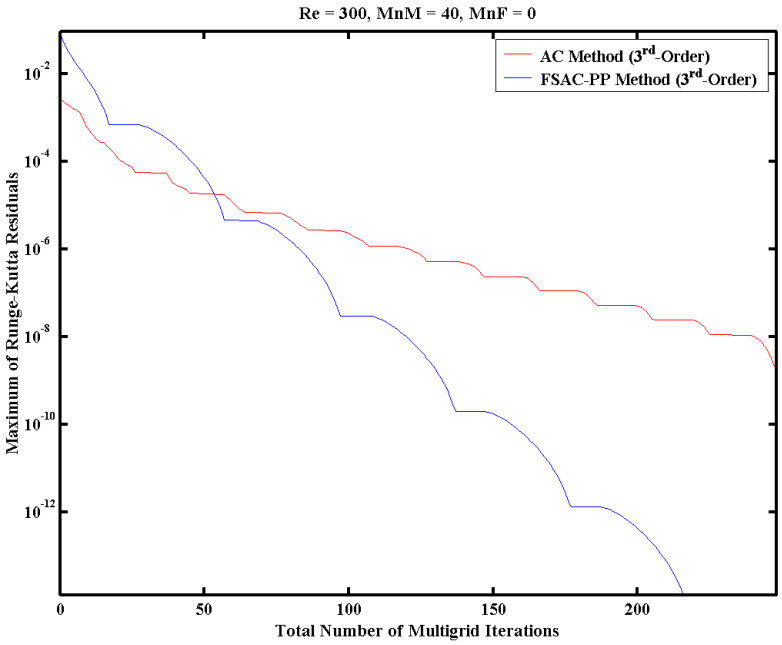

Figure 8.6: Comparison of the numerical convergence of the AC and FSAC-PP methods using non-Newtonian power law fluid model in the presence of uniform localized magnetic field in the microfluidic straight channel; maximum values of Runge-Kutta residuals versus total number of multigrid iterations on the fine grid using 3^{rd}-order interpolation at $Re = 300$, $Mn_M = 40$, $Mn_F = 0$.

	$Re = 300$, $Mn_M = 40$, $Mn_F = 0$
	Order of Intercell Flux Interpolation: 3^{rd}-Order
	Total Number of Multigrid Iterations on the Fine Grid
AC Method	248
FSAC-PP Method	228

Table 8.4: Comparison of the numerical convergence of the AC and FSAC-PP methods using non-Newtonian power law fluid model in the presence of uniform localized magnetic field in the microfluidic straight channel; total number of multigrid iterations on the fine grid using 3^{rd}-order interpolation at $Re = 300$, $Mn_M = 40$, $Mn_F = 0$.

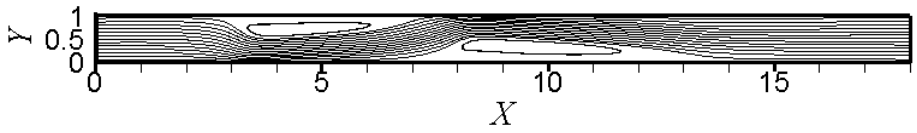

Figure 8.7: Streamline pattern for two-dimensional, steady-state, incompressible, non-Newtonian power law fluid flow in the presence of uniform magnetic field obtained by the author of this thesis at $Re = 300$, $Mn_M = 0$, $Mn_F = 11.39$.

8.5 Summary and Conclusions

In this chapter, the proposed FSAC-PP method in conjunction with the FMG-FAS multigrid technique [7] has been tested for steady-state, incompressible, non-isothermal, Newtonian and non-Newtonian biofluid flow in the presence of uniform magnetic field in a two-dimensional straight microfluidic channel at $Re = 300$, $Mn_M = 40$, and $Mn_F = 0$. The model equations of Tzirtzilakis and Loukopoulos [9] have been further extended and generalized to use any types of constitutive equation for the blood. In the present test case, the non-Newtonian blood rheological model was relying on a version of the power law fluid model as proposed by Walburn and Schneck [54]. The numerical results of the proposed FSAC-PP method have been compared to the classical AC method and to the computational data of Tzirtzilakis and Loukopoulos [9]. In terms of accuracy, the overall results of the non-Newtonian power law fluid approach show very similar agreement with the obtained results of the Newtonian fluid model. In terms of efficiency, the proposed FSAC-PP method is slightly more efficient than the classical AC method; therefore, overall, the accuracy and efficiency of FSAC-PP and AC methods exhibit minor differences for the present two-dimensional benchmark. When the magnetic field strength is increased by the FHD effect, the magnitude of the source terms may become relatively high in the momentum and temperature equations (8.13)-(8.14) which may lead to numerical instabilities by employing either the AC or FSAC-PP methods. Consequently the inclusion of the velocity field of the magnetic source terms in the eigenvalue system of scalar equations (4.2) may improve further the stability of the numerical solution. As future work, relying on the generalized FHD and MHD model equations (8.4)-(8.6) for using any constitutive relationships, other types of non-Newtonian blood fluid models may be further investigated on the present two-dimensional benchmark.

Chapter 9

Acoustic Wave and ssDNA Flow Modelling in a Microfluidic T-Channel

9.1 Introduction

This chapter focuses on acoustic wave modelling in conjunction with high-resolution characteristics-based (CB) Godunov-type method for solving unsteady, incompressible, laminar flow problem in a three-dimensional microfluidic T-channel. A simplified acoustic wave source term model has been adopted and further developed to investigate the effects of acoustic waves on the Newtonian fluid flow pattern under the continuum hypothesis. The adopted acoustic wave model appears as the source term of the divergence of acoustic intensity in the momentum equation. The hyperbolic-type second-order acoustic wave equation has been solved for the acoustic pressure and both, the FSAC-PP and AC formulations have been employed for solving the system of governing equations. The proposed acoustic source term model is a closer approach to Poesio and Ooms theory [193] rather than to Lighthill's theory [194] or to the theory of perturbation [195]. In the presented numerical study, the acoustic waves interact with ssDNA strands that have been released in the investigated microfluidic T-channel; and have been modelled through a coupled Eulerian-Lagrangian dynamics developed by Benke et al. [10, 11].

In the last two decades, researchers devoted significant attention to surface acoustic waves (SAW) in the fields of micro- and nanofluidics. The reason for this interest is the possibility to transfer acoustic waves (AW) in the fluid flow that can dynamically cause changes in the material properties such as density and viscosity, and impact the pressure and velocity fields. SAW were discovered and explained by Lord Rayleigh in 1885 [196, 197], therefore, these are also known as Rayleigh waves. Rayleigh discussed the mode of wave propagation, and described the properties of these waves that consist of

longitudinal and vertical shear components. These Rayleigh wave components can also be coupled with any kind of medium on the surface giving the idea of SAW devices [197].

Rocha-Gaso et al. [196] published a review paper on Surface Generated Acoustic Wave (SGAW) technology considering technological and scientific improvements in the last 40 years. According to their classification [196], three groups of AW devices exist upon the AW guiding process; such as Bulk Acoustic Wave (BAW), SAW and Acoustic Plate Mode (APM) devices [196]. These devices operate with AW propagation in different ways and a wave propagates as a) "unguided through the volume of substrate" (BAW device), b) "guided or unguided along a single surface of substrate" (SAW device), and c) "guided by reflection from multiple surface of the substrate" (APM device) [196, p. 5742]. SAW and APM biosensors can potentially be considered for DNA detection as reported recently in [196, 197, 198]. These devices were further developed in the last two decades, therefore, SAW and APM type devices can work in liquid media [196, 197, 198] for biosensing applications as well. These devices are also capable of detecting pathogen agents such as bacteria and viruses reported by Rocha-Gaso et al. [196].

The modelling of physical phenomena in the SAW devices is indispensable to improve further the sensor design [196, 197, 198]. Mathematical models and Finite Element Method (FEM) based simulations in SAW devices can be found in the literature [199, 200]. These physical phenomena are essentially complex multiphysics problems, because the AW appears as acoustic pressure in the flow field, which can cause significant changes in the flow behaviour; therefore, these changes can lead to physical instabilities in the flow pattern. Multiphysics problems related to fluid dynamics in small-scale microfluidic devices are substantially different from physical problems in macro-scale systems. In terms of AW in macro-scale systems [196, 197, 198, 199, 200], the density and pressure changes due to the presence of AW are much smaller than the changes due to the fluid flow; therefore, the AW model can be separated from the fluid flow model. There are even cases, when AW can be neglected [195]. Thus, the AW model in small-scale devices has to be taken into account coupled with the fluid flow. In this thesis, a simplified AW model has been adopted [193] and further developed to investigate the effects of AW on the Newtonian fluid flow pattern under the continuum hypothesis. The adopted AW model appears as the divergence of acoustic intensity in the momentum equation. The AW equation has been solved for the acoustic pressure, which can be derived from the continuity, momentum and energy equations of compressible fluid using perturbation decomposition [195, 201]. A theoretical description of aerodynamic acoustic sources was developed by Lighthill [194] relying on the acoustic analogy. Lighthill gave a tensor description of acoustic source terms [194, 195], which may become too complicated for complex flow cases, therefore, Lilley [202] further developed Lighthill's theory in order to take into account the convection and refraction on AW in the fluid flow.

Different theoretical and practical applications can be found for AW modelling in the literature. Governing equations of acoustic perturbation was used by Shi [201] modelling structural-acoustic interaction relying on the Euler equation. For low speed, unsteady, compressible flow, Wang et al. [203] derived a system of acoustic perturbation equations investigating two-dimensional automobile door cavity in turbulent flow. Poesio and Ooms [193] proposed a relatively simple acoustic source term model for high-frequency AW on the liquid flow through porous material; and they compared their theoretical approach with experimental data. Chu [204] investigated SAW on the laminar microflow stability using the fourth-order streamfunction equation eliminating the pressure term from the Navier-Stokes equations; and coupled the system of equations with the Orr-Sommerfeld equation [204]. As a matter of fact, many authors dealt with the perturbation theory or simplified acoustic source models for solving flow problems including flow instability investigations [195, 194, 202, 203, 193]. Although the mathematical and physical background of AW are often investigated related to SAW devices, one can find only a few references relying on high-resolution CB Godunov-type method for modelling AW in conjunction with selective microfluidic sensors for DNA detection.

For capturing AW in microfluidic devices, the high-resolution CB Godunov-type method is a reliable FVM based mathematical tool for solving hyperbolic system of equations with discontinuous solutions. Therefore, this thesis focuses on AW modelling in conjunction with high-resolution CB Godunov-type method in the case of an unsteady, incompressible, laminar flow in a three-dimensional microfluidic T-channel test geometry. In this thesis, AW interact with DNA strands that have been released in the T-channel test case, and have been modelled through a coupled Eulerian-Lagrangian dynamics.

9.2 Acoustic Wave and ssDNA Flow Modelling

For solving unsteady, incompressible, laminar microfluidic flow problem with the presence of acoustic wave and DNA strands in the Newtonian fluid, the governing equations of conservation of mass and momentum may be written as

$$\nabla \cdot \mathbf{u} = 0 \tag{9.1}$$

$$\frac{D\mathbf{u}}{Dt} = \mathbf{g} - \frac{1}{\rho}\nabla p + \upsilon \nabla^2 \mathbf{u} + \frac{1}{\rho c_s}\nabla \cdot \mathbf{i}_s + \mathbf{f}_{DNA} \tag{9.2}$$

where D/Dt is the substantial (total) derivative, $\mathbf{u}$ is the velocity vector, t is the physical time, $\mathbf{g}$ is the gravity vector, p is the hydrodynamic pressure, ρ is the fluid density, υ is

the kinematic viscosity of the fluid, c_s is the speed of sound in the medium, and

$$\mathbf{i}_s = p_s \mathbf{u} \tag{9.3}$$

is the acoustic intensity (sound intensity in the medium), which is the product of the acoustic pressure p_s (acoustic pressure in the medium) and the particle velocity using Eulerian-description of the fluid flow motion. The divergence of the acoustic intensity (9.2) can be expressed as

$$\nabla \cdot \mathbf{i}_s = \nabla \cdot (p_s \mathbf{u}) = \mathbf{u} \cdot \nabla p_s + p_s (\nabla \cdot \mathbf{u}) \tag{9.4}$$

and taking into account the divergence-free (incompressibility) constraint (9.1), the second term of Eq. (9.4) will vanish, therefore, the divergence of the acoustic intensity is reduced to be the product of the particle velocity and the acoustic pressure gradient, which can also be written as

$$\nabla \cdot \mathbf{i}_s = \mathbf{u} \cdot \nabla p_s \tag{9.5}$$

consequently, Eq. (9.2) will be

$$\frac{D\mathbf{u}}{Dt} = \mathbf{g} - \frac{1}{\rho}\nabla p + \upsilon \nabla^2 \mathbf{u} + \frac{1}{\rho c_s}\mathbf{u} \cdot \nabla p_s + \mathbf{f}_{DNA} \tag{9.6}$$

where $\mathbf{f}_{DNA}$ represents an external force field modelling the dsDNA or ssDNA molecule motion. The meta-model of DNA strands, used in this thesis, including Brownian-motion and coupling Eulerian-Lagrangian description of fluid flow motion, was developed by Benke et al. [10, 11]. In order to determine the acoustic intensity relying on Eq. (9.3), the hyperbolic second-order partial differential equation (acoustic wave equation [195]) has been solved for the acoustic pressure as

$$\frac{1}{c_s^2}\frac{\partial^2 p_s}{\partial t^2} = \nabla^2 p_s. \tag{9.7}$$

To non-dimensionalise the governing equations from Eq. (9.1) to (9.7), the following

$$t^* = \frac{t u_\infty}{h}, \;\; X = \frac{x}{h}, \;\; Y = \frac{y}{h}, \;\; Z = \frac{z}{h},$$

$$U = \frac{u}{u_\infty}, \;\; V = \frac{v}{u_\infty}, \;\; W = \frac{w}{u_\infty}, \;\; \mathbf{g}^* = \frac{h}{u_\infty^2}\mathbf{g},$$

$$P = \frac{p}{\rho_\infty u_\infty^2}, \;\; P_s = \frac{p_s}{\rho_\infty u_\infty^2}, \;\; Re = \frac{2hu_\infty}{\upsilon},$$

$$Ma = \frac{u_\infty}{c_s}, \quad \mathbf{F} = \frac{h}{u_\infty^2}\mathbf{f},$$

dimensionless quantities have been introduced for time, spatial coordinates, velocity components, gravity field, hydrodynamic pressure field, acoustic pressure in the medium, and for external force field; where h, u_∞, ρ_∞ are constant reference quantities for characteristic length, velocity and fluid density. The Reynolds number Re represents the ratio of the momentum transported by convection and viscous diffusion. The Mach number Ma is the ratio of the characteristic speed of the fluid flow to the speed of sound propagation in the medium. Since, the density is constant, therefore, the reference density is equal to the fluid density as $\rho_\infty = \rho$. The average velocity magnitude u_a has been considered as the characteristic speed of the flow, therefore, $u_\infty = u_a$. Using dimensionless quantities and neglecting the gravity field $\mathbf{g}^*$, the non-dimensionalized system of perturbed governing equations relying on the AC formulation can be written as

$$\frac{1}{\beta}\frac{\partial P}{\partial \tau} + \nabla \cdot \mathbf{U} = 0 \tag{9.8}$$

which is the perturbed continuity equation [27], and

$$\frac{\partial \mathbf{U}}{\partial \tau} = -\frac{\partial \mathbf{U}}{\partial t^*} - \nabla \cdot \left(\tilde{\mathbf{U}} \otimes \tilde{\mathbf{U}}\right) - \nabla P + \frac{2}{Re}\nabla^2 \mathbf{U} + Ma\mathbf{u} \cdot \nabla P_s + \mathbf{F}_{DNA} \tag{9.9}$$

is the equation of fluid motion for unsteady, incompressible, Newtonian fluid flow using the dual-time stepping procedure; where β is the AC parameter to ensure convergence, and τ is the pseudo-time step size, which is computed in each control cell [16]. The convective flux term in the momentum equation (9.9) has been discretized and computed by applying the CB Godunov-type scheme [16]. The system of dimensionless governing equations (9.8)-(9.9) is hyperbolic-type, therefore, the Riemann method can be applied to determine the intercell CB flux values. To capture the AW in the Newtonian fluid flow field coupled with Eulerian-Lagrangian meta-modelling of the motion of DNA strands, high-resolution convective flux treatment has been recommended. Note that the non-linear convective term is the most sensitive part of the momentum equation (9.9) from the point of view of numerical stability. Therefore, to achieve a higher-order of accuracy, the 3^{rd}-order interpolation has been employed to approximate the intercell flux quantities. After performing a high accurate flow field computation, the following

$$\frac{1}{\beta^2}\frac{\partial^2 P_s}{\partial \tau^2} = \frac{1}{Ma^2}\nabla^2 P_s \tag{9.10}$$

dimensionless hyperbolic-type AW equation has been solved for the acoustic pressure to compute the acoustic pressure gradient term in the momentum Eq. (9.9). The pseudo-time

stepping procedure is advanced by using a fourth-order explicit Runge-Kutta scheme. Both of the proposed FSAC-PP and the classical AC solution methods have been employed for solving the system of governing equations (9.8)-(9.10).

9.3 Three-Dimensional Microfluidic T-Channel Test Case

The aim of this chapter is to provide information to those researchers and engineers who design highly selective microfluidic sensors for DNA detection. It might be difficult to perform accurate and trustable measurements in these devices, because of the small physical scales and geometrical sizes. Therefore, it is reasonable to develop sophisticated mathematical models and set up simulation test cases to investigate the physical phenomena operating at these small-scales. In this study, longitudinal AW interact with ssDNA chains aiming to investigate the effects of AW on the ssDNA motion. The current numerical study may essentially be important to determine the optimum location of the sensor within a DNA detection device. The ssDNA motion takes place within a three-dimensional microfluidic T-channel and is modelled through a coupled Eulerian-Lagrangian scheme [10, 11]. The sketch of the microfluidic T-channel has been shown in Figure 9.1 along with the corresponding notations of geometrical sizes.

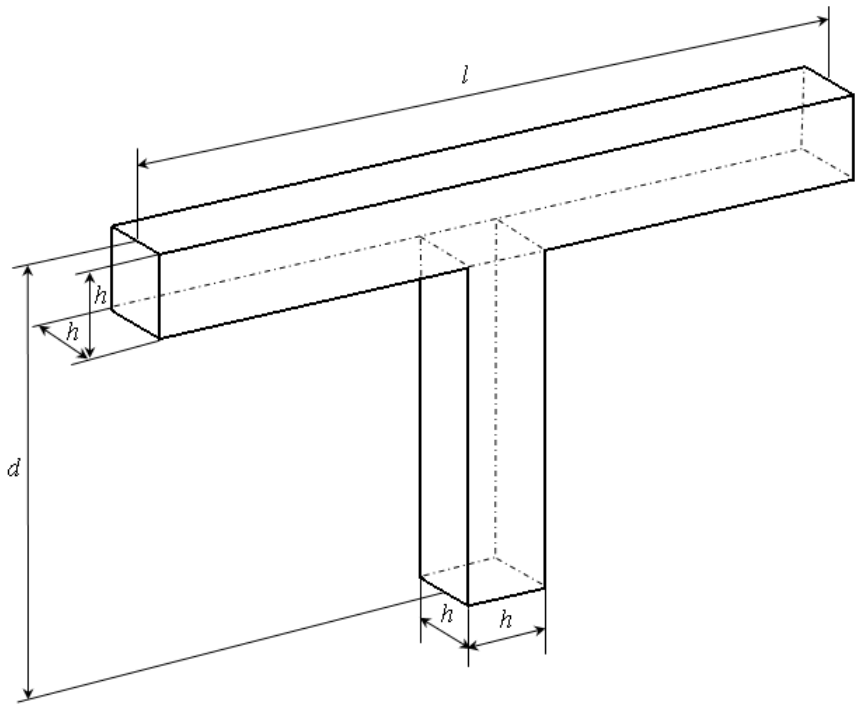

Figure 9.1: Sketch of the three-dimensional microfluidic T-channel geometry.

The dimensions of the microfluidic T-channel (*l*,*d*), corresponding to the length and depth, have been summarized in Table 9.1. The non-dimensionalization of the spatial coordinates has been carried out based on the height of the inlet sections *h*.

	Microfluidic T-channel Geometry	
Sizes	μm	dimensionless
l	110	11
h	10	1
d	60	6

Table 9.1: Geometrical sizes of the three-dimensional T-channel.

The left hand side and bottom rectangular cross sections have been considered as inlet sections with volume flow rates $Q_1 = 0.08343\, m^3/s$ and $Q_2 = 0.66750\, m^3/s$, respectively. The propagation of longitudinal AW has been modelled from the left hand side inlet to the right hand side outlet section. The longitudinal waves appear as pressure waves travelling through the liquid; and relying on the model of Poesio and Ooms [193], these waves are proportional to the gradient of acoustic pressure in the momentum equations (9.6) and (9.9). The inlet velocity profiles are parabolic surfaces related to volume flow rate, and the normal derivative of velocity components vanish at the right hand side outlet cross section of the T-channel. For the acoustic pressure, Dirichlet boundary conditions have been prescribed in the inlet and outlet sections representing the dimensionless acoustic pressure difference between 0 and 1. In the present study, the longitudinal wave, travelling through the liquid, has only been taken into account; and any other possible acoustic sources have been neglected on the boundaries of the T-channel.

9.3.1 Grid Convergence Study

To determine the optimum number of computational cells, the results of the grid convergence study have been presented in this subsection. A grid convergence study, which may also be called grid-independency study, has been performed to determine the optimum number of cells for each simulation test case. We assume that the continuum hypothesis for water is valid up to the smallest characteristic length scale of the detection system, which is bigger than 0.3 nanometer according to the Eq. (5.10). The left hand side and bottom side located inlet sections of the channel have been divided into *N* parts ($N = 10, 20, 40, 50, 100, 120, \ldots, 200$). The grid density has also been increased proportional to *N*. The expected outcome of the grid convergence study is that the numerical solution of the laminar flow problem has not to be changed above a certain number of computational cells. This way it becomes possible to decrease the computational time when the optimum number of cells is known. To compute the optimum number of cells,

the following relative errors of the main physical quantities have been defined as

$$\Delta P_{error}^{relative} = \frac{\left|\left(\int P\mathrm{dV}\right)_{fine\,grid} - \left(\int P\mathrm{dV}\right)_{coarse\,grid}\right|}{\left|\int P\mathrm{dV}\right|_{fine\,grid}}, \tag{9.11}$$

$$\Delta U_{error}^{relative} = \frac{\left|\left(\int U\mathrm{dV}\right)_{fine\,grid} - \left(\int U\mathrm{dV}\right)_{coarse\,grid}\right|}{\left|\int U\mathrm{dV}\right|_{fine\,grid}}, \tag{9.12}$$

$$\Delta V_{error}^{relative} = \frac{\left|\left(\int V\mathrm{dV}\right)_{fine\,grid} - \left(\int V\mathrm{dV}\right)_{coarse\,grid}\right|}{\left|\int V\mathrm{dV}\right|_{fine\,grid}}, \tag{9.13}$$

$$\Delta W_{error}^{relative} = \frac{\left|\left(\int W dV\right)_{fine\,grid} - \left(\int W\mathrm{dV}\right)_{coarse\,grid}\right|}{\left|\int W\mathrm{dV}\right|_{fine\,grid}}, \tag{9.14}$$

where $\Delta P_{error}^{relative}$ is the relative error of the pressure field, $\Delta U_{error}^{relative}$ is the relative error of the velocity component U, $\Delta V_{error}^{relative}$ is the relative error of velocity component V, and $\Delta W_{error}^{relative}$ is the relative error of the velocity component W relating to the volume integral of the investigated physical quantity for fine and coarse grids as well.

	T-Channel Test Case		
	N = 20 (4536 Cells)	N = 50 (19455 Cells)	N = 100 (30816 Cells)
$\left\|\Delta P_{error}^{relative}\right\|_{(\infty)}$	0.00485	0.00007	0.00006
$\left\|\Delta U_{error}^{relative}\right\|_{(\infty)}$	0.00168	0.00050	0.00048
$\left\|\Delta V_{error}^{relative}\right\|_{(\infty)}$	0.00137	0.00045	0.00041
$\left\|\Delta W_{error}^{relative}\right\|_{(\infty)}$	0.00116	0.00032	0.00029

Table 9.2: Results of grid convergence study.

The results of the grid convergence study show that the maximum norm of the relative errors decreases when N is increased, and the relative error of primitive variables does not change significantly above $N = 50$ (see Table 9.2); therefore, the optimum number of computational cells has been determined between $N = 50$ and $N = 100$. Consequently, the simulations for unsteady, incompressible, laminar, Newtonian fluid flow with and without the presence of acoustic wave and ssDNA strands have been performed by employing 27 508 node points in the three-dimensional microfluidic T-channel test case.

9.4 Results and Discussion

Simulations have been performed to investigate the pathlines of ssDNA with longitudinal AW in the macroscopic flow field at $Re = 10$ and at $Ma = 3.4 \cdot 10^{-6}$; where the speed of sound in the water has been taken as $c_s = 1497\ m/s$. The longitudinal wave length $\lambda_{longitudinal} = 4.25 \cdot 10^{-6}\ m$, which is smaller than the length of the microfluidic T-channel. The DNA sensing area has been assumed to be located in the upper wall close to the T-shape junction. Although the Mach number is very small due to the small velocity components in each flow direction; the gradient of the acoustic intensity has an apparent impact on the velocity field in the small-scale physics. The importance of the simulations presented in this chapter is that the presence of AW in the macroscopic flow field can induce flow instabilities that may also cause DNA-breaking, which should be avoided in a detection device. In the simulation, longitudinal AW have been modelled by travelling through the water medium with ssDNA molecule chain in the microfluidic T-channel. The adopted AW model takes into account the longitudinal propagation of AW as the gradient of acoustic pressure in the right hand side of the momentum equation (9.9); therefore, the velocity field is influenced via this source term. The acoustic pressure gradient is connected to hyperbolic-type and second-order acoustic wave equation (9.10). The dimensionless velocity components U, V, and W without and with the presence of longitudinal AW have been shown in Figures 9.2 to 9.9. The FSAC-PP method consumes 43.19 times less total number of multigrid iterations on the fine grid than the AC method using 3^{rd}-order intercell flux interpolation for the present benchmark at $Re = 10$. It means that the FSAC-PP method is much more efficient than the AC method in these test cases (see Figure 9.10 and Table 9.3). The velocity component U and ssDNA pathlines without and with the presence of longitudinal AW have been shown in Figures 9.11 to 9.12.

The simulation result shows that the presence of AW is the main influence on the dimensionless velocity component U. The direction of the flow approaches the sensor area from the left hand side upper inlet and the flow becomes fully developed in the right hand side outlet section (see Figure 9.12). The distribution of velocity component V with the presence of AW is slightly different in Figure 9.14 than the distribution without the presence of AW in Figure 9.13. Higher velocity components can be observed close to the ssDNA sensing area (see Figures 9.12 and 9.14) than in the simulation case without taking into account the presence of AW in the flow field (see Figures 9.11 and 9.13). These simulation results suggest that the presence of AW in the macroscopic flow field has significant influence on the pathlines of ssDNA flow without breaking the molecule chain. The results also show that the ssDNA chain flows towards the upper wall effectively without the presence of longitudinal AW in the flow field. It is important to mention that the ssDNA chain has been released when the fluid flow becomes fully developed in the

microfluidic T-channel; thus, the criterion of DNA-breaking remains unknown. To gain deeper understanding of the presence of AW in a DNA detection device, an acoustic source should be located in the opposite side of the DNA sensing area. The effect of the location of an acoustic source has to be further investigated in another study, because the results suggest that the presence of an acoustic source near the DNA sensing area could be advantageous to force the ssDNA chain to reach the sensor. The acoustic source generator could be chosen in different ways, such as using a microphone, piezoelectric crystal, or a magnetostriction device that could be attached to T-channel boundary.

The velocity magnitude and ssDNA pathlines without and with the presence of longitudinal AW have been shown in Figures 9.17 to 9.18, respectively. Although the velocity magnitudes are similar to each other, the ssDNA flow stream shows small differences as shown in Figures 9.11 to 9.18. This is due to the the wave length of longitudinal AW present in the flow field, and because the ssDNA chain mainly follow the path of the flow streamlines. For modelling ssDNA flow, the number of particles is 206 with number of bead-rod structure 20; the relative particle radius is $4.56 \cdot 10^{-5}$ m, the relative particle density is $8.005 \cdot 10^{-15}$ kg/m^3, and the rod length of chain elements is $9.15 \cdot 10^{-5}$ m in the ssDNA meta-modelling approach (see more details in [10, 11]). To ensure converged solution of the pseudo-time stepping procedure, the AC parameter β has been chosen to be 20. Note that difficulty may arise to obtain a converged numerical solution within very small tolerance values of ε (e.g. 10^{-8}). The reason for this difficulty is the gradient of the acoustic pressure in the right hand side of the momentum equation (9.9); because the velocity field might change rapidly due to the presence of longitudinal AW in the microfluidic T-channel. To overcome this numerical problem, the ssDNA meta-modelling approach has been performed after the flow field becomes fully developed; then the ssDNA chain is released in the upper inlet section. Consequently, the strong gradients of the acoustic pressure may cause numerical instability in the Eulerian-Lagrangian simulation of ssDNA flow. The results show that the FSAC-PP method consumes 15.58 times less total number of multigrid iterations on the fine grid than the AC method using 3^{rd}-order intercell flux interpolation with the presence of longitudinal AW at $Re = 10$. It means that the FSAC-PP method is more efficient than the AC method in this test case (see Figure 9.19 and Table 9.4). Overall, the numerical results suggest that the presence of AW generator near the DNA sensing area could be advantangeous, because the ssDNA chain might reach the sensing area faster than without the presence of the acoustic source generator.

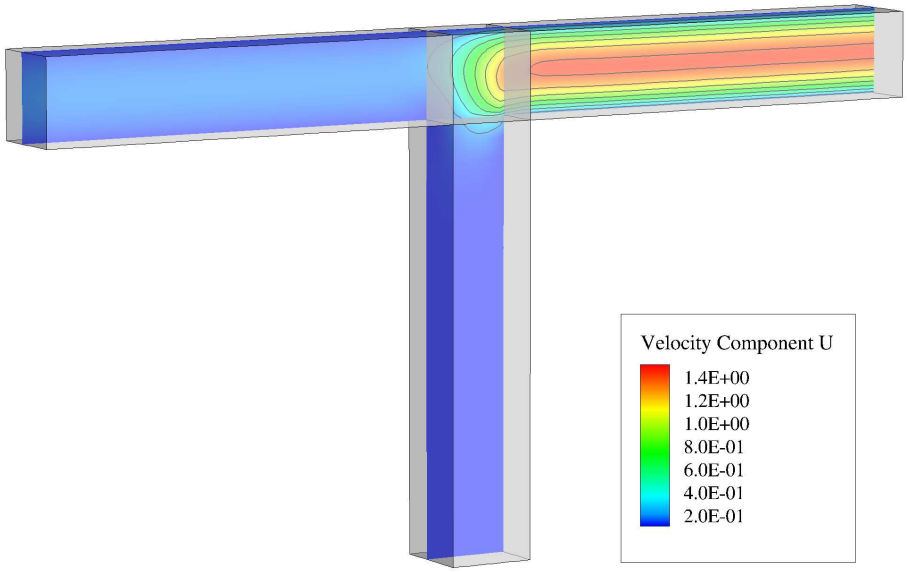

Figure 9.2: Velocity component U without the presence of AW at $Re = 10$.

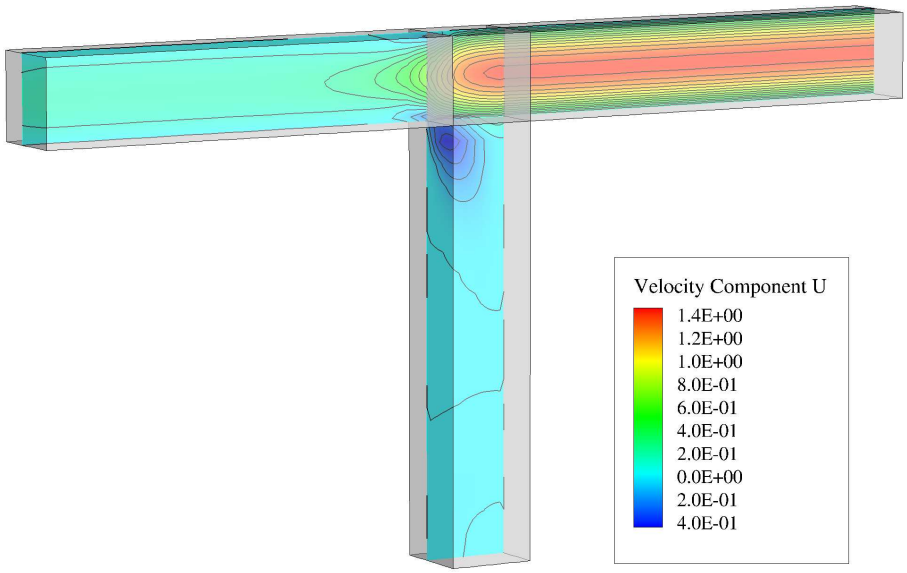

Figure 9.3: Velocity component U with the presence of AW at $Re = 10$.

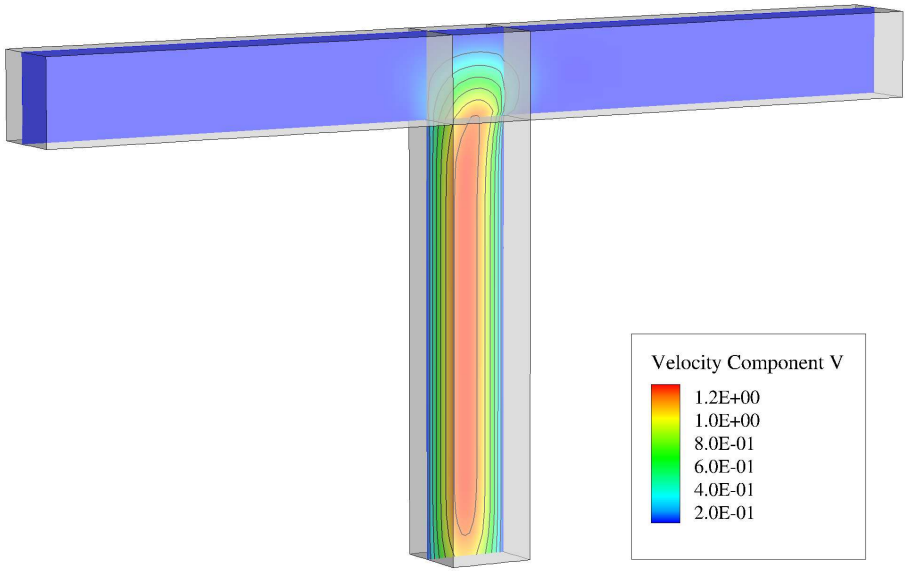

Figure 9.4: Velocity component V without the presence of AW at $Re = 10$.

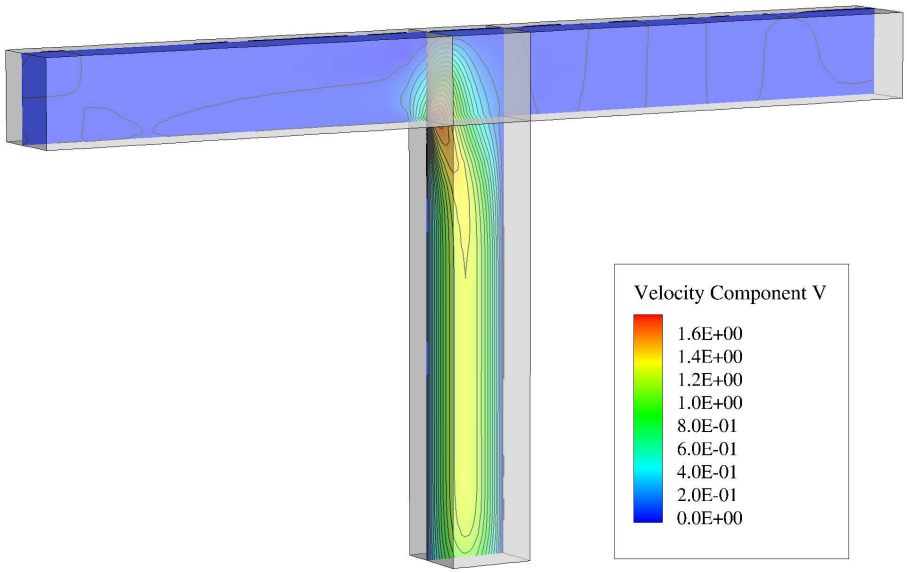

Figure 9.5: Velocity component V with the presence of AW at $Re = 10$.

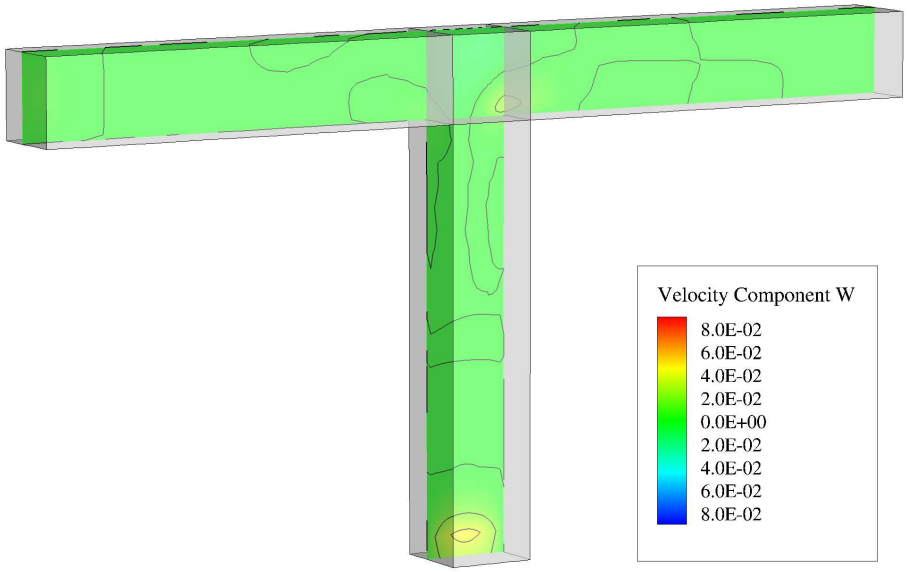

Figure 9.6: Velocity component W without the presence of AW at $Re = 10$.

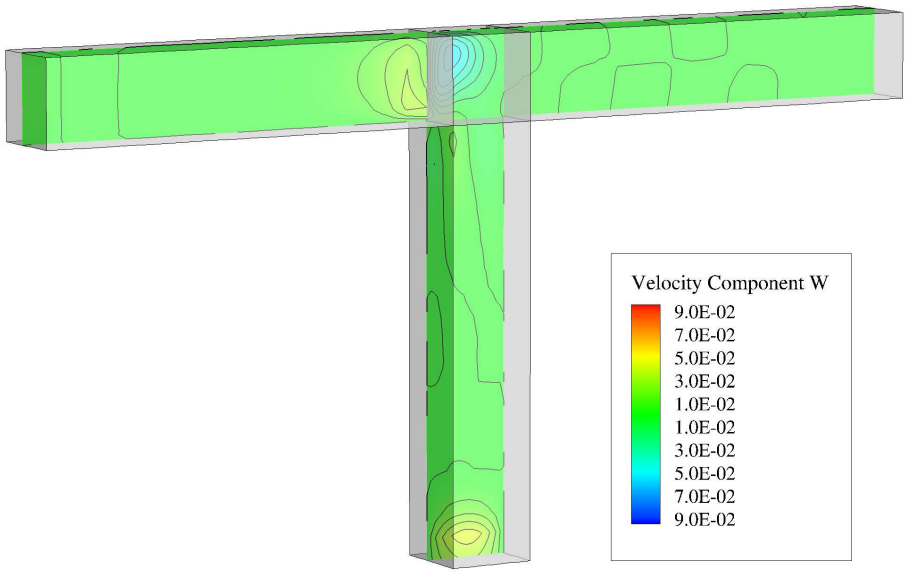

Figure 9.7: Velocity component W with the presence of AW at $Re = 10$.

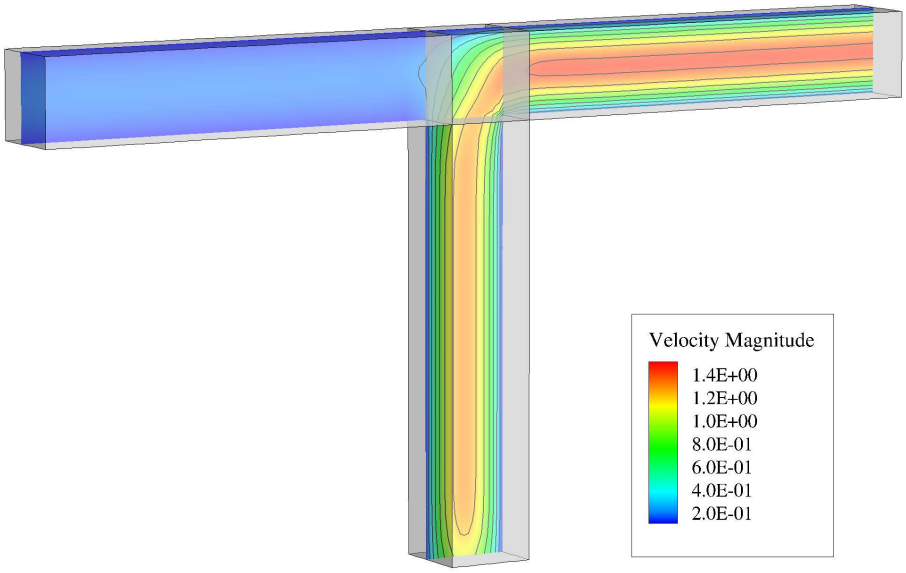

Figure 9.8: Velocity magnitude without the presence of AW at $Re = 10$.

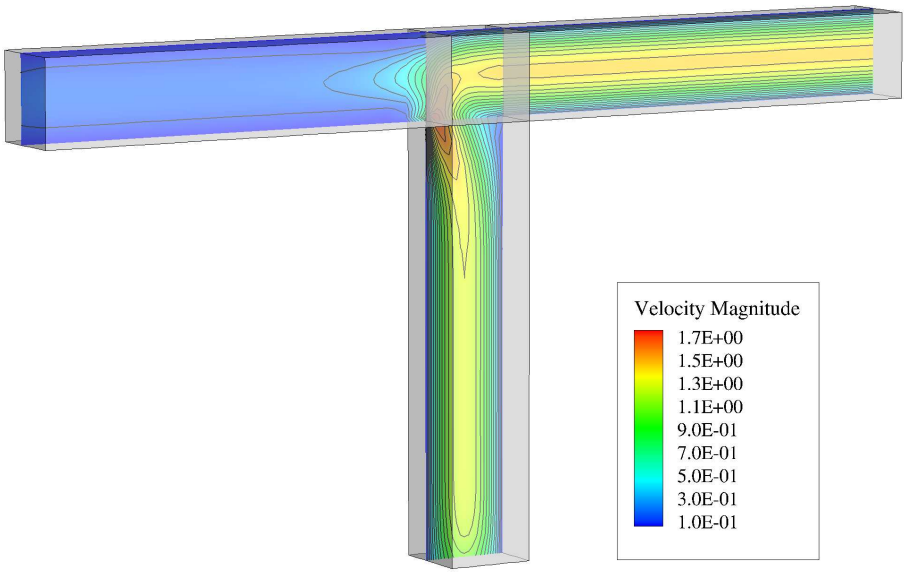

Figure 9.9: Velocity magnitude with the presence of AW at $Re = 10$.

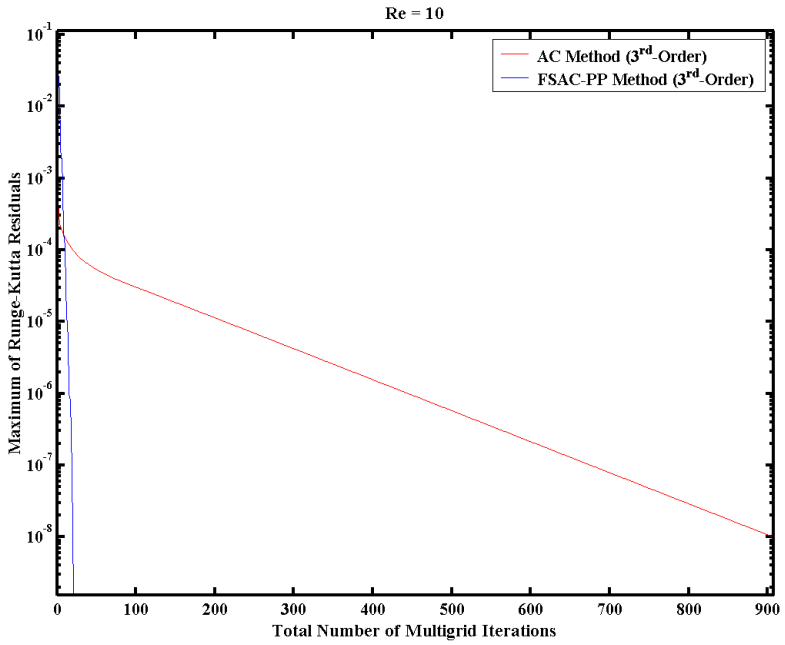

Figure 9.10: Comparison of the numerical convergence of the AC and FSAC-PP methods without modelling AW in the microfluidic T-channel; maximum values of Runge-Kutta residuals versus total number of multigrid iterations on the fine grid using 3^{rd}-order interpolation at $Re = 10$.

	$Re = 10$
	Order of Intercell Flux Interpolation: 3^{rd}-Order
	Total Number of Multigrid Iterations on the Fine Grid
AC Method	907
FSAC-PP Method	21

Table 9.3: Comparison of the numerical convergence of the AC and FSAC-PP methods without modelling AW in the microfluidic T-channel; total number of multigrid iterations on the fine grid using 3^{rd}-order interpolation at $Re = 10$.

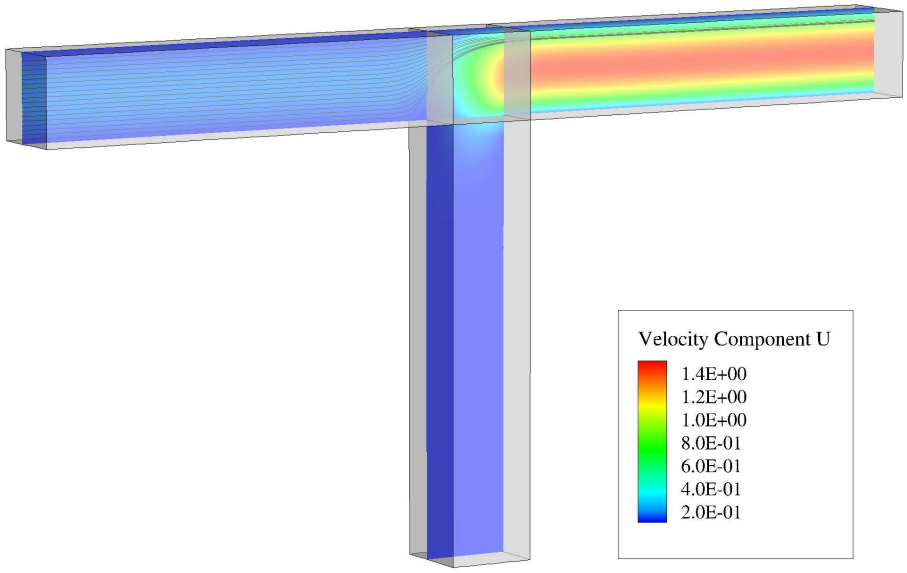

Figure 9.11: Distribution of the velocity component U and ssDNA pathlines without the presence of AW at $Re = 10$.

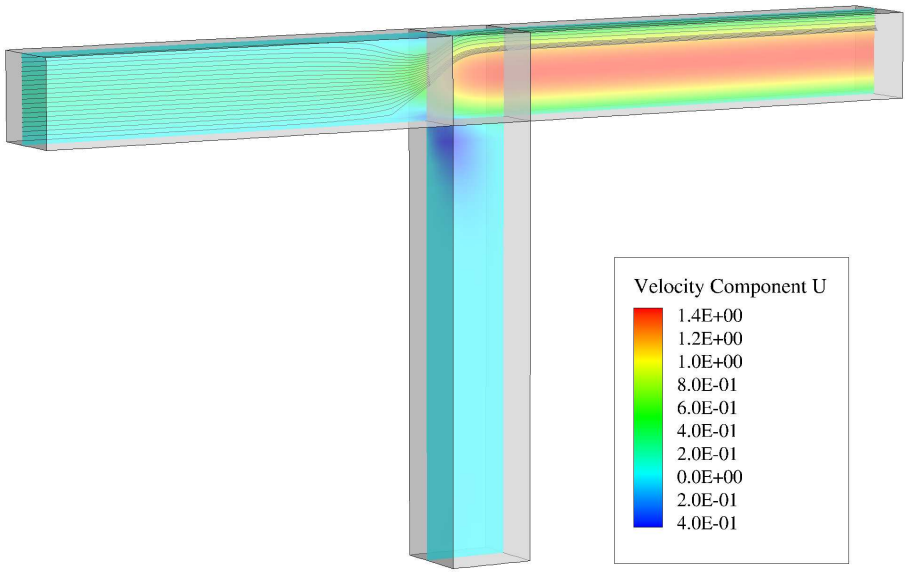

Figure 9.12: Distribution of the velocity component U and ssDNA pathlines with the presence of AW at $Re = 10$.

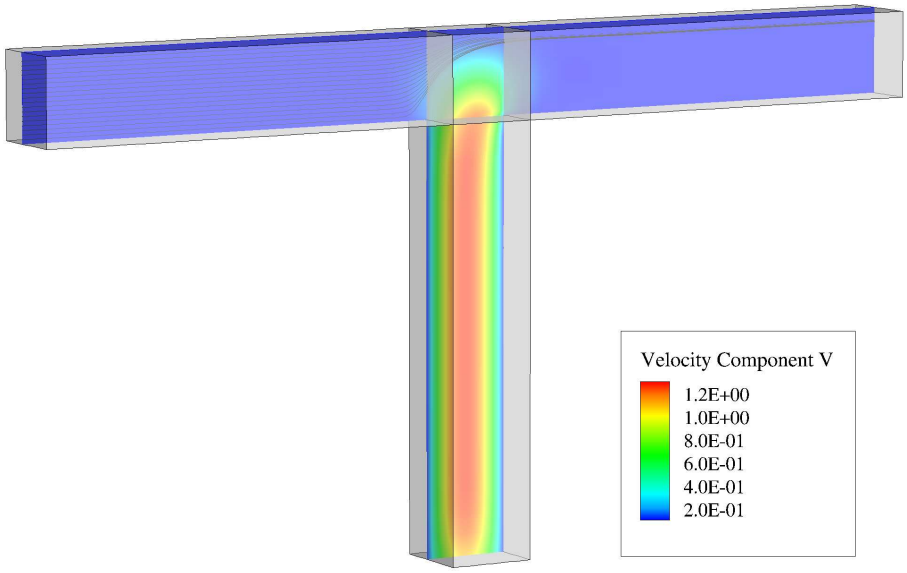

Figure 9.13: Distribution of the velocity component V and ssDNA pathlines without the presence of AW at $Re = 10$.

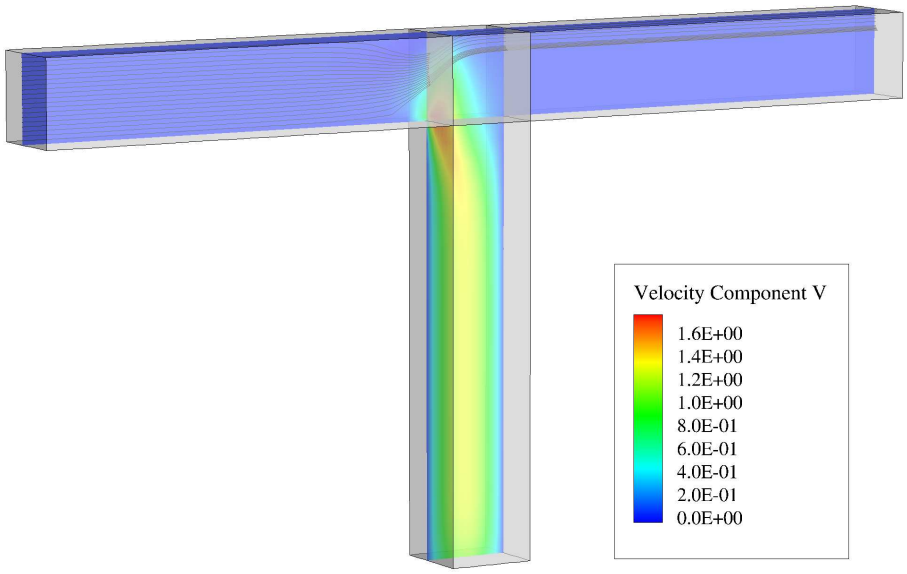

Figure 9.14: Distribution of the velocity component V and ssDNA pathlines with the presence of AW at $Re = 10$.

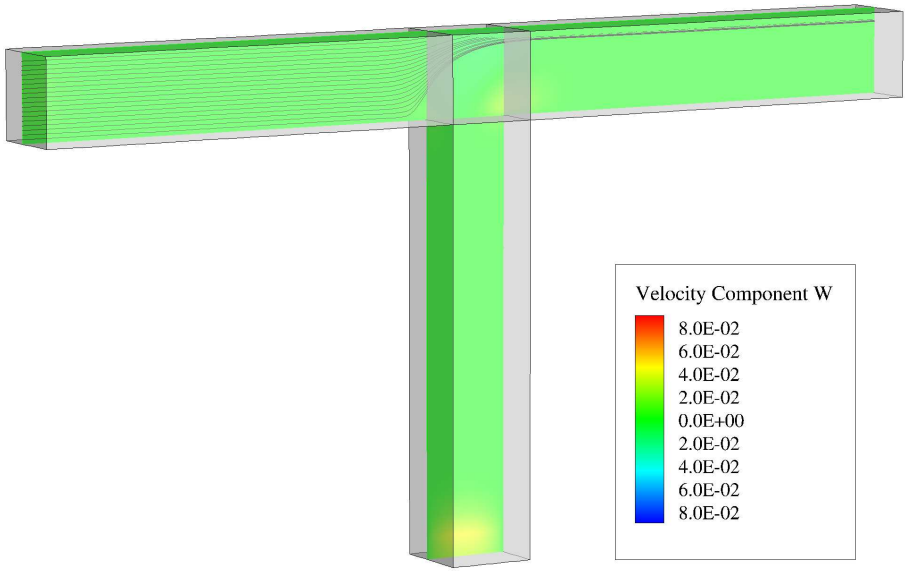

Figure 9.15: Distribution of the velocity component W and ssDNA pathlines without the presence of AW at $Re = 10$.

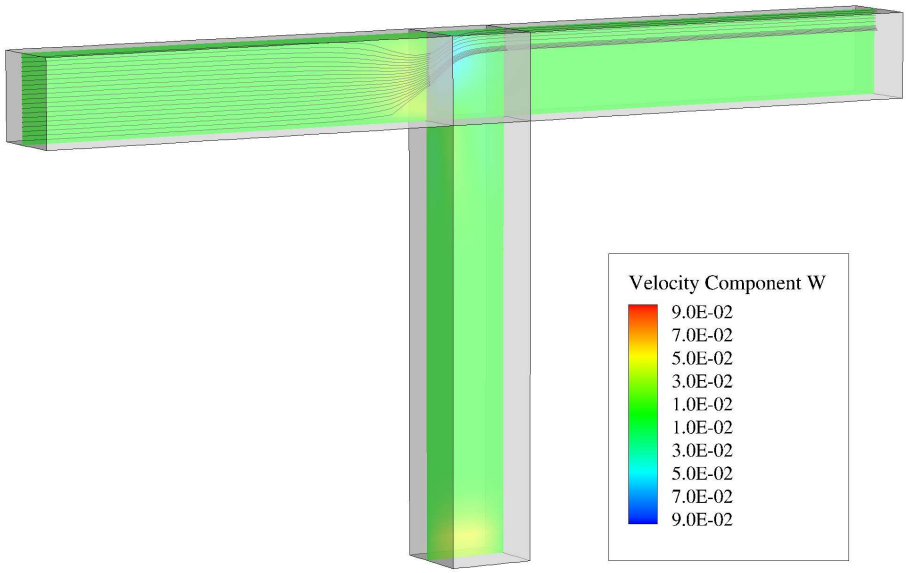

Figure 9.16: Distribution of the velocity component W and ssDNA pathlines with the presence of AW at $Re = 10$.

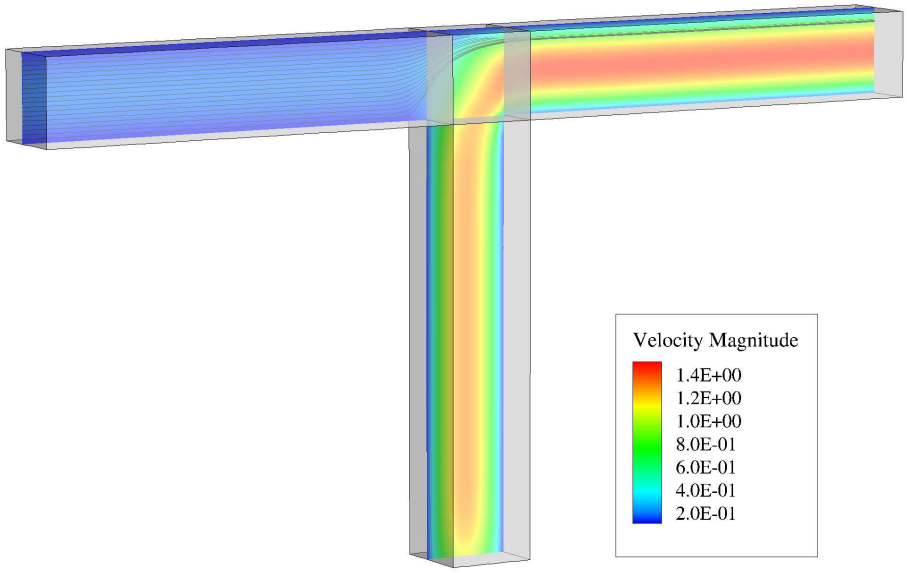

Figure 9.17: Distribution of velocity magnitude and ssDNA pathlines without the presence of AW at $Re = 10$.

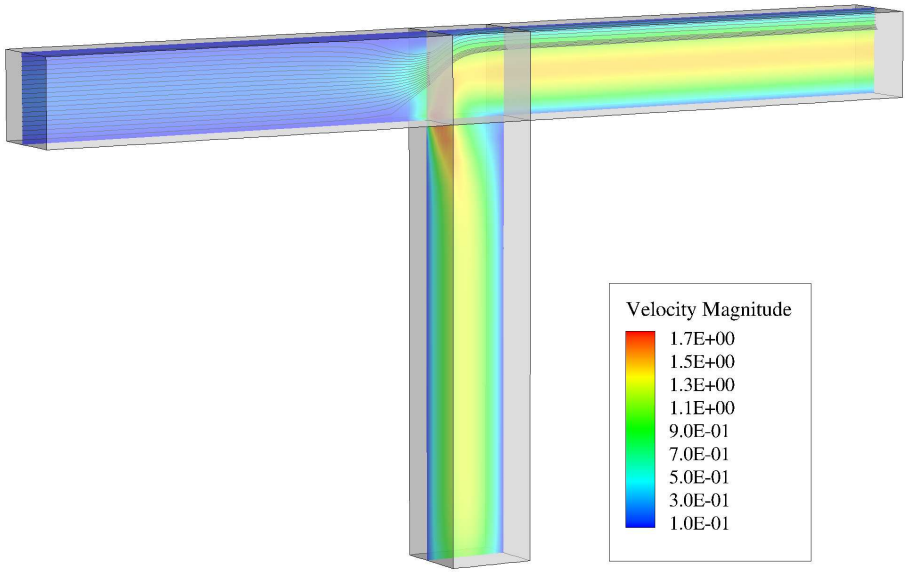

Figure 9.18: Distribution of velocity magnitude and ssDNA pathlines with the presence of AW at $Re = 10$.

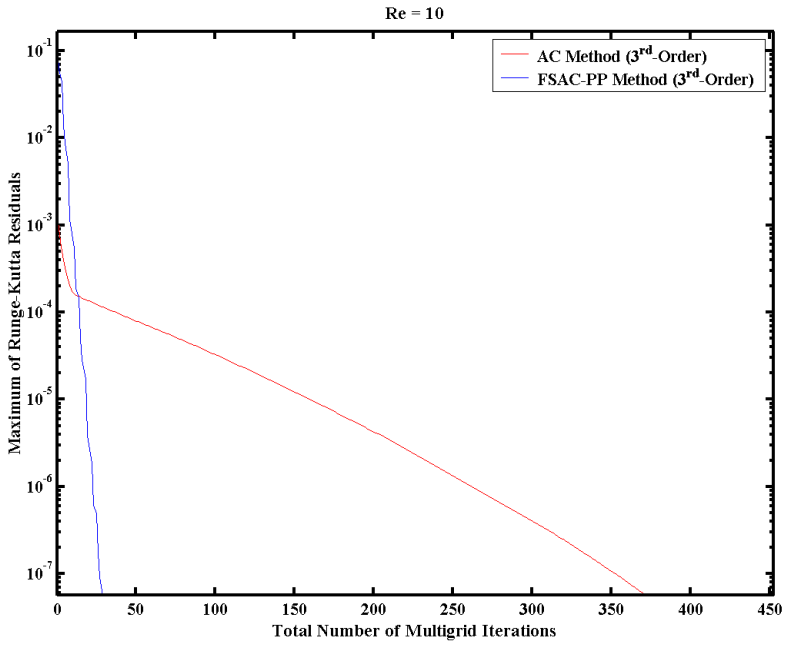

Figure 9.19: Comparison of the numerical convergence of the AC and FSAC-PP methods with modelling AW in the microfluidic T-channel; maximum values of Runge-Kutta residuals versus total number of multigrid iterations on the fine grid using 3^{rd}-order interpolation at $Re = 10$.

	$Re = 10$
	Order of Intercell Flux Interpolation: 3^{rd}-Order
	Total Number of Multigrid Iterations on the Fine Grid
AC Method	452
FSAC-PP Method	29

Table 9.4: Comparison of the numerical convergence of the AC and FSAC-PP methods with modelling AW in the microfluidic T-channel; total number of multigrid iterations on the fine grid using 3^{rd}-order interpolation at $Re = 10$.

9.5 Summary and Conclusions

In this chapter, the proposed FSAC-PP method in conjunction with the FMG-FAS multigrid technique [7] has been tested for acoustic wave (AW) modelling and for solving unsteady, incompressible, laminar flow problem in a three-dimensional microfluidic T-channel at $Re = 10$. A simplified AW model has been adopted and further developed to investigate the effects of AW on the Newtonian fluid flow pattern. According to this simplified AW model, the longitudinal AW propagation, appearing as pressure wave travelling in the liquid, is proportional to the particle velocity multiplied by the acoustic pressure gradient represented in the momentum equations (9.6) and (9.9) as a source term. The proposed acoustic source term model is a closer approach to Poesio and Ooms theory [193] rather than to Lighthill's theory [194], or to the perturbation theory [195]. In this chapter, the AW interacted with ssDNA strands that have been released in the three-dimensional microfluidic T-channel, and have been modeled through a coupled Eulerian-Lagrangian dynamics [10, 11]. The following main conclusions might be drawn: a) the presence of AW in the flow field has influence on the pathlines of ssDNA flow without breaking the molecule chain; b) the ssDNA chain flows towards the upper wall effectively without the presence of AW in the flow field; c) the ssDNA chain has been released when the fluid flow becomes fully developed, thus, the criterion of a possible DNA-breaking remains unknown; d) the proposed FSAC-PP method is more efficient than the classical AC method using 3^{rd}-order intercell flux interpolation for the present benchmark at $Re = 10$. It is important to mention that in order to decrease the computational cost, an alternative solution is that the fully developed flow field has been computed with the presence of AW, but without meta-modelling of the ssDNA flow. When the flow field becomes nearly fully developed with the presence of AW propagation, the ssDNA chain has been released in the microfluidic T-channel to avoid numerical instabilities in the flow field. Overall, the numerical results presented in this chapter suggest that the presence of AW generator near the DNA sensing area could be advantageous, because the ssDNA chain might reach the sensing area faster than without the presence of the acoustic source generator. The outcomes of the current numerical study might be of great importance in the design process of highly selective micro- and nanofluidic sensors for DNA detection. Note that the author of this thesis is not aware of any publications in conjunction with acoustic wave modelling coupled with ssDNA flow in a three-dimensional microfluidic T-channel.

Chapter 10

Summary and Conclusions

10.1 Summary and Conclusions of the Research Work

The outcome of this project is a novel numerical method for solving the unsteady, incompressible Navier-Stokes equations. The proposed FSAC-PP approach encompasses both artificial compressibility (AC) and fractional step (FS) pressure-projection (PP) methods of Chorin [3, 4] in a unified solution concept. The aim of the method development was to further improve the accuracy and efficiency of the classical AC and PP methods. A useful software tool is also an outcome of this work, which has the capability of handling multiphysics problems at (very) low and moderate Reynolds numbers including constant and variable density flows, interface tracking, magnetic field, and acoustic wave modelling with ssDNA flow all together. However, different multiphysics software packages are available on the market, such as ANSYS Multiphysics, CFD-ACE+, CoventrorWare^{TM} and COMSOL packages, but there are shortages of quick and reliable high-resolution Godunov-type method based software tools to design microfluidic devices. For microfluidic applications, the surface forces, surface tension and viscosity dominate at low Reynolds numbers. Therefore, the main scope of this project was to develop, analyse and validate a new efficient high-resolution Godunov-type method based numerical procedure for solving the unsteady, incompressible Navier-Stokes equations at low and moderate Reynolds numbers; and implement a multiphysics FORTRAN 90/95 software package, called HIRECOM-MULTIPHYSICS Unified Code v1.0. This software might be a bridge between the market leader packages and the daily engineering demand in the design of microfluidic devices. The problem classes of the developed multiphysics software tool have been shown in Figure 10.1.

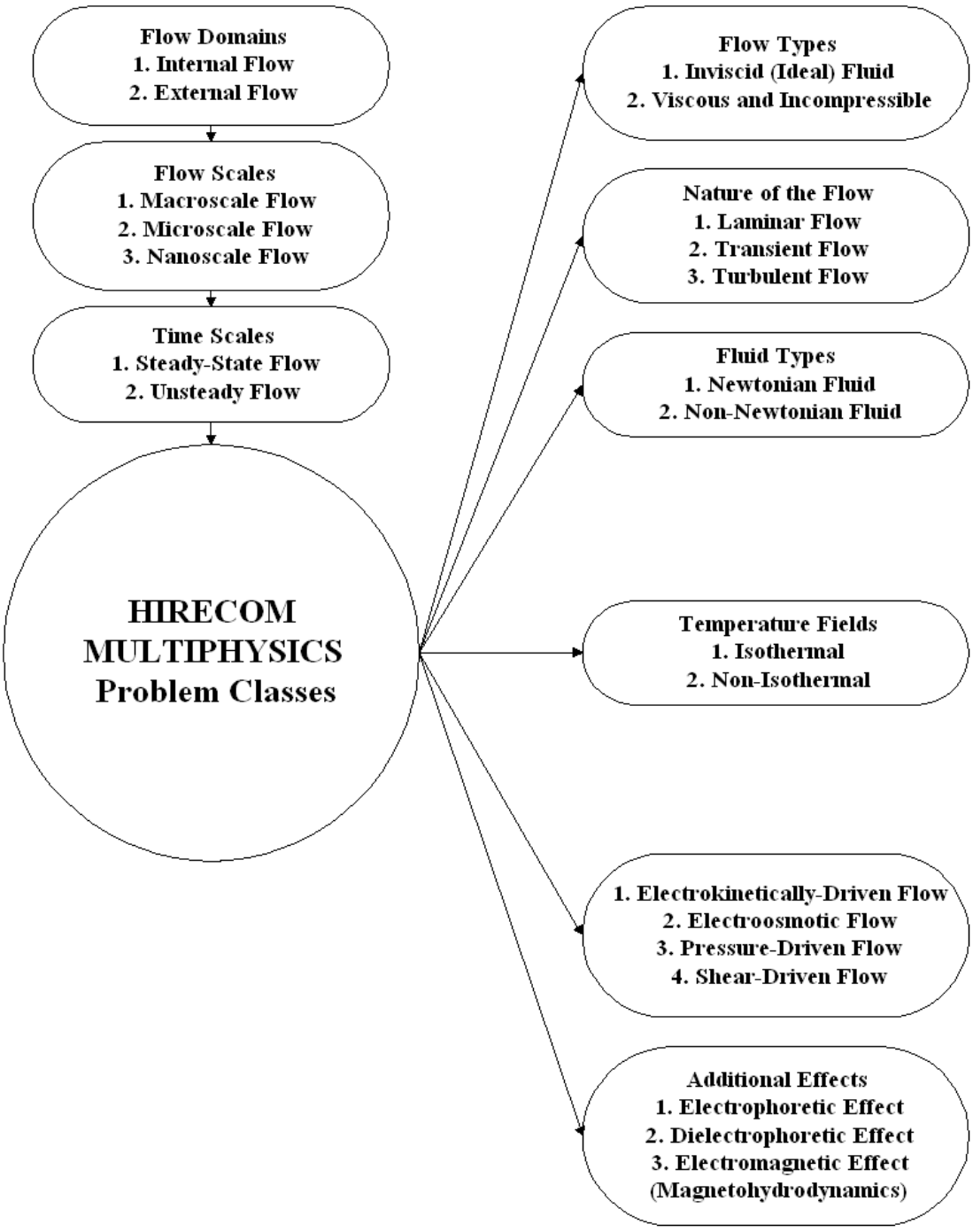

Figure 10.1: Problem classes of the developed multiphysics software.

10. Summary and Conclusions

To circumvent convergence and associated accuracy problems of the classical AC formulation when used for low Reynolds and/or unsteady problems, a new FSAC-PP approach has been proposed in Chapter 4. The proposed FSAC-PP method incorporates the CB scheme with PP methods via FSAC formulation. The FSAC-PP method retains the hyperbolic, inviscid counterpart of the AC formulation in order to enable the use of Riemann method for solving the Riemann problem. The pressure field has been updated by solving a pressure-Poisson equation. The pressure-Poisson equation has been implemented in the in-house HIRECOM-MULTIPHYSICS Unified Code v1.0 in curvilinear coordinate system. To provide time-accurate solutions, the dual-time stepping procedure is utilized. Taking the advantage of the hyperbolic nature of the inviscid part of the AC formulation, high-resolution CB Godunov-type scheme is employed to discretize the non-linear advective fluxes. High-order of accuracy is achieved by employing from first- up to ninth-order interpolation schemes. Time integration is obtained from a fourth-order Runge-Kutta scheme. A non-linear full-multigrid, full-approximation storage (FMG-FAS) acceleration technique [7] has been further extended to the FSAC-PP method for solving constant and variable density flow problems. Relying on this method, it is possible to further improve the efficiency of the classical AC method, because excellent convergence properties of the high-resolution CB Godunov-type schemes can be gained to avoid spurious oscillations in the non-linear convective/advective terms.

In Chapter 5, the proposed FSAC-PP method has been validated compared to the AC, PP methods and an analytical solution for steady-state, incompressible, constant density, pressure-driven laminar flow in a straight microfluidic channel. Four-hundred and eighty simulations have been performed using three different methods with five different intercell flux interpolation formulas on four different girds at eight different Reynolds numbers from 10 to 10^{-4}. The convergence histories overall show that the FSAC-PP method requires significantly smaller number of multigrid iterations than the classical AC and PP methods to achieve convergence at each Reynolds number. For $Re < 0.1$, the convergence of the AC method exhibits relatively high values related to the lowest maximum Runge-Kutta residuals, therefore, the numerical solution is not able to resolve the fully developed laminar velocity profile at the outlet boundary section. Thus, the AC method fails to give physically correct results at extremely low Reynolds number flows ($10^{-4} < Re < 0.1$), whereas both PP and FSAC-PP methods exhibited a good agreement with the analytical solution. Numerical solutions to the AC formulation of the Navier-Stokes equations exhibit slow convergence rates irrespective of the values of the AC parameter. In the case of the PP method, the rate of convergence is also slow and the number of multigrid cycles is the highest. Due to these reasons, the proposed FSAC-PP solution method has been developed and investigated as an alternative method. The presented results in Chapter 5 overall showed that the FSAC-PP method is more efficient than the classical AC and

PP methods for the investigated two-dimensional microfluidic benchmark channel. The computational results were overall better than the the ones obtained by the AC and PP methods. From the present benchmark test case, it can also be concluded that both PP and FSAC-PP methods are capable of handling extremely low Reynolds numbers more accurately than the classical AC method. According to the computational experience gained, the FSAC-PP method performs at a very slow convergence rate when the Reynolds number is smaller than 10^{-4}. Therefore, further investigation is required to understand the convergence properties of the proposed FSAC-PP method for $Re < 10^{-4}$. The FSAC-PP method has to be tested for complex microfluidic geometries.

In Chapter 6, the proposed FSAC-PP method in conjunction with the FMG-FAS multigrid technique [7] has been validated for steady-state, incompressible, constant density laminar flow in a lid driven square cavity at $Re = 100$, 400, and 1000. The proposed FSAC-PP method has also been tested for unsteady turbulent flows in a lid driven cubical cavity at $Re = 3200$, and 10 000. The numerical results of the FSAC-PP method has also been compared to the classical AC and PP methods; and to the DNS based computational data of Ghia et al. [8] for two-dimensional laminar flows; and to experimental data of Prasad and Koseff [17] for three-dimensional turbulent flows. The aforementioned turbulent flow simulations have been performed by using Implicit Large Eddy Simulation (ILES) method. For two-dimensional laminar flows, the overall results suggest that in terms of accuracy, the FSAC-PP method shows better results in most cases compared to the AC and PP methods; especially when low-order (first- and second-order) intercell flux interpolation schemes have been employed. In terms of efficiency, the FSAC-PP method is the most efficient method compared to the AC and PP methods for the presented two-dimensional benchmark at $Re = 100, 400,$ and 1000. It is important to emphasize that the FSAC-PP method required and consumed the lowest number of multigrid iterations in each two-dimensional test case. For three-dimensional, unsteady turbulent flows, the overall results show that the AC, PP and FSAC-PP methods capture the mean velocity components better than the RMS main and shear stress profiles compared to the experimental data of Prasad and Koseff [17] at $Re = 3200$, and 10 000. The RMS main and shear stress profiles follow the tendency of the measured values with significant discrepancy between experiments and simulations, which are similar to the DNS results of Leriche et al. [177]. According to Leriche et al. [177], the differences between the simulation and the experiment are caused by the measurement errors approaching the moving wall.

In Chapter 7, the proposed FSAC-PP method in conjunction with the FMG-FAS multigrid technique [7] has been tested for steady-state, incompressible, multi-species variable density flow, taking two different miscible liquids with different densities, in a three-dimensional Y-junction microfluidic channel at $Re = 50$ and $Pe = 1000$. The dimensionless outlet velocity distribution has numerically been compared to the analytical solution

of Marco and Han [18, 19, p. 5.67]. The obtained overall results showed that in terms of accuracy, the FSAC-PP method exhibits minor difference compared to the AC and PP methods; and in terms of efficiency, the FSAC-PP method is more efficient than the AC and PP methods for the Y-junction microfluidic benchmark test case. The presented results in Chapter 7 showed good agreement with the theoretical investigations of Ismagilov et al. [180], and the numerical investigations of Shapiro and Drikakis [6].

In Chapter 8, the proposed FSAC-PP method in conjunction with the FMG-FAS multigrid technique [7] has been tested for steady-state, incompressible, non-isothermal, Newtonian and non-Newtonian biofluid flow in the presence of uniform magnetic field in a two-dimensional straight microfluidic channel at $Re = 300$, $Mn_M = 40$, and $Mn_F = 0$. The model equations of Tzirtzilakis and Loukopoulos [9] have been further extended and generalized to use any types of constitutive equation for the blood. In Chapter 8, the non-Newtonian blood rheological model was relying on a version of power law fluid model as proposed by Walburn and Schneck [54]. The numerical results of the FSAC-PP method has also been compared to the AC method and to the computational data of Tzirtzilakis and Loukopoulos [9]. In terms of accuracy, the overall results of the non-Newtonian power law fluid approach show very similar agreement with the obtained results of the Newtonian fluid model. In terms of efficiency, the proposed FSAC-PP method is slightly more efficient than the classical AC method; therefore, overall, the accuracy and efficiency of FSAC-PP and AC methods exhibit minor differences for the two-dimensional microfluidic benchmark channel under the presence of uniform magnetic field. When the magnetic field strength is increased by the FHD effect, the magnitude of source terms may become high in the momentum and temperature equations, which may lead to numerical instabilities when employing either the AC or FSAC-PP methods. The inclusion of the velocity field of the magnetic source terms in the eigenvalue system of scalar equations may further improve the stability of the solution.

In Chapter 9, the proposed FSAC-PP method in conjunction with the FMG-FAS multigrid technique [7] has been tested for acoustic wave (AW) modelling and for solving unsteady, incompressible, laminar flow problem in a three-dimensional microfluidic T-channel at $Re = 10$. A simplified AW model has been adopted and further developed to investigate the effects of AW on the Newtonian fluid flow pattern. According to this simplified AW model, the longitudinal AW propagation, appearing as pressure wave travelling in the liquid, is proportional to the particle velocity multiplied by the acoustic pressure gradient represented in the momentum equation as a source term. The proposed acoustic source term model is a closer approach to Poesio and Ooms theory [193] rather than to Lighthill's theory [194], or to the perturbation theory [195]. In Chapter 9, the AW interacted with ssDNA strands that have been released in the three-dimensional microfluidic T-channel, and have been modeled through a coupled Eulerian-Lagrangian dynamics

[10, 11]. The following main conclusions might be drawn: a) the presence of AW in the flow field has influence on the pathlines of ssDNA flow without breaking the molecule chain; b) the ssDNA chain flows towards the upper wall effectively without the presence of AW in the flow field; c) the ssDNA chain has been released when the fluid flow becomes fully developed, thus, the criterion of a possible DNA-breaking remains unknown; d) the proposed FSAC-PP method is much more efficient than the classical AC method using 3^{rd}-order intercell flux interpolation for the present benchmark at $Re = 10$. The presented results in Chapter 9 overall suggested that the presence of AW generator near the DNA sensing area could be advantageous, because the ssDNA chain might reach the sensing area faster than without the presence of the acoustic source generator. Note that the author of this thesis is not aware of any publications in conjunction with acoustic wave modelling coupled with ssDNA flow in a three-dimensional microfluidic T-channel.

All in all, the conclusion of the present Ph.D. thesis is that in terms of accuracy, the proposed FSAC-PP method showed similar results in the most benchmark test cases compared to the classical AC and PP methods. In terms of efficiency, the FSAC-PP method was the most efficient method in each presented test case. It means that the FSAC-PP method required and consumed the lowest number of multigrid iterations in each test case. Relying on the results of this thesis, the proposed FSAC-PP has been recommended to use as an efficient solution method for physical problems at low or extremely low Reynolds numbers, especially for microfluidic applications.

10.2 Contribution to the Knowledge

The contribution to the knowledge in the present Ph.D. thesis has been summarized as

1. A novel high-resolution Godunov-type numerical procedure has been developed for solving the unsteady, incompressible Navier-Stokes equations for constant and variable density flows. The proposed FSAC-PP approach encompasses both artificial compressibility (AC) and fractional step (FS) pressure-projection (PP) methods of Chorin [3, 4] in a unified solution concept. The objective of the method development was to further improve the accuracy and efficiency of the classical AC and PP methods. An advantageous feature of the FSAC-PP method that incorporates the CB scheme with PP methods via FSAC formulation.

2. The proposed FSAC-PP high-resolution Godunov-type solution method based multiphysics software tool, called HIRECOM-MULTIPHYSICS Unified Code v1.0, has been implemented in FORTRAN 90/95 programming language, which have the capability of handling multiphysics problems at (very) low and moderate Reynolds numbers including constant and variable density flows, interface tracking, magnetic field, and acoustic wave modelling with ssDNA flow all together.

3. The pressure-Poisson equation has been implemented in the in-house HIRECOM-MULTIPHYSICS Unified Code v1.0 in curvilinear coordinate system for constant and variable density flow problems.

4. A non-linear full-multigrid, full-approximation storage (FMG-FAS) acceleration technique [7] has been further extended to the novel FSAC-PP method for solving constant and variable density flow problems.

5. The proposed FSAC-PP method has been validated by comparison to AC, PP, and analytical solution methods for steady-state, incompressible, constant density, pressure driven laminar flow in a straight microfluidic channel. Four-hundred and eighty simulations have been performed using three different methods with five different intercell flux interpolation formulas on four different girds at eight different Reynolds numbers from 10 to 0.0001. The AC method fails to give physically correct results at extremely low Reynolds number flows ($0.0001 < Re < 0.1$), whereas both PP and FSAC-PP methods exhibits a good agreement with the analytical solution for the two-dimensional straight microfluidic benchmark channel.

6. The proposed FSAC-PP method in conjunction with the FMG-FAS multigrid technique [7] has been validated for steady-state, incompressible, constant density laminar flow in a lid driven square cavity at $Re = 100, 400,$ and 1000. To provide numerical data for validation purposes, different intercell flux interpolation formulas

have been employed from first- up to ninth-order for the lid driven square cavity test case; and the numerical results have been summarized and compared to the computational data of Ghia et al. [8] in comparative tables in Appendix B.

7. The proposed FSAC-PP method has been tested for unsteady turbulent flows in a lid driven cubical cavity at $Re = 3200$, and 10 000. The turbulent flow simulations have been performed by using Implicit Large Eddy Simulation (ILES) method relying on the novel FSAC-PP solution method.

8. The proposed FSAC-PP method in conjunction with the FMG-FAS multigrid technique [7] has been tested for steady-state, incompressible, multi-species variable density flow, taking two different miscible liquids with different densities, in a three-dimensional Y-junction microfluidic channel at $Re = 50$ and $Pe = 1000$.

9. The proposed FSAC-PP method in conjunction with the FMG-FAS multigrid technique [7] has been tested for steady-state, incompressible, non-isothermal, Newtonian and non-Newtonian biofluid flow in the presence of uniform magnetic field in a two-dimensional straight microfluidic channel at $Re = 300$, $Mn_M = 40$, and $Mn_F = 0$. The model equations of Tzirtzilakis and Loukopoulos [9] have been further extended to use any types of constitutive equation for blood.

10. The proposed FSAC-PP method in conjunction with the FMG-FAS multigrid technique [7] has been tested for acoustic wave (AW) modelling and for solving unsteady, incompressible, laminar flow problem in a three-dimensional microfluidic T-channel at $Re = 10$. A simplified AW model has been adopted and further developed to investigate the effects of AW on the Newtonian fluid flow pattern. In the presented benchmark test case, the AW interacted with ssDNA strands that have been released in the microfluidic T-channel, and have been modeled through a coupled Eulerian-Lagrangian dynamics [10, 11]. The author of this thesis is not aware of any publications in conjunction with acoustic wave modelling coupled with ssDNA flow in a three-dimensional microfluidic T-channel.

11. Relying on the results of the present Ph.D. thesis, the proposed FSAC-PP has been recommended to use as an efficient solution method for physical problems at low or extremely low Reynolds numbers, especially for microfluidic applications.

10.3 Future Work

The effect of compressibility was not a scope of the present Ph.D. thesis, therefore, the proposed FSAC-PP solution method might be further extended to compressible flows. It might be important to mention that Hetsroni et al. [205] considered this problem of liquid and gas flow in microchannels using small Knudsen and Mach numbers. The pressure drop were analyzed in circular, rectangular, triangular, and trapezoidal microchannels. Their study considered the Reynolds number at transition from laminar to turbulent flow, and discussed the sources of unexpected effects in microfluidics [205]. Therefore, the FSAC-PP method would probably also be an efficient method for investigating these unexpected effects in microfluidic applications. As a future work, relying on the generalized FHD and MHD model equations for using any constitutive relationships, other types of non-Newtonian blood fluid models may be further investigated on the presented two-dimensional benchmark in Chapter 8. The effects of the temperature field on the solution have to be further investigated as well. The author of this thesis is not aware of any multiphysics software package on the market relying on the high-resolution Godunov-type FSAC-PP solution method, therefore, there is potential possibility to commercialize the further developed software package. Furthermore, the FSAC-PP method has to be further investigated at high Reynolds numbers for both constant and variable density flows, especially for unsteady flows, which should be a major target in the future work.

Appendix A

Computation of the Derivatives of the Curvilinear Coordinates

A.1 First Derivatives in the Cell-Centres and Faces

The first derivatives of the curvilinear coordinates (ξ, η, ζ), according to Cartesian coordinates (X, Y, Z), can be computed [27, p. 60] as

$$\xi_X = \frac{\partial \xi}{\partial X} = \frac{1}{J}\left(\frac{\partial Y}{\partial \eta}\frac{\partial Z}{\partial \zeta} - \frac{\partial Y}{\partial \zeta}\frac{\partial Z}{\partial \eta}\right) = \frac{Y_\eta Z_\zeta - Y_\zeta Z_\eta}{J}, \tag{A.1}$$

$$\xi_Y = \frac{\partial \xi}{\partial Y} = \frac{1}{J}\left(\frac{\partial X}{\partial \zeta}\frac{\partial Z}{\partial \eta} - \frac{\partial X}{\partial \eta}\frac{\partial Z}{\partial \zeta}\right) = \frac{X_\zeta Z_\eta - X_\eta Z_\zeta}{J}, \tag{A.2}$$

$$\xi_Z = \frac{\partial \xi}{\partial Z} = \frac{1}{J}\left(\frac{\partial X}{\partial \eta}\frac{\partial Y}{\partial \zeta} - \frac{\partial X}{\partial \zeta}\frac{\partial Y}{\partial \eta}\right) = \frac{X_\eta Y_\zeta - X_\zeta Y_\eta}{J}, \tag{A.3}$$

$$\eta_X = \frac{\partial \eta}{\partial X} = \frac{1}{J}\left(\frac{\partial Y}{\partial \zeta}\frac{\partial Z}{\partial \xi} - \frac{\partial Y}{\partial \xi}\frac{\partial Z}{\partial \zeta}\right) = \frac{Y_\zeta Z_\xi - Y_\xi Z_\zeta}{J}, \tag{A.4}$$

$$\eta_Y = \frac{\partial \eta}{\partial Y} = \frac{1}{J}\left(\frac{\partial X}{\partial \xi}\frac{\partial Z}{\partial \zeta} - \frac{\partial X}{\partial \zeta}\frac{\partial Z}{\partial \xi}\right) = \frac{X_\xi Z_\zeta - X_\zeta Z_\xi}{J}, \tag{A.5}$$

$$\eta_Z = \frac{\partial \eta}{\partial Z} = \frac{1}{J}\left(\frac{\partial X}{\partial \zeta}\frac{\partial Y}{\partial \xi} - \frac{\partial X}{\partial \xi}\frac{\partial Y}{\partial \zeta}\right) = \frac{X_\zeta Y_\xi - X_\xi Y_\zeta}{J}, \tag{A.6}$$

$$\zeta_X = \frac{\partial \zeta}{\partial X} = \frac{1}{J}\left(\frac{\partial Y}{\partial \xi}\frac{\partial Z}{\partial \eta} - \frac{\partial Y}{\partial \eta}\frac{\partial Z}{\partial \xi}\right) = \frac{Y_\xi Z_\eta - Y_\eta Z_\xi}{J}, \tag{A.7}$$

$$\zeta_Y = \frac{\partial \zeta}{\partial Y} = \frac{1}{J}\left(\frac{\partial X}{\partial \eta}\frac{\partial Z}{\partial \xi} - \frac{\partial X}{\partial \xi}\frac{\partial Z}{\partial \eta}\right) = \frac{X_\eta Z_\xi - X_\xi Z_\eta}{J}, \tag{A.8}$$

$$\zeta_Z = \frac{\partial \zeta}{\partial Z} = \frac{1}{J}\left(\frac{\partial X}{\partial \xi}\frac{\partial Y}{\partial \eta} - \frac{\partial X}{\partial \eta}\frac{\partial Y}{\partial \xi}\right) = \frac{X_\xi Y_\eta - X_\eta Y_\xi}{J}, \tag{A.9}$$

where

$$\begin{aligned} J = \left|\frac{\partial (X,Y,Z)}{\partial (\xi,\eta,\zeta)}\right| &= \frac{\partial X}{\partial \xi}\left(\frac{\partial Y}{\partial \eta}\frac{\partial Z}{\partial \zeta} - \frac{\partial Y}{\partial \zeta}\frac{\partial Z}{\partial \eta}\right) + \\ &+ \frac{\partial X}{\partial \eta}\left(\frac{\partial Y}{\partial \zeta}\frac{\partial Z}{\partial \xi} - \frac{\partial Y}{\partial \xi}\frac{\partial Z}{\partial \zeta}\right) + \\ &+ \frac{\partial X}{\partial \zeta}\left(\frac{\partial Y}{\partial \xi}\frac{\partial Z}{\partial \eta} - \frac{\partial Y}{\partial \eta}\frac{\partial Z}{\partial \xi}\right) \end{aligned} \tag{A.10}$$

is the Jacobian determinant, which can also be expressed as

$$\begin{aligned} J = \det \mathbf{J} = |\mathbf{J}| &= \begin{vmatrix} X_\xi & X_\eta & X_\zeta \\ Y_\xi & Y_\eta & Y_\zeta \\ Z_\xi & Z_\eta & Z_\zeta \end{vmatrix} = \\ &= X_\xi \left(Y_\eta Z_\zeta - Y_\zeta Z_\eta\right) + X_\eta \left(Y_\zeta Z_\xi - Y_\xi Z_\zeta\right) + X_\zeta \left(Y_\xi Z_\eta - Y_\eta Z_\xi\right), \end{aligned} \tag{A.11}$$

where the cell-centred first derivatives of the Cartesian coordinates (X,Y,Z), according to curvilinear coordinates (ξ,η,ζ), can be computed by central approximations relying on the Taylor-series [27, p. 60] as

$$\begin{aligned} \left.\frac{\partial X}{\partial \xi}\right|_{i,j,k} &= \frac{1}{4}\left(X_{i+1,j,k} + X_{i+1,j+1,k} + X_{i+1,j+1,k+1} + X_{i+1,j,k+1} - \right. \\ &\left. - X_{i,j,k} - X_{i,j+1,k} - X_{i,j+1,k+1} - X_{i,j,k+1}\right), \end{aligned} \tag{A.12}$$

$$\begin{aligned} \left.\frac{\partial Y}{\partial \xi}\right|_{i,j,k} &= \frac{1}{4}\left(Y_{i+1,j,k} + Y_{i+1,j+1,k} + Y_{i+1,j+1,k+1} + Y_{i+1,j,k+1} - \right. \\ &\left. - Y_{i,j,k} - Y_{i,j+1,k} - Y_{i,j+1,k+1} - Y_{i,j,k+1}\right), \end{aligned} \tag{A.13}$$

$$\begin{aligned} \left.\frac{\partial Z}{\partial \xi}\right|_{i,j,k} &= \frac{1}{4}\left(Z_{i+1,j,k} + Z_{i+1,j+1,k} + Z_{i+1,j+1,k+1} + Z_{i+1,j,k+1} - \right. \\ &\left. - Z_{i,j,k} - Z_{i,j+1,k} - Z_{i,j+1,k+1} - Z_{i,j,k+1}\right), \end{aligned} \tag{A.14}$$

$$\begin{aligned} \left.\frac{\partial X}{\partial \eta}\right|_{i,j,k} &= \frac{1}{4}\left(X_{i,j+1,k} + X_{i,j+1,k+1} + X_{i+1,j+1,k+1} + X_{i+1,j+1,k} - \right. \\ &\left. - X_{i,j,k} - X_{i,j,k+1} - X_{i+1,j,k+1} - X_{i+1,j,k}\right), \end{aligned} \tag{A.15}$$

$$\left.\frac{\partial Y}{\partial \eta}\right|_{i,j,k} = \frac{1}{4}\left(Y_{i,j+1,k} + Y_{i,j+1,k+1} + Y_{i+1,j+1,k+1} + Y_{i+1,j+1,k} -\right.$$

$$\left. - Y_{i,j,k} - Y_{i,j,k+1} - Y_{i+1,j,k+1} - Y_{i+1,j,k}\right), \tag{A.16}$$

$$\left.\frac{\partial Z}{\partial \eta}\right|_{i,j,k} = \frac{1}{4}\left(Z_{i,j+1,k} + Z_{i,j+1,k+1} + Z_{i+1,j+1,k+1} + Z_{i+1,j+1,k} -\right.$$

$$\left. - Z_{i,j,k} - Z_{i,j,k+1} - Z_{i+1,j,k+1} - Z_{i+1,j,k}\right), \tag{A.17}$$

$$\left.\frac{\partial X}{\partial \zeta}\right|_{i,j,k} = \frac{1}{4}\left(X_{i,j,k+1} + X_{i,j+1,k+1} + X_{i+1,j+1,k+1} + X_{i+1,j,k+1} -\right.$$

$$\left. - X_{i,j,k} - X_{i,j+1,k} - X_{i+1,j+1,k} - X_{i+1,j,k}\right), \tag{A.18}$$

$$\left.\frac{\partial Y}{\partial \zeta}\right|_{i,j,k} = \frac{1}{4}\left(Y_{i,j,k+1} + Y_{i,j+1,k+1} + Y_{i+1,j+1,k+1} + Y_{i+1,j,k+1} -\right.$$

$$\left. - Y_{i,j,k} - Y_{i,j+1,k} - Y_{i+1,j+1,k} - Y_{i+1,j,k}\right), \tag{A.19}$$

$$\left.\frac{\partial Z}{\partial \zeta}\right|_{i,j,k} = \frac{1}{4}\left(Z_{i,j,k+1} + Z_{i,j+1,k+1} + Z_{i+1,j+1,k+1} + Z_{i+1,j,k+1} -\right.$$

$$\left. - Z_{i,j,k} - Z_{i,j+1,k} - Z_{i+1,j+1,k} - Z_{i+1,j,k}\right), \tag{A.20}$$

and where the first derivatives of the Cartesian coordinates (X,Y,Z), according to curvilinear coordinates (ξ,η,ζ), at the cell faces can also be computed by central approximations relying on the Taylor-series as

$$\left.\frac{\partial X}{\partial \xi}\right|_{i-\frac{1}{2},j,k} = \frac{1}{8}\left(X_{i+1,j,k} + X_{i+1,j+1,k} + X_{i+1,j+1,k+1} + X_{i+1,j,k+1} -\right.$$

$$\left. - X_{i-1,j,k} - X_{i-1,j+1,k} - X_{i-1,j+1,k+1} - X_{i-1,j,k+1}\right), \tag{A.21}$$

$$\left.\frac{\partial Y}{\partial \xi}\right|_{i-\frac{1}{2},j,k} = \frac{1}{8}\left(Y_{i+1,j,k} + Y_{i+1,j+1,k} + Y_{i+1,j+1,k+1} + Y_{i+1,j,k+1} -\right.$$

$$\left. - Y_{i-1,j,k} - Y_{i-1,j+1,k} - Y_{i-1,j+1,k+1} - Y_{i-1,j,k+1}\right), \tag{A.22}$$

$$\left.\frac{\partial Z}{\partial \xi}\right|_{i-\frac{1}{2},j,k} = \frac{1}{8}\left(Z_{i+1,j,k} + Z_{i+1,j+1,k} + Z_{i+1,j+1,k+1} + Z_{i+1,j,k+1} -\right.$$

$$\left. - Z_{i-1,j,k} - Z_{i-1,j+1,k} - Z_{i-1,j+1,k+1} - Z_{i-1,j,k+1}\right), \tag{A.23}$$

$$\left.\frac{\partial X}{\partial \eta}\right|_{i-\frac{1}{2},j,k} = \frac{1}{2}\left(X_{i,j+1,k} + X_{i,j+1,k+1} - X_{i,j,k} - X_{i,j,k+1}\right), \tag{A.24}$$

$$\left.\frac{\partial Y}{\partial \eta}\right|_{i-\frac{1}{2},j,k} = \frac{1}{2}\left(Y_{i,j+1,k} + Y_{i,j+1,k+1} - Y_{i,j,k} - Y_{i,j,k+1}\right), \tag{A.25}$$

$$\left.\frac{\partial Z}{\partial \eta}\right|_{i-\frac{1}{2},j,k} = \frac{1}{2}\left(Z_{i,j+1,k} + Z_{i,j+1,k+1} - Z_{i,j,k} - Z_{i,j,k+1}\right), \tag{A.26}$$

$$\left.\frac{\partial X}{\partial \zeta}\right|_{i-\frac{1}{2},j,k} = \frac{1}{2}\left(X_{i,j,k+1} + X_{i,j+1,k+1} - X_{i,j,k} - X_{i,j+1,k}\right), \tag{A.27}$$

$$\left.\frac{\partial Y}{\partial \zeta}\right|_{i-\frac{1}{2},j,k} = \frac{1}{2}\left(Y_{i,j,k+1} + Y_{i,j+1,k+1} - Y_{i,j,k} - Y_{i,j+1,k}\right), \tag{A.28}$$

$$\left.\frac{\partial Z}{\partial \zeta}\right|_{i-\frac{1}{2},j,k} = \frac{1}{2}\left(Z_{i,j,k+1} + Z_{i,j+1,k+1} - Z_{i,j,k} - Z_{i,j+1,k}\right), \tag{A.29}$$

$$\left.\frac{\partial X}{\partial \xi}\right|_{i,j-\frac{1}{2},k} = \frac{1}{2}\left(X_{i+1,j,k} + X_{i+1,j,k+1} - X_{i,j,k} - X_{i,j,k+1}\right), \tag{A.30}$$

$$\left.\frac{\partial Y}{\partial \xi}\right|_{i,j-\frac{1}{2},k} = \frac{1}{2}\left(Y_{i+1,j,k} + Y_{i+1,j,k+1} - Y_{i,j,k} - Y_{i,j,k+1}\right), \tag{A.31}$$

$$\left.\frac{\partial Z}{\partial \xi}\right|_{i,j-\frac{1}{2},k} = \frac{1}{2}\left(Z_{i+1,j,k} + Z_{i+1,j,k+1} - Z_{i,j,k} - Z_{i,j,k+1}\right), \tag{A.32}$$

$$\left.\frac{\partial X}{\partial \eta}\right|_{i,j-\frac{1}{2},k} = \frac{1}{8}\left(X_{i,j+1,k} + X_{i+1,j+1,k} + X_{i+1,j+1,k+1} + X_{i,j+1,k+1} - \right.$$
$$\left. - X_{i,j-1,k} - X_{i+1,j-1,k} - X_{i+1,j-1,k+1} - X_{i,j-1,k+1}\right), \tag{A.33}$$

$$\left.\frac{\partial Y}{\partial \eta}\right|_{i,j-\frac{1}{2},k} = \frac{1}{8}\left(Y_{i,j+1,k} + Y_{i+1,j+1,k} + Y_{i+1,j+1,k+1} + Y_{i,j+1,k+1} - \right.$$
$$\left. - Y_{i,j-1,k} - Y_{i+1,j-1,k} - Y_{i+1,j-1,k+1} - Y_{i,j-1,k+1}\right), \tag{A.34}$$

$$\left.\frac{\partial Z}{\partial \eta}\right|_{i,j-\frac{1}{2},k} = \frac{1}{8}\left(Z_{i,j+1,k} + Z_{i+1,j+1,k} + Z_{i+1,j+1,k+1} + Z_{i,j+1,k+1} - \right.$$
$$\left. - Z_{i,j-1,k} - Z_{i+1,j-1,k} - Z_{i+1,j-1,k+1} - Z_{i,j-1,k+1}\right), \tag{A.35}$$

$$\left.\frac{\partial X}{\partial \zeta}\right|_{i,j-\frac{1}{2},k} = \frac{1}{2}\left(X_{i,j,k+1} + X_{i+1,j,k+1} - X_{i,j,k} - X_{i+1,j,k}\right), \tag{A.36}$$

$$\left.\frac{\partial Y}{\partial \zeta}\right|_{i,j-\frac{1}{2},k} = \frac{1}{2}\left(Y_{i,j,k+1} + Y_{i+1,j,k+1} - Y_{i,j,k} - Y_{i+1,j,k}\right), \tag{A.37}$$

$$\left.\frac{\partial Z}{\partial \zeta}\right|_{i,j-\frac{1}{2},k} = \frac{1}{2}\left(Z_{i,j,k+1} + Z_{i+1,j,k+1} - Z_{i,j,k} - Z_{i+1,j,k}\right), \tag{A.38}$$

$$\left.\frac{\partial X}{\partial \xi}\right|_{i,j,k-\frac{1}{2}} = \frac{1}{2}\left(X_{i+1,j,k} + X_{i+1,j+1,k} - X_{i,j,k} - X_{i,j+1,k}\right), \tag{A.39}$$

$$\left.\frac{\partial Y}{\partial \xi}\right|_{i,j,k-\frac{1}{2}} = \frac{1}{2}\left(Y_{i+1,j,k} + Y_{i+1,j+1,k} - Y_{i,j,k} - Y_{i,j+1,k}\right), \tag{A.40}$$

$$\left.\frac{\partial Z}{\partial \xi}\right|_{i,j,k-\frac{1}{2}} = \frac{1}{2}\left(Z_{i+1,j,k} + Z_{i+1,j+1,k} - Z_{i,j,k} - Z_{i,j+1,k}\right), \tag{A.41}$$

$$\left.\frac{\partial X}{\partial \eta}\right|_{i,j,k-\frac{1}{2}} = \frac{1}{2}\left(X_{i,j+1,k} + X_{i+1,j+1,k} - X_{i,j,k} - X_{i+1,j,k}\right), \tag{A.42}$$

$$\left.\frac{\partial Y}{\partial \eta}\right|_{i,j,k-\frac{1}{2}} = \frac{1}{2}\left(Y_{i,j+1,k} + Y_{i+1,j+1,k} - Y_{i,j,k} - Y_{i+1,j,k}\right), \tag{A.43}$$

$$\left.\frac{\partial Z}{\partial \eta}\right|_{i,j,k-\frac{1}{2}} = \frac{1}{2}\left(Z_{i,j+1,k} + Z_{i+1,j+1,k} - Z_{i,j,k} - Z_{i+1,j,k}\right), \tag{A.44}$$

$$\left.\frac{\partial X}{\partial \zeta}\right|_{i,j,k-\frac{1}{2}} = \frac{1}{8}\left(X_{i,j,k+1} + X_{i+1,j,k+1} + X_{i+1,j+1,k+1} + X_{i,j+1,k+1} - \right.$$
$$\left. - X_{i,j,k-1} - X_{i+1,j,k-1} - X_{i+1,j+1,k-1} - X_{i,j+1,k-1}\right), \tag{A.45}$$

$$\left.\frac{\partial Y}{\partial \zeta}\right|_{i,j,k-\frac{1}{2}} = \frac{1}{8}\left(Y_{i,j,k+1} + Y_{i+1,j,k+1} + Y_{i+1,j+1,k+1} + Y_{i,j+1,k+1} - \right.$$
$$\left. - Y_{i,j,k-1} - Y_{i+1,j,k-1} - Y_{i+1,j+1,k-1} - Y_{i,j+1,k-1}\right), \tag{A.46}$$

$$\left.\frac{\partial Z}{\partial \zeta}\right|_{i,j,k-\frac{1}{2}} = \frac{1}{8}\left(Z_{i,j,k+1} + Z_{i+1,j,k+1} + Z_{i+1,j+1,k+1} + Z_{i,j+1,k+1} - \right.$$
$$\left. - Z_{i,j,k-1} - Z_{i+1,j,k-1} - Z_{i+1,j+1,k-1} - Z_{i,j+1,k-1}\right). \tag{A.47}$$

A.2 Second Derivatives in the Cell-Centres and Faces

The second derivatives of the curvilinear coordinates (ξ,η,ζ), according to Cartesian coordinates (X,Y,Z), can be computed by central approximations as

$$\xi_{XX} = \frac{\partial^2 \xi}{\partial X^2} = \frac{\partial}{\partial X}\left(\frac{\partial \xi}{\partial X}\right) = \frac{\left(\frac{\partial \xi}{\partial X}\right)_{i+\frac{1}{2},j,k} - \left(\frac{\partial \xi}{\partial X}\right)_{i-\frac{1}{2},j,k}}{\frac{1}{2}\left(X_{i+1,j,k} - X_{i-1,j,k}\right)}, \tag{A.48}$$

$$\xi_{YY} = \frac{\partial^2 \xi}{\partial Y^2} = \frac{\partial}{\partial Y}\left(\frac{\partial \xi}{\partial Y}\right) = \frac{\left(\frac{\partial \xi}{\partial Y}\right)_{i,j+\frac{1}{2},k} - \left(\frac{\partial \xi}{\partial Y}\right)_{i,j-\frac{1}{2},k}}{\frac{1}{2}\left(Y_{i,j+1,k} - Y_{i,j-1,k}\right)}, \tag{A.49}$$

$$\xi_{ZZ} = \frac{\partial^2 \xi}{\partial Z^2} = \frac{\partial}{\partial Z}\left(\frac{\partial \xi}{\partial Z}\right) = \frac{\left(\frac{\partial \xi}{\partial Z}\right)_{i,j,k+\frac{1}{2}} - \left(\frac{\partial \xi}{\partial Z}\right)_{i,j,k-\frac{1}{2}}}{\frac{1}{2}\left(Z_{i,j,k+1} - Z_{i,j,k-1}\right)}, \tag{A.50}$$

$$\eta_{XX} = \frac{\partial^2 \eta}{\partial X^2} = \frac{\partial}{\partial X}\left(\frac{\partial \eta}{\partial X}\right) = \frac{\left(\frac{\partial \eta}{\partial X}\right)_{i+\frac{1}{2},j,k} - \left(\frac{\partial \eta}{\partial X}\right)_{i-\frac{1}{2},j,k}}{\frac{1}{2}\left(X_{i+1,j,k} - X_{i-1,j,k}\right)}, \tag{A.51}$$

$$\eta_{YY} = \frac{\partial^2 \eta}{\partial Y^2} = \frac{\partial}{\partial Y}\left(\frac{\partial \eta}{\partial Y}\right) = \frac{\left(\frac{\partial \eta}{\partial Y}\right)_{i,j+\frac{1}{2},k} - \left(\frac{\partial \eta}{\partial Y}\right)_{i,j-\frac{1}{2},k}}{\frac{1}{2}\left(Y_{i,j+1,k} - Y_{i,j-1,k}\right)}, \tag{A.52}$$

$$\eta_{ZZ} = \frac{\partial^2 \eta}{\partial Z^2} = \frac{\partial}{\partial Z}\left(\frac{\partial \eta}{\partial Z}\right) = \frac{\left(\frac{\partial \eta}{\partial Z}\right)_{i,j,k+\frac{1}{2}} - \left(\frac{\partial \eta}{\partial Z}\right)_{i,j,k-\frac{1}{2}}}{\frac{1}{2}\left(Z_{i,j,k+1} - Z_{i,j,k-1}\right)}, \tag{A.53}$$

$$\zeta_{XX} = \frac{\partial^2 \zeta}{\partial X^2} = \frac{\partial}{\partial X}\left(\frac{\partial \zeta}{\partial X}\right) = \frac{\left(\frac{\partial \zeta}{\partial X}\right)_{i+\frac{1}{2},j,k} - \left(\frac{\partial \zeta}{\partial X}\right)_{i-\frac{1}{2},j,k}}{\frac{1}{2}\left(X_{i+1,j,k} - X_{i-1,j,k}\right)}, \tag{A.54}$$

$$\zeta_{YY} = \frac{\partial^2 \zeta}{\partial Y^2} = \frac{\partial}{\partial Y}\left(\frac{\partial \zeta}{\partial Y}\right) = \frac{\left(\frac{\partial \zeta}{\partial Y}\right)_{i,j+\frac{1}{2},k} - \left(\frac{\partial \zeta}{\partial Y}\right)_{i,j-\frac{1}{2},k}}{\frac{1}{2}\left(Y_{i,j+1,k} - Y_{i,j-1,k}\right)}, \tag{A.55}$$

$$\zeta_{ZZ} = \frac{\partial^2 \zeta}{\partial Z^2} = \frac{\partial}{\partial Z}\left(\frac{\partial \zeta}{\partial Z}\right) = \frac{\left(\frac{\partial \zeta}{\partial Z}\right)_{i,j,k+\frac{1}{2}} - \left(\frac{\partial \zeta}{\partial Z}\right)_{i,j,k-\frac{1}{2}}}{\frac{1}{2}\left(Z_{i,j,k+1} - Z_{i,j,k-1}\right)}, \tag{A.56}$$

where the computation of the first derivatives of the curvilinear coordinates (ξ,η,ζ), according to Cartesian coordinates (X,Y,Z), can be found in section A.1. The cell-centred second derivatives of the Cartesian coordinates (X,Y,Z), according to curvilinear coordi-

nates (ξ,η,ζ), can be computed by central approximations as

$$\left.\frac{\partial^2 X}{\partial \xi^2}\right|_{i,j,k} = \frac{1}{4}\left(X_{i+1,j,k}+X_{i+1,j+1,k}+X_{i+1,j+1,k+1}+X_{i+1,j,k+1}+\right.$$
$$\left.+X_{i-1,j,k}+X_{i-1,j+1,k}+X_{i-1,j+1,k+1}+X_{i-1,j,k+1}\right)-$$
$$-\frac{1}{2}\left(X_{i,j,k}+X_{i,j+1,k}+X_{i,j+1,k+1}+X_{i,j,k+1}\right), \tag{A.57}$$
$$\left.\frac{\partial^2 Y}{\partial \xi^2}\right|_{i,j,k} = \frac{1}{4}\left(Y_{i+1,j,k}+Y_{i+1,j+1,k}+Y_{i+1,j+1,k+1}+Y_{i+1,j,k+1}+\right.$$
$$\left.+Y_{i-1,j,k}+Y_{i-1,j+1,k}+Y_{i-1,j+1,k+1}+Y_{i-1,j,k+1}\right)-$$
$$-\frac{1}{2}\left(Y_{i,j,k}+Y_{i,j+1,k}+Y_{i,j+1,k+1}+Y_{i,j,k+1}\right), \tag{A.58}$$
$$\left.\frac{\partial^2 Z}{\partial \xi^2}\right|_{i,j,k} = \frac{1}{4}\left(Z_{i+1,j,k}+Z_{i+1,j+1,k}+Z_{i+1,j+1,k+1}+Z_{i+1,j,k+1}+\right.$$
$$\left.+Z_{i-1,j,k}+Z_{i-1,j+1,k}+Z_{i-1,j+1,k+1}+Z_{i-1,j,k+1}\right)-$$
$$-\frac{1}{2}\left(Z_{i,j,k}+Z_{i,j+1,k}+Z_{i,j+1,k+1}+Z_{i,j,k+1}\right), \tag{A.59}$$
$$\left.\frac{\partial^2 X}{\partial \eta^2}\right|_{i,j,k} = \frac{1}{4}\left(X_{i,j+1,k}+X_{i+1,j+1,k}+X_{i+1,j+1,k+1}+X_{i,j+1,k+1}+\right.$$
$$\left.+X_{i,j-1,k}+X_{i+1,j-1,k}+X_{i+1,j-1,k+1}+X_{i,j-1,k+1}\right)-$$
$$-\frac{1}{2}\left(X_{i,j,k}+X_{i+1,j,k}+X_{i+1,j,k+1}+X_{i,j,k+1}\right), \tag{A.60}$$
$$\left.\frac{\partial^2 Y}{\partial \eta^2}\right|_{i,j,k} = \frac{1}{4}\left(Y_{i,j+1,k}+Y_{i+1,j+1,k}+Y_{i+1,j+1,k+1}+Y_{i,j+1,k+1}+\right.$$
$$\left.+Y_{i,j-1,k}+Y_{i+1,j-1,k}+Y_{i+1,j-1,k+1}+Y_{i,j-1,k+1}\right)-$$
$$-\frac{1}{2}\left(Y_{i,j,k}+Y_{i+1,j,k}+Y_{i+1,j,k+1}+Y_{i,j,k+1}\right), \tag{A.61}$$
$$\left.\frac{\partial^2 Z}{\partial \eta^2}\right|_{i,j,k} = \frac{1}{4}\left(Z_{i,j+1,k}+Z_{i+1,j+1,k}+Z_{i+1,j+1,k+1}+Z_{i,j+1,k+1}+\right.$$
$$\left.+Z_{i,j-1,k}+Z_{i+1,j-1,k}+Z_{i+1,j-1,k+1}+Z_{i,j-1,k+1}\right)-$$
$$-\frac{1}{2}\left(Z_{i,j,k}+Z_{i+1,j,k}+Z_{i+1,j,k+1}+Z_{i,j,k+1}\right), \tag{A.62}$$

$$\left.\frac{\partial^2 X}{\partial \zeta^2}\right|_{i,j,k} = \frac{1}{4}\left(X_{i,j,k+1} + X_{i+1,j,k+1} + X_{i+1,j+1,k+1} + X_{i,j+1,k+1} + \right.$$

$$\left. + X_{i,j,k-1} + X_{i+1,j,k-1} + X_{i+1,j+1,k-1} + X_{i,j+1,k-1}\right) -$$

$$-\frac{1}{2}\left(X_{i,j,k} + X_{i+1,j,k} + X_{i+1,j+1,k} + X_{i,j+1,k}\right), \tag{A.63}$$

$$\left.\frac{\partial^2 Y}{\partial \zeta^2}\right|_{i,j,k} = \frac{1}{4}\left(Y_{i,j,k+1} + Y_{i+1,j,k+1} + Y_{i+1,j+1,k+1} + Y_{i,j+1,k+1} + \right.$$

$$\left. + Y_{i,j,k-1} + Y_{i+1,j,k-1} + Y_{i+1,j+1,k-1} + Y_{i,j+1,k-1}\right) -$$

$$-\frac{1}{2}\left(Y_{i,j,k} + Y_{i+1,j,k} + Y_{i+1,j+1,k} + Y_{i,j+1,k}\right), \tag{A.64}$$

$$\left.\frac{\partial^2 Z}{\partial \zeta^2}\right|_{i,j,k} = \frac{1}{4}\left(Z_{i,j,k+1} + Z_{i+1,j,k+1} + Z_{i+1,j+1,k+1} + Z_{i,j+1,k+1} + \right.$$

$$\left. + Z_{i,j,k-1} + Z_{i+1,j,k-1} + Z_{i+1,j+1,k-1} + Z_{i,j+1,k-1}\right) -$$

$$-\frac{1}{2}\left(Z_{i,j,k} + Z_{i+1,j,k} + Z_{i+1,j+1,k} + Z_{i,j+1,k}\right). \tag{A.65}$$

The second derivatives of the Cartesian coordinates (X,Y,Z), according to curvilinear coordinates (ξ,η,ζ), at the cell faces can also be computed by central approximations relying on the Taylor-series as

$$\left.\frac{\partial^2 X}{\partial \xi^2}\right|_{i-\frac{1}{2},j,k} = \frac{1}{4}\left(X_{i+1,j,k} + X_{i+1,j+1,k} + X_{i+1,j+1,k+1} + X_{i+1,j,k+1} + \right.$$

$$\left. + X_{i-1,j,k} + X_{i-1,j+1,k} + X_{i-1,j+1,k+1} + X_{i-1,j,k+1}\right) -$$

$$-\frac{1}{2}\left(X_{i,j,k} + X_{i,j+1,k} + X_{i,j+1,k+1} + X_{i,j,k+1}\right), \tag{A.66}$$

$$\left.\frac{\partial^2 Y}{\partial \xi^2}\right|_{i-\frac{1}{2},j,k} = \frac{1}{4}\left(Y_{i+1,j,k} + Y_{i+1,j+1,k} + Y_{i+1,j+1,k+1} + Y_{i+1,j,k+1} + \right.$$

$$\left. + Y_{i-1,j,k} + Y_{i-1,j+1,k} + Y_{i-1,j+1,k+1} + Y_{i-1,j,k+1}\right) -$$

$$-\frac{1}{2}\left(Y_{i,j,k} + Y_{i,j+1,k} + Y_{i,j+1,k+1} + Y_{i,j,k+1}\right), \tag{A.67}$$

$$\left.\frac{\partial^2 Z}{\partial \xi^2}\right|_{i-\frac{1}{2},j,k} = \frac{1}{4}\left(Z_{i+1,j,k} + Z_{i+1,j+1,k} + Z_{i+1,j+1,k+1} + Z_{i+1,j,k+1} + \right.$$

$$\left. + Z_{i-1,j,k} + Z_{i-1,j+1,k} + Z_{i-1,j+1,k+1} + Z_{i-1,j,k+1}\right) -$$

$$-\frac{1}{2}\left(Z_{i,j,k}+Z_{i,j+1,k}+Z_{i,j+1,k+1}+Z_{i,j,k+1}\right), \tag{A.68}$$

$$\left.\frac{\partial^2 X}{\partial \eta^2}\right|_{i-\frac{1}{2},j,k}=\frac{1}{2}\left(X_{i,j+1,k}+X_{i,j+1,k+1}+X_{i,j-1,k}+X_{i,j-1,k+1}\right)-$$

$$-\left(X_{i,j,k}+X_{i,j,k+1}\right), \tag{A.69}$$

$$\left.\frac{\partial^2 Y}{\partial \eta^2}\right|_{i-\frac{1}{2},j,k}=\frac{1}{2}\left(Y_{i,j+1,k}+Y_{i,j+1,k+1}+Y_{i,j-1,k}+Y_{i,j-1,k+1}\right)-$$

$$-\left(Y_{i,j,k}+Y_{i,j,k+1}\right), \tag{A.70}$$

$$\left.\frac{\partial^2 Z}{\partial \eta^2}\right|_{i-\frac{1}{2},j,k}=\frac{1}{2}\left(Z_{i,j+1,k}+Z_{i,j+1,k+1}+Z_{i,j-1,k}+Z_{i,j-1,k+1}\right)-$$

$$-\left(Z_{i,j,k}+Z_{i,j,k+1}\right), \tag{A.71}$$

$$\left.\frac{\partial^2 X}{\partial \zeta^2}\right|_{i-\frac{1}{2},j,k}=\frac{1}{2}\left(X_{i,j,k+1}+X_{i,j+1,k+1}+X_{i,j,k-1}+X_{i,j+1,k-1}\right)-$$

$$-\left(X_{i,j,k}+X_{i,j+1,k}\right), \tag{A.72}$$

$$\left.\frac{\partial^2 Y}{\partial \zeta^2}\right|_{i-\frac{1}{2},j,k}=\frac{1}{2}\left(Y_{i,j,k+1}+Y_{i,j+1,k+1}+Y_{i,j,k-1}+Y_{i,j+1,k-1}\right)-$$

$$-\left(Y_{i,j,k}+Y_{i,j+1,k}\right), \tag{A.73}$$

$$\left.\frac{\partial^2 Z}{\partial \zeta^2}\right|_{i-\frac{1}{2},j,k}=\frac{1}{2}\left(Z_{i,j,k+1}+Z_{i,j+1,k+1}+Z_{i,j,k-1}+Z_{i,j+1,k-1}\right)-$$

$$-\left(Z_{i,j,k}+Z_{i,j+1,k}\right), \tag{A.74}$$

$$\left.\frac{\partial^2 X}{\partial \xi^2}\right|_{i,j-\frac{1}{2},k}=\frac{1}{2}\left(X_{i+1,j,k}+X_{i+1,j,k+1}+X_{i-1,j,k}+X_{i-1,j,k+1}\right)-$$

$$-\left(X_{i,j,k}+X_{i,j,k+1}\right), \tag{A.75}$$

$$\left.\frac{\partial^2 Y}{\partial \xi^2}\right|_{i,j-\frac{1}{2},k}=\frac{1}{2}\left(Y_{i+1,j,k}+Y_{i+1,j,k+1}+Y_{i-1,j,k}+Y_{i-1,j,k+1}\right)-$$

$$-\left(Y_{i,j,k}+Y_{i,j,k+1}\right), \tag{A.76}$$

$$\left.\frac{\partial^2 Z}{\partial \xi^2}\right|_{i,j-\frac{1}{2},k}=\frac{1}{2}\left(Z_{i+1,j,k}+Z_{i+1,j,k+1}+Z_{i-1,j,k}+Z_{i-1,j,k+1}\right)-$$

$$-\left(Z_{i,j,k}+Z_{i,j,k+1}\right), \tag{A.77}$$

$$\left.\frac{\partial^2 X}{\partial \eta^2}\right|_{i,j-\frac{1}{2},k} = \frac{1}{4}\left(X_{i,j+1,k} + X_{i+1,j+1,k} + X_{i+1,j+1,k+1} + X_{i,j+1,k+1} + \right.$$
$$\left. + X_{i,j-1,k} + X_{i+1,j-1,k} + X_{i+1,j-1,k+1} + X_{i,j-1,k+1}\right) -$$
$$- \frac{1}{2}\left(X_{i,j,k} + X_{i+1,j,k} + X_{i+1,j,k+1} + X_{i,j,k+1}\right), \tag{A.78}$$

$$\left.\frac{\partial^2 Y}{\partial \eta^2}\right|_{i,j-\frac{1}{2},k} = \frac{1}{4}\left(Y_{i,j+1,k} + Y_{i+1,j+1,k} + Y_{i+1,j+1,k+1} + Y_{i,j+1,k+1} + \right.$$
$$\left. + Y_{i,j-1,k} + Y_{i+1,j-1,k} + Y_{i+1,j-1,k+1} + Y_{i,j-1,k+1}\right) -$$
$$- \frac{1}{2}\left(Y_{i,j,k} + Y_{i+1,j,k} + Y_{i+1,j,k+1} + Y_{i,j,k+1}\right), \tag{A.79}$$

$$\left.\frac{\partial^2 Z}{\partial \eta^2}\right|_{i,j-\frac{1}{2},k} = \frac{1}{4}\left(Z_{i,j+1,k} + Z_{i+1,j+1,k} + Z_{i+1,j+1,k+1} + Z_{i,j+1,k+1} + \right.$$
$$\left. + Z_{i,j-1,k} + Z_{i+1,j-1,k} + Z_{i+1,j-1,k+1} + Z_{i,j-1,k+1}\right) -$$
$$- \frac{1}{2}\left(Z_{i,j,k} + Z_{i+1,j,k} + Z_{i+1,j,k+1} + Z_{i,j,k+1}\right), \tag{A.80}$$

$$\left.\frac{\partial^2 X}{\partial \zeta^2}\right|_{i,j-\frac{1}{2},k} = \frac{1}{2}\left(X_{i,j,k+1} + X_{i+1,j,k+1} + X_{i,j,k-1} + X_{i+1,j,k-1}\right) -$$
$$- \left(X_{i,j,k} + X_{i+1,j,k}\right), \tag{A.81}$$

$$\left.\frac{\partial^2 Y}{\partial \zeta^2}\right|_{i,j-\frac{1}{2},k} = \frac{1}{2}\left(Y_{i,j,k+1} + Y_{i+1,j,k+1} + Y_{i,j,k-1} + Y_{i+1,j,k-1}\right) -$$
$$- \left(Y_{i,j,k} + Y_{i+1,j,k}\right), \tag{A.82}$$

$$\left.\frac{\partial^2 Z}{\partial \zeta^2}\right|_{i,j-\frac{1}{2},k} = \frac{1}{2}\left(Z_{i,j,k+1} + Z_{i+1,j,k+1} + Z_{i,j,k-1} + Z_{i+1,j,k-1}\right) -$$
$$- \left(Z_{i,j,k} + Z_{i+1,j,k}\right), \tag{A.83}$$

$$\left.\frac{\partial^2 X}{\partial \xi^2}\right|_{i,j,k-\frac{1}{2}} = \frac{1}{2}\left(X_{i+1,j,k} + X_{i+1,j+1,k} + X_{i-1,j,k} + X_{i-1,j+1,k}\right) -$$
$$- \left(X_{i,j,k} + X_{i,j+1,k}\right), \tag{A.84}$$

$$\left.\frac{\partial^2 Y}{\partial \xi^2}\right|_{i,j,k-\frac{1}{2}} = \frac{1}{2}\left(Y_{i+1,j,k} + Y_{i+1,j+1,k} + Y_{i-1,j,k} + Y_{i-1,j+1,k}\right) -$$
$$- \left(Y_{i,j,k} + Y_{i,j+1,k}\right), \tag{A.85}$$

$$\left.\frac{\partial^2 Z}{\partial \xi^2}\right|_{i,j,k-\frac{1}{2}} = \frac{1}{2}\left(Z_{i+1,j,k} + Z_{i+1,j+1,k} + Z_{i-1,j,k} + Z_{i-1,j+1,k}\right) -$$

$$- \left(Z_{i,j,k} + Z_{i,j+1,k}\right), \tag{A.86}$$

$$\left.\frac{\partial^2 X}{\partial \eta^2}\right|_{i,j,k-\frac{1}{2}} = \frac{1}{2}\left(X_{i,j+1,k} + X_{i+1,j+1,k} + X_{i,j-1,k} + X_{i+1,j-1,k}\right) -$$

$$- \left(X_{i,j,k} + X_{i+1,j,k}\right), \tag{A.87}$$

$$\left.\frac{\partial^2 Y}{\partial \eta^2}\right|_{i,j,k-\frac{1}{2}} = \frac{1}{2}\left(Y_{i,j+1,k} + Y_{i+1,j+1,k} + Y_{i,j-1,k} + Y_{i+1,j-1,k}\right) -$$

$$- \left(Y_{i,j,k} + Y_{i+1,j,k}\right), \tag{A.88}$$

$$\left.\frac{\partial^2 Z}{\partial \eta^2}\right|_{i,j,k-\frac{1}{2}} = \frac{1}{2}\left(Z_{i,j+1,k} + Z_{i+1,j+1,k} + Z_{i,j-1,k} + Z_{i+1,j-1,k}\right) -$$

$$- \left(Z_{i,j,k} + Z_{i+1,j,k}\right), \tag{A.89}$$

$$\left.\frac{\partial^2 X}{\partial \zeta^2}\right|_{i,j,k-\frac{1}{2}} = \frac{1}{4}\left(X_{i,j,k+1} + X_{i+1,j,k+1} + X_{i+1,j+1,k+1} + X_{i,j+1,k+1} +\right.$$

$$\left. + X_{i,j,k-1} + X_{i+1,j,k-1} + X_{i+1,j+1,k-1} + X_{i,j+1,k-1}\right) -$$

$$- \frac{1}{2}\left(X_{i,j,k} + X_{i+1,j,k} + X_{i+1,j+1,k} + X_{i,j+1,k}\right), \tag{A.90}$$

$$\left.\frac{\partial^2 Y}{\partial \zeta^2}\right|_{i,j,k-\frac{1}{2}} = \frac{1}{4}\left(Y_{i,j,k+1} + Y_{i+1,j,k+1} + Y_{i+1,j+1,k+1} + Y_{i,j+1,k+1} +\right.$$

$$\left. + Y_{i,j,k-1} + Y_{i+1,j,k-1} + Y_{i+1,j+1,k-1} + Y_{i,j+1,k-1}\right) -$$

$$- \frac{1}{2}\left(Y_{i,j,k} + Y_{i+1,j,k} + Y_{i+1,j+1,k} + Y_{i,j+1,k}\right), \tag{A.91}$$

$$\left.\frac{\partial^2 Z}{\partial \zeta^2}\right|_{i,j,k-\frac{1}{2}} = \frac{1}{4}\left(Z_{i,j,k+1} + Z_{i+1,j,k+1} + Z_{i+1,j+1,k+1} + Z_{i,j+1,k+1} +\right.$$

$$\left. + Z_{i,j,k-1} + Z_{i+1,j,k-1} + Z_{i+1,j+1,k-1} + Z_{i,j+1,k-1}\right) -$$

$$- \frac{1}{2}\left(Z_{i,j,k} + Z_{i+1,j,k} + Z_{i+1,j+1,k} + Z_{i,j+1,k}\right). \tag{A.92}$$

Appendix B

Comparative Tables

B.1 Laminar Flow in a Lid Driven Cavity at *Re* = 100, 400, and 1000

To provide numerical data for validation purposes, different intercell flux interpolation formulas have been employed from first- up to ninth-order in each test case, and the results have been summarized in comparative tables at $Re = 100$, 400, and 1000. The AC, PP and FSAC-PP solution method based numerical results have been compared to the computational data of Ghia et al. [8] in a lid driven square cavity.

Different interpolation formulas have been employed for first-, second- and third-order intercell flux interpolations based on the work of Shapiro and Drikakis [16, pp. 599-600]. The following relationships

$$\mathbf{U}_{L,i-\frac{1}{2}} = \mathbf{U}_i, \text{ and } \mathbf{U}_{R,i+\frac{1}{2}} = \mathbf{U}_{i+1}, \tag{B.1}$$

are valid for first-order intercell flux interpolation, and

$$\mathbf{U}_{L,i-\frac{1}{2}} = \frac{3}{2}\mathbf{U}_i - \frac{1}{2}\mathbf{U}_{i-1}, \text{ and } \mathbf{U}_{R,i+\frac{1}{2}} = \frac{3}{2}\mathbf{U}_{i+1} - \frac{1}{2}\mathbf{U}_{i+2}, \tag{B.2}$$

are valid for second-order intercell flux interpolation, and

$$\mathbf{U}_{L,i-\frac{1}{2}} = \frac{5}{6}\mathbf{U}_i - \frac{1}{6}\mathbf{U}_{i-1} + \frac{1}{3}\mathbf{U}_{i+1}, \text{ and } \mathbf{U}_{R,i+\frac{1}{2}} = \frac{5}{6}\mathbf{U}_{i+1} - \frac{1}{6}\mathbf{U}_{i+2} + \frac{1}{3}\mathbf{U}_i, \tag{B.3}$$

are valid for third-order intercell flux interpolation. The intercell flux value can be com-

puted by employing a fifth-order WENO interpolation formula [166, 27] as

$$\mathbf{U}_{L,i-\frac{1}{2}} = \underline{\alpha}_1 \frac{(2\mathbf{U}_{i-1} + 5\mathbf{U}_i - \mathbf{U}_{i+1})}{6\,(\underline{\alpha}_1 + \underline{\alpha}_2 + \underline{\alpha}_3)} +$$
$$+ \underline{\alpha}_2 \frac{5\mathbf{U}_{i-1} + 2\mathbf{U}_i - \mathbf{U}_{i-2}}{6\,(\underline{\alpha}_1 + \underline{\alpha}_2 + \underline{\alpha}_3)} +$$
$$+ \underline{\alpha}_3 \frac{2\mathbf{U}_{i-3} - 7\mathbf{U}_{i-2} + 11\mathbf{U}_{i-1}}{6\,(\underline{\alpha}_1 + \underline{\alpha}_2 + \underline{\alpha}_3)}, \tag{B.4}$$

where the vectors $\underline{\alpha}_1, \underline{\alpha}_2, \underline{\alpha}_3$ are

$$\underline{\alpha}_1 = \frac{(3/10)}{(\varepsilon + \mathbf{C}_1)^2}, \qquad \underline{\alpha}_2 = \frac{(6/10)}{(\varepsilon + \mathbf{C}_2)^2}, \qquad \underline{\alpha}_3 = \frac{(1/10)}{(\varepsilon + \mathbf{C}_3)^2},$$

where ε is a very small number to avoid division by zero (e.g. 10^{-10}), and the vectors $\mathbf{C}_1, \mathbf{C}_2, \mathbf{C}_3$ are

$$\mathbf{C}_1 = \frac{13}{12}\,(\mathbf{U}_{i-1} - 2\mathbf{U}_i + \mathbf{U}_{i+1})^2 + \frac{1}{4}\,(3\mathbf{U}_{i-1} - 4\mathbf{U}_i + \mathbf{U}_{i+1})^2, \tag{B.5}$$

$$\mathbf{C}_2 = \frac{13}{12}\,(\mathbf{U}_{i-2} - 2\mathbf{U}_{i-1} + \mathbf{U}_i)^2 + \frac{1}{4}\,(\mathbf{U}_{i-2} - \mathbf{U}_i)^2, \tag{B.6}$$

$$\mathbf{C}_3 = \frac{13}{12}\,(\mathbf{U}_{i-3} - 2\mathbf{U}_{i-2} + \mathbf{U}_{i-1})^2 + \frac{1}{4}\,(3\mathbf{U}_{i-1} - 4\mathbf{U}_{i-2} + \mathbf{U}_{i-3})^2. \tag{B.7}$$

For ninth-order WENO interpolation, the following formula is used [166, p. 416] as

$$\mathbf{U}_{L,i-\frac{1}{2}} = (1/630)\,\mathbf{U}_{i-4} - (41/2520)\,\mathbf{U}_{i-3} + (199/2520)\,\mathbf{U}_{i-2} -$$
$$- (641/2520)\,\mathbf{U}_{i-1} + (1879/2520)\,\mathbf{U}_i + (275/504)\,\mathbf{U}_{i+1} -$$
$$- (61/504)\,\mathbf{U}_{i+2} + (11/504)\,\mathbf{U}_{i+3} - (1/504)\,\mathbf{U}_{i+4}. \tag{B.8}$$

For fifth- and ninth-order WENO reconstruction schemes, the author of this thesis refers to the literature of [166, 27].

B. Comparative Tables

	$Re = 100$			
	Order of Interpolation: 1^{st}-Order			
X	Ghia et al. [8]	AC Method	PP Method	FSAC-PP Method
1.0000	0.00000	0.00000	0.00000	0.00000
0.9688	-0.05906	-0.06023	-0.05667	-0.06341
0.9609	-0.07391	-0.07478	-0.07015	-0.07916
0.9531	-0.08864	-0.08889	-0.08325	-0.09467
0.9453	-0.10313	-0.10243	-0.09593	-0.10985
0.9063	-0.16914	-0.15878	-0.15140	-0.17754
0.8594	-0.22445	-0.19562	-0.19617	-0.23134
0.8047	-0.24533	-0.19743	-0.21461	-0.24801
0.5000	0.05454	0.04386	0.03128	0.05511
0.2344	0.17527	0.14035	0.17371	0.17710
0.2266	0.17507	0.14078	0.17406	0.17701
0.1563	0.16077	0.13452	0.16254	0.16346
0.0938	0.12317	0.10621	0.12512	0.12584
0.0781	0.10890	0.09440	0.11095	0.11139
0.0703	0.10091	0.08767	0.10308	0.10328
0.0625	0.09233	0.08035	0.09466	0.09455
0.0000	0.00000	0.00000	0.00000	0.00000

Table B.1: Results of the AC, PP, and FSAC-PP methods for the dimensionless velocity component V along horizontal centre-line of the square cavity using 1^{st}-order interpolation compared to the results of [8] at $Re = 100$.

	AC Method		
Minimum Absolute Error [-]	Maximum Absolute Error [-]	Minimum Relative Error [-]	Maximum Relative Error [-]
0.00025	0.04790	0.00278	0.19925
	PP Method		
Minimum Absolute Error [-]	Maximum Absolute Error [-]	Minimum Relative Error [-]	Maximum Relative Error [-]
0.00101	0.03072	0.00578	0.42650
	FSAC-PP Method		
Minimum Absolute Error [-]	Maximum Absolute Error [-]	Minimum Relative Error [-]	Maximum Relative Error [-]
0.00057	0.00840	0.01047	0.07362

Table B.2: Absolute and relative errors of the AC, PP, and FSAC-PP methods for the dimensionless velocity component V along horizontal centre-line of the square cavity using 1^{st}-order interpolation compared to the results of [8] at $Re = 100$.

B. Comparative Tables

	$Re = 100$			
	Order of Intercell Flux Interpolation: 1^{st}-Order			
Y	Ghia et al. [8]	AC Method	PP Method	FSAC-PP Method
1.0000	1.00000	1.00000	1.00000	1.00000
0.9766	0.84123	0.81966	0.86112	0.84171
0.9688	0.78871	0.76113	0.81533	0.78939
0.9609	0.73722	0.70423	0.77010	0.73815
0.9531	0.68717	0.64937	0.72559	0.68836
0.8516	0.23151	0.16551	0.25411	0.23376
0.7344	0.00332	-0.04871	-0.04238	0.00099
0.6172	-0.13641	-0.13430	-0.17479	-0.13968
0.5000	-0.20581	-0.15683	-0.20664	-0.20642
0.4531	-0.21090	-0.15456	-0.20110	-0.21041
0.2813	-0.15662	-0.12098	-0.14171	-0.15501
0.1719	-0.10150	-0.09000	-0.09441	-0.10047
0.1016	-0.06434	-0.06362	-0.06165	-0.06373
0.0703	-0.04775	-0.04849	-0.04561	-0.04615
0.0625	-0.04192	-0.04423	-0.04138	-0.04155
0.0547	-0.03717	-0.03974	-0.03705	-0.03685
0.0000	0.00000	0.00000	0.00000	0.00000

Table B.3: Results of the AC, PP, and FSAC-PP methods for the dimensionless velocity component U along vertical centre-line of the square cavity using 1^{st}-order interpolation compared to the results of [8] at $Re = 100$.

	AC Method		
Minimum Absolute Error [-]	Maximum Absolute Error [-]	Minimum Relative Error [-]	Maximum Relative Error [-]
0.00072	0.06600	0.01116	15.67207
	PP Method		
Minimum Absolute Error [-]	Maximum Absolute Error [-]	Minimum Relative Error [-]	Maximum Relative Error [-]
0.00012	0.04570	0.00320	13.76639
	FSAC-PP Method		
Minimum Absolute Error [-]	Maximum Absolute Error [-]	Minimum Relative Error [-]	Maximum Relative Error [-]
0.00032	0.00327	0.00057	0.70087

Table B.4: Absolute and relative errors of the AC, PP, and FSAC-PP methods for the dimensionless velocity component U along vertical centre-line of the square cavity using 1^{st}-order interpolation compared to the results of [8] at $Re = 100$.

B. Comparative Tables

	$Re = 100$			
	Order of Intercell Flux Interpolation: 2^{nd}-Order			
X	Ghia et al. [8]	AC Method	PP Method	FSAC-PP Method
1.0000	0.00000	0.00000	0.00000	0.00000
0.9688	-0.05906	-0.06208	-0.06579	-0.06191
0.9609	-0.07391	-0.07764	-0.08252	-0.07740
0.9531	-0.08864	-0.09303	-0.09915	-0.09273
0.9453	-0.10313	-0.10815	-0.11556	-0.10778
0.9063	-0.16914	-0.17664	-0.19034	-0.17590
0.8594	-0.22445	-0.23319	-0.25117	-0.23212
0.8047	-0.24533	-0.25324	-0.26835	-0.25208
0.5000	0.05454	0.05731	0.06953	0.05756
0.2344	0.17527	0.17954	0.17638	0.17824
0.2266	0.17507	0.17934	0.17608	0.17802
0.1563	0.16077	0.16480	0.16158	0.16351
0.0938	0.12317	0.12638	0.12451	0.12539
0.0781	0.10890	0.11178	0.11039	0.11090
0.0703	0.10091	0.10360	0.10247	0.10278
0.0625	0.09233	0.09481	0.09394	0.09406
0.0000	0.00000	0.00000	0.00000	0.00000

Table B.5: Results of the AC, PP, and FSAC-PP methods for the dimensionless velocity component V along horizontal centre-line of the square cavity using 2^{nd}-order interpolation compared to the results of [8] at $Re = 100$.

	AC Method		
Minimum Absolute Error [-]	Maximum Absolute Error [-]	Minimum Relative Error [-]	Maximum Relative Error [-]
0.00248	0.00874	0.02436	0.05110
	PP Method		
Minimum Absolute Error [-]	Maximum Absolute Error [-]	Minimum Relative Error [-]	Maximum Relative Error [-]
0.00081	0.02672	0.00503	0.27482
	FSAC-PP Method		
Minimum Absolute Error [-]	Maximum Absolute Error [-]	Minimum Relative Error [-]	Maximum Relative Error [-]
0.00173	0.00767	0.01684	0.05531

Table B.6: Absolute and relative errors of the AC, PP, and FSAC-PP methods for the dimensionless velocity component V along horizontal centre-line of the square cavity using 2^{nd}-order interpolation compared to the results of [8] at $Re = 100$.

B. Comparative Tables

	$Re = 100$			
	Order of Intercell Flux Interpolation: 2^{nd}-Order			
Y	Ghia et al. [8]	AC Method	PP Method	FSAC-PP Method
1.0000	1.00000	1.00000	1.00000	1.00000
0.9766	0.84123	0.84350	0.84368	0.84363
0.9688	0.78871	0.79164	0.79207	0.79181
0.9609	0.73722	0.74076	0.74146	0.74093
0.9531	0.68717	0.69126	0.69208	0.69140
0.8516	0.23151	0.23685	0.23353	0.23566
0.7344	0.00332	0.00424	0.00543	0.00304
0.6172	-0.13641	-0.13892	-0.13493	-0.13947
0.5000	-0.20581	-0.20927	-0.20913	-0.20906
0.4531	-0.21090	-0.21407	-0.21538	-0.21354
0.2813	-0.15662	-0.15754	-0.15887	-0.15642
0.1719	-0.10150	-0.10155	-0.10138	-0.10069
0.1016	-0.06434	-0.06426	-0.06370	-0.06371
0.0703	-0.04775	-0.04651	-0.04600	-0.04612
0.0625	-0.04192	-0.04187	-0.04139	-0.04152
0.0547	-0.03717	-0.03712	-0.03670	-0.03682
0.0000	0.00000	0.00000	0.00000	0.00000

Table B.7: Results of the AC, PP, and FSAC-PP methods for the dimensionless velocity component U along vertical centre-line of the square cavity using 2^{nd}-order interpolation compared to the results of [8] at $Re = 100$.

	AC Method		
Minimum Absolute Error [-]	Maximum Absolute Error [-]	Minimum Relative Error [-]	Maximum Relative Error [-]
0.00005	0.00534	0.00052	0.27663
	PP Method		
Minimum Absolute Error [-]	Maximum Absolute Error [-]	Minimum Relative Error [-]	Maximum Relative Error [-]
0.00012	0.00491	0.00115	0.63502
	FSAC-PP Method		
Minimum Absolute Error [-]	Maximum Absolute Error [-]	Minimum Relative Error [-]	Maximum Relative Error [-]
0.00020	0.00423	0.00130	0.08482

Table B.8: Absolute and relative errors of the AC, PP, and FSAC-PP methods for the dimensionless velocity component U along vertical centre-line of the square cavity using 2^{nd}-order interpolation compared to the results of [8] at $Re = 100$.

B. Comparative Tables

	$Re = 100$			
	Order of Intercell Flux Interpolation: 3^{rd}-Order			
X	Ghia et al. [8]	AC Method	PP Method	FSAC-PP Method
1.0000	0.00000	0.00000	0.00000	0.00000
0.9688	-0.05906	-0.06226	-0.06227	-0.06217
0.9609	-0.07391	-0.07786	-0.07789	-0.07775
0.9531	-0.08864	-0.09329	-0.09333	-0.09315
0.9453	-0.10313	-0.10845	-0.10852	-0.10828
0.9063	-0.16914	-0.17702	-0.17723	-0.17672
0.8594	-0.22445	-0.23347	-0.23372	-0.23307
0.8047	-0.24533	-0.25321	-0.25310	-0.25279
0.5000	0.05454	0.05746	0.05889	0.05709
0.2344	0.17527	0.17934	0.17744	0.17917
0.2266	0.17507	0.17914	0.17720	0.17898
0.1563	0.16077	0.16460	0.16261	0.16454
0.0938	0.12317	0.12622	0.12466	0.12622
0.0781	0.10890	0.11163	0.11026	0.11165
0.0703	0.10091	0.10346	0.10220	0.10348
0.0625	0.09233	0.09468	0.09354	0.09471
0.0000	0.00000	0.00000	0.00000	0.00000

Table B.9: Results of the AC, PP, and FSAC-PP methods for the dimensionless velocity component V along horizontal centre-line of the square cavity using 3^{rd}-order interpolation compared to the results of [8] at $Re = 100$.

	AC Method		
Minimum Absolute Error [-]	Maximum Absolute Error [-]	Minimum Relative Error [-]	Maximum Relative Error [-]
0.00235	0.00902	0.02324	0.05420
	PP Method		
Minimum Absolute Error [-]	Maximum Absolute Error [-]	Minimum Relative Error [-]	Maximum Relative Error [-]
0.00121	0.00927	0.01142	0.07968
	FSAC-PP Method		
Minimum Absolute Error [-]	Maximum Absolute Error [-]	Minimum Relative Error [-]	Maximum Relative Error [-]
0.00238	0.00862	0.02225	0.05270

Table B.10: Absolute and relative errors of the AC, PP, and FSAC-PP methods for the dimensionless velocity component V along horizontal centre-line of the square cavity using 3^{rd}-order interpolation compared to the results of [8] at $Re = 100$.

B. Comparative Tables

	$Re = 100$			
	Order of Intercell Flux Interpolation: 3^{rd}-Order			
Y	Ghia et al. [8]	AC Method	PP Method	FSAC-PP Method
1.0000	1.00000	1.00000	1.00000	1.00000
0.9766	0.84123	0.84339	0.84317	0.84334
0.9688	0.78871	0.79150	0.79125	0.79142
0.9609	0.73722	0.74059	0.74030	0.74049
0.9531	0.68717	0.69106	0.69071	0.69093
0.8516	0.23151	0.23644	0.23464	0.23577
0.7344	0.00332	0.00410	0.00256	0.00371
0.6172	-0.13641	-0.13874	-0.13925	-0.13842
0.5000	-0.20581	-0.20892	-0.20856	-0.20842
0.4531	-0.21090	-0.21373	-0.21305	-0.21330
0.2813	-0.15662	-0.15748	-0.15612	-0.15737
0.1719	-0.10150	-0.10164	-0.10051	-0.10161
0.1016	-0.06434	-0.06436	-0.06361	-0.06436
0.0703	-0.04775	-0.04659	-0.04606	-0.04660
0.0625	-0.04192	-0.04194	-0.04147	-0.04195
0.0547	-0.03717	-0.03719	-0.03677	-0.03720
0.0000	0.00000	0.00000	0.00000	0.00000

Table B.11: Results of the AC, PP, and FSAC-PP methods for the dimensionless velocity component U along vertical centre-line of the square cavity using 3^{rd}-order interpolation compared to the results of [8] at $Re = 100$.

	AC Method		
Minimum Absolute Error [-]	Maximum Absolute Error [-]	Minimum Relative Error [-]	Maximum Relative Error [-]
0.00002	0.00493	0.00028	0.23427
	PP Method		
Minimum Absolute Error [-]	Maximum Absolute Error [-]	Minimum Relative Error [-]	Maximum Relative Error [-]
0.00040	0.00354	0.00231	0.22983
	FSAC-PP Method		
Minimum Absolute Error [-]	Maximum Absolute Error [-]	Minimum Relative Error [-]	Maximum Relative Error [-]
0.00002	0.00426	0.00027	0.11597

Table B.12: Absolute and relative errors of the AC, PP, and FSAC-PP methods for the dimensionless velocity component U along vertical centre-line of the square cavity using 3^{rd}-order interpolation compared to the results of [8] at $Re = 100$.

B. Comparative Tables

	$Re = 100$			
	Order of Intercell Flux Interpolation: 5^{th}-WENO			
X	Ghia et al. [8]	AC Method	PP Method	FSAC-PP Method
1.0000	0.00000	0.00000	0.00000	0.00000
0.9688	-0.05906	-0.06226	-0.06233	-0.06218
0.9609	-0.07391	-0.07786	-0.07795	-0.07776
0.9531	-0.08864	-0.09328	-0.09340	-0.09316
0.9453	-0.10313	-0.10844	-0.10859	-0.10829
0.9063	-0.16914	-0.17702	-0.17726	-0.17674
0.8594	-0.22445	-0.23350	-0.23367	-0.23309
0.8047	-0.24533	-0.25326	-0.25291	-0.25281
0.5000	0.05454	0.05748	0.05867	0.05709
0.2344	0.17527	0.17937	0.17719	0.17918
0.2266	0.17507	0.17916	0.17695	0.17899
0.1563	0.16077	0.16462	0.16246	0.16455
0.0938	0.12317	0.12623	0.12458	0.12623
0.0781	0.10890	0.11164	0.11019	0.11166
0.0703	0.10091	0.10347	0.10213	0.10349
0.0625	0.09233	0.09469	0.09347	0.09472
0.0000	0.00000	0.00000	0.00000	0.00000

Table B.13: Results of the AC, PP, and FSAC-PP methods for the dimensionless velocity component V along horizontal centre-line of the square cavity using 5^{th}-order WENO interpolation compared to the results of [8] at $Re = 100$.

	AC Method		
Minimum Absolute Error [-]	Maximum Absolute Error [-]	Minimum Relative Error [-]	Maximum Relative Error [-]
0.00236	0.00905	0.02338	0.05415
	PP Method		
Minimum Absolute Error [-]	Maximum Absolute Error [-]	Minimum Relative Error [-]	Maximum Relative Error [-]
0.00114	0.00922	0.01054	0.07575
	FSAC-PP Method		
Minimum Absolute Error [-]	Maximum Absolute Error [-]	Minimum Relative Error [-]	Maximum Relative Error [-]
0.00239	0.00864	0.02229	0.05283

Table B.14: Absolute and relative errors of the AC, PP, and FSAC-PP methods for the dimensionless velocity component V along horizontal centre-line of the square cavity using 5^{th}-order WENO interpolation compared to the results of [8] at $Re = 100$.

B. Comparative Tables

	$Re = 100$			
	Order of Intercell Flux Interpolation: 5^{th}-WENO			
Y	Ghia et al. [8]	AC Method	PP Method	FSAC-PP Method
1.0000	1.00000	1.00000	1.00000	1.00000
0.9766	0.84123	0.84340	0.84286	0.84338
0.9688	0.78871	0.79152	0.79080	0.79147
0.9609	0.73722	0.74061	0.73973	0.74054
0.9531	0.68717	0.69109	0.69004	0.69098
0.8516	0.23151	0.23647	0.23409	0.23580
0.7344	0.00332	0.00415	0.00233	0.00373
0.6172	-0.13641	-0.13872	-0.13885	-0.13840
0.5000	-0.20581	-0.20896	-0.20799	-0.20842
0.4531	-0.21090	-0.21378	-0.21250	-0.21330
0.2813	-0.15662	-0.15751	-0.15606	-0.15738
0.1719	-0.10150	-0.10164	-0.10064	-0.10163
0.1016	-0.06434	-0.06436	-0.06374	-0.06437
0.0703	-0.04775	-0.04659	-0.04616	-0.04661
0.0625	-0.04192	-0.04194	-0.04156	-0.04196
0.0547	-0.03717	-0.03719	-0.03685	-0.03721
0.0000	0.00000	0.00000	0.00000	0.00000

Table B.15: Results of the AC, PP, and FSAC-PP methods for the dimensionless velocity component U along vertical centre-line of the square cavity using 5^{th}-order WENO interpolation compared to the results of [8] at $Re = 100$.

	AC Method		
Minimum Absolute Error [-]	Maximum Absolute Error [-]	Minimum Relative Error [-]	Maximum Relative Error [-]
0.00002	0.00496	0.00024	0.24897
	PP Method		
Minimum Absolute Error [-]	Maximum Absolute Error [-]	Minimum Relative Error [-]	Maximum Relative Error [-]
0.00032	0.00287	0.00193	0.29880
	FSAC-PP Method		
Minimum Absolute Error [-]	Maximum Absolute Error [-]	Minimum Relative Error [-]	Maximum Relative Error [-]
0.00003	0.00429	0.00046	0.12395

Table B.16: Absolute and relative errors of the AC, PP, and FSAC-PP methods for the dimensionless velocity component U along vertical centre-line of the square cavity using 5^{th}-order WENO interpolation compared to the results of [8] at $Re = 100$.

B. Comparative Tables

	$Re = 100$			
	Order of Intercell Flux Interpolation: 9^{th}-WENO			
X	Ghia et al. [8]	AC Method	PP Method	FSAC-PP Method
1.0000	0.00000	0.00000	0.00000	0.00000
0.9688	-0.05906	-0.06224	-0.06210	-0.06218
0.9609	-0.07391	-0.07784	-0.07767	-0.07775
0.9531	-0.08864	-0.09326	-0.09308	-0.09316
0.9453	-0.10313	-0.10842	-0.10822	-0.10829
0.9063	-0.16914	-0.17701	-0.17671	-0.17674
0.8594	-0.22445	-0.23349	-0.23300	-0.23308
0.8047	-0.24533	-0.25326	-0.25227	-0.25280
0.5000	0.05454	0.05747	0.05861	0.05709
0.2344	0.17527	0.17937	0.17700	0.17917
0.2266	0.17507	0.17917	0.17675	0.17898
0.1563	0.16077	0.16462	0.16216	0.16454
0.0938	0.12317	0.12624	0.12430	0.12623
0.0781	0.10890	0.11165	0.10993	0.11165
0.0703	0.10091	0.10348	0.10189	0.10349
0.0625	0.09233	0.09470	0.09325	0.09471
0.0000	0.00000	0.00000	0.00000	0.00000

Table B.17: Results of the AC, PP, and FSAC-PP methods for the dimensionless velocity component V along horizontal centre-line of the square cavity using 9^{th}-order WENO interpolation compared to the results of [8] at $Re = 100$.

	AC Method		
Minimum Absolute Error [-]	Maximum Absolute Error [-]	Minimum Relative Error [-]	Maximum Relative Error [-]
0.00237	0.00904	0.02341	0.05391
	PP Method		
Minimum Absolute Error [-]	Maximum Absolute Error [-]	Minimum Relative Error [-]	Maximum Relative Error [-]
0.00092	0.00855	0.00864	0.07455
	FSAC-PP Method		
Minimum Absolute Error [-]	Maximum Absolute Error [-]	Minimum Relative Error [-]	Maximum Relative Error [-]
0.00238	0.00863	0.02225	0.05277

Table B.18: Absolute and relative errors of the AC, PP, and FSAC-PP methods for the dimensionless velocity component V along horizontal centre-line of the square cavity using 9^{th}-order WENO interpolation compared to the results of [8] at $Re = 100$.

B. Comparative Tables

	$Re = 100$			
	Order of Intercell Flux Interpolation: 9^{th}-WENO			
Y	Ghia et al. [8]	AC Method	PP Method	FSAC-PP Method
1.0000	1.00000	1.00000	1.00000	1.00000
0.9766	0.84123	0.84342	0.84294	0.84335
0.9688	0.78871	0.79154	0.79089	0.79144
0.9609	0.73722	0.74063	0.73983	0.74050
0.9531	0.68717	0.69111	0.69015	0.69094
0.8516	0.23151	0.23649	0.23411	0.23578
0.7344	0.00332	0.00414	0.00210	0.00372
0.6172	-0.13641	-0.13874	-0.13941	-0.13841
0.5000	-0.20581	-0.20898	-0.20837	-0.20841
0.4531	-0.21090	-0.21379	-0.21272	-0.21329
0.2813	-0.15662	-0.15751	-0.15564	-0.15737
0.1719	-0.10150	-0.10164	-0.10017	-0.10162
0.1016	-0.06434	-0.06435	-0.06340	-0.06436
0.0703	-0.04775	-0.04658	-0.04590	-0.04660
0.0625	-0.04192	-0.04194	-0.04133	-0.04195
0.0547	-0.03717	-0.03718	-0.03665	-0.03720
0.0000	0.00000	0.00000	0.00000	0.00000

Table B.19: Results of the AC, PP, and FSAC-PP methods for the dimensionless velocity component U along vertical centre-line of the square cavity using 9^{th}-order WENO interpolation compared to the results of [8] at $Re = 100$.

	AC Method		
Minimum Absolute Error [-]	Maximum Absolute Error [-]	Minimum Relative Error [-]	Maximum Relative Error [-]
0.00001	0.00498	0.00019	0.24727
	PP Method		
Minimum Absolute Error [-]	Maximum Absolute Error [-]	Minimum Relative Error [-]	Maximum Relative Error [-]
0.00052	0.00300	0.00203	0.36641
	FSAC-PP Method		
Minimum Absolute Error [-]	Maximum Absolute Error [-]	Minimum Relative Error [-]	Maximum Relative Error [-]
0.00002	0.00427	0.00036	0.12054

Table B.20: Absolute and relative errors of the AC, PP, and FSAC-PP methods for the dimensionless velocity component U along vertical centre-line of the square cavity using 9^{th}-order WENO interpolation compared to the results of [8] at $Re = 100$.

B. Comparative Tables

	$Re = 400$			
	Order of Intercell Flux Interpolation: 1^{st}-Order			
X	Ghia et al. [8]	AC Method	PP Method	FSAC-PP Method
1.0000	0.00000	0.00000	0.00000	0.00000
0.9688	-0.12146	-0.08917	-0.06127	-0.12631
0.9609	-0.15663	-0.11109	-0.07627	-0.16165
0.9531	-0.19254	-0.13190	-0.09100	-0.19708
0.9453	-0.22847	-0.15124	-0.10537	-0.23181
0.9063	-0.23827	-0.21838	-0.16944	-0.37189
0.8594	-0.44993	-0.23287	-0.22177	-0.42647
0.8047	-0.38598	-0.19227	-0.24144	-0.36956
0.5000	0.05186	0.06414	0.04411	0.06250
0.2344	0.30174	0.11467	0.17733	0.27742
0.2266	0.30203	0.11494	0.17764	0.27734
0.1563	0.28124	0.11355	0.16802	0.25895
0.0938	0.22965	0.09853	0.13562	0.21340
0.0781	0.20920	0.09042	0.12302	0.19454
0.0703	0.19713	0.08540	0.11594	0.18333
0.0625	0.18360	0.07964	0.10833	0.17072
0.0000	0.00000	0.00000	0.00000	0.00000

Table B.21: Results of the AC, PP, and FSAC-PP methods for the dimensionless velocity component V along horizontal centre-line of the square cavity using 1^{st}-order interpolation compared to the results of [8] at $Re = 400$.

	AC Method		
Minimum Absolute Error [-]	Maximum Absolute Error [-]	Minimum Relative Error [-]	Maximum Relative Error [-]
0.01228	0.21706	0.08350	0.61997
	PP Method		
Minimum Absolute Error [-]	Maximum Absolute Error [-]	Minimum Relative Error [-]	Maximum Relative Error [-]
0.00775	0.22816	0.14940	0.53882
	FSAC-PP Method		
Minimum Absolute Error [-]	Maximum Absolute Error [-]	Minimum Relative Error [-]	Maximum Relative Error [-]
0.00334	0.13362	0.01463	0.56081

Table B.22: Absolute and relative errors of the AC, PP, and FSAC-PP methods for the dimensionless velocity component V along horizontal centre-line of the square cavity using 1^{st}-order interpolation compared to the results of [8] at $Re = 400$.

B. Comparative Tables

	$Re = 400$			
	Order of Intercell Flux Interpolation: 1^{st}-Order			
Y	Ghia et al. [8]	AC Method	PP Method	FSAC-PP Method
1.0000	1.00000	1.00000	1.00000	1.00000
0.9766	0.75837	0.68566	0.85359	0.75094
0.9688	0.68439	0.59385	0.80509	0.67568
0.9609	0.61756	0.51160	0.75730	0.60797
0.9531	0.55892	0.43932	0.71052	0.54866
0.8516	0.29093	0.08144	0.24914	0.26977
0.7344	0.16256	0.00766	-0.01191	0.15167
0.6172	0.02135	-0.04522	-0.15202	0.01721
0.5000	-0.11477	-0.08734	-0.20777	-0.11992
0.4531	-0.17119	-0.09926	-0.20877	-0.17620
0.2813	-0.32726	-0.11484	-0.15336	-0.30012
0.1719	-0.24299	-0.10378	-0.10265	-0.22178
0.1016	-0.14612	-0.08335	-0.06872	-0.13897
0.0703	-0.10338	-0.06741	-0.05259	-0.10019
0.0625	-0.09266	-0.06241	-0.04838	-0.09018
0.0547	-0.08186	-0.05693	-0.04409	-0.07998
0.0000	0.00000	0.00000	0.00000	0.00000

Table B.23: Results of the AC, PP, and FSAC-PP methods for the dimensionless velocity component U along vertical centre-line of the square cavity using 1^{st}-order interpolation compared to the results of [8] at $Re = 400$.

	AC Method		
Minimum Absolute Error [-]	Maximum Absolute Error [-]	Minimum Relative Error [-]	Maximum Relative Error [-]
0.02493	0.21242	0.09588	3.11797
	PP Method		
Minimum Absolute Error [-]	Maximum Absolute Error [-]	Minimum Relative Error [-]	Maximum Relative Error [-]
0.03758	0.17447	0.12556	8.12039
	FSAC-PP Method		
Minimum Absolute Error [-]	Maximum Absolute Error [-]	Minimum Relative Error [-]	Maximum Relative Error [-]
0.00188	0.02714	0.00980	0.19398

Table B.24: Absolute and relative errors of the AC, PP, and FSAC-PP methods for the dimensionless velocity component U along vertical centre-line of the square cavity using 1^{st}-order interpolation compared to the results of [8] at $Re = 400$.

B. Comparative Tables

	$Re = 400$			
	Order of Intercell Flux Interpolation: 2^{nd}-Order			
X	Ghia et al. [8]	AC Method	PP Method	FSAC-PP Method
1.0000	0.00000	0.00000	0.00000	0.00000
0.9688	-0.12146	-0.12327	-0.12085	-0.12285
0.9609	-0.15663	-0.15875	-0.15468	-0.15808
0.9531	-0.19254	-0.19487	-0.18927	-0.19395
0.9453	-0.22847	-0.23092	-0.22403	-0.22977
0.9063	-0.23827	-0.38495	-0.37822	-0.38436
0.8594	-0.44993	-0.45159	-0.45846	-0.45522
0.8047	-0.38598	-0.38653	-0.40130	-0.39102
0.5000	0.05186	0.05175	0.06903	0.05068
0.2344	0.30174	0.30282	0.29292	0.30586
0.2266	0.30203	0.30317	0.29152	0.30628
0.1563	0.28124	0.28273	0.26027	0.28582
0.0938	0.22965	0.23084	0.20825	0.23343
0.0781	0.20920	0.21021	0.18907	0.21262
0.0703	0.19713	0.19804	0.17791	0.20035
0.0625	0.18360	0.18440	0.16548	0.18658
0.0000	0.00000	0.00000	0.00000	0.00000

Table B.25: Results of the AC, PP, and FSAC-PP methods for the dimensionless velocity component V along horizontal centre-line of the square cavity using 2^{nd}-order interpolation compared to the results of [8] at $Re = 400$.

	AC Method		
Minimum Absolute Error [-]	Maximum Absolute Error [-]	Minimum Relative Error [-]	Maximum Relative Error [-]
0.00011	0.14668	0.00141	0.61561
	PP Method		
Minimum Absolute Error [-]	Maximum Absolute Error [-]	Minimum Relative Error [-]	Maximum Relative Error [-]
0.00061	0.13995	0.00505	0.58735
	FSAC-PP Method		
Minimum Absolute Error [-]	Maximum Absolute Error [-]	Minimum Relative Error [-]	Maximum Relative Error [-]
0.00118	0.14609	0.00571	0.61311

Table B.26: Absolute and relative errors of the AC, PP, and FSAC-PP methods for the dimensionless velocity component V along horizontal centre-line of the square cavity using 2^{nd}-order interpolation compared to the results of [8] at $Re = 400$.

B. Comparative Tables

	$Re = 400$			
	Order of Intercell Flux Interpolation: 2^{nd}-Order			
Y	Ghia et al. [8]	AC Method	PP Method	FSAC-PP Method
1.0000	1.00000	1.00000	1.00000	1.00000
0.9766	0.75837	0.76001	0.76944	0.76403
0.9688	0.68439	0.68656	0.69835	0.69134
0.9609	0.61756	0.62024	0.63267	0.62527
0.9531	0.55892	0.56205	0.57348	0.56698
0.8516	0.29093	0.29242	0.28704	0.29473
0.7344	0.16256	0.16226	0.16361	0.16341
0.6172	0.02135	0.02025	0.01759	0.02056
0.5000	-0.11477	-0.11637	-0.12948	-0.11663
0.4531	-0.17119	-0.17300	-0.19164	-0.17367
0.2813	-0.32726	-0.32847	-0.33177	-0.33302
0.1719	-0.24299	-0.24142	-0.21605	-0.24278
0.1016	-0.14612	-0.14376	-0.11961	-0.14285
0.0703	-0.10338	-0.10130	-0.08195	-0.10010
0.0625	-0.09266	-0.09072	-0.07293	-0.08953
0.0547	-0.08186	-0.08008	-0.06400	-0.07893
0.0000	0.00000	0.00000	0.00000	0.00000

Table B.27: Results of the AC, PP, and FSAC-PP methods for the dimensionless velocity component U along vertical centre-line of the square cavity using 2^{nd}-order interpolation compared to the results of [8] at $Re = 400$.

	AC Method		
Minimum Absolute Error [-]	Maximum Absolute Error [-]	Minimum Relative Error [-]	Maximum Relative Error [-]
0.00030	0.00313	0.00187	0.05174
	PP Method		
Minimum Absolute Error [-]	Maximum Absolute Error [-]	Minimum Relative Error [-]	Maximum Relative Error [-]
0.00105	0.02694	0.00645	0.21816
	FSAC-PP Method		
Minimum Absolute Error [-]	Maximum Absolute Error [-]	Minimum Relative Error [-]	Maximum Relative Error [-]
0.00021	0.00806	0.00087	0.03716

Table B.28: Absolute and relative errors of the AC, PP, and FSAC-PP methods for the dimensionless velocity component U along vertical centre-line of the square cavity using 2^{nd}-order interpolation compared to the results of [8] at $Re = 400$.

B. Comparative Tables

	$Re = 400$			
	Order of Intercell Flux Interpolation: 3^{rd}-Order			
X	Ghia et al. [8]	AC Method	PP Method	FSAC-PP Method
1.0000	0.00000	0.00000	0.00000	0.00000
0.9688	-0.12146	-0.12435	-0.11466	-0.12283
0.9609	-0.15663	-0.16010	-0.14772	-0.15819
0.9531	-0.19254	-0.19650	-0.18162	-0.19422
0.9453	-0.22847	-0.23279	-0.21573	-0.23018
0.9063	-0.23827	-0.38692	-0.36584	-0.38371
0.8594	-0.44993	-0.45108	-0.43923	-0.44917
0.8047	-0.38598	-0.38450	-0.38223	-0.38310
0.5000	0.05186	0.05209	0.06863	0.05158
0.2344	0.30174	0.30170	0.28041	0.29975
0.2266	0.30203	0.30203	0.27864	0.30015
0.1563	0.28124	0.28165	0.24579	0.28031
0.0938	0.22965	0.22997	0.19507	0.22902
0.0781	0.20920	0.20940	0.17679	0.20854
0.0703	0.19713	0.19726	0.16621	0.19647
0.0625	0.18360	0.18366	0.15447	0.18293
0.0000	0.00000	0.00000	0.00000	0.00000

Table B.29: Results of the AC, PP, and FSAC-PP methods for the dimensionless velocity component V along horizontal centre-line of the square cavity using 3^{rd}-order interpolation compared to the results of [8] at $Re = 400$.

	AC Method		
Minimum Absolute Error [-]	Maximum Absolute Error [-]	Minimum Relative Error [-]	Maximum Relative Error [-]
0.00000	0.14865	0.00002	0.62387
	PP Method		
Minimum Absolute Error [-]	Maximum Absolute Error [-]	Minimum Relative Error [-]	Maximum Relative Error [-]
0.00375	0.12757	0.00971	0.53539
	FSAC-PP Method		
Minimum Absolute Error [-]	Maximum Absolute Error [-]	Minimum Relative Error [-]	Maximum Relative Error [-]
0.00028	0.14544	0.00168	0.61038

Table B.30: Absolute and relative errors of the AC, PP, and FSAC-PP methods for the dimensionless velocity component V along horizontal centre-line of the square cavity using 3^{rd}-order interpolation compared to the results of [8] at $Re = 400$.

B. Comparative Tables

	$Re = 400$			
	Order of Intercell Flux Interpolation: 3^{rd}-Order			
Y	Ghia et al. [8]	AC Method	PP Method	FSAC-PP Method
1.0000	1.00000	1.00000	1.00000	1.00000
0.9766	0.75837	0.75963	0.75825	0.75969
0.9688	0.68439	0.68602	0.68403	0.68600
0.9609	0.61756	0.61948	0.61623	0.61925
0.9531	0.55892	0.56104	0.55599	0.56050
0.8516	0.29093	0.29081	0.27788	0.28730
0.7344	0.16256	0.16173	0.15598	0.15904
0.6172	0.02135	0.02056	0.01138	0.02010
0.5000	-0.11477	-0.11543	-0.13289	-0.11401
0.4531	-0.17119	-0.17181	-0.19252	-0.16992
0.2813	-0.32726	-0.32700	-0.31512	-0.32532
0.1719	-0.24299	-0.24160	-0.20189	-0.24021
0.1016	-0.14612	-0.14473	-0.11229	-0.14347
0.0703	-0.10338	-0.10228	-0.07736	-0.10125
0.0625	-0.09266	-0.09165	-0.06896	-0.09071
0.0547	-0.08186	-0.08095	-0.06062	-0.08010
0.0000	0.00000	0.00000	0.00000	0.00000

Table B.31: Results of the AC, PP, and FSAC-PP methods for the dimensionless velocity component U along vertical centre-line of the square cavity using 3^{rd}-order interpolation compared to the results of [8] at $Re = 400$.

	AC Method		
Minimum Absolute Error [-]	Maximum Absolute Error [-]	Minimum Relative Error [-]	Maximum Relative Error [-]
0.00012	0.00212	0.00042	0.03705
	PP Method		
Minimum Absolute Error [-]	Maximum Absolute Error [-]	Minimum Relative Error [-]	Maximum Relative Error [-]
0.00012	0.04111	0.00015	0.46706
	FSAC-PP Method		
Minimum Absolute Error [-]	Maximum Absolute Error [-]	Minimum Relative Error [-]	Maximum Relative Error [-]
0.00076	0.00363	0.00174	0.05844

Table B.32: Absolute and relative errors of the AC, PP, and FSAC-PP methods for the dimensionless velocity component U along vertical centre-line of the square cavity using 3^{rd}-order interpolation compared to the results of [8] at $Re = 400$.

B. Comparative Tables

	$Re = 400$			
	Order of Intercell Flux Interpolation: 5^{th}-WENO			
X	Ghia et al. [8]	AC Method	PP Method	FSAC-PP Method
1.0000	0.00000	0.00000	0.00000	0.00000
0.9688	-0.12146	-0.12421	-0.11031	-0.12273
0.9609	-0.15663	-0.15996	-0.14290	-0.15807
0.9531	-0.19254	-0.19637	-0.17639	-0.19408
0.9453	-0.22847	-0.23271	-0.21013	-0.23003
0.9063	-0.23827	-0.38717	-0.35900	-0.38356
0.8594	-0.44993	-0.45144	-0.43174	-0.44906
0.8047	-0.38598	-0.38445	-0.37563	-0.38301
0.5000	0.05186	0.05206	0.07147	0.05158
0.2344	0.30174	0.30200	0.27141	0.29965
0.2266	0.30203	0.30235	0.26935	0.30005
0.1563	0.28124	0.28200	0.23554	0.28019
0.0938	0.22965	0.23028	0.18625	0.22892
0.0781	0.20920	0.20970	0.16871	0.20846
0.0703	0.19713	0.19756	0.15859	0.19638
0.0625	0.18360	0.18394	0.14738	0.18285
0.0000	0.00000	0.00000	0.00000	0.00000

Table B.33: Results of the AC, PP, and FSAC-PP methods for the dimensionless velocity component V along horizontal centre-line of the square cavity using 5^{th}-order WENO interpolation compared to the results of [8] at $Re = 400$.

	AC Method		
Minimum Absolute Error [-]	Maximum Absolute Error [-]	Minimum Relative Error [-]	Maximum Relative Error [-]
0.00020	0.14890	0.00087	0.62492
	PP Method		
Minimum Absolute Error [-]	Maximum Absolute Error [-]	Minimum Relative Error [-]	Maximum Relative Error [-]
0.01035	0.12073	0.02680	0.50669
	FSAC-PP Method		
Minimum Absolute Error [-]	Maximum Absolute Error [-]	Minimum Relative Error [-]	Maximum Relative Error [-]
0.00028	0.14529	0.00193	0.60976

Table B.34: Absolute and relative errors of the AC, PP, and FSAC-PP methods for the dimensionless velocity component V along horizontal centre-line of the square cavity using 5^{th}-order WENO interpolation compared to the results of [8] at $Re = 400$.

B. Comparative Tables

	$Re = 400$			
	Order of Intercell Flux Interpolation: 5^{th}-WENO			
Y	Ghia et al. [8]	AC Method	PP Method	FSAC-PP Method
1.0000	1.00000	1.00000	1.00000	1.00000
0.9766	0.75837	0.75954	0.75175	0.75989
0.9688	0.68439	0.68594	0.67573	0.68617
0.9609	0.61756	0.61942	0.60683	0.61939
0.9531	0.55892	0.56099	0.54618	0.56060
0.8516	0.29093	0.29093	0.27157	0.28722
0.7344	0.16256	0.16178	0.15115	0.15897
0.6172	0.02135	0.02062	0.00879	0.02006
0.5000	-0.11477	-0.11529	-0.13521	-0.11403
0.4531	-0.17119	-0.17161	-0.19446	-0.16993
0.2813	-0.32726	-0.32732	-0.30649	-0.32523
0.1719	-0.24299	-0.24196	-0.19159	-0.24010
0.1016	-0.14612	-0.14483	-0.10555	-0.14338
0.0703	-0.10338	-0.10230	-0.07256	-0.10118
0.0625	-0.09266	-0.09167	-0.06466	-0.09065
0.0547	-0.08186	-0.08096	-0.05683	-0.08005
0.0000	0.00000	0.00000	0.00000	0.00000

Table B.35: Results of the AC, PP, and FSAC-PP methods for the dimensionless velocity component U along vertical centre-line of the square cavity using 5^{th}-order WENO interpolation compared to the results of [8] at $Re = 400$.

	AC Method		
Minimum Absolute Error [-]	Maximum Absolute Error [-]	Minimum Relative Error [-]	Maximum Relative Error [-]
0.00000	0.00207	0.00001	0.03432
	PP Method		
Minimum Absolute Error [-]	Maximum Absolute Error [-]	Minimum Relative Error [-]	Maximum Relative Error [-]
0.00662	0.05140	0.00873	0.58807
	FSAC-PP Method		
Minimum Absolute Error [-]	Maximum Absolute Error [-]	Minimum Relative Error [-]	Maximum Relative Error [-]
0.00074	0.00371	0.00200	0.06039

Table B.36: Absolute and relative errors of the AC, PP, and FSAC-PP methods for the dimensionless velocity component U along vertical centre-line of the square cavity using 5^{th}-order WENO interpolation compared to the results of [8] at $Re = 400$.

B. Comparative Tables

	$Re = 400$			
	Order of Intercell Flux Interpolation: 9^{th}-WENO			
X	Ghia et al. [8]	AC Method	PP Method	FSAC-PP Method
1.0000	0.00000	0.00000	0.00000	0.00000
0.9688	-0.12146	-0.12424	-0.11342	-0.12293
0.9609	-0.15663	-0.16002	-0.14672	-0.15832
0.9531	-0.19254	-0.19646	-0.18090	-0.19437
0.9453	-0.22847	-0.23283	-0.21528	-0.23035
0.9063	-0.23827	-0.38746	-0.36587	-0.38395
0.8594	-0.44993	-0.45175	-0.43689	-0.44931
0.8047	-0.38598	-0.38463	-0.37766	-0.38306
0.5000	0.05186	0.05201	0.06847	0.05136
0.2344	0.30174	0.30221	0.27778	0.29994
0.2266	0.30203	0.30256	0.27602	0.30038
0.1563	0.28124	0.28223	0.24342	0.28080
0.0938	0.22965	0.23049	0.19307	0.22954
0.0781	0.20920	0.20989	0.17496	0.20904
0.0703	0.19713	0.19774	0.16449	0.19694
0.0625	0.18360	0.18412	0.15288	0.18337
0.0000	0.00000	0.00000	0.00000	0.00000

Table B.37: Results of the AC, PP, and FSAC-PP methods for the dimensionless velocity component V along horizontal centre-line of the square cavity using 9^{th}-order WENO interpolation compared to the results of [8] at $Re = 400$.

	AC Method		
Minimum Absolute Error [-]	Maximum Absolute Error [-]	Minimum Relative Error [-]	Maximum Relative Error [-]
0.00015	0.14919	0.00154	0.62612
	PP Method		
Minimum Absolute Error [-]	Maximum Absolute Error [-]	Minimum Relative Error [-]	Maximum Relative Error [-]
0.00804	0.12760	0.02157	0.53552
	FSAC-PP Method		
Minimum Absolute Error [-]	Maximum Absolute Error [-]	Minimum Relative Error [-]	Maximum Relative Error [-]
0.00011	0.14568	0.00046	0.61141

Table B.38: Absolute and relative errors of the AC, PP, and FSAC-PP methods for the dimensionless velocity component V along horizontal centre-line of the square cavity using 9^{th}-order WENO interpolation compared to the results of [8] at $Re = 400$.

B. Comparative Tables

	$Re = 400$			
	Order of Intercell Flux Interpolation: 9^{th}-WENO			
Y	Ghia et al. [8]	AC Method	PP Method	FSAC-PP Method
1.0000	1.00000	1.00000	1.00000	1.00000
0.9766	0.75837	0.75976	0.75268	0.75988
0.9688	0.68439	0.68618	0.67696	0.68619
0.9609	0.61756	0.61967	0.60848	0.61945
0.9531	0.55892	0.56125	0.54825	0.56070
0.8516	0.29093	0.29114	0.27531	0.28740
0.7344	0.16256	0.16190	0.15410	0.15905
0.6172	0.02135	0.02067	0.01137	0.02023
0.5000	-0.11477	-0.11528	-0.13123	-0.11371
0.4531	-0.17119	-0.17162	-0.19012	-0.16955
0.2813	-0.32726	-0.32754	-0.31219	-0.32536
0.1719	-0.24299	-0.24217	-0.20069	-0.24079
0.1016	-0.14612	-0.14495	-0.11186	-0.14398
0.0703	-0.10338	-0.10239	-0.07716	-0.10165
0.0625	-0.09266	-0.09174	-0.06880	-0.09107
0.0547	-0.08186	-0.08103	-0.06050	-0.08043
0.0000	0.00000	0.00000	0.00000	0.00000

Table B.39: Results of the AC, PP, and FSAC-PP methods for the dimensionless velocity component U along vertical centre-line of the square cavity using 9^{th}-order WENO interpolation compared to the results of [8] at $Re = 400$.

	AC Method		
Minimum Absolute Error [-]	Maximum Absolute Error [-]	Minimum Relative Error [-]	Maximum Relative Error [-]
0.00021	0.00233	0.00074	0.03205
	PP Method		
Minimum Absolute Error [-]	Maximum Absolute Error [-]	Minimum Relative Error [-]	Maximum Relative Error [-]
0.00569	0.04230	0.00750	0.46733
	FSAC-PP Method		
Minimum Absolute Error [-]	Maximum Absolute Error [-]	Minimum Relative Error [-]	Maximum Relative Error [-]
0.00106	0.00353	0.00199	0.05240

Table B.40: Absolute and relative errors of the AC, PP, and FSAC-PP methods for the dimensionless velocity component U along vertical centre-line of the square cavity using 9^{th}-order WENO interpolation compared to the results of [8] at $Re = 400$.

B. Comparative Tables

	$Re = 1000$			
	Order of Intercell Flux Interpolation: 1^{st}-Order			
X	Ghia et al. [8]	AC Method	PP Method	FSAC-PP Method
1.0000	0.00000	0.00000	0.00000	0.00000
0.9688	-0.21388	-0.12151	-0.06519	-0.22543
0.9609	-0.27669	-0.14810	-0.08130	-0.28405
0.9531	-0.33714	-0.17137	-0.09716	-0.33750
0.9453	-0.39188	-0.19087	-0.11268	-0.38359
0.9063	-0.51550	-0.23233	-0.18230	-0.48051
0.8594	-0.42665	-0.19986	-0.23928	-0.40206
0.8047	-0.31966	-0.13063	-0.25999	-0.29023
0.5000	0.02526	0.05454	0.04605	0.03246
0.2344	0.32235	0.08658	0.18304	0.29893
0.2266	0.33075	0.08697	0.18360	0.30406
0.1563	0.37095	0.08944	0.17780	0.31947
0.0938	0.32627	0.08483	0.15187	0.28149
0.0781	0.30353	0.08038	0.14139	0.26338
0.0703	0.29012	0.07725	0.13546	0.25224
0.0625	0.27485	0.07336	0.12904	0.23919
0.0000	0.00000	0.00000	0.00000	0.00000

Table B.41: Results of the AC, PP, and FSAC-PP methods for the dimensionless velocity component V along horizontal centre-line of the square cavity using 1^{st}-order interpolation compared to the results of [8] at $Re = 1000$.

	AC Method		
Minimum Absolute Error [-]	Maximum Absolute Error [-]	Minimum Relative Error [-]	Maximum Relative Error [-]
0.02928	0.28317	0.43189	1.15918
	PP Method		
Minimum Absolute Error [-]	Maximum Absolute Error [-]	Minimum Relative Error [-]	Maximum Relative Error [-]
0.02079	0.33320	0.18666	0.82317
	FSAC-PP Method		
Minimum Absolute Error [-]	Maximum Absolute Error [-]	Minimum Relative Error [-]	Maximum Relative Error [-]
0.00036	0.05148	0.00108	0.28518

Table B.42: Absolute and relative errors of the AC, PP, and FSAC-PP methods for the dimensionless velocity component V along horizontal centre-line of the square cavity using 1^{st}-order interpolation compared to the results of [8] at $Re = 1000$.

B. Comparative Tables

	$Re = 1000$			
	Order of Intercell Flux Interpolation: 1^{st}-Order			
Y	Ghia et al. [8]	AC Method	PP Method	FSAC-PP Method
1.0000	1.00000	1.00000	1.00000	1.00000
0.9766	0.65928	0.53519	0.85287	0.63959
0.9688	0.57492	0.42214	0.80405	0.55195
0.9609	0.51117	0.33200	0.75599	0.48481
0.9531	0.46604	0.26187	0.70901	0.43564
0.8516	0.33304	0.04307	0.25612	0.29190
0.7344	0.18719	0.01641	0.00737	0.17187
0.6172	0.05702	-0.00936	-0.13843	0.05156
0.5000	-0.06080	-0.04010	-0.20858	-0.05697
0.4531	-0.10648	-0.05288	-0.21423	-0.09845
0.2813	-0.27805	-0.09067	-0.16381	-0.26441
0.1719	-0.38289	-0.09754	-0.11191	-0.33267
0.1016	-0.29730	-0.08704	-0.07828	-0.26467
0.0703	-0.22220	-0.07393	-0.06285	-0.20904
0.0625	-0.20196	-0.06930	-0.05888	-0.19274
0.0547	-0.18109	-0.06397	-0.05486	-0.17518
0.0000	0.00000	0.00000	0.00000	0.00000

Table B.43: Results of the AC, PP, and FSAC-PP methods for the dimensionless velocity component U along vertical centre-line of the square cavity using 1^{st}-order interpolation compared to the results of [8] at $Re = 1000$.

	AC Method		
Minimum Absolute Error [-]	Maximum Absolute Error [-]	Minimum Relative Error [-]	Maximum Relative Error [-]
0.02070	0.28997	0.18821	1.16409
	PP Method		
Minimum Absolute Error [-]	Maximum Absolute Error [-]	Minimum Relative Error [-]	Maximum Relative Error [-]
0.07692	0.27098	0.23097	3.42777
	FSAC-PP Method		
Minimum Absolute Error [-]	Maximum Absolute Error [-]	Minimum Relative Error [-]	Maximum Relative Error [-]
0.00383	0.05022	0.02987	0.13116

Table B.44: Absolute and relative errors of the AC, PP, and FSAC-PP methods for the dimensionless velocity component U along vertical centre-line of the square cavity using 1^{st}-order interpolation compared to the results of [8] at $Re = 1000$.

B. Comparative Tables

	$Re = 1000$			
	Order of Intercell Flux Interpolation: 2^{nd}-Order			
X	Ghia et al. [8]	AC Method	PP Method	FSAC-PP Method
1.0000	0.00000	0.00000	0.00000	0.00000
0.9688	-0.21388	-0.21224	-0.20686	-0.19142
0.9609	-0.27669	-0.27314	-0.26245	-0.24869
0.9531	-0.33714	-0.33178	-0.31713	-0.30516
0.9453	-0.39188	-0.38526	-0.36912	-0.35837
0.9063	-0.51550	-0.51315	-0.53641	-0.51035
0.8594	-0.42665	-0.42345	-0.49229	-0.43330
0.8047	-0.31966	-0.31458	-0.34907	-0.31787
0.5000	0.02526	0.02791	0.03672	0.03976
0.2344	0.32235	0.32278	0.35897	0.33969
0.2266	0.33075	0.33036	0.36595	0.34508
0.1563	0.37095	0.35864	0.37784	0.34019
0.0938	0.32627	0.30664	0.31235	0.26590
0.0781	0.30353	0.28383	0.28839	0.24265
0.0703	0.29012	0.27060	0.27462	0.23007
0.0625	0.27485	0.25568	0.25911	0.21642
0.0000	0.00000	0.00000	0.00000	0.00000

Table B.45: Results of the AC, PP, and FSAC-PP methods for the dimensionless velocity component V along horizontal centre-line of the square cavity using 2^{nd}-order interpolation compared to the results of [8] at $Re = 1000$.

	AC Method		
Minimum Absolute Error [-]	Maximum Absolute Error [-]	Minimum Relative Error [-]	Maximum Relative Error [-]
0.00039	0.01970	0.00119	0.10497
	PP Method		
Minimum Absolute Error [-]	Maximum Absolute Error [-]	Minimum Relative Error [-]	Maximum Relative Error [-]
0.00689	0.06564	0.01857	0.45352
	FSAC-PP Method		
Minimum Absolute Error [-]	Maximum Absolute Error [-]	Minimum Relative Error [-]	Maximum Relative Error [-]
0.00179	0.06088	0.00560	0.57405

Table B.46: Absolute and relative errors of the AC, PP, and FSAC-PP methods for the dimensionless velocity component V along horizontal centre-line of the square cavity using 2^{nd}-order interpolation compared to the results of [8] at $Re = 1000$.

B. Comparative Tables

	$Re = 1000$			
	Order of Intercell Flux Interpolation: 2^{nd}-Order			
Y	Ghia et al. [8]	AC Method	PP Method	FSAC-PP Method
1.0000	1.00000	1.00000	1.00000	1.00000
0.9766	0.65928	0.65365	0.72185	0.65518
0.9688	0.57492	0.56866	0.64314	0.56839
0.9609	0.51117	0.50457	0.57562	0.50197
0.9531	0.46604	0.45901	0.52041	0.45454
0.8516	0.33304	0.32766	0.35826	0.33544
0.7344	0.18719	0.18693	0.20382	0.19634
0.6172	0.05702	0.05489	0.05778	0.05238
0.5000	-0.06080	-0.06791	-0.07994	-0.08679
0.4531	-0.10648	-0.11465	-0.13273	-0.13818
0.2813	-0.27805	-0.28383	-0.33603	-0.31562
0.1719	-0.38289	-0.37512	-0.39763	-0.36002
0.1016	-0.29730	-0.27156	-0.24484	-0.20617
0.0703	-0.22220	-0.19662	-0.16450	-0.13328
0.0625	-0.20196	-0.17739	-0.14547	-0.11692
0.0547	-0.18109	-0.15798	-0.12689	-0.10130
0.0000	0.00000	0.00000	0.00000	0.00000

Table B.47: Results of the AC, PP, and FSAC-PP methods for the dimensionless velocity component U along vertical centre-line of the square cavity using 2^{nd}-order interpolation compared to the results of [8] at $Re = 1000$.

	AC Method		
Minimum Absolute Error [-]	Maximum Absolute Error [-]	Minimum Relative Error [-]	Maximum Relative Error [-]
0.00026	0.02574	0.00140	0.12761
	PP Method		
Minimum Absolute Error [-]	Maximum Absolute Error [-]	Minimum Relative Error [-]	Maximum Relative Error [-]
0.00076	0.06822	0.01329	0.31473
	FSAC-PP Method		
Minimum Absolute Error [-]	Maximum Absolute Error [-]	Minimum Relative Error [-]	Maximum Relative Error [-]
0.00240	0.09113	0.00622	0.44063

Table B.48: Absolute and relative errors of the AC, PP, and FSAC-PP methods for the dimensionless velocity component U along vertical centre-line of the square cavity using 2^{nd}-order interpolation compared to the results of [8] at $Re = 1000$.

B. Comparative Tables

	$Re = 1000$			
	Order of Intercell Flux Interpolation: 3^{rd}-Order			
X	Ghia et al. [8]	AC Method	PP Method	FSAC-PP Method
1.0000	0.00000	0.00000	0.00000	0.00000
0.9688	-0.21388	-0.22257	-0.20835	-0.21492
0.9609	-0.27669	-0.28634	-0.26641	-0.27700
0.9531	-0.33714	-0.34706	-0.32298	-0.33661
0.9453	-0.39188	-0.40148	-0.37557	-0.39071
0.9063	-0.51550	-0.51950	-0.51781	-0.51499
0.8594	-0.42665	-0.42502	-0.43948	-0.42016
0.8047	-0.31966	-0.31862	-0.31850	-0.31026
0.5000	0.02526	0.02568	0.03625	0.02598
0.2344	0.32235	0.32333	0.33668	0.31707
0.2266	0.33075	0.33178	0.34313	0.32537
0.1563	0.37095	0.37246	0.35300	0.36436
0.0938	0.32627	0.32818	0.28877	0.31926
0.0781	0.30353	0.30535	0.26577	0.29665
0.0703	0.29012	0.29180	0.25280	0.28330
0.0625	0.27485	0.27632	0.23834	0.26810
0.0000	0.00000	0.00000	0.00000	0.00000

Table B.49: Results of the AC, PP, and FSAC-PP methods for the dimensionless velocity component V along horizontal centre-line of the square cavity using 3^{rd}-order interpolation compared to the results of [8] at $Re = 1000$.

	AC Method		
Minimum Absolute Error [-]	Maximum Absolute Error [-]	Minimum Relative Error [-]	Maximum Relative Error [-]
0.00042	0.00992	0.00303	0.04062
	PP Method		
Minimum Absolute Error [-]	Maximum Absolute Error [-]	Minimum Relative Error [-]	Maximum Relative Error [-]
0.00116	0.03776	0.00362	0.43522
	FSAC-PP Method		
Minimum Absolute Error [-]	Maximum Absolute Error [-]	Minimum Relative Error [-]	Maximum Relative Error [-]
0.00031	0.00940	0.00098	0.02942

Table B.50: Absolute and relative errors of the AC, PP, and FSAC-PP methods for the dimensionless velocity component V along horizontal centre-line of the square cavity using 3^{rd}-order interpolation compared to the results of [8] at $Re = 1000$.

B. Comparative Tables

	$Re = 1000$			
	Order of Intercell Flux Interpolation: 3^{rd}-Order			
Y	Ghia et al. [8]	AC Method	PP Method	FSAC-PP Method
1.0000	1.00000	1.00000	1.00000	1.00000
0.9766	0.65928	0.66158	0.68084	0.65912
0.9688	0.57492	0.57800	0.59514	0.57410
0.9609	0.51117	0.51486	0.52529	0.50928
0.9531	0.46604	0.47002	0.47173	0.46284
0.8516	0.33304	0.33417	0.33302	0.32446
0.7344	0.18719	0.18703	0.19270	0.18196
0.6172	0.05702	0.05610	0.05516	0.05447
0.5000	-0.06080	-0.06230	-0.07563	-0.06169
0.4531	-0.10648	-0.10815	-0.12483	-0.10639
0.2813	-0.27805	-0.27990	-0.30180	-0.27379
0.1719	-0.38289	-0.38383	-0.37445	-0.37836
0.1016	-0.29730	-0.29390	-0.24528	-0.28608
0.0703	-0.22220	-0.21784	-0.17017	-0.20989
0.0625	-0.20196	-0.19763	-0.15191	-0.18993
0.0547	-0.18109	-0.17696	-0.13387	-0.16964
0.0000	0.00000	0.00000	0.00000	0.00000

Table B.51: Results of the AC, PP, and FSAC-PP methods for the dimensionless velocity component U along vertical centre-line of the square cavity using 3^{rd}-order interpolation compared to the results of [8] at $Re = 1000$.

	AC Method		
Minimum Absolute Error [-]	Maximum Absolute Error [-]	Minimum Relative Error [-]	Maximum Relative Error [-]
0.00016	0.00436	0.00085	0.02469
	PP Method		
Minimum Absolute Error [-]	Maximum Absolute Error [-]	Minimum Relative Error [-]	Maximum Relative Error [-]
0.00002	0.05203	0.00005	0.26077
	FSAC-PP Method		
Minimum Absolute Error [-]	Maximum Absolute Error [-]	Minimum Relative Error [-]	Maximum Relative Error [-]
0.00009	0.01231	0.00024	0.06324

Table B.52: Absolute and relative errors of the AC, PP, and FSAC-PP methods for the dimensionless velocity component U along vertical centre-line of the square cavity using 3^{rd}-order interpolation compared to the results of [8] at $Re = 1000$.

B. Comparative Tables

	$Re = 1000$			
	Order of Intercell Flux Interpolation: 5^{th}-WENO			
X	Ghia et al. [8]	AC Method	PP Method	FSAC-PP Method
1.0000	0.00000	0.00000	0.00000	0.00000
0.9688	-0.21388	-0.22214	-0.18757	-0.21091
0.9609	-0.27669	-0.28603	-0.24461	-0.27221
0.9531	-0.33714	-0.34696	-0.30065	-0.33131
0.9453	-0.39188	-0.40164	-0.35295	-0.38516
0.9063	-0.51550	-0.51981	-0.49165	-0.51106
0.8594	-0.42665	-0.42444	-0.41620	-0.41788
0.8047	-0.31966	-0.31838	-0.30388	-0.30860
0.5000	0.02526	0.02550	0.03666	0.02799
0.2344	0.32235	0.32270	0.32110	0.31811
0.2266	0.33075	0.33119	0.32652	0.32592
0.1563	0.37095	0.37274	0.32686	0.35810
0.0938	0.32627	0.32883	0.26128	0.30845
0.0781	0.30353	0.30596	0.23953	0.28580
0.0703	0.29012	0.29239	0.22754	0.27261
0.0625	0.27485	0.27690	0.21438	0.25770
0.0000	0.00000	0.00000	0.00000	0.00000

Table B.53: Results of the AC, PP, and FSAC-PP methods for the dimensionless velocity component V along horizontal centre-line of the square cavity using 5^{th}-order WENO interpolation compared to the results of [8] at $Re = 1000$.

	AC Method		
Minimum Absolute Error [-]	Maximum Absolute Error [-]	Minimum Relative Error [-]	Maximum Relative Error [-]
0.00024	0.00982	0.00108	0.03863
	PP Method		
Minimum Absolute Error [-]	Maximum Absolute Error [-]	Minimum Relative Error [-]	Maximum Relative Error [-]
0.00125	0.06499	0.00389	0.45148
	FSAC-PP Method		
Minimum Absolute Error [-]	Maximum Absolute Error [-]	Minimum Relative Error [-]	Maximum Relative Error [-]
0.00273	0.01782	0.00861	0.10794

Table B.54: Absolute and relative errors of the AC, PP, and FSAC-PP methods for the dimensionless velocity component V along horizontal centre-line of the square cavity using 5^{th}-order WENO interpolation compared to the results of [8] at $Re = 1000$.

B. Comparative Tables

	$Re = 1000$			
	Order of Intercell Flux Interpolation: 5^{th}-WENO			
Y	Ghia et al. [8]	AC Method	PP Method	FSAC-PP Method
1.0000	1.00000	1.00000	1.00000	1.00000
0.9766	0.65928	0.66127	0.65126	0.65595
0.9688	0.57492	0.57775	0.56229	0.56996
0.9609	0.51117	0.51470	0.49328	0.50438
0.9531	0.46604	0.46998	0.44340	0.45740
0.8516	0.33304	0.33389	0.31293	0.32218
0.7344	0.18719	0.18684	0.18005	0.18275
0.6172	0.05702	0.05610	0.04852	0.05443
0.5000	-0.06080	-0.06215	-0.07737	-0.06410
0.4531	-0.10648	-0.10794	-0.12430	-0.10945
0.2813	-0.27805	-0.27934	-0.29606	-0.27622
0.1719	-0.38289	-0.38426	-0.34636	-0.37404
0.1016	-0.29730	-0.29463	-0.21101	-0.27483
0.0703	-0.22220	-0.21792	-0.14115	-0.19922
0.0625	-0.20196	-0.19759	-0.12492	-0.17976
0.0547	-0.18109	-0.17683	-0.10919	-0.16011
0.0000	0.00000	0.00000	0.00000	0.00000

Table B.55: Results of the AC, PP, and FSAC-PP methods for the dimensionless velocity component U along vertical centre-line of the square cavity using 5^{th}-order WENO interpolation compared to the results of [8] at $Re = 1000$.

	AC Method		
Minimum Absolute Error [-]	Maximum Absolute Error [-]	Minimum Relative Error [-]	Maximum Relative Error [-]
0.00035	0.00437	0.00185	0.02355
	PP Method		
Minimum Absolute Error [-]	Maximum Absolute Error [-]	Minimum Relative Error [-]	Maximum Relative Error [-]
0.00714	0.08629	0.01216	0.39702
	FSAC-PP Method		
Minimum Absolute Error [-]	Maximum Absolute Error [-]	Minimum Relative Error [-]	Maximum Relative Error [-]
0.00183	0.02298	0.00505	0.11584

Table B.56: Absolute and relative errors of the AC, PP, and FSAC-PP methods for the dimensionless velocity component U along vertical centre-line of the square cavity using 5^{th}-order WENO interpolation compared to the results of [8] at $Re = 1000$.

B. Comparative Tables

	$Re = 1000$			
	Order of Intercell Flux Interpolation: 9^{th}-WENO			
X	Ghia et al. [8]	AC Method	PP Method	FSAC-PP Method
1.0000	0.00000	0.00000	0.00000	0.00000
0.9688	-0.21388	-0.22262	-0.20402	-0.21365
0.9609	-0.27669	-0.28671	-0.26415	-0.27551
0.9531	-0.33714	-0.34784	-0.32246	-0.33502
0.9453	-0.39188	-0.40269	-0.37597	-0.38909
0.9063	-0.51550	-0.52085	-0.50466	-0.51390
0.8594	-0.42665	-0.42481	-0.41293	-0.41913
0.8047	-0.31966	-0.31880	-0.30390	-0.30959
0.5000	0.02526	0.02546	0.03718	0.02659
0.2344	0.32235	0.32308	0.32286	0.31737
0.2266	0.33075	0.33160	0.32875	0.32551
0.1563	0.37095	0.37351	0.33528	0.36239
0.0938	0.32627	0.32970	0.27151	0.31581
0.0781	0.30353	0.30680	0.24919	0.29318
0.0703	0.29012	0.29321	0.23677	0.27987
0.0625	0.27485	0.27770	0.22307	0.26476
0.0000	0.00000	0.00000	0.00000	0.00000

Table B.57: Results of the AC, PP, and FSAC-PP methods for the dimensionless velocity component V along horizontal centre-line of the square cavity using 9^{th}-order WENO interpolation compared to the results of [8] at $Re = 1000$.

	AC Method		
Minimum Absolute Error [-]	Maximum Absolute Error [-]	Minimum Relative Error [-]	Maximum Relative Error [-]
0.00020	0.01081	0.00226	0.04084
	PP Method		
Minimum Absolute Error [-]	Maximum Absolute Error [-]	Minimum Relative Error [-]	Maximum Relative Error [-]
0.00051	0.05476	0.00159	0.47184
	FSAC-PP Method		
Minimum Absolute Error [-]	Maximum Absolute Error [-]	Minimum Relative Error [-]	Maximum Relative Error [-]
0.00023	0.01046	0.00108	0.05262

Table B.58: Absolute and relative errors of the AC, PP, and FSAC-PP methods for the dimensionless velocity component V along horizontal centre-line of the square cavity using 9^{th}-order WENO interpolation compared to the results of [8] at $Re = 1000$.

B. Comparative Tables

	$Re = 1000$			
	Order of Intercell Flux Interpolation: 9^{th}-WENO			
Y	Ghia et al. [8]	AC Method	PP Method	FSAC-PP Method
1.0000	1.00000	1.00000	1.00000	1.00000
0.9766	0.65928	0.66194	0.64733	0.65809
0.9688	0.57492	0.57846	0.55880	0.57268
0.9609	0.51117	0.51543	0.49109	0.50758
0.9531	0.46604	0.47071	0.44244	0.46096
0.8516	0.33304	0.33454	0.31645	0.32368
0.7344	0.18719	0.18721	0.18502	0.18232
0.6172	0.05702	0.05627	0.05366	0.05452
0.5000	-0.06080	-0.06216	-0.07213	-0.06249
0.4531	-0.10648	-0.10802	-0.11929	-0.10741
0.2813	-0.27805	-0.27956	-0.28705	-0.27440
0.1719	-0.38289	-0.38503	-0.35968	-0.37702
0.1016	-0.29730	-0.29555	-0.23696	-0.28271
0.0703	-0.22220	-0.21862	-0.16421	-0.20664
0.0625	-0.20196	-0.19824	-0.14662	-0.18682
0.0547	-0.18109	-0.17742	-0.12928	-0.16671
0.0000	0.00000	0.00000	0.00000	0.00000

Table B.59: Results of the AC, PP, and FSAC-PP methods for the dimensionless velocity component U along vertical centre-line of the square cavity using 9^{th}-order WENO interpolation compared to the results of [8] at $Re = 1000$.

	AC Method		
Minimum Absolute Error [-]	Maximum Absolute Error [-]	Minimum Relative Error [-]	Maximum Relative Error [-]
0.00002	0.00467	0.00010	0.02236
	PP Method		
Minimum Absolute Error [-]	Maximum Absolute Error [-]	Minimum Relative Error [-]	Maximum Relative Error [-]
0.00217	0.06034	0.01157	0.28609
	FSAC-PP Method		
Minimum Absolute Error [-]	Maximum Absolute Error [-]	Minimum Relative Error [-]	Maximum Relative Error [-]
0.00093	0.01556	0.00181	0.07939

Table B.60: Absolute and relative errors of the AC, PP, and FSAC-PP methods for the dimensionless velocity component U along vertical centre-line of the square cavity using 9^{th}-order WENO interpolation compared to the results of [8] at $Re = 1000$.

Bibliography

[1] L. Könözsy. Computational multiphysics modelling for microfluidic biomedical devices. *Cranfield University, Department of Aerospace Sciences, Ninth Month Progress Review Report, Cranfield, Bedfordshire, MK43 0AL, United Kingdom*, 2009.

[2] L. Könözsy. Computational multiphysics modelling of incompressible micro/macroscale flow problems at low and high reynolds numbers using high-resolution method. *Cranfield University, Department of Aerospace Sciences, Twenty-First Month Progress Review Report, Cranfield, Bedfordshire, MK43 0AL, United Kingdom*, 2010.

[3] A. J. Chorin. A numerical method for solving incompressible viscous flow problems. *Journal of Computational Physics*, 2:12–26, 1967.

[4] A. J. Chorin. Numerical solution of the navier-stokes equations. *Math. Comp.*, 22:745–762, 1968.

[5] R. Peyret and T. Taylor. Computational methods for fluid flow. *Springer-Verlag, Berlin*, 1983.

[6] E. Shapiro and D. Drikakis. Artificial compressibility, characteristics-based schemes for variable-density, incompressible, multispecies flows: Part ii. multigrid implementation and numerical tests. *Journal of Computational Physics*, 210:608–631, 2005.

[7] D. Drikakis, O. P. Iliev, and D. P. Vassileva. A nonlinear multigrid method for the three-dimensional incompressible navier-stokes equations. *Journal of Computational Physics*, 146:301–321, 1998.

[8] U. Ghia, K. N. Ghia, and C. T. Shin. High-re solutions for incompressible flow using the navier-stokes equations and a multigrid method. *Journal of Computational Physics*, 48:387–411, 1982.

[9] E. E. Tzirtzilakis and V. C. Loukopoulos. Biofluid flow in a channel under the action of a uniform localized magnetic field. *Comput Mech*, 36:360–374, 2005.

[10] M. Benke, E. Shapiro, and D. Drikakis. An efficient multi-scale modelling approach for ssdna motion in fluid flow. *Journal of Bionic Engineering*, 5:299–307, 2008.

[11] M. Benke. Mesoscale modeling and simulation of macromolecule transport in microfluidic channels. *Cranfield University, Department of Aerospace Sciences, Ph.D. thesis*, 2010.

[12] Nikolaos Asproulis. Hybrid molecular and continuum fluid dynamics models for micro and nanofluidic flows. *Cranfield University, Department of Aerospace Sciences, Ph.D. thesis*, 2009.

[13] Pasi Kallio and Johanna Kuncova. Microfluidics. *Technology Review 158/2004, National Technology Agency, Helsinki*, 2004.

[14] J. D. Newman and A. P. F. Turner. Home blood glucose biosensors: A commercial perspective. *Biosensors and Bioelectronics*, 20:2435–2453, 2005.

[15] J. H. Ferziger and M. Peric. Computational methods for fluid dynamics. *Third, Rev. Edition, Springer-Verlag, Berlin*, 2002.

[16] E. Shapiro and D. Drikakis. Artificial compressibility, characteristics-based schemes for variable density, incompressible, multi-species flows. part i. derivation of different formulations and constant density limit. *Journal of Computational Physics*, 210:584–607, 2005.

[17] A. K. Prasad and J. R. Koseff. Reynolds number and end-wall effects on a lid-driven cavity flow. *Physics of Fluids A*, 1(2):208–218, 1989.

[18] S. M. Marco and L. S. Han. A note on limiting laminar nusselt number in ducts with constant temperature gradient by analogy to thin-plate theory. *Trans. ASME*, 77:625–630, 1955.

[19] W. M. Rohsenow, J. P. Hartnett, and Y. I. Cho. Handbook of heat transfer. *McGraw-Hill, Third Edition, New York*, 1998.

[20] P. Neofytou and D. Drikakis. Non-newtonian flow instability in a channel with a sudden expansion. *Journal of Non-Newtonian Fluid Mechanics*, 111:127–150, 2003.

[21] J. D. Bronzino. The biomedical engineering handbook (2nd ed). *CRC Press, New York*, 1, 2000.

[22] H. K. Versteeg and W. Malalasekera. Introduction to computational fluid dynamics - the finite volume method. *Longman Group Ltd.*, 1995.

[23] G. Karniadakis, A. Beskok, and N. Aluru. Microflows and nanoflows. *Springer, New York*, 2005.

[24] H. Bruus. Theoretical microfluidics. *Oxford University Press*, 2008.

[25] N.-T. Nguyen and S. T. Wereley. Fundamentals and applications of microfluidics (2nd ed). *Artech House, London*, 2006.

[26] M. Gad el Hak. The mems handbook (2nd ed). *CRC Press, New York*, 2006.

[27] D. Drikakis and W. Rider. High-resolution methods for incompressible and low-speed flows. *Springer-Verlag, Berlin*, 2005.

[28] R. P. Feynman. There's plenty of room at the bottom: An invitation to enter a new field of physics. *Engineering and Science*, 23:22–36, 1960.

[29] R. P. Feynman. There's plenty of room at the bottom. *Journal of Microelectromechanical Systems*, 1(1):60–66, 1992.

[30] J. N. Mazumdar. Biofluid mechanics. *World Scientific Publishing*, 1992.

[31] K. Nill. Glossary of biotechnology terms (3rd ed). *CRC Press, New York*, 2002.

[32] M. L. Yarmush, M. Toner, R. Plonsey, and J. D. Bronzino. Biotechnology for biomedical engineers. *CRC Press, New York*, 2003.

[33] J. Moore and G. Zouridakis. Biomedical technology and devices handbook. *CRC Press, New York*, 2004.

[34] B. Engquist, P. Lötstedt, and O. Runborg. Multiscale methods in science and engineering. *Springer-Verlag, Berlin*, 2005.

[35] D. Drikakis and M. Kalweit. Computational modeling of flow and mass transport processes in nanotechnology (chapter 34). *Handbook of Theoretical and Computational Nanotechnology*, 2005.

[36] Challa S. S. R. Kumar, J. Hormes, and C. Leuschner. Nanofabrication towards biomedical applications. *WILEY-VCH Verlag, Weinheim*, 2005.

[37] U. R. Müller and D. V. Nicolau. Microarray technology and its applications. *Springer-Verlag, Berlin*, 2005.

[38] J. D. Enderle, S. M. Blanchard, and J. D. Bronzino. Introduction to biomedical engineering (2nd ed). *Elsevier Academic Press, New York*, 2005.

[39] N. H. Malsch. Biomedical nanotechnology. *CRC Press, New York*, 2005.

[40] K. E. Petersen. Silicon as mechanical material. *Proceedings of the IEEE*, 70(5):420–457, 1982.

[41] M. Akay. Encyclopedia of biomedical engineering. *Wiley, New Jersey*, 2006.

[42] J. G. Webster. Encyclopedia of medical devices and instrumentation. *Wiley, New Jersey*, 1-6, 2006.

[43] J. D. Enderle, D. C. Farden, and D. J. Krause. Basic probability theory for biomedical engineers. *Morgan and Claypool Publishers*, 2006.

[44] J. D. Enderle, D. C. Farden, and D. J. Krause. Intermediate probability theory for biomedical engineers. *Morgan and Claypool Publishers*, 2006.

[45] J. D. Enderle, D. C. Farden, and D. J. Krause. Advanced probability theory for biomedical engineers. *Morgan and Claypool Publishers*, 2006.

[46] M. Ozkan and M. J. Heller. Biomems and biomedical nanotechnology (micro/nano technology for genomics and proteomics biomems). *Springer, New York*, 2, 2006.

[47] R. Bashir and S. Wereley. Biomems and biomedical nanotechnology (biomolecular sensing, processing and analysis). *Springer, New York*, 4, 2006.

[48] W. Wang and S. A. Soper. Bio-mems technologies and applications. *CRC Press, New York*, 2007.

[49] L. Waite and J. Fine. Applied biofluid mechanics. *McGraw-Hill, New York*, 2007.

[50] J. Berthier. Microdrops and digital microfluidics. *William Andrew Inc., Norwich, NY, USA*, 2008.

[51] W. C. Tian and E. Finehout. Microfluidics for biological applications. *Springer, New York*, 2008.

[52] D. R. Peterson and J. D. Bronzino. Biomechanics principles and applications. *CRC Press, New York*, 2008.

[53] N. A. Casson. A flow equation for pigment-oil suspensions of the printing ink type. *Rheology of Disperse Systems. C. C. Mills (Ed.). Pergamon Press, New York*, pages 84–102, 1959.

[54] F. J. Walburn and D. J. Schneck. A constitutive equation for whole human blood. *Biorheology*, 13:201–210, 1976.

[55] D. Quemada. Rheology of concentrated disperse systems iii. general features of the proposed non-newtonian model. comparison with experimental data. *Rheologica Acta*, 17:643–653, 1977.

[56] R. Himeno. Blood flow simulation toward actual application at hospital. *The 5th Asian Computational Fluid Dynamics, Busan, Korea*, pages 27–30, 2003.

[57] L. Grinberg and G. E. Karniadakis. A scalable domain decomposition method for ultra-parallel arterial flow simulations. *Communications in Computational Physics*, 4(5):1151–1169, 2008.

[58] L. Grinberg, T. Anor, J. R. Madsen, A. Yakhot, and G. E. Karniadakis. Large-scale simulation of the human arterial tree. *Clinical and Experimental Pharmacology and Physiology*, pages 1–10, 2008.

[59] S. J. Sherwin, J. Peiró, O. Shah, G.-S. Karamanos, and D. J. Doorly. Computational haemodynamics - geometry and non-newtonian modelling using spectral-hp element methods. *Comput Visual Sci*, 3:77–83, 2000.

[60] P. Neofytou and S. Tsangaris. Computational haemodynamics and the effects of blood rheological models on the flow through an arterial stenosis. *European Congress on Computational Methods in Applied Sciences and Engineering*, pages 1–13, 2004.

[61] Md. A. Ikbal, S. Chakravarty, Kelvin K.L. Wongb, J. Mazumdar, and P.K. Mandal. Unsteady response of non-newtonian blood flow through a stenosed artery in magnetic field. *Journal of Computational and Applied Mathematics*, 230:243–259, 2009.

[62] Y. H. Kim, P. J. VandeVord, and J. S. Lee. Multiphase non-newtonian effects on pulsatile hemodynamics in a coronary artery. *Int. J. Numer. Meth. Fluids*, 58:803–825, 2008.

[63] J. Jung, R. W. Lyczkowski, C. B. Panchal, and A. Hassanein. Multiphase hemodynamic simulation on pulsatile flow in a coronary artery. *Journal of Biomechanics*, 39:2064–2073, 2006.

[64] J.R. Buchanan, C. Kleinstreuer, and J. K. Comer. Rheological effects on pulsatile hemodynamics in a stenosed tube. *Computers and Fluids*, 29:695–724, 2001.

[65] M. Ohta, S. G. Wetzel, P. Dantan, C. Bachelet, K. O. Lovblad, H. Yilmaz, P. Flaud, and D. A. Rüfenacht. Rheological changes after stenting of a cerebral aneurysm: A finite element modeling approach. *CardioVascular and Interventional Radiology*, 28:768–772, 2005.

[66] H. A. Gonzalez and N. O. Moraga. On predicting unsteady non-newtonian blood flow. *Applied Mathematics and Computation*, 170:909–923, 2005.

[67] V. Franke, J. Peiró, S. Sherwin, K. Parker, Wee Ling, and N. M. Fisk. Computational modelling of 1d blood flow and its applications. *ESAIM: Proceedings, November 2002*, 12:48–54, 2002.

[68] S. J. Sherwin, V. Franke, J. Peiró, and K. Parker. One-dimensional modelling of a vascular network in space-time variables. *Kluwer Academic Publishers*, pages 1–42, 2003.

[69] L. Bitsch. Blood flow in microchannels. *Department of Micro- and Nanotechnology, Technical University of Denmark, M.Sc. thesis*, 2002.

[70] G. H. Tang, X. F. Li, Y. L. He, and W. Q. Tao. Electroosmotic flow of non-newtonian fluid in microchannels. *Journal of Non-Newtonian Fluid Mechanics*, 157:133–137, 2009.

[71] S. Das and S. Chakraborty. Analytical solutions for velocity temperature and concentration distribution in electroosmotic microchannel flows of a non-newtonian bio-fluid. *Analytica Chimica Acta*, 559:15–14, 2006.

[72] A. Fortin, D. Coté, and P. A. Tanguy. On the imposition of friction boundary conditions for the numerical simulation of bingham fluid flows. *Computer Methods in Applied Mechanics and Engineering*, 88:97–109, 1991.

[73] K. G. Kornev and A. V. Neimark. Modeling of spontaneous penetration of viscoelastic fluids and biofluids into capillaries. *Journal of Colloid and Interface Science*, 262:253–262, 2003.

[74] Y. Xiao, F. Yang, and R. Pitchumani. A generalized analysis of capillary flows in channels. *Journal of Colloid and Interface Science*, 298:880–888, 2006.

[75] S. Chakraborty and D. Paul. Microchannel flow control through a combined electromagnetohydrodynamic transport. *J. Phys. D: Appl. Phys.*, 39:5364–5371, 2006.

[76] S. Das, T. Das, and S. Chakraborty. Analytical solutions for the rate of dna hybridization in a microchannel. *Sensors and Actuators*, 114:957–963, 2006.

[77] S. Das, T. Das, and S. Chakraborty. Modeling of coupled momentum heat and solute transport during dna hybridization in a microchannel. *Microfluid Nanofluid*, 2:37–49, 2006.

[78] E. Shapiro, D. Drikakis, J. Gargiuli, and P. Vadgama. Interface capturing in dual-flow microfluidics. *Journal of Computational and Theoretical Nanoscience*, 4(4):802–806, 2007.

[79] J. Gargiuli, E. Shapiro, H. Gulhane, G. Nair, D. Drikakis, and P. Vadgama. Microfluidic systems for in situ formation of nylon 6,6 membranes. *Journal of Membrane Science*, 282:257–265, 2006.

[80] S. Chakraborty. Electroosmotically driven capillary transport of typical non-newtonian biofluids in rectangular microchannels. *Analytica Chimica Acta*, 605:175–184, 2007.

[81] S. Chakraborty and A. K. Srivastava. Generalized model for time periodic electroosmotic flows with overlapping electrical double layers. *Langmuir*, 23:12421–12428, 2007.

[82] D. Paul and S. Chakraborty. Wall effects in microchannel-based macromolecular separation under electromagnetohydrodynamic influences. *Journal OF Applied Physics*, 102(074921):1–10, 2007.

[83] B. H. Schneider. Biosensor and bioelectrocatalysis studies of enzymes immobilized on graphite electrode materials. *Cranfield University of Technology, Biotechnology Centre, Ph.D. thesis*, 1987.

[84] B. R. Eggins. Chemical sensors and biosensors. *Wiley, San Francisco*, 2002.

[85] J. Y. Wong and J. D. Bronzino. Biomaterials. *CRC Press, New York*, 2007.

[86] M. Reza Mozafari. Nanomaterials and nanosystems for biomedical applications. *Springer, New York*, 2007.

[87] Y. Takeuchi, Y. Iwasa, and K. Sato. Mathematics for life sciences and medicine. *Springer-Verlag, Berlin*, 2007.

[88] M. Zourob, S. Elwary, and A. Turner. Principles of bacterial detection: Biosensors, recognition, receptors and microsystems. *Springer, New York*, 2008.

[89] M. J. Jensen. Bubbles in microchannels. *Department of Micro- and Nanotechnology, Technical University of Denmark, M.Sc. thesis*, 2002.

[90] F. R. Hansen. Dispersion in electrokinetically and pressure driven microflows. *Department of Micro- and Nanotechnology, Technical University of Denmark, M.Sc. thesis*, 2002.

[91] A. Brask. Principles of electroosmotic pumps. *Department of Micro- and Nanotechnology, Technical University of Denmark, M.Sc. thesis*, 2003.

[92] G. Goranovic. Electrohydrodynamic aspects of two-fluid microfluidic systems: Theory and simulation. *Department of Micro- and Nanotechnology, Technical University of Denmark, Ph.D. thesis*, 2003.

[93] L. H. Olesen. Cfd in microfluidic systems. *Department of Micro- and Nanotechnology, Technical University of Denmark, M.Sc. thesis*, 2003.

[94] L. Belmon. Electrohydrodynamics of the asymmetric electrode array micropump. *Department of Micro- and Nanotechnology, Technical University of Denmark, M.Sc. thesis*, 2004.

[95] M. Heller. Dynamics of finite-sized particles in microfluidic systems. *Department of Micro- and Nanotechnology, Technical University of Denmark, M.Sc. thesis*, 2005.

[96] M. J. Jensen. Numerical simulations of interface dynamics in microfluidics. *Department of Micro- and Nanotechnology, Technical University of Denmark, Ph.D. thesis*, 2005.

[97] Z. Xueyu. Brownian dynamics simulation of polymer beheaviors in microfluidic systems. *Department of Micro- and Nanotechnology, Technical University of Denmark, M.Sc. thesis*, 2005.

[98] A. Brask. Electroosmotic micropumps. *Department of Micro- and Nanotechnology, Technical University of Denmark, Ph.D. thesis*, 2005.

[99] M. M. Gregersen. Ac asymmetric electrode micropumps. *Department of Micro- and Nanotechnology, Technical University of Denmark, M.Sc. thesis*, 2005.

[100] C. I. Mikkelsen. Magnetic separation and hydrodynamic interactions in microfluidic systems. *Department of Micro- and Nanotechnology, Technical University of Denmark, Ph.D. thesis*, 2005.

[101] L. Bitsch. Critical components in microfluidic systems for drug delivery: Energy consumption in safe turning microvalves. *Department of Micro- and Nanotechnology, Technical University of Denmark, Ph.D. thesis*, 2006.

[102] L. H. Olesen. Ac electrokinetic micropumps. *Department of Micro- and Nanotechnology, Technical University of Denmark, Ph.D. thesis*, 2006.

[103] T. E. Hansen. Flow in micro porous silicon carbide. *Department of Micro- and Nanotechnology, Technical University of Denmark, M.Sc. thesis*, 2007.

[104] M. Heller. Numerical study of free surfaces and particle sorting in microfluidic systems. *Department of Micro- and Nanotechnology, Technical University of Denmark, Ph.D. thesis*, 2008.

[105] M. B. Andersen. Theoretical aspects of nonlinear electrokinetic phenomena in microfluidics. *Department of Micro- and Nanotechnology, Technical University of Denmark, M.Sc. thesis*, 2009.

[106] M. M. Gregersen. Electrokinetics and catalysis in microfluidic systems. *Department of Micro- and Nanotechnology, Technical University of Denmark, Ph.D. thesis*, 2009.

[107] D. Mantzalis, K. Karantonis, N. Asproulis, L. Könözsy, and D. Drikakis. Computational modelling of aqueous environments in micro and nanochannels. *Book of Detection of Pathogens in Water Using Micro and Nano-Technology, Edited by G. Zuccheri and N. Asproulis, IWA Publishing, London, New York*, pages 135–161, 2012.

[108] R. Temam. Sur l'approximation de la solution des equations de navier-stokes par la methode des pas fractionnaires (i). *Arch. Rat. Mech. Anal.*, 32:377–385, 1969.

[109] O. A. Ladyzhenskaya. Mathematical problems in the dynamics of a viscous incompressible flow. *Gordon and Breach, New York*, 1963.

[110] J. Kim and P. Moin. Application of a fractional-step method to incompressible navier-stokes equations. *Journal of Computational Physics*, 59:308–323, 1985.

[111] A. Eberle. Characteristic flux averaging approach to the solution of euler's equation. *VKI Lecture Series, Computational FLuid Dynamics 1987-04*, 1987.

[112] D. Drikakis, P. A. Govatsos, and D. E. Papatonis. A characteristic-based method for incompressible flows. *International Journal for Numerical Methods in Fluids*, 19:667–685, 1994.

[113] E. Turkel. Preconditioned methods for solving the incompressible and low speed compressible equations. *Journal of Computational Physics*, 72:277–298, 1987.

[114] J. B. Bell, P. Colella, and J. A. Trangenstein. Higher order godunov methods for general systems of hyperbolic conservation laws. *Journal of Computational Physics*, 82:362–397, 1989.

[115] J. B. Bell, P. Colella, and H. M. Glaz. A second-order projection method for the incompressible navier-stokes equations. *Journal of Computational Physics*, 85:257–283, 1989.

[116] P. Colella. Multidimensional upwind methods for hyperbolic conservation laws. *Journal of Computational Physics*, 87:171–200, 1990.

[117] G. E. Karniadakis, M. Israeli, and S. A. Orszag. High-order splitting methods for the incompressible navier-stokes equations. *Journal of Computational Physics*, 97:414–443, 1991.

[118] J. B. Bell and D. L. Marcus. A second-order projection method for variable-density flows. *Journal of Computational Physics*, 101:334–348, 1992.

[119] J. B. Perot. An analysis of the fractional step method. *Journal of Computational Physics*, 108:51–58, 1993.

[120] D. Drikakis. A parallel multiblock characteristic-based method for three-dimensional incompressible flows. *Advances in Engineering Software*, 26:111–119, 1996.

[121] Ann S. Almgren, John B. Bell, Phillip Colella, Louis H. Howell, and Michael L. Welcome. A conservative adaptive projection method for the variable density incompressible navier-stokes equations. *Journal of Computational Physics*, 142:1–46, 1998.

[122] E. Turkel. Preconditioning techniques in computational fluid dynamics. *Annu. Rev. Fluid Mech.*, 31:385–416, 1999.

[123] S. Patel and D. Drikakis. Effects of preconditioning on the accuracy and efficiency of incompressible flows. *International Journal for Numerical Methods in Fluids*, 47:963–970, 2005.

[124] H. S. Tang and F. Sotiropoulos. Fractional step artificial compressibility schemes for the unsteady incompressible navier-stokes equations. *Computers and Fluids*, 36:974–986, 2007.

[125] K. Zamzamian and S. E. Razavi. Multidimensional upwinding for incompressible flows based on characteristics. *Journal of Computational Physics*, 227:8699–8713, 2008.

[126] T. J. Chung. Computational fluid dynamics. *Cambridge University Press, Cambridge*, 2002.

[127] J. A. Stratton. Electromagnetic theory. *McGraw Hill, New York*, 1941.

[128] R. B. Pember, L. H. Howell, J. B. Bell, P. Colella, W. Y. Crutchfield, W. A. Fiveland, and J. P. Jessee. An adaptive projection method for unsteady low-mach number combustion. *Combustion Science and Technology*, 140:123–168, 1998.

[129] J. O. Wilkes. The finite difference computation of natural convection in an enclosed cavity. *PhD Thesis, University of Michigan, Ann Arbor, Michigan*, 1963.

[130] K. E. Torrance. Comparison of finite-difference computations of natural convection. *Journal of Research of National Bureau of Standards*, 72B:281–301, 1968.

[131] K. E. Torrance and J. A. Rockett. Numerical study of natural convection in an enclosure with localized heating from below-creeping flow to the oneset of laminar instability. *Journal of Fluid Mechanics*, 36:33–54, 1969.

[132] R. M. Kopecky and K. E. Torrance. Initiation and structure of axisymmetric eddies in a rotating stream. *Computers and Fluids*, 1:289–300, 1973.

[133] R. D. Raithby and K. E. Torrance. Upstream-weighted differencing schemes and their application to elliptic problems involving fluid flow. *Computers and Fluids*, 2:191–206, 1974.

[134] Chuen-Yen Chow. An introduction to computational fluid mechanics. *Seminole Publishing Company, Boulder, Colorado*, 1979.

[135] M. Griebel, T. Dornseifer, and T. Neunhoeffer. Numerical simulation in fluid dynamics. *Society for Industrial and Applied Mathematics (SIAM)*, 1998.

[136] Richard Barrett, Michael Berry, Tony F. Chan, James Demmel, June M. Donato, Jack Dongarra, Victor Eijkhout, Roldan Pozo, Charles Romine, and Henk Van der Vorst. Templates for the solution of linear systems: Building blocks for iterative methods, 2nd edition. *SIAM, Philadelphia, PA, http://www.netlib.org/templates/Templates.html*, 1994.

[137] M. F. Tome and S. McKee. Gensmac - a computational marker and cell method for free surface flows in general domains. *Journal of Computational Physics*, 110:171–186, 1994.

[138] P. Roache. Computational fluid dynamics. *Albuquerque: Hermosa*, 1976.

[139] S. V. Patankar and D. B. Spalding. A calculation procedure for heat mass and momentum transfer in three-dimensional parabolic flows. *Int. J. Heat and Mass Transfer*, 15:1787–1806, 1972.

[140] B. P. Leonard. A stable and accurate convective modelling procedure based on quadratic upstream interpolation. *Computer Methods in Applied Mechanics and Engineering*, 19:59–98, 1979.

[141] S. V. Patankar. Numerical hear transfer and fluid flow. *Hemisphere Publishing Corporation, Taylor and Francis Group, New York*, 1980.

[142] J. P. Van Doormaal and G. D. Raithby. Enhancements of the simple method for predicting incompressible fluid flows. *Numerical Heat Transfer*, 7:147–163, 1984.

[143] R. I. Issa. Solution of the implicitly discretised fluid flow equations by operator-splitting. *Journal of Computational Physics*, 62:40–65, 1985.

[144] F. H. Harlow and J. E. Welch. Numerical calculation of time-dependent incompressible flow of fluid with free surfaces. *Physics of Fluids*, 8(12):2182–2189, 1965.

[145] M. Peric, R. Kessler, and G. Scheuerer. Comparison of finite-volume numerical method with staggered and collocated grids. *Computers and Fluids*, 16(4):389–403, 1988.

[146] B. J. Daly and W. E. Pracht. Numerical study of density-current surges. *Physics of Fluids*, 11(1):15–30, 1968.

[147] A. A. Amsden and F. H. Harlow. A simplified mac technique for incompressible fluid flow calculations. *Journal of Computational Physics*, 6:322–325, 1970.

[148] B. D. Nichols and C. W. Hirt. Improved free surface boundary conditions for numerical incompressible-flow calculations. *Journal of Computational Physics*, 8:434–448, 1971.

[149] J. A. Viecelli. A computing method for incompressible flows bounded by moving walls. *Journal of Computational Physics*, 8:119–143, 1971.

[150] C. W. Hirt and J. L. Cook. Calculating three-dimensional flows around structures and over rough terrain. *Journal of Computational Physics*, 10:324–340, 1972.

[151] H. Miyata, S. Nishimura, and A. Masuko. Finite difference simulation of nonlinear waves generated by ships of arbitrary three-dimensional configuration. *Journal of Computational Physics*, 60:391–436, 1985.

[152] H. Miyata. Finite-difference simulation of breaking waves. *Journal of Computational Physics*, 65:179–214, 1986.

[153] C. W. Hirt and B. D. Nichols. Volume of fluid (vof) method for the dynamics of free boundaries. *Journal of Computational Physics*, 39:201–225, 1981.

[154] B. Lafaurie, C. Nardone, R. Scardovelli, and G. Zanetti. Modelling merging and fragmentation in multiphase flows with surfer. *Journal of Computational Physics*, 113:134–147, 1994.

[155] M. Vinokur. Conservation equations of gas dynamics in curvilinear coordinate systems. *Journal of Computational Physics*, 14:105–125, 1974.

[156] H. Viviand. Conservative forms of gas dynamic equations. *Rech. Aerosp.*, 1971-1:65–68, 1974.

[157] D. Trebotich, P. Colella, and G. H. Miller. A stable and convergent scheme for viscoelastic flow in contraction channels. *Journal of Computational Physics*, 205:315–342, 2005.

[158] T.C. Papanastasiou. Flow of materials with yield. *J. Rheol.*, 31:385, 1987.

[159] S. E. Charm, W. McComis, and G. Kurland. Rheology and structure of blood suspension. *J. Appl. Physiol.*, 19:127, 1964.

[160] S. Charm and G. Kurland. 1965. 206:617, Viscometry of Human Blood for Shear Rates of 0-100,000 s-1.

[161] P. Nithiarasu. An efficient artificial compressibility (ac) scheme based on the characteristic based split (cbs) method for incompressible flows. *Int. J. Numer. Meth. Engng.*, 56:1815–1845, 2003.

[162] N. Massarotti, F. Arpino, R. W. Lewis, and P. Nithiarasu. Explicit and semi-implicit cbs procedures for incompressible viscous flows. *Int. J. Numer. Meth. Engng.*, 66:1618–1640, 2006.

[163] R. Courant and D. Hilbert. Methods of mathematical physics. *John Wiley and Sons Inc., New York*, 1991.

[164] G.-S. Jiang and C.-W. Shu. Efficient implementation of weighted eno schemes. *Journal of Computational Physics*, 126:202–228, 1996.

[165] C.-W. Shu. Essentially non-oscillatory and weighted essentially non-oscillatory schemes for hyperbolic conservation laws. *NASA/CR-97-206253, ICASE Report No. 97-65*, 1997.

[166] D. S. Balsara and C.-W. Shu. Monotonicity preserving weighted essentially non-oscillatory schemes with increasingly high order of accuracy. *Journal of Computational Physics*, 160:405–452, 2000.

[167] C.-W. Shu and S. Osher. Efficient implementation of essentially non-oscillatory shock-capturing schemes. *Journal of Computational Physics*, 77:439–471, 1988.

[168] A. Quarteroni, R. Sacco, and F. Saleri. Numerical mathematics. *Springer-Verlag, New York*, 2000.

[169] G. E. Karniadakis and S. Sherwin. Spectral/hp element methods for cfd (2nd ed). *Oxford University Press*, 2005.

[170] J.-L. Guermond, C. Migeon, G. Pineau, and L. Quartapelle. Start-up flows in a three-dimensional rectangular driven cavity of aspect ratio 1:1:2 at re = 1000. *Journal of Fluid Mechanics*, 450:169–199, 2002.

[171] A. Brandt. A multilevel adaptive solutions of boundary value problems. *Math. Comput.*, 31:333, 1977.

[172] S. Kotake, K. Hijikata, and T. Fusegi. Numerical simulations of heat transfer and fluid flow on a personal computer. *Transport Processes in Engineering, Elsevier, London*, 3, 1993.

[173] X. Y. Chen, K. C. Toh, J. C. Chai, and C. Yang. Developing pressure-driven liquid flow in microchannels under the electrokinetic effect. *International Journal of Engineering Science*, 42:609–622, 2004.

[174] S. Chakraborty. Augmentation of peristaltic microflows through electroosmotic mechanisms. *J. Phys. D: Appl. Phys.*, 39:5356–5363, 2006.

[175] P. J. Roache. Perspective: A method for uniform reporting of grid refinement studies. *ASME Journal of Fluids Engineering*, 116:405–413, 1994.

[176] W. Y. Soh and J. W. Goodrich. Unsteady solution of incompressible navier-stokes equations. *Journal of Computational Physics*, 79:113–134, 1988.

[177] E. Leriche, S. Gavrilakis, and M. O. Deville. A spectral direct simulation method for a 3d inhomogeneous domain. *24th Workshop Proceedings, Speedup Journal*, 12(2):17–21, 1998.

[178] E. Leriche. Direct numerical simulation in a lid-driven cubical cavity at high reynolds number by a chebyshev spectral method. *SIAM J. Sci. Comput.*, 27(1-3):335–345, 2006.

[179] F. F. Grinstein, L. G. Margolin, and W. J. Rider. Implicit large eddy simulation: computing turbulent fluid dynamics. *Cambridge University Press*, 2007.

[180] R. F. Ismagilov, A. D. Stroock, P. J. A. Kenis, G. Whitesides, and H. A. Stone. Experimental and theoretical scaling laws for transverse diffusive broadening in two phase laminar flows in microchannels. *Appl. Phys. Lett.*, 76(17):2376–2378, 2000.

[181] H. F. P. Purday. An introduction to the mechanics of viscous flow. *Dover, New York*, 1949.

[182] N. M. Natarajan and S. M. Lakshmanan. Laminar flow in rectangular ducts: Prediction of velocity profiles and friction factor. *Indian J. Technol.*, 10:435–438, 1972.

[183] Y. Haik, J. C. Chen, and V. M. Pai. Development of bio-magnetic fluid dynamics. *Proceedings of the IX International Symposium on Transport Properties in Thermal Fluids Engineering, Singapore, Pacific Center of Thermal Fluid Engineering, S. H. Winoto, Y. T. Chew, N. E. Wijeysundera (eds.), Hawaii, USA, June 25-28*, pages 121–126, 1996.

[184] Y. Haik, V. Pai, and C. J. Chen. Development of magnetic device for cell separation. 194:254–261, 1999.

[185] Y. Haik, V. Pai, and C. J. Chen. Biomagnetic fluid dynamics. *Fluid Dynamics at Interfaces, W. Shyy, R. Narayanan (eds.), Cambridge University Press, London*, pages 439–452, 1999.

[186] R. E. Rosensweig. Ferrohydrodynamics. *Cambridge University Press*, 1985.

[187] B. Berkovski and V. Bashtovoy. Magnetic fluids and applications handbook. *Begell House Inc., New York*, 1996.

[188] V. G. Bashtovoy, B. M. Berkovsky, and A. N. Vislovich. Introduction to thermodynamics of magnetic fluids. *Hemisphere Publishing co., Springer-Verlag, New York*, 1998.

[189] V. E. Fertman. Magnetic fluids guidebook: Properties and applications. *Hemisphere Publishing co., New York*, 1990.

[190] E. Blums, A. Cebers, and M. M. Maiorov. Magnetic fluids. *Walter de Gruyter, Berlin*, 1997.

[191] R. A. Frewer. The electrical conductivity of flowing blood. *Biomed. Eng.*, 9:552–554, 1974.

[192] S. Gabriel, R. W. Lau, and C. Gabriel. The dielectric properties of biological tissues: Iii. parametric models for the dielectric spectrum of tissues. *Phys. Medicine Biol.*, 41:2271–2293, 1996.

[193] Pietro Poesio and Gijs Ooms. Influence of high-frequency acoustic waves on the flow of a liquid through porous material. *Jacques M. Huyghe et al. (eds), IUTAM Proceedings on Physicochemical and Electromechanical Interactions in Porous Media, Springer, Printed in the Netherlands*, pages 61–66, 2005.

[194] J. M. Lighthill. On sound generated aerodynamically, i generally theory. *Proc. R. Soc.*, 211:564–587, 1952.

[195] A. P. Dowling and J. E. Ffowcs Williams. Sound and sources of sound. *Ellis Horwood Limited, John Wiley and Sons, New York*, 1983.

[196] María-Isabel Rocha-Gaso, Carmen March-Iborra, Ángel Montoya-Baides, and Antonio Arnau-Vives. Surface generated acoustic wave biosensors for the detection of pathogens: A review. *Sensors*, 9:5740–5769, 2009.

[197] D. S. Ballantine, R. M. White, S. J. Martin, A. J. Ricco, G. C. Frye, E. T. Zellers, and H. Wohltjen. Acoustic wave sensors, theory, design, and physico-chemical applications. *Academic Press, San Diego*, 1997.

[198] J. C. Andle, J. T. Weaver, J. F. Vetelino, and D. J. McAllister. Selective acoustic plate mode dna sensor. *Sensors and Actuators B*, 24:129–133, 1995.

[199] S. J. Ippolito, K. Kalantar-Zadeh, D. A. Powell, and W. Wlodarski. A 3-dimensional finite element approach for simulating acoustic wave propagation in layered saw devices. *IEEE Ultrason. Symp.*, pages 303–306, 2003.

[200] A. Abdollahi, A. Jiang, and S. A. Arabshahi. Evaluation on mass sensitivity of saw sensors for different piezoelectric materials using finite-element analyisis. *IEEE Trans. Ultrason. Ferroelectr. Freq. Cont.*, 54:2446–2455, 2007.

[201] Yucheng Shi. The modeling of structural-acoustic interaction using coupled fe/be method and control of interior acoustic pressure using piezoelectric actuators. *Faculty of Old Dominion University, Ph.D. thesis*, 1996.

[202] G. M. Lilley. On the noise from jets. *AGARD CP-131*, pages 13.1–13.12, 1974.

[203] Zong-Kang Wang, Georgi Djambazov, Choi-Hong Lai, and Koulis Pericleous. Numerical simulation of flow-induced cavity noise in self-sustained oscillations. *Comput. Visual. Sci.*, 10:123–134, 2007.

[204] R. Kwang-Hua Chu. Effects of slip velocity and surface acoustic wave on the laminar flow stability. *Meccanica*, 42:1–7, 2007.

[205] G. Hetsroni, A. Mosyak, E. Pogrebnyak, and L. P. Yarin. Fluid flow in microchannels. *International Journal of Heat and Mass Transfer*, 48:1982–1998, 2005.